Fall 12-2015

From Dye Sensitized Solar Cells to Organic Field Effect Transistors: A Computational Investigation into the Structural and Electronic Properties of Novel Phthalocyanines

Patrick J. Dwyer
Seton Hall University, patrick.dwyer@student.shu.edu

From Dye Sensitized Solar Cells to Organic Field Effect Transistors: A Computational Investigation into the Structural and Electronic Properties of Novel Phthalocyanines

DISSERTATION

Submitted to the faculty of the Department of Chemistry and Biochemistry

in the School of Arts and Sciences as partial fulfillment of the requirements for the degree of

Doctor of Philosophy.

Seton Hall University
400 South Orange Avenue
South Orange, New Jersey 07079

Patrick J. Dwyer

December 2015

We certify that we have read this dissertation and that in our opinion it is adequate in scientific scope and quality as a dissertation for the degree of Doctor of Philosophy.

APPROVED

11/18/15

Stephen P. Kelty, Ph.D. Date
Research Mentor, Member of Dissertation Committee
Seton Hall University

11/20/15

Wyatt. R. Murphy, Ph.D. Date
Member of Dissertation Committee
Seton Hall University

11/21/15

Sergiu M. Gorun, Ph.D. Date
Member of Dissertation Committee
Seton Hall University

12/7/15

Nicholas H. Snow, Ph.D. Date
Chair, Department of Chemistry and Biochemistry
Seton Hall University

"…the need for at least a cursory understanding

of the theory/computation/modeling is

by no means restricted to practitioners of the art

…To take advantage of readily accessible theoretical tools,

and to understand the results reported by theoretical collaborators (or competitors),

even the wettest of wet chemist can benefit from some familiarity with theoretical chemistry."

Christopher J. Cramer
Essentials of Computational Chemistry (2nd Edition)

Contents

Abstract

Phthalocyanines (Pc) have gained intense research attention in many diverse application areas due to their highly tunable electronic and structural properties through modification of the molecular periphery and metal center. Throughout this work a series of novel perfluoro-isopropyl substituted MPc have been investigated through theoretical methods. First, the synthetic mechanisms of these Pcs will be explored to gain insight into the experimentally observed Pc product distribution. By examining the electronic structure and formation energies of the various Pc precursors, we explain the product distribution as well as propose the formation of additional Pcs, which were not currently believed to form.

The effect of metal center and peripheral modification on the Pc structural and electronic properties is also determined through a systematic investigation of several Pcs with varying degree of peripheral modification as well as several different metal centers. Increased modification of the Pc periphery with strongly electron withdrawing groups lowers the energy of the molecular frontier orbitals; increasing the chemical stability of the Pc. Open d-shell metal centers also introduce several partially occupied states near the top of the Pc valence band, which have electron density localized on the metal center.

The bulky groups on the periphery of the Pc also act to mitigate molecular aggregation. To access the degree of aggregation as a function of peripheral modification, a molecular dynamics forcefield within the CHARMM parameterization model was developed specific to these Pcs. This also allows for the simulation of bulk and thin film properties important to

various application areas. Finally, we propose a completely solid state dye sensitized solar cell (DSSC) design in which these chemically robust modified Pcs are sandwiched between n-TiO_2 and p-NiO, acting as both photosensitizer and electron shuttle. Through analysis of the electronic structure of the Pc|semiconductor systems, the free energy associated with hole injection into the valence band of NiO upon photoexcitation of the sensitizer and electron injection into the conduction band of TiO_2 from the reduced form of the Pc are calculated. Significant molecular orbital coupling between the Pc and semiconductors results in estimated charge transfer lifetimes on the femtosecond time scale on both NiO and TiO_2. Additionally, the calculated excited state lifetimes of the Pc is found to be on the nanoseconds time scale, allowing ample time for charge transfer prior to the spontaneous relaxation of the Pc excited state.

In the absence of a liquid electrolyte solution, the Pc molecule will need to also act as electron shuttle in our cell design. The charge transfer properties within the Marcus-Hush electron transfer theoretical framework are calculated. Results indicate that intermediate modification of the Pc periphery leads to high hole and electron mobilities. This is a promising result for our proposed DSSC design, but also makes these Pcs a viable semiconducting material in other application areas, such as light emitting diodes (LEDs) or organic field effect transistors (OFETs).

Acknowledgments

First and foremost I would like to extend my deepest appreciations to my mentor, Prof. Stephen P. Kelty, for his unconditional support and guidance over the years that has made this work possible. Steve, I will forever cherish the time we have spent together and all you have taught me. I stand proud of the work we have accomplished together and look forward to fruitful collaborations in the future.

I also want to express my appreciation to my fellow colleagues, past and present, in the Kelty research group. I thank Jack Ferguson and Vito Cataldo for their assistance and guidance during the early adventures of this journey; as well as Kelly Raymond and Frank Hung for the current support and knowledge they provide. A special thanks to Rory Vander Valk who has been my right hand man throughout the years. Rory, in addition to being an excellent research collaborator, you have served as a brilliant first line of defense against all of my bad ideas. You have been an essential part of my research, thank you.

I have also greatly benefited from an exceptional working relationship with Prof. Sergiu M. Gorun and a few of the outstanding members of his research team, Andrei Loas and Hemantbhai Patel. I thank all of you for the stimulating debates we have had and the contributions you have made to this work.

I would also like to thank Dr. Cosimo Antonacci. We have had a close relationship since my first days here at SHU. In addition to being a good friend over the years, you have always been an excellent source of wisdom that has helped me in completing this work. Thank you.

Much appreciation is also extended to Porter Scientific Inc., and the U.S. Air Force Research Laboratory (AFRL) for financial support throughout this work (SBIR program Grant Nos. FA8501-12-P-0096 and FA8501-13-C-0024.)

I now need to thank several people outside of the Seton Hall community. Pursuing this degree has been one of the most selfish things have done to date. I have dedicated the majority of my time and thoughts towards this work and, in turn, left many important people waiting in the background. But they have waited patiently and supported me more than ever.

I'll begin with the amazing young lady who somehow finds a way to deal with me on a daily basis, my Samantha Lynn. Your love and support has been the biggest contributor to my success, and it would have been impossible without you by my side. While everybody mentioned previously has helped make me a better chemist, researcher, etc.; you have made me a better man. Additionally, I extend my gratitude to the rest of the Nogueira family. Luis, Paula, Tiffany, and Sunny, you have all welcomed me into the Portuguese circle with open arms. I am thankful for all that you have done and continue to do for me.

My greatest acknowledgment goes to those who made me who I am and supported me not just during this work but all my life, my family. To my siblings, Jason and Colleen; although I am terrible at showing it, there are few people I admire and think about more than the two of you. I look forward to spending more time with you now this long adventure is coming to an end. To my aunt and uncle, Dave and Judy Jones; I am grateful every day for all that you do for me. You have been much more like a second set of parents throughout my life and taught me so much. Thank you for always being there for us and just being who you are. Finally, to the most remarkable person I know, my mother. You are the strongest woman in the world and I could not have done any of this without your endless support, encouragement, and love. You deserve so much more than a simple thank you from me, but that's all I can provide here. Thank you.

List of Tables

List of Tables Cont.

List of Tables Cont.

List of Figures

List of Figures Cont.

List of Figures Cont.

List of Figures Cont.

List of Figures Cont.

List of Figures Cont.

Introduction to Phthalocyanines

Phthalocyanines (Pcs) and their derivatives have attracted extensive research attention for many years. First structurally characterized by Linstead[1-4] in 1934, these materials have been found to have application in many diverse fields. Structurally, Pcs are planar highly aromatic macrocycles made up of four isoindole units (Figure 1). This high degree of conjugation presents a delocalized 18 π-electron arrangement across the carbon and nitrogen atoms.

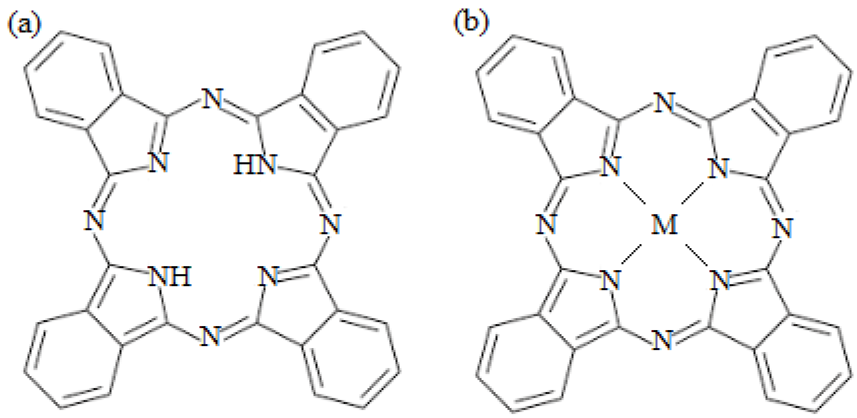

Figure 1. General schematic representing the structure of (a) Phthalocyanine an1d (b) Metallo-phthalocyanine.

As a result of intense absorption centered around 620-700 nm[5], Pcs original application was in the area of textiles and inks as dye materials[6]. In more recent past, research in Pcs has seen a strong resurgence for application in molecular devices including:[7-17] photovoltaics, industrial catalytic systems, electrochromism devices, optical data storage, laser dyes, liquid crystals, chemical sensors, and photodynamic therapy.

The primary driving force for Pc based interest is attributed to their outstanding electrical and photophysical properties, as well as their thermal and chemical stability[18]. Pcs also have extraordinary adaptability. To date, approximately 70 different metal ions and nonmetals have been shown to form coordination complexes with Pc exhibiting a variety of functional properties[19]. Optical and electronic properties can also be tuned by rational design of the symmetry and chemical composition of substituents on the molecular periphery and/or at the axial positions. It has become recognized that chemical modification of the molecular periphery, particularly low symmetry modifications, offers significant opportunity to exploit novel properties[20-21].

One particular modification of Pcs is in eliminating labile C-H bonds and replacing them with more inert C-F bonds[22]. . For electronic device applications, hexadecylfluoro-phthalocyanine ($F_{16}Pc$) been shown to exhibit far greater ambient stability than the parent per-hydro $H_{16}Pc$[23]. Another advantageous property of $F_{16}Pc$ for electronic application is the stacking of the planar molecules through their intrinsic π-π interactions. However, this aggregation is not always desired, as in catalytic applications. The introduction of bulky peripheral substituents is commonly used to prevent the aggregation phenomena.

Throughout this several Pc substitution schemes of different peripheral substituents will be explored. The Pcs of interest include: zinc phthalocyanine (**$H_{16}ZnPc$**); zinc hexadecyl-perfluoro-phthalocyanine (**$F_{16}ZnPc$**); zinc 1,2,4-Tris-(perfluoroisopropyl)-tridecafluoro-phthalocyanine (**$F_{34}ZnPc$**); 1,4,8,11,15,16,17,18,22,23,24,25-dodecylfluoro-2,3,9,10-tetrakisperfluoro(isopropyl) phthalocyanine (**$F_{40}ZnPc$**); 1,2,4,8,9,11-Hexa-(perfluoroisopropyl)-decafluoro-phthalocyanine (**$F_{52}ZnPc$**); 1,4,8,11,15,18,22,23,24,25-decacylfluoro-2,3,9,10,16,17-tetrakisperfluoro(isopropyl) phthalocyanine (**$F_{52a}ZnPc$**); and 1,4,8,11,15,18,22,25-octafluoro-

2,3,9,10,16,17,23,24-octakisperfluoro(isopropyl) phthalocyanine, (**F_{64}ZnPc**). Hereafter, these Pc molecules, shown in Figure 2a-g, will be referred to by the names in the parentheses.

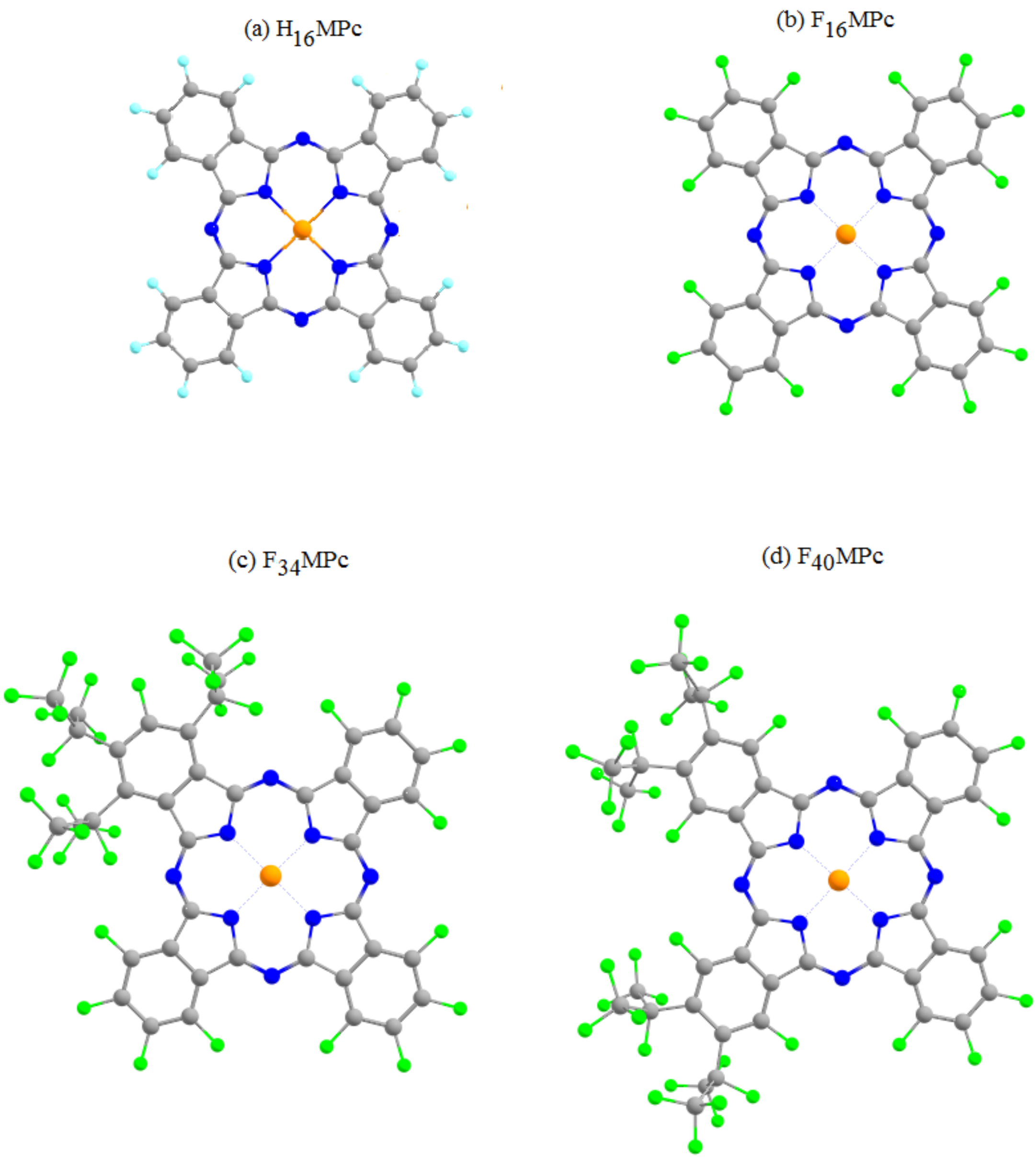

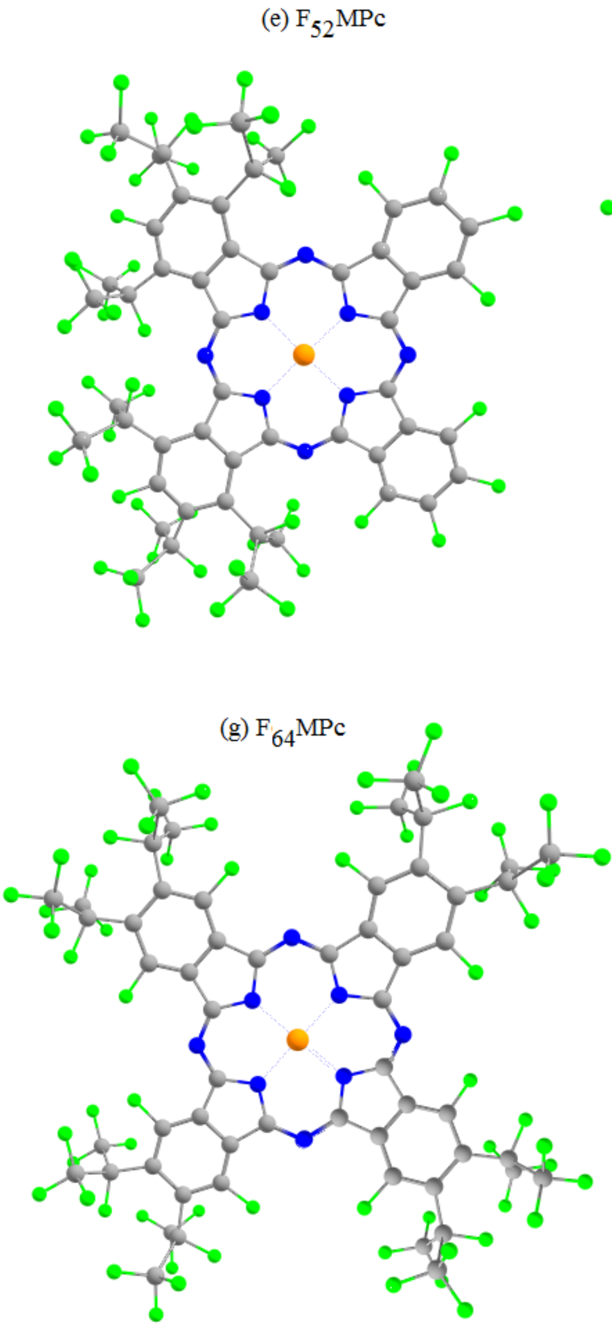

Figure 2. Molecular structure of target Pcs: (a) $H_{16}MPc$, (b) $F_{16}MPc$, (c) $F_{34}MPc$, (d) $F_{40}MPc$, (e) $F_{52}MPc$, (f) $F_{52a}MPc$, and (g) $F_{64}MPc$. Coloring scheme: metal (orange), nitrogen (dark blue), carbon (gray), and fluorine (green).

CHAPTER 1

Theoretical Investigation into the Synthetic Mechanism of F_xZnPc

1.1 Introduction

The synthetic pathway of the fluorinated precursors to form the Pcs of interest is hypothesized as illustrated in Figure 1.1. Four unique Pc precursors: phthalonitrile (***1***); perfluoro-3,4,6-diisopropylphthalonitrile (***3***); perfluoro-4,5-diisopropylphthalonitrile (***4***); and perfluoro-3,6-diisopropylphthalonitrile (***5***) lead to the production of six Pcs of various degree of peripheral fluorination. Precursor ***1*** in combination with precursor ***4*** leads to the formation of F_{16}ZnPc, F_{40}ZnPc, F_{52a}ZnPc, and F_{64}ZnPc. Experimentally, the relative amount of products formed is as follows: F_{64}MPc > F_{52a}MPc >> F_{40}MPc >> F_{16}MPc.[24] While the molecular structure of F_{40}ZnPc allows for both a cis- and trans- isomers; only the cis-F_{40}ZnPc isomer is thought to be formed based on the identified crystal structure.

Pc precursor ***3*** allows for the formation of the highly asymmetric Pcs. Combination of precursors ***1*** and ***3*** leads to the formation of F_{34}ZnPc, F_{52}ZnPc, and F_{16}ZnPc. As with F_{40}ZnPc, F_{52}ZnPc can, in principle, be produced as a mixture of cis- and trans- isomers. Although, to date, only the cis isomer is observed in the crystal structure. If ***1*** is used excess, F_{16}ZnPc is the majority product with minority yield of F_{34}ZnPc and F_{52}ZnPc. Conversely, excess amounts of precursor ***3*** added to the reaction vessel results in equally low yields of F_{52}ZnPc, F_{34}ZnPc, and F_{16}ZnPc products.[24] Surprisingly, precursor ***5*** exhibits no reactivity with itself or in combination with precursor ***1***. [24] This lack of reactivity leads to no Pc products when precursor ***5*** is employed. This is an unanticipated result given the reactivity of precursor ***3*** and ***4*** despite the increased steric hindrance of both precoursors.[24]

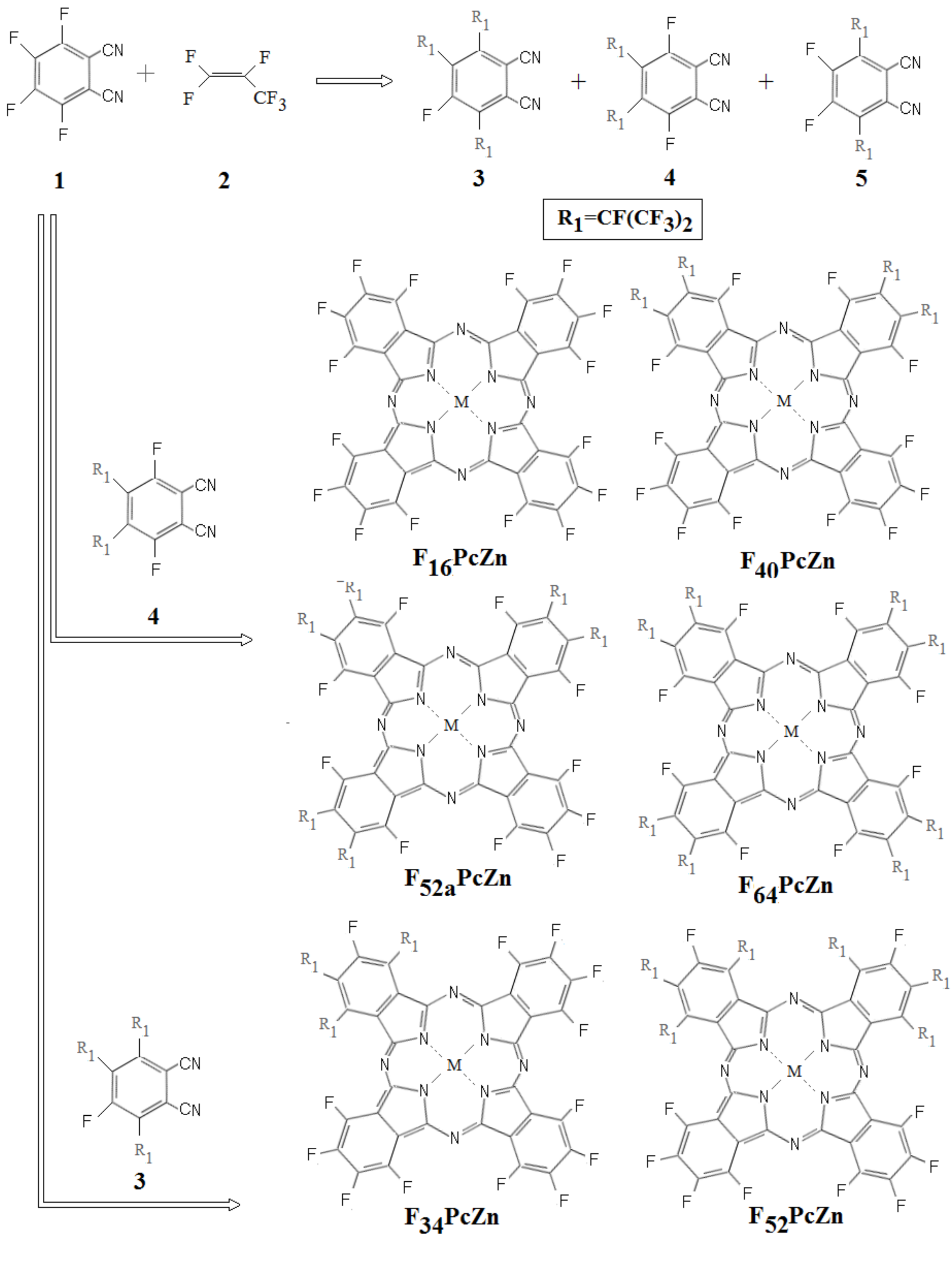

Figure 1.1. Synthetic pathway of all modified perfluoroisopropyl-phthalocyanines.

Based on these experimental findings, computational studies were carried out to further understand these results. Specifically, the kinetic and thermodynamic aspects of the product distributions observed experimentally as well as the possibility of trans-F_{40}ZnPc and trans-F_{52}ZnPc isomers.

1.2 RESULTS

1.2.1 Reactivity of Pc Monomer Precursors

The formation of the Pc macrocycle begins with the intermolecular activation of the precursor to form a zwitterionic monomer species (Figure 1.2).[25] The reduced form of these zwitterionic monomers is also present from a one-electron reduction.

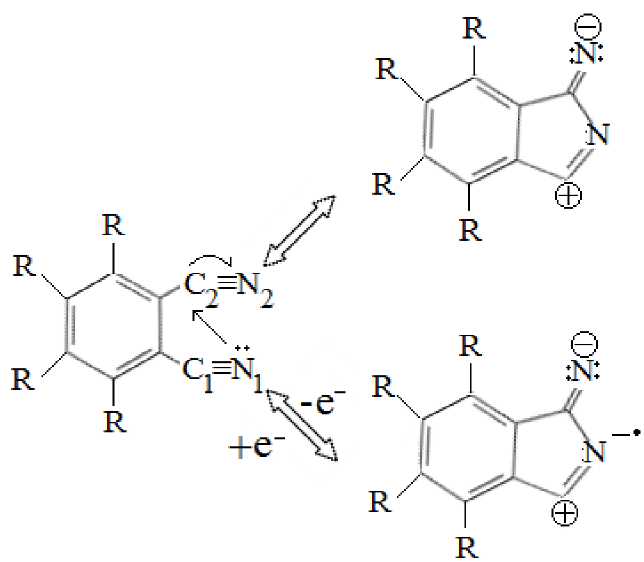

Figure 1.2. Intramolecular activation of monomer precursors.

Analysis of the frontier molecular orbitals (HOMO and LUMO) electron density distribution of the starting precursors (Figure 1.3) reveal that the bulky electron withdrawing –C_3F_7 peripheral ligands affects the electronic distribution required for intermolecular activation. The proposed intermolecular activation requires adequate electron density on the –CN groups in both the HOMO and LUMO states. As seen in Figure 1.3, this requirement is satisfied in both symmetric precursors ***1*** and ***4***. However, precursor ***5*** shows no carbon centered LUMO electron density on either –CN group. This explains its lack of reactivity of ***5*** despite its symmetry and low steric hindrance relative to precursor ***4***. Replacement of a single peripheral fluorine with a –C_3F_7 group (precursor ***3***) restores the reactivity; but the intermolecular activation is forced in one direction unlike the symmetric precursors ***1*** and ***4***.

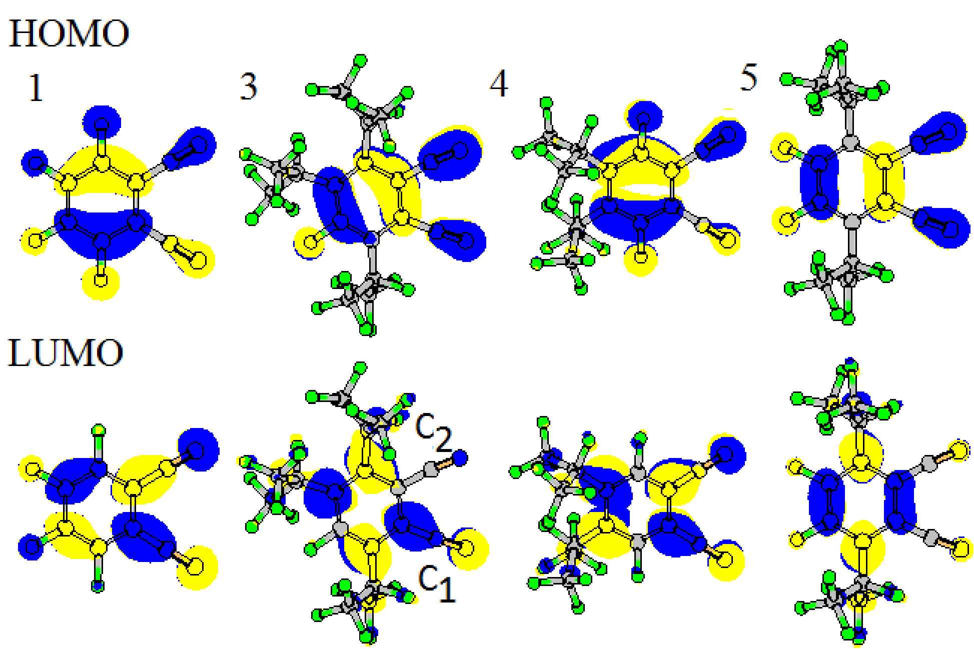

Figure 1.3. Electron density distribution plot of HOMO and LUMO states for precursors ***1***, ***3***, ***4***, and ***5***.

The C_2 position of the –CN group of precursor ***3*** has no LUMO electron density. Therefore, activation can only occur at C_1 at not at C_2. The importance of this directional activation will be discussed in further detail when examining the $F_{34}ZnPc/F_{52}ZnPc$ product distribution in section 1.2.5. Additionally, from an energetic standpoint, formation of the zwitterionic neutral monomer of precursor ***1*** is favored over the zwitterionic monomer of precursor ***3*** and ***4*** by 3.49 kcal/mol and 0.05 kcal/mol, respectively.

1.2.2 Formation of Pc Dimer Intermediates

From the zwitterionic monomer species, formation of the various Pcs proceeds through the formation of zwitterionic dimer intermediates.[26] Subsequently, it is believed that these dimers join together to form the final Pc molecule. As in the zwitterionic monomers, we will first examine the electron density of the zwitterionic monomers in an attempt to provide rational for dimer intermediate formation and, in turn, the overall Pc product distribution. The proposed mechanism for the formation of the neutral dimers is presented in Figure 1.4.

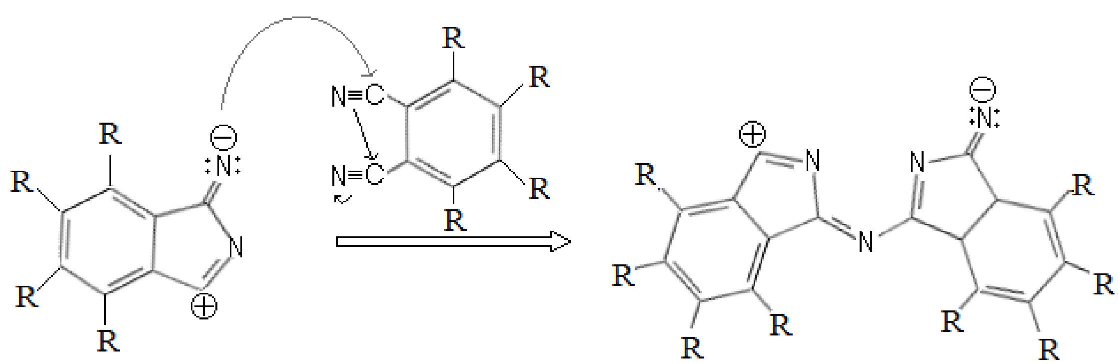

Figure 1.4. Formation of the neutral dimer Pc intermediates.

Localization of HOMO electron density on the attacking nitrogen of the monomer is a prerequisite for dimer formation. Electron density distribution plots for the zwitterionic monomers of precursors ***1***, ***3***, and ***4*** are illustrated in Figure 1.5. For the remainder of the discussion, the zwitterionic monomers of precursors ***1***, ***3***, and ***4*** will be referred to as ***1′***, ***3′***, and ***4′***, respectively.

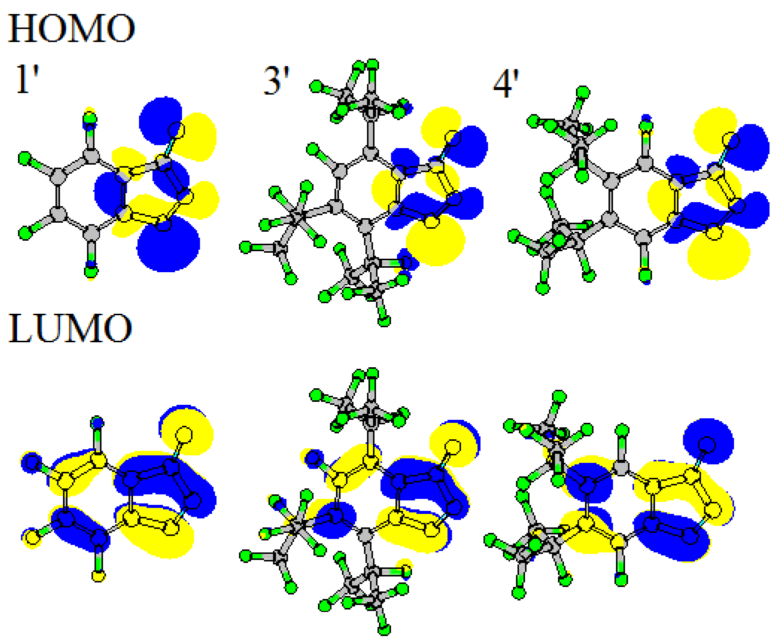

Figure 1.5. Electron density distribution plots of HOMO (top) and LUMO (bottom) of zwitterionic Pc precursors ***1'***, ***3'***, and ***4'***.

There are no significant differences in the HOMO and LUMO state electron density distribution of the zwitterionic monomer species. Therefore, in terms of the distribution of the frontier orbitals, the formation of all dimer intermediates from these monomer species should be possible. To gain a better description on the probability of the dimer construction, the formation energies of each dimer has been calculated. The discussion on each of these dimers is elaborated on in the following sections.

1.2.3 Synthetic Pathway of $F_{16}ZnPc$, $F_{40}ZnPc$, $F_{52a}ZnPc$ and $F_{64}ZnPc$

The synthetic pathway for the production of $F_{16}ZnPc$, $F_{40}ZnPc$, $F_{52a}ZnPc$, and $F_{64}ZnPc$ involves reaction of the symmetric phthalonitrile precursor, ***1***, as well as perfluoro-4,5-diisopropylphthalonitrile precursor, ***4***. The reaction of these two precursors leads to a mixture of the various phthalocyanines. Pcs from ***1*** and ***4*** alone leads to the formation of $F_{16}ZnPc$ and $F_{64}ZnPc$, respectively. While a combination of both precursors leads to the formation of $F_{40}ZnPc$ and $F_{52a}ZnPc$. Experimentally, the relative amount of products formed is as follows: F64ZnPc > F52aZnPc >> F40ZnPc >> F16ZnPc.[24] Additionally, the formation of the trans-$F_{40}ZnPc$ isomer is not believed to occur based on the crystallized structure of $F_{40}ZnPc$ in which only the cis isomer is found. The proposed mechanism showing all possible routes for the production of $F_{16}ZnPc$, $F_{40}ZnPc$, $F_{52a}ZnPc$, and $F_{64}ZnPc$ is presented in Figure 1.6.

Combination of any neutral and doubly reduced dimer pairs generate the various Pc molecules. For example, formation of $F_{64}ZnPc$ would result from the combination of neutral dimer ***4a*** and doubly reduced dimer ***4b***. Additionally, trans-$F_{40}ZnPc$ would be produced by the combination of the neutral dimer ***1c*** and its doubly reduced form ***1c'***. Under the assumption that the formation of the dimer intermediates directly controls the formation of the Pcs, the energy of formation of each intermediate may be used to predict the final Pc product distribution. This section will focus on explaining the product distribution of $F_{16}ZnPc$, $F_{40}ZnPc$, $F_{52a}ZnPc$, and $F_{64}ZnPc$ based on the respective dimer intermediates.

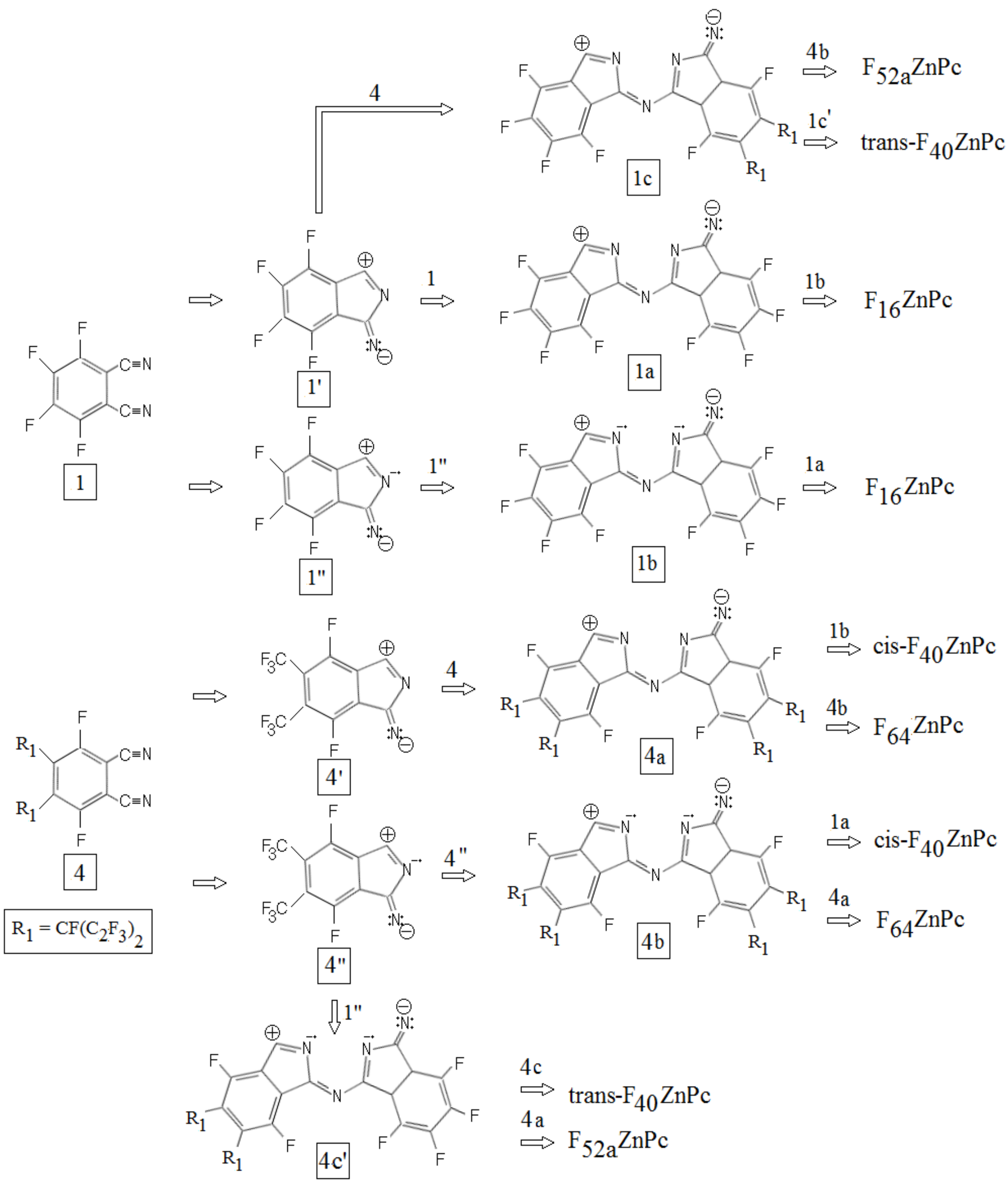

Figure 1.6. Proposed mechanism for the formation of $F_{16}ZnPc$, $F_{40}ZnPc$, $F_{52a}ZnPc$ and $F_{64}ZnPc$.[24]

We will begin our discussion by focusing on the formation of the neutral dimer intermediates ***1a***, ***4a***, ***1c*** and ***4c***; which as previously mentioned make up half of the total Pc macrocycle. While the electron density distribution of the frontier molecular orbitals of monomers ***1′*** and ***4′*** indicate that the formation of all of the dimer intermediates should be possible, differences arise when considering the calculated formation energies for each of the neutral dimer intermediates.

The formation energies of the four neutral dimers are presented in Table 1.1. The dimer formation energies are calculated as:

$$E_{formation} = E_{ij} - \left(E_i + E_j\right) \tag{1.1}$$

where E_{ij} is the energy of the dimer and E_i / E_j represent the energy of the relevant monomers. Based on the formation energy, the most probable neutral dimer is ***4a*** while the least likely dimer to form is ***1a***. Since dimer ***4a*** is thermodynamically favored over the other neutral dimer species, monomer ***4*** will largely be consumed in the formation of dimer ***4a***. Neutral dimers ***1c*** and ***4c***, which are composed from monomers ***1*** and ***4***, will be in direct competition with dimer ***4a*** for monomer precursor ***4***. A Boltzmann distribution (Equation 1.2) between these dimers indicates that ***4a*** is favored 16:1 and 2:1 over ***4c*** and ***1c***, respectively.

Table 1.1. Formation energies of the $F_{16}ZnPc$, $F_{40}ZnPc$, $F_{52a}ZnPc$, and $F_{64}ZnPc$ neutral dimer Pc intermediates.

Dimer	Formation Scheme	Formation Energy (kcal/mol)
1a	***1′*** + ***1***	-13.4722
4a	***4′*** + ***4***	-17.1744
1c	***1′*** + ***4***	-16.6917
4c	***4′*** + ***1***	-15.5456

Additionally, dimer ***1c*** and ***4c*** are also in competition with ***1a*** for monomer precursor ***1***. As already stated dimer ***1a*** is the least likely to form based on the formation energies of the dimers. A Boltzmann distribution between these dimers is calculated as follows:

$$\frac{N_1}{N_2} = e^{-\Delta E / kT} \tag{1.2}$$

where ***k*** is the Boltzmann constant and ***T*** is temperature. Pc dimer ***1c*** is favored 228:1 over ***1a*** while ***4c*** is favored 33:1 over ***1a***. Therefore, compared to the other possible dimers, ***1a*** is expected to form in minimal amounts, if any. In terms of Pc production; as an initial estimation of the product distribution based upon the neutral dimers, the low amounts of the neutral ***1a*** should lead to minimal amounts of $F_{16}ZnPc$ while the abundant ***3a*** should lead to large amounts of $F_{64}ZnPc$. A more detailed prediction of the Pc product distribution may be made once the reduced dimer species have been considered.

In addition to the neutral dimer intermediates, formation of the final Pc product requires a doubly reduced dimer intermediate as well. These doubly reduced dimers are assembled from the reduced zwitterionic monomer precursors, ***1″*** and/or ***4″***. Thus, calculation of the electron affinity

(EA) of ***1′*** and ***4′*** is a logical starting place. The adiabatic electron affinities are calculated from the change in total energy when transitioning from the neutral molecule in its equilibrium geometry, E^0, to the anionic species in its equilibrium geometry, E^-.

$$EA_{ad} = E^0 - E^- \tag{1.3}$$

The calculated adiabatic EA are 41.49 kcal/mol and 72.69 kcal/mol for precursor ***1′*** and ***4′***, respectively. Furthermore, in terms of energy, the reduction of ***4′*** to ***4″*** is 40.0 kcal/mol lower in energy than that of the reduction of ***1′*** to ***1″***. Therefore, precursor ***4*** is much more capable of accommodating the additional electron during the one electron reduction process. This is not an unexpected result given the introduction of the highly electron withdrawing $-C_3F_7$ groups on precursor ***4***.

While it is clear precursor ***4*** has a greater ability to be reduced, the formation energy of each of the possible reduced dimers is calculated (Table 1.2) to further explore these intermediates.

Table 1.2. Formation energies of the F_{16}ZnPc, F_{40}ZnPc, F_{52a}ZnPc, and F_{64}ZnPc reduced Pc dimer intermediates.

Dimer	Formation Scheme	Formation Energy (kcal/mol)
1b	***1″*** + ***1″***	-80.6448
4b	***4″*** + ***4″***	-58.4033
1c’	***1″*** + ***4″***	-16.6917
4c’	***4″*** + ***1″***	-15.5456

The reduced dimer ***1b*** is the lowest in energy and therefore most likely to form. It should however be noted that this low formation energy is the direct result of the reduced monomer ***1″*** being quite unstable compared to that of ***4″***. Therefore, assuming the reduced monomer ***1″*** is formed in relatively low amounts; formation of dimer ***1b*** is likely to be lower than what is indicated in Table 1.2. Putting that assumption aside, for now, the predicted product distribution, based on the reduced dimer formation energy is as follows: ***1b*** > ***4b*** >> ***1c′*** > ***4c′***.

This predicted ordering of the reduced dimers, along with the predicted order of the neutral dimers (***4a*** > ***1c*** > ***4c*** > ***1a***), allows for the prediction of the overall Pc product distribution. Combination of the most likely neutral dimer (***4a***) with the most likely reduced dimer (***1b***) leads to the formation of cis-F_{40}ZnPc as the major product; followed then by the combination of ***4a*** with ***4b*** to produce F_{64}ZnPc. The mixed dimers (***1c*** and ***4c***) along with ***4b*** will lead to substantial amounts of F_{52a}ZnPc. Since ***4a*** is favored over ***1c*** and ***4c***, production of F_{52a}ZnPc will be less than that of F_{64}ZnPc. The mixed neutral dimers may also combine with the reduced form of a mixed dimer (***1c′*** or ***4c′***) to form trans-F_{40}ZnPc. While the trans-F_{40}ZnPc is likely to form in relatively small amounts, the possibility of formation is still probable. This will be debated further is the following section. Finally, the low amounts of the neutral dimer ***1a***, along with the reduced ***1b*** being consumed to produce the other Pcs, F_{16}ZnPc is expected to form is relatively low amounts. Therefore, following the predicted distribution of the dimers in Tables 1.1 and 1.2, the predicted Pc distribution is as follows: cis-F_{40}ZnPc > F_{64}ZnPc > F_{52}ZnPc > trans-F_{40}ZnPc > F_{16}ZnPc. This however does not agree with unpublished experimental findings of F_{64}ZnPc > F_{52a}ZnPc > cis-F_{40}ZnPc > F_{16}ZnPc.

If we return to the assumption that ***1′*** is difficult to reduce compared to ***4′***, the reduced dimer distribution may be more likely to be: ***4b*** > ***1c′*** > ***4c′*** > ***1b***. Under this assumption, the dimers containing monomers of ***4′*** are more likely to form. The final Pc product distribution changes significantly. Now the most likely neutral dimer (***4a***) and most likely reduced dimer (***4b***) will combine to produce F_{64}ZnPc as the major product. Slightly less but sill in large amounts will be the production of F_{52a}ZnPc (***4a*** + ***1c′*** or ***4c′***). The trans- isomer of F_{40}ZnPc, formed by the mixed dimers, is now more favorable than the cis- isomer. F_{16}ZnPc is however still predicted to form is relatively low amount. Under this assumption the predicted product distribution of the Pcs becomes: F_{64}ZnPc > F_{52a}ZnPc > trans-F_{40}ZnPc > cis-F_{40}ZnPc > F_{16}ZnPc. This agrees much better with the experimental findings except for the prediction of a trans-F_{40}ZnPc isomer.

Regardless of the assumption about the reduction capabilities of ***1b***, the lack of formation of an F_{28}ZnPc is unexpected. If the reduced dimer ***1b*** is found in relatively high amounts, it should combine with a mixed neutral ***1c*** or ***4c*** to form significant amounts of F_{28}ZnPc. This however does not occur and no evidence to the existence of F_{28}ZnPc is present in the experimental product distribution.

1.2.4 Isomers of F_{40}ZnPc

As discussed in the previous section, the formation of both cis- and trans- isomer of F_{40}ZnPc should be thermodynamically allowed. DFT calculations preformed on both isomers reveal that the trans- isomer is slightly more energetically favored over the cis- form. The difference in ground state energy of these two geometric isomers is merely 2.274 $\times 10^{-3}$ Ha (0.597

kJ/mol). A Boltzmann distribution of these two states indicates that neither isomer of F_{40}ZnPc is thermodynamically favored; both have essentially equal (1.2:1) probability of formation. The optimized structures of the cis- and trans- isomers of F_{40}ZnPc are presented in Figure 1.7.

Additionally, the cis- and trans- isomers present distinct differences in the electron structure of the molecule. The electron density distribution plot for the HOMO and LUMO states of each isomer is illustrated in Figure 1.8.

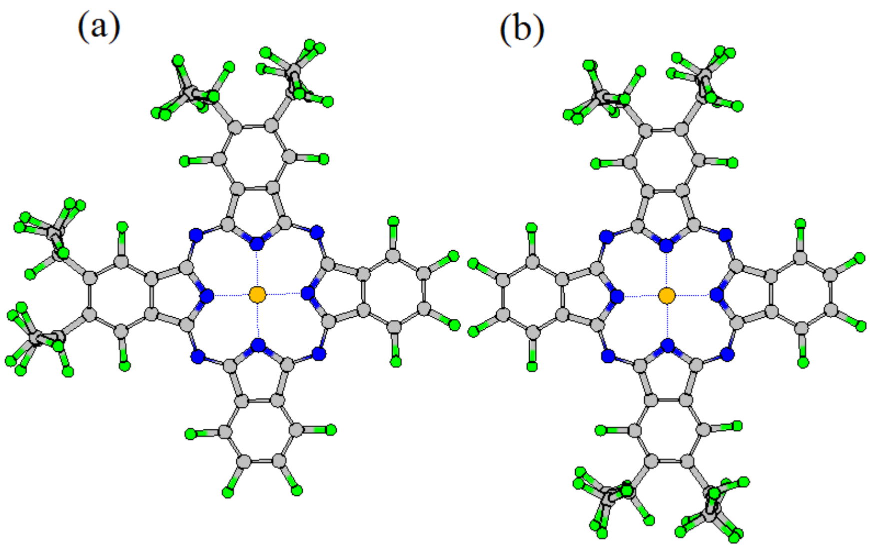

Figure 1.7. Geometry optimized structure of (a) cis-F_{40}ZnPc and (b) trans-F_{40}ZnPc. Color code: green=fluorine, orange=zinc, gray=carbon, blue=nitrogen.

There is no significant difference in the HOMO electron density distribution. However, the first two unoccupied states (LUMO and LUMO+1) for trans-F_{40}ZnPc has an electron distribution that occupies only two of the isoindole units while the distribution on the LUMO and LUMO+1 in cis-F_{40}ZnPc is more delocalized across all four isoindole units. This leads to a significant variation in the calculated energies of the LUMO and LUMO+1 state. These two unoccupied states in the cis- isomer are nearly degenerate with an energy separation of only 0.02 eV. In the trans- isomer there is a significant (0.17 eV) separation in the LUMO and LUMO+1 states. The differences in the unoccupied orbitals results in a unique absorbance spectrum for each isomer. The experimental and TDDFT calculated absorption spectrum for both cis- and tans-F_{40}ZnPc is presented in Figure 1.9. The experimental absorbance spectrum shows two distinct peaks; one at 638 nm and another at 670 nm. It has been proposed that the slightly less intense peak at 638 is caused by aggregation of the cis-F_{40}ZnPc isomer.[24]

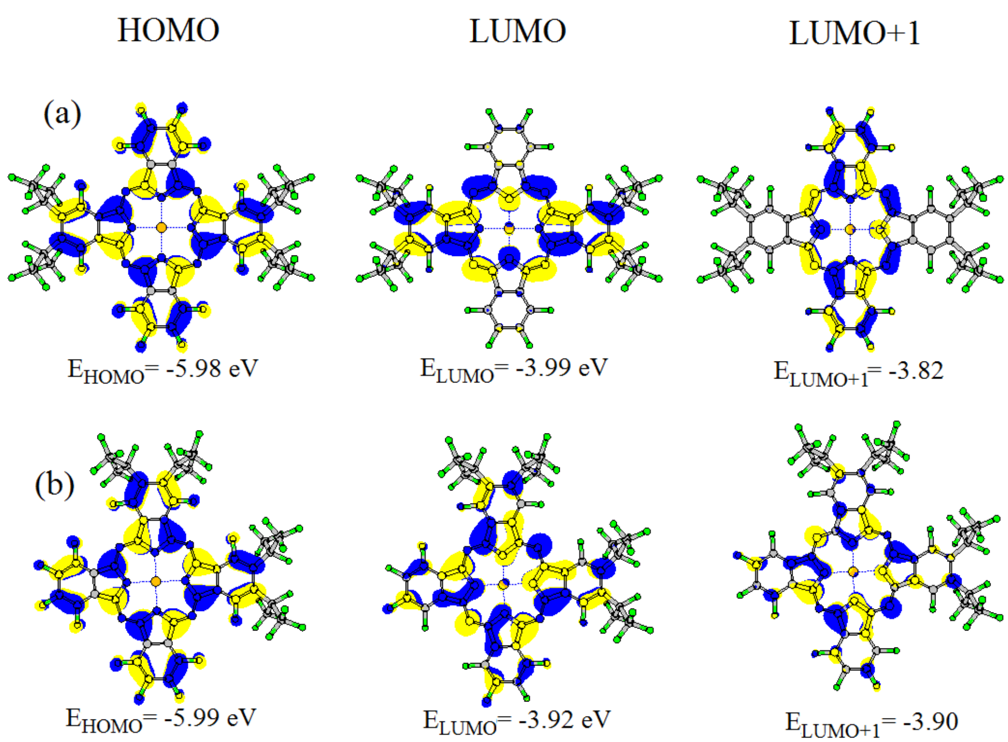

Figure 1.8. Electron density distribution plot of HOMO and LUMO states for (a) trans-F_{40}ZnPc and (b) cis-F_{40}ZnPc.

While aggregation is probable with the cis isomer, since half of the molecular structure is free from the bulky $–C_3F_7$ groups, the calculated absorbance spectrums of both isomers reveal that the two peaks may be caused by the existence of a mixture of cis- and trans- isomers. The calculated spectra take into account ethanol solvent effects, to better mimic the experimental spectrum, and reproduce the experimental absorbance spectra quite well. As seen in Figure 1.9, the calculated spectrums for both isomers are quite different.

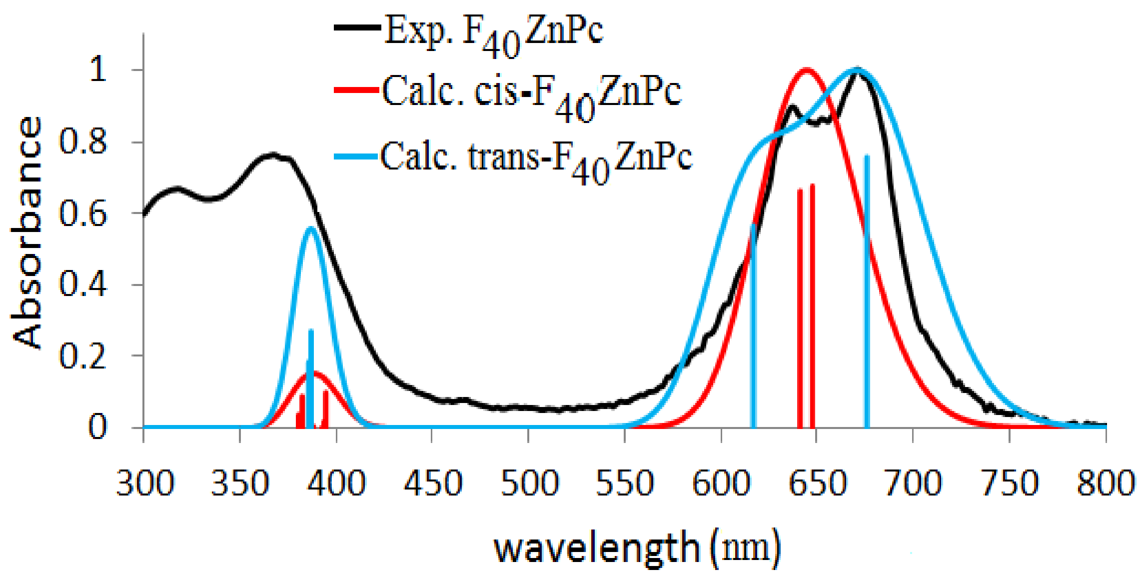

Figure 1.9. Absorbance Spectrum of F_{40}ZnPc; Experimental spectrum (black line), Calculated absorbance spectrum for cis-F_{40}ZnPc (red line), Calculated absorbance spectrum for trans-F_{40}ZnPc (blue line). Calculated cure normalized to 1. Height of vertical lines indicated the oscillator strength of the transitions.

It is noted that the calculated spectra provide transition oscillator strengths rather than absorbance values. The oscillator strength is related to absorbance, in that is describes the probability of the transition. In Figure 1.9, the oscillator strengths are indicated by the vertical lines. The curve for the calculated spectra are generated via a Gaussian fit to the oscillator strengths. The broadening of these curves is artificial and has been normalized and loosely fit to the experimental peaks. The calculated absorbance spectrum for cis-F_{40}ZnPc has two highly probable excitations, both around 650 nm. The first transition, at 648 nm, is an excitation from the HOMO to LUMO of the molecule. The second transition, at 641 nm is an excitation from the HOMO to LUMO+1. These two excitations correlate well with the experimental peak found at 638 nm. For trans-F_{40}ZnPc, there is again two major excitations. The first excitation is found at 675 nm, which is a transition from the HOMO to LUMO. The second excitation is found at 617 nm, which is a transition from HOMO to LUMO+1. The first calculated excitation for the trans isomer agrees well with the experimental peak found at 670 nm. The second calculated excitation also closely resembles the experimental peak found at 638 nm.

Additionally, absorbance spectrum of F_{28}ZnPc (Figure 1.10) have also been calculated. Like trans-F_{40}ZnPc, the HOMO to LUMO and HOMO to LUMO+1 transitions appear as two distinct peaks in the calculated spectrum (Figure 1.11).

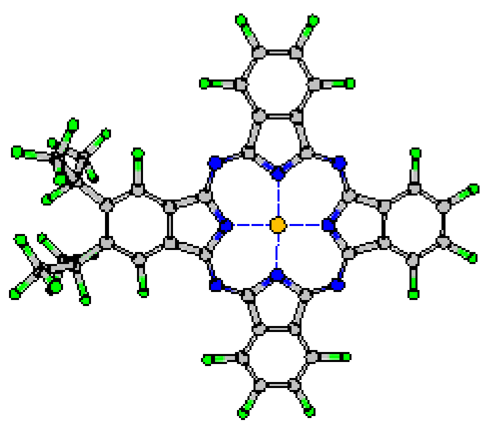

Figure 1.10. Geometry of the optimized structure of F_{28}ZnPc.

The first transition appears at 657 nm, and the second at 627 nm. The calculated absorbance spectrum of F_{28}ZnPc also closly resembles the multiple peaks seen in the experimental spectrum. Based on the calculated absorbance spectra of trans-F_{40}ZnPc and F_{28}ZnPc, we believe that not only does a trans-F_{40}ZnPc isomer exist, but an additional F_{28}ZnPc is being produced. Based on the formation energies of the dimer intermediates, $F_{28}ZnPc$ is expected to form in relatively high amounts as well.

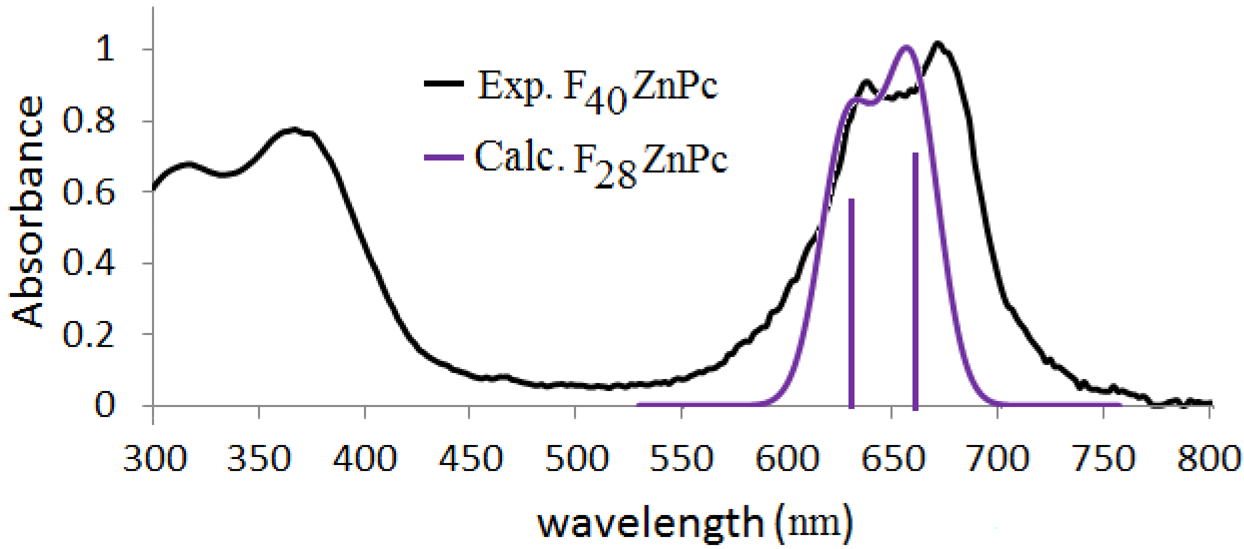

Figure 1.11. Experimental absorbance spectrum of $F_{40}ZnPc$ (black line) and calculated absorbance spectrum of $F_{28}ZnPc$ (purple line). Calculated cure normalized to 1. Height of vertical lines indicated the oscillator strength of the transitions.

1.2.5 Synthetic Pathway of $F_{34}ZnPc$ and $F_{52}ZnPc$

The synthetic pathway for the production of $F_{34}ZnPc$ and $F_{52}ZnPc$ involves reaction of the symmetric precursor, ***1***, as well as the asymmetric, ***3***. The reaction of these two precursors leads to a mixture of $F_{16}ZnPc$, $F_{34}ZnPc$, and $F_{52}ZnPc$. The experimental product distribution is found to be dependent on the initial ratio of precursors ***1*** and ***3*** added to the reaction. When ***1*** is added in excess, 3:1 ratio with ***3***, $F_{16}ZnPc$ is the major product with only trace amounts of the desired $F_{34}ZnPc$ and $F_{52}ZnPc$. If precursor ***3*** is added in excess, 3:1 ratio with ***1***, the yield of $F_{34}ZnPc$ and $F_{52}ZnPc$ increases and the three various Pcs are all formed in relatively equal amounts: $F_{34}ZnPc$ (38%), $F_{16}ZnPc$ (32%), and $F_{34}ZnPc$ (30%).[24]

As with $F_{40}ZnPc$, the experimental crystal structure of $F_{52}ZnPc$ contains no trans-$F_{52}ZnPc$. This section will precede much like Section 1.4. We will examine the intermediate dimer species in an attempt to explain the experimentally found Pc product distribution. Discussion will also focus on the formation of $F_{52}ZnPc$ cis- and trans- isomers. The proposed mechanism for the synthesis of $F_{34}ZnPc$ and $F_{52}ZnPc$ is presenting in Figure 1.12.

Prior to starting the discussion on the dimer intermediates, let's first return to reactivity of precursor ***3*** from Section 1.2. As seen in Figure 1.12, the asymmetric precursor ***3*** leads to the possibility of two zwitterionic monomer species following intermolecular activation, $\boldsymbol{3'}$ and $\boldsymbol{3'''}$. The number of isomers of both $F_{34}ZnPc$ and $F_{52}ZnPc$ would increase if both of these monomers were to exist. As previously discussed, the LUMO electron density distribution (Figure 1.3) for precursor ***3*** directs the formation of the ***3'*** monomer as indicated in Figure 1.12. Additionally, calculations preformed indicate a >98% probability of the formation of monomer $\boldsymbol{3'}$ over $\boldsymbol{3'''}$.

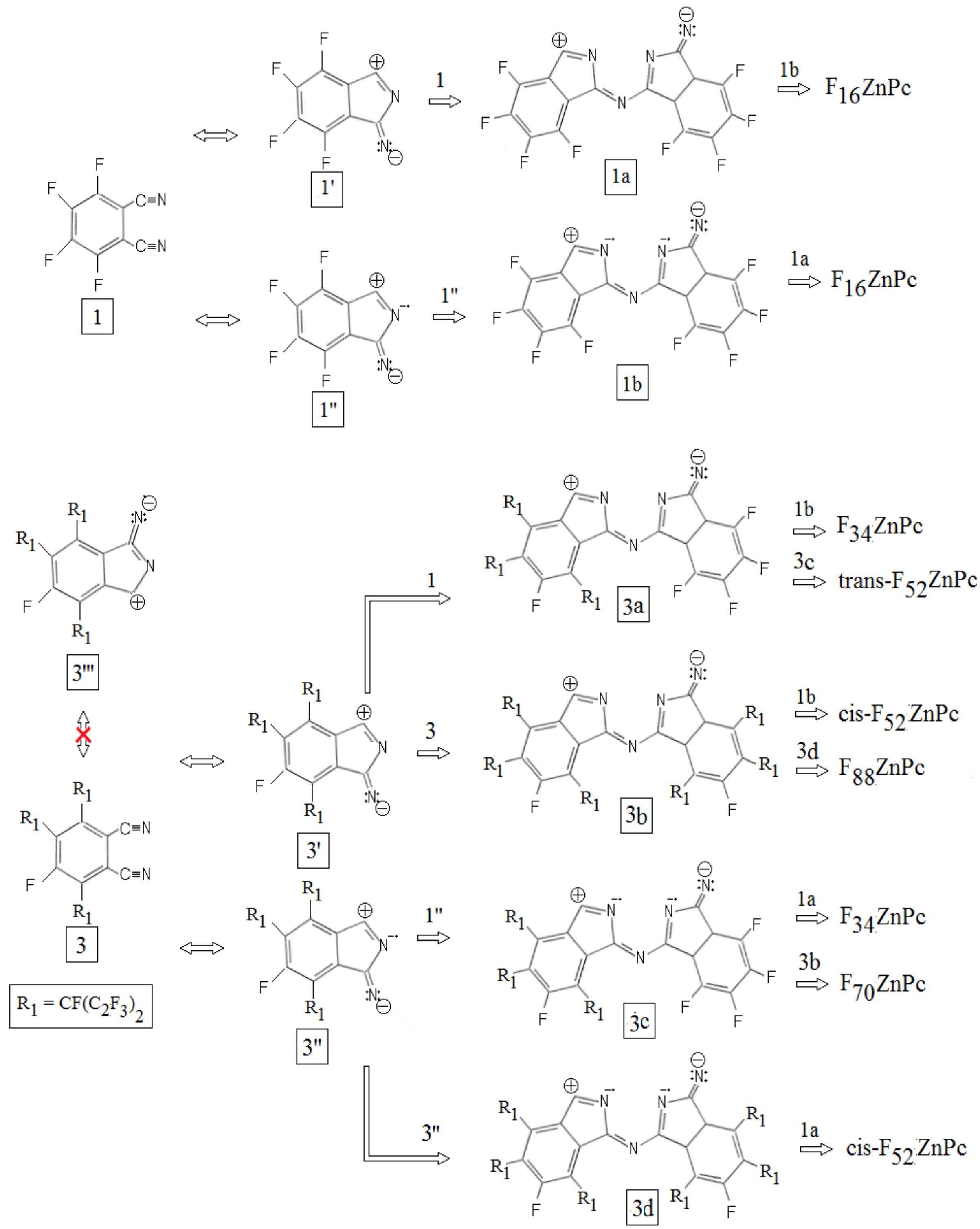

Figure 1.12. Proposed mechanism for the formation of $F_{34}ZnPc$ and $F_{52}ZnPc$.

Dimers ***1a*** and ***1b*** are the same that were discussed in section 1.2.3. However, the neutral and reduced dimers ***3a-d*** are unique to the synthesis of F_{34}ZnPc and F_{52}ZnPc. The calculated formation energy of each dimer species is presented in Table 1.3.

Table 1.3. Formation energies of F_{34}ZnPc and F_{52}ZnPc dimer intermediates.

Dimer	Formation Scheme	Formation Energy (kcal/mol)
1a	***1′ + 1***	-13.4722
3a	***3′ + 1***	+963.83555
3b	***3′ + 3***	+1469.7232
1b	***1″ + 1″***	-80.6448
3c	***3″ + 1″***	+968.0651
3d	***3″ + 3″***	+1504.2246

Focusing first on the neutral intermediate dimers, ***1a*** is the only dimer in the synthesis of F_{34}ZnPc and F_{52}ZnPc with favorable (negative) formation energy. The neutral dimers ***3a*** and ***3b*** both require a significant amount of energy for formation to be possible. Therefore, based on the calculated energies of formation, neutral dimer ***1a*** is by far the most likely to form. A similar finding observed for the reduced dimer intermediates as well. Reduced dimer ***1b*** is significantly favored over that of ***3c*** and ***3d***.

The addition of three bulky $–C_3F_7$ groups on the periphery of precursor ***3*** results in a large degree of steric hindrance. During dimer formation this steric hindrance alters the geometry of the optimized dimer structure. This ultimately leads to an increase in the calculated formation energy of the dimer intermediates that are prepared from precursor ***3***. The optimized structures of dimers ***1a***, ***3a***, and ***3b*** are illustrated in Figure 1.13; ***4a*** is also included for comparison.

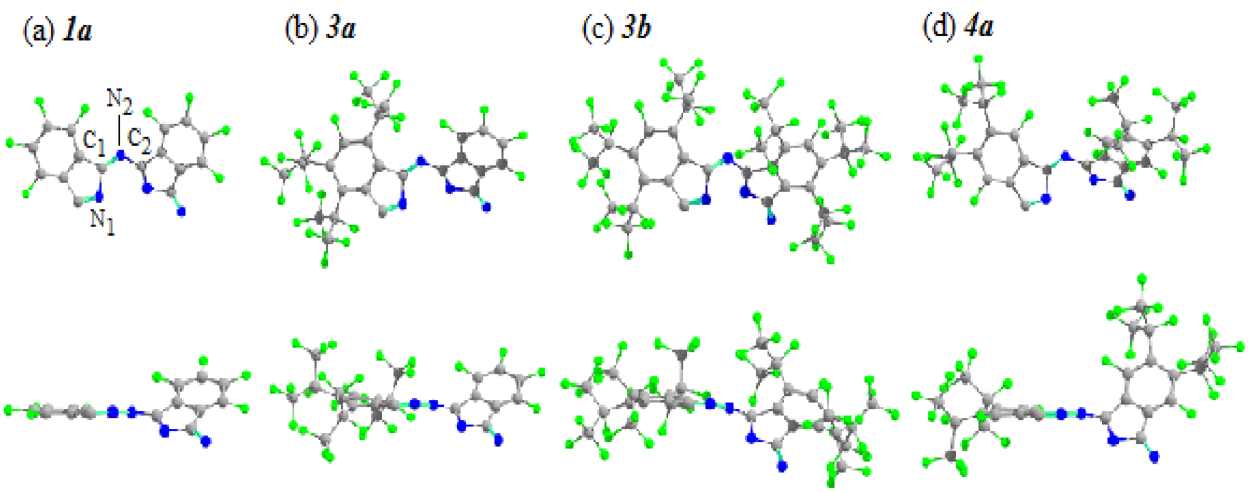

Figure 1.13. Optimized structure of dimer intermediates: (a) ***1a***, (b) ***3a***, (c) ***3b***, and (d) ***4a***.

Dimers formed from the monomer precursor ***3*** experience a decrease in the C_1-N_2-C_2 bond angle as a result of the electronic repulsion between the bulky $–C_3F_7$ groups on the periphery of ***3*** during dimer formation. For the same reasons, there is also an observed increase in the bowing of the dimer across the bridging Nitrogen atom as indicated in the N_1-C_1-N_2-C_2 dihedral angle of the optimized dimer structures (Table 1.4). For comparison, ***4a*** was also included in this analysis. Dimer ***4a*** does not experience the same degree of structural deformation seen in ***3a*** and ***3b***. Therefore, it is believed that the increased formation energies of dimers ***3a*** and ***3b*** is a direct result of the steric hindrance of monomer ***3***.

Table 1.4. Select bond and dihedral angles for intermediate dimers ***1a***, ***3a***, ***3b***, and ***4a***.

Precursor	***1a***	***3a***	***3b***	***4a***
C_1-N_2-C_2	126.56°	126.64°	122.31°	126.80°
N_1-C_1-N_2-C_2	5.02°	9.05°	10.19°	8.42°

Formation of dimers ***1a*** (neutral) and ***1b*** (reduced) are significantly thermodynamically favored over the more bulky dimers formed from monomer ***3***. This explains why F_{16}ZnPc (***1a*** + ***1b***) is produced as the major product when ***1*** is used in excess. Given the calculated formation energies of dimers ***3a-d***; is not a surprise that, even with excess ***3***, F_{34}ZnPc and F_{52}ZnPc are synthesized in awfully low yields. Although production of the reduced dimers ***3c*** and ***3d*** will be difficult, ***3c*** is predicted to form in greater amounts than ***3d***. This would result in increased formation of F_{34}ZnPc (***1a*** + ***3c***) over F_{52}ZnPc (***1a*** + ***3d***).

Due to the lack available ***3a*** (neutral) and ***3c*** (reduced) mixed dimers; it is possible that the majority of these dimers will be consumed in the production of F_{34}ZnPc. This may result in no formation of trans-F_{52}ZnPc which would require combination of ***3a*** and ***3c***. However, with excess ***3*** available, the mixed dimers should be able to form the trans- isomer. Additionally, there is no evidence of the production of an F_{70}ZnPc or F_{88}ZnPc molecule; which would require combination of two bulky dimer intermediates. This may be simply explained by the large steric hindrance of these dimers restricting their ability to combine as seen in Figure 1.14. The F_{52}ZnPc cis- vs. trans- will be covered in more detail in the next section. Assuming, for now, that trans-F_{52}ZnPc is not formed; the predicted final Pc product distribution based on the calculated formation energies of the dimer intermediates agrees with the experimental findings. F_{34}ZnPc and cis-F_{52}ZnPc are predicted to form is relatively equal amounts, but with low overall yields when excess ***3*** is introduced into the system. If precursor ***1*** is in excess, $F_{16}ZnPc$ will dominate the Pc product formation.

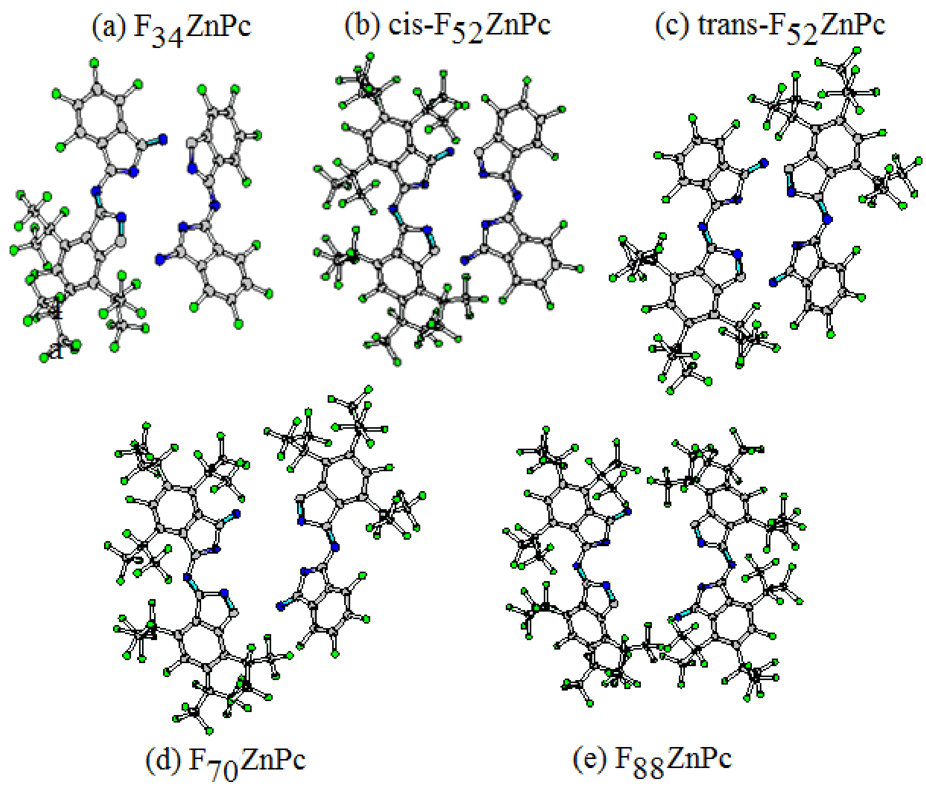

Figure 1.14. Spatial orientation of Pc dimer intermediates for the production of: (a) $F_{34}ZnPc$, (b) cis-$F_{52}ZnPc$, (c) trans-$F_{52}ZnPc$, (d) $F_{70}ZnPc$, and (e) $F_{88}ZnPc$.

1.2.6 Isomers of $F_{52}ZnPc$

As discussed in the previous section trans-$F_{52}ZnPc$ may not form due to the predicted low formation of ***3a*** and ***3c*** dimer intermediates. This could be the only explanation of the lack of experimental evidence of trans-$F_{52}ZnPc$ since calculations of the two isomers of $F_{52}ZnPc$ (Figure 1.15) reveal that the tran- isomer has a considerably lower (-19.65 kcal/mol) ground state energy than the cis isomer. This is not an unexpected result given the high steric hindrance for the cis-isomer compare to the trans- isomer.

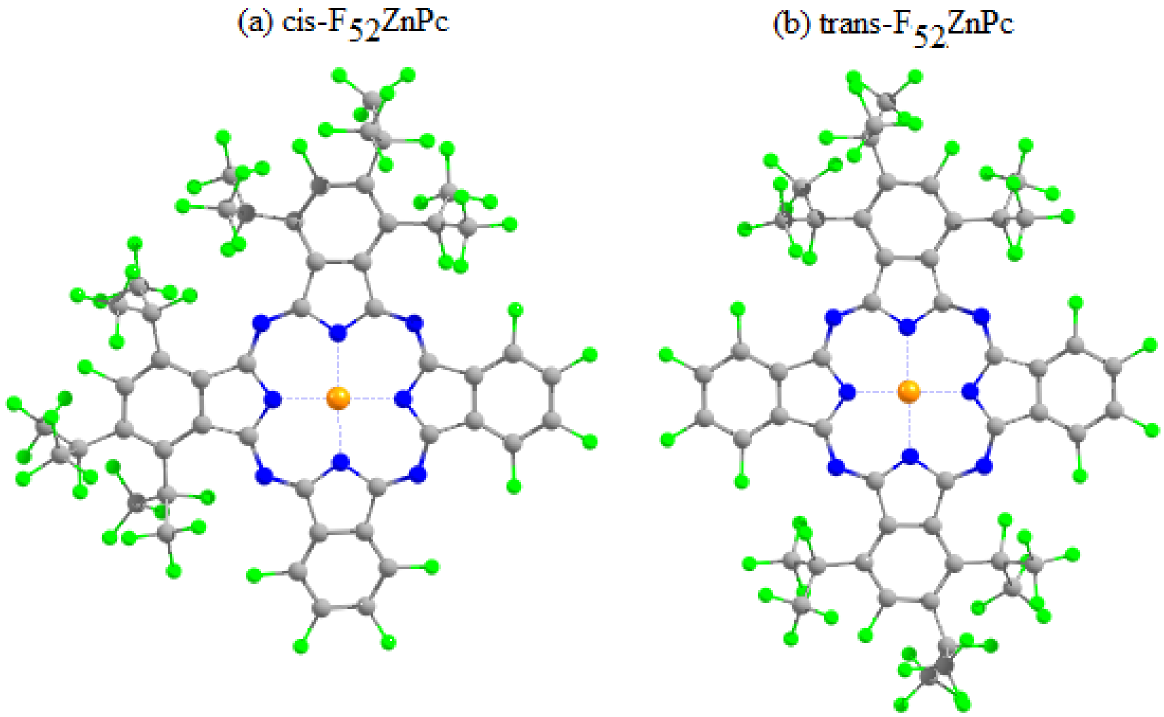

Figure 1.15. Geometry optimized structures of (a) cis-$F_{52}ZnPc$ and (b) trans-$F_{52}ZnPc$.

As with the isomers of $F_{40}ZnPc$, analysis of the electronic structure of the isomers of $F_{52}ZnPc$ reveals distinct characteristics that may be used to identify the isomers via the calculated absorbance spectra. Electron density distribution plots of the HOMO, LUMO, and LUMO+1 state for each isomer are illustrated in Figure 1.16. There is little variation in the HOMO state of the two isomers. The electron density of both HOMO states is highly delocalized across the Carbon atoms of the Pc macrocycle. There is also only a 0.03 eV difference is the calculated energies of the HOMO states.

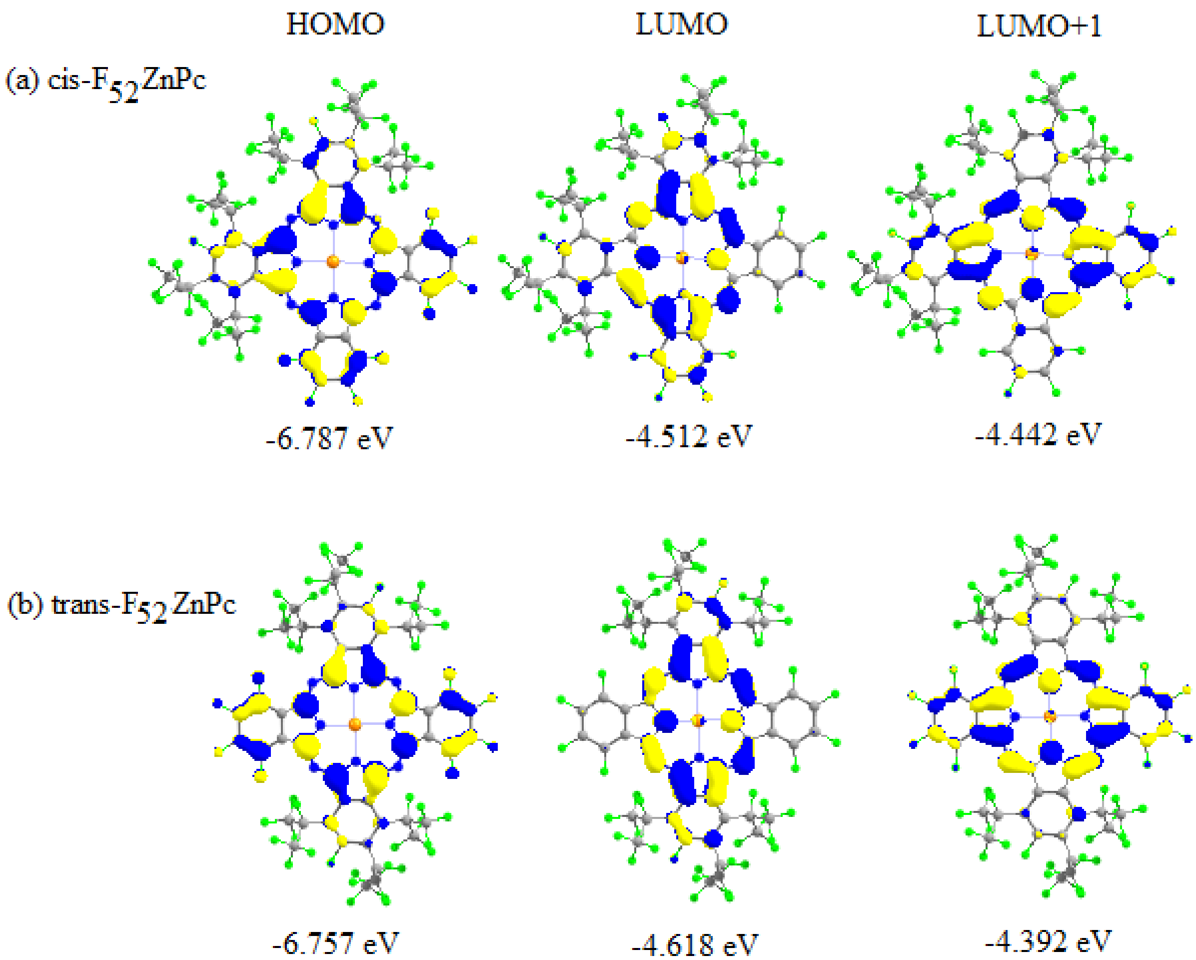

Figure 1.16. Electron density distribution plots of the HOMO, LUMO, and LUMO+1 states of (a) cis-F_{52}ZnPc and (b) trans-F_{52}ZnPc. Electron density sampled at 0.03 e/au

However, there are distinctive differences is the LUMO and LUMO+1 states of the two isomers. The LUMO state for trans-F_{52}ZnPc is calculated to be 0.11 eV lower in energy than the cis-F_{52}ZnPc LUMO state; this results in a 0.14 eV smaller band gap for the trans- isomer. Additionally, the LUMO and LUMO+1 state are essentially degenerate for the cis-isomer (0.07 eV separation), while there is a 0.23 eV separation in these states in the trans- isomer. These differences in the electron structure of the two isomers leads to distinguishing calculated absorbance spectra (Figure 1.17).

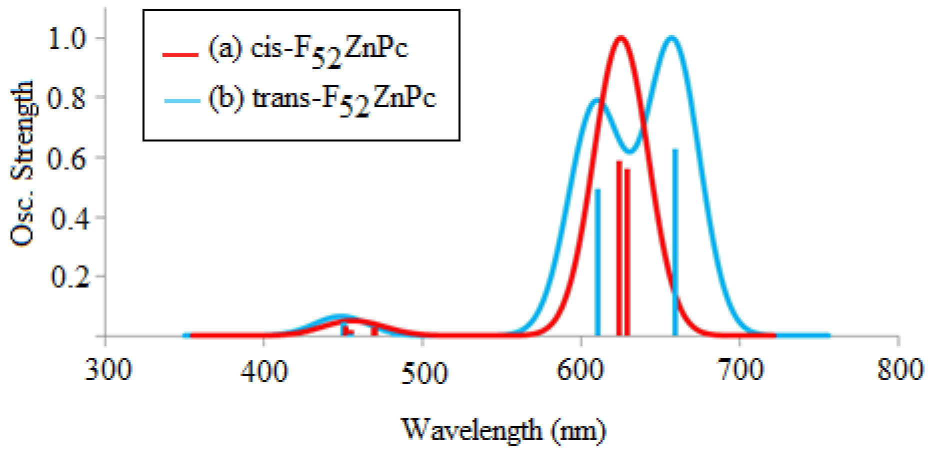

Figure 1.17. Calculated absorbance spectrum of (a) cis-F_{52}ZnPc (red line), and (b) trans-F_{52}ZnPc (blue line).

The non-degenerate LUMO and LUMO+1 state of trans-F_{52}ZnPc results in two distinct peaks in the calculated absorbance spectrum. The first transition for the trans- isomer is HOMO to LUMO in nature at 658 nm and the second transition is HOMO to LUMO+1 in nature at 609 nm. On the contrary, the nearly degenerate LUMO and LUMO+1 state results in two transitions at nearly identical energy. The first cis- transition, HOMO to LUMO, is found at 627 nm and the second, HOMO to LUMO+1, is found at 623 nm.

The experimental absorbance spectrum of F_{52}ZnPc is broad containing two major peaks at 701 nm and 674 nm, with a significant shoulder at 640 nm. The calculated absorbance spectrum of F_{52}ZnPc do not reproduce these λ_{max} values perfectly, but the spacing between the peaks matches quite well. If we shift the of calculated λ_{max} up 40 nm we have a spectrum with peaks at 698 nm (trans- H→L), 667 nm (cis- H→L, H→L+1), and 649 nm (trans- H→L+1). Therefore, we believe that the thermodynamically preferred trans-F_{52}ZnPc is produced in this reaction.

1.6 Conclusions

Within this study we have investigated the proposed synthetic pathways for the production of $F_{16}ZnPc$, $F_{34}ZnPc$, $F_{40}ZnPc$, $F_{52}ZnPc$, $F_{52a}ZnPc$, and $F_{64}ZnPc$. For the symmetric precursors ***1*** and ***4***, analysis of the reduction potential of the monomer precursors and formation energies of the dimer intermediates predicts a product distribution of $F_{64}ZnPc > F_{52a}ZnPc >$ trans-$F_{40}ZnPc >$ cis-$F_{40}ZnPc > F_{28}ZnPc > F_{16}ZnPc$. This prediction matches well and helps explain the experimental Pc product distribution. For the asymmetric precursor ***3***, thermodynamically unfavored formation energies of the dimer intermediates predict low yields of both $F_{34}ZnPc$ and $F_{52}ZnPc$. However, $F_{34}ZnPc$ is found to be slightly favored over $F_{52}ZnPc$. The major problem in the formation of these asymmetric Pcs is the large degree of steric hindrance imposed during formation of the dimer intermediates.

Additionally, the possibility of cis- and trans- isomers of $F_{40}ZnPc$ and $F_{52}ZnPc$ has been investigated. The calculated formation energies of the dimer intermediates of trans-$F_{40}ZnPc$ reveal that formation of trans- isomer is not only possible, but may be favored over cis-$F_{40}ZnPc$. A finding that is further supported by a 1.2:1 Boltzmann distribution favoring the trans- isomer, and calculated absorbance spectra that correspond to a mixture of both cis- and trans- isomers, as well as $F_{28}ZnPc$. The dimer intermediates of $F_{52}ZnPc$ indicate a relatively low probability of trans-$F_{52}ZnPc$ formation compared to the cis- isomer. Yet, the calculated absorbance spectrum of both isomers indicates that both cis- and trans- $F_{52}ZnPc$ are being produced.

1.7 Computation Details

All calculations are performed using density functional theory (DFT)[27-28] as implemented in the General Atomic and Molecular Electronic Structure System (GAMESS)[29-30] software package. The B3LYP[31-33] functional was employed for all single molecule vacuum state geometry optimizations. For the precursor monomer and dimer species, Popel's double zeta 6-31G[34-35] basis was used for all atoms. All calculations in this study had convergence tolerances of 1.0 x 10^{-3} Ha/bohr for the geometry optimization and 1.0 x 10^{-5} Ha for the SCF gradient. The selection of basis set and convergence tolerances are modest, but adequate for the relative comparisons in the ground state energies made in this study. We have also found that this basis set and convergence criteria accurately reproduces experimental geometries of the full F_xZnPc molecules.[36]

For calculation of the monomer EA, an extra polarization and diffuse function on all heavy atoms was added in the larger 6-31+G(d)[37-38] basis to better account for the polarization effects on the charged molecular species. The F_xZnPc absorbance spectra are calculated via time-dependant density functional theory (TDDFT).[39] Several functionals and basis sets were tested to find the optimal level of theory to reproduce experimental absorbance spectra. For more information see Appendix A. The B3LYP functional with 6-31G(d) basis set provided the best agreement with experimental results while maintain computational efficiency. Bulk solvent (ethanol) effects were also included in the absorbance spectra calculations using the polarizable continuum model (PCM);[40] analogy with experimental. The first ten vertical excitations were calculated for $F_{40}ZnPc$ and first five excitations for $F_{52}ZnPc$.

Electron density distribution plots, absorbance spectra, and optimized structures were visualized using the ChemCraft[41] software package.

CHAPTER 2

Effect of Peripheral Modification and Metal Center on the Structural and Electronic Properties of Phthalocyanines

2.1 Introduction

The recent surge in Pc based application is largely attributed to their extraordinary adaptability. To date, approximately 70 different metal ions and nonmetals have been shown to form coordination complexes with Pc exhibiting a variety of functional properties[19]. Optical and electronic properties can also be tuned by rational design of the symmetry and chemical composition of substituents on the molecular periphery and/or at the axial positions.[20-21]

In this chapter we will focus on the effect of both peripheral substitution as well as the choice of metal center on the structural and electronic properties of Pcs. The effect of the substation pattern on various Pc properties will be a recurring theme in several chapters throughout this work while variation of the metal center will only be address within this chapter. The Pcs of interest include the parent perhydro $H_{16}MPc$ as well as the fully fluorinated $F_{16}MPc$. Increased fluorination through the addition of bulky perfluoroisopropyl groups leads to the 3-D Pcs: $F_{34}MPc$, $F_{40}MPc$, $F_{52}MPc$, $F_{52a}MPc$, and $F_{64}MPc$.

While trans- isomers of $F_{40}ZnPc$ and $F_{52}ZnPc$ may exist (Chapter 1), only the cis-isomers are included in this study. To investigate the effect of the metal center, several metals are placed within the central cavity of the Pc. These metals include Zinc, Magnesium, Cobalt, Copper, and Iron. This series of metal centers was chosen to include both open d-shell transition metals (Fe, Co, and Cu) as well as the closed d shell transition metal Zn. Open shell Pc's often have a more complex electronic structures with a number of semi-occupied electronic states located energetically close together[42]. For comparison between transition and main group metals, Mg is also selected as a metal center lacking d shell electrons.

2.2 Results

2.2.1 Analysis of the Molecular Geometry

We will begin our discussion with the analysis of the molecular geometry of the various Pcs. While the planar $H_{16}MPc$ and $F_{16}MPc$ have high symmetry[43] (D_4h, Figure 2.1), the geometry of all Pc molecules was optimized without imposing any symmetry constraints. The introduction of the 3D $–C_3F7$ groups, which are not found to be perfectly eclipsed, on the periphery of the Pc greatly reduce the symmetry of the molecule.

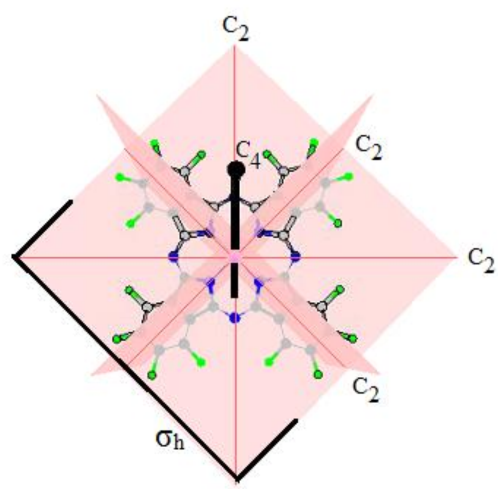

Figure 2.1. Calculated D_{4h} symmetry for $F_{16}ZnPc$ indicating rotational axes and mirror planes.

As an initial analysis of the effect of the various metal centers, as well as the peripheral fluorination, the root mean squared deviation (RMSD) from D_4h symmetry for $H_{16}MPc$ and $F_{16}MPc$ was calculated. This also served as validation if the computational methods employed in this study (Section 2.7). Although the 3-D F_xMPcs have lower symmetry, the RMSD from D_{4h} for the central conjugated region of the molecule was calculated to access relative deviations within this area. The calculated RMSD values are presented in Table 2.1; a RMSD value of zero indicates perfect D_4h molecular symmetry.

Table 2.1. Calculated RMSD (nm) from D_{4h} symmetry for various MPcs.

	$H_{16}MPc$	$F_{16}MPc$	$F_{34}MPc$	$F_{40}MPc$	$F_{52}MPc$	$F_{52a}MPc$	$F_{64}MPc$
Zn	0.597	0.595	0.908	0.930	2.637	0.763	0.801
Mg	0.586	0.567	0.901	0.919	2.633	0.724	0.770
Cu	0.868	0.197	0.874	0.846	2.606	0.724	0.765
Co	0.569	0.206	0.857	0.860	2.617	0.732	0.741
Fe	0.574	0.209	0.861	0.845	2.614	0.695	0.724

As expected, the calculated geometry of all $H_{16}MPc$ and $F_{16}MPc$ molecules maintain the expected D_{4h} symmetry best. The largest deviations from D_{4h} occur in the closed shell (Zn and Mg) systems. This is a result of these metal atoms residing farther out of the molecular plane in the optimized structure. As peripheral substitution increases there is an observed increase in the calculated deviations. Bond lengths and 3-body angles are slightly altered near the $–C_3F_7$ substation positions. There is also a significant bowing in the Pc structure in $F_{52}MPc$, which leads to the largest deviations from D_{4h} symmetry. The symmetric substitution pattern of $F_{64}ZnPc$ restores D_{4h} symmetry in the conjugated region of the Pc. To better understand the effect of peripheral substitution and metal center on the molecular geometry, the calculated average bond lengths of the various Pcs are presented in Table 2.2 and compared to experimental XRD bond lengths where available. This analysis has been restricted to the central conjugated region and is based on average bond length values of the Pc macrocycle. All bond lengths for each MPc are available in Appendix B.

Table 2.2. Comparison between Experimental XRD and calculated bond lengths for H_{16}MPc. F_{16}MPc, F_{34}MPc, F_{40}MPc, F_{52}MPc, F_{52a}MPc, and F_{64}MPc where M=Zn, Mg, Co, Cu, and Fe. All values reported in Å. XRD values pertain to the metal marked with an asterisk for each Pc. Labeling scheme: N_1, the nitrogen atom bonded to central Zn; C_1, C_2, C_3, C_4 represent the carbon atoms starting at N_1 and proceeding around the isoindole ring unit.

F_xPc	M	M-N_1	N_1-C_1	C_1-N_2	C_1-C_2	C_2-C_2	C_2-C_3	C_3-C_4	C_4-C_4	M out of plane
H_{16}Pc	XRD	1.979	1.369	1.331	1.401	1.401	1.393	1.391	1.396	?
	Zn	2.003	1.387	1.335	1.461	1.417	1.396	1.399	1.411	0.083
	Mg	2.003	1.387	1.335	1.461	1.417	1.396	1.399	1.411	0.083
	Co	1.904	1.395	1.327	1.457	1.411	1.400	1.399	1.412	0.028
	Cu	2.052	1.351	1.328	1.478	1.399	1.377	1.395	1.391	0.397
	Fe	1.961	1.399	1.331	1.461	1.414	1.401	1.400	1.412	0.026
F_{16}Pc	XRD	1.952	1.378	1.319	1.467	1.361	1.381	1.359	1.407	?
	Zn	2.007	1.385	1.331	1.459	1.422	1.391	1.394	1.399	0.096
	Mg	2.019	1.384	1.334	1.461	1.423	1.391	1.394	1.399	0.044
	Co	1.939	1.392	1.322	1.452	1.414	1.392	1.393	1.400	0.001
	Cu*	1.966	1.385	1.325	1.455	1.417	1.391	1.394	1.401	0.004
	Fe	1.956	1.389	1.325	1.451	1.417	1.392	1.393	1.401	0.003
F_{34}Pc	XRD	2.030	1.362	1.327	1.472	1.398	1.402	1.388	1.377	?
	Zn*	2.020	1.382	1.325	1.471	1.415	1.402	1.396	1.398	0.078
	Mg	2.032	1.381	1.329	1.472	1.431	1.401	1.397	1.397	0.033
	Co	1.961	1.391	1.320	1.460	1.425	1.407	1.396	1.399	0.011
	Cu	1.984	1.384	1.321	1.469	1.426	1.404	1.396	1.398	0.019
	Fe	1.975	1.388	1.321	1.468	1.421	1.406	1.396	1.399	0.029
F_{40}Pc	XRD	1.925	1.373	1.321	1.445	1.390	1.387	1.390	1.338	?
	Zn	2.007	1.385	1.330	1.460	1.411	1.389	1.403	1.424	0.102
	Mg	2.007	1.385	1.330	1.460	1.411	1.389	1.403	1.424	0.095
	Co*	1.940	1.392	1.322	1.446	1.405	1.390	1.402	1.423	0.013
	Cu	1.960	1.386	1.325	1.453	1.407	1.388	1.401	1.424	0.004
	Fe	1.955	1.390	1.324	1.453	1.408	1.390	1.402	1.424	0.003
F_{52}Pc	XRD	2.024	1.355	1.334	1.475	1.406	1.396	1.384	1.393	?
	Zn*	2.027	1.386	1.330	1.480	1.433	1.410	1.398	1.396	0.062
	Mg	2.027	1.383	1.330	1.480	1.433	1.407	1.398	1.396	0.062
	Co	1.964	1.391	1.320	1.476	1.427	1.414	1.408	1.396	0.067
	Cu	1.983	1.425	1.326	1.477	1.430	1.409	1.399	1.396	0.028
	Fe	1.987	1.389	1.325	1.478	1.429	1.414	1.398	1.396	0.028
F_{52a}Pc	XRD									?
	Zn	2.009	1.385	1.329	1.461	1.397	1.406	1.409	1.438	0.109
	Mg	2.019	1.384	1.334	1.462	1.407	1.388	1.408	1.437	0.051
	Co	1.955	1.394	1.323	1.460	1.402	1.393	1.409	1.439	0.008
	Cu	1.976	1.389	1.326	1.461	1.403	1.392	1.408	1.439	0.026
	Fe	1.963	1.391	1.325	1.457	1.402	1.391	1.408	1.439	0.020

$F_{64}Pc$	XRD	1.925	1.373	1.321	1.445	1.392	1.387	1.390	1.417	?
	Zn	2.010	1.387	1.332	1.462	1.400	1.388	1.412	1.450	0.097
	Mg	2.022	1.384	1.336	1.464	1.401	1.388	1.413	1.449	0.046
	Co	1.942	1.393	1.322	1.454	1.395	1.389	1.411	1.450	0.013
	Cu*	1.960	1.387	1.324	1.454	1.396	1.387	1.411	1.450	0.003
	Fe	1.958	1.394	1.323	1.457	1.396	1.390	1.412	1.451	0.016

For all MPc molecules the calculated vacuum ground state geometry is in good agreement with the experimental XRD structures. It should be noted that several of the XRD crystals contain solvent molecules which contribute to the slight variation in bond lengths compared to the vacuum state calculated structures. The open-shell metals are located more in the plain of the Pc macrocycle, which results in shortening of the metal-nitrogen bond distances in the Co, Cu, and Fe systems compared to the Zn and Mg systems. The metal-nitrogen bond distances increase as follows: Co < Fe < Cu < Zn <Mg. As expected, this trend is reversed in all systems when considering the N_1-C_1 bond distances. The remaining bond lengths presented in Table 2.2, which are more distance from the metal center, are less dependent on the nature of the metal. It is also observed that the substitution pattern on the periphery of the Pc has little effect in the calculated bond lengths throughout the central conjugated region of the molecule. The same observations are made when considering the calculated 3-body angles. The calculated 3-body angles for each system are provided in Appendix B.

2.2.2 Binding Strength of Various Metal Centers

One aspect contributing to the long term stability of the Pc, is the binding strength of the metal center to the Pc macrocycle. The metal binding strength is calculated as follows:

$$E_{Binding} = E_{MPc} - \left[E_{Pc^{2-}} + E_{M^{2+}} \right] \qquad 2.1$$

where E_{MPc} is the ground state energy of the metal coordinated Pc, E_{Pc}^{2-} is the energy of the metal free Pc, and E_M^{2+} is the energy of the metal cation alone in vacuum. Metal binding strengths have been calculated for the various substitution patterns for each of the five metals centers (Zn, Mg, Co, Cu, Fe). The calculated binding energies are presented in Table 2.3.

Table 2.3. Calculated metal binding strength for: F_{16}MPc, F_{34}MPc, F_{40}MPc, F_{52}MPc, F_{52a}MPc, and F_{64}MPc where M=Zn, Mg, Co, Cu, and Fe. All values reported in eV.

PcM	Zn	Mg	Co	Cu	Fe
F_{16}Pc	-29.439	-26.501	-32.782	-31.144	-31.101
F_{34}Pc	-28.819	-25.995	-32.018	-30.469	-30.385
F_{40}Pc	-20.270	-17.322	-24.181	-22.451	-22.416
F_{52}Pc	-28.274	-25.365	-31.539	-29.886	-29.666
F_{52a}Pc	-28.018	-25.093	-31.403	-29.711	-29.662
F_{64}Pc	-27.562	-24.623	-30.952	-29.322	-28.960

As indicated in Table 2.3, each metal displays strong binding to Pc macrocycle. Depending on the metal center and substitution pattern, several distinct trends develop. For each substitution pattern, it is found that the metal binding strength follows: Co > Cu > Fe > Zn > Mg. This agrees well with the calculated M-N_1 bond lengths calculated in Table 2.1 and will be further discussed when examining the charge distribution of the various Pcs in the following section.

It is expected that the increase in fluorination on the periphery would lead to increasing electron density on the periphery of the molecule which would, in turn, result in a weaker metal binding strength. With the exception of F_{40}MPc, this trend is observed with the metal binding strength following the trend: F_{16}MPc > F_{34}MPc > F_{52}MPc > F_{52a}MPc > F_{64}MPc > F_{40}MPc. The calculated metal binding strength of F_{40}MPc is significantly lower (~7.5 eV) than any of the other substation patterns analyzed. There is no indication in the calculated bond lengths as to what may be causing this effect.

2.2.3 Charge Distribution of F_xMPc

Several methods exist for determining partial atomic charges, two of which are the Merz-Kollman[44] (MK) and Mulliken[45-48] methods. In other studies,[36] which will be discussed in the next chapter, we have found that both methods provide an acceptable description of the partial atomic charges. Since obtaining MK charges requires additional post-optimization calculations, we have decided to use the Mulliken method to investigate the effects of peripheral substation and metal center on the atomic charges. Additionally, we are only interested in making relative comparisons between systems, so the Mulliken method is adequate.

The calculated Mulliken partial atomic charges for all F_xMPcs are collected in Table 2.4. These values are averages of each symmetry unique atom type as depicted in Figure 2.2, where $F_{34}MPc$ is depicted. Although all of the metal centers have a formal charge of +2, the calculated effective atomic charge is found to be between +0.96 and +1.29. If the M-Pc bonding was purely ionic in nature, these calculated atomic charges should be closer to +2. This suggests that the M-Pc bonding is significantly covalent in nature. This is in agreement with the strong binding energy calculated for all metal centers in section 2.3.

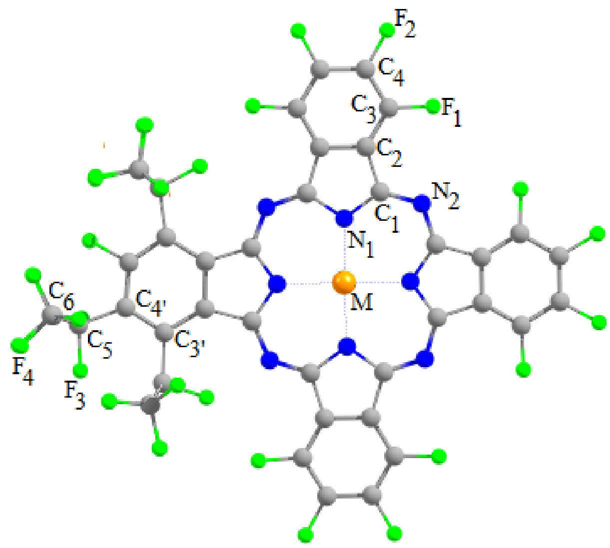

Figure 2.2. Atom labeling scheme for MPc calculated Milliken charges.

There is little variation in the metal atomic charge for Cu, Co, and Fe; as expected according to the electronegativities of these metals. The lower electronegativity of Zn and Mg results in a slightly greater atomic charge for these metal centers. Due to the orbital overlap with the metal, N1 is significantly more negative than N2 for all systems. While the atomic charge of N1 is slightly affected by the nature of the metal center, the remainder of the Pc macrocycle is relatively unaltered. The degree of peripheral modification has little observed effect of the partial atomic charges. A complete description of the calculated Mulliken atomic charges for all MPcs is provided in Appendix B.

Table 2.4. Calculated Mulliken atomic charges for FxMPc, where M = Zn, Mg, Co, Cu, and Fe.

		Metal Center							Metal Center				
F_xPc		Zn	Mg	Cu	Co	Fe	F_xPc		Zn	Mg	Cu	Co	Fe
F_{16}	M	1.04	1.27	0.98	0.96	1.01	**F_{34}**	M	1.04	1.27	0.98	0.96	1.02
	N_1	-0.68	-0.74	-0.68	-0.69	-0.68		N_1	-0.67	-0.73	-0.67	-0.68	-0.70
	N_2	-0.33	-0.34	-0.32	-0.32	-0.32		N_2	-0.33	-0.34	-0.33	-0.33	-0.33
	C_1	0.36	0.37	0.35	0.35	0.36		C_1	0.36	0.37	0.36	0.36	0.36
	C_2	0.04	0.03	0.04	0.04	0.04		C_2	0.03	0.03	0.04	0.04	0.04
	C_3	0.25	0.25	0.25	0.25	0.25		C_3	0.25	0.25	0.25	0.25	0.25
	$C_{3'}$	-	-	-	-	-		$C_{3'}$	0.08	0.07	0.08	0.08	0.08
	C_4	0.28	0.28	0.28	0.28	0.28		C_4	0.27	0.27	0.27	0.27	0.27
	$C_{4'}$	-	-	-	-	-		$C_{4'}$	0.06	0.06	0.06	0.06	0.06
	C_5	-	-	-	-	-		C_5	0.07	0.07	0.08	0.07	0.07
	C_6	-	-	-	-	-		C_6	0.80	0.80	0.80	0.80	0.80
	F_1	-0.26	-0.26	-0.26	-0.26	-0.26		F_1	-0.26	-0.26	-0.26	-0.26	-0.26
	F_2	-0.28	-0.28	-0.28	-0.28	-0.28		F_2	-0.28	-0.28	-0.28	-0.28	-0.28
	F_3	-	-	-	-	-		F_3	-0.27	-0.27	-0.27	-0.27	-0.27
	F_4	-	-	-	-	-		F_4	-0.25	-0.25	-0.25	-0.25	-0.25
F_{40}	M	1.05	1.29	0.99	1.01	1.02	**F_{52}**	M	1.04	1.27	0.99	1.08	1.16
	N_1	-0.68	-0.75	-0.68	-0.70	-0.71		N_1	-0.67	-0.73	-0.67	-0.69	-0.71
	N_2	-0.32	-0.32	-0.31	-0.31	-0.32		N_2	-0.34	-0.35	-0.34	-0.33	-0.34
	C_1	0.37	0.37	0.36	0.35	0.37		C_1	0.38	0.38	0.37	0.36	0.37
	C_2	0.04	0.04	0.05	0.05	0.05		C_2	0.03	0.04	0.03	0.04	0.03
	C_3	0.25	0.25	0.25	0.26	0.26		C_3	0.25	0.25	0.25	0.25	0.25
	$C_{3'}$	-	-	-	-	-		$C_{3'}$	0.05	0.05	0.05	0.06	0.06
	C_4	0.28	0.28	0.28	0.28	0.28		C_4	0.28	0.28	0.28	0.28	0.28
	$C_{4'}$	0.04	0.04	0.04	0.04	0.04		$C_{4'}$	0.03	0.03	0.03	0.03	0.03
	C_5	0.06	0.06	0.05	0.06	0.06		C_5	0.07	0.07	0.07	0.07	0.07
	C_6	0.80	0.80	0.82	0.82	0.82		C_6	0.81	0.81	0.81	0.81	0.81
	F_1	-0.26	-0.26	-0.26	-0.26	-0.26		F_1	-0.26	-0.26	-0.26	-0.26	-0.26
	F_2	-0.27	-0.27	-0.27	-0.27	-0.27		F_2	-0.28	-0.13	-0.28	-0.28	-0.28
	F_3	-0.28	-0.28	-0.28	-0.29	-0.29		F_3	-0.28	-0.28	-0.28	-0.28	-0.28
	F_4	-0.25	-0.25	-0.25	-0.25	-0.25		F_4	-0.25	-0.25	-0.25	-0.25	-0.25
F_{52a}	M	1.05	1.28	0.99	1.08	1.02	**F_{64}**	M	1.05	1.28	1.00	0.98	1.03
	N_1	-0.68	-0.74	-0.68	-0.69	-0.68		N_1	-0.68	-0.74	-0.68	-0.68	-0.73
	N_2	-0.32	-0.35	-0.31	-0.31	-0.32		N_2	-0.32	-0.32	-0.31	-0.30	-0.31
	C_1	0.37	0.38	0.37	0.36	0.37		C_1	0.37	0.38	0.36	0.36	0.36
	C_2	0.04	0.04	0.05	0.05	0.05		C_2	0.04	0.04	0.05	0.05	0.05
	C_3	0.25	0.25	0.25	0.25	0.26		C_3	0.25	0.25	0.26	0.26	0.26
	$C_{3'}$	-	-	-	-	-		$C_{3'}$	-	-	-	-	-
	C_4	0.28	0.28	0.28	0.28	0.28		C_4	-	-	-	-	-
	$C_{4'}$	0.04	0.04	0.04	0.04	0.04		$C_{4'}$	0.04	0.04	0.04	0.04	0.04
	C_5	0.07	0.07	0.07	0.07	0.07		C_5	0.07	0.07	0.06	0.07	0.07
	C_6	0.80	0.80	0.80	0.80	0.80		C_6	0.80	0.80	0.80	0.80	0.80
	F_1	-0.26	-0.26	-0.26	-0.26	-0.26		F_1	-0.26	-0.26	-0.26	-0.26	-0.26
	F_2	-0.27	-0.27	-0.27	-0.27	-0.27		F_2	-	-	-	-	-
	F_3	-0.28	-0.28	-0.28	-0.28	-0.28		F_3	-0.28	-0.28	-0.28	-0.28	-0.28
	F_4	-0.25	-0.25	-0.25	-0.25	-0.25		F_4	-0.25	-0.25	-0.24	-0.25	-0.25

2.2.4 Electronic Structure of F_xMPc

For all metal centers, increased fluorination on the periphery of the Pc leads to a significant lowering of the molecular frontier orbitals. This lowering of the frontier orbitals results in increased chemical stability of the Pc molecule. For the closed shell metal centers (Zn and Mg) there is very little variation observed in the calculated MO diagram. However, as previously mentioned, the open d-shell metal centers (Co, Cu, and Fe) are slightly more complicated with singly occupied molecular orbitals (SOMO) located in between the HOMO and LUMO states. For all substitution patterns, the Co and Cu SOMO levels are significantly more stable than the SOMOs of Fe, with the exception of $F_{64}FePc$. Possible explanations of this will be discussed below. As with the HOMO and LUMO states, the SOMO levels are also stabilized with increases fluorination on the periphery of the Pc. The calculated MO diagrams for the ground state F_xMPcs are illustrated in Figure 2.3. It is noted that these MO diagrams are focused on displaying the occupied and unoccupied MOs near the band gap, rather than all of the states.

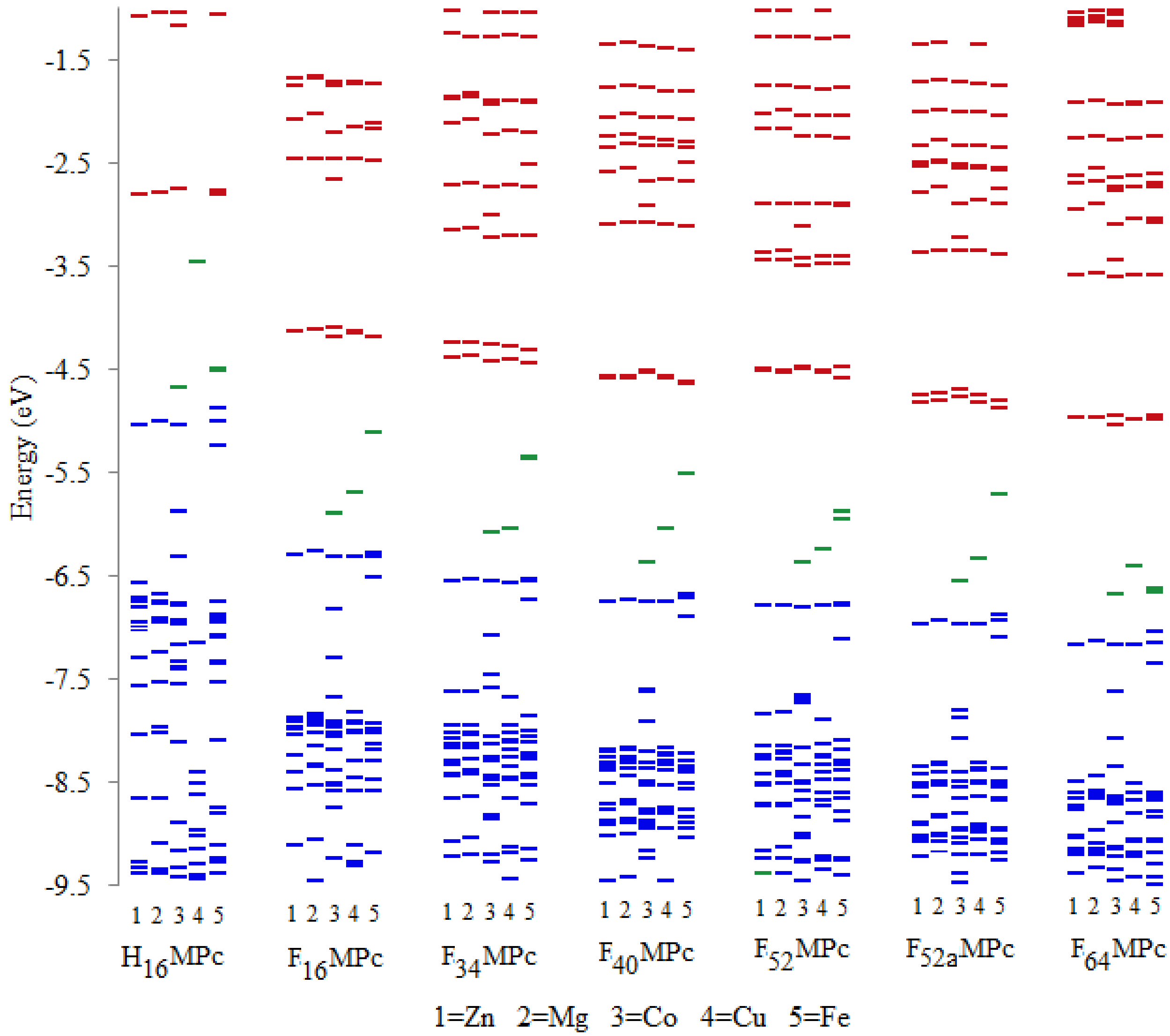

Figure 2.3. Molecular orbital diagram of upper occupied and lower unoccupied states of F_{16}MPc, F_{34}MPc, F_{40}MPc, F_{52}MPc, F_{52a}MPc, and F_{64}MPc. Occupied MOs are indicated by blue lines, partially occupied MOs by green lines, and unoccupied MOs by red lines.

The resulting energy gap between the HOMO (SOMO) and LUMO are summarized in Table 2.5. For the closed d-shell metals there is little variation observed in the HOMO-LUMO energy gap upon increased peripheral substitution. The only exception to this is a slight widening of the gap for F_{52}MPc. Due to higher lying SOMOs of the open d-shell metals, the calculated HOMO-LUMO energy gap is significantly decreased compared to that of Zn and Mg. There is also more significant deviations present in the calculated energy gaps for M = Co, Cu, and Fe. It is also noted that the SOMO levels of the open d-shell metals allow for additional low energy excitations than the SOMO to LUMO transitions indicated in Table 2.5

Table 2.5. Calculated HOMO (SOMO) - LUMO energy gap for F_xMPc. All values reported in eV.

	M = Zn	M = Mg	M = Co	M = Cu	M = Fe
H_{16}MPc					
F_{16}MPc	2.171	2.150	1.709	1.559	0.925
F_{34}MPc	2.163	2.150	1.657	1.644	0.920
F_{40}MPc	2.169	2.150	1.834	1.450	0.873
F_{52}MPc	2.275	2.260	1.878	1.703	1.293
F_{52a}MPc	2.133	2.117	1.769	1.491	0.825
F_{64}MPc	2.185	2.161	1.641	1.420	1.644

Density of states (DOS) and partial density of states (PDOS) plots are constructed for each molecule to further explore the electronic properties of the various MPcs. Focusing on the frontier orbitals, the PDOS is employed to examine the electron density distribution of each state. We will first explore the effect of peripheral substitution, then the effects of the various metal centers. DOS and PDOS plots for F_xZnPc are illustrated in Figure 2.4 a-e.

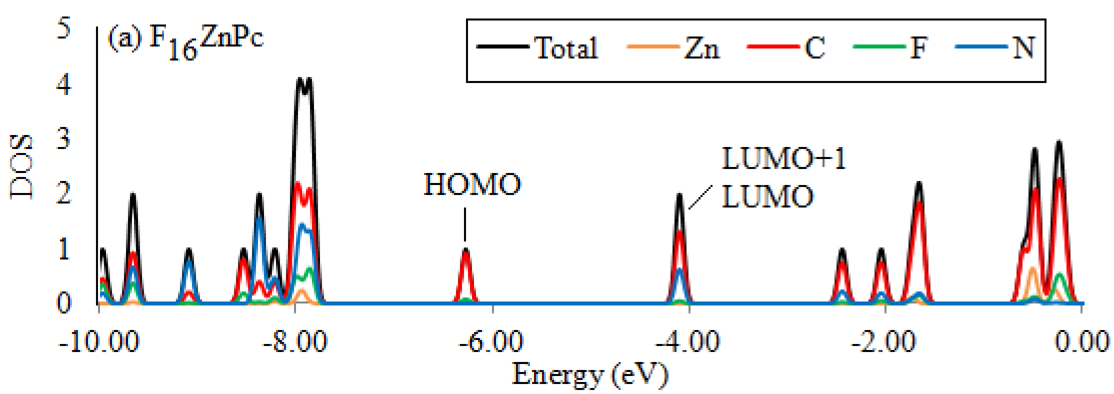

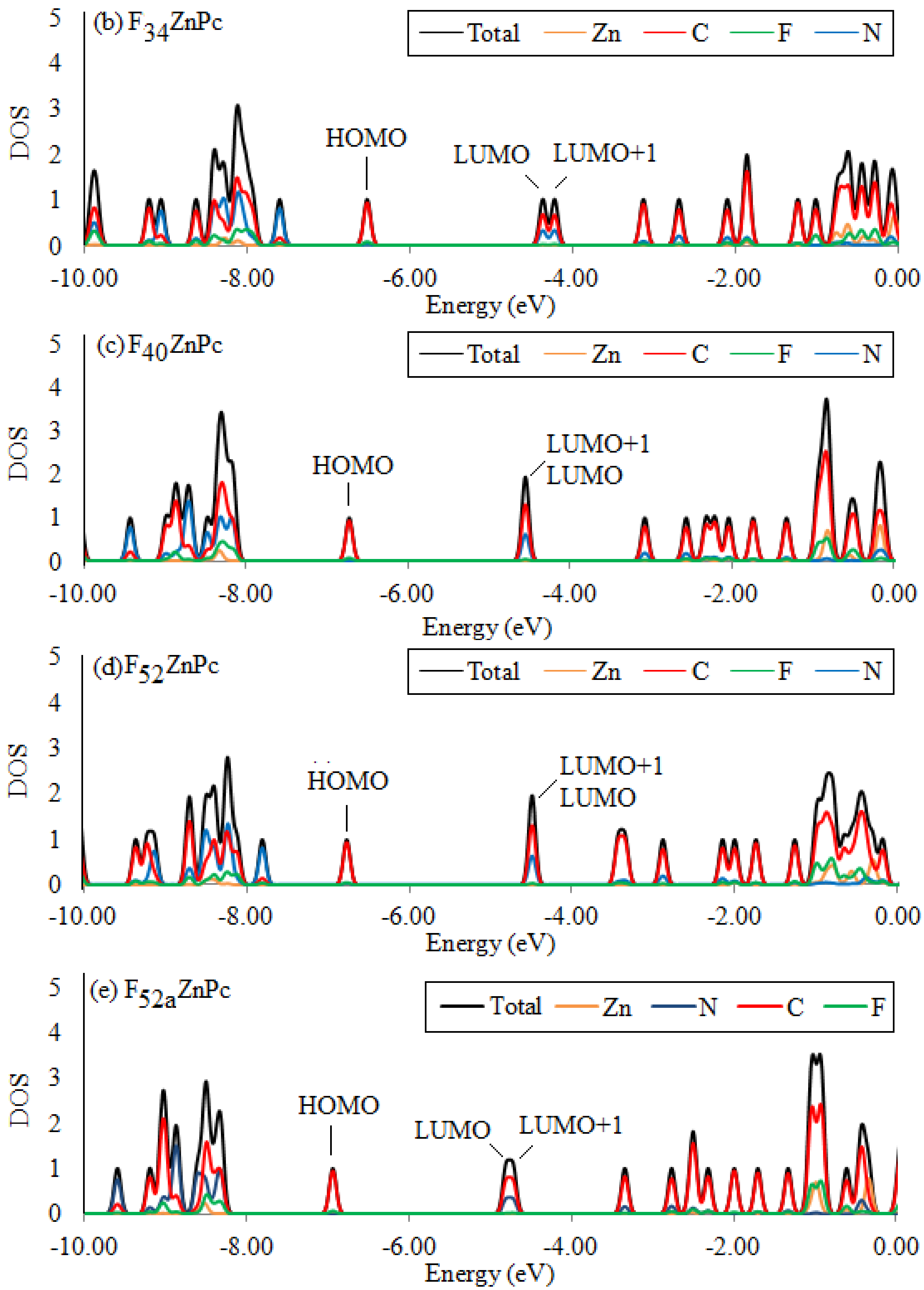
(b) F34ZnPc
Total Zn C F N
HOMO
LUMO
LUMO+1
DOS
Energy (eV)
(c) F40ZnPc
Total Zn C F N
HOMO
LUMO+1
LUMO
DOS
Energy (eV)
(d)F52ZnPc
Total Zn C F N
HOMO
LUMO+1
LUMO
DOS
Energy (eV)
(e) F52aZnPc
Total Zn N C F
HOMO
LUMO
LUMO+1
DOS
Energy (eV)

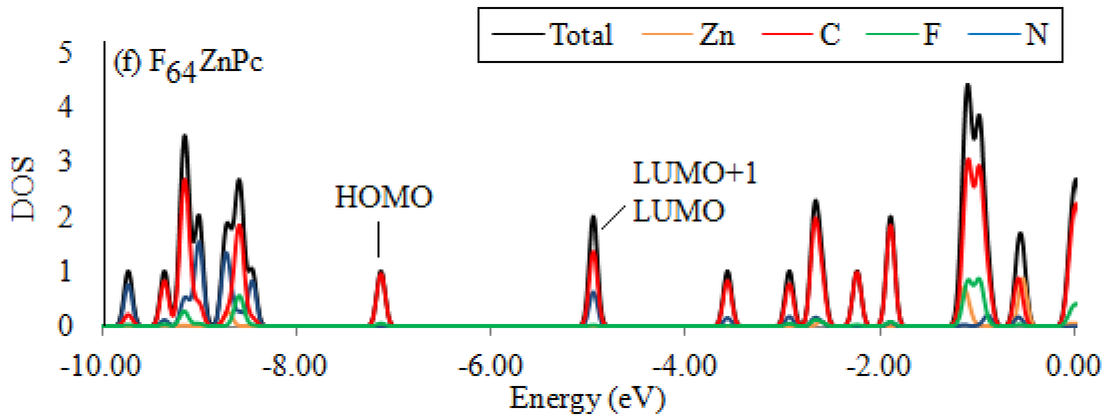

Figure 2.4. DOS and PDOS of (a) $F_{16}ZnPc$, (b) $F_{34}ZnPc$, (c) $F_{40}ZnPc$, (d) $F_{52}ZnPc$, (e) $F_{52a}ZnPc$ and (f) $F_{64}ZnPc$.

All F_xZnPc systems contain a discrete HOMO state that is composed of large (~93%) delocalized contributions from the Carbon atoms of the Pc macrocycle and minor contributions located on the peripheral Fluorine atoms (Table2.6). The HOMO electron density is highly delocalized across all four isoindole units of the Pc macrocycle. $F_{34}ZnPc$ and $F_{52}ZnPc$ also have a discrete HOMO-1 state with major Nitrogen contributions which is not present in the other F_xZnPcs. However, the HOMO state of all F_xZnPc is > 1 eV higher in energy than the next occupied MO. With the exception of a lowering in energy, the peripheral substitution pattern has little effect on the F_xZnPc HOMO state. Electron density plots of these states are illustrated in Figure 2.5a-f.

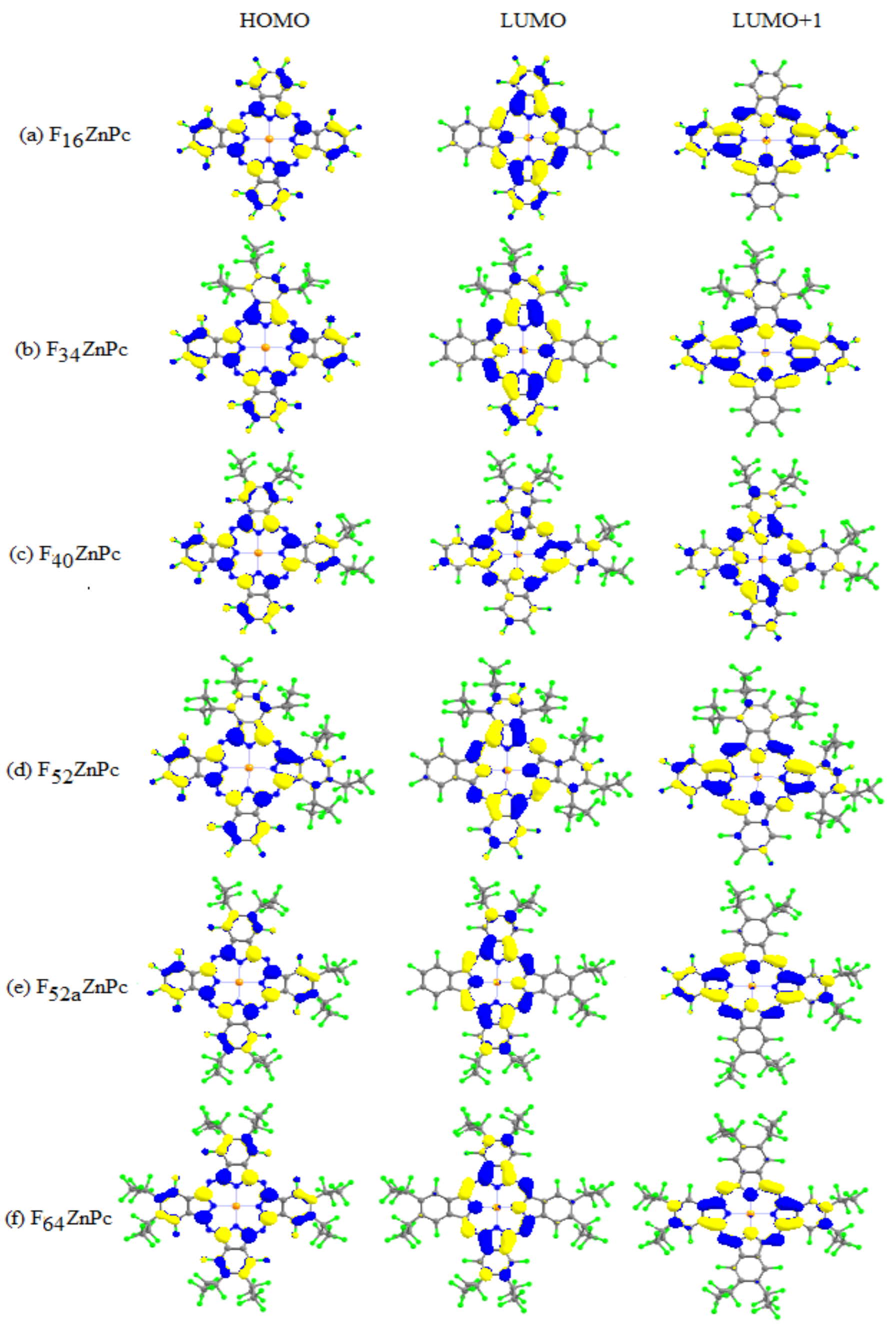

Figure 2.5. Electron density distribution plot of HOMO (left), LUMO (middle), and LUMO+1(left) for; (a) $F_{16}ZnPc$, (b) $F_{34}ZnPc$, (c) $F_{40}ZnPc$, (d) $F_{52}ZnPc$, (e) $F_{52a}ZnPc$, and (f) $F_{64}ZnPc$.

All F_xZnPc contain a LUMO and LUMO+1 state which are located energetically close together. The spacing and electron density distribution in these unoccupied states is greatly affected by the peripheral substitution. The greatest difference in energy of the LUMO and LUMO+1 state is observed for $F_{34}ZnPc$ (0.144 eV); followed by $F_{52a}ZnPc$ (0.087 eV), $F_{52}ZnPc$ (0.070 eV), $F_{40}ZnPc$ (0.019), $F_{64}ZnPc$ (0.003 eV), and $F_{16}ZnPc$ (0.000 eV). Therefore, asymmetric peripheral substitution of the Pc results in an increased energy separation between the first two unoccupied states.

Table 2.6. Calculated energy and electron density atom contributions of select MOs for F_xZnPc

			% Contribution to MO			
Pc	MO	Energy(eV)	Zn	N	C	F
$F_{16}ZnPc$	HOMO	-6.286	0.00	0.00	91.87	8.13
	LUMO	-4.114	0.31	31.23	65.93	2.53
	LUMO+1	-4.114	0.31	31.23	65.93	2.53
$F_{34}ZnPc$	HOMO	-6.536	0.00	0.54	92.32	7.13
	LUMO	-4.373	0.32	31.11	66.62	1.94
	LUMO+1	-4.229	0.30	31.72	65.58	2.41
$F_{40}ZnPc$	HOMO	-6.740	0.00	0.35	92.94	6.71
	LUMO	-4.572	0.31	30.95	66.97	1.78
	LUMO+1	-4.553	0.31	30.95	66.97	1.78
$F_{52}ZnPc$	HOMO	-6.787	0.02	1.47	92.93	5.56
	LUMO	-4.512	0.31	31.69	66.06	1.94
	LUMO+1	-4.442	0.31	31.69	66.06	1.94
$F_{52a}ZnPc$	HOMO	-6.944	0.00	0.26	93.66	6.07
	LUMO	-4.811	0.31	31.10	67.45	1.15
	LUMO+1	-4.724	0.31	31.03	66.99	1.68
$F_{64}ZnPc$	HOMO	-7.146	0.00	0.02	94.74	5.22
	LUMO	-4.961	0.31	31.25	67.44	0.99
	LUMO+1	-4.958	0.31	31.25	67.44	0.99

In terms of the PDOS of the FxZnPcs, the LUMO and LUMO+1 state have similar atom contributions. The LUMO and LUMO+1 state in all systems have significant contributions from the Carbon(~ 66%) and Nitrogen (~31%) atoms of the Pc macrocycle. For all systems except $F_{40}ZnPc$, the electron density in the LUMO and LUMO+1 is distributed across two adjacent isoindole units. $F_{40}ZnPc$ is unique in that the electron density distribution of these states is more delocalized across all four isoindole units; much like the HOMO state. Electron density plots of these states are illustrated in Figure 2.5a-f.

The effects of various metal centers on the electron structure of the MPc frontier orbitals is slightly more complicated due to the SOMO levels of the open d-shell metals. The DOS and PDOS of $F_{16}MPc$ are presented in Figure 2.6 a-e

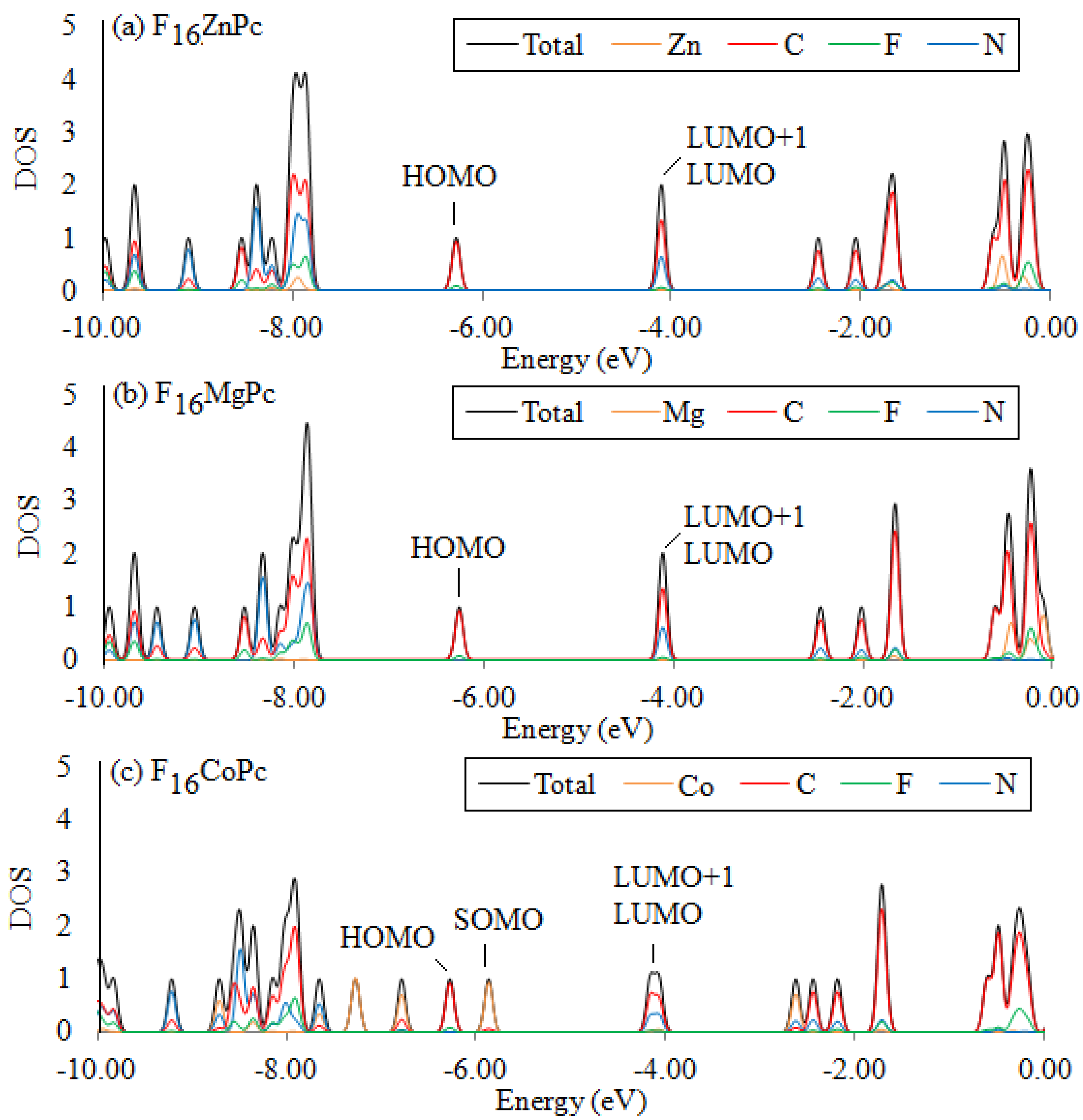

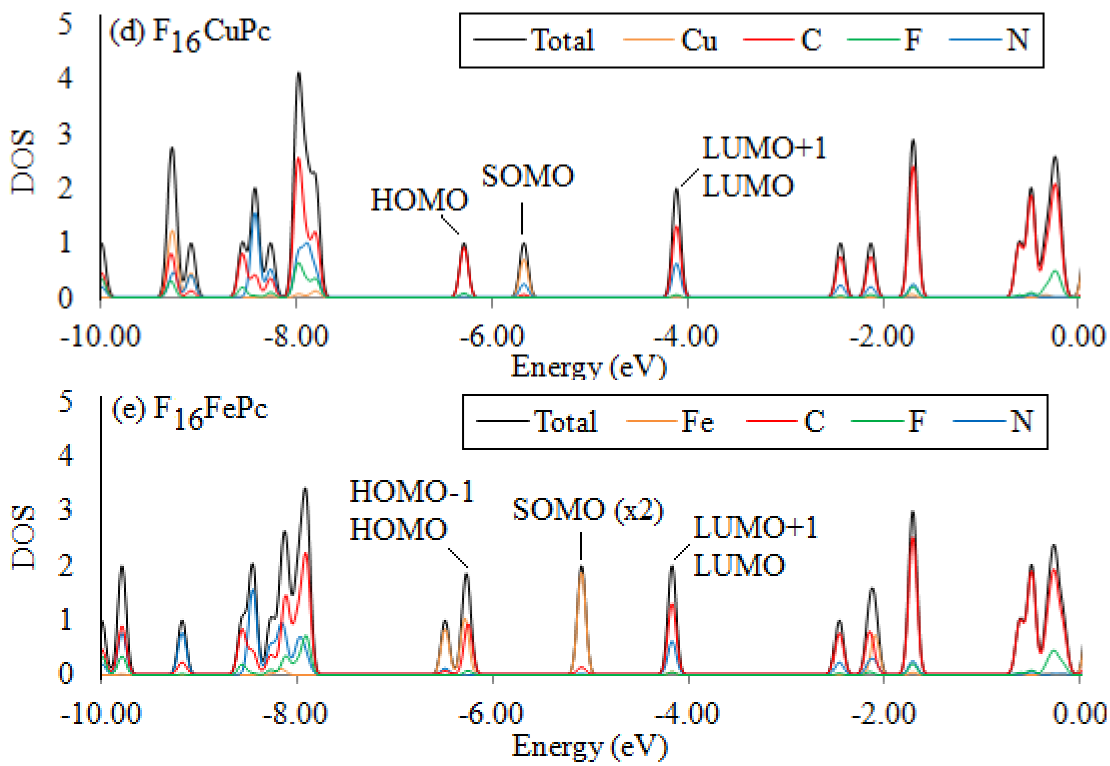

Figure 2.6. DOS and PDOS of (a) $F_{16}ZnPc$, (b) $F_{16}MgPc$, (c) $F_{16}CoPc$, (d) $F_{16}CuPc$, and (e) $F_{16}FePc$.

Considering first the HOMO state of the various MPc. With the exception of $F_{16}FePc$, all systems contain a discrete HOMO with large (~92%) contributions for the Carbon atoms and minor (~8%) contributions for the peripheral Fluorine atoms. The HOMO of $F_{16}FeZn$ has the same atom contributions, but there is an essentially degenerate HOMO-1 state which is entirely center on the central Fe atom. As seen in Figure 2.7 this HOMO-1 MO is exclusively Fe d_{x^2} in nature. The energy difference between these two occupied levels is only 0.032 eV. The HOMO-2 is also entirely Fe centered ($d_{z^2-y^2}$) and located near the HOMO; only 0.201 eV lower in energy than the HOMO-1. The HOMO-1 and HOMO-2 of $F_{16}CoPc$ also have large contributions from the central metal atom, but are located 0.509 eV and 0.996 eV lower in energy than the HOMO, respectively. The F_{16}CoPc HOMO-1 has significant Fe d_{xz} and d_{xy} character (Figure 2.7) and the HOMO-2 is entirely made up of the $d_x{}^2$ atomic orbital (AO). The energy and atom contributions are summarized in Table 2.7.

Table 2.7. Calculated energy and atom contributions of select MOs of F_{16}MPc, where M = Zn, Co, Cu, and Fe.

			% Contribution to MO			
Pc	MO	Energy(eV)	Zn	N	C	F
F_{16}ZnPc	HOMO	-6.286	0.00	0.00	91.87	8.13
	LUMO	-4.114	0.31	31.23	65.93	2.53
	LUMO+1	-4.114	0.31	31.23	65.93	2.53
F_{16}MgPc	HOMO	-6.264	0.00	0.00	91.93	8.06
	LUMO	-4.114	0.00	30.99	66.47	2.54
	LUMO+1	-4.112	0.00	30.99	66.47	2.54
F_{16}CoPc	HOMO	-6.286	0.00	0.00	91.87	8.13
	SOMO	-5.878	93.71	6.65	5.43	0.21
	LUMO	-4.169	2.25	29.92	65.28	2.56
	LUMO+1	-4.076	4.55	31.45	61.64	2.37
F_{16}CuPc	HOMO	-6.294	0.00	0.00	91.85	8.13
	SOMO	-5.682	70.04	24.25	5.60	0.09
	LUMO	-4.123	1.00	31.11	65.38	2.51
	LUMO+1	-4.120	1.00	31.11	65.38	2.51
F_{16}FePc	HOMO-1	-6.291	100.00	0.00	0.00	0.00
	HOMO	-6.259	0.00	0.00	92.00	8.00
	SOMO	-5.097	93.17	0.41	6.19	0.22
	SOMO	-5.097	93.17	0.41	6.19	0.22
	LUMO	-4.172	2.80	30.55	64.14	2.50
	LUMO+1	-4.172	2.80	30.55	64.14	2.50

The open d-shell Cu center does not introduce any new metal centered occupied states near the HOMO. The HOMO-1 level for F_{16}ZnPc, F_{16}MgPc, and F_{16}CuPc is located far (~1.5 eV) from the HOMO state. The degenerate LUMO and LUMO+1 seen in F_{16}ZnPc are also observed for F_{16}MgPc, F_{16}CuPc, and F_{16}FePc. However, for F_{16}CoPc there is a 0.093 eV separation in these two unoccupied levels. The electron density distribution of these states is mostly located on the carbon and nitrogen atoms of opposing isoindole units. Electron density distribution plots for all of these states are provided in Appendix C.

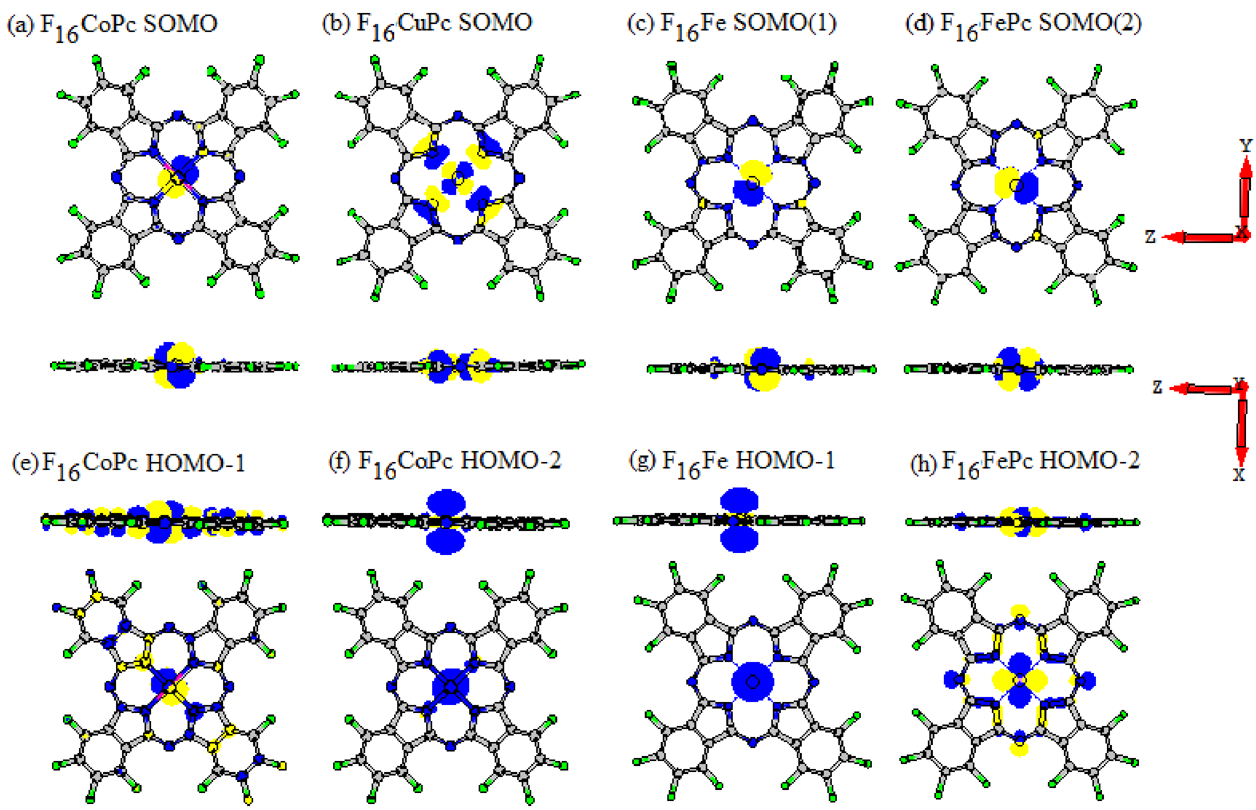

Figure 2.7. Electron density distribution ploys of: (a) F_{16}CoPc SOMO, (b) F_{16}CuPc SOMO, (c) F_{16}FePc SOMO(1), (d) F_{16}FePc SOMO(2), (e) F_{16}CoPc HOMO-1, (f) F_{16}CoPc HOMO-2, (g) F_{16}FePc HOMO-1, and (h) F_{16}FePc HOMO-2. All plots sampled at 0.03 e/au.

The most significant alteration to the electronic structure of the various MPcs is the introduction of SOMO levels between the HOMO and LUMO in the open d-shell systems. Electron density distributions plots for these SOMO states are illustrated in Figure 2.7. F_{16}CoPc has a single SOMO level located 0.408 eV above the HOMO. This MO has large contributions from the Co d_{xy} and d_{xz} AOs. F_{16}CuPc also has a single SOMO, but this level is 0.612 eV higher in energy than the HOMO. This SOMO MO contains significant contributions from the Cu d_{yz} AO, as well as the N p AOs. $F_{16}FePc$ is somewhat unique in that there are two degenerate SOMOs with electron density residing in the Fe d_{xy} and d_{xz} AOs. These degenerate SOMO levels are 1.162 eV above the HOMO.

$F_{34}MPc$ shows the same non-degenerate LUMO and LUMO+1 levels with all metal centers as previously discussed for $F_{34}ZnPc$. The greatest degree of separation (0.163 eV) is observed for $F_{34}CoPc$. This is an expected result given the slight separation between these states seen in $F_{16}CoPc$. The DOS, PDOS, and electron density distribution plots for $F_{34}MPc$ show no significant variation compared to $F_{16}MPc$.

For the $F_{40}MPc$ systems, the increased delocalization of the LUMO and LUMO+1 across the entire conjugated region seen in $F_{40}ZnPc$ is observed for all metals. However, some differences are found in the electron density distribution of the SOMO and HOMO levels. $F_{40}CoPc$ has a SOMO level between the HOMO and LUMO as seen previously in $F_{16}CoPc$ and $F_{34}CoPc$. But the electron density in this MO (Figure 2.8) is located in the Co d_x^2 AO instead of the d_{xy} and d_{xz} AOs, as seen in $F_{16}CoPc$ and $F_{34}CoPc$.

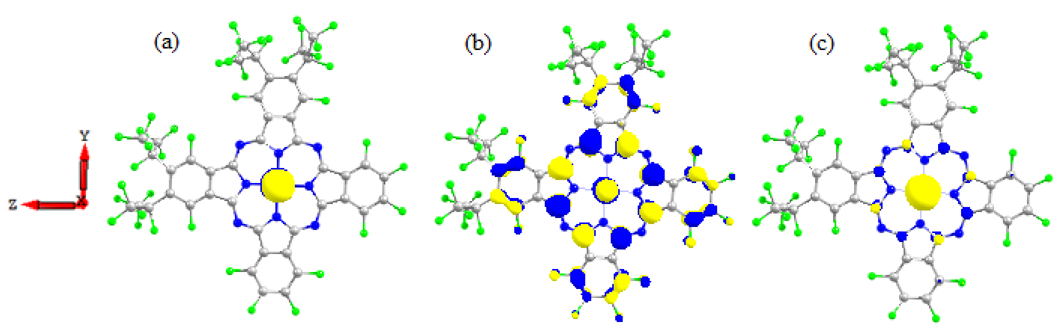

Figure 2.8. Electron density distribution plot of: (a) $F_{40}CoPc$ SOMO, (b) $F_{40}FePc$ HOMO-1, and (c) $F_{40}FePc$ HOMO. Sampled at 0.03 e/a

Additionally, the HOMO state of $F_{40}FePc$ is localized entirely on Fe (d_x^2). The HOMO-1 of $F_{16}FePc$ resembles the highly delocalized HOMO that $F_{16}FePc$ and $F_{34}FePc$ possess. The SOMOs of $F_{16}CuPc$ and $F_{16}FePc$ are consistent with the observations made for $F_{16}MPc$ and $F_{34}MPc$.

For the $F_{52}MPc$, $F_{52}aMPc$, and $F_{64}MPc$, system, there is no significant difference in the DOS, PDOS, and electron density distribution of the unoccupied MOs compared to $F_{16}MPc$. The SOMO of $F_{52}CoPc$ and $F_{52a}Co$ is the same as that seen in $F_{40}CoPc$. The SOMO of $F_{64}CoPc$ resembles that of F16CoPc and $F_{34}CoPc$. The electron density distribution of the HOMO and HOMO-1 of $F_{52}FePc$, $F_{52a}FePc$, and $F_{64}FePc$ is also the same as what was seen for $F_{40}FePc$. DOS, PDOS, and electron density distribution plots for all FxMPcs are available in Appendix C. Additionally, Tables summarizing the energy and atom contributions are provided.

2.3 Conclusions

A systematic study of the effects of peripheral fluorination and metal center on the electronic and structural properties of Pcs has been carried out. Asymmetric substitution patterns on the periphery of the Pc, such as $F_{52}MPc$, leads to a slight bowing of the Pc as indicated by the overall RMSD from D_{4h} symmetry in the central highly conjugated region. It should be noted that the significant bowing of $F_{52}MPc$ observed is most likely caused by the extreme steric hindrance rather than the presence of the strong electron with drawing groups. Overall the calculated bond lengths of the macrocycle are unaffected by the degree of fluorination on the periphery of the Pc. However, the metal-nitrogen bond lengths are dependent upon the metal center. The metal-nitrogen bond lengths for all substitution patterns are found to increase as: Co < Fe < Cu < Zn < Mg. As expected, the binding strength of the metal center to the Pc increases as the metal-nitrogen bond lengths decrease.

These observed trends in metal-nitrogen bond lengths and metal center binding strength is explained through analysis of the partial atomic charges. Although all metal centers in this study have a formal charge of +2, the calculated partial atomic charges when coordinated to the Pc macrocycle range from +0.96 to +1.29. Therefore, the metal-nitrogen bond is significantly covalent in nature. The partial atomic charges correlate with the calculated bond lengths and metal center binding strengths.

Analysis of the electronic structure of the various F_xMPcs presents several interesting findings. A significant lowering of the molecular frontier orbitals is observed with increased fluorination on the periphery of the Pc. All of the MPcs have degenerate or nearly degenerate LUMO and LUMO+1 level. Increasing the asymmetry of the Pc through peripheral substitution increases the separation of these unoccupied MOs. Additionally, Co as the metal center has also shown to separate these unoccupied states. The electron density distribution of the LUMO and LUMO+1 is localized across opposing isoindole units for all F_xMPcs except F_{40}MPc. For F40MPc, the electron density is delocalized across all four isoindole like in the HOMO MO of all MPcs.

Overall, there is very little differences observed when Zn and Mg are used as the metal center. The open d-shell metals (Co, Cu, and Fe) have SOMO levels located between the HOMO and LUMO states. The electron density of these MOs is largely localized on the metal center. Co and Fe also introduce additional metal centered MOs slightly below the HOMO level.

2.4 Computational Details

All calculations are performed using density functional theory (DFT)[27-28] as implemented in the General Atomic and Molecular Electronic Structure System (GAMESS)[29-30] software package. The B3LYP[31-33] functional was employed for all single molecule vacuum state geometry optimizations. Popel's double zeta 6-31G[34-35] basis was used for all atoms. All calculations in this study had convergence tolerances of 1.0 x 10^{-3} Ha/bohr for the geometry optimization and 1.0 x 10^{-5} Ha for the SCF gradient. The selection of basis set and convergence tolerances are modest, but adequate for the relative comparisons in the ground state properties made in this study. It is also shown that this basis set and convergence criteria accuracy reproduce the experimental geometries.

The open d-shell Co and Cu systems were treated as ground state doublets via restricted open-shell Hartree-Fock (ROHF)[49] calculations. The Fe systems were treated as ground state triplets. These ground state multiplicities are consistent with other theoretical investigations on open d-shell MPcs.[42] Electron density distribution plots and optimized structures were visualized using the Chemcraft[41] software package. DOS and PDOS plots were generated via GaussSum.[50]

CHAPTER 3

All-Atom CHARMM Force Field for Perfluoro-Zinc-Phthalocyanines

3.1 Introduction

Metal phthalocyanines have diverse application areas including solar energy conversion,[51-53] electrocatalysis,[54] chemical sensors,[55] organic device electronics,[56] and anticancer therapeutics.[57] Optical and electronic properties can be tuned by rational design of the symmetry and chemical composition of substituents on the molecular periphery.[20-21] The presence of bulky $–C_3F_7$ substituents can be used to influence intermolecular interactions which effect stacking patterns. $F_{34}ZnPn$, $F_{40}ZnPc$, and $F_{64}ZnPc$ exhibit enhanced solubility and favorable electronic structure over the planar $F_{16}ZnPc$ and $H_{16}ZnPc$; which are known to aggregate through π-π interactions, hindering solubility and accessibility to the central metal ion which is believed to be important for catalytic activity.[21] Continued progress the development of material applications will critically depend on the ability to employ classical models on large scale ensembles of these molecules to accurately predict bulk and thin film properties.

Current interest in Pc-based emerging technologies has also driven the need for advanced modeling and simulation techniques to corroborate experimental results and provide a reliable means for novel property prediction. Accordingly, classical modeling methods have been employed to probe the thin film and bulk properties using available or derived force-field models.[58-71] In most cases the model employed was either coarse grain (non-atomistic), or generically derived due to the lack of available force fields specific to Pcs. An all-atom COMPASS[72] force field was recently reported using the COMPASS parameterization method[73] for the $H_{16}CuPc$ molecule.

In this chapter the development of a new set of force-fields parameters within the CHARMM[74] parameterization model specific to perfluoro-modified ZnPcs will be reported. The preparation and X-ray Diffraction (XRD) data of $H_{16}ZnPc$, $F_{16}ZnPc$ and $F_{64}ZnPc$ have been described in the literature,[21,42,75-77] which we use for validation of the force-fields. For all molecules, we also validate the force fields with DFT optimized structures. It is noted that while we predict $F_{40}ZnPc$ to form as a mixture of both the cis- and trans- isomers (Section 3.4); we are interested in the possible stacking interactions in lower symmetry systems, only the cis isomer is included in this chapter.

As with most pseudo-two-dimensional molecular systems, one of the key properties of thin film and bulk ensembles is tendency for molecular stacking interactions. For planar organic molecules composed of poly-cyclic conjugated π molecular orbitals, these interactions are commonly caused by attractive intermolecular short range π-π interaction forces. Clearly, the CHARMM force field model does not explicitly treat π-π interactions but treats them within the non-bonded van der Waals interaction potential. It should be noted that as the subject materials are all heterocyclic molecules, the localized atomic charges are also expected to contribute significantly to molecular stacking interactions. Such interactions are modeled by the inverse square distance-dependent electrostatic force law. It is critically important that the force fields for Pcs adequately predict the intermolecular stacking geometry.

Our development of an explicit all-atom force field for the modified Pc's is derived from a combination of DFT calculations, interaction potentials previously developed for similar functional groups, assuming transferability, and experimental results. Although our force field is not specifically designed to treat π-π stacking interactions; we find that they provide good approximations to XRD determined stacking order and geometry. Our primary objective in developing of a set optimal force field parameters specific to modified perfluoro F_xZnPc

phthalocyanines is to provide an enhanced computational technique aimed at characterizing bulk and thin film properties.

3.2 Force Field Development Methodology

Spin-restricted DFT calculations were performed using the General Atomic and Molecular Electronic Structure System (GAMESS) package[29-30] on the F_xZnPc systems (x= 16, 34, 40, 64) and $H_{16}ZnPc$. Geometry optimization was carried out at the B3LYP level of approximation.[31-33] This is a hybrid GGA method combining five functionals, namely Becke + Slater + HF exchange and LYP (Lee-Yang-Parr) + VWN1 (Vosko-Wilk-Nusair) correlation. In order to select the optimal basis set that provided the best fit for geometry optimization while avoiding prohibitively high computational cost, we compared the 6-31G[37] and 6-31G(d)[38] split valence basis sets. As the materials under study all contain a zinc atom, it is anticipated that larger 6-31G* basis set, which includes d orbital terms for C, N, and F and f orbital terms for Zn, would provide a better fit when comparing optimized molecular geometries with those from experimental XRD data. Full molecule (all atoms unique) geometry optimizations were performed for all five molecules using the 6-31G basis set. We also optimized geometries for the $H_{16}ZnPc$ and $F_{16}ZnPc$ molecules (57 atoms each) using the 6-31G(d) basis set. In order to reduce the computational complexity associated with using the 6-31G(d) basis set for the $F_{34}ZnPc$, $F_{40}ZnPc$ and $F_{64}ZnPc$ molecules (84, 93, and 129 atoms respectively), we optimized the geometries for portions of these molecules that represent the two structural fragments, shown in Figure 3.1. Broken bonds between fragments and the central zinc atom were passivated with hydrogen atoms. The rationale for this approach was driven by our observation that the optimized geometry of molecular core was essentially invariant using either basis set for $H_{16}ZnPc$ and $F_{16}ZnPc$.

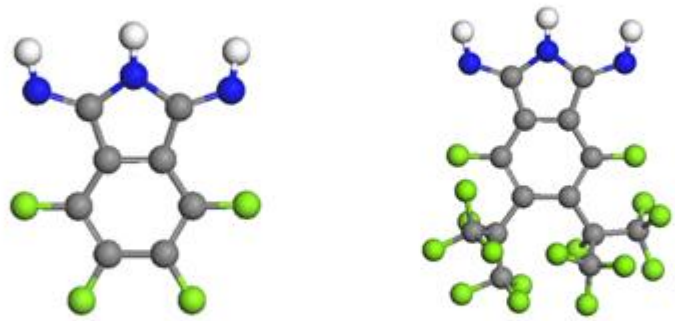

Figure 3.1. Molecular fragments for geometry optimizations using the 6-31G* basis set. Color scheme: gray =C, blue = N, green = F, and white = H

In all cases, the optimized geometries represent those of isolated molecules (vacuum state) rather than those of bulk condensed phases and so do not include the effects of intermolecular interactions. Convergence tolerances were 1.0×10^{-3} ha/bohr for the geometry search. The $H_{16}ZnPc$ and $F_{16}ZnPc$ exhibit inherent D_{4h} symmetry whereas the other F_xZnPc (x = 34, 40, 64) only exhibit global symmetry greater than C_1. Rather than impose symmetry on only the former molecules we optimized all molecules as C_1 symmetry in which all atoms are unique. In order to ensure convergence while avoiding reduced computational efficiency for these comparatively large molecular systems (up to 129 atoms), we selected a convergence tolerance somewhat lower than that typically used for smaller molecular systems. In fact, optimized geometries for $F_{16}ZnPc$ obtained using C_1 symmetry (57 unique atoms) at 1.0×10^{-3} ha/bohr tolerance versus D_{4h} symmetry (8 unique atoms) at 1.0×10^{-5} ha/bohr tolerance did not lead to a noticeable improvement in comparison with experimental XRD data. The tolerance for density gradient changes between consecutive SCF cycles was set at $1.0x10^{-5}$ ha. Equilibrium 2-body bond lengths, 3-body bond angles and 4-body dihedral angles were obtained from the optimized geometries.

Ground state partial atomic charges were obtained from DFT calculations at the B3LYP 6-31G level of approximation as described above for each of the molecular species. Atomic charges were calculated using the Mulliken,[45-48] and Merz-Kollman[44] methods for comparison. CHARMM 2-, 3-, and 4-body bonded force constants and non-bonded interaction potential were obtained from previously published force fields for functionally related molecular systems and used as-is assuming transferability.[58,78]

Validation of the force fields was performed by comparing intra- and inter-molecular geometry properties from MD simulations with DFT calculations with available experimental results. All MD simulations were carried out using NAMD.[79] We conducted MD simulations on bulk simulation cells as well as single crystal unit cells based on available experimental XRD data. MD bulk simulation cells contained 256 molecular species. The simulation cells were initially amorphized at a temperature of 600K to eliminate initial state effects followed by annealing to 300K until equilibrium was achieved. All high temperature amorphizations were done under canonical NVT ensemble conditions (Langevin dynamics) and equilibrated under NPT ensemble conditions at 300 K and 1 atm. All temperature and pressure coupling was done using the Langevin coupling scheme.[80] The time step in all MD simulations was 1 fs. Bulk system MD simulations were found to achieve stable equilibrium in the volume, pressure and ensemble energy within 1-5 ns of simulation time. The resulting equilibrium bond lengths, angles dihedrals and intermolecular geometries were compared to DFT and available XRD data results.

As previously mentioned; three of the molecular systems, XRD crystal structures have been previously published,[21,76-77] namely $H_{16}ZnPc$, $F_{16}PcCu$, and $F_{64}PcCu$. These materials crystalize in the $P\bar{1}$, $P2_1/a$ and $P2_1/n$ space groups respectively. It should be noted that the $F_{16}PcCu$ and $F_{64}PcCu$ XRD refinement were done for the Copper complexes and that the $F_{64}PcCu$ crystal refinement contained co-crystallized ethyl acetate solvent. MD simulations of the lattice structures were conducted under NPT conditions with adjustable cell parameters using Langevin dynamics for pressure and temperature coupling. The simulations were run at 1 fs time steps for 0.5 ns time length trajectories until equilibrium was reached.

Employing source code developed by Rory Vander Valk, the intermolecular stacking order was determined by defining a unit vector normal to the molecular plane for each molecule in the ensemble. This vector was defined as the normalized cross-product of two in-plane vectors between the central zinc atom and two nearest adjacent nitrogen atoms. The dot product of the normal vectors for adjacent molecules within a cut off range was then used to provide a scalar ranging between 0 (perpendicular alignment) and 1 (parallel alignment). The intermolecular pair interaction cut off was taken as 0.6 nm for $F_{16}ZnPc$ and $H_{16}ZnPc$, 0.9 nm for $F_{34}ZnPc$ and $F_{40}ZnPc$, and 1.2 nm for $F_{64}ZnPc$ so as to only include nearest neighbor pair interactions. The sum of all $\boldsymbol{i \cdot j}$ values within the cut off is plotted of as a function of $\cos(\Theta)$ to quantify the stacking order parameters.

In addition, rotational pair correlation functions of the in-plane Zn-N vectors between adjacent molecules were used to determine the relative rotation of stacked molecules within the same cut off distance as for stacking interactions. An ensemble average over the equilibrium MD trajectories for each molecule was used to determine the relative intermolecular rotation of stacked molecules.

3.3 Results

3.3.1 Force Field Parameterization and Validation

The labeling scheme for the atom types is shown in Figure 3.2. For $H_{16}ZnPc$, hydrogen atoms on the periphery result in atom types CAH, CBH, HPA, and HPB replacing CAF, CBF, FPA, and FPB respectively. Substitution of fluorine with perfluoro-isopropyl groups generates the atom type naming scheme for $F_{34}ZnPc$, $F_{40}ZnPc$, and $F_{64}ZnPc$. Diagrams of all molecules are presented in Appendix D.

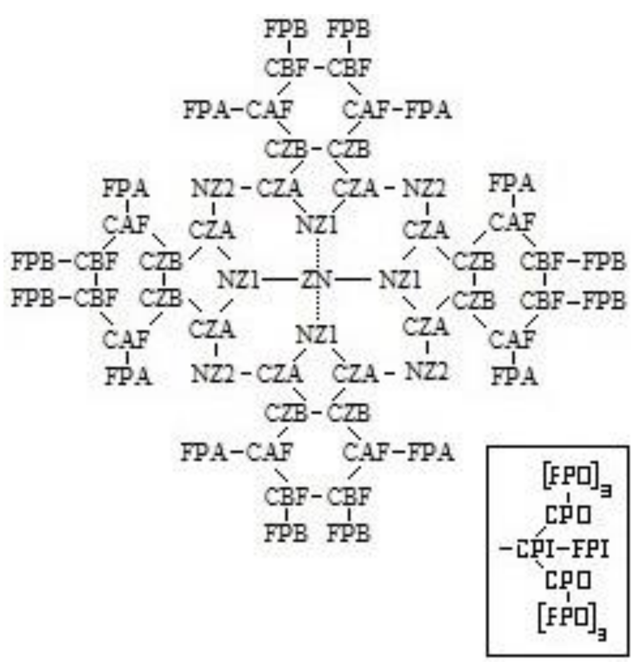

Figure 3.2. Naming scheme for force field atom types. $F_{16}ZnPc$ molecule depicted with perfluoro-isopropyl

Force field parameters for the equilibrium 2-body bond lengths, 3-body angles and 4-body dihedral angles were obtained from DFT calculations. A comparison of the calculated molecular geometry for the two DFT basis sets used (6-31G and 6-31G(d)) with experimental results[21,76-77] is presented in Table 3.1. The percent variance between the experimental XRD values and DFT-calculated values for each basis set do not indicate a significant improvement using the larger B3LYP 6-31G* basis set versus the 6-31G basis set. This is indicated by the overall root mean square deviation (RMSD) indicated in Table 3.1. It should again be noted that the F_{16}MPc XRD data is for the Cu complex, not Zn. This explains the relatively high deviation seen in the ZN-NZI bond lengths.

Table 3.1. Percent variation of calculated bond lengths with experimental XRD for H_{16}ZnPc and F_{16}ZnPc.

	Bond Type	XRD (Å)	6-31G (%)	6-31G* (%)
H_{16}ZnPc				
	ZN-NZ1	1.979	1.219	1.107
	NZ1-CZA	1.369	1.299	0.110
	CZA-NZ2	1.331	0.293	0.391
	CZA-CZB	1.456	0.322	0.227
	CZB-CZB	1.401	1.125	0.414
	CZB-CAH	1.393	0.238	0.201
	CAH-CBA	1.391	0.570	0.165
	CBH-CBH	1.396	1.057	0.458
	CAH-HPA	1.140	4.902	5.149
	CBH-HPB	1.140	4.827	5.096
	RMSD (Å)	-	0.0289	0.0290
F_{16}ZnPc				
	ZN-NZ1	1.952	2.818	2.444
	NZ1-CZA	1.378	0.508	0.581
	CZA-NZ2	1.319	0.910	0.379
	CZA-CZB	1.467	0.545	0.620
	CZB-CZB	1.361	4.445	3.828
	CZB-CAF	1.381	0.724	0.565
	CAF-CBA	1.359	2.575	2.428
	CBF-CBF	1.407	0.552	0.526
	CAF-FPA	1.354	1.329	1.773
	CBF-FPB	1.332	2.041	1.441
	RMSD (Å)	-	0.0285	0.0237

The same comparison for the F_{64}ZnPc molecular fragment (Table 3.2) shows similar results. In fact, both basis set provides acceptable results given that most of the calculated bond lengths shown in Table 4.1 and 4.2 are within 1-2% of experimental values. Given that no clear advantage between basis sets is indicated based on comparisons of optimized geometry with experiment, we adopted the B3LYP/6-31G basis set for development of the bond, angle and dihedral force field parameters. Comparison with experimental XRD data for the calculated 3-body angles for the two DFT basis sets is presented in Appendix D.

Table 3.2. Percent variation of calculated bond lengths with experimental XRD for the F_{64}ZnPc fragment.

Bond Type	XRD (Å)	6-31G (%)	6-31G* (%)
CZA-CZB	1.445	1.150	2.550
CZB-CZB	1.392	0.575	0.776
CZB-CAF	1.387	0.081	0.507
CAF-CBA	1.390	1.593	1.401
CBF-CBF	1.417	2.365	1.531
CAF-FPA	1.335	2.819	0.363
CBC-CPI	1.543	0.259	0.548
CPI-CPO	1.572	0.143	0.580
CPI-FPI	1.367	4.497	0.922
CPO-FPO	1.329	3.772	0.583
RMSD (Å)	-	0.0380	0.0138

A key component of the CHARMM parameterization model, particularly involving molecules with large numbers of heteroatoms, is the atomic charge assignments on each atom. We compared validation results for atomic charges determined using the Mulliken[45-48] and Merz-Kollman[44] (MK) methods. Atomic charges for the various atom types were obtained through DFT calculations as discussed above. It is expected that atomic charges determined using these two methods will vary depending on the level of approximation used to obtain the equilibrium geometry and corresponding electron density profile around each atom. As discussed above, we adopted the 6-31G basis set and so the Mulliken and MK atomic charge models were determined using this basis set for comparison in order to determine the optimum charge parameterization method. Comparisons of the calculated atomic charges derived from both methods are presented in Table B.2. In order to validate the selection of atomic charges derived from the Mulliken or MK methods, we constructed force field sets using equilibrium 2- 3- and 4-body parameters from DFT calculations described above and force constants and non-bonded (van der Walls) interaction parameters from existing parameter sets for similar structural motifs.[58,78]

Force field sets constructed using the Mulliken and MK atomic charge methods were compared using MD simulations of the crystal structures for H_{16}ZnPc, F_{16}PcCu, and F_{64}PcCu. Our results indicate that both atomic charge methods provide acceptable results but we observe a slight improvement using the MK method versus the Mulliken method in the MD simulated crystal structures. Hence, the charge parameters adopted for the force fields are taken from the MK method. The results of this comparison for the H_{16}ZnPc and F_{16}ZnPc are shown in Table 3.3.

The RMSD was calculated for both a molecular mechanics minimization and an MD simulation. Of particular concern among developers of classical force fields that include Zinc containing systems is the charge assigned to the Zinc atom. Although we are not aware of published work describing classical force fields for Zinc-phthalocyanines specifically, previous efforts to develop force fields for related molecular systems containing Zinc have been reported.[81-82] In fact, the atomic charges for Zinc in these reports are similar to those described herein.

Table 3.3. Absolute Percent Variation in Crystal Lattice Parameters Compared with Experimental XRD

	$H_{16}ZnPc$		$F_{16}ZnPc$	
Basis set	6-31G		6-31G	
Lattice param.	Mull.	MK	Mull.	MK
a	6.708	9.110	10.685	2.905
b	5.279	8.867	7.203	1.246
c	2.033	3.321	5.537	2.142
α	0.000	0.000	0.093	0.318
β	1.295	1.586	0.123	0.023
γ	0.000	0.000	2.055	0.225
Density	1.422	0.609	7.305	6.299
RMSD (Å) (minimization)	0.177	0.122	0.533	0.151
RMSD (Å) (MD run)	1.295	1.812	1.188	0.659

A further assessment of the validity of the force fields can be determined by quantifying the geometry obtained from bulk amorphous MD simulated cells and geometry from XRD data and DFT calculations. We find that the bond distances within each molecule type are highly conserved in the MD simulated bulk cells as compared to DFT (B3LYP/6-31G) and XRD results (Table 3.4) further validating the force fields. We expand on the bulk properties of F_xZnPc in the next section.

Table 3.4. Absolute Percent Variation in MD Simulated Bond Lengths from DFT* and Experimental XRD values.

Bond	$H_{16}ZnPc$		$F_{16}ZnPc$		$F_{34}ZnPc$		$F_{40}ZnPc$		$F_{64}ZnPc$	
	DFT	Exp.	DFT	Exp.	DFT	Exp.	DFT	Exp.	DFT	Exp.
ZN-NZ1	2.80	1.62	2.94	1.57	3.52	-	2.99	-	3.09	0.51
NZ1-CZA	1.01	0.23	0.94	0.22	0.58	-	0.80	-	0.94	0.22
CZA-CZB	0.07	0.41	0.55	0.34	0.48	-	0.00	-	0.14	0.55
CZA-NZ2	1.80	1.50	1.80	1.80	1.28	-	1.65	-	1.66	1.43
CZB-CZB	1.13	0.0	0.14	1.64	0.14	-	0.78	-	1.29	2.01
CZB-CAF	1.58	1.80	1.37	1.22	1.07	-	1.59	-	1.51	0.71
CZB-CBC	-	-	-	-	1.92	-	-	-	-	-
CAF-CBF	1.07	1.62	1.94	4.56	1.86	-	1.57	-	1.13	2.73
CAF-FPA	0.19	-	0.29	1.63	0.44	-	0.00	-	0.51	1.71
CAF-CBC	-	-	-	-	-	-	1.74	-	1.14	1.75
CBF-FPB	0.18	-	0.66	3.75	0.51	-	0.80	-	-	-
CBF-CBF	1.35	2.44	2.07	1.49	2.29	-	1.48	-	-	-
CBF-CBC	-	-	-	-	2.81	-	-		-	-
CBC-CBC	-	-	-	-	1.52	-	2.61	-	0.94	1.33
CBC-CPI	-	-	-	-	2.77	-	2.50	-	2.79	2.85
CPI-CPO	-	-	-	-	1.21	-	1.08	-	1.40	1.99
CPI-FPI	-	-	-	-	1.13	-	0.49	-	0.35	4.60
CPO-FPO	-	-	-	-	0.22	-	0.15	-	0.29	4.06

* DFT results are for B3LYP/6-31G

As shown in Table 3.4, most of the MD bond lengths agree with optimized DFT and experimental structures to within 2%. We note that in the case of $F_{16}PcM$ and $F_{64}PcM$ that M = Cu in the XRD data. Furthermore, the crystal structure of $F_{64}PcM$ includes ethyl acetate coordinated to the central metal atom. Although these differences are expected to result in some variation with the solvent-free, Zn complexes reported here, the differences are expected to be sufficiently small that using these experimental results for validation is warranted. Then primary effect of the solvent is expected to alter the planarity and bond lengths at the molecular center, although the results indicate that indeed, this effect is not significant.

The largest degree of variation occurs in the central ZN-NZ1 bond lengths for all molecules. This is most likely caused by the zinc oscillation above and below the molecular plane during the MD simulation, whereas DFT geometry optimization predicts that the zinc atom is coplanar. The ZN-NZ1 bond lengths appear to be in better agreement with experimental XRD values than with DFT predictions. Several experimental bond lengths are significantly greater (>3%) than predicted in the MD simulations. In general, these variations occur in the perfluoropropyl substituents at the molecular periphery. Overall, the DFT and MD values exhibit greater agreement since neither contains coordinated solvent molecules and contain the same metal center atom type. Comparison of the 3-body angles is provided in Table 3.5 which also indicates good agreement.

Table 3.5. Absolute Percent Variation in MD Simulated 3-Body Angles from DFT and Experimental values.

Angle	$H_{16}ZnPc$		$F_{16}ZnPc$		$F_{34}ZnPc$		$F_{40}ZnPc$		$F_{64}ZnPc$	
	DFT	Exp.	DFT	Exp.	DFT	Exp.	DFT	Exp.	DFT	Exp.
NZ1-ZN-NZ1 (adjacent)	0.07	0.40	0.09	0.05	0.07	-	0.11	-	0.12	0.05
NZ1-ZN-NZ1 (opposite)	0.41	2.24	0.51	2.19	0.43	-	0.72	-	0.94	1.97
ZN-NZ1-CZA	0.35	0.37	0.50	0.38	0.63	-	0.54	-	0.54	0.19
NZ1-CZA-CZB	1.21	1.03	1.40	1.88	1.30	-	1.59	-	1.74	0.83
NZ1-CZA-NZ2	0.32	0.98	0.67	2.19	0.03	-	0.64	-	0.57	1.77
NZ2-CZA-CZB	0.86	0.03	0.67	0.56	1.51	-	0.88	-	1.06	0.43
CZA-CZB-CZB	0.82	0.62	0.85	1.45	0.60	-	0.99	-	1.15	0.46
CZA-CZB-CAF	0.50	0.53	0.19	0.83	0.36	-	0.23	-	0.15	1.61
CZA-CZB-CBC	-	-	-	-	0.28	-	-	-	-	-
CZA-NZ2-CZA	0.35	1.04	0.03	3.62	1.66	-	0.11	-	0.25	2.77
CZA-NZ1-CZA	1.64	1.66	1.27	1.45	1.58	-	1.38	-	1.36	0.67
CZB-CAF-CBF	0.23	0.28	0.41	0.76	1.05	-	2.03	-	3.66	4.36
CZB-CAF-CBC	-	-	-	-	-	-	2.35	-	3.66	4.36
CZB-CZB-CAF	0.01	0.20	0.36	0.25	0.31	-	0.22	-	0.38	0.76
CZB-CZB-CBC	-	-	-	-	1.70	-	-	-	-	-

CZB-CBC-CBC	-	-	-	-	1.56	-	-	-	-	-
CZB-CBC-CBF	-	-	-	-	3.85	-	-	-	-	-
CZB-CBC-CPI	-	-	-	-	0.34	-	-	-	-	-
CZB-CAF-FPA	1.07	1.56	1.11	0.95	1.31	-	1.76	-	5.04	3.74
CAF-CBF-CBF	0.17	0.45	0.35	0.21	1.68	-	1.47	-	1.92	1.46
CAF-CBF-FPB	0.22	0.01	0.31	1.61	0.04	-	0.05	-	-	-
CAF-CBC-CBC	-	-	-	-	-	-	3.80	-	1.92	1.46
CAF-CBC-CPI	-	-	-	-	-	-	1.31	-	1.73	2.39
CBF-CBC-CBC	-	-	-	-	1.26	-	-	-	-	-
CBF-CBC-CPI	-	-	-	-	2.38	-	-	-	-	-
CBF-CBF-FPB	0.23	0.14	0.13	1.11	0.20	-	0.03	-	-	-
CBC-CBF-FPB	-	-	-	-	1.12	-	-	-	-	-
CBF-CAF-FPA	0.72	0.95	1.05	1.30	1.26	-	0.78	-	2.97	1.04
CAF-CBF-CPI	-	-	-	-	0.49	-	0.93	-	1.73	2.39
CZB-CAF-CPI	-	-	-	-	0.34	-	-	-	-	-
CBF-CAF-CPI	-	-	-	-	0.06	-	-	-	-	-
CBC-CAF-FPA	-	-	-	-	-	-	1.48	-	2.97	1.04
CBC-CBF-CBC	-	-	-	-	1.26	-	-	-	-	-
CBC-CBC-CPI	-	-	-	-	1.09	-	0.93	-	1.31	1.03
CBC-CPI-CPO	-	-	-	-	0.92	-	0.31	-	0.17	1.20
CBC-CPI-FPI	-	-	-	-	1.91	-	1.37	-	1.11	1.11
CPI-CPO-FPO	-	-	-	-	1.14	-	1.13	-	1.31	1.31
CPO-CPI-CPO	-	-	-	-	3.33	-	3.11	-	3.75	1.40
FPI-CPI-CPO	-	-	-	-	2.28	-	1.93	-	1.84	2.56
FPO-CPO-FPO	-	-	-	-	1.46	-	1.44	-	1.65	1.69

Given the significant agreement of structural intra- and intermolecular properties between the force fields, we conclude that the force field parameters reported herein using the 6-31G basis set and MK atomic charge method are acceptable without further optimization or modification. Our results did not indicate a significant enhancement in optimized geometry using the expanded 6-31G* basis set for vacuum state individual molecules or bulk amorphous systems. However, we did observe a slight improvement in Molecular Dynamics (MD) single crystal unit cell parameters using partial atomic charges derived from MK atomic charge method versus the Mulliken method. The final force field parameters are provided in Appendix D.

3.3.2 MD Simulated Bulk Properties

Among the more important structural properties for bulk Pcs is the extent of aggregation. Specifically, the predicted optical properties of modified Pcs are strongly affected by the formation of stacked associations, particularly among low-dimensional (pseudo-2D) molecular species.[83] It is well recognized that the electronic and optical properties are expected to undergo significant changes resulting from stacking aggregation in which the π-molecular orbitals overlap, possibly leading to excitonic electronic structure. The π molecular orbitals contribute significantly to the HOMO and LUMO orbitals as evidenced in our DFT results. A primary motivation to incorporate bulky substituents on the periphery of Pc molecules is to provide a means to modify stacking aggregation. In this section we present the results of stacking order assessment of MD simulated bulk F_xZnPc systems.

We characterized the stacked pair correlation functions for bulk MD simulation trajectories for each molecule type to determine both the propensity of intermolecular stacking as well as the relative rotational order of molecules in stacked layers. Figure 3.3 shows the ensemble average stacking probability for each material. Stacking order parameters were determined for molecular pairs within a specific cut off distance for each molecular system. Abscissa values range between 0 (perpendicular orientation) and 1 (parallel, stacked). The ordinate indicates the normalized frequency (probability) for stacked molecular pairs.

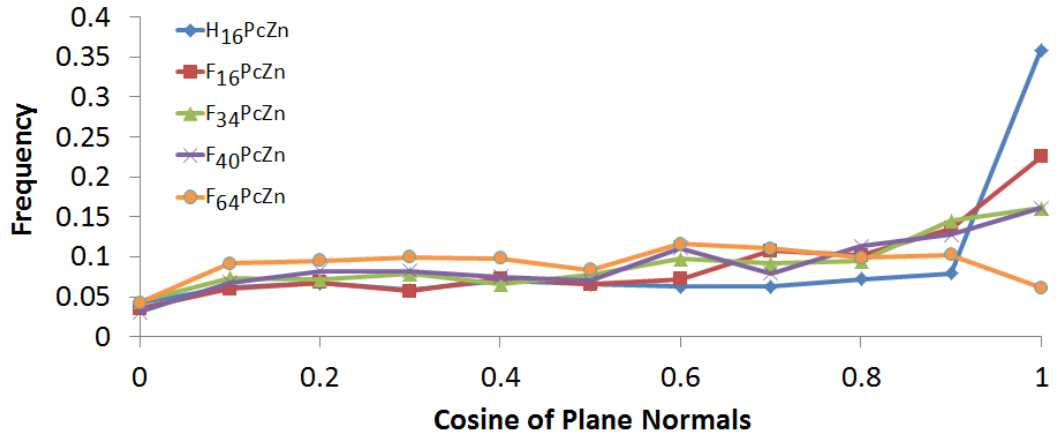

Figure 3.3. MD Simulated stacking propensity for F_xZnPc.

We observe significant stacking for the $H_{16}ZnPc$ and $F_{16}ZnPc$ molecules, as expected, since these molecules lack any bulky peripheral substituents that would induce steric hindrance. The fluorine substituted $F_{16}ZnPc$ molecule exhibits slightly less stacking probability which we interpret as increased charge repulsion among fluorine atoms in this otherwise planar molecule. We also observe a measureable amount of stacking in $F_{34}ZnPc$ and $F_{40}ZnPc$. This can be interpreted as the formation of dimers. $F_{34}ZnPc$ has ¼ of its surface plane hindered leaving ¾ available for stacking interactions while $F_{40}ZnPc$, in the cis- isomer, has ½ of its surface plane available for stacking. The $F_{64}ZnPc$ system does not indicate any significant short range stacking order as expected.

To further evaluate the stacking interaction details, we determined the interaction potential as a function of inter-plane separation between two isolated $F_{16}ZnPc$ and $F_{64}ZnPc$ molecules in a simulation cell (Figure 3.4). The equilibrium distance was found to be 0.328 nm for $F_{16}ZnPc$ and 0.980 nm for $F_{64}ZnPc$ in good agreement with XRD data results of 0.326 and 1.035 respectively. It is interesting to note that the inter-plane stabilization energy, indicated by the well depth, is significantly larger for $F_{16}ZnPc$ (36.2 kcal/mol) than for the more bulky

$F_{64}ZnPc$ molecule (5.3 kcal/mol). This is a strong indication that the bulky peripheral substituents do result in reduced stacking, consistent with the bulk system studies described above.

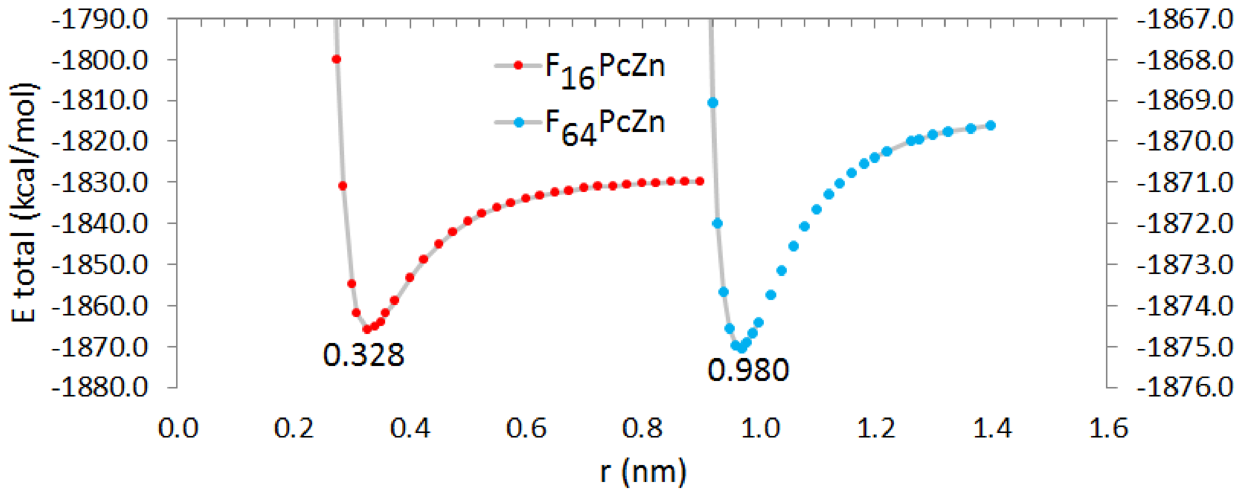

Figure 3.4. Intermolecular Potential Energy vs. separation for $F_{16}ZnPc$ (energy scale at left) and $F_{64}ZnPc$ (energy scale at right).

In addition to the stacking order parameter of the various F_xZnPc, we investigated the rotational orientation of stacked dimers. As mentioned above, $F_{34}ZnPc$ and $F_{40}ZnPc$ have ¾ and ½ of the molecule accessible, respectively, for stacking interactions. By considering only the F_xZnPc's previously determined as stacked ($\cos\theta > 0.95$, Figure 3.3) the relative orientation of the vectors from the central ZN to a NZ1 vector on adjacent molecules can be used to quantify the relative orientation. In this case, we take the cosine of the angle between these vectors on adjacent stacked molecules as a measure of the rotational order parameter, shown in Figure 3.5

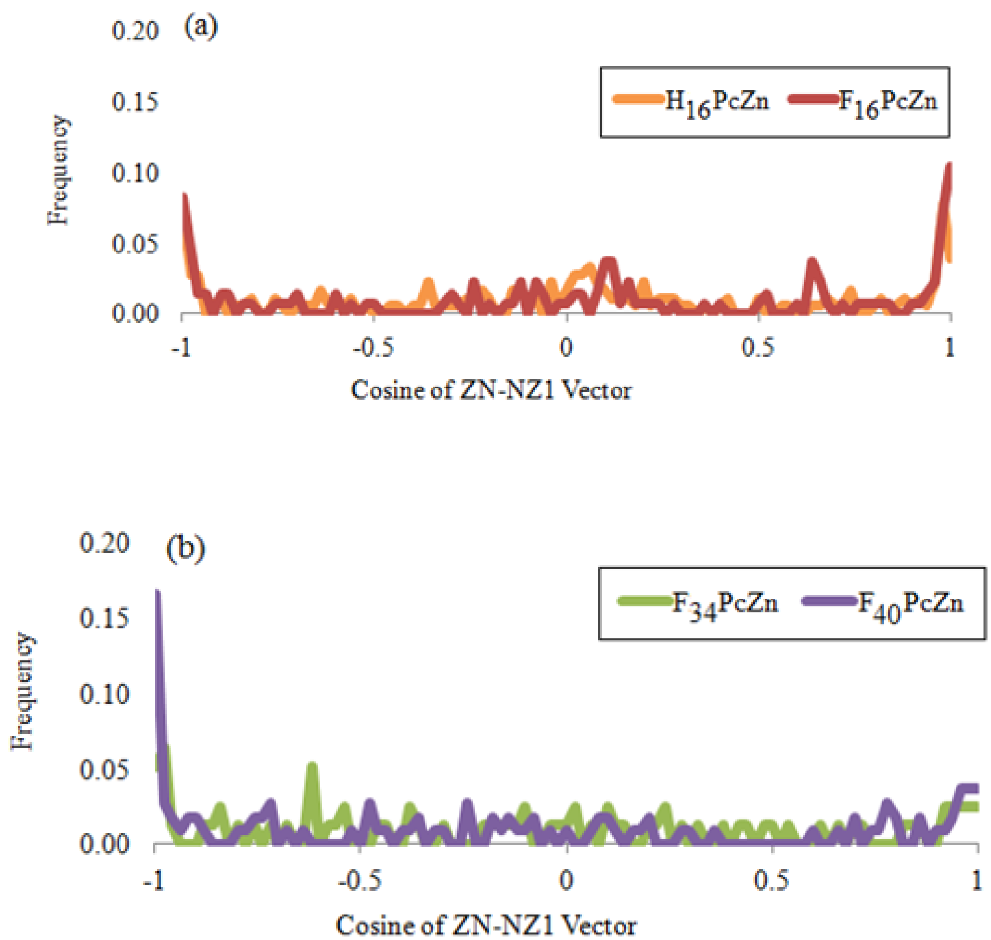

Figure 3.5. Rotational order parameter for (a) H_{16}ZnPc and F_{16}ZnPc; (b) F_{34}ZnPc and F_{40}ZnPc.

Values for F_{64}ZnPc are excluded as they exhibited minimal observed stacking. Values of 1 indicate no rotation, values of zero indicate either 90 or 270 degree orientation, and values of -1 indicate 180 degree rotation. It is evident that stacked F_{40}ZnPc molecules indicate a preferred orientation of 180 degrees as shown in Figure 3.5b. The F_{34}ZnPc also indicates both a preferred orientation of 180 degrees ($\cos\theta = -1$), and another orientation at 135 or 225 degrees ($\cos\theta \cong -0.7$). This indicates that the bulky substituents adopt orientations with the bulky groups staggered by 45 degrees for F34ZnPc. Figure 3.6a-b shows the preferred orientation for F_{40}ZnPc and $F_{34}ZnPc$. It should be noted that all systems undergo a lateral shift which, for the $H_{16}ZnPc$, $F_{16}ZnPc$, and $F_{34}ZnPc$ systems, accommodates parallel orientation ($\cos\theta = 1$).

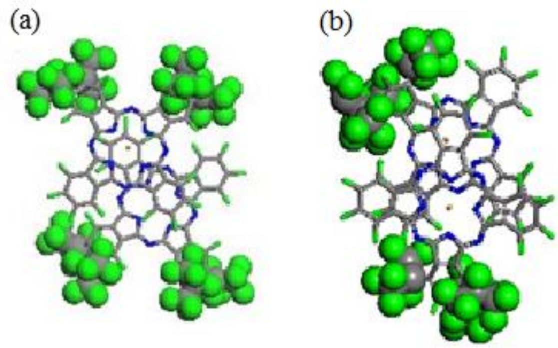

Figure 3.6. Preferred stacking orientation of (a) $F_{40}ZnPc$ at 180 degree orientation and (b) $F_{34}ZnPc$ at 135 degree orientation.

The water diffusion coefficient (*D*) is also calculated for the bulk F_xZnPc systems. The lack of aggregation seen for $F_{64}ZnPc$ results in a lower density bulk system compared to the other F_xZnPcs; which leads to a greater water diffusion coefficient. The water diffusion coefficient was calculated as:

$$D = \frac{\langle x^2 \rangle}{q_i t} \tag{3.1}$$

where $\langle x^2 \rangle$ is the mean-squared displacement of the water molecules over time, q_i is a numerical constant which depends on the dimensionality of diffusion (q_i = 2, 4, 6, for 1, 2, 3 dimensions), and *t* is time. The water diffusion was allowed to equilibrate over 3 ns of simulation time for each system (Figure 3.7). The calculated diffusion coefficients for water in bulk $F_{16}ZnPc$, $F_{34}ZnPc$, and $F_{64}ZnPc$ are $6.32\text{x}10^{-7}$ cm^2/s, $7.18\text{x}10^{-7}$ cm^2/s, and $2.03\text{x}10^{-6}$ cm^2/s, respectively.

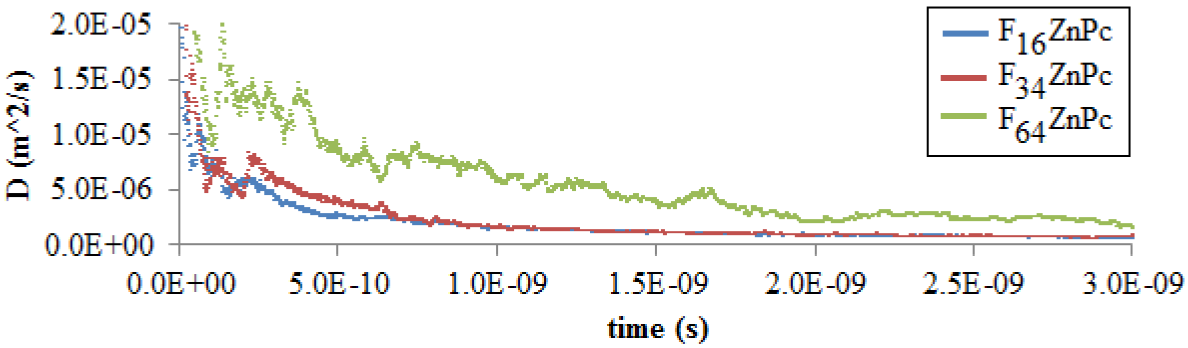

Figure 3.7. Calculated diffusion coefficient of water over time in: bulk $F_{16}ZnPc$ (blue line), $F_{34}ZnPc$ (red line), and $F_{64}ZnPc$ (green line).

3.3.3 MD Simulated Thin Film Properties

In addition to simulated bulk properties, the above developed MD force field has been employed to simulate the formation of Pc thin films. The focus of this study is on how the peripheral $–C_3F_7$ groups effect the growth of the film. This includes calculation of the density of the film created as well as the adsorption energy of each of the layers within the film. While similar MD simulations are underway to investigate the Pc interaction with various TiO_2 surfaces, substrate effects are not included in these simulations. Instead, ideal monolayer coverage is assumed by restricting the motion of the first layer of the film. The target Pcs for this section include the highly aggregating $F_{16}ZnPc$, intermediate aggregating $F_{40}ZnPc$, and extremely bulky (low aggregating) $F_{64}ZnPc$. We have also considered two different starting orientations for the Pcs: (1) the Pcs are orientated parallel to the surface (Figure 3.8a), and (2) perpendicular to the surface (Figure 3.8b). It is noted that this perpendicular orientation would likely require some modification to the molecular structure to incorporate an anchoring group on the periphery.

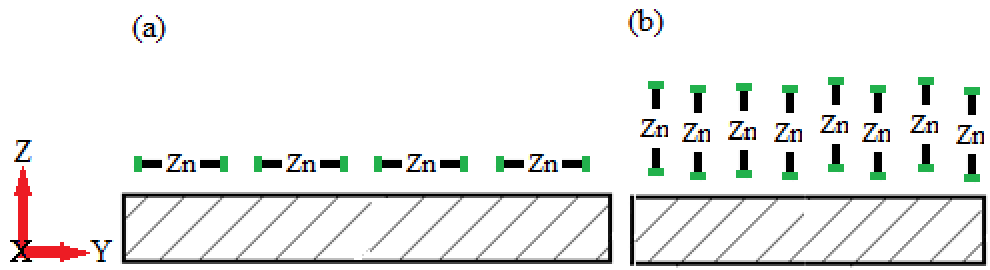

Figure 3.8. Constrained initial layer orientation; (a) parallel orientation and (b) perpendicular orientation.

As with the bulk simulations, all thin film MD simulations were carried out using NAMD.[79] The thin film MD simulation cells contained an initial layer of Pcs which are meant to mimic monolayer coverage on any generic surface. This is accomplished by imposing constraints in the Pc z-coordinate of layer 1 while allowing the Pc to move free in the x-y plane. To effectively model the surface, ~15Å of vacuum space was added in the z-direction. The simulation cells are amorphized at a temperature of ~600K to eliminate initial state effects followed by annealing to 300K until equilibrium was achieved. All high temperature amorphizations were done under canonical NVT ensemble conditions. The equilibration of the system was also done under NVT ensemble conditions to ensure the vacuum space above the film was maintained. Once a layer of Pc molecules was equilibrated, an additional layer was added to the system and the same amorphization and equilibration procedures were employed. All temperature and pressure coupling was done using the Langevin coupling scheme.[80] The time step in all MD simulations was 1 fs.

Considering first the Pc thin films with parallel orientation to the surface, the $F_{16}ZnPc$ system is presented in Figure 3.9a-b. This system consists of five layers of $F_{16}ZnPc$.

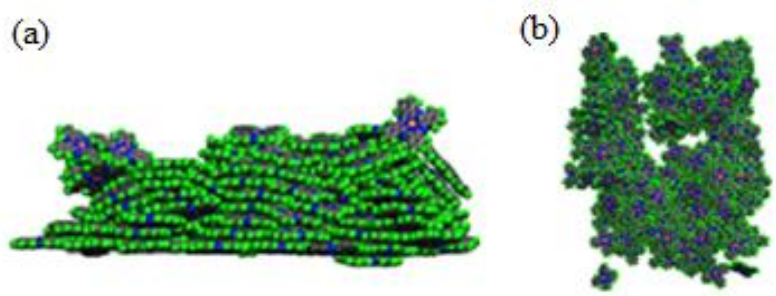

Figure 3.9. Equilibrated $F_{16}ZnPc$ thin film oriented parallel to the surface viewed: (a) edge on and (b) top down.

Given the high stacking propensity of $F_{16}ZnPc$, this film forms highly stacked layers perpendicular to the surface. The degree of stacking in all layers (Figure 3.10) of the $F_{16}ZnPc$ film is greater than that found in the bulk simulations. The high frequency of stacking found in layers 2, 3, and 4 lead to the formation of tall stacked columns. However, the formation of these columns causes voids to develop throughout the film to develop and leads to a low density film. The final density of this film is calculated to be 0.6251 g/cm^3.

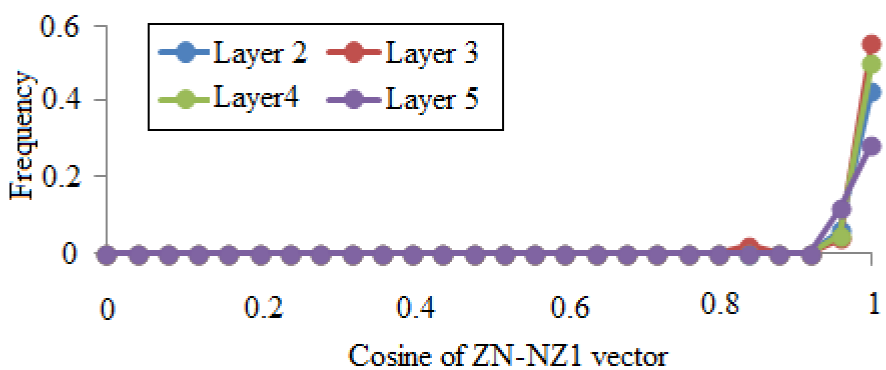

Figure 3.10. Calculated degree of stacking in the $F_{16}ZnPc$ thin film orientated parallel to the surface. Values on 1 indicate perfectly stacked Pcs.

Increased stacking in the layers will lead to larger adsorption energy due to the greater π-π interactions between Pc's. Given the large degree of stacking found in each layer of this system the adsorption energy for each layer is significant. The calculated adsorption energies for each layer are presented in Table 3.6.

Table 3.6. Average adsorption energy of each layer in the $F_{16}ZnPc$ thin film oriented parallel to the surface.

Layer	Adsorption E (kcal/mol)
2	-63.79
3	-61.54
4	-61.56
5	-55.12

Thin films of $F_{40}ZnPc$ in which the fixed layer of Pcs is orientated parallel to the surface are depicted in Figure 3.11. This system consists of five layers of $F_{40}ZnPc$.

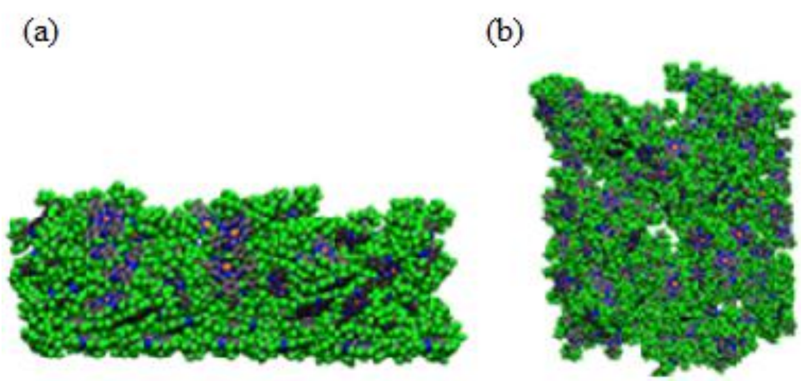

Figure 3.11. Equilibrated $F_{40}ZnPc$ thin film oriented parallel to the surface viewed: (a) edge on and (b) top down.

The $F_{40}ZnPc$ film layered parallel to surface forms a slightly more dense film than that of $F_{16}ZnPc$ in the same orientation. This is an expected result given the introduction of the bulky groups on half of the $F_{40}ZnPc$ molecule reduced the stacking (Figure 3.12) and not as many voids in the film are observed. The calculated density of this film is 0.7459 g/cm^3.

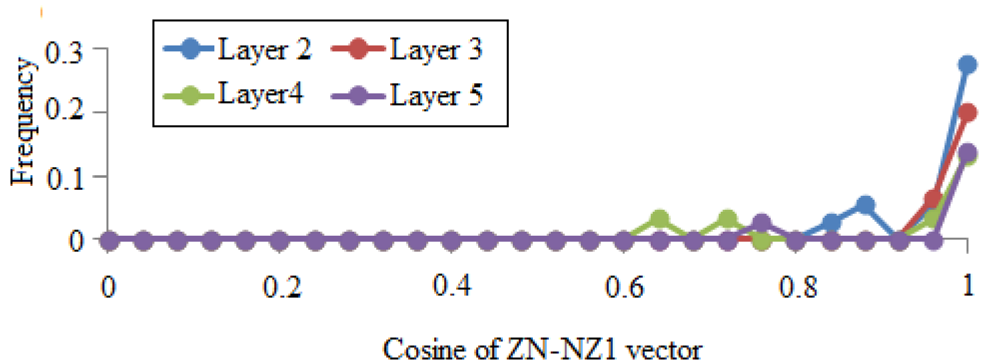

Figure 3.12. Calculated degree of stacking in the $F_{40}ZnPc$ thin film orientated parallel to the surface. Values on 1 indicate perfectly stacked Pcs.

As expected, the adsorption energies for layers 2 and 3, where the degree of stacking is greater, are significantly greater than layers 4 and 5. However, all layers in this system have lover adsorption energies than the $F_{16}ZnPc$ film of the same orientation. This is a direct effect of the lower stacking caused by the steric hindrance of the $F_{40}ZnPc$ molecule. The adsorption energy of each layer in this system is presented in Table 3.7.

Table 3.7. Average adsorption energy of each layer in the $F_{40}ZnPc$ thin film oriented parallel to the surface.

Layer	Adsorption E (kcal/mol)
2	-40.11
3	-45.91
4	-23.34
5	-28.49

Thin films of $F_{64}ZnPc$ in which the restricted layer of Pc's is orientated parallel to the surface are depicted in Figure 3.13. This system consists of five layers of $F_{64}ZnPc$.

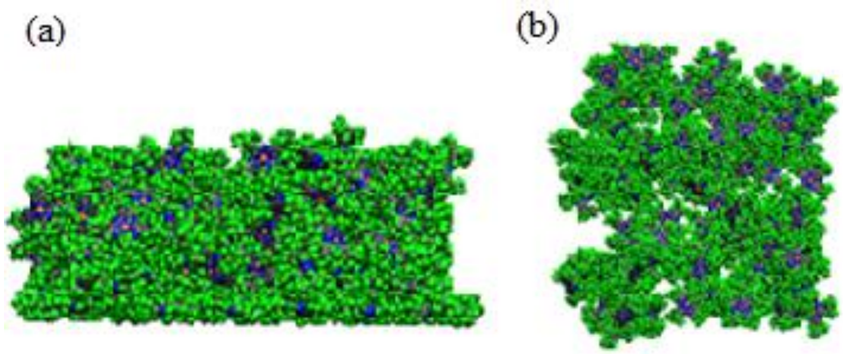

Figure 3.13. Equilibrated $F_{64}ZnPc$ thin film oriented parallel to the surface viewed: (a) edge on and (b) top down.

As seen with the $F_{40}ZnPc$ films, the introduction of the bulky $–C_3F_7$ groups hinder aggregation throughout the $F_{64}ZnPc$ film. Since the $F_{64}ZnPc$ molecule is fully substituted with the bulky substituents, there is very little stacking observed in this film. This observation is also present in the bulk simulations of $F_{64}ZnPc$. This indicates that all additional layers of this film have little interaction with the previous layers. Therefore, adsorption energies for each layer are relatively low compared to that of $F_{16}ZnPc$ and $F_{40}ZnPc$ in the same orientation. The calculated adsorption energies are displayed in Table 3.8. In addition of the low adsorption energies, the lack of stacking caused by the bulky substituents also leads to the lowest film density. The calculated film density is 0.4974 g/cm^3.

Table 3.8. Average adsorption energy of each layer in the $F_{64}ZnPc$ thin film oriented parallel to the surface.

Layer	Adsorption E (kcal/mol)
2	-20.17
3	-16.62
4	-13.58
5	-15.44

We will now examine the Pc thin films in which the initial constrained layer is oriented perpendicular to the surface. It is noted again that this type or Pc orientation is not expected to occur without the introduction of some anchoring group(s) on the periphery of the molecule. Thin films of $F_{16}ZnPc$ in which the fixed layer of Pc's is orientated perpendicular to the surface are depicted in Figure 3.14. This system consists of five layers of $F_{16}ZnPc$.

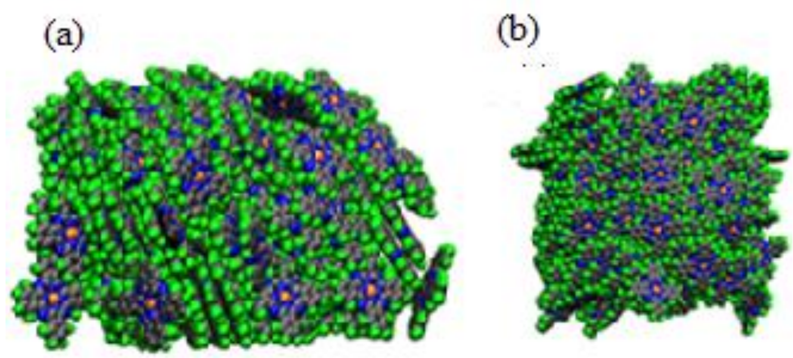

Figure 3.14. Equilibrated $F_{16}ZnPc$ thin film oriented perpendicular to the surface viewed: (a) edge on and (b) top down.

As seen in Figure 3.13, having the initial Pc layer orientated perpendicular to the surface leads to a more dense film than when the initial layer is parallel to the surface. The calculated density of this system is 1.62 g/cm^3. The orientation of the layers is important for the adsorption energy for each layer. As seen in the previous $F_{16}ZnPc$ film which had a parallel orientation; the strength of adsorption is dependent upon the amount of available π-π interactions. These stacking interactions are limited in the perpendicular orientation which results in low calculated adsorption energies (Table 3.9).

Table 3.9. Average adsorption energy of each layer in the $F_{16}ZnPc$ thin film oriented parallel to the surface.

Layer	Adsorption E (kcal/mol)
2	-15.57
3	-24.40
4	-28.80
5	-47.60

An interesting trend is observed in the calculated adsorptions energies presented in Table 4.9. The adsorption energy of each additional added to this system increases. This is explained by examining the Pc orientation in each of the layers. With layer 1 restricted to maintain the perpendicular orientation, there is very little opportunity for π-π interactions with layer 2. Some of the Pc's of layer 2 have settled in between the initial Pcs but not enough to lead to a strong adsorption of layer 2. However, the adsorption energy in layers 3, 4, and 5 increases, this is consistent with these layers reverting to a parallel orientation in an attempt to maximize their π-π interactions. As the Pc's of each addition layer tilt closer to a parallel orientation, more of the molecule is available for π-π interactions and the calculated adsorption energies increase. Nevertheless, the adsorption energies for the parallel F_{16}ZnPc film are still far greater than this perpendicular film.

Thin films of F_{40}ZnPc in which the initial layer of Pc's is orientated perpendicular to the surface are depicted in Figure 3.15. This system contains four layers of F_{40}ZnPc.

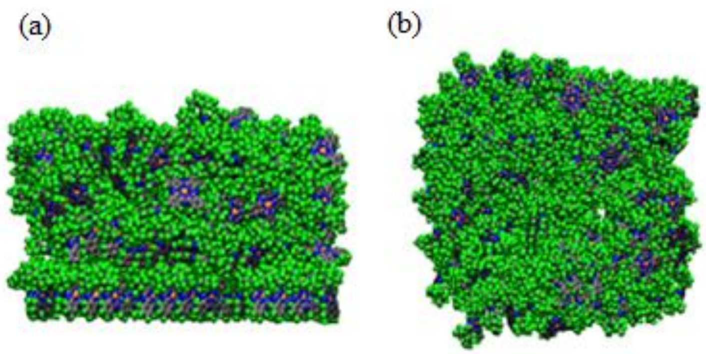

Figure 3.15. Equilibrated F_{40}ZnPc thin film oriented perpendicular to the surface viewed: (a) edge on and (b) top down.

There is little order to this film with the exception of layer 1 which is restricted in the x-coordinate. As addition layers are added the density of the film slightly increases but the lack of stacking interactions results in a random layering in this $F_{40}ZnPc$ film. Untimely this leads to relatively low film density. The calculated film density is 0.77 g/cm^3. As expected, the lack of strong stacking interactions affects the adsorption energy of each layer in this system. The calculated adsorption energy for each layer is shown in Table 3.10.

Table 3.10. Average adsorption energy of each layer in the $F_{40}ZnPc$ thin film oriented parallel to the surface.

Layer	Adsorption E (kcal/mol)
2	-6.86
3	-14.06
4	-11.09

The calculated adsorption energy for all of the layers are significantly less than any of the previous films studied. There is a slight increase in adsorption energy for layers 3 and 4 which is caused by the Pcs in these layers beginning to adapting a more parallel orientation; much like what was seen in the $F_{16}ZnPc$ film of perpendicular orientation but to a much lesser degree.

Thin films of $F_{64}ZnPc$ orientated perpendicular to the surface showed little adsorption in all layers. Not an unexpected result given the high degree of bulky substituents on the periphery of the molecule. This caused the creation of a film in this orientation to be extremely difficult. The lack of adsorption leads to the $F_{64}ZnPc$ molecules to fill the vacuum space instead of layering onto the surface (Layer 1). This system is illustrated in Figure 3.16.

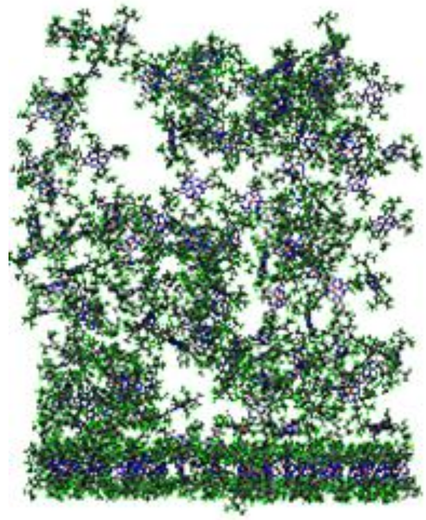

Figure 3.16. $F_{64}ZnPc$ thin film oriented perpendicular to the surface viewed edge on.

3. 4 Conclusions

The force fields described herein validate favorably with available experimental and calculated results. We have used the parameters to model bulk and thin film systems and found that the degree and orientation of stacking in low to moderately bulky molecules is constant with available experimental results. Of special note is the intermolecular interaction geometry of low symmetry F_xZnPc (x = 34, 40) molecules containing partial steric hindrance on the molecular periphery. These molecules are predicted to exhibit directed stacking orientation in which the bulky substituents are oriented so as to minimize steric interactions. For $F_{64}ZnPc$, the most bulky of the molecules investigated, little or no intermolecular stacking interactions are indicated in both bulk and thin film studies.

In the thin film simulations of F_xZnPc with two different layering orientations it is found that the introduction of the bulky $–C_3F_7$ groups on the periphery of the molecule hinder stacking with in turn results in lower density films with weaker adsorption of the various layers. F16ZnPc shows the strongest adsorption which is an expected result due to the propensity of aggregation through stronger π-π stacking interactions seen in the bulk simulations. Assuming a strong adsorption to the substrate, to build a thin film the adsorption of layer 2 to layer 1 is of most interest. If layer 2 does not adsorb to layer 1 there will be no growth in the film. The calculated adsorption energies of layer 2 for all systems studied are summarized in Table 3.11.

Table 3.11. Summary of the calculated adsorption energies for F_{16}ZnPc, F_{40}ZnPc, and F_{64}ZnPc oriented parallel (=) and perpendicular (⊥) to the surface.

Film	Adsorption E (kcal/mol)
F_{16}ZnPc =	-63.79
F_{16}ZnPc ⊥	-15.57
F_{40}ZnPc =	-40.11
F_{40}ZnPc ⊥	-6.86
F_{64}ZnPc =	-20.17
F_{64}ZnPc ⊥	-

The lower adsorption energies of the modified Pc's compared to F16ZnPc also leads to films of lower density. The calculated final film densities of all systems studied are summarized in Table 3.12.

Table 3.12. Summary of the calculated film densities for $F_{16}ZnPc$, $F_{40}ZnPc$, and $F_{64}ZnPc$ oriented parallel (=) and perpendicular (┴) to the surface.

Film	Density (g/cm^3)
$F_{16}ZnPc$ ═	0.6251
$F_{16}ZnPc$ ┴	1.6208
$F_{40}ZnPc$ ═	0.7459
$F_{40}ZnPc$ ┴	0.7653
$F_{64}ZnPc$ ═	0.4974
$F_{64}ZnPc$ ┴	-

CHAPTER 4

Theoretical Investigation of Chemically Robust Phthalocyanines for Solar Energy Conversion

4.1 Introduction

4.1.1 n-Type Dye Sensitized Solar Cells

Since their invention in 1991 by Michael Grätzel and Brian O'Regan,[84] dye-sensitized solar cells (DSSCs) have attracted extensive research attention and have become one of the most promising renewable energy sources.[85-86] The main advantages of DSSCs include:[87] (a) stable performance under nonstandard conditions of temperature, irradiation, and solar incidence angle; (b) low cost; (c) availability and environmentally friendly materials; and (d) semi-transparency and multicolor range possibilities. Commercialization of Grätzel cells are currently underway in the European Union and are predicted to be a significant source of renewable energy by 2020.[88] Conventional Grätzel cells consist of a photosensitized anode and a liquid electrolyte solution. The general operational scheme for a Grätzel cell is presented in Figure 4.1.

The cell is activated by photoexcitation of the adsorbed sensitizer. From the excited state (D^*) of the dye material an ultrafast electron transfer into the conduction band (CB) of the working electrode occurs. The oxidized form of the sensitizer (D^+) is then regenerated by oxidizing iodide in the liquid electrolyte solution to iodine and eventually into triiodide. The triiodide is then regenerated at the counter electrode. There are also several charge recombination processes that must be considered in conventional Grätzel cells. These processes are shown as broken lines in Figure 4.1 and include; relaxation of the sensitizer excited state prior to electron transfer, electron transfer from the electrode to the oxidized form the sensitizer, and electron transfer from the electrode to the redox mediator in the electrolyte solution.

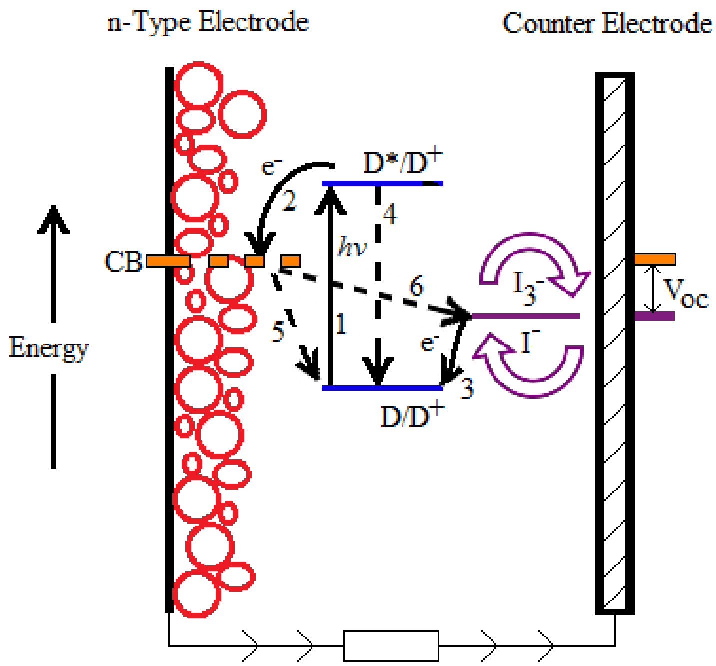

Figure 4.1. Schematic diagram of the electron transfer processes occurring in a Grätzel cell.

The overall energy conversion efficiency of DSSCs is thought to be governed by four fundamental properties:[85] (a) the light-harvesting efficiency of the sensitizer; (b) the charge injection efficiency from the sensitizer to the electrodes; (c) the electron transport efficiency in the electrodes; and (d) the sensitizer regeneration efficiency of the liquid electrolyte solution. Extensive experimental and theoretical efforts to understand and tune these properties of Grätzel cells over the past two decades have led to conversion efficiencies as high as 13%.[89] However, all of the key components of DSSCs including; semiconductor films, dye sensitizers, and the redox electrolyte, are still under great investigation. This is evident in numerous recent review articles accessing the progress being made in n-DSSCs development.[90-104]

4.1.2 n-Type Sensitizers

One of the largest advantages in the DSSC design is the ability to molecular engineer a vast amount of diverse sensitizing materials. For efficient solar energy conversion, the ideal n-type photosensitizer must encompass several essential properties, [105] including: (a) the ability to absorb incident light covering the visible to near-infrared region of the solar spectrum; (b) a LUMO state above the edge of the CB of the metal oxide electrode to ensure electron injection; (c) a sufficiently low HOMO state to allow electron donation from the liquid electrolyte solution; and (d) enough chemical and thermal stability to endure ~20 years of exposure to sunlight without significant degradation. It is also common practice to incorporate a carboxylate or phosphonate group(s) into the molecular framework to securely anchor the sensitizer to the surface of the electrode.

Since its introduction in 1993,[106] cis-RuL_2-$(NCS)_2$ (N3 dye) has been one the most efficient charge transfer sensitizers for nanocrystalline TiO_2 films. More recently, another Ruthenium based sensitizer, black dye N749, has also emerged as an excellent photosensitizer with reported energy conversion efficiencies as high as 11.1%.[107] However, Ru based dyes contain several major drawbacks, including the high cost and limited availability of Ru. In an attempt to tackle these issues, many metal free organic based sensitizers have also been synthesized and applied to n-type DSSCs.[108] A conversion efficiency as high as 9.1% has been reported by Hwang et al. based on the metal free TA-St-CA dye.[109] The most promising n-type sensitizers to date have emerged based on zinc-porphyrin dyes. The TD2-*o*-C8 and SM315 dyes have shown efficiencies of 12.3% and 13.0%, respectively.[89,110] These zinc-porphyrin sensitizers represent the highest energy conversion efficiencies to date.

Although the zinc-porphyrin sensitizers present the highest energy conversion efficiencies, their low photostability and molar extinction coefficients in the red-near IR region of the solar spectrum are major disadvantages. These shortcomings may be overcome by employing phthalocyanines molecules (porphyrin analogues). Pcs are known for their high molar extinction coefficients and remarkable robustness.[111-113] Additionally, Pcs are chemically and thermally stable, thus providing the perfect light harvesting sensitizers. Although a significant amount of progress has been made in Pc based DSSCs,[16,114-125] they do tend to suffer from strong aggregation, which is thought to limit the energy conversion efficiencies.[126] To enhance the conversion efficiencies of Pc sensitizers, bulky groups are often introduced on the periphery of the Pc to limit the degree of aggregation. Efficiencies as high as 4.6% have been reported from ZnPc with bulky 2,6-diphenylphenoxy groups.[127]

However, Aranyos et al. have reported several metal-free and ZnPcs without bulky substituents with conversion efficiencies ranging 5-9%.[128] Interestingly, not only the adsorbed monolayer displayed electron injection into TiO_2, but the aggregating Pcs on top were found to contribute to the overall photocurrent. This beneficial aggregation has also been reported for porphyrin dimers.[129] Additionally, the aggregating Pcs in Aranyos report were introduced without any conventional anchoring groups.

4.1.3 Semiconductor Metal Oxide Electrode

Titanium dioxide (TiO_2) is by far the most utilized semiconductor oxide in n-type DSSCs. TiO_2 is found in three crystal forms: rutile, anatase, and brookite. The most thermodynamically stable form of TiO_2 is rutile. However, anatase is typically preferred for solar energy conversion applications due a slightly larger band gap as well as a higher CB edge, which leads to greater open circuit voltages. Rutile also has a smaller specific surface area compared to anatase which results in a lower amount of dye molecules adsorbed on rutile films compared to anatase. The packing density of the rutile form is also larger resulting in slower electron transport. One of the few drawbacks of TiO_2 is a relatively low electron mobility (0.1 – 1 $cm^2\ V^{-1}\ s^{-1}$).[130]

Several other semiconductor oxides have also been investigated in n-type DSSCs. Zinc oxide (ZnO) has a similar band structure as TiO_2 but relatively high electron mobility (1 – 5 $cm^2\ V^{-1}\ s^{-1}$)[131], which makes it a potential alternative electrode material. The first n-DSSC based on ZnO was sensitized with the N3 dye and produced a modest efficiency of < 1%. This initial low conversion efficiency was attributed to the tendency of the ZnO film to dissociate and form $Zn2^+$/N3 aggregates. More recently, this obstacle with ZnO has been overcome[132-133] and efficiency values as high as 6.58% have been reported.[134]

Another potential alternative to TiO_2 is Tin oxide (SnO_2). SnO_2 presents two major advantages over that of TiO_2 and ZnO. First, the electron mobility is three orders of magnitude greater than TiO_2 (100-200 $cm^2\ V^{-1}\ s^{-1}$).[135] SnO_2 also has a larger band gap than both TiO_2 and ZnO. The band gap of TiO_2 and ZnO is ~3.2 eV, while SnO_2 has a gap of ~3.8 eV. Under UV illumination photoexcitation of the semiconductor oxide results in charge separation within the oxide. The resulting holes in the semiconductor VB are capable of oxidizing the dye material; leading to more rapid degradation of the sensitizer. The larger band gap of SnO_2 would create fewer of these oxidative holes and, in turn, increase the overall stability of the n-DSSC.

In addition to a greater band gap, the energetic location of the SnO_2 bands differs from TiO_2 and ZnO. The CB edge of SnO_2 is ~0.6 eV lower in energy.[136] The advantage of this is the LUMO state of most common n-type sensitizers will be deeper into the CB of SnO_2, which would facilitate electron injection upon photoexcitation. Conversely, the HOMO state of the same dyes would be much closer to the CB edge which would promote charge recombination between injected electrons and the resulting hole on the sensitizer. In fact, the reported performances of SnO_2 based DSSCs are less than that of TiO_2.[137] In recent years, optimization of the cell design by introducing addition isolating oxide layers of ZnO, MgO, or Al_2O_3 onto the SnO_2 electrode have resulted in efficiencies as high as 7%.[138]

4.1.4 Electrolyte Solution

The final fundamental component of the DSSC design to be discussed is the electrolyte solution. The main function of the electrolyte in n-DSSCs is to collect electrons at the cathode and shuttle them across the cell to regenerate the oxidized dye material. The most commonly employed electrolyte is the iodide/triiodide redox couple. This electrolyte is mainly a favorite due to the large (~0.7 eV) open circuit potential when paired with TiO_2, which as previously stated, is the most common semiconductor oxide in n-DSSCs.[139] However, as with all liquid electrolytes, the iodide/triiodide redox couple does display some undesirable properties. Temperature stability issues result in difficulties in achieving long term durability. The iodide/triiodide concentration within the cell is also an important issue that needs to be considered. At low concentrations, efficient regeneration of the dye becomes problematic and promotes the charge recombination reactions between the semiconductor oxide and the dye. At high concentrations, charge recombination between the semiconductor oxide and I^-/I_3^- increases which ultimately results in a lowering of the DSSC efficiency. The I^-/I_3^- also absorbs small amounts of visible light, which is intensified at high concentrations.[140]

Several other redox couples have also been studied in an attempt to further increase the open circuit voltage as well as resolve the stability issues of I^-/I_3^-. Some of these alternative redox couples include: Br^-/Br_3^-, $SCN^-/(SCN)_2$, $SeCN^-/(SeCN)_3^-$, $Fe(CN)_6^{3-/4-}$, and Co(II)/Co(III).[141] Room temperature ionic liquids have also shown promise as liquid electrolytes.[142] The structure of these solutions allow for chemical and thermal stability as well as high ionic conductivity, while acting as both an electron source and as a solvent.[143] Efficiencies of >8% have been reported for these types of electrolytes.[144-145]

Solid state electrolytes have also been investigated as potential alternatives to liquid redox coupled mediators. The major advantage of solid state electrolytes is the improved stability and simplification of cell fabrication. Typical solid state electrolytes are p-type semiconductors or hole transporting organic materials. While solid state electrolytes solve the evaporation and leakage problems of traditional liquid electrolytes; they suffer low overall conversion efficiencies due to poor contacts within the cell. The initial hole transporting materials used as electrolytes, CuSCN[146] and CuI[147], achieved conversion efficiencies < 1%. More recently, solid state systems such as a TiO_2/CuI/Cu electrode[148] and organic semiconductor spiro-OMe[149] have produced efficiencies of 4.73% and 4.0%, respectively.

4.1.5 Tandem Dye Sensitized Solar Cells

The DSSC design and components discussed so far relies on a single light harvester. Therefore, it is limited by the thermodynamic Shockley-Queisser[150] limit for a single junction solar cell to a maximum efficiency of 31%. In addition to improving the performance of these single component n-DSSCs, tandem pn-DSSCs are capable of achieving much higher conversion efficiencies. A tandem DSSC incorporates an additional dye to sensitize the cathode and increase the overall light harvesting capabilities of the cell. With both electrodes photoactive, the theoretical thermodynamic efficiency limit is increased to 43%.[151] In addition to the expected increase in conversion efficiency, the tandem DSSCs design further lowers the material cost by replacing the expensive platinum counter electrode with a sensitized p-type semiconductor. The pn-DSSC design indicating the desired electron transfer process is illustrated in Figure 4.2.

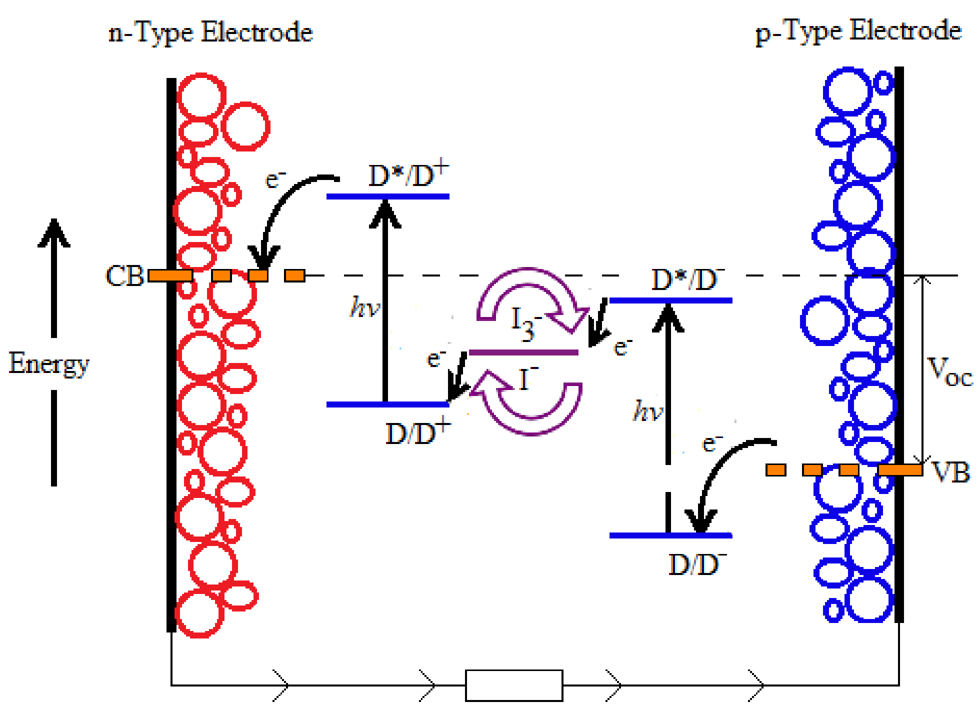

Figure 4.2. Representation of the electron transfer and ideal band alignment for the tandem DSSC design.

Like conventional Grätzel cells, the tandem DSSC is activated through the photoexcitation of the dye material. The two sensitizers adsorbed on either electrode are usually chosen so that one dye absorbs high energy photons, while the other absorbs lower energy photons. The operational processes on the n-type electrode are the same as discussed in section 4.1.1. On the p-type electrode, the photoexcited sensitizer injects a hole into the VB of the p-type semiconductor resulting in the reduced form of the dye. Therefore, the HOMO state of the p-type sensitizer must be below the VB edge of the photocathode to allow efficient hole injection. The redox couple within the electrolyte is then reduced by the p-type dye prior to reducing the n-type dye. In this pn-DSSC design, the open circuit potential is determined by the difference between the VB edge of the photocathode and the CB edge of the photoanode. It does not depend on the redox potential of the electrolyte as seen in n-DSSCs. However, the redox potential of the electrolyte must be matched with the HOMO and LUMO states of the two dyes to ensure efficient electron transfer across the cell.

While the tandem DSSC design is promising in theory, the research and development of these devices is still in its very early stages. Unlike the n-type cells, there have been very few studies conducted on p-type cells. Of the few p-type DSSCs investigated to date, nickel oxide (NiO) has been the common p-type semiconductor employed. NiO is a transparent (in the visible spectrum) semiconductor with a rock-salt crystal structure. The band gap energy is ~3.6 eV with a VB edge around -5.0 eV vs. vacuum. Sensitized nanostructured NiO photocathodes were first introduced in p-DSSCs in 1999 by He et al.[152] Erythrosin B and tetrakis(4-carboxyphenyl)-porphyrin (TPPC) were used as the photosensitizers in conjunction with the standard I^-/I_3^- redox couple. The overall conversion efficiency produced with this cells was extremely low at <0.01%. The open circuit potential was also restricted (0.1 eV) by the small difference in energy between the NiO VB and the I^-/I_3^- redox mediator. The redox potential of I^-/I_3^- is ~ -4.8 eV which only allows for a maximum open circuit potential of ~ 0.2 eV when paired with NiO. Therefore, sensitized NiO photocathodes in tandem with conventional sensitized TiO_2 and I^-/I_3^- redox couple may not provide any significant improvements over the n-DSSC alone.

He, et al. has also reported the construction of a pn-DSSC based on the erythrosine B sensitized NiO previously discussed and TiO_2 sensitized with the N3 dye.[153] The I^-/I_3^- redox mediator for this cell was replaced with Co(II)/Co(III) in an attempt to increase the open circuit potential on the NiO photocathode. The overall V_{oc} was reported to be 0.732 eV; however, this large V_{oc} is the sum of a 0.650 eV V_{oc} on the TiO_2 photoanode and only 0.083 eV V_{oc} on the NiO photocathode. Low current on the p-side of this tandem cell resulted in a low conversion efficiency of 0.39%.

To better understand the dye/NiO interface, Morandeira et al. investigated the charge transfer dynamics of coumarin 343 sensitized NiO with the I^-/I_3^- redox couple.[154] Coumarin 343 had previously been reported for the successful sensitization of TiO_2[155-159] and NiO[160]. On NiO, coumarin 343 has a HOMO state sufficiently (~ 1.0 eV) below the VB edge to allow hole injection; and a LUMO state significantly (~ 1.6 eV) above the VB edge to discourage charge recombination. Analysis of the charge transfer dynamics of this system revealed that efficient hole injection into the VB of NiO occurs in ~ 200 fs. However, the energy conversion efficiency of this cell remained extremely low. This was attributed to the comparatively fast charge recombination (~ 20 ps) at the NiO interface despite the proper band alignment. Regeneration of the dye before the fast charge recombination process is difficult for the I^-/I_3^- redox couple.

Keeping in mind that the current research on pn-DSSCs remains scarce, the best tandem cells are only providing overall conversion efficiencies of ~ 2%.[161] Obviously it is the p-side of these tandem cells that need improvement; and it is becoming clear that any significant advances in p-DSSCs will require replacements of either the NiO semiconductor or the traditional I^-/I_3^- redox couple. To date, there have not been any reports of p-type semiconductors that perform better than NiO. Recently, several novel p-type redox couples have been proposed, including cobalt based redox couples, which have been shown to provide a 3-fold increase in the cell photovoltage compared to the I^-/I_3^- redox couple.[162]

4.1.6 Novel Electrolyte-free DSSC Design based on Perfluoro-Zinc-Phthalocyanines

Extensive experimental and theoretical efforts over the past 25 years to understand and tune the properties of n-DSSCs has led to conversion efficiencies as high as 13.0%.[89] Although the research into pn-DSSCs remains in its infancy, tandem DSSCs are the most promising DSSC design in achieving solar energy conversion efficiencies capable of rivaling that of traditional silicon based solar cells. However, the inclusion of a liquid electrolyte redox couple to shuttle electrons between the electrodes in these cell designs will continue to be an obstacle in achieving long term device stability. Removing the need for the electrolyte in the cell design will not only increase device stability, but will allow for even more simplified cell fabrication procedures. Throughout the remainder of the chapter, we will introduce and investigate a completely solid state DSSC based on chemically and thermally robust perfluoro-isopropyl-zinc-phthalocyanines. Within this cell design, the Pc molecule will be acting as both photosensitizer and electron shuttle. The ideal band alignment and proposed electron transfer processes for this novel DSSC design is illustrated in Figure 4.3.

The proposed solid state DSSC incorporates the fundamental working processes involved in both n-DSSCs and p-DSSCs. Activation of the cell occurs by (1) photoexcitation of the Pc sensitizer. Upon charge separation on the Pc molecule, the Pc may either be oxidized by the photoanode or reduced by the photocathode. Given the exceptionally low lying HOMO state of the F_xZnPc molecules seen in section 2.4, oxidation of the Pc is improbable. It is far more likely that these Pcs will be reduced. Therefore, upon photoexcitation, the Pc molecule is (2) reduced via hole injection into the VB of the p-type photocathode. Subsequently, the reduced form of the Pc is returned to the neutral ground state through (3) an electron transfer into the CB of the n-type photoanode. For these electron transfer processes to occur, the Pc sensitizer must have a HOMO state below the VB edge of the photocathode and a LUMO above the CB edge of the photoanode.

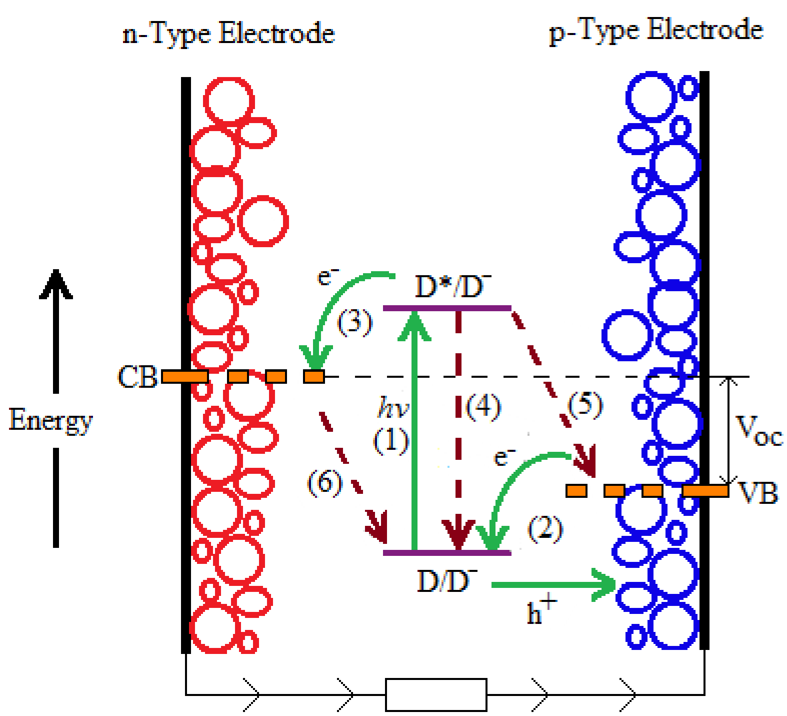

Figure 4.3. Representation of the electron transfer and ideal energy level alignment for proposed Pc based solid state DSSC.

As with all DSSC designs, there are also several charge recombination processes at the interfaces that must be taken into account. Hole injection into the VB of the photocathode must occur prior to (4) the spontaneous relaxation of the Pc excited state. Following hole injection into the VB, the reduced form of the Pc must efficiency transfer the excess electron into the CB of the photoanode before (5) charge recombination with the hole present on the photocathode. Finally, the electrons injected into the CB of the photoanode must be rapidly collected or (6) electron transfer back to the Pc may occur.

A solid state DSSC with similar cell design was first reported in 1995 by Tennakone et al.[146] In this study the natural flower pigment cyaniding was employed as a sensitizer on the n-type semiconductor TiO_2 and p-type semiconductor CuI. Photoexcitation of the dye results in electron injection into the CB of TiO_2 leaving the oxidized form of the sensitizer. The sensitizer is regenerated by injection of a hole into the valence band of CuI. The resulting conversion efficiency was a modest 0.8% but serves as a fundamental proof of concept for out proposed Pc based DSSC design.

Since the target F_xZnPc sensitizers lack any conventional anchoring groups, adsorption to the semiconductor surface will need to occur through electrostatic interactions and/or molecular orbital overlap. These interactions are highly dependent on the ability of the various Pcs to get close to the surfaces. Therefore the most promising F_xZnPcs are those with little or no bulky periphery substitution; namely, $F_{16}ZnPc$, $F_{34}ZnPc$, and $F_{40}ZnPc$. However the completely substituted $F_{64}ZnPc$ will often be presented for comparative purposes.

It is noted that achieving a single monolayer of sensitizing Pcs sandwiched between both electrodes during cell fabrication, as depicted in Figure 4.3, is not to be expected. The electron transport properties of F_xZnPc will be addressed separately in the next chapter. The focus of this chapter will be on investigating the various charge transfer processes occurring at the electrode interfaces.

4.2 Results

4.2.1 Light Harvesting Efficiency and Excited State Lifetimes of F_xZnPc

As previously stated, the introduction of bulky $i\text{–}C_3F_7$ substituents on the periphery of the Pc molecule has been shown to expand the optical absorbance spectrum as well as lowers the energetic position of the molecular frontier orbitals.[21,75] The electron accepting properties of the Pc is also enhanced by the introduction of the strong electron withdrawing peripheral groups. The vertical and adiabatic ionization potential (IP) and electron affinity (EA) of F_xZnPc are calculated via DFT calculations as follows:

$$IP_{adiabatic} = E_{+}^{+} - E_{0}^{0} \tag{4.1}$$

$$IP_{vertical} = E_{0}^{+} - E_{0}^{0} \tag{4.2}$$

$$EA_{adiabatic} = E_{0}^{0} - E_{-}^{-} \tag{4.3}$$

$$EA_{vertical} = E_{0}^{0} - E_{0}^{-} \tag{4.4}$$

Where the subscripts and superscripts, 0 (neutral), + (cationic), and – (anionic), indicate the molecular geometry and charge state of the Pc, respectively. The calculated IP and EA are presented in Table 4.1. In all cases; the energy of the Pc cationic state is higher than the neutral state, and the energy of the anionic state is lower than the neutral state. Therefore, all F_xZnPc

molecules in this study are most stable in their anionic form, consistent with being excellent electron acceptors (hole injectors). The calculated EA also increases as peripheral substitution increases.

Table 4.1. Calculated Ionization Potential and Electron Affinities for Gas Phase FxZnPc. All values reported in eV.

	IP_{ad}	IP_{vert}	EA_{ad}	EA_{vert}
$F_{16}ZnPc$	7.341	7.381	3.083	2.979
$F_{34}ZnPc$	7.263	7.326	3.299	3.155
$F_{40}ZnPc$	7.417	7.476	3.430	3.349
$F_{64}ZnPc$	7.660	7.721	3.826	3.716

It is of fundamental importance that the Pc sensitizers are excellent light absorbers. Sensitizing materials are typically classified according to their light harvesting efficiency (LHE); which is estimated experimentally from the absorbance strength corresponding to the maximum absorption wavelength, λ_{max}(abs):[163]

$$LHE = 1 - 10^{-A} \tag{4.5}$$

Theoretically, the calculation of absorbance spectra provides oscillator strength, *f*, rather than absorbance values. Consequently, estimation of the LHE of a dye may be estimated by:[164]

$$LHE = 1 - 10^{-f} \tag{4.6}$$

The calculated absorbance spectra of the first two transitions are illustrated in Figure 4.4; with corresponding λ_{max}(abs), oscillator strengths, and transition nature for F_xZnPc are presented in Table 4.2.

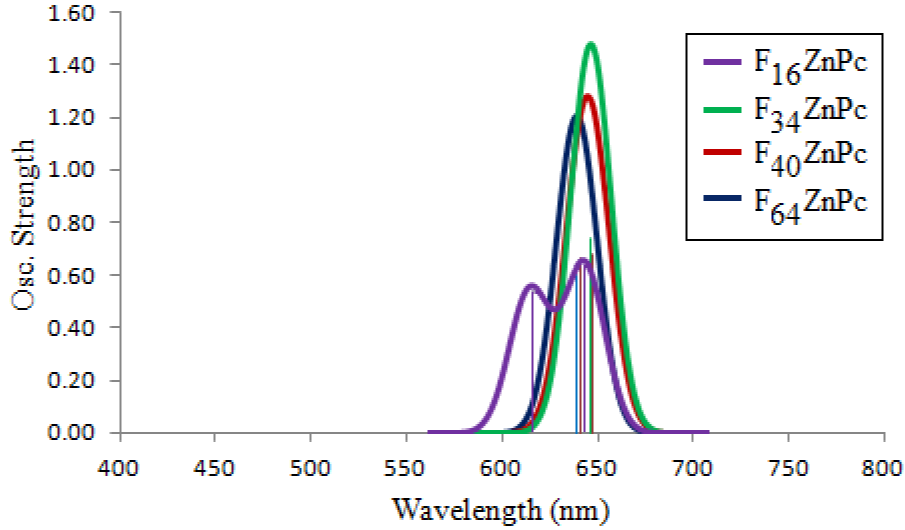

Figure 4.4. Calculated absorbance spectra. All spectra calculated with ethanol solvent for better agreement with experimental absorbance spectra.

There is little deviation observed in the calculated absorbance maximum for the various F_xZnPcs. As peripheral fluorination is increased, there is a slight red shift in λ_{max} compared to $F_{16}ZnPc$. This is an expected result given the lowering of the unoccupied states as the degree of fluorination is increased. With the exception of $F_{34}ZnPc$, the absorbance λ_{max} corresponds to two probable transitions; HOMO→LUMO and HOMO→LUMO+1. This is a result of the nearly degenerate LUMO and LUMO+1 states for these Pcs discussed in Chapter 2. Theses multiple possible transitions lead to exceptionally large oscillator strength and, in turn, high LHE for $F_{16}ZNPc$, $F_{40}ZnPc$, and $F_{64}ZnPc$. For $F_{34}ZnPc$ the non-degenerate LUMO and LUMO+1 level results in a 29 nm separation of the first two possible transitions. This leads to a lower light harvesting efficiency compared to the other F_xZnPcs. Overall, the calculated λ_{max} values are in good agreement with the experimental values given the inherent limitations of TDDFT calculations.

Table 4.2. Calculated absorbance maxima (λ_{max}) compared to experimental values, oscillator strength of $S_0 \rightarrow S_1$ transition, and calculated LHE.

	Absorbance λ_{max} (nm)			
	Calc.	Exp.	Osc.	LHE
F_{16}ZnPc	639.10 638.77	636	0.602 0.601	0.937
F_{34}ZnPc	643.08 614.40	679 637	0.641 0.544	0.771
F_{40}ZnPc	647.44 641.08	670 638	0.675 0.662	0.947
F_{64}ZnPc	646.09 646.09	680	0.740 0.740	0.967

To avoid charge recombination prior to hole injection, the excited state lifetime of the Pc sensitizer must be sufficiently long relative to the charge injection rate. Excited state lifetimes for spontaneous emission from the first excited state (S_1) are obtained from TDDFT calculations of the fluorescence energies (E_{fluor}) and oscillator strength (f), which represents the transition probability (in atomic units):[165]

$$\tau = \frac{2\pi\varepsilon_0 m_e \hbar^2 c^3}{e^4 \left(E_{fluor}\right)^2 f} \tag{4.7}$$

Where c is the speed of light, e the elementary charge, m_e the electron mass, ε_0 the vacuum permittivity, and $\hbar$ is the reduced Planck constant. The fluorescence electronic transitions ($S_1 \rightarrow S_0$) are treated as vertical de-excitations from the geometry optimized first excited state of the F_xZnPc. The calculated fluorescence energies, oscillator strength, and excited state lifetimes are presented in Table 4.2.

Table 4.3. Calculated fluorescence maxima (λ_{max}) compared to experimental values, oscillator strength of $S_1 \rightarrow S_0$ transition, and calculated excited state lifetimes.

	Fluorescence λ_{max} (nm)			
	Calc.	Exp.	Osc. Strength	τ (ns)
$F_{16}ZnPc$	681	-	0.880	3.95
$F_{34}ZnPc$	722	-	0.917	4.26
cis-$F_{40}ZnPc$	687	689	0.942	3.75
$F_{64}ZnPc$	682	-	0.998	3.49

It is noted that these fluorescence spectra are simulated in ethanol solvent to be consistent with the experimental spectra. As peripheral fluorination of the Pc is increased, there is little variation in the fluorescence energy for $F_{16}ZnPc$, $F_{40}ZnPc$, and $F_{64}ZnPc$, but a slight decrease in the calculated excited state lifetimes is observed. $F_{34}ZnPc$ is again unique with the highest fluorescence λ_{max} and longest lived first excited state.

4.2.2. F_xZnPc | NiO Interface

Following photoexcitation of the Pc sensitizer, it is proposed that hole injection into the VB of the photocathode with occur. As previously stated, the ability to easily produce inexpensive NiO films in conjunction with its excellent photostability make NiO the most common p-type semiconductor employed in p-DSSCs to date. It is also noted that for p-DSSCs in which a conventional electrolyte is employed, NiO has not been found to be the greatest photocathode material. The VB edge is too close to common redox couples, which produces very low cell $V_{ov.}$[166-169] NiO may be more promising in our proposed cell design because there is no need of an electrolyte redox mediator for dye regeneration. Therefore, NiO was chosen as a starting point for the investigation of hole injection from the Pcs. The preferred NiO surface preparation is to cleave along the (100) crystal plane.[154,168-171]

For efficient hole injection into the VB of NiO to be possible, we need the HOMO state of the Pc sensitizer to be: (1) below the VB edge of NiO; and (2) significantly coupled with NiO VB states. To access the band alignment of the Pc on NiO (100) surfaces, large scale periodic DFT calculations were preformed. The optimized geometry of F_{16}ZnPc, F_{34}ZnPc, and F_{40}ZnPc on NiO (100) are presented in Figure 4.5.

The bulky –C_3F_7 groups on the periphery of F_{34}ZnPc and F_{40}ZnPc result in an increased distance between the Pc and the NiO surface compared to F_{16}ZnPc. Unexpectedly, the less bulky F_{34}ZnPc is farther from the surface (3.48 Å) than F_{40}ZnPc (2.59 Å). The reason for this remains unknown. The lack of any steric hindrance of F_{16}ZnPc results in a distance of 2.09 Å from the surface.

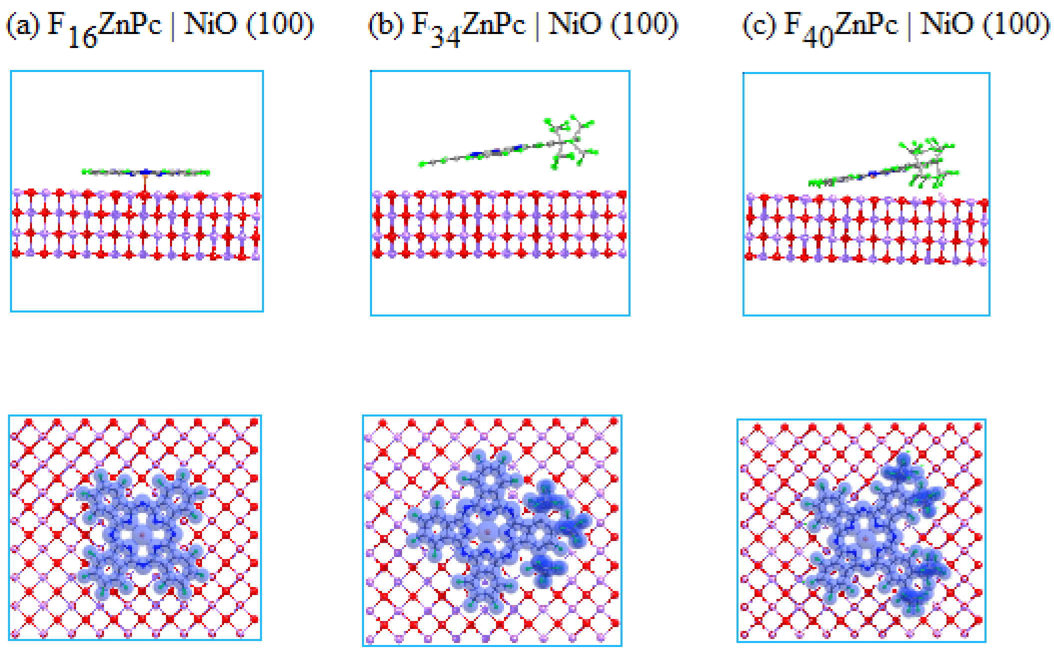

Figure 4.5. Geometry optimized Pc | NiO systems: (a) $F_{16}ZnPc$, (b) $F_{34}ZnPc$, and (c) $F_{40}ZnPc$. Viewed edge on (top) and top down (bottom). VDW spheres used to illustrate Pc in top down view for clarity.

The total density of states (DOS) and partial density of states (PDOS) are calculated from the optimized systems to examine the Pc | NiO band alignment. The total DOS are illustrated in Figure 4.6. There is little difference in the calculated DOS of the various Pcs. This is an expected result since the total DOS is dominated by surface states. From Figure 4.6, there are minor fluctuations in the calculated energy of the VB edge depending of the adsorbed Pc. This is a result of interaction of the Pc states with the surface states near the VB edge.

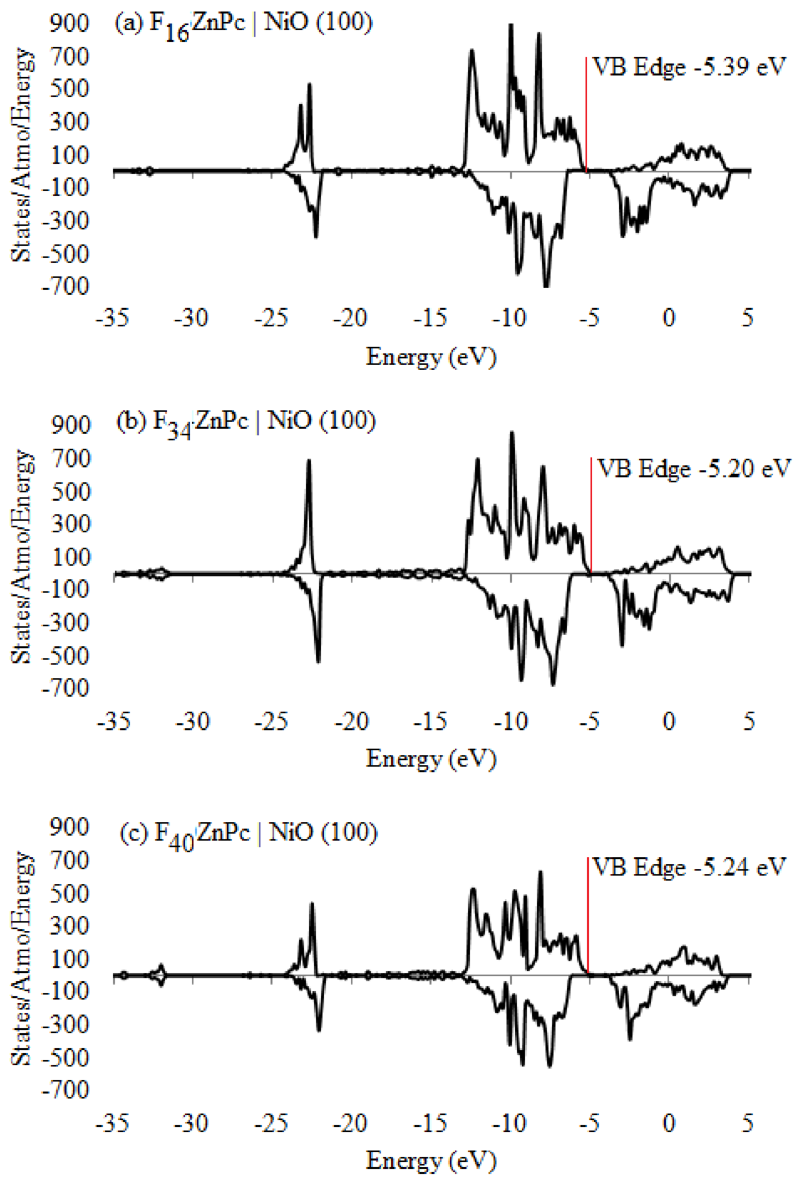

Figure 4.6. Calculated total DOS of (a) $F_{16}ZnPc$, (b) $F_{34}ZnPc$, and (c) $F_{40}ZnPc$ on NiO (100).

To get a better description of the Pc contributions near the VB edge; the DOS is parsed into Pc contributions and surface contributions to each MO (Figure 4.7).

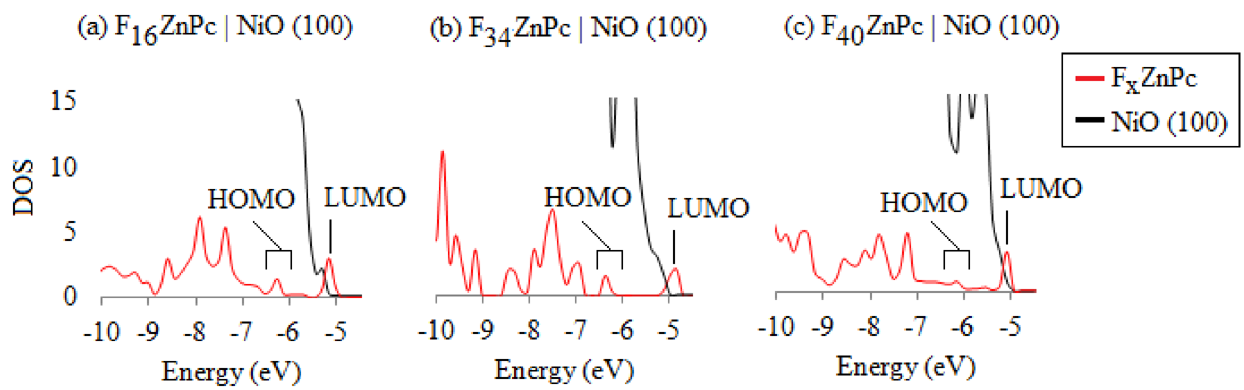

Figure 4.7. Magnified PDOS of (a) $F_{16}ZnPc$, (b) $F_{34}ZnPc$, and (c) $F_{40}ZnPc$. Pc contributions multiplied by a factor of 3 for clarity.

The HOMO state of all Pc sensitizers is found to be significantly below the top of the NiO VB, which allows for hole injection from the excited sensitizer. Further enhancing the hole tunneling process, the HOMO states for both sensitizers show substantial orbital coupling with the VB. The degree of coupling in the HOMO state with the surface states can be seen (qualitatively) by comparison of the HOMO peak height with the discrete LUMO state located above the VB edge. The Pc HOMO state is not discrete, but distributed across several Pc|NiO mixed states. The first occupied MO with significant Pc contribution for $F_{16}ZnPc$ and $F_{40}ZnPc$ is at -6.44 eV and -6.42 eV, respectively. However, the Pc contribution to both of these states is a modest 18%. The first occupied MO with significant $F_{34}ZnPc$ contribution is at -6.42 eV. This MO is less mixed than that seen for $F_{16}ZnPc$ and $F_{40}ZnPc$, with 65% $F_{34}ZnPc$ contribution. The less orbital coupling with the surface seen for $F_{34}ZnPc$ is a direct result of increased distance of the Pc from the surface.

It is this orbital coupling and resulting distribution of the HOMO state that allows for efficient hole injection into the VB of NiO. For estimation of the hole injection lifetime between the Pc and NiO surface, we employ the Newns-Anderson model,[172-173] following the approach set forth by Lundqvist et al.[174-181] This method of estimating charge injection lifetimes has typically been used for the electron injection into the CB of TiO_2. However, there is no indication of the direction of charge transfer. Therefore, it is perfectly reasonable to employ this methodology for hole injection into the VB of NiO.

Through further analysis of the Pc | NiO PDOS in Figure 4.7, the Newns-Anderson model uses the coupled Pc HOMO states to estimate a lifetime broadening. Described by a Lorentzian distribution, this HOMO broadening allows for estimation of the adsorbed Pc excited state decay.[182] The analysis begins with examination of the MO expansion coefficients (cij) to find the portion (*p*) of each MO that is centered on the Pc molecule to construct the PDOS plots.

$$p_i = \sum_j^{Pc} \left(c_{ij}\right)^2 \Big/ \sum_j^{n} \left(c_{ij}\right)^2 \tag{4.6}$$

The HOMO of the Pc adsorbed on NiO, HOMO(ads), energy levels are selected so that $\sum p_i \approx 1$. A weighted average of the distribution of HOMO(ads) states provides the energy of the adsorbed Pc HOMO:

$$E_{HOMO}(ads) = \sum_i p_i \varepsilon_i \tag{4.7}$$

The width of the HOMO(ads) broadening ($\hbar\Gamma$) is calculated from the mean deviation of the HOMO(ads) levels:

$$\hbar\Gamma = \sum_i p_i \left|\varepsilon_i - E_{HOMO}(ads)\right| \tag{4.8}$$

The hole injection rate from the adsorbed Pc to the VB of NiO is calculated directly from the HOMO broadening as:

$$\tau(\text{fs}) = 658/\,\hbar\Gamma(\text{meV}) \tag{4.9}$$

Where the leading constant 658 is derived from the reduced Planck's constant (ħ) in meV• fs. The calculated HOMO energy of the adsorbed Pcs, energy of NiO VB edge, HOMO broadening, and estimated hole injection lifetimes are presented in table 4.3. Other important properties that are critical for efficient hole injection that can be obtained from the PDOS of Figure 4.7 are the Gibbs free energy of both hole injection and charge recombination. The free energy associated with hole injection (recombination) is calculated from the difference in energy between the Pc $HOMO_{(ads)}$ (LUMO) and the VB edge of NiO.

Table 4.4. Calculated energy of NiO VB edge (E_{VB}), Pc HOMO(ads), Pc LUMO (E_{LUMO}), HOMO broadening (ħΓ), Gibbs free energy for hole injection (ΔG_{h+}), Gibbs free energy for charge recombination at the NiO surface (ΔG_{CR}), and estimated hole injection lifetime (τ). All values reported in eV, unless noted otherwise.

	E_{VB}	E_{HOMO}(ads)	E_{LUMO}	ħΓ (meV)	τ (fs)	ΔG_{h+}	ΔG_{CR}
F_{16}ZnPc	-5.39	-6.38	-5.21	101.93	6	-0.99	+0.18
F_{34}ZnPc	-5.20	-6.39	-5.10	2.90	226	-1.19	+0.10
F_{40}ZnPc	-5.24	-6.36	-5.13	206.77	3	-1.12	+0.11

As previously stated, the calculated energy of the VB edge of NiO shows slight variation depending on the Pc adsorbed on the surface. The E_{HOMO}(ads) state for all of the F_xZnPc is found to be ~ -6.4 eV. This results in significantly negative Gibbs free energy for hole injection. An observer increase (more negative) in ΔG_{h+} occurs from F_{16}ZnPc to F_{40}ZnPc. This is an expected result given the lowering of the HOMO states of the Pcs in vacuum as peripheral fluorination is increased. Additionally, the estimated hole injection lifetimes are found to be exceptionally fast; all are on the fs timescale. This predicted fast hole injection is a direct result of the large degree of orbital coupling of the Pc HOMO with NiO surface states indicated by the HOMO(ads) broadening (ħΓ). The Lorentzian distribution illustrating the broadening of the HOMO(ads) state is plotted in Figure 4.8 as:

$$\rho = \frac{1}{\pi} \frac{\hbar\Gamma/2}{\left(E - E_{HOMO}(ads)\right)^2 + \left(\hbar\Gamma/2\right)^2} \tag{4.10}$$

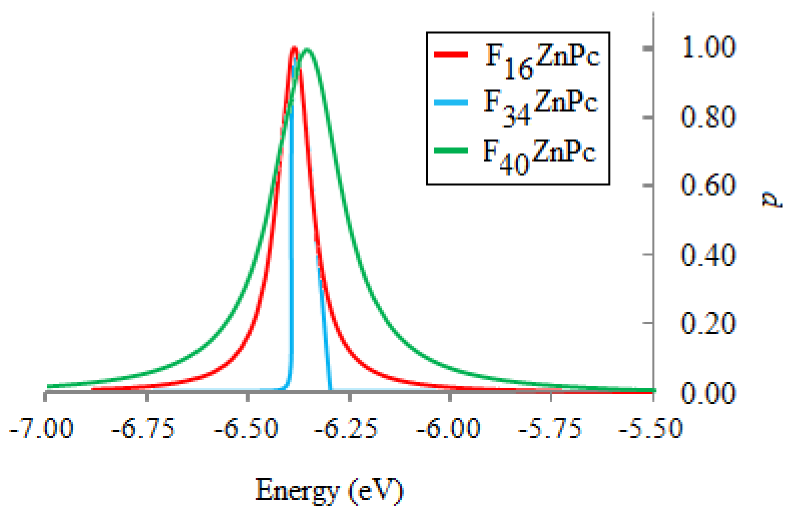

Figure 4.8. Lorentzian distribution of Pc HOMO(ads) states to illustrate the degree of broadening for $F_{16}ZnPc$ (red line), $F_{34}ZnPc$ (blue line), and $F_{40}ZnPc$ (green line).

The greatest amount of coupling is seen for F_{40}ZnPc; twice that of F_{16}ZnPc and two orders of magnitude greater than F_{34}ZnPc. The lower orbital coupling of F_{34}ZnPc is attributed to the increased distance from the surface compared to F_{16}ZnPc and F_{40}ZnPc. However, F_{40}ZnPc is 0.5 Å farther from the surface than F_{16}ZnPc, but displays better coupling with the surface. The only possible explanation of this is that the HOMO of F_{40}ZnPc is 0.2 eV deeper into the VB of NiO, where there are more surface states available to mix with.

The estimated fs timescale hole injection lifetimes for all Pcs is sufficient to ensure charge injection given the ns excited state lifetimes calculated previously. However, charge recombination on the NiO surface after hole injection is a great concern. As seen in Table 4.4, the calculated Gibbs free energy for charge recombination is positive, but very small for all Pcs. Therefore, charge recombination between the newly injected hole and the reduced form of the Pc may occur. This may be avoided if a thermodynamic driving force can be established to push the electron in the opposite direction; that is toward the photoanode.

It should be noted that DFT is a ground state approach; simply meaning it is relatively poor at predicting band gaps. As expected, the calculated band gap of the Pcs (and NiO) is significantly underestimated. Employing larger basis sets to better account for the exchange and correlation effects in known to improve the band gap prediction; which we do observe for the vacuum state Pc calculations discussed in Chapter 2. However, the enormous size of these calculations restricts us to a relatively small basis. Since the Pc gap is actually greater than what is found in these calculations (~ 1.2 eV); it is entirely possible that the Pc LUMO is located higher above the VB than indicated. This would increase ΔG_{CR} and charge recombination may not be such a concern. Regardless, additional p-type semiconductors with slightly lower VB are investigated in section 4.2.4.

4.2.3 F_xZnPc | TiO_2 Interface

Following hole injection from the photoexcited Pc, the reduced form of the Pc molecule will be returned to its neutral ground state through an electron transfer into the CB of the photoanode. In conventional n-DSSCs, the most common photoanode employed is TiO_2. Largely due to its high abundance, low toxicity, good chemical and photo stability, and low cost. In our solid state Pc based DSSC design, we will investigate TiO_2 as a potential photoanode material. Following the same analysis preformed for the adsorbed Pcs on NiO, we will examine the band structure and orbital coupling to examine the probability of electron injection from the Pc into the CB of TiO_2.

Selection of a suitable TiO_2 surface to sensitize with the Pcs is slightly more complicated with TiO_2. TiO_2 is found in nature in three different polymorphs; rutile, anatase, and brookite. Of the three crystal phases, rutile is known to be the most thermodynamically stable, while anatase is the more preferred crystal phase for DSSC applications. This is due to a slightly larger band gap for anatase (~ 3.3 eV) compared to rutile (~ 3.0 eV); as well as a higher CB in the anatase form. The higher CB leads to increase cell V_{OC} when paired with common electrolyte redox mediators. Brookite is relatively unstable and less photoactive than anatase. Given the incredible computational cost of running numerous periodic DFT calculations of the Pc adsorbed on a TiO_2

surface, semiempirical PM7 methods are employed to provide an initial evaluation of which TiO_2 surfaces are most promising for the Pc electron injection process.

Several stoichiometric low-index rutile and anatase surfaces were cleaved from previously optimized bulk crystal structures. A total of eight TiO_2 surfaces were investigated; four rutile surfaces, and four anatase surfaces. These surfaces include the rutile (110), (100), (001) and (101) surfaces, as well as the anatase (001), (100), (110), and (101) surfaces. The optimized structures of the TiO_2 surfaces are presented in Figure 4.9.

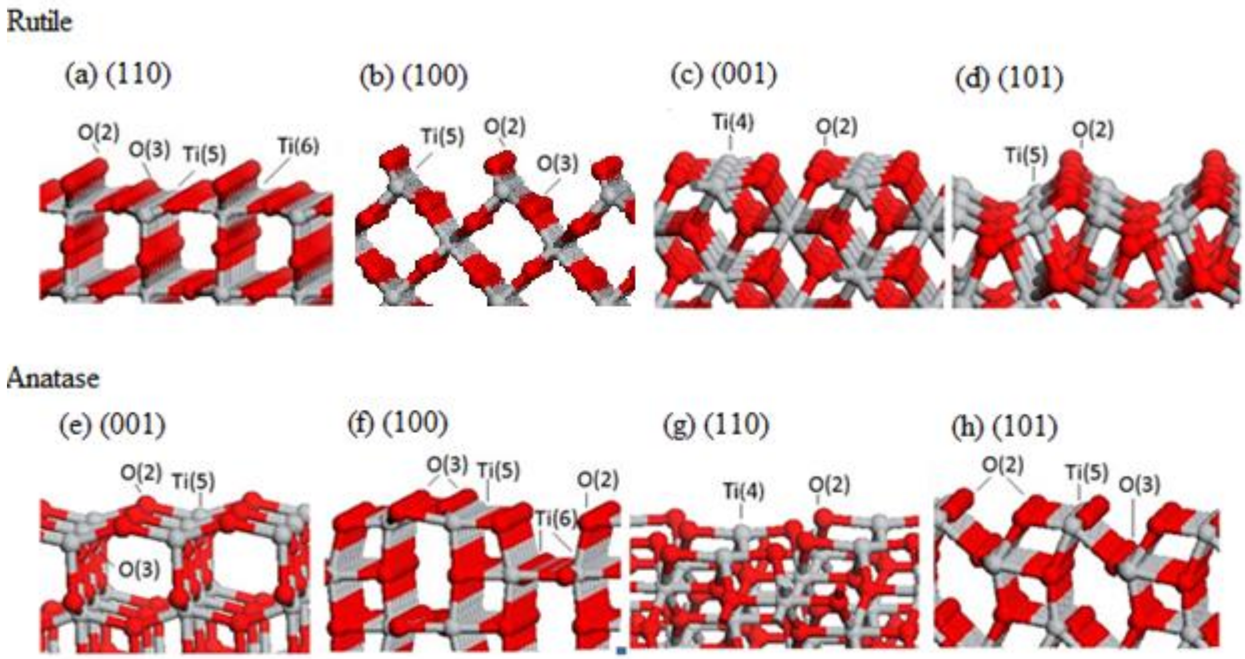

Figure 4.9. Optimized geometry of low index TiO_2 surfaces: rutile (a) (110), (b) (100), (c) (001) and (d) (101). As well as anatase (e) (001), (f) (100), (g) (110), and (h) (101). Coordination of select surface atoms indicated.

The resulting cleaved surfaces contain both undercoordinated titanium and oxygen atoms exposed to vacuum. The rutile (110) face (Figure 4.9a) has a five-fold coordinated Ti, denoted

Ti(5), as well as two types of O atoms; a three-fold coordinated O on the surface, O(3), and a bridging two-fold coordinated O above the surface, O(2). Optimization of this surface results in the bridging O(2) atoms and undercoordinated Ti(5) relaxing down toward the surface. However, the degree of relaxation of these surface atoms is minimal with average root mean square deviation (RMSD) of the surface atoms of 0.247 Å and 0.144 Å, for O(2) and Ti(5), respectively. The rutile (100) face (Figure 4.9b) exhibits a different orientation than the rutile (110) face, but contains the same kinds of undercoordinated surface atoms. The O(2) and Ti(5) surface atoms relax down toward the surface, while the O(3) atoms relax upward slightly. The degree of relaxation is slightly greater than the rutile (110) surface, with average RMSD for surface O and Ti of 0.363 Å and 0.255 Å, respectively.

The rutile (001) surface (Figure 4.9c) exhibits a tetra-coordinated, highly unsaturated, titanium atom as well as a two-fold oxygen atom. These Ti(4) and O(2) atoms show the largest reconstruction of any of the rutile surface studied. The Ti(4) atoms relax down (RMSD 0.334 Å) and O(2) show large relaxation away from the surface (RMSD 0.783 Å). The rutile (101) surface (Figure 4.9d) looks much like the (100) surface but only consists of two different types of surface atoms. A pentacoordinated titanium and a two-fold oxygen atom with two different Ti-O bond lengths. As with the (100) surface, minor surface relaxation is observed; RMSD 0.214 Å and 0.206 Å for O(2) and Ti(5), respectively.

The relaxed anatase (001) and (101) face (Figure 4.9e,h) contain the same five-fold coordinated Ti atoms, as well as two- and three-fold coordinated O atoms. The (001) surface shows much larger relaxation of the surface atoms than the (101) anatase surface. In both surface, Ti(5) and O(3) relax down toward the surface causing a relaxation upward for O(2). The average RMDS for surface O is 1.33 Å and 0.024 Å for the (001) and (101) surfaces, respectively. Likewise, RMSD for Ti(5) is greater for the (001) surface (1.27 Å) than the (101) surface (0.053 Å). The anatase (110) (Figure 4.9g) also displays large surface relaxations. The highly undercoordinated Ti(4) relaxed toward the surface 0.325 Å and O(2) relax up 0.658 Å. Finally, the anatase (100) face (Figure 4.9f) contains five-fold coordinated Ti and both two- and three-fold coordinated O atoms on the top most layer. The Ti(5) and O(2) relax down toward the surface while O(3) relax away from the surface. The average RMSD of surface O is greater (0.460 Å) compared to the surface Ti atoms (0.236 Å).

The degree of surface relaxation seen in all of the low index TiO_2 surfaces has a direct affect on the calculated surface energies. The surface energy of each system was calculated by semiempirical PM7 and DFT LDA methods. The effect of slab thickness on surface energy calculations has been demonstrated in previous reports.[183-189] For all surfaces of interest in this report, surface energies were calculated as a function of the number of layers, where a layer is defined as a row of titanium atoms. The slab thickness was increased until convergence in the surface energy of 0.02 J/m^2 was achieved. The number of layers required to reach this convergence criteria varied for each surface as seen in Figure 4.10.

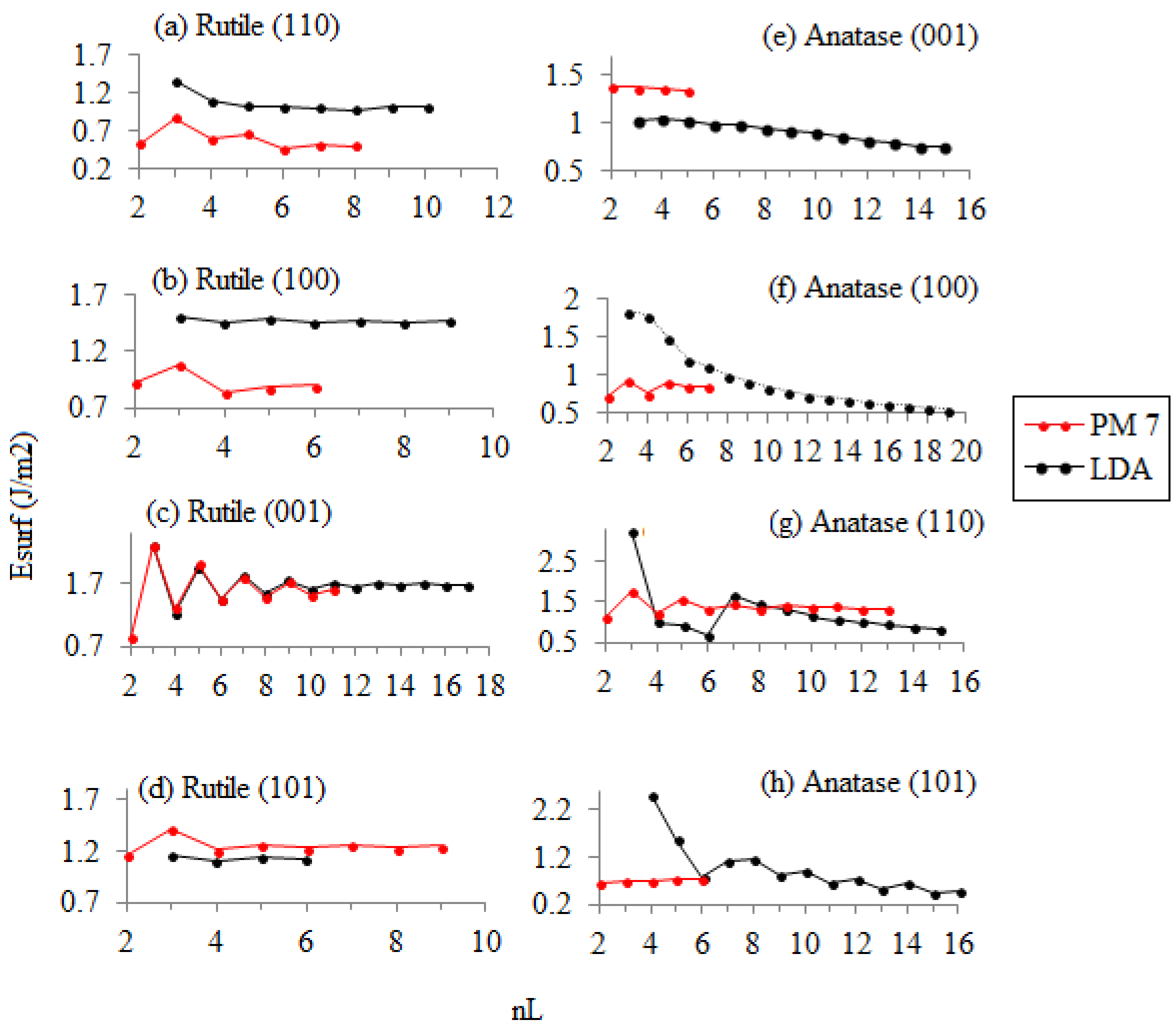

Figure 4.10. Calculated surface energies (J/m^2) of optimized (a) Rutile (110), (b) Rutile (100), (c) Rutile (001), (d) Rutile (101), (e) Anatase (001), (f) Anatase (100), (g) Anatase (110), and (h) Anatase (101). Comparison between PM7 methods (black line) and DFT LDA methods (red line).

As seen in figure 4.10, the calculated surface energies vary depending on the level of theory employed. This is an expected result; we will be interested in the relative differences in surface energy of the various low index surfaces for each method. The calculated surface energies along with the number of layers required to achieve convergence are presented in Table

4.5. There is also a comparison with several other calculated values from additional levels of theory.

Table 4.5. Comparison of calculated surface energy (J/m2) of various low index TiO_2 surfaces at different levels of theory. Calculated values from this study in red. The number of layers in each system indicated in parenthesis for each surface.

	Rutile				Anatase			
Method	**(110)**	**(001)**	**(100)**	**(101)**	**(101)**	**(100)**	**(001)**	**(110)**
HF	0.92[a] (9) 1.00[b] (9)	2.08[a] (13) 2.20[e] (11)	1.13[a] (5) 1.21[f] (3)		0.89[a] (10)	1.02[a] (8)		
MOPAC	1.02 (10)	1.68 (17)	1.46 (9)	1.11 (9)	0.42 (16)	0.56 (19)	0.73 (15)	0.83 (15)
LDA	0.91[a] (9) 0.90[b] (9) 0.50 (8)	1.88[a] (13) 1.87[e] (11) 1.63 (13)	1.20[a] (5) 1.30[f] (3) 0.90 (6)	1.23 (6)	0.85[a] (10) 0.84[h] (6) 0.72 (6)	0.97[a] (8) 0.96[h] (6) 0.86 (7)	1.38[h] (6) 1.36 (4)	1.32 (13)
PBE	0.48[a] (9)	1.39[a] (13)	0.69[a] (5)		0.53[a] 0.49[h] (6)	0.63[a] 0.58[h] (6)	0.98[h] (6)	1.15[h] (7)
B3LYP	0.46[a] 1.00[d] (8)	1.45[a]	0.70[a]		0.58[a] 1.45[g] (4)	0.67[a] 1.80[g] (4)		2.30[g] (7)
GGA	0.50[c] (9)	1.25[c] (13)	0.69[c] (5)	1.03[c] (10)				
PBE0	0.60[a]	1.59[a]	0.83[a]		0.62[a]	0.73[a]		

a[184] b[189] c[187] d[188] e[190] f[186] g[183] h[185]

Although the values for surface energies vary depending on the level of theory employed; a general trend in the calculated surface energies is observed. For rutile, the surfaces energies increase: (110) < (100) < (101) < (001). For anatase, the calculated surface energies increase as: (101) < (100) < (001) < (110). Therefore, moving forward we decided to focus on the two lowest energy rutile and anatase surfaces for Pc sensitization. However, with four TiO_2 surfaces and three Pc molecules; semiempirical PM7 methods were employed again as an initial investigation.

Considering first the anatase surfaces; the total DOS and Pc projected PDOS for the combined Pc | TiO_2 systems are displayed in Figure 4.11. For comparison, the DOS computed of the clean anatase surfaces are also reported. As expected for TiO_2, the calculated DOS of the surfaces show distinct valence and conduction bands along with a significant band gap. It is noted that the calculated DOS displays a significantly overestimated TiO_2 band gap. The same is true for the band gap of the Pcs as well. In these calculations we are not interested in the exact energy of the bands. It is the energy of the Pc LUMO state relative to the CB of TiO_2 that is of interest. Although the PM7 methods overestimate the exact energy of these states, the relative energy differences are maintained. Therefore the less computationally demanding PM7 methodology is perfectly adequate. Validation of the PM7 method with periodic DFT calculations is provided in section 4.5.

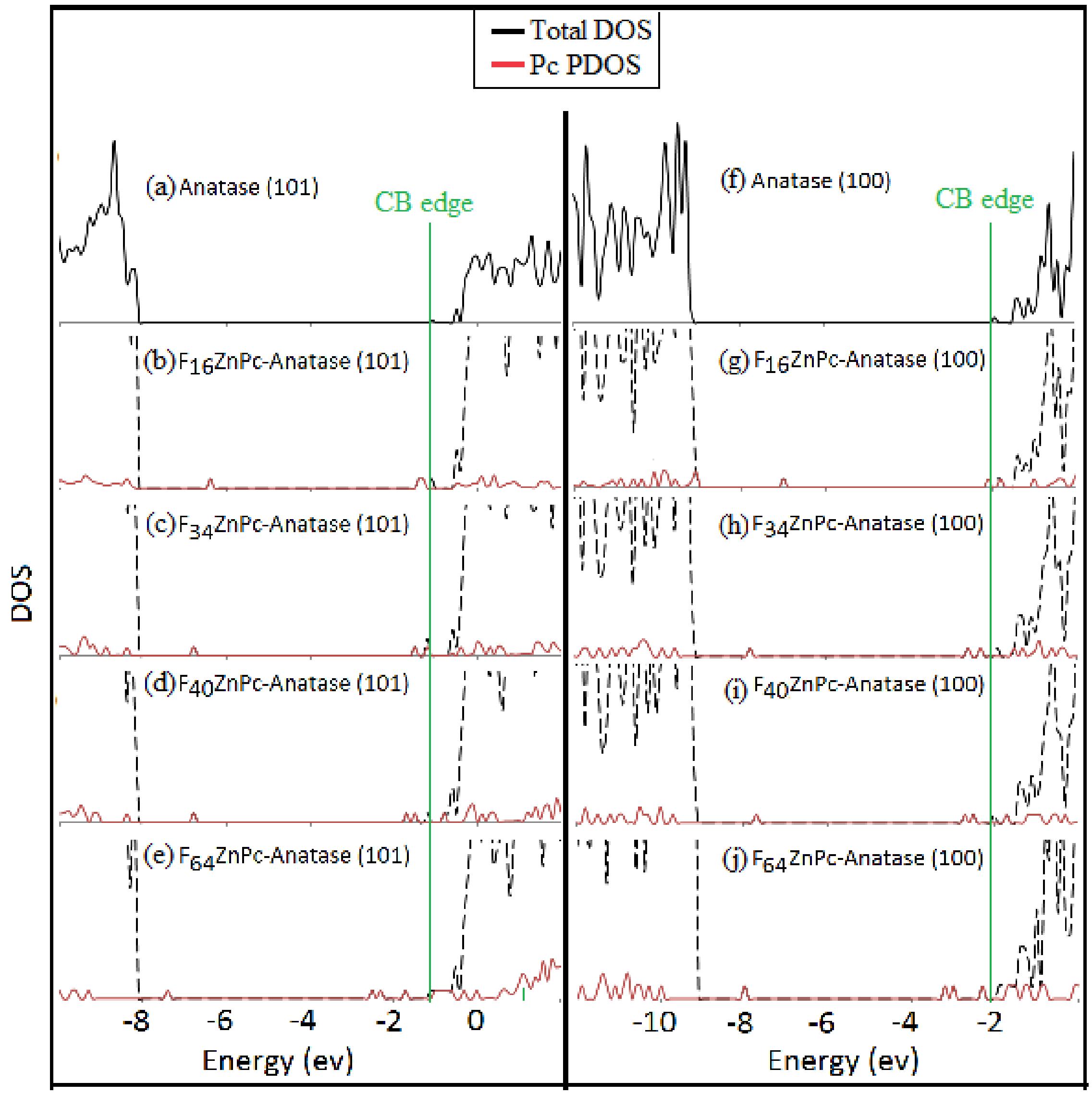

Figure 4.11. Calculated DOS (black line) and PDOS (red line) of Pc on anatase surfaces. Anatase (101): (b) F_{16}ZnPc, (c) F_{34}ZnPc, (d) F_{40}ZnPc, (e) F_{64}ZnPc. Anatase (100): (g) F_{16}ZnPc, (h) F_{34}ZnPc, (i) F_{40}ZnPc, (j) F_{64}ZnPc

In all cases, adsorption of the Pc on the surface extends the top of the valence band into the band gap of the clean anatase surface. This is a result of the HOMO of the combined systems belonging entirely to the Pc molecule. Likewise; the first unoccupied states consists entirely of Pc states with no contribution from the substrate. As the degree of Pc fluorination increases, the Pc HOMO and LUMO state decreases in energy as seen in the vacuum state Pcs. A fundamental prerequisite for electron injection from the Pc into the CB of TiO_2 is a Pc LUMO state above the CB edge. As previously stated, anatase is known to have a high CB edge compared to rutile, which is usually a desired property. However, the Pc LUMO state is below the CB edge for all Pcs studied. Therefore, electron infection into the CB of the anatase surfaces is highly improbable.

Turning now to the rutile surfaces; the total DOS and Pc PDOS for the combined Pc | rutile systems are displayed in Figure 4.12. As with the anatase surfaces; the HOMO state of the adsorbed Pc is energetically located within the band gap the rutile surface for all Pcs. Unlike anatase, the Pc LUMO states on the rutile surfaces are above the CB edge. As seen in Figure 4.12, the LUMO state of F_{16}ZnPc is located deep into the CB; but increased fluorination leads to a lowering in the Pc LUMO state. For the fully substituted F_{64}ZnPc, the LUMO state is right at the CB edge on the (100) surface and below the CB on the (110) surface. As a potential sensitizer, F_{64}ZnPc had already been ruled out due the large degree of bulkiness; but the band alignment is also not promising for efficient electron injection into the CB. These initial semiempirical calculations reveal that F_{16}ZnPc, F_{34}ZnPc, and F_{40}ZnPc have the proper band alignment for electron injection into the CB of rutile (100) and/or (110)

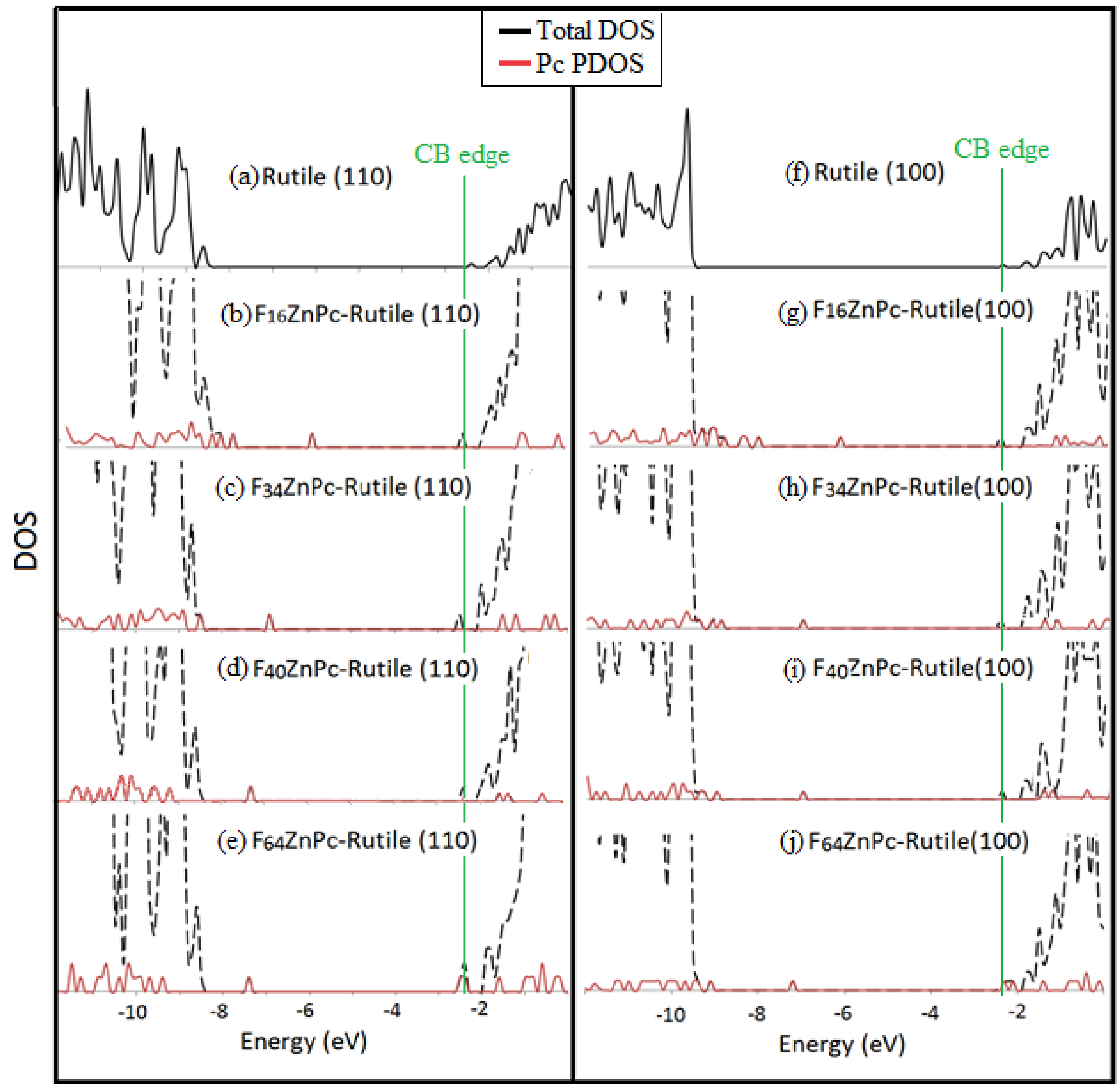

Figure 4.12. Calculated DOS (black line) and PDOS (red line) of Pc on rutile surfaces. Rutile (110): (b) $F_{16}ZnPc$, (c) $F_{34}ZnPc$, (d) $F_{40}ZnPc$, (e) $F_{64}ZnPc$. Rutile (100): (g) $F_{16}ZnPc$, (h) $F_{34}ZnPc$, (i) $F_{40}ZnPc$, (j) $F_{64}ZnPc$.

Examination of the Pc LUMO states within the CB of TiO_2 shows an increase in Pc | TiO_2 orbital coupling on the rutile (100) surface compared to the rutile (110) surface (Figure 4.13). Because of this increased coupling; large scale DFT calculations were performed on the rutile (100) surface sensitized with $F_{16}ZnPc$, $F_{34}ZnPc$, and $F_{40}ZnPc$ to investigate the electron injection process.

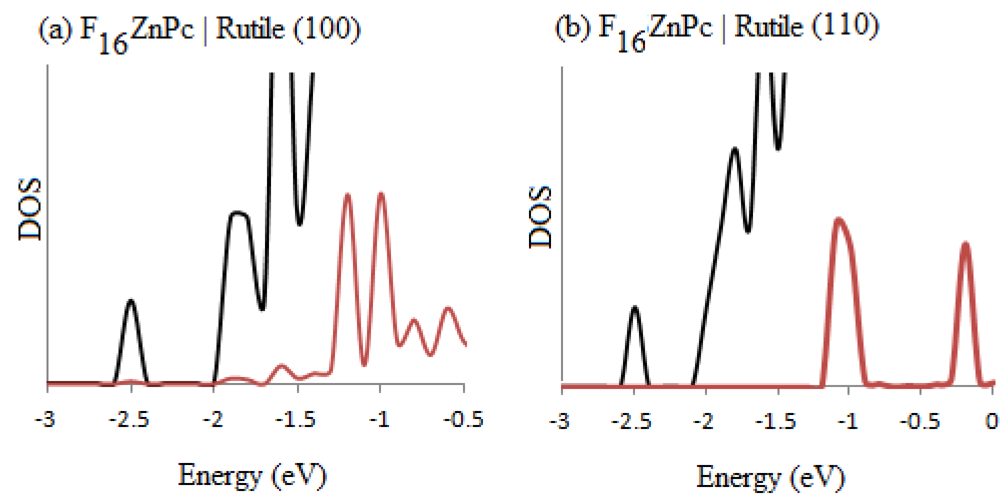

Figure 4.13. Magnified CB edge of (a) rutile (100) and (b) rutile (110) surface sensitized with $F_{16}ZnPc$. PM7 Methods.

The DFT optimized Pc | TiO_2 systems are presented in Figure 4.14. Overall, the optimized structures show a slightly increased distance between the Pc and surface compared to the NiO surface. But a more expected trend is observed; $F_{16}ZnPc$ is the closest to the surface (2.708 Å), followed by $F_{34}ZnPc$ (2.927 Å), and $F_{40}ZnPc$ (3.125 Å). Increased bulky substitution restricts the Pc's approach to the surface. This is expected to influence the Pc orbital coupling with the CB and, in turn, the estimated electron injection lifetimes.

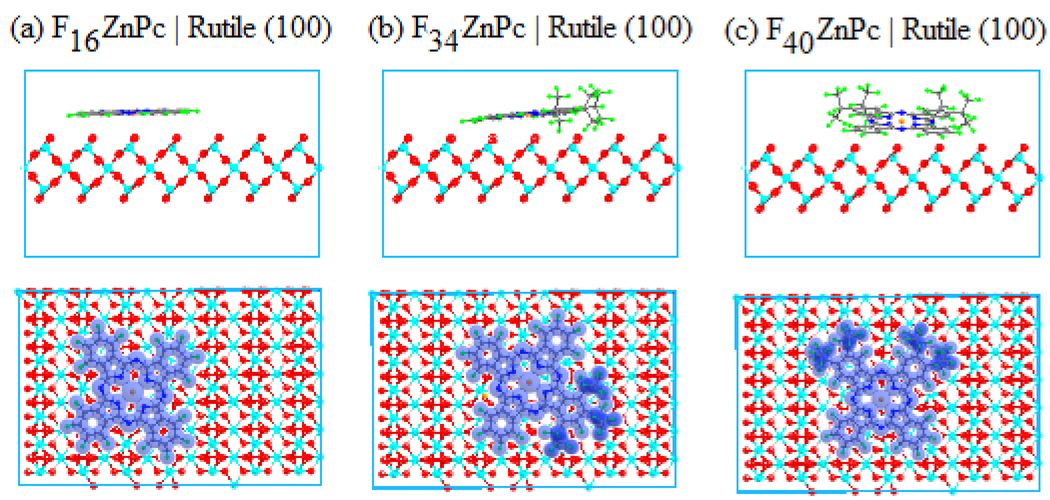

Figure 4.14. Geometry optimized Pc | TiO_2 systems: (a) $F_{16}ZnPc$, (b) $F_{34}ZnPc$, and (c) $F_{40}ZnPc$. Viewed edge on (top) and top down (bottom). VDW spheres used to illustrate Pc in top down view for clarity.

As with the Pc sensitized NiO calculations, we will employ the Newns-Anderson model to examine the molecular orbital coupling within the rutile CB to estimate electron injection lifetimes. The DOS and PDOS are calculated from the optimized systems to examine the Pc | TiO_2 band alignment. The total DOS are illustrated in Figure 4.15. There is little deviation in the energy of the CB edge when sensitized with the various Pcs. The DOS peaks of the $F_{34}ZnPc$ | rutile (100) system are broader than the other DOS due to a slightly larger energy interval sampling. This only affects the graphical representation of the DOS not the MO analysis used to estimate the hole injection lifetime. Between the distinct rutile VB and CB, there is a small population of occupied MOs belonging entirely to the Pc molecule. This is in agreement with the semiempirical calculations discussed previously.

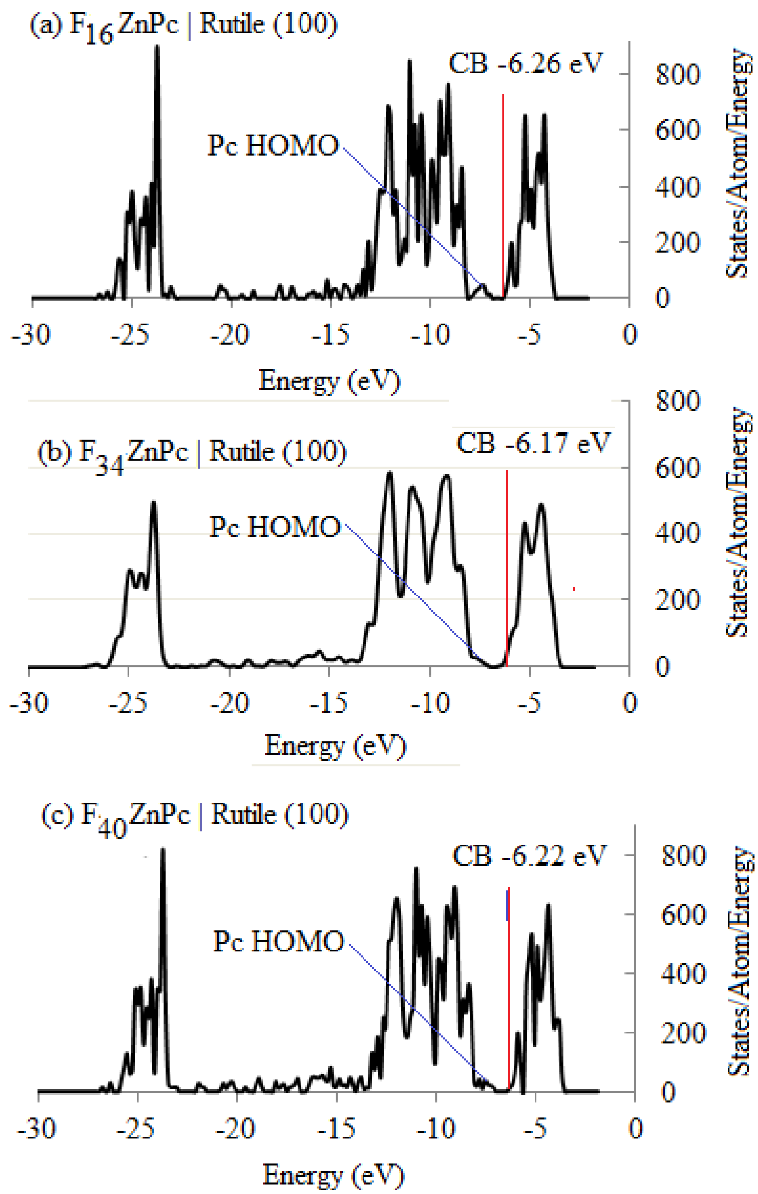

Figure 4.15. Calculated total DOS of (a) $F_{16}ZnPc$, (b) $F_{34}ZnPc$, and (c) $F_{40}ZnPc$ on rutile (100).

To get a better description of the Pc contributions near the CB edge; the DOS is parsed into Pc contributions and surface contributions to each MO (Figure 4.16).

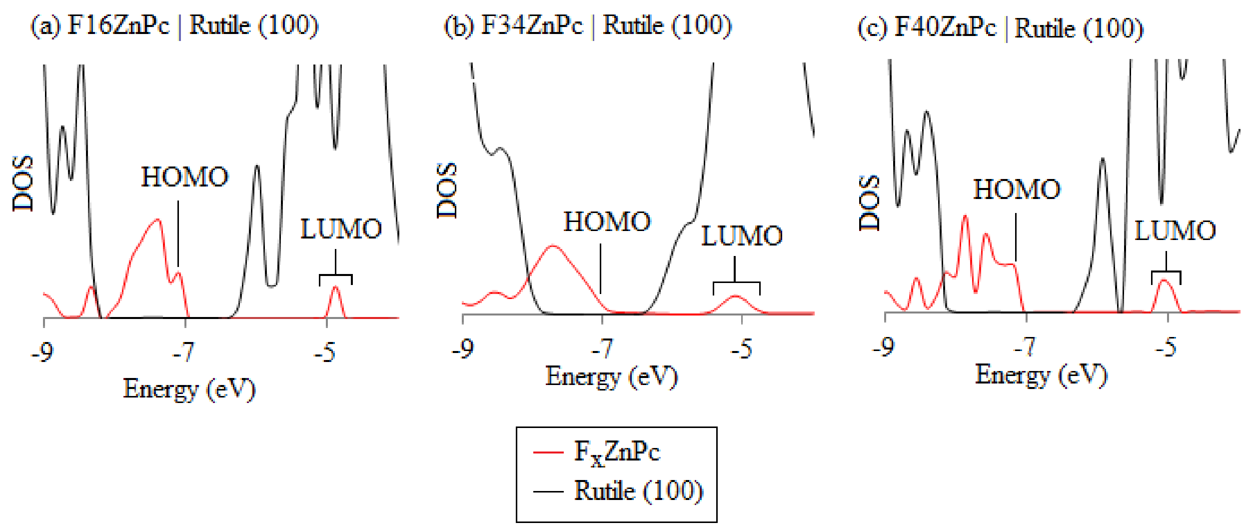

Figure 4.16. Magnified PDOS of (a) F_{16}ZnPc, (b) F_{34}ZnPc, and (c) F_{40}ZnPc. Pc contributions multiplied by a factor of 5 for clarity.

The LUMO state of all Pc sensitizers is found to be significantly above the rutile VB; which allows for electron injection from the excited sensitizer. Additionally, the LUMO state of all Pcs displays orbital coupling with the CB states. As seen in Figure 4.17, the broadening of the Pc LUMO state is greatest for F_{34}ZnPc, followed by F_{40}ZnPc, and F_{16}ZnZnPc. This is unexpected result given that the ability of F_{16}ZnPc to get closer to the surface should allow for increased orbital coupling with the surface. Analysis of each MO reveals that F_{16}ZnPc does show slightly more coupling with the surface, but it is restricted a few Pc states; resulting in the lower broadening. The first unoccupied MO in the F_{16}ZnPc | rutile (100) system with significant Pc contributions is found to have 68% of the electron density localized on F_{16}ZnPc. The first unoccupied MO in the F_{34}ZnPc | rutile (100) and F_{40}ZnPc | rutile (100) systems with significant Pc contribution have 76% and 80% Pc contributions, respectively. The Pc contributions of the LUMO(ads) states, along with the LUMO(ads) Lorentzian distribution is presenting in Figure 4.17.

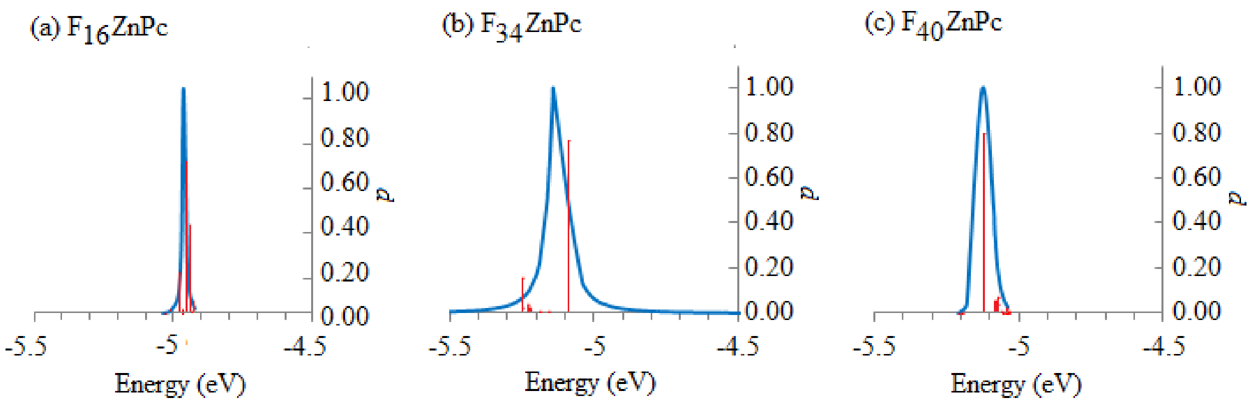

Figure 4.17. Lorentzian distribution of Pc LUMO(ads) states to illustrate the degree of broadening for; (a) $F_{16}ZnPc$, (b) $F_{34}ZnPc$, and (c) $F_{40}ZnPc$. The distribution is normalized. Vertical red lines indicate the energy and Pc contribution in the LUMO(ads) states.

The degree of coupling for all Pcs is less on rutile (100) than the NiO (100) surface discussed previously. This results in longer charge injection lifetimes on the rutile surface (Table 4.6). Nevertheless, the estimated fs timescale electron injection into the rutile (100) CB is a promising result for our proposed DSSC design. This ultrafast electron transfer from the Pc may also reduce the opportunity for charge recombination on the NiO surface.

Table 4.6. Calculated energy of CB edge (E_{CB}), Pc LUMO(ads), Pc HOMO (E_{LUMO}), LUMO broadening ($\hbar\Gamma$), Gibbs free energy for electron injection (ΔG_{e-}), Gibbs free energy for charge recombination at the TiO_2 surface (ΔG_{CR}), and estimated hole injection lifetime (τ). All values reported in eV, unless noted otherwise.

	E_{CB}	E_{LUMO}(ads)	E_{HOMO}	$\hbar\Gamma$ (meV)	τ (fs)	ΔG_{e-}	ΔG_{CR}
$F_{16}ZnPc$	-6.25	-4.96	-7.16	13.06	50	-1.29	+0.91
$F_{34}ZnPc$	-6.17	-5.13	-7.25	58.73	11	-1.04	+1.08
$F_{40}ZnPc$	-6.22	-5.11	-7.24	24.56	27	-1.11	+1.02

4.2.4 Other Potential P-type Semiconductors

As previously discussed, the VB band alignment of NiO with common electrolyte redox couples has proven to be inadequate for p-DSSCs. Our proposed cell design removes the need for an electrolyte, but the energy of the NiO VB is located near the Pc LUMO state. This could ultimately lead to the promotion of charge recombination on the NiO surface. NiO is also know to have poor hole mobility (~ 50 $cm^2/V \cdot s$), which would also increase the amount of charge recombination. Therefore, several additional p-type semiconductors have been investigated as a potential photocathode material. To lower the possibility of charge recombination, the VB edge should be lower than that of NiO to allow a greater ΔG_{CR}. However, we still need the VB to sufficiently high enough so that the Pc HOMO state is below and coupled with VB states. The p-type semiconductors that meet these requirements are: AlAs (100 $cm^2/V \cdot s$), CdTe (100 $cm^2/V \cdot s$), GaAs (400 $cm^2/V \cdot s$), InAs (460 $cm^2/V \cdot s$), Si (450 $cm^2/V \cdot s$), SiC (50 $cm^2/V \cdot s$). [191] It should be noted that these semiconductors have drawbacks of their own. The major flaw for all is a relatively low band gap; which may lead to low photostability and decreased longevity of the cell.

Currently calculations of these semiconductors sensitized with F_{16}ZnPc and F_{40}ZnPc have only been carried out via PM7 semiempirical methods. But these methods have proven apt for the prediction of the Pc | semiconductor band alignment (see section 4.5). The PM7 methods have not been as successful in reproducing the DFT charge injection lifetimes; but they are still calculated and presented for these surfaces. The methodology for estimating hole injection lifetimes is the same that was used for NiO. All of these additional semiconductors have zinc-blend crystal structure, with the exception of Si, which has diamond structure. Low index (110) surfaces were cleaved for the analysis in all systems. All of the PM7 optimized structures are available in Appendix E.

The key characteristics for efficient hole injection for each system studied is presented in Table 4.7. Since these are all semiempirical PM7 calculations, a direct comparison of the calculated Pc HOMO(ads), Pc LUMO, and VB energies to the DFT NiO systems is not warranted. We are interested in the relative difference in energy between these states, which allows for calculation of ΔG_{h+} and ΔG_{CR}. The free energy associated with charge recombination is difficult to obtain accurately due to the significant overestimation of the Pc band gap in the PM7 calculations. The Pc LUMO for all systems is artificially high, leading to inflated ΔG_{CR}. Although the Pc gap is underestimated in the DFT calculations, 1.30 eV for F_{16}ZnPc and 1.11 for F_{40}ZnPc, we will use these gaps for the prediction of ΔG_{CR} in the following systems. As previously discussed, this may lead to an underestimation of ΔG_{CR}; but it will serve as a comparison with the NiO systems.

Table 4.7. Calculated energies of the valence band edge (VBE), Pc $HOMO_{(ads)}$ level, Pc LUMO, $HOMO_{(ads)}$ broadening (ħΓ), Gibbs free energy of hole ininjection (ΔG_{h+}), and free energy of charge recombination (ΔG_{CR}) for AlAs, CdTe, GaAs, InAs, Si, and SiC surfaces. All values reported in eV unless noted otherwise.

	Pc	VBE	$HOMO_{(ads)}$	ΔG_{h+}	LUMO	ΔG_{CR}	ħΓ (meV)	τ (fs)
AlAs	$F_{16}ZnPc$	-8.47	-7.90	+0.57	-6.60	+1.87	---	---
	$F_{40}ZnPc$	-8.46	-8.36	+0.10	-7.26	+1.20	---	---
CdTe	$F_{16}ZnPc$	-7.97	-7.68	+0.29	-6.38	+1.61	---	---
	$F_{40}ZnPc$	-7.89	-8.46	-0.57	-7.36	+0.53	50.46	13
GaAs	$F_{16}ZnPc$	-7.56	-7.80	-0.24	-6.50	+1.06	11.35	58
	$F_{40}ZnPc$	-7.54	-8.30	-0.76	-7.20	+0.34	48.08	14
InAs	$F_{16}ZnPc$	-7.21	-7.33	-0.12	-6.03	+1.18	---	---
	$F_{40}ZnPc$	-7.21	-7.76	-0.55	-6.66	+0.55	17.21	38
Si	$F_{16}ZnPc$	-7.12	-8.62	-1.50	-7.32	-0.20	78.89	8
	$F_{40}ZnPc$	-7.01	-8.76	-1.75	-7.66	-0.65	1.18	557
SiC	$F_{16}ZnPc$	-6.90	-7.74	-0.84	-6.44	+0.46	50.11	13
	$F_{40}ZnPc$	-6.90	-7.92	-1.02	-6.82	+0.08	22.30	30

The calculated DOS, PDOS, and HOMO(ads) Lorentzian distributions of $F_{16}ZnPc$ and $F_{40}ZnPc$ on all of these surfaces are provided in Appendix E. The Pc HOMO state for both Pc sensitizers is found to be above the VB of AlAs. Therefore hole injection from the Pc is not possible in these systems. The same result is found for $F_{16}ZnPc$ on CdTe. However, the lowering of the Pc HOMO as peripheral fluorination is increased results in an $F_{40}ZnPc$ HOMO below the VB of CdTe. This HOMO state is not as deep into the VB as $F_{40}ZnPc$ on NiO resulting in a ΔG_{h+} of -0.57 eV; which leads to an increase in ΔG_{CR} (+0.53 eV) compared to the NiO system (+0.11 eV). The $F_{40}ZnPc$ HOMO is also significantly coupled with the CdTe VB states. The calculated hole injection lifetime is on the fs timescale, suitable for hole injection prior to relaxation of the Pc excited state.

GaAs is overall the most promising of this set of additional p-type semiconductors. Both F_{16}ZnPc and F_{40}ZnPc have a HOMO below the VB of GaAs. There is also a significant amount of orbital coupling between the Pc and the surface in both systems. More importantly, there is in increase in the calculated ΔG_{CR} compared to NiO. As with F_{16}ZnPc and F_{40}ZnPc on NiO, fs hole injection lifetimes are found. Expectedly, the HOMO(ads) state of F_{40}ZnPc is deeper into the VB which allows for increased coupling and shorter injection lifetime.

Sensitization of InAs with F_xZnPc provides similar results as CdTe. F_{16}ZnPc has a HOMO slightly below the VB, but the lack of amiable surface states in this region results in no orbital coupling with the surface. The F_{40}ZnPc HOMO is lowered enough by the peripheral fluorination to be located significantly below the VB. The F_{40}ZnPc is also significantly coupled with the surface leading to fs injection lifetime.

F_xZnPc on Si show promising band alignment with the HOMO of both Pcs extensively below and coupled with the VB. However, the Si VB is too high. The Pc LUMO state of both Pcs is below the VB, which would strongly promote charge recombination. Finally, SiC shows promising band alignment for the injection of a hole from the photoexcited Pc into the VB. The HOMO of both Pcs is located below the VB of SiC and a large degree of orbital coupling with the surface is observed in these states. Charge recombination may be a concern for F_{40}ZnPc on SiC given the calculated ΔG_{CR} of +0.08 eV. The LUMO state is essentially at the VB edge.

4.3 Conclusions

A completely solid state, electrolyte free, DSSC has been proposed in which the chemically robust F_xZnPcs are sandwiched between n-TiO_2 and p-NiO. In the absence of a liquid electrolyte solution, the Pc molecule will act as both photosensitizer and electron shuttle in this cell design. The electronic structure of F_xZnPc adsorbed on n-TiO_2 and p-NiO has been calculated to describe free energy and lifetimes associated with the various charge transfer processes. The semiconducting properties of F_xZnPc important for shuttling electrons across the cell are discussed separately in the following chapter.

The DSSC is activated through photoexcitation of the Pc sensitizer. The nearly degenerate LUMO and LUMO+1 state of $F_{16}ZnPc$, $F_{40}ZnPc$ and $F_{64}ZnPc$ results in exceptional light harvesting efficiencies. $F_{34}ZnPc$ has a slightly lower LHF, but is still suitable as a sensitizing material. Following photoexcitation, charge transfer occurs into the active electrode from the Pc excited state. The highly electronegative -C_3F_7 substituents on the periphery of the Pc results in high ionization potential and electron affinity. The high IP of F_xZnPc (> 7 eV) restricts their application as sensitizers in conventional Grätzel cells. Oxidation of the Pc via electron injection into the CB of TiO_2 is an extremely unlikely process. Conversely, the high EA (> 3 eV) of F_xZnPc favors reduction of the Pc through hole injection into the VB of NiO.

Calculations preformed with the Pc adsorbed on NiO and TiO_2 indicate favorable band alignment for charge transfer through the proposed photovoltaic cell. Significant orbital coupling between the Pc and NiO results in an estimated fs hole injection lifetime. Therefore, hole injections is predicted to occur before the spontaneous relaxation of the Pc excited state. Charge recombination on the NiO remains a concern given the low energetic spacing between the Pc

LUMO and NiO VB. Several other p-type semiconductors have been investigated as potential alternatives to NiO. Based on initial semiempirical PM7 calculations, GaAs shows promising results. On the opposing end of the cell, electron injection into the CB of TiO_2 has been estimated to occur on the fs timescale as well. Overall, F_xZnPc presents the proper band alignment and orbital coupling with NiO and TiO_2 for efficient charge transfer; combined with the calculated chare injection lifetimes, the proposed NiO|Pc|TiO_2 DSSC is a promising solar energy conversion device.

4.4 Computational Details

Vacuum state Pc geometry optimizations preformed for calculating the IP and EA were done using density functional theory (DFT)[27-28] as implemented in the General Atomic and Molecular Electronic Structure System (GAMESS)[29-30] software package. The B3LYP[31-33] functional and 6-31+G(d)[37-38] basis set was employed for all single molecule vacuum state calculations; with closed-shell singlet calculations for the neutral species and open-shell doublets for the charged species. Convergence tolerances of 1.0×10^{-3} Ha/bohr for the geometry optimization and 1.0×10^{-5} Ha for the SCF gradient were employed. The selection these tolerances are modest, but we have found this convergence criteria accurately reproduces experimental geometries.[36]

The F_xZnPc absorbance spectra are calculated via time-dependant density functional theory (TDDFT).[39] Several functionals and basis sets were tested to find the optimal level of theory to reproduce experimental absorbance spectra. For more information see Appendix A. The B3LYP functional with 6-31G(d) basis set provided the best agreement with experimental results while maintain computational efficiency. Bulk solvent (ethanol) effects were also included in the absorbance spectra calculations using the polarizable continuum model (PCM);[40] analogy with experimental. The first five vertical excitations were calculated to better describe the first one.

For the investigation of the Pc|semiconductor interface, calculations were performed using the semiempirical Molecular Orbital PACkage (MOPAC)[192] version 2012. The PM7[193] parameterization values based on Dewar and Thiel's neglect of diatomic differential overlap (NDDO)[194] approximation was employed for all calculations. Due to the large size of these systems, the Broyden-Fletcher-Goldfarb-Shanno (BFGS)[195] procedure was used for the optimizations. Additionally select systems were studied via ab initio calculations using the Vienna Ab-initio Simulation Package (VASP)[196-199]. Projector-augmented wave (PAW)[200-201] basis functions were used. Due to the size of these systems the cut-off energy for the plane wave basis set was 400 eV. Additionally, the *k* point sampling was limited to Monkhorst-Pack[202] meshes of 1x1x1. The partial occupancies of wave functions were estimated using the Gaussian smearing method for both optimization and band structure analysis. Optimization convergence criteria were set to 5×10^{-4} eV/Å and 0.5 eV/Å for the SCF loops and geometry, respectively.

Due to the antiferromagnetic nature of NiO, a local spin density approximation (LSDA)+U[203] correction was employed. Previously studies[204] have reported that *U* in the range of 6.0 - 6.3 eV and J = 1.0 eV are best for reproducing the experimental band gap of NiO. However, these correction terms still only prove a NiO band gap of ~ 3 eV; compared to the 4.0 eV experimental gap. For calculations in this study; *U* and *J* values of 6.0 and 1.0 were used, respectively.

4.5 Validation of Semiempirical PM7 Methods

Investigation of the Pc|semiconductor interface requires constructing exceptionally large systems. To reduce the computational cost of these calculations, semiempirical PM7 methods were often employed. Compared to the DFT calculations that were carried out on select interfaces, the PM7 method resulted in significant differences in the calculated MO energies. There was also a severe overestimation of the band gap of both the Pcs and semiconductor surfaces. However, the exact energy of these various states is not vital to the investigation of the charge transfer dynamics. The primary focus is on the location of the Pc and surface states relative to one another.

Fundamental to the operation of our proposed DSSC is that: (a) the HOMO of the Pc is below the VB of the photocathode and, (b) the Pc LUMO is above the CB edge of the photoanode. The semiempirical methods used in this study provide a quality description of the location of Pc HOMO (LUMO) relative to the VB (CB) edge. Since both PM7 and DFT methods were employed for the Pc|rutile (100) systems; comparison of the results may be used to validate the PM7 calculations (Table 4.8)

Table 4.8. Comparison between calculated energies of the CB, LUMO(ads), and ΔG_{e-} obtained by PM7 and DFT methods. All values reported in eV.

	PM7			**DFT**		
	E_{CB}	E_{LUMO}(ads)	ΔG_{e-}	E_{CB}	E_{LUMO}(ads)	ΔG_{e-}
F_{16}ZnPc	-2.50	-1.20	1.30	-6.26	-4.96	1.29
F_{34}ZnPc	-2.42	-1.49	0.93	-6.17	-5.13	1.11
F_{40}ZnPc	-2.43	-1.52	0.91	-6.22	-5.11	1.04

As seen in Table 4.8, the PM7 energies of the CB and LUMO(ads) are very different than the corresponding DFT values. But the free energy associated with electron injection is accurately calculated via PM7 methods. The average variation between DFT and PM7 is only 0.11 eV; acceptable given the significant increase in computational efficiency provided by the semiempirical methods. Therefore, the PM7 methodology employed throughout this study to screen for semiconductors with the proper band alignment is justified.

CHAPTER 5

Charge Transfer Properties in Modified Perfluoroisopropyl-Phthalocyanines

5.1 Introduction

Recent interest in the electronic structure and charge transport properties of organic semiconductors has focused on a number of promising application areas, including photovoltaic cells,[205] light-emitting diodes,[206-207] and field-effect transistors.[208] Although it is not expected that organic semiconductors will match or exceed the performance level of inorganic semiconductors, they do offer distinct advantages such as reduced materials and processing cost and in tenability.[209] Planar molecular frameworks with extended π conjugation have become the most popular and best performing semiconductor materials for organic field-effect transistors (OFET) resulting from charge transport pathways provided by the intermolecular π orbital overlap in molecular dimers. Significant progress has been made, to date, in developing n-type, p-type, and ambipolar semiconductors although the majority of the reported materials display predominantly p-type (hole transfer) behavior. These p-type materials include several different oligoacenes, such as pentacene,[210-211] tetracene,[212] rubrene,[213] and oligofluorenes.[211]

Development of organic n-type materials has been challenging due to the high electron injection barrier from the electrode to the lowest unoccupied molecular orbital (LUMO) of the molecule. The charge injection barrier for organic semiconductors is the difference between the work function of the electrode, most commonly gold (4.8-5.1 eV), and the LUMO (electron injection) or HOMO (hole injection) of the semiconductor.[208] The LUMO of many organic semiconductors is in the range of 2-3 eV which presents an electron injection barrier of 2-3 eV. Metal electrodes with lower work functions such as calcium, magnesium, or aluminum do not present a solution to this problem given the low environmental stability of these electrodes.[208] One strategy to improve n-type properties is through the introduction of strong electron withdrawing groups into the molecular framework. The electron withdrawing groups act to lower the energy of the LUMO which, in turn, improves the electron injection into the material from the electrode.

Metal phthalocyanines (MPc) have long received extensive research attention in the field of organic device electronics. Much of this interest is attributed to their highly tunable electronic properties based upon the choice of metal center and modification of the molecular periphery. Commonly used Pcs in OFETs include metal-free phthalocyanines (H2Pc),[159] copper phthalocyanine (CuPc),[56,214] tin phthalocyanine (SnPc),[215-216] and zinc phthalocyanine (ZnPc).[217] These reports indicate that Pc-based materials exhibit among the highest carrier mobilities reported in OFET technology. The focus of these studies primarily involved the effect of varying the type of metal center rather than modification of the molecular periphery. It is well-recognized that substitution of the peripheral hydrogen atoms with electron withdrawing fluorine or per-fluoroalkyl groups can significantly increase the chemical stability particularly in electronic device applications.[23] Moreover, the introduction of electron withdrawing groups results in electronically stabilized HOMO and LUMO electronic states that would be expected to exhibit enhanced n-type carrier mobilities. However, it would also be expected that with the introduction of bulky per-fluoroalkyl groups on the molecular periphery, intermolecular orbital overlap would be reduced. In that case, one would expect a reduction in carrier mobilities. Although some experimental investigations have appeared in the literature involving fluorinated phthalocyanines, particularly the planar perfluoro-copper-phthalocyanine ($F_{16}CuPc$), as semiconducting materials,[218-221] the relative effects of these two opposing effects have not, to our knowledge, been investigated.

Herein, we report the results of computational investigations of the charge transport properties of three ZnPc species derivatized with peripheral perfluoro-isopropyl groups. The target Pcs include; $F_{16}ZnPc$, $F_{34}ZnPc$, $F_{40}ZnPc$, and $F_{64}ZnPc$.

5.2 Methodology

In conjunction with experimental investigations into OFET device preparation and fabrication techniques; extensive efforts have been made via theoretical studies to better understand the relationship between OFET performance and molecular material design. From a theoretical standpoint, the intrinsic semiconducting properties of OFET materials are influenced by the: (1) energy of the HOMO and LUMO state, (2) ionization potential (IP) and electron affinity (EA) of the material, (3) reorganization energy for hole (λ_+) and electron (λ_-), (4) charge transfer integral for hole (J_+) and electron (J_-), and (5) distance of charge transfer.[209]

P-type semiconductors should have a high HOMO state (low IP), and n-type semiconductors should have a low LUMO (large EA). As previously stated, to ensure efficient charge injection from the source-drain electrode, the IP (hole injection) and EA (electron injection) should be close to the work function potential of the electrode.[208] The reorganization energy, charge transfer integral, and charge transfer distance, all dictate the charge transfer mobility; thus, determining the performance of the semiconductor material.

The first three of these five fundamental properties are intrinsic properties of the molecule; while the last two are determined by the intermolecular interactions between neighboring molecules. It has been shown in previous chapters, and elsewhere,[21] that increasing peripheral perfluoro-isopropyl substitution leads to a lowering of the molecular frontier orbitals and the degree of Pc aggregation. As potential n-type organic semiconductors, the various F_xZnPcs of interest in this study allow for determination of the optimal substitution pattern that presents a high EA while maintaining strong intermolecular interactions with neighboring Pcs.

Solid state charge transfer in organic semiconductors is modeled following the charge hopping mechanism.[209,222-225] The hopping mechanism describes charge transfer as a self-exchange electron transfer reaction between a neutral molecule and a neighboring cation (p-type) or anion (n-type). The rate constant, *W*, for charge transfer can then be obtained via classical Marcus theory as:[226-227]

$$W = \frac{2J^2}{h}\sqrt{\frac{\pi^3}{\lambda k_B T}}\exp\left(\frac{-\lambda}{4k_B T}\right) \tag{5.1}$$

where T, k_B, and *h*, are temperature, Boltzmann, and Planck constants, respectively. The reorganization energy, λ_+ (λ_-) for hole (electron) transfer, is calculated from: (1) the energy of vertical ionization of the neutral molecule to the charged species followed by geometry relaxation and, (2) the energy of vertical neutralization of the charged species followed by geometry relaxation:

$$\begin{aligned} \lambda_- &= \left(E_0^- - E_-^-\right) + \left(E_-^0 - E_0^0\right) \\ \lambda_+ &= \left(E_0^+ - E_-^+\right) + \left(E_+^0 - E_0^0\right) \end{aligned} \tag{5.2}$$

where the subscripts and superscripts 0, -, and + represent the molecular geometry and charge state, respectively. Low reorganization energy is preferable in order to maximize the charge transfer rate and carrier mobility.[216,228-229] The charge transfer integral, *J*, describes the intermolecular electronic coupling between neighboring molecules. To achieve high carrier mobility, the transfer integral must be maximized. In this study, nearest neighboring molecular pairs are selected from previously reported crystal structures for $F_{16}PcCu$[77] and $F_{64}PcCu$.[21] It is noted that the $F_{16}PcCu$ and $F_{64}PcCu$ XRD refinement were done for the Copper complexes and the $F_{64}PcCu$ crystal refinement contained co-crystallized ethyl acetate solvent. In the absence of $F_{40}ZnPc$ and $F_{34}ZnPc$ crystal structures, molecular pairs for these system were obtained from the calculated stacking orientations previously reported via molecular dynamics simulations.[36] The transfer integral is calculated using the direct dimer Hamiltonian method:[230-231]

$$J_{+/-} = \left\langle \Phi^{fragment1}_{HOMO/LUMO} \middle| F^0 \middle| \Phi^{fragment2}_{HOMO/LUMO} \right\rangle \tag{5.3}$$

In this approach, each molecule of the dimer is treated as separate molecular fragments with non-interacting molecular orbitals. The transfer integral is obtained through directly evaluating the dimer Fock matrix with the unperturbed monomer orbitals and associated density matrix. This method has been shown to be more reliable[230,232-234] than the "energy splitting in dimer" scheme,[235] which evaluates the transfer integral as half of the splitting of the HOMO and LUMO levels of the dimer.

Using the obtained transfer integral and spatial overlap matrix elements (*S*), the effective charge transfer integral is calculated as:

$$J_{eff} = J_{ij} - \frac{1}{2}\left[S_{ij}\left(\varepsilon_i + \varepsilon_j\right)\right] \tag{5.4}$$

Where the site energies of the two frontier molecular orbitals, HOMO for hole transfer and LUMO for electron transfer, are denoted by ε_i and ε_j. Once the charge transfer rate constant (*W*) between neighboring dimer pairs is acquired from eq. 5.1, the diffusion coefficient (*D*) is calculated as:

$$D = \frac{1}{2d} \frac{\sum_i r_i^2 W_i^2}{\sum_i W_i} \tag{5.5}$$

with the dimensionality of the crystal, 3 for all systems in this study, is represented by *d*, and *r* denoting the distance between neighboring monomer pairs; measured as the molecular center to center distance. The summation is carried out over several charge transfer pathways, *i*. Finally, the charge carrier mobility (μ) is obtained via the Einstein relation:

$$\mu = \frac{e}{k_B T} D \tag{5.6}$$

5.3 Results

5.3.1 F_xZnPc Electronic Properties

The calculated energy of the HOMO and LUMO orbital states along with the corresponding HOMO-LUMO gap of the target molecules are presented in Table 5.1. All Pcs have a calculated HOMO-LUMO gap of 2.09 eV. Therefore, the degree of fluorination on the periphery has no effect on the gap. However, the addition of the peripheral electron withdrawing groups lowers the energy of both the HOMO and LUMO states. This results in an increase in the

IP and EA as Pc fluorination increases. Considering the work function of the standard gold electrode (~ 5 eV); the energetic barrier for electron injection into the LUMO of the Pc is lowered ($F_{16}ZnPc > F_{34}ZnPc > F_{40}ZnPc > F_{64}ZnPc$), while the barrier for hole injection into the HOMO is increased ($F_{16}ZnPc < F_{34}ZnPc < F_{40}ZnPc < F_{64}ZnPc$). This suggests that increased fluorination of F_xZnPc tunes the molecule to favor n-type semiconducting behavior.

Table 5.1. Energy of F_xZnPc Frontier Orbitals and Corresponding HOMO-LUMO Gap. Calculated Vertical and Adiabatic Ionization Potentials and Electron Affinities. All values reported in eV.

	E_{HOMO}	E_{LUMO}	$\Delta E_{H\text{-}L}$	IP_v	IP_a	EA_v	EA_a
$F_{16}ZnPc$	-6.14	-4.05	2.09	7.38	7.34	2.98	3.08
$F_{34}ZnPc$	-6.30	-4.21	2.09	7.33	7.26	3.15	3.30
$F_{40}ZnPc$	-6.48	-4.39	2.09	7.48	7.42	3.35	3.43
$F_{64}ZnPc$	-6.78	-4.69	2.09	7.72	7.66	3.72	3.83

5.3.2 Reorganization Energy

As previously discussed, the reorganization energy of the molecule has a direct impact on the rate of charge transfer. For a maximal transfer rate, the reorganization energy upon oxidation and/or reduction of the molecule should be minimized. Calculated hole and electron reorganization energies are presented in Table 5.2. For all Pc's in this study, λ_+ is lower than that of λ_-, indicating favored hole transfer (p-type) over electron transfer (n-type). Increased peripheral fluorination leads to an increase in λ_+. Therefore, based on calculated reorganization energy, the rate of hole transfer is predicted to decrease with increased fluorination while the rate of electron transfer does not show a particular dependence on the degree of peripheral fluorination. Interestingly, we do note that $F_{40}ZnPc$ shows a uniquely low λ_- in comparison to $F_{16}ZnPc$, $F_{34}ZnPc$, and $F_{64}ZnPc$. Although λ_+ for $F_{40}ZnPc$ is greater than that of $F_{16}ZnPc$ and $F_{34}ZnPc$, there is a greater balance between λ_+ and λ_-, which may lead to a unique ability to transfer both holes and electrons.

Table 5.2. Calculated Hole and Electron Reorganization Energies of $F_{16}ZnPc$, $F_{34}ZnPc$, $F_{40}ZnPc$, and $F_{64}ZnPc$.

	$F_{16}ZnPc$	$F_{34}ZnPc$	$F_{40}ZnPc$	$F_{64}ZnPc$
λ_-	0.217	0.277	0.165	0.228
λ_+	0.080	0.114	0.117	0.125

Table 5.3 displays the average bond lengths for $F_{16}ZnPc$, $F_{34}ZnPc$, $F_{40}ZnPc$, and $F_{64}ZnPc$ in the optimized neutral (Pc^0), anionic (Pc^-), and cationic (Pc^+) state. This analysis has been restricted to the central conjugated region of the Pc since this is where the HOMO and LUMO states of each neutral molecule are localized as shown in Figure 5.1. Oxidation or reduction of the molecule would have the greatest effect on the bond lengths in this region of the Pc. All bond lengths and 3-body angles for these systems are available in Appendix F. For all systems in this

study, we observe little change in the calculated bond lengths upon oxidation and reduction of the neutral molecule, as indicated by the overall RMSD values in Table 5.3. This is consistent with our observation of small reorganization energies for both hole and electron transfer. It is also observed that the variation in bond lengths of the anions is greater than that of the cations; confirming a greater reorganization energy for electrons than holes, potentially leading to enhanced hole transfer over electron transfer for these materials.

Table 5.3. Comparison of Optimized Average Bond Lengths of Neutral, Anionic, and Cationic $F_{16}ZnPc$, $F_{34}ZnPc$, $F_{40}ZnPc$, and $F_{64}ZnPc$.

	$F_{16}ZnPc$			$F_{34}ZnPc$			$F_{40}ZnPc$			$F_{64}ZnPc$		
bond[a]	Pc	Pc^-	Pc^+	Pc	Pc^-	Pc^+	Pc	Pc^-	Pc^+	Pc	Pc^-	Pc^+
Zn-N_1	2.007	2.011	2.005	2.016	2.020	2.011	2.001	2.006	2.000	2.001	2.006	1.997
N_1-C_1	1.385	1.389	1.386	1.369	1.373	1.371	1.372	1.376	1.374	1.372	1.376	1.373
N_2-C_1	1.331	1.335	1.332	1.324	1.328	1.325	1.328	1.330	1.334	1.327	1.330	1.327
C_1-C_2	1.459	1.455	1.461	1.440	1.467	1.478	1.463	1.458	1.466	1.464	1.456	1.461
C_2-C_2	1.422	1.427	1.421	1.425	1.432	1.423	1.406	1.411	1.406	1.396	1.402	1.397
C_2-C_3	1.391	1.395	1.387	1.404	1.407	1.402	1.391	1.394	1.388	1.392	1.393	1.386
C_3-C_4	1.394	1.391	1.396	1.396	1.392	1.406	1.403	1.400	1.409	1.407	1.402	1.414
C_4-C_4	1.399	1.402	1.395	1.401	1.403	1.397	1.429	1.434	1.421	1.449	1.457	1.447
RMSD (Å10^{-4})	---	1.442	0.357	---	1.296	0.421	---	0.521	0.310	---	1.085	0.387

[a] N_1, the nitrogen atom bonded to central Zn; C_1, C_2, C_3, C_4 represent the carbon atoms starting at N_1 and proceeding around the isoindole ring unit.

$F_{40}ZnPc$ is unique in that there is no significant variation in the bond length between the cation and anion. This finding supports the better balanced λ_+ and λ_- values previously discussed. This may be explained by examining the HOMO and LUMO electron density plots in Figure 5.1. The HOMO for all Pcs is distributed symmetrically over all four isoindole units of the Pc molecule. Conversely, the LUMO electron density of $F_{16}ZnPc$, $F_{34}ZnPc$ and $F_{64}ZnPc$ is distributed across only two isoindole units while the $F_{40}ZnPc$ LUMO maintains a distribution similar to that of the HOMO states. The more delocalized LUMO state of $F_{40}ZnPc$ allows for smaller geometry changes upon reduction. Therefore, oxidation and reduction of $F_{40}ZnPc$ should have similar effects on the bond length variations and as a result, similar reorganization energy for hole and electron transfer.

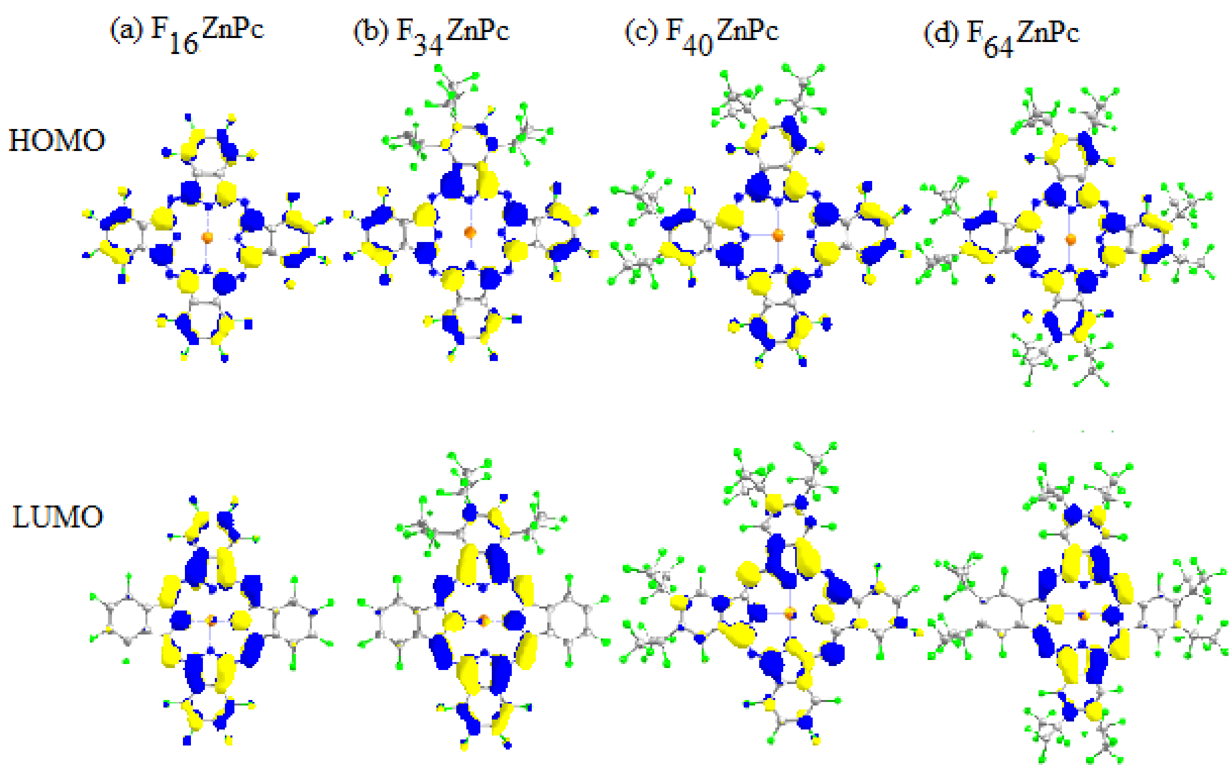

Figure 5.1. Electron Density Plots for the HOMO (top) and LUMO (bottom) of a) $F_{16}ZnPc$, b) $F_{34}ZnPc$, c) $F_{40}ZnPc$, and d) $F_{64}ZnPc$. Density for all figures sampled at 0.03 e/au^3

5.3.3 Charge Transfer Integrals and Mobility

Investigation of the reorganization energy as well as the hopping matrix elements (charge transfer integral) leads to a better understanding of the charge transport and mobility. The charge transfer properties of molecules greatly depend upon the ability to form molecular aggregates in solution or crystal form. Introduction of the bulky $–C_3F_7$ groups on the periphery greatly hinders the ability to form π-stacked dimers as reported elsewhere.[36] The propensity for stacking in F_{16}ZnPc, in which the entire molecular plane is available for π-π interactions, is much greater than that of F_{34}ZnPC and F_{40}ZnPc, in which only one quarter and half of the molecule is available, respectively. The fully substituted F_{64}ZnPc shows very little stacking interactions which may lead to low charge mobility despite the low reorganization energy for this molecule. Charge transfer integrals are calculated based on three potential hopping pathways for each system studied. For F_{16}ZnPc and F_{64}ZnPc molecular dimers found in published crystal structures,[21,77] are used to calculate the transfer integrals.

Since no crystal structure is available for F_{34}ZnPc and F_{40}ZnPc in the literature, dimers found from previous bulk MD simulations[36] on the stacking orientations were used to generate the most likely dimer pairs. These include a dimer in which the monomers are stacked and rotated 180° relative to one another, and a dimer which is rotated 180° and laterally shifted. As well as an F_{40}ZnPc dimer which is not rotated but slightly offset due to the steric hindrance and an F_{34}ZnPc dimer which is stacked and rotated 135 degrees. All of the hopping pathways are illustrated in Figure 5.2.

Calculated charge transfer integrals and charge mobility determined in this study are presented in Table 5.4. For F_{16}ZnPc, the hole transfer integral is larger than the electron transfer integral for all three dimer configurations. For both hole and electron, the transfer integrals decrease in dimer 2 and dimer 3 compared to dimer 1. We interpret this as a direct result of the stacking orientations and interplanar distances of the dimers. The orientation of $F_{16}ZnPc$ dimer 1 has the lowest interplanar distance allowing for the greatest amount of π-π interaction and thus leading to the highest transfer integral value for all $F_{16}ZnPc$ dimers.

For $F_{34}ZnPc$ and $F_{40}ZnPc$, the charge transfer integrals calculated for both hole and electron transfer of the stacked dimers are significantly different than that of $F_{16}ZnPc$. As with $F_{16}ZnPc$, the reduced π-π interaction in some $F_{34}ZnPc$ and $F_{40}ZnPc$ dimers resulting from increased interplanar distances results in negligible charge transfer integral values.

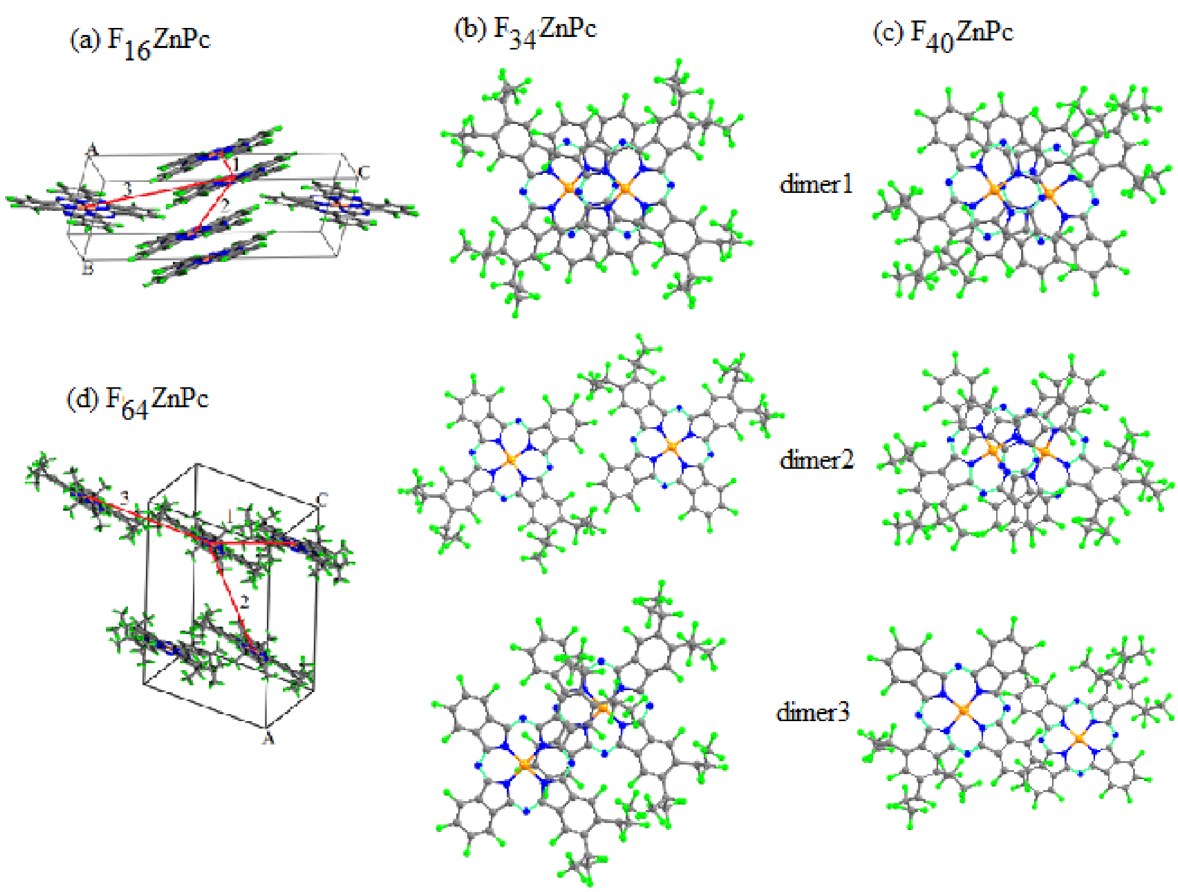

Figure 5.2. F_xZnPc dimer charge hopping pathways studied for calculating charge transfer integrals: (a) $F_{16}ZnPc$, (b) $F_{34}ZnPc$, (c) $F_{40}ZnPc$, and (d) $F_{64}ZnPc$.

While dimer 1 of $F_{16}ZnPc$, $F_{34}ZnPc$, and $F_{40}ZnPc$ have similar stacking orientations, the introduction of the peripheral $–C_3F_7$ groups leads to an increase in the hole transfer integral. This ultimately leads to an increase in the hole mobility. Compared to $F_{16}ZnPc$, $F_{34}ZnPc$ has much lower electron mobility. The calculated charge transfer integrals of the $F_{34}ZnPc$ dimers are not much lower than $F_{16}ZnPc$, but $F_{34}ZnPc$ has the largest electron reorganization energy of any of the F_xZnPc in this study. The low charge transfer integral and high reorganization energy leads to the low electron mobility of $F_{34}ZnPc$.

Table 5.4. Calculated Effective Charge Transfer Integral ($J_{\pm}$), Dimer Energy of Formation (E_f), Interplanar Distance between Monomers (r_{ij}), and Carrier Mobility (μ).

		r_{ij} (Å)	E_f (kcal/mol)	J_+ (eV)	J_- (eV)	μ_{hole} ($cm^2/V\cdot s$)	$\mu_{electron}$ ($cm^2/V\cdot s$)
$F_{16}ZnPc$	1	4.80	-60.04	0.0975	0.0649		
	2	11.93	-15.86	-0.0224	0.0154	3.71	0.265
	3	15.59	-2.17	-0.0003	0.0001		
$F_{34}ZnPc$	1	5.61	-61.05	0.1435	0.0374		
	2	5.62	-60.11	0.1435	0.0374	6.85	0.068
	3	11.06	-2.333	0.0000	0.0000		
$F_{40}ZnPc$	1	5.08	-65.73	0.1718	0.0706		
	2	11.05	-1.15	0.0000	0.0000	7.82	0.697
	3	14.40	-7.83	0.0001	0.0003		
$F_{64}ZnPc$	1	12.16	-30.66	0.0008	-0.0015		
	2	16.91	-1.05	0.0000	0.0000	$8.58x10^{-4}$	$8.25x10^{-4}$
	3	21.06	-2.50	0.0000	0.0000		

The reduced values for the charge transfer integral for both holes and electrons for $F_{64}ZnPc$ strongly suggest that the bulky peripheral groups significantly inhibit intermolecular stacking interactions compared to $F_{16}ZnPc$, $F_{34}ZnPc$, and $F_{40}ZnPc$. This finding is not unexpected given the importance of orbital overlap previously discussed. It should be noted that for dimer 1 of $F_{64}ZnPc$, in which some overlap is observed, the charge transfer integral for electrons is greater than that of holes. This further supports the idea that electron withdrawing groups may.

The charge transfer integral of $F_{40}ZnPc$ dimer 1 is the greatest of all systems investigated. This surprising increase in J_- of $F_{40}ZnPc$ may be explained by the increase dimer orbital overlap allowed by the more delocalized LUMO distribution of $F_{40}ZnPc$ in Figure 5.1. Combining this high charge transfer integral with the exceptionally low electron reorganization energy; $F_{40}ZnPc$ displays high electron mobility.

Overall, hole mobility for all systems is greater than that of electron mobility. Nevertheless, we find that the calculated electron mobilities for these systems, especially $F_{40}ZnPc$, make them promising materials for organic n-type semiconductors compared to other calculated values, including lead phthalocyanine[236] (0.39 $cm^2/V \cdot s$), tin phthalocyanine[215] (0.270 $cm^2/V \cdot s$), coronene[237] (0.163 $cm^2/V \cdot s$), derivatives of 1,3,5-triazine[238] ($6.28 \times 10^{-4} – 3.44 \times 10^{-1}$ $cm^2/V \cdot s$), derivatives of tris(1,2,4)triazolo(1,3,5)-triazine[238] ($2.45 \times 10^{-2} – 1.25 \times 10^{-1}$ $cm^2/V \cdot s$) or metal free phthalocyainine[159,239] (0.32 – 0.43 $cm^2/V \cdot s$). In addition, a few reports have appeared that describe experimentally measured carrier mobilities for the commercially available $F_{16}CuPc$ thin films.[219,240-241] These reports show mobilities no greater that 4 – 6 x 10^{-3} $cm^2/V \cdot s$.

5. 4 Conclusions

In this study, we have focused on analyzing the effect of peripheral fluorination on the electronic and charge transfer properties of per-fluoro-zinc phthalocyanines. Introduction of the strong electron withdrawing $–C_3F_7$ groups shifts the HOMO and LUMO states to lower energies while maintaining low molecular reorganization energies. This leads to a decrease (increase) of the charge injection barrier from the electrode for electron (hole) carriers. The calculated charge mobilities indicate that the hole mobility for both F_{16}ZnPc, F_{34}ZnPc, and F_{40}ZnPc is significantly greater than the electron mobility. However, F_{40}ZnPc displays a greater balance in the hole and electron reorganization energy as well as a substantial improvement in both hole and electron mobility compared to F_{16}ZnPc. The inhibition of intermolecular stacking interactions in F_{64}ZnPc is predicted to result in reduced hole and electron mobility despite the low reorganization energies calculated. Within this study we have shown that design of a molecular framework containing strong electron withdrawing groups while maintaining accessible conjugated regions leads to a significant improvement in the charge transfer properties.

5.5 Computational Details

All calculations are performed using density functional theory (DFT) as implemented in the General Atomic and Molecular Electronic Structure System (GAMESS) software package. The B3LYP functional was employed for all single molecule vacuum state geometry optimizations; with closed-shell singlet calculations for the neutral species and open-shell doublets for the charged species. The 6-31+G(d) basis set was used for all non-Zinc atoms.

Diffuse functions are not available for Zinc within this basis set so the 6-31G(d) basis set was augmented with diffuse functions from the cc-pVDZ basis. The large basis sets are used in all calculations to account for the polarization effects on the charged molecular species. Optimizations were performed to convergence tolerances for geometry optimization and for the SCF gradient of 1.0×10^{-3} Ha/bohr and 1.0×10^{-5} Ha, respectively. These tolerances are adequate given the size of target molecules. We have also found in previous studies that these tolerances accurately reproduce experimental geometries. The dimer systems were calculated using the long range dispersion corrected ωB97x-D[242] DFT functional to better account for the dispersion interactions in the stacked molecular systems. The electron structure of the dimer systems were analyzed using the AOMix program.

Appendix A

Effect of DFT Functional and Basis Set on the Calculated F_xZnPc Absorbance Spectra

TDDFT calculated F_xZnPc absorbance spectra have been used on multiple occasions throughout this work. They have been employed to validate the presence of trans- isomers of $F_{40}ZnPc$ and $F_{52}ZnPc$ in Chapter 1; as well as to quantify the light harvesting efficiency of the various FxZnPcs in Chapter 4. Therefore is it vital that our computational methodology in calculating the absorbance spectra provide accurate results. Comparison with experimental absorbance spectra is the best way to validate the computational parameters.

TDDFT is the most popular method to treat excited states within the DFT framework. While the calculation of excited states has its limitations, TDDFT is capable of producing reliable results.[243-247] There are three major factors that have been found to influence the calculated absorbance spectra: the DFT functional, the size of the basis set, and inclusion of bulk solvent effects. $F_{16}ZnPc$ is the smallest (fewest atoms) of the modified perfluoroisopropyl-phthalocyanines, so it has been used to address each of these factors individually. Calculation of the larger Pcs is significantly more computational demanding; which is compounded with increasing the size of the basis set. Throughout the entirety of this work, the hybrid B3LYP functional with Popel's double zeta 6-31G[34-35] basis set has produced accurate FxZnPc molecular geometries compared to experimental values. Therefore, this functional and basis set was initially used to calculate the absorbance spectra. The calculated $F_{16}ZnPc$ absorbance spectra with the B3LYP[31-33] functional and 6-31G basis set is compared to the experimental spectrum in Figure A.1.

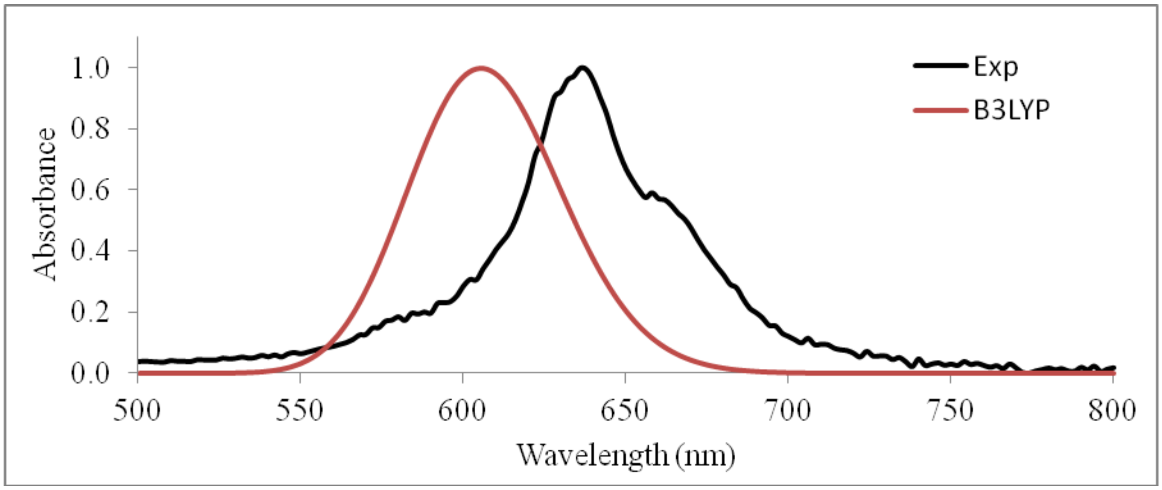

Figure A.1. Calculated Absorbance spectrum of $F_{16}ZnPc$ with B3LYP functional and 6-31G basis set (red line) compared to the experimental spectrum (black line).

The B3LYP functional with 6-31G basis set results in a $F_{16}ZnPc$ absorbance peak at 605 nm compared to the experimental peak at 638 nm. It is noted that the calculation of absorbance spectra provides excitation energies and corresponding oscillator strengths. The oscillator strengths are the transition probabilities. The curve in the calculated spectrum is a normalized Gaussian fit to the excitation energies and oscillator strength. The broadening of this cure is completely arbitrary. The experimental spectrum is in ethanol solvent, while the calculated spectrum in A.1 is vacuum state. To improve on the calculated spectrum of $F_{16}ZnPc$, bulk solvent (ethanol) effects were included using the polarizable continuum model (PCM).[40] This results in a slightly better calculated spectrum as seen in Figure A.2. The calculated absorbance λ_{max} with ethanol solvent effects is at 614 nm.

In an attempt to further improve upon the calculated $F_{16}ZnPc$ absorbance spectrum, the other DFT functionals were employed; including, the hybrid PBE0[248] and long-range corrected

CAM-B3LYP[249] functionals. The calculated absorbance spectra with these new functionals, with solvent effects included, are compared to B3LYP and experimental spectra in Figure A.3.

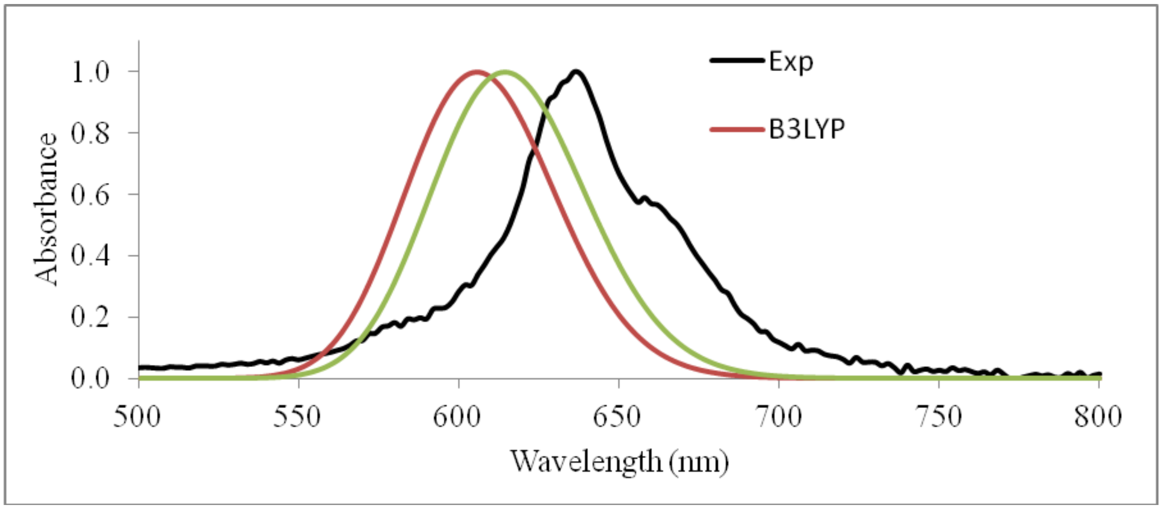

Figure A.2. Calculated Absorbance spectrum of $F_{16}ZnPc$: solvent free B3LYP functional and 6-31G basis set (red line), ethanol solvent (green line), and experimental spectrum (black line).

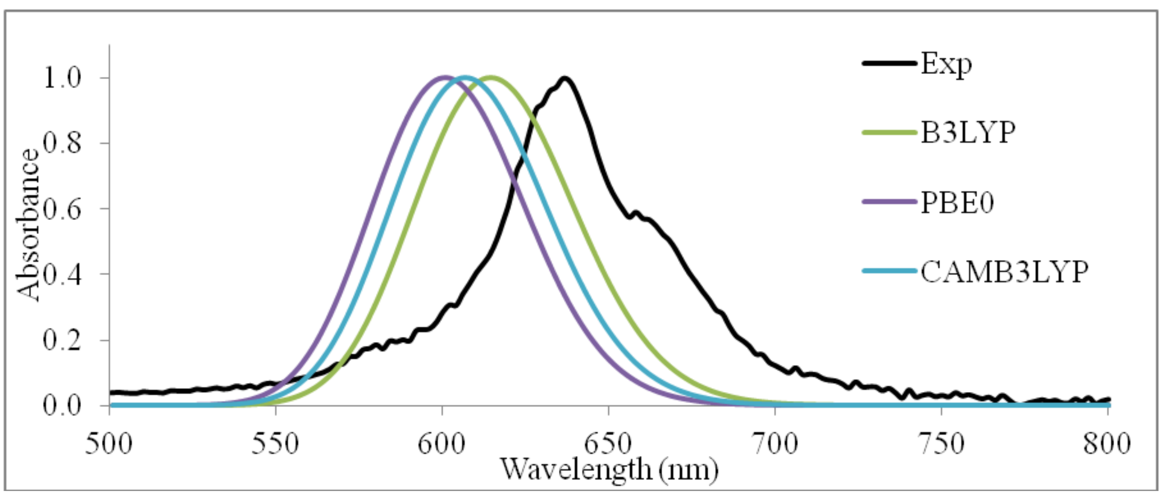

Figure A.3. Calculated Absorbance spectrum of $F_{16}ZnPc$ in ethanol solvent and 6-31G basis set: B3LYP functional (green line), PBE0 (purple line), CAM-B3LYP (blue line), and experimental spectrum (black line).

The additional DFT functionals do not provide more accurate results compared to the experimental spectrum. The calculated λ_{max} for the PBE0 and CAM-B3LYP functionals are located at 600 nm and 607 nm, respectively. Instead of continuing to search for functional to test, we chose to increase the size of the basis set. The much larger 6-31+G(d)[37-38] basis set provides a calculated F_{16}ZnPc absorbance in good agreement with experiment (Figure A.4).

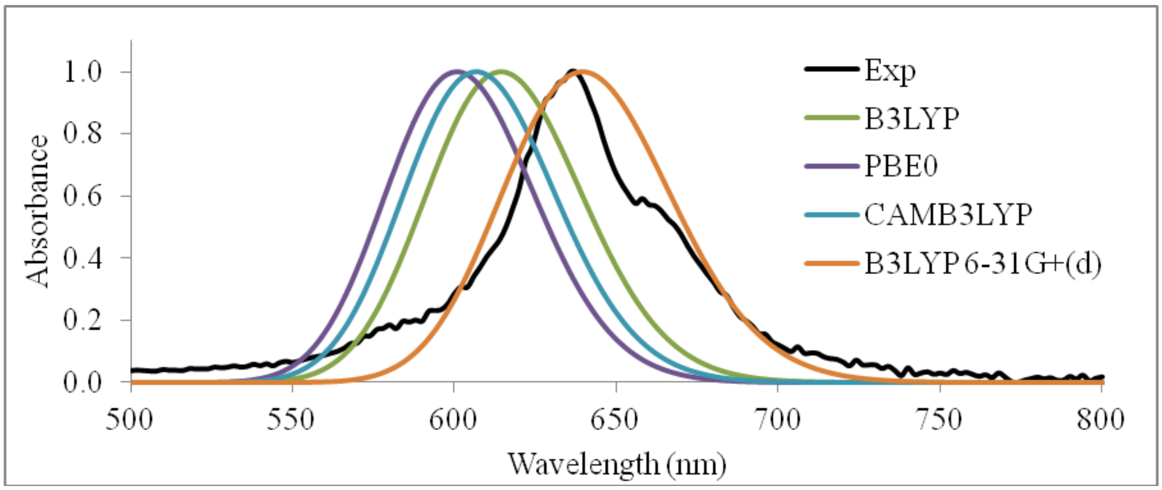

Figure A.4. Calculated Absorbance spectrum of F_{16}ZnPc in ethanol solvent and 6-31G basis set: B3LYP functional (green line), PBE0 (purple line), CAM-B3LYP (blue line), and experimental spectrum (black line). B3LYP with ethanol solvent and larger 6-31G+(d) basis set (orange line).

The larger basis set provided a λ_{max} of 639 nm; excellent agreement with the experimental value of 638 nm. However, using this large basis set is not computationally efficient for the larger F_xZnPc molecules. For excited state calculations, the inclusion of additional polarization functions is more important than diffuse functions. Diffuse functions are important for charged species, such as cation and/or anions. Therefore, removal of the extra diffuse functions should have little effect on the calculated F_{16}ZnPc absorbance spectrum. This is fact observed when the 6-31G(d) basis set is used. Comparison between the 6-31G(d) and 6-

31G+(d) basis set is illustrated in Figure A.5. There is no difference in the calculated $F_{16}ZnPc$ absorbance spectrum without the additional diffuse basis set functions. Therefore, the B3LYP functional with 6-31G(d) basis set is optimal for accurately calculating the absorbance spectrum of the modified perfluoroisopropyl Pcs.

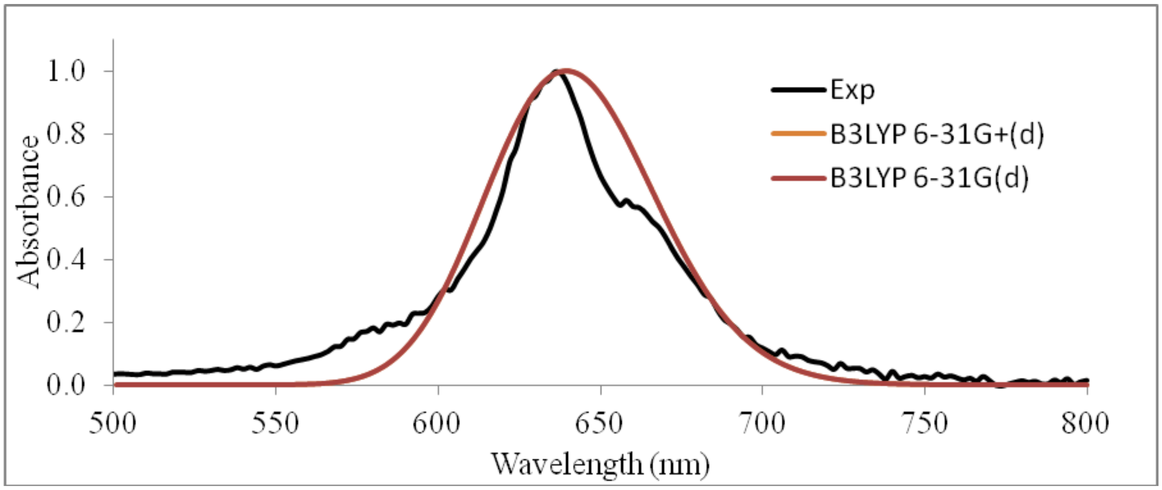

Figure A.5. Comparison between calculated absorbance spectrum of $F_{16}ZnPc$ in ethanol solvent using the 6-31G(d) and 6-31G basis set.

APPENDIX B

Calculated Geometry and Atomic Charge of F_xMPc

All of the MPc structures are optimized with the B3LYP DFT functional and 6-31G basis set. The calculated 2-body bond lengths, 3-body bond angles, and atomic charges for $H_{16}MPc$ are presented in Tables B.1-3 following the atom labeling scheme depicted in Figure B.1.

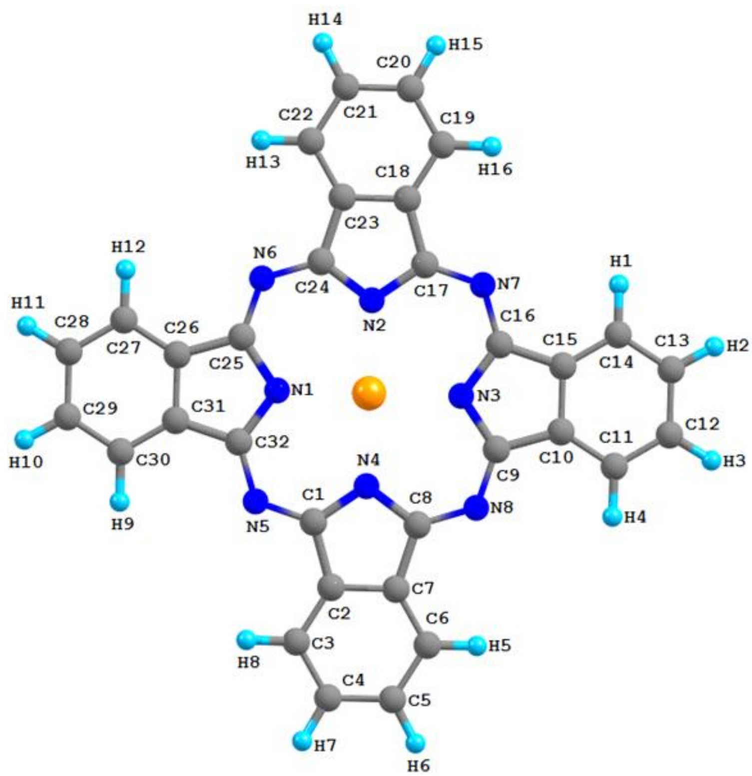

Figure B.1. Atom labeling scheme of $H_{16}MPc$ bond lengths, 3-body angles, and atomic charges.

Table B.1. Calculated bond lengths of $H_{16}MPc$ with B3LYP functional and 6-31G basis set.

	$H_{16}ZnPc$	$H_{16}MgPc$	$H_{16}CoPc$	$H_{16}CuPc$	$H_{16}FePc$
M-N1	2.004	2.004	1.940	2.051	1.965
M-N2	2.003	2.003	1.939	2.057	1.956
M-N3	2.004	2.004	1.940	2.048	1.965
M-N4	2.002	2.002	1.939	2.050	1.956
N1-C25	1.387	1.387	1.395	1.390	1.398
N1-C32	1.387	1.387	1.395	1.315	1.398

N2-C17	1.387	1.387	1.395	1.332	1.400
N2-C24	1.387	1.387	1.395	1.355	1.400
N3-C9	1.387	1.387	1.395	1.322	1.398
N3-C16	1.387	1.387	1.395	1.384	1.399
N4-C1	1.387	1.387	1.395	1.360	1.400
N4-C8	1.387	1.387	1.395	1.347	1.400
N5-C1	1.335	1.335	1.327	1.309	1.329
N5-C32	1.335	1.335	1.327	1.355	1.333
N6-C24	1.335	1.335	1.327	1.352	1.329
N6-C25	1.335	1.335	1.327	1.291	1.333
N7-C16	1.335	1.335	1.327	1.292	1.333
N7-C17	1.335	1.335	1.327	1.362	1.329
N8-C8	1.335	1.335	1.327	1.318	1.329
N8-C9	1.335	1.335	1.327	1.345	1.333
C1-C2	1.461	1.461	1.457	1.486	1.464
C2-C3	1.396	1.396	1.399	1.374	1.399
C2-C7	1.417	1.417	1.411	1.396	1.412
C3-C4	1.399	1.399	1.399	1.398	1.401
C3-H8	1.084	1.084	1.084	1.072	1.084
C4-C5	1.411	1.411	1.412	1.388	1.410
C4-H7	1.085	1.085	1.086	1.074	1.086
C5-C6	1.399	1.399	1.399	1.398	1.401
C5-H6	1.085	1.085	1.086	1.073	1.086
C6-C7	1.396	1.396	1.400	1.374	1.399
C6-H5	1.084	1.084	1.084	1.072	1.084
C7-C8	1.461	1.461	1.457	1.488	1.464
C9-C10	1.461	1.461	1.457	1.486	1.458
C10-C11	1.396	1.396	1.399	1.376	1.402
C10-C15	1.417	1.417	1.411	1.397	1.416
C11-C12	1.399	1.399	1.399	1.397	1.398
C11-H4	1.084	1.084	1.084	1.072	1.084
C12-C13	1.411	1.411	1.412	1.390	1.413
C12-H3	1.085	1.085	1.086	1.074	1.086
C13-C14	1.399	1.399	1.399	1.396	1.398
C13-H2	1.085	1.085	1.086	1.074	1.087
C14-C15	1.397	1.397	1.400	1.374	1.403
C14-H1	1.084	1.084	1.084	1.072	1.084
C15-C16	1.461	1.461	1.458	1.481	1.459
C17-C18	1.46	1.46	1.457	1.464	1.464
C18-C19	1.396	1.396	1.399	1.383	1.399
C18-C23	1.417	1.417	1.411	1.404	1.412
C19-C20	1.399	1.399	1.399	1.389	1.401
C19-H16	1.084	1.084	1.084	1.072	1.084
C20-C21	1.411	1.411	1.412	1.397	1.410
C20-H15	1.085	1.085	1.086	1.074	1.086
C21-C22	1.399	1.399	1.399	1.389	1.401
C21-H14	1.085	1.085	1.086	1.074	1.086

C22-C23	1.396	1.396	1.400	1.385	1.399
C22-H13	1.084	1.084	1.084	1.072	1.084
C23-C24	1.461	1.461	1.457	1.458	1.464
C25-C26	1.461	1.461	1.457	1.476	1.458
C26-C27	1.397	1.397	1.399	1.376	1.402
C26-C31	1.417	1.417	1.411	1.398	1.416
C27-C28	1.399	1.399	1.399	1.395	1.398
C27-H12	1.084	1.084	1.084	1.073	1.084
C28-C29	1.411	1.411	1.412	1.390	1.413
C28-H11	1.085	1.085	1.086	1.073	1.087
C29-C30	1.399	1.399	1.399	1.396	1.398
C29-H10	1.085	1.085	1.086	1.073	1.086
C30-C31	1.396	1.396	1.400	1.377	1.403
C30-H9	1.084	1.084	1.084	1.072	1.084
C31-C32	1.461	1.461	1.457	1.484	1.459

Table B.2. Calculated 3-body bond angles of H_{16}MPc with B3LYP functional and 6-31G basis set.

	H_{16}ZnPc	H_{16}MgPc	H_{16}CoPc	H_{16}CuPc	H_{16}FePc
N1-M-N2	89.89	89.89	90.00	89.99	89.99
N1-M-N3	175.08	175.08	178.10	178.12	178.43
N1-M-N4	89.93	89.93	90.00	89.99	90.00
M-N1-C25	125.47	125.47	126.60	126.62	126.17
M-N1-C32	125.47	125.47	126.60	126.64	126.17
N2-M-N3	89.88	89.88	90.00	89.99	89.99
N2-M-N4	175.39	175.39	178.60	178.58	178.65
M-N2-C17	125.41	125.41	126.60	126.62	126.36
M-N2-C24	125.46	125.46	126.60	126.64	126.39
N3-M-N4	89.91	89.91	90.00	89.99	89.99
M-N3-C9	125.42	125.42	126.60	126.62	126.17
M-N3-C16	125.51	125.51	126.60	126.64	126.19
M-N4-C1	125.39	125.39	126.60	126.62	126.36
M-N4-C8	125.47	125.47	126.60	126.64	126.38
C25-N1-C32	109.07	109.07	106.70	110.80	107.63
N1-C25-N6	126.93	126.93	126.70	127.80	126.82
N1-C25-C26	108.71	108.71	110.10	107.30	109.42
N1-C32-N5	126.9	126.9	126.70	127.90	126.80
N1-C32-C31	108.71	108.71	110.10	109.30	109.42
C17-N2-C24	109.11	109.11	106.70	110.50	107.25
N2-C17-N7	127.03	127.03	126.70	127.10	126.88
N2-C17-C18	108.66	108.66	110.10	109.00	109.65
N2-C24-N6	126.97	126.97	126.70	126.70	126.85

N2-C24-C23	108.69	108.69	110.10	108.60	109.66
C9-N3-C16	109.06	109.06	106.70	110.80	107.63
N3-C9-N8	126.96	126.96	126.70	128.00	126.82
N3-C9-C10	108.7	108.7	110.10	109.20	109.43
N3-C16-N7	126.87	126.87	126.70	128.00	126.78
N3-C16-C15	108.74	108.74	110.10	107.50	109.43
C1-N4-C8	109.12	109.12	106.70	110.90	107.25
N4-C1-N5	127.01	127.01	126.70	128.20	126.88
N4-C1-C2	108.66	108.66	110.10	108.10	109.65
N4-C8-N8	126.95	126.95	126.70	128.40	126.84
N4-C8-C7	108.67	108.67	110.10	108.40	109.65
C1-N5-C32	125.2	125.2	123.30	124.40	123.76
N5-C1-C2	124.32	124.32	123.20	123.70	123.47
N5-C32-C31	124.39	124.39	123.20	122.80	123.77
C24-N6-C25	125.19	125.19	123.30	126.70	123.76
N6-C24-C23	124.33	124.33	123.20	124.70	123.48
N6-C25-C26	124.36	124.36	123.20	124.90	123.76
C16-N7-C17	125.18	125.18	123.30	125.90	123.77
N7-C16-C15	124.39	124.39	123.20	124.60	123.79
N7-C17-C18	124.31	124.31	123.20	123.90	123.47
C8-N8-C9	125.2	125.2	123.30	124.20	123.77
N8-C8-C7	124.38	124.38	123.20	123.30	123.50
N8-C9-C10	124.34	124.34	123.20	122.90	123.75
C1-C2-C3	132.16	132.16	132.40	132.30	132.22
C1-C23-C7	106.78	106.78	106.50	106.30	106.73
C3-C2-C7	121.06	121.06	121.10	121.50	121.05
C2-C3-C4	117.87	117.87	117.80	117.50	117.93
C2-C3-H8	120.53	120.53	120.90	121.10	120.84
C2-C7-C6	121	121	121.10	121.40	121.01
C2-C7-C8	106.76	106.76	106.50	106.30	106.70
C4-C3-H8	121.61	121.61	121.30	121.40	121.23
C3-C4-C5	121.09	121.09	121.10	121.00	121.02
C3-C4-H7	119.6	119.6	119.70	119.50	119.67
C5-C4-H7	119.3	119.3	119.30	119.40	119.31
C4-C5-C6	121.12	121.12	121.10	121.00	121.06
C4-C5-H6	119.3	119.3	119.30	119.40	119.29
C6-C5-H6	119.58	119.58	119.70	119.60	119.66
C5-C6-C7	117.86	117.86	117.80	117.60	117.92
C5-C6-H5	121.53	121.53	121.30	121.30	121.18
C7-C6-H5	120.6	120.6	120.90	121.10	120.89
C6-C7-C8	132.24	132.24	132.40	132.30	132.28
C9-C10-C11	132.17	132.17	132.40	132.70	132.28
C9-C10-C15	106.78	106.78	106.50	106.10	106.78
C11-C10-C15	121.05	121.05	121.10	121.20	120.93
C10-C11-C12	117.9	117.9	117.80	117.60	118.00
C10-C11-H4	120.55	120.55	120.90	121.20	120.69
C10-C15-C14	120.98	120.98	121.00	121.60	120.90

C10-C15-C16	106.72	106.72	106.50	106.40	106.73
C12-C11-H4	121.55	121.55	121.30	121.20	121.31
C11-C12-C13	121.05	121.05	121.10	121.10	121.06
C11-C12-H3	119.57	119.57	119.70	119.70	119.72
C13-C12-H3	119.37	119.37	119.20	119.30	119.21
C12-C13-C14	121.14	121.14	121.10	121.00	121.13
C12-C13-H2	119.27	119.27	119.30	119.50	119.16
C14-C13-H2	119.58	119.58	119.70	119.50	119.70
C13-C14-C15	117.87	117.87	117.90	117.60	117.97
C13-C14-H1	121.53	121.53	121.30	121.50	121.29
C15-C14-H1	120.6	120.6	120.90	120.90	120.74
C14-C15-C16	132.29	132.29	132.50	132.00	132.36
C17-C18-C19	132.14	132.14	132.40	132.90	132.20
C17-C18-C23	106.8	106.8	106.50	106.00	106.74
C19-C18-C23	121.06	121.06	121.10	121.10	121.06
C18-C19-C20	117.85	117.85	117.80	117.90	117.92
C18-C19-H16	120.51	120.51	120.90	120.90	120.84
C18-C23-C22	121.02	121.02	121.10	121.10	121.01
C18-C23-C24	106.74	106.74	106.50	105.90	106.70
C20-C19-H16	121.64	121.64	121.30	121.30	121.24
C19-C20-C21	121.11	121.11	121.10	121.10	121.03
C19-C20-H15	119.59	119.59	119.70	119.70	119.67
C21-C20-H15	119.3	119.3	119.30	119.20	119.29
C20-C21-C22	121.11	121.11	121.10	121.10	121.05
C20-C21-H14	119.3	119.3	119.20	119.20	119.29
C22-C21-H14	119.58	119.58	119.70	119.60	119.66
C21-C22-C23	117.84	117.84	117.80	117.80	117.92
C21-C22-H13	121.59	121.59	121.30	121.30	121.20
C23-C22-H13	120.56	120.56	120.90	120.90	120.87
C22-C23-C24	132.25	132.25	132.40	133.00	132.28
C25-C26-C27	132.17	132.17	132.40	132.10	132.28
C25-C26-C31	106.77	106.77	106.50	106.40	106.77
C27-C26-C31	121.07	121.07	121.10	121.50	120.94
C26-C27-C28	117.86	117.86	117.80	117.60	117.98
C26-C27-H12	120.56	120.56	120.90	121.00	120.71
C26-C31-C30	120.98	120.98	121.10	121.20	120.88
C26-C31-C32	106.74	106.74	106.50	106.10	106.75
C28-C27-H12	121.59	121.59	121.30	121.40	121.32
C27-C28-C29	121.08	121.08	121.10	121.00	121.09
C27-C28-H11	119.67	119.67	119.70	119.50	119.74
C29-C28-H11	119.25	119.25	119.30	119.50	119.17
C28-C29-C30	121.13	121.13	121.10	121.10	121.11
C28-C29-H10	119.3	119.3	119.20	119.30	119.18
C30-C29-H10	119.57	119.57	119.70	119.60	119.71
C29-C30-C31	117.88	117.88	117.80	117.60	117.99
C29-C30-H9	121.49	121.49	121.30	121.10	121.28
C31-C30-H9	120.63	120.63	120.90	121.30	120.74

C30-C31-C32	132.27	132.27	132.40	132.70	132.36

Table B.3. Calculated Mulliken Atomic Charges of $H_{16}MPc$ with B3LYP functional and 6-31G basis set.

	$H_{16}ZnPc$	$H_{16}MgPc$	$H_{16}CoPc$	$H_{16}CuPc$	$H_{16}FePc$
M	1.015	1.261	1.049	0.853	
N1	-0.684	-0.750	-0.694	-0.858	
N2	-0.683	-0.749	-0.694	-0.841	
N3	-0.684	-0.750	-0.694	-0.801	
N4	-0.684	-0.749	-0.694	-0.829	
N5	-0.391	-0.391	-0.378	-0.662	
N6	-0.391	-0.391	-0.378	-0.656	
N7	-0.391	-0.391	-0.378	-0.620	
N8	-0.391	-0.391	-0.378	-0.620	
C1	0.347	0.535	0.330	0.671	
C2	0.028	0.027	0.037	-0.147	
C3	-0.118	-0.199	-0.115	-0.119	
C4	-0.133	-0.133	-0.133	-0.204	
C5	-0.133	-0.133	-0.133	-0.204	
C6	-0.118	-0.119	-0.114	-0.155	
C7	0.028	0.028	0.038	-0.155	
C8	0.347	0.353	0.330	0.684	
C9	0.347	0.353	0.330	0.690	
C10	0.028	0.027	0.037	-0.177	
C11	-0.119	-0.119	-0.114	-0.120	
C12	-0.133	-0.132	-0.133	-0.207	
C13	-0.133	-0.133	-0.133	-0.203	
C14	-0.118	-0.119	-0.114	-0.119	
C15	0.028	0.028	0.038	-0.129	
C16	0.347	0.352	0.330	0.627	
C17	0.347	0.353	0.330	0.627	
C18	0.028	0.026	0.037	-0.168	
C19	-0.119	-0.119	-0.115	-0.112	
C20	-0.133	-0.133	-0.133	-0.210	
C21	-0.133	-0.133	-0.133	-0.208	
C22	-0.118	-0.119	-0.115	-0.112	
C23	0.028	0.026	0.038	-0.146	
C24	0.347	0.353	0.330	0.602	
C25	0.347	0.353	0.330	0.608	
C26	0.028	0.027	0.037	-0.125	
C27	-0.119	-0.119	-0.114	-0.118	
C28	-0.133	-0.133	-0.133	-0.203	

C29	-0.133	-0.132	-0.133	-0.208
C30	-0.118	-0.119	-0.114	-0.119
C31	0.028	0.028	0.037	-0.176
C32	0.347	0.353	0.330	0.686
H1	0.156	0.155	0.155	0.249
H2	0.130	0.129	0.130	0.208
H3	0.130	0.129	0.130	0.208
H4	0.156	0.155	0.155	0.248
H5	0.156	0.155	0.155	0.250
H6	0.130	0.129	0.130	0.210
H7	0.130	0.129	0.130	0.210
H8	0.156	0.155	0.155	0.250
H9	0.156	0.155	0.155	0.248
H10	0.130	0.129	0.130	0.207
H11	0.130	0.129	0.130	0.208
H12	0.156	0.155	0.155	0.247
H13	0.156	0.155	0.155	0.247
H14	0.130	0.129	0.130	0.203
H15	0.130	0.129	0.130	0.202
H16	0.156	0.155	0.155	0.241

The calculated 2-body bond lengths, 3-body bond angles, and atomic charges for F_{16}MPc are presented in Tables B.4-6 following the atom labeling scheme depicted in Figure B.2.

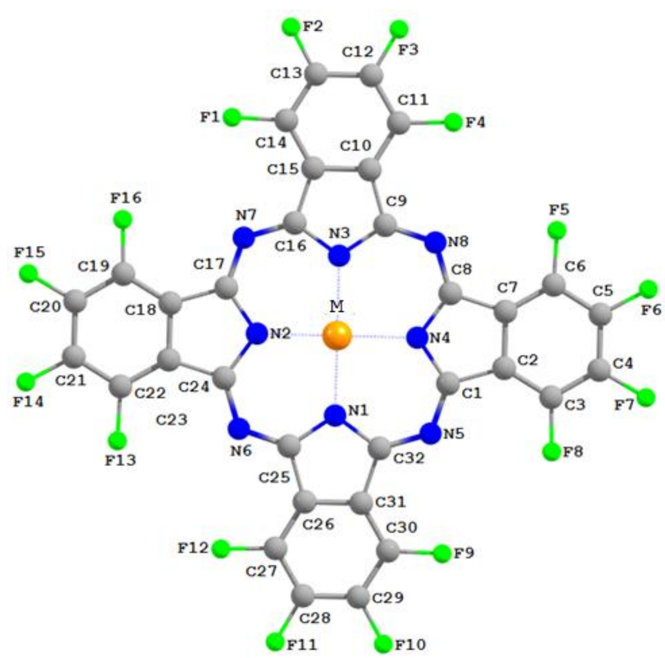

Figure B.2. Atom labeling scheme for F_{16}MPc bond lengths, 3-body angles, and atomic charges.

Table B.4. Calculated bond lengths of $F_{16}MPc$ with B3LYP functional and 6-31G basis set.

	$F_{16}ZnPc$	$F_{16}MgPc$	$F_{16}CoPc$	$F_{16}CuPc$	$F_{16}FePc$
M-N1	2.007	2.019	1.939	1.966	1.956
M-N2	2.007	2.019	1.939	1.966	1.956
M-N3	2.007	2.019	1.939	1.966	1.956
M-N4	2.007	2.018	1.940	1.966	1.957
N1-C25	1.385	1.384	1.392	1.385	1.389
N1-C32	1.385	1.384	1.392	1.385	1.389
N2-C17	1.385	1.384	1.391	1.386	1.389
N2-C24	1.385	1.384	1.392	1.385	1.389
N3-C9	1.385	1.384	1.391	1.385	1.389
N3-C16	1.385	1.384	1.392	1.385	1.39
N4-C1	1.385	1.384	1.391	1.385	1.389
N4-C8	1.385	1.384	1.392	1.385	1.389
N5-C1	1.331	1.334	1.322	1.325	1.325
N5-C32	1.331	1.334	1.322	1.325	1.325
N6-C24	1.331	1.334	1.322	1.326	1.325
N6-C25	1.331	1.334	1.322	1.326	1.325
N7-C16	1.331	1.334	1.322	1.325	1.325
N7-C17	1.331	1.334	1.322	1.325	1.325
N8-C8	1.331	1.334	1.322	1.325	1.325
N8-C9	1.331	1.334	1.322	1.326	1.325
C1-C2	1.459	1.461	1.451	1.455	1.451
C2-C3	1.391	1.391	1.391	1.391	1.391
C2-C7	1.421	1.423	1.414	1.417	1.417
C3-C4	1.394	1.394	1.393	1.394	1.393
C3-F8	1.371	1.372	1.371	1.372	1.371
C4-C5	1.399	1.399	1.40	1.401	1.401
C4-F7	1.373	1.373	1.372	1.373	1.372
C5-C6	1.394	1.394	1.393	1.394	1.393
C5-F6	1.373	1.373	1.373	1.373	1.372
C6-C7	1.391	1.391	1.392	1.391	1.392
C6-F5	1.372	1.372	1.371	1.372	1.371
C7-C8	1.459	1.461	1.453	1.455	1.452
C9-C10	1.459	1.461	1.451	1.455	1.451
C10-C11	1.391	1.391	1.391	1.391	1.391
C10-C15	1.422	1.423	1.414	1.417	1.417
C11-C12	1.394	1.394	1.393	1.394	1.393
C11-F4	1.372	1.372	1.372	1.372	1.371
C12-C13	1.399	1.399	1.400	1.401	1.401
C12-F3	1.372	1.372	1.372	1.373	1.372
C13-C14	1.394	1.394	1.393	1.394	1.393
C13-F2	1.372	1.373	1.373	1.373	1.372
C14-C15	1.391	1.391	1.392	1.391	1.392
C14-F1	1.372	1.372	1.371	1.372	1.372

C15-C16	1.459	1.461	1.452	1.455	1.451
C17-C18	1.459	1.461	1.451	1.455	1.451
C18-C19	1.391	1.391	1.391	1.391	1.391
C18-C23	1.421	1.423	1.414	1.417	1.417
C19-C20	1.394	1.394	1.393	1.394	1.393
C19-F16	1.372	1.372	1.372	1.372	1.371
C20-C21	1.400	1.399	1.400	1.401	1.401
C20-F15	1.372	1.373	1.372	1.373	1.372
C21-C22	1.394	1.394	1.393	1.394	1.393
C21-F14	1.372	1.373	1.373	1.373	1.372
C22-C23	1.391	1.391	1.392	1.391	1.392
C22-F13	1.372	1.372	1.371	1.372	1.372
C23-C24	1.459	1.461	1.453	1.455	1.452
C25-C26	1.459	1.461	1.452	1.455	1.451
C26-C27	1.391	1.391	1.391	1.391	1.391
C26-C31	1.422	1.424	1.414	1.417	1.417
C27-C28	1.394	1.394	1.393	1.394	1.393
C27-F12	1.371	1.372	1.372	1.372	1.371
C28-C29	1.399	1.399	1.400	1.401	1.401
C28-F11	1.373	1.373	1.372	1.373	1.372
C29-C30	1.394	1.394	1.393	1.394	1.393
C29-F10	1.373	1.373	1.373	1.373	1.372
C30-C31	1.391	1.391	1.392	1.391	1.392
C30-F9	1.372	1.372	1.372	1.372	1.372
C31-C32	1.459	1.461	1.452	1.455	1.451

Table B.5. Calculated 3-body bond angles of $F_{16}MPc$ with B3LYP functional and 6-31G basis set.

	$F_{16}ZnPc$	$F_{16}MgPc$	$F_{16}CoPc$	$F_{16}CuPc$	$F_{16}FePc$
N1-M-N2	89.86	89.97	89.99	90.01	90.00
N1-M-N3	174.38	177.41	179.82	179.68	179.93
N1-M-N4	89.89	90.00	90.02	90.00	90.00
M-N1-C25	125.24	125.04	126.35	125.87	126.02
M-N1-C32	125.20	125.02	126.32	125.84	126.05
N2-M-N3	89.86	89.97	90.02	90.00	90.00
N2-M-N4	174.69	177.63	179.96	179.94	179.65
M-N2-C17	125.21	125.00	126.29	125.87	126.01
M-N2-C24	125.20	125.01	126.36	125.84	126.05
N3-M-N4	89.87	89.97	89.98	90.00	90.00
M-N3-C9	125.22	125.02	126.33	125.86	126.01
M-N3-C16	125.24	125.02	126.34	125.84	126.06
M-N4-C1	125.19	124.98	126.30	125.87	126.01
M-N4-C8	125.22	125.03	126.38	125.86	126.06
C25-N1-C32	109.56	109.94	107.33	108.27	107.92

N1-C25-N6	127.14	127.09	127.19	127.13	127.26
N1-C25-C26	108.47	108.27	109.75	109.33	109.41
N1-C32-N5	127.15	127.09	127.19	127.14	127.23
N1-C32-C31	108.48	108.25	109.79	109.30	109.43
C17-N2-C24	109.56	109.99	107.35	108.28	107.94
N2-C17-N7	127.13	127.16	127.23	127.10	127.28
N2-C17-C18	108.45	108.23	109.76	109.32	109.40
N2-C24-N6	127.15	127.14	127.18	127.17	127.21
N2-C24-C23	108.49	108.20	109.76	109.30	109.41
C9-N3-C16	109.53	109.96	107.33	108.29	107.93
N3-C9-N8	127.11	127.14	127.23	127.14	127.27
N3-C9-C10	108.49	108.23	109.75	109.33	109.40
N3-C16-N7	127.13	127.14	127.16	127.14	127.21
N3-C16-C15	108.50	108.25	109.77	109.28	109.42
C1-N4-C8	109.57	109.99	107.33	108.26	107.93
N4-C1-N5	127.13	127.16	127.23	127.11	127.28
N4-C1-C2	108.44	108.22	109.78	109.35	109.41
N4-C8-N8	127.11	127.14	127.15	127.15	127.20
N4-C8-C7	108.50	108.22	109.76	109.31	109.42
C1-N5-C32	125.32	125.74	122.95	124.03	123.43
N5-C1-C2	124.43	124.62	122.99	123.54	123.30
N5-C32-C31	124.37	124.66	123.02	123.56	123.34
C24-N6-C25	125.27	125.73	122.93	123.97	123.45
N6-C24-C23	124.36	124.66	123.07	123.53	123.38
N6-C25-C26	124.38	124.63	123.06	123.54	123.34
C16-N7-C17	125.31	125.69	122.96	124.04	123.44
N7-C16-C15	124.36	124.62	123.07	123.58	123.38
N7-C17-C18	124.42	124.60	123.02	123.57	123.32
C8-N8-C9	125.34	125.70	122.94	123.98	123.44
N8-C8-C7	124.39	124.64	123.09	123.54	123.38
N8-C9-C10	124.40	124.64	123.02	123.53	123.30
C1-C2-C3	132.90	132.90	132.73	132.95	132.73
C1-C2-C7	106.78	106.80	106.63	106.53	106.66
C3-C2-C7	120.31	120.30	120.65	120.51	120.61
C2-C3-C4	118.87	118.91	118.55	118.72	118.60
C2-C3-F8	122.29	122.33	122.52	122.27	122.36
C2-C7-C6	120.35	120.28	120.46	120.39	120.49
C2-C7-C8	106.71	106.78	106.50	106.54	106.58
C4-C3-F8	118.84	118.76	118.93	119.01	119.05
C3-C4-C5	120.86	120.81	120.88	120.83	120.81
C3-C4-F7	120.10	120.01	120.04	120.06	120.06
C5-C4-F7	119.04	119.18	119.08	119.11	119.13
C4-C5-C6	120.72	120.79	120.85	120.70	120.94
C4-C5-F6	119.08	119.15	119.02	119.08	119.09
C6-C5-F6	120.20	120.07	120.13	120.23	119.97
C5-C6-C7	118.89	118.91	118.62	118.84	118.56
C5-C6-F5	118.91	118.78	118.74	118.79	119.07

C7-C6-F5	122.20	122.31	122.64	122.37	122.37
C6-C7-C8	132.94	132.94	133.05	133.06	132.93
C9-C10-C11	132.95	132.91	132.75	132.96	132.75
C9-C10-C15	106.76	106.80	106.64	106.52	106.66
C11-C10-C15	120.29	120.29	120.62	120.52	120.59
C10-C11-C12	118.92	118.94	118.56	118.72	118.60
C10-C11-F4	122.26	122.33	122.52	122.27	122.36
C10-C15-C14	120.36	120.28	120.48	120.38	120.51
C10-C15-C16	106.72	106.76	106.50	106.58	106.59
C12-C11-F4	118.82	118.72	118.92	119.01	119.04
C11-C12-C13	120.78	120.76	120.89	120.84	120.81
C11-C12-F3	120.18	120.04	120.05	120.06	120.06
C13-C12-F3	119.04	119.20	119.06	119.10	119.13
C12-C13-C14	120.77	120.80	120.84	120.69	120.94
C12-C13-F2	118.98	119.14	119.04	119.09	119.10
C14-C13-F2	120.25	120.05	120.13	120.22	119.96
C13-C14-C15	118.87	118.92	118.62	118.84	118.55
C13-C14-F1	118.82	118.76	118.73	118.77	119.05
C15-C14-F1	122.31	122.32	122.65	122.39	122.40
C14-C15-C16	132.92	132.96	133.02	133.02	132.90
C17-C18-C19	132.88	132.94	132.74	132.94	132.74
C17-C18-C23	106.78	106.77	106.63	106.54	106.66
C19-C18-C23	120.34	120.29	120.63	120.52	120.60
C18-C19-C20	118.90	118.92	118.56	118.72	118.60
C18-C19-F16	122.30	122.31	122.52	122.29	122.36
C18-C23-C22	120.34	120.29	120.47	120.39	120.50
C18-C23-C24	106.73	106.81	106.51	106.56	106.59
C20-C19-F16	118.80	118.77	118.92	119.00	119.04
C19-C20-C21	120.78	120.78	120.89	120.84	120.82
C19-C20-F15	120.14	120.04	120.04	120.06	120.06
C21-C20-F15	119.08	119.19	119.08	119.10	119.13
C20-C21-C22	120.76	120.82	120.84	120.68	120.93
C20-C21-F14	119.06	119.16	119.03	119.09	119.10
C22-C21-F14	120.18	120.02	120.14	120.23	119.97
C21-C22-C23	118.88	118.90	118.63	118.86	118.56
C21-C22-F13	118.88	118.77	118.74	118.78	119.07
C23-C22-F13	122.24	122.32	122.63	122.36	122.37
C22-C23-C24	132.93	132.91	133.03	133.05	132.92
C25-C26-C27	132.93	132.96	132.81	133.01	132.80
C25-C26-C31	106.76	106.76	106.61	106.50	106.64
C27-C26-C31	120.31	120.28	120.58	120.49	120.55
C26-C27-C28	118.87	118.96	118.57	118.73	118.60
C26-C27-F12	122.30	122.31	122.53	122.27	122.36
C26-C31-C30	120.36	120.26	120.53	120.41	120.52
C26-C31-C32	106.74	106.78	106.52	106.59	106.60
C28-C27-F12	118.83	118.73	118.91	119.00	119.03
C27-C28-C29	120.82	120.77	120.89	120.85	120.83

C27-C28-F11	120.02	120.07	120.06	120.06	120.05
C29-C28-F11	119.16	119.16	119.05	119.09	119.11
C28-C29-C30	120.77	120.77	120.83	120.68	120.91
C28-C29-F10	119.01	119.14	119.06	119.10	119.12
C30-C29-F10	120.23	120.09	120.10	120.22	119.97
C29-C30-C31	118.86	118.95	118.60	118.84	118.56
C29-C30-F9	118.88	118.74	118.73	118.78	119.06
C31-C30-F9	122.26	122.31	122.67	122.38	122.38
C30-C31-C32	132.90	132.95	132.95	133.00	132.87

Table B.6. Calculated Mullikan Atomic Charges of $F_{16}MPc$ with B3LYP functional and 6-31G basis set.

	$F_{16}ZnPc$	$F_{16}MgPc$	$F_{16}CoPc$	$F_{16}CuPc$	$F_{16}FePc$
M	1.038	1.271	0.956	0.983	1.005
N1	-0.680	-0.742	-0.697	-0.676	-0.704
N2	-0.680	-0.743	-0.673	-0.676	-0.704
N3	-0.679	-0.742	-0.697	-0.676	0.704
N4	-0.679	-0.743	-0.673	-0.677	-0.704
N5	-0.332	-0.336	-0.317	-0.322	-0.324
N6	-0.332	-0.336	-0.318	-0.322	-0.325
N7	-0.332	-0.336	-0.318	-0.322	-0.324
N8	-0.332	-0.336	-0.318	-0.322	-0.325
C1	0.359	0.370	0.346	0.350	0.358
C2	0.035	0.031	0.041	0.040	0.039
C3	0.247	0.245	0.253	0.250	0.253
C4	0.275	0.275	0.275	0.275	0.276
C5	0.276	0.275	0.275	0.276	0.276
C6	0.248	0.246	0.251	0.249	0.253
C7	0.036	0.032	0.047	0.041	0.043
C8	0.359	0.370	0.346	0.352	0.358
C9	0.359	0.369	0.355	0.351	0.359
C10	0.036	0.032	0.041	0.041	0.040
C11	0.247	0.245	0.253	0.250	0.253
C12	0.275	0.275	0.275	0.275	0.276
C13	0.275	0.275	0.275	0.276	0.276
C14	0.248	0.246	0.252	0.249	0.253
C15	0.035	0.032	0.046	0.041	0.043
C16	0.359	0.369	0.354	0.351	0.357
C17	0.359	0.369	0.346	0.350	0.358
C18	0.035	0.032	0.041	0.040	0.040
C19	0.247	0.245	0.253	0.251	0.253
C20	0.275	0.275	0.275	0.275	0.276

C21	0.275	0.275	0.275	0.276	0.276
C22	0.248	0.246	0.252	0.249	0.253
C23	0.036	0.031	0.046	0.041	0.043
C24	0.359	0.370	0.347	0.352	0.358
C25	0.359	0.369	0.355	0.351	0.358
C26	0.036	0.032	0.042	0.040	0.041
C27	0.247	0.245	0.253	0.250	0.253
C28	0.275	0.275	0.275	0.275	0.276
C29	0.275	0.275	0.275	0.276	0.276
C30	0.248	0.245	0.253	0.249	0.253
C31	0.035	0.032	0.045	0.042	0.041
C32	0.359	0.370	0.354	0.351	0.358
F1	-0.264	-0.264	-0.263	-0.264	-0.263
F2	-0.277	-0.277	-0.276	-0.277	-0.277
F3	-0.277	-0.277	-0.276	-0.277	-0.277
F4	-0.264	-0.264	-0.263	-0.263	-0.263
F5	-0.264	-0.264	-0.263	-0.265	-0.263
F6	-0.277	-0.277	-0.277	-0.277	-0.277
F7	-0.277	-0.277	-0.277	-0.277	-0.277
F8	-0.264	-0.264	-0.263	-0.263	-0.263
F9	-0.264	-0.264	-0.263	-0.264	-0.263
F10	-0.277	-0.277	-0.276	-0.277	-0.277
F11	-0.277	-0.277	-0.276	-0.277	-0.277
F12	-0.264	-0.265	-0.263	-0.263	-0.263
F13	-0.264	-0.264	-0.263	-0.264	-0.263
F14	-0.277	-0.277	-0.277	-0.277	-0.277
F15	-0.277	-0.277	-0.277	-0.277	-0.277
F16	-0.264	-0.264	-0.263	-0.263	-0.263

The calculated 2-body bond lengths, 3-body bond angles, and atomic charges for $F_{34}MPc$ are presented in Tables B.7-9 following the atom labeling scheme depicted in Figure B.3.

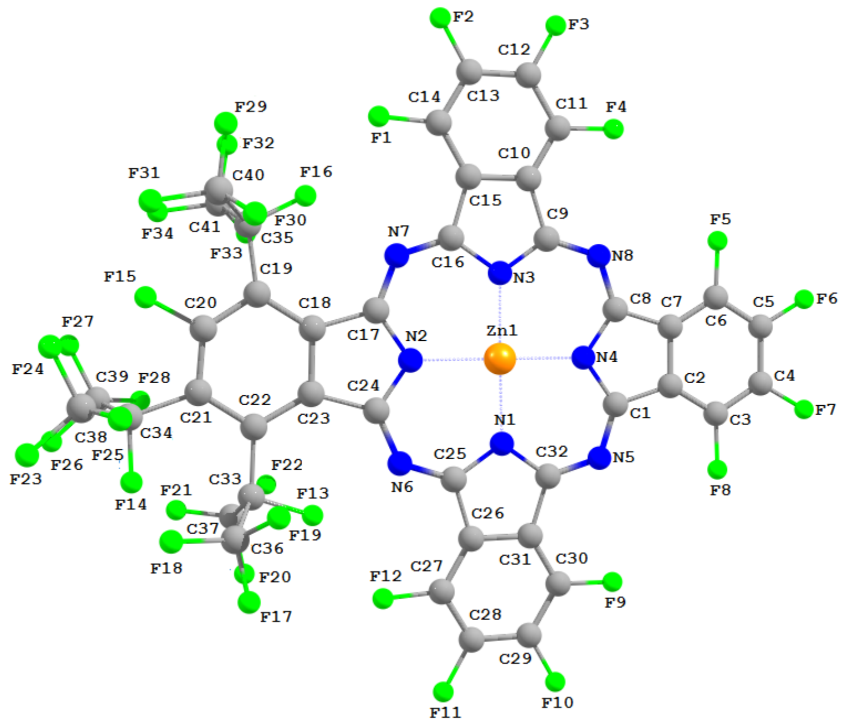

Figure B.3. Atom labeling scheme for $F_{34}MPc$ bond lengths, 3-body angles, and atomic charges.

Table B.7. Calculated bond lengths of $F_{34}MPc$ with B3LYP functional and 6-31G basis set.

	$F_{34}ZnPc$	$F_{34}MgPc$	$F_{34}CoPc$	$F_{34}CuPc$	$F_{34}FePc$
M-N1	1.978	2.049	1.931	1.946	1.940
M-N2	2.074	2.075	2.015	2.044	2.033
M-N3	1.981	2.004	1.937	1.950	1.946
M-N4	2.045	2.049	1.960	1.995	1.979
N1-C25	1.389	1.388	1.394	1.390	1.393
N1-C32	1.379	1.375	1.386	1.380	1.383
N2-C17	1.370	1.372	1.381	1.374	1.377
N2-C24	1.376	1.378	1.390	1.381	1.385
N3-C9	1.380	1.377	1.386	1.381	1.384
N3-C16	1.392	1.390	1.397	1.393	1.396
N4-C1	1.384	1.385	1.396	1.387	1.392
N4-C8	1.383	1.384	1.395	1.387	1.392

N5-C1	1.328	1.329	1.320	1.323	1.322
N5-C32	1.333	1.337	1.328	1.329	1.329
N6-C24	1.327	1.331	1.319	1.323	1.322
N6-C25	1.312	1.317	1.309	1.309	1.309
N7-C16	1.318	1.322	1.314	1.315	1.315
N7-C17	1.331	1.335	1.324	1.327	1.327
N8-C8	1.327	1.329	1.320	1.322	1.322
N8-C9	1.334	1.337	1.329	1.330	1.330
C1-C2	1.461	1.462	1.460	1.458	1.458
C2-C3	1.389	1.389	1.393	1.391	1.393
C2-C7	1.419	1.420	1.414	1.416	1.416
C3-C4	1.396	1.396	1.397	1.396	1.396
C3-F8	1.371	1.371	1.371	1.371	1.371
C4-C5	1.398	1.398	1.398	1.399	1.399
C4-F7	1.372	1.372	1.372	1.372	1.372
C5-C6	1.396	1.396	1.397	1.396	1.396
C5-F6	1.372	1.372	1.373	1.372	1.372
C6-C7	1.389	1.389	1.394	1.392	1.393
C6-F5	1.371	1.371	1.371	1.371	1.371
C7-C8	1.462	1.463	1.462	1.460	1.459
C9-C10	1.457	1.457	1.451	1.454	1.452
C10-C11	1.392	1.391	1.396	1.393	1.394
C10-C15	1.421	1.423	1.419	1.418	1.419
C11-C12	1.393	1.393	1.392	1.393	1.393
C11-F4	1.371	1.371	1.372	1.372	1.371
C12-C13	1.397	1.397	1.399	1.397	1.398
C12-F3	1.372	1.372	1.372	1.372	1.372
C13-C14	1.395	1.396	1.394	1.395	1.395
C13-F2	1.372	1.372	1.372	1.372	1.372
C14-C15	1.393	1.392	1.397	1.394	1.395
C14-F1	1.370	1.370	1.370	1.370	1.369
C15-C16	1.469	1.471	1.464	1.467	1.465
C17-C18	1.481	1.482	1.484	1.481	1.481
C18-C19	1.420	1.419	1.427	1.424	1.426
C18-C23	1.456	1.457	1.448	1.451	1.450
C19-C20	1.382	1.383	1.384	1.382	1.382
C19-C35	1.543	1.542	1.545	1.545	1.545
C20-C21	1.398	1.397	1.398	1.398	1.399
C20-F15	1.383	1.384	1.384	1.383	1.383
C21-C22	1.418	1.421	1.420	1.419	1.419
C21-C34	1.541	1.545	1.547	1.546	1.547
C22-C23	1.450	1.448	1.458	1.456	1.458
C22-C33	1.556	1.550	1.555	1.555	1.555
C23-C24	1.510	1.511	1.514	1.510	1.510
C25-C26	1.467	1.471	1.462	1.465	1.463
C26-C27	1.392	1.391	1.396	1.393	1.394
C26-C31	1.421	1.423	1.418	1.417	1.418

C27-C28	1.395	1.396	1.394	1.395	1.395
C27-F12	1.370	1.370	1.370	1.370	1.369
C28-C29	1.397	1.397	1.399	1.398	1.398
C28-F11	1.372	1.372	1.372	1.372	1.372
C29-C30	1.394	1.394	1.393	1.394	1.394
C29-F10	1.372	1.372	1.372	1.372	1.372
C30-C31	1.391	1.391	1.395	1.393	1.394
C30-F9	1.371	1.371	1.372	1.372	1.371
C31-C32	1.459	1.458	1.452	1.455	1.454
C35-F16	1.410	1.410	1.410	1.410	1.410
C35-C40	1.559	1.560	1.561	1.561	1.561
C35-C41	1.560	1.565	1.563	1.562	1.562
C40-F29	1.375	1.375	1.375	1.375	1.375
C40-F30	1.378	1.379	1.378	1.378	1.378
C40-F31	1.387	1.386	1.387	1.387	1.387
C41-F32	1.387	1.386	1.387	1.387	1.387
C41-F33	1.376	1.378	1.376	1.376	1.376
C41-F34	1.378	1.376	1.378	1.378	1.378
C34-F14	1.417	1.417	1.417	1.417	1.417
C34-C39	1.568	1.576	1.570	1.570	1.570
C34-C38	1.568	1.570	1.571	1.570	1.570
C39-F26	1.375	1.377	1.375	1.375	1.375
C39-F27	1.378	1.376	1.378	1.378	1.378
C39-F28	1.385	1.384	1.384	1.384	1.384
C38-F23	1.384	1.384	1.384	1.384	1.384
C38-F24	1.374	1.374	1.374	1.374	1.374
C38-F25	1.378	1.379	1.379	1.379	1.379
C33-F13	1.423	1.423	1.421	1.422	1.422
C33-C37	1.583	1.581	1.585	1.584	1.585
C33-C36	1.581	1.581	1.583	1.582	1.582
C37-F20	1.372	1.374	1.373	1.373	1.373
C37-F21	1.378	1.376	1.378	1.378	1.378
C37-F22	1.392	1.392	1.392	1.392	1.392
C36-F17	1.392	1.393	1.392	1.392	1.392
C36-F18	1.372	1.371	1.373	1.373	1.373
C36-F19	1.377	1.376	1.378	1.378	1.378

Table B.8. Calculated 3-body bond angles of F_{34}MPc with B3LYP functional and 6-31G basis set.

	F_{34}ZnPc	F_{34}MgPc	F_{34}CoPc	F_{34}CuPc	F_{34}FePc
N1-M-N2	91.30	91.47	91.01	91.10	91.04
N1-M-N3	174.68	176.50	178.06	177.65	178.01
N1-M-N4	88.29	88.36	88.86	88.72	88.82
M-N1-C25	123.00	122.78	124.46	123.97	124.24

M-N1-C32	127.41	127.04	127.83	127.63	127.68
N2-M-N3	91.19	91.17	90.73	90.88	90.77
N2-M-N4	175.72	178.52	179.49	179.03	179.51
M-N2-C17	123.92	123.82	125.44	124.72	125.03
M-N2-C24	125.10	124.82	126.35	125.77	125.98
N3-M-N4	88.89	88.94	89.39	89.28	89.36
M-N3-C9	126.43	126.12	126.93	126.69	126.77
M-N3-C16	123.93	123.76	125.34	124.89	125.14
M-N4-C1	125.50	125.43	126.70	126.13	126.35
M-N4-C8	125.31	125.16	126.54	125.95	126.19
C25-N1-C32	109.59	110.17	107.71	108.39	108.07
N1-C25-N6	127.22	126.98	126.93	127.12	127.00
N1-C25-C26	108.22	107.79	109.35	108.98	109.15
N1-C32-N5	127.32	127.24	127.05	127.22	127.15
N1-C32-C31	108.77	108.57	109.97	109.61	109.77
C17-N2-C24	110.97	111.36	108.20	109.51	108.99
N2-C17-N7	124.49	124.79	124.37	124.45	124.46
N2-C17-C18	108.65	108.36	110.32	109.56	109.84
N2-C24-N6	121.81	122.21	121.85	121.86	121.90
N2-C24-C23	109.05	108.65	110.66	109.94	110.20
C9-N3-C16	109.63	110.11	107.72	108.42	108.09
N3-C9-N8	127.75	127.59	127.43	127.62	127.53
N3-C9-C10	108.75	108.56	109.99	109.61	109.78
N3-C16-N7	126.83	126.68	126.59	126.75	126.66
N3-C16-C15	108.09	107.79	109.23	108.87	109.03
C1-N4-C8	109.19	109.40	106.75	107.92	107.45
N4-C1-N5	127.13	127.19	127.03	127.06	127.09
N4-C1-C2	108.78	108.61	110.21	109.57	109.79
N4-C8-N8	126.88	127.04	126.82	126.84	126.88
N4-C8-C7	108.79	108.62	110.21	109.58	109.79
C1-N5-C32	124.29	124.74	122.53	123.24	122.89
N5-C1-C2	124.08	124.19	122.76	123.36	123.12
N5-C32-C31	123.90	124.19	122.98	123.17	123.08
C24-N6-C25	131.47	131.71	129.39	130.17	129.83
N6-C24-C23	129.13	129.14	127.49	128.20	127.90
N6-C25-C26	124.55	125.23	123.70	123.88	123.84
C16-N7-C17	129.57	129.73	127.52	128.30	127.94
N7-C16-C15	125.08	125.53	124.17	124.37	124.30
N7-C17-C18	126.86	126.82	125.31	125.98	125.70
C8-N8-C9	124.66	125.12	122.90	123.61	123.27
N8-C8-C7	124.33	124.34	122.97	123.58	123.34
N8-C9-C10	123.50	123.85	122.57	122.76	122.68
C1-C2-C3	132.79	132.83	133.04	132.92	132.95
C1-C2-C7	106.67	106.71	106.46	106.51	106.54
C3-C2-C7	120.54	120.46	120.50	120.56	120.51
C2-C3-C4	118.76	118.83	118.86	118.71	118.78
C2-C3-F8	122.36	122.38	122.71	122.57	122.62

C2-C7-C6	120.36	120.33	120.33	120.40	120.34
C2-C7-C8	106.57	106.65	106.37	106.42	106.44
C4-C3-F8	118.88	118.79	118.44	118.72	118.60
C3-C4-C5	120.74	120.74	120.69	120.77	120.74
C3-C4-F7	120.01	120.01	120.11	120.02	120.08
C5-C4-F7	119.26	119.24	119.20	119.22	119.18
C4-C5-C6	120.81	120.78	120.74	120.83	120.81
C4-C5-F6	119.21	119.22	119.16	119.18	119.13
C6-C5-F6	119.98	120.00	120.10	120.00	120.06
C5-C6-C7	118.79	118.87	118.89	118.74	118.81
C5-C6-F5	118.83	118.76	118.39	118.67	118.55
C7-C6-F5	122.38	122.37	122.72	122.59	122.64
C6-C7-C8	133.06	133.02	133.29	133.17	133.20
C9-C10-C11	132.05	132.02	132.21	132.12	132.15
C9-C10-C15	106.99	106.98	106.72	106.76	106.75
C11-C10-C15	120.96	121.00	121.07	121.12	121.10
C10-C11-C12	118.94	118.90	118.87	118.81	118.83
C10-C11-F4	122.35	122.28	122.53	122.54	122.54
C10-C15-C14	119.37	119.37	119.30	119.37	119.35
C10-C15-C16	106.54	106.57	106.34	106.35	106.35
C12-C11-F4	118.72	118.81	118.60	118.65	118.63
C11-C12-C13	120.39	120.41	120.38	120.39	120.39
C11-C12-F3	120.28	120.20	120.35	120.26	120.28
C13-C12-F3	119.33	119.39	119.27	119.35	119.33
C12-C13-C14	121.01	121.04	121.06	121.06	121.06
C12-C13-F2	119.23	119.14	119.14	119.22	119.19
C14-C13-F2	119.76	119.82	119.80	119.73	119.75
C13-C14-C15	119.33	119.28	119.32	119.25	119.27
C13-C14-F1	117.53	117.84	117.34	117.42	117.39
C15-C14-F1	123.14	122.88	123.34	123.33	123.34
C14-C15-C16	134.09	134.07	134.37	134.28	134.30
C17-C18-C19	131.84	131.94	132.17	132.04	132.09
C17-C18-C23	107.22	107.27	107.00	107.06	107.05
C19-C18-C23	120.94	120.76	120.83	120.90	120.85
C18-C19-C20	114.30	114.44	114.41	114.29	114.36
C18-C19-C35	129.28	129.35	129.82	129.69	129.73
C18-C23-C22	121.21	121.13	121.16	121.20	121.15
C18-C23-C24	104.11	104.34	103.82	103.93	103.92
C20-C19-C35	116.42	116.21	115.77	116.02	115.91
C19-C20-C21	128.34	128.36	128.51	128.53	128.54
C19-C20-F15	117.12	116.86	117.25	117.17	117.22
C19-C35-F16	110.32	110.34	110.11	110.20	110.16
C19-C35-C40	114.02	113.76	114.14	114.04	114.08
C19-C35-C41	114.19	114.37	114.44	114.38	114.40
C21-C20-F15	114.54	114.77	114.24	114.30	114.24
C20-C21-C22	118.53	118.08	118.15	118.29	118.24
C20-C21-C34	114.40	113.63	114.22	114.21	114.20

C22-C21-C34	127.08	128.28	127.63	127.49	127.56
C21-C22-C23	116.67	117.01	116.92	116.77	116.86
C21-C22-C33	121.13	120.61	120.50	120.77	120.65
C21-C34-F14	107.94	108.83	108.00	107.98	107.99
C21-C34-C39	114.82	114.73	115.11	115.08	115.10
C21-C34-C38	115.17	114.21	115.32	115.21	115.27
C23-C22-C33	122.20	122.34	122.58	122.46	122.49
C22-C23-C24	134.68	134.53	135.02	134.86	134.93
C22-C33-F13	106.91	108.53	106.90	106.99	106.94
C22-C33-C37	115.90	114.44	115.92	115.76	115.84
C22-C33-C36	115.31	115.09	115.27	115.32	115.28
C25-C26-C27	133.59	133.83	133.88	133.81	133.83
C25-C26-C31	106.57	106.60	106.38	106.39	106.39
C27-C26-C31	119.83	119.57	119.73	119.80	119.78
C26-C27-C28	119.09	119.19	119.11	119.05	119.06
C26-C27-F12	123.08	122.90	123.27	123.26	123.27
C26-C31-C30	120.69	120.87	120.80	120.86	120.83
C26-C31-C32	106.84	106.88	106.59	106.62	106.62
C28-C27-F12	117.83	117.91	117.62	117.69	117.67
C27-C28-C29	120.93	120.99	120.97	120.97	120.97
C27-C28-F11	119.81	119.84	119.87	119.80	119.81
C29-C28-F11	119.25	119.17	119.15	119.24	119.21
C28-C29-C30	120.55	120.49	120.55	120.56	120.56
C28-C29-F10	119.24	119.34	119.18	119.26	119.23
C30-C29-F10	120.21	120.17	120.28	120.19	120.21
C29-C30-C31	118.90	118.89	118.84	118.77	118.79
C29-C30-F9	118.74	118.82	118.63	118.67	118.65
C31-C30-F9	122.36	122.29	122.53	122.55	122.56
C30-C31-C32	132.46	132.26	132.61	132.52	132.55
F16-C35-C40	100.75	100.40	100.82	100.82	100.82
F16-C35-C41	101.02	103.12	101.19	101.19	101.19
C40-C35-C41	114.70	113.29	114.28	114.38	114.34
C35-C40-F29	115.60	115.85	115.72	115.67	115.69
C35-C40-F30	110.07	109.39	109.96	109.95	109.95
C35-C40-F31	107.65	107.87	107.70	107.72	107.71
C35-C41-F32	107.80	108.95	107.90	107.91	107.91
C35-C41-F33	115.62	114.06	115.70	115.64	115.67
C35-C41-F34	110.02	110.36	109.94	109.94	109.94
F29-C40-F30	107.20	107.52	107.10	107.12	107.11
F29-C40-F31	107.91	107.56	107.90	107.91	107.90
F30-C40-F31	108.20	108.44	108.25	108.25	108.25
F32-C41-F33	107.99	108.31	108.01	108.01	108.01
F32-C41-F34	108.19	108.03	108.20	108.22	108.21
F33-C41-F34	107.00	106.94	106.87	106.90	106.89
F14-C34-C39	102.06	103.69	102.06	102.11	102.08
F14-C34-C38	101.40	100.79	101.30	101.35	101.32
C39-C34-C38	113.41	112.94	112.97	113.06	113.01

C34-C39-F26	114.82	113.87	114.88	114.87	114.88
C34-C39-F27	109.48	109.80	109.47	109.44	109.45
C34-C39-F28	108.78	109.64	108.86	108.87	108.87
C34-C38-F23	108.63	108.65	108.71	108.73	108.72
C34-C38-F24	115.32	115.86	115.40	115.39	115.40
C34-C38-F25	109.13	108.81	109.09	109.06	109.07
F26-C39-F27	107.08	106.88	106.95	106.98	106.96
F26-C39-F28	107.94	108.10	107.95	107.94	107.95
F27-C39-F28	108.59	108.39	108.56	108.57	108.57
F23-C38-F24	107.94	107.34	107.95	107.94	107.94
F23-C38-F25	108.64	108.73	108.63	108.64	108.64
F24-C38-F25	107.00	107.26	106.89	106.91	106.90
F13-C33-C37	95.22	95.32	95.30	95.28	95.29
F13-C33-C36	95.76	95.93	95.91	95.90	95.90
C37-C33-C36	121.30	122.03	121.19	121.28	121.25
C33-C37-F20	121.60	120.53	121.67	121.61	121.63
C33-C37-F21	109.12	109.81	109.08	109.08	109.08
C33-C37-F22	104.85	105.04	104.84	104.88	104.86
C33-C36-F17	104.83	104.76	104.79	104.81	104.80
C33-C36-F18	121.17	120.78	121.21	121.15	121.17
C33-C36-F19	109.44	109.75	109.42	109.42	109.41
F20-C37-F21	106.33	107.03	106.31	106.33	106.33
F20-C37-F22	105.68	105.15	105.65	105.66	105.65
F21-C37-F22	108.74	108.75	108.76	108.76	108.76
F17-C36-F18	105.71	105.36	105.68	105.68	105.68
F17-C36-F19	108.67	108.74	108.75	108.75	108.75
F18-C36-F19	106.49	106.91	106.48	106.52	106.51

Table B.9. Calculated Mullikan Atomic Charges of F_{34}MPc with B3LYP functional and 6-31G basis set.

	F_{34}ZnPc	F_{34}MgPc	F_{34}CoPc	F_{34}CuPc	F_{34}FePc
M	1.039	1.266	0.957	0.983	1.016
N1	-0.690	-0.753	-0.698	-0.683	-0.706
N2	-0.648	-0.707	-0.646	-0.644	-0.676
N3	-0.693	-0.754	-0.700	-0.685	-0.708
N4	-0.661	-0.721	-0.663	-0.663	-0.695
N5	-0.330	-0.334	-0.321	-0.323	-0.326
N6	-0.338	-0.345	-0.328	-0.331	-0.333
N7	-0.337	-0.343	-0.330	-0.331	-0.334
N8	-0.331	-0.335	-0.323	-0.324	-0.328
C1	0.356	0.367	0.352	0.352	0.361
C2	0.035	0.033	0.044	0.040	0.042
C3	0.249	0.248	0.254	0.253	0.255
C4	0.278	0.278	0.277	0.277	0.278

C5	0.278	0.278	0.277	0.278	0.278
C6	0.248	0.247	0.252	0.252	0.254
C7	0.042	0.037	0.049	0.046	0.047
C8	0.356	0.367	0.353	0.352	0.361
C9	0.368	0.376	0.363	0.359	0.366
C10	0.010	0.006	0.018	0.015	0.017
C11	0.255	0.253	0.261	0.258	0.260
C12	0.275	0.275	0.275	0.275	0.275
C13	0.278	0.279	0.279	0.278	0.279
C14	0.238	0.236	0.242	0.239	0.241
C15	0.066	0.062	0.070	0.069	0.070
C16	0.365	0.373	0.363	0.359	0.365
C17	0.370	0.383	0.364	0.366	0.372
C18	-0.044	-0.043	-0.036	-0.041	-0.039
C19	0.081	0.077	0.084	0.085	0.086
C20	0.236	0.238	0.234	0.235	0.234
C21	0.056	0.059	0.059	0.058	0.058
C22	0.070	0.058	0.066	0.068	0.068
C23	0.062	0.055	0.072	0.068	0.071
C24	0.353	0.370	0.345	0.346	0.353
C25	0.363	0.374	0.362	0.358	0.364
C26	0.062	0.062	0.065	0.065	0.065
C27	0.242	0.238	0.246	0.243	0.245
C28	0.278	0.279	0.279	0.278	0.279
C29	0.275	0.275	0.275	0.275	0.275
C30	0.253	0.253	0.260	0.257	0.259
C31	0.018	0.009	0.025	0.023	0.025
C32	0.366	0.375	0.361	0.357	0.364
C33	0.051	0.053	0.052	0.068	0.052
C34	0.058	0.059	0.062	0.061	0.061
C35	0.099	0.095	0.100	0.100	0.100
C36	0.797	0.799	0.795	0.797	0.797
C37	0.795	0.796	0.797	0.795	0.795
C38	0.808	0.806	0.808	0.808	0.808
C39	0.810	0.820	0.810	0.810	0.810
C40	0.793	0.793	0.793	0.793	0.793
C41	0.794	0.801	0.794	0.794	0.794
F1	-0.262	-0.262	-0.261	-0.261	-0.261
F2	-0.274	-0.275	-0.274	-0.274	-0.274
F3	-0.275	-0.276	-0.275	-0.275	-0.275
F4	-0.263	-0.263	-0.261	-0.263	-0.262
F5	-0.262	-0.262	-0.261	-0.261	-0.261
F6	-0.275	-0.275	-0.274	-0.274	-0.274
F7	-0.275	-0.275	-0.274	-0.274	-0.274
F8	-0.261	-0.262	-0.261	-0.261	-0.261
F9	-0.263	-0.263	-0.263	-0.263	-0.263
F10	-0.276	-0.276	-0.275	-0.276	-0.275

F11	-0.274	-0.275	-0.273	-0.274	-0.273
F12	-0.260	-0.262	-0.260	-0.260	-0.260
F13	-0.256	-0.256	-0.257	-0.256	-0.256
F14	-0.288	-0.286	-0.288	-0.287	-0.288
F15	-0.289	-0.290	-0.290	-0.290	-0.289
F16	-0.256	-0.257	-0.256	-0.256	-0.256
F17	-0.242	-0.242	-0.242	-0.242	-0.242
F18	-0.238	-0.238	-0.238	-0.238	-0.238
F19	-0.266	-0.265	-0.265	-0.266	-0.265
F20	-0.243	-0.242	-0.243	-0.243	-0.243
F21	-0.238	-0.243	-0.239	-0.238	-0.238
F22	-0.265	-0.264	-0.265	-0.265	-0.265
F23	-0.241	-0.243	-0.240	-0.241	-0.241
F24	-0.257	-0.257	-0.237	-0.235	-0.235
F25	-0.235	-0.235	-0.257	-0.257	-0.257
F26	-0.240	-0.240	-0.241	-0.240	-0.240
F27	-0.236	-0.261	-0.236	-0.237	-0.237
F28	-0.258	-0.242	-0.258	-0.259	-0.258
F29	-0.239	-0.261	-0.239	-0.239	-0.239
F30	-0.262	-0.238	-0.243	-0.243	-0.243
F31	-0.242	-0.245	-0.262	-0.262	-0.262
F32	-0.262	-0.242	-0.239	-0.239	-0.243
F33	-0.241	-0.238	-0.241	-0.241	-0.241
F34	-0.242	-0.263	-0.262	-0.262	-0.262

The calculated 2-body bond lengths, 3-body bond angles, and atomic charges for $F_{40}MPc$ are presented in Tables B.10-12 following the atom labeling scheme depicted in Figure B.4.

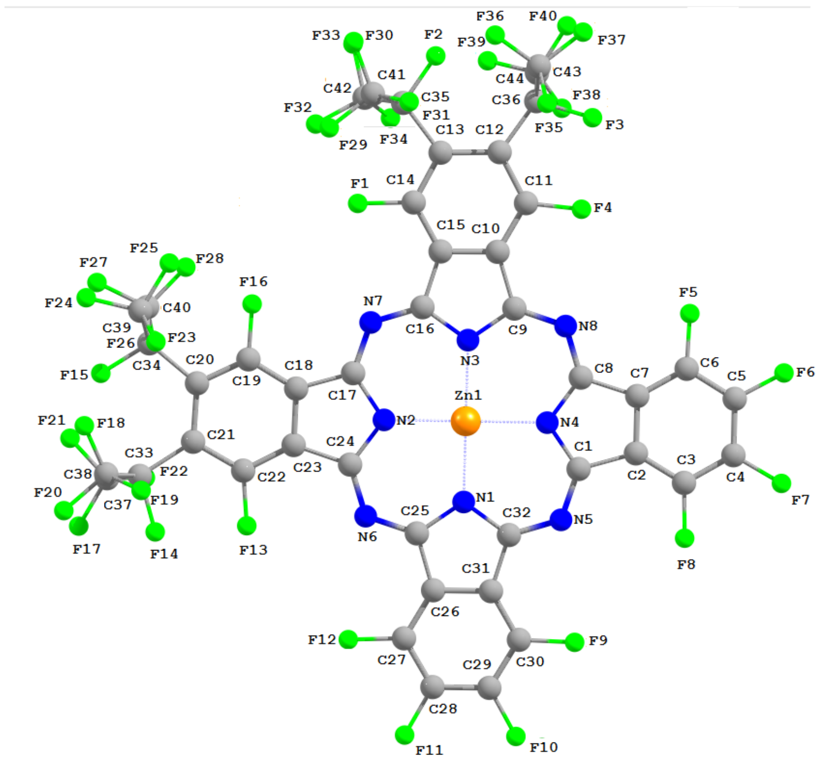

Figure B.4. Atom labeling scheme for $F_{40}MPc$ bond lengths, 3-body angles, and atomic charges.

Table B.10. Calculated bond lengths of $F_{40}MPc$ with B3LYP functional and 6-31G basis set.

	$F_{40}ZnPc$	$F_{40}MgPc$	$F_{40}CoPc$	$F_{40}CuPc$	$F_{40}FePc$
M-N1	2.002	2.002	1.938	1.958	1.953
M-N2	2.012	2.012	1.941	1.960	1.957
M-N3	2.009	2.009	1.942	1.962	1.958
M-N4	2.006	2.006	1.938	1.958	1.953
N1-C25	1.390	1.390	1.395	1.389	1.393
N1-C32	1.382	1.382	1.389	1.384	1.387
N2-C17	1.384	1.384	1.394	1.387	1.391
N2-C24	1.385	1.385	1.391	1.385	1.388
N3-C9	1.384	1.384	1.390	1.384	1.388
N3-C16	1.384	1.384	1.394	1.388	1.391
N4-C1	1.382	1.382	1.390	1.384	1.387
N4-C8	1.388	1.388	1.395	1.389	1.392

N5-C1	1.331	1.331	1.323	1.326	1.325
N5-C32	1.332	1.332	1.323	1.326	1.325
N6-C24	1.335	1.335	1.325	1.328	1.328
N6-C25	1.329	1.329	1.319	1.321	1.321
N7-C16	1.327	1.327	1.321	1.323	1.323
N7-C17	1.327	1.327	1.322	1.324	1.324
N8-C8	1.327	1.327	1.318	1.321	1.321
N8-C9	1.334	1.334	1.325	1.328	1.327
C1-C2	1.461	1.461	1.454	1.454	1.454
C2-C3	1.390	1.390	1.391	1.389	1.391
C2-C7	1.421	1.421	1.413	1.415	1.416
C3-C4	1.396	1.396	1.395	1.395	1.395
C3-F8	1.371	1.371	1.371	1.371	1.370
C4-C5	1.398	1.398	1.400	1.400	1.400
C4-F7	1.371	1.371	1.372	1.371	1.371
C5-C6	1.396	1.396	1.395	1.395	1.396
C5-F6	1.371	1.371	1.371	1.371	1.371
C6-C7	1.390	1.390	1.391	1.389	1.391
C6-F5	1.370	1.370	1.370	1.370	1.370
C7-C8	1.461	1.461	1.454	1.454	1.454
C9-C10	1.464	1.464	1.454	1.454	1.455
C10-C11	1.394	1.394	1.395	1.393	1.395
C10-C15	1.400	1.400	1.397	1.399	1.399
C11-C12	1.420	1.420	1.417	1.416	1.417
C11-F4	1.372	1.372	1.373	1.373	1.372
C12-C13	1.451	1.451	1.446	1.446	1.446
C12-F3	1.552	1.552	1.554	1.554	1.554
C13-C14	1.399	1.399	1.399	1.398	1.399
C13-C35	1.538	1.538	1.531	1.530	1.531
C14-C15	1.382	1.382	1.385	1.382	1.384
C14-F1	1.377	1.377	1.379	1.379	1.378
C15-C16	1.452	1.452	1.450	1.449	1.450
C17-C18	1.451	1.451	1.449	1.449	1.450
C18-C19	1.380	1.380	1.384	1.382	1.384
C18-C23	1.401	1.401	1.398	1.399	1.400
C19-C20	1.398	1.398	1.399	1.399	1.399
C19-F16	1.377	1.377	1.378	1.378	1.378
C20-C21	1.450	1.450	1.448	1.448	1.448
C20-C34	1.534	1.534	1.532	1.532	1.532
C21-C22	1.424	1.424	1.416	1.415	1.415
C21-C33	1.559	1.559	1.552	1.551	1.551
C22-C23	1.396	1.396	1.395	1.393	1.395
C22-F13	1.373	1.373	1.373	1.373	1.373
C23-C24	1.469	1.469	1.455	1.454	1.455
C25-C26	1.463	1.463	1.454	1.454	1.455
C26-C27	1.390	1.390	1.391	1.389	1.391
C26-C31	1.421	1.421	1.413	1.415	1.416

C27-C28	1.396	1.396	1.396	1.395	1.396
C27-F12	1.370	1.370	1.370	1.370	1.370
C28-C29	1.398	1.398	1.399	1.400	1.400
C28-F11	1.371	1.371	1.371	1.371	1.371
C29-C30	1.395	1.395	1.395	1.395	1.395
C29-F10	1.371	1.371	1.372	1.372	1.371
C30-C31	1.390	1.390	1.391	1.389	1.391
C30-F9	1.371	1.371	1.371	1.371	1.370
C31-C32	1.460	1.460	1.454	1.453	1.454
C33-F14	1.439	1.439	1.430	1.430	1.430
C33-C38	1.580	1.580	1.581	1.580	1.580
C33-C37	1.568	1.568	1.565	1.564	1.565
C38-F20	1.372	1.372	1.380	1.380	1.379
C38-F21	1.378	1.378	1.377	1.377	1.377
C38-F22	1.388	1.388	1.382	1.382	1.382
C37-F17	1.386	1.386	1.386	1.386	1.386
C37-F18	1.373	1.373	1.376	1.376	1.376
C37-F19	1.380	1.380	1.378	1.378	1.378
C34-F15	1.415	1.415	1.419	1.419	1.419
C34-C40	1.564	1.564	1.567	1.567	1.566
C34-C39	1.564	1.564	1.573	1.573	1.573
C40-F26	1.372	1.372	1.374	1.374	1.374
C40-F27	1.380	1.380	1.381	1.381	1.381
C40-F28	1.385	1.385	1.380	1.380	1.380
C39-F23	1.384	1.384	1.383	1.383	1.383
C39-F24	1.378	1.378	1.381	1.380	1.380
C39-F25	1.376	1.376	1.374	1.374	1.374
C35-F2	1.416	1.416	1.418	1.417	1.417
C35-C41	1.562	1.562	1.559	1.559	1.559
C35-C42	1.570	1.570	1.575	1.574	1.575
C41-F29	1.375	1.375	1.376	1.376	1.376
C41-F30	1.378	1.378	1.378	1.378	1.378
C41-F31	1.384	1.384	1.383	1.384	1.383
C42-F32	1.383	1.383	1.382	1.382	1.382
C42-F33	1.376	1.376	1.380	1.380	1.380
C42-F34	1.378	1.378	1.376	1.376	1.375
C36-F3	1.441	1.441	1.429	1.429	1.429
C36-C44	1.580	1.580	1.576	1.574	1.574
C36-C43	1.570	1.570	1.581	1.582	1.582
C44-F35	1.370	1.370	1.370	1.370	1.370
C44-F36	1.378	1.378	1.380	1.380	1.380
C44-F37	1.390	1.390	1.388	1.388	1.388
C43-F38	1.387	1.387	1.377	1.377	1.377
C43-F39	1.375	1.375	1.387	1.387	1.387
C43-F40	1.377	1.377	1.378	1.378	1.378

Table B.11. Calculated 3-body bond angles of $F_{40}MPc$ with B3LYP functional and 6-31G basis set.

	$F_{40}ZnPc$	$F_{40}MgPc$	$F_{40}CoPc$	$F_{40}CuPc$	$F_{40}FePc$
N1-M-N2	89.33	89.33	89.95	89.95	89.93
N1-M-N3	174.35	174.35	178.84	179.45	179.49
N1-M-N4	90.32	90.32	89.91	89.93	89.97
M-N1-C25	125.58	125.58	126.30	126.00	126.07
M-N1-C32	124.78	124.78	126.41	126.09	126.11
N2-M-N3	90.51	90.51	90.14	90.15	90.13
N2-M-N4	174.81	174.81	179.56	179.87	179.90
M-N2-C17	124.13	124.13	126.03	125.73	125.76
M-N2-C24	126.18	126.18	126.50	126.18	126.22
N3-M-N4	89.33	89.33	89.99	89.97	89.96
M-N3-C9	125.99	125.99	126.44	126.13	126.18
M-N3-C16	124.41	124.41	126.12	125.73	125.80
M-N4-C1	124.90	124.90	126.46	126.13	126.15
M-N4-C8	125.53	125.53	126.29	125.98	126.04
C25-N1-C32	109.63	109.63	107.28	107.90	107.82
N1-C25-N6	127.21	127.21	127.19	127.06	127.18
N1-C25-C26	108.19	108.19	109.69	109.44	109.40
N1-C32-N5	127.34	127.34	127.22	127.09	127.20
N1-C32-C31	108.58	108.58	109.89	109.62	109.59
C17-N2-C24	109.67	109.67	107.47	108.10	108.01
N2-C17-N7	127.69	127.69	127.29	127.16	127.29
N2-C17-C18	108.04	108.04	109.18	108.91	108.87
N2-C24-N6	126.24	126.24	126.91	126.81	126.92
N2-C24-C23	107.90	107.90	109.40	109.13	109.11
C9-N3-C16	109.59	109.59	107.43	108.04	107.98
N3-C9-N8	126.63	126.63	126.95	126.80	126.93
N3-C9-C10	107.99	107.99	109.45	109.20	109.13
N3-C16-N7	127.48	127.48	127.18	127.04	127.22
N3-C16-C15	108.06	108.06	109.19	108.93	108.89
C1-N4-C8	109.55	109.55	107.25	107.86	107.80
N4-C1-N5	127.03	127.03	127.16	127.04	127.16
N4-C1-C2	108.58	108.58	109.90	109.65	109.59
N4-C8-N8	127.22	127.22	127.18	127.05	127.19
N4-C8-C7	108.36	108.36	109.74	109.50	109.44
C1-N5-C32	125.40	125.40	122.81	123.70	123.38
N5-C1-C2	124.37	124.37	122.93	123.31	123.25
N5-C32-C31	124.07	124.07	122.89	123.29	123.20
C24-N6-C25	125.41	125.41	123.10	123.96	123.63
N6-C24-C23	125.85	125.85	123.66	124.05	123.96
N6-C25-C26	124.59	124.59	123.12	123.49	123.42
C16-N7-C17	125.50	125.50	123.01	123.91	123.56
N7-C16-C15	124.46	124.46	123.62	124.01	123.89
N7-C17-C18	124.23	124.23	123.40	123.81	123.70

C8-N8-C9	125.24	125.24	123.15	124.04	123.70
N8-C8-C7	124.42	124.42	123.08	123.44	123.37
N8-C9-C10	125.39	125.39	123.59	123.97	123.93
C1-C2-C3	132.92	132.92	132.87	132.93	132.86
C1-C2-C7	106.71	106.71	106.55	106.49	106.58
C3-C2-C7	120.37	120.37	120.57	120.57	120.55
C2-C3-C4	118.84	118.84	118.60	118.60	118.60
C2-C3-F8	122.35	122.35	122.49	122.40	122.44
C2-C7-C6	120.38	120.38	120.61	120.59	120.58
C2-C7-C8	106.79	106.79	106.56	106.50	106.59
C4-C3-F8	118.81	118.81	118.91	119.00	118.95
C3-C4-C5	120.77	120.77	120.82	120.81	120.82
C3-C4-F7	120.01	120.01	120.00	119.98	119.98
C5-C4-F7	119.23	119.23	119.18	119.19	119.17
C4-C5-C6	120.79	120.79	120.82	120.81	120.84
C4-C5-F6	119.22	119.22	119.16	119.17	119.15
C6-C5-F6	119.99	119.99	120.02	120.01	120.01
C5-C6-C7	118.83	118.83	118.58	118.59	118.58
C5-C6-F5	118.84	118.84	118.94	119.02	118.97
C7-C6-F5	122.33	122.33	122.48	122.39	122.45
C6-C7-C8	132.83	132.83	132.83	132.89	132.81
C9-C10-C11	133.40	133.40	132.63	132.71	132.63
C9-C10-C15	106.76	106.76	106.68	106.60	106.69
C11-C10-C15	119.84	119.84	120.67	120.66	120.64
C10-C11-C12	122.56	122.56	122.17	122.17	122.18
C10-C11-F4	113.95	113.95	114.37	114.28	114.37
C10-C15-C14	118.97	118.97	118.44	118.46	118.45
C10-C15-C16	107.61	107.61	107.22	107.20	107.26
C12-C11-F4	123.49	123.49	123.46	123.53	123.44
C11-C12-C13	116.71	116.71	116.35	116.35	116.37
C11-C12-C36	117.17	117.17	117.61	117.54	117.48
C13-C12-C36	126.11	126.11	126.02	126.10	126.11
C12-C13-C14	118.79	118.79	119.64	119.66	119.68
C12-C13-C35	126.23	126.23	125.31	125.34	125.35
C12-C36-F3	109.02	109.02	107.91	107.81	107.83
C12-C36-C44	115.92	115.92	115.83	115.95	115.56
C12-C36-C43	113.72	113.72	114.55	114.50	114.85
C14-C13-C35	114.97	114.97	115.01	114.98	114.91
C13-C14-C15	123.11	123.11	122.63	122.60	122.62
C13-C14-F1	119.25	119.25	118.78	118.87	118.82
C13-C35-F2	108.62	108.62	108.91	108.94	108.87
C13-C35-C41	113.75	113.75	112.59	112.50	112.57
C13-C35-C42	115.17	115.17	115.33	115.39	115.28
C15-C14-F1	117.63	117.63	118.56	118.51	118.53
C14-C15-C16	133.42	133.42	134.34	134.34	134.30
C17-C18-C19	133.13	133.13	134.06	134.07	134.05
C17-C18-C23	107.82	107.82	107.26	107.23	107.30

C19-C18-C23	119.04	119.04	118.63	118.66	118.62
C18-C19-C20	123.15	123.15	122.62	122.62	122.59
C18-C19-F16	117.73	117.73	118.65	118.56	118.64
C18-C23-C22	119.64	119.64	120.43	120.45	120.41
C18-C23-C24	106.55	106.55	106.63	106.57	106.66
C20-C19-F16	119.12	119.12	118.72	118.76	118.77
C19-C20-C21	119.03	119.03	119.22	119.26	119.24
C19-C20-C34	114.78	114.78	114.94	114.81	114.90
C21-C20-C34	126.18	126.18	125.76	125.77	125.77
C20-C21-C22	116.30	116.30	116.55	116.60	116.57
C20-C21-C33	126.58	126.58	125.61	125.55	125.64
C20-C34-F15	108.11	108.11	108.84	108.82	108.84
C20-C34-C40	115.05	115.05	114.19	114.18	114.09
C20-C34-C39	114.36	114.36	114.52	114.47	114.53
C22-C21-C33	117.09	117.09	117.60	117.59	117.58
C21-C22-C23	122.77	122.77	122.20	122.16	122.18
C21-C22-F13	123.73	123.73	122.90	122.98	122.97
C21-C33-F14	107.54	107.54	108.67	108.65	108.67
C21-C33-C38	116.37	116.37	116.35	116.29	116.41
C21-C33-C37	115.65	115.65	113.64	113.67	113.51
C23-C22-F13	113.50	113.50	114.89	114.84	114.85
C22-C23-C24	133.81	133.81	132.94	132.98	132.93
C25-C26-C27	133.02	133.02	132.87	132.93	132.86
C25-C26-C31	106.80	106.80	106.57	106.51	106.59
C27-C26-C31	120.18	120.18	120.56	120.56	120.54
C26-C27-C28	118.87	118.87	118.58	118.60	118.60
C26-C27-F12	122.35	122.35	122.48	122.38	122.45
C26-C31-C30	120.57	120.57	120.62	120.62	120.59
C26-C31-C32	106.79	106.79	106.57	106.52	106.60
C28-C27-F12	118.77	118.77	118.93	119.02	118.95
C27-C28-C29	120.87	120.87	120.82	120.81	120.85
C27-C28-F11	120.02	120.02	119.99	119.98	119.99
C29-C28-F11	119.12	119.12	119.19	119.21	119.16
C28-C29-C30	120.69	120.69	120.83	120.84	120.83
C28-C29-F10	119.32	119.32	119.17	119.15	119.18
C30-C29-F10	120.00	120.00	120.00	120.01	120.00
C29-C30-C31	118.82	118.82	118.58	118.58	118.60
C29-C30-F9	118.88	118.88	118.93	119.02	118.96
C31-C30-F9	122.31	122.31	122.49	122.41	122.44
C30-C31-C32	132.63	132.63	132.82	132.85	132.82
F14-C33-C38	98.08	98.08	102.39	102.37	102.45
F14-C33-C37	97.05	97.05	97.96	97.98	97.97
C38-C33-C37	117.53	117.53	115.14	115.20	115.17
C33-C38-F20	118.49	118.49	113.10	113.07	113.10
C33-C38-F21	109.82	109.82	110.50	110.57	110.47
C33-C38-F22	106.53	106.53	110.52	110.57	110.50
C33-C37-F17	106.60	106.60	107.37	107.38	107.39

C33-C37-F18	118.72	118.72	116.95	116.90	116.91
C33-C37-F19	109.09	109.09	109.57	109.58	109.56
F20-C38-F21	105.89	105.89	106.75	106.68	106.79
F20-C38-F22	107.67	107.67	108.94	108.87	108.97
F21-C38-F22	108.07	108.07	106.77	106.82	106.75
F17-C37-F18	106.21	106.21	106.35	106.35	106.39
F17-C37-F19	108.82	108.82	108.38	108.41	108.38
F18-C37-F19	107.07	107.07	107.91	107.93	107.93
F15-C34-C40	100.30	100.30	100.75	100.75	100.80
F15-C34-C39	104.37	104.37	105.76	105.85	105.77
C40-C34-C39	112.91	112.91	111.47	111.47	111.51
C34-C40-F26	115.90	115.90	115.21	115.29	115.19
C34-C40-F27	108.87	108.87	108.65	108.67	108.67
C34-C40-F28	107.91	107.91	109.10	109.19	109.10
C34-C39-F23	109.59	109.59	110.58	110.51	110.59
C34-C39-F24	113.17	113.17	111.89	111.90	111.90
C34-C39-F25	110.38	110.38	110.54	110.45	110.53
F26-C40-F27	107.42	107.42	108.06	107.97	108.04
F26-C40-F28	107.95	107.95	107.14	107.12	107.15
F27-C40-F28	108.61	108.61	108.50	108.42	108.51
F23-C39-F24	108.02	108.02	107.84	107.89	107.83
F23-C39-F25	108.24	108.24	108.17	108.21	108.15
F24-C39-F25	107.30	107.30	107.69	107.76	107.71
F2-C35-C41	102.35	102.35	102.40	102.36	102.35
F2-C35-C42	102.65	102.65	104.28	104.35	104.36
C41-C35-C42	112.73	112.73	112.10	112.08	112.18
C35-C41-F29	114.42	114.42	113.74	113.82	113.79
C35-C41-F30	109.68	109.68	110.00	110.01	109.94
C35-C41-F31	108.80	108.80	108.70	108.67	108.64
C35-C42-F32	109.48	109.48	110.90	110.90	110.93
C35-C42-F33	114.21	114.21	112.29	112.35	112.26
C35-C42-F34	109.47	109.47	109.98	109.98	110.00
F29-C41-F30	107.59	107.59	108.46	108.47	108.50
F29-C41-F31	107.65	107.65	107.18	107.10	107.19
F30-C41-F31	108.55	108.55	108.62	108.63	108.63
F32-C42-F33	108.18	108.18	108.34	108.30	108.32
F32-C42-F34	108.37	108.37	107.86	107.81	107.87
F33-C42-F34	106.97	106.97	107.31	107.34	107.30
F3-C36-C44	95.67	95.67	98.58	98.78	98.87
F3-C36-C43	97.96	97.96	101.80	101.71	101.70
C44-C36-C43	120.11	120.11	115.37	115.29	115.26
C36-C44-F35	120.00	120.00	118.35	118.21	118.01
C36-C44-F36	109.70	109.70	109.11	109.17	109.18
C36-C44-F37	105.23	105.23	106.61	106.61	106.72
C36-C43-F38	106.52	106.52	110.36	110.42	110.44
C36-C43-F39	117.31	117.31	112.12	112.05	111.96
C36-C43-F40	110.61	110.61	111.85	111.90	111.96

F35-C44-F36	106.32	106.32	106.64	106.77	106.79
F35-C44-F37	106.70	106.70	107.35	107.31	107.38
F36-C44-F37	108.45	108.45	108.45	108.45	108.46
F38-C43-F39	105.35	105.35	105.83	105.81	105.88
F38-C43-F40	108.82	108.82	107.43	107.39	107.28
F39-C43-F40	107.86	107.86	108.98	109.00	109.06

Table B.12. Calculated Mullikan Atomic Charges of $F_{40}MPc$ with B3LYP functional and 6-31G basis set.

	$F_{40}ZnPc$	$F_{40}MgPc$	$F_{40}CoPc$	$F_{40}CuPc$	$F_{40}FePc$
M	1.046	1.290	1.083	0.992	1.015
N1	-0.682	-0.750	-0.695	-0.677	-0.704
N2	-0.681	-0.746	-0.698	-0.680	-0.707
N3	-0.682	-0.747	-0.697	-0.679	-0.706
N4	-0.680	-0.747	-0.695	-0.677	-0.704
N5	-0.332	-0.333	-0.315	-0.321	-0.325
N6	-0.327	-0.327	-0.308	-0.313	-0.317
N7	-0.314	-0.314	-0.303	-0.308	-0.312
N8	-0.324	-0.324	-0.307	-0.313	-0.317
C1	0.368	0.375	0.350	0.357	0.367
C2	0.036	0.034	0.044	0.041	0.041
C3	0.250	0.249	0.254	0.253	0.255
C4	0.279	0.279	0.278	0.279	0.279
C5	0.279	0.279	0.279	0.279	0.279
C6	0.251	0.250	0.255	0.254	0.256
C7	0.037	0.035	0.047	0.045	0.045
C8	0.362	0.369	0.344	0.351	0.361
C9	0.362	0.368	0.343	0.350	0.360
C10	0.042	0.039	0.040	0.038	0.038
C11	0.268	0.267	0.268	0.267	0.269
C12	0.014	0.014	0.025	0.026	0.026
C13	0.061	0.061	0.054	0.056	0.054
C14	0.234	0.233	0.243	0.243	0.245
C15	0.044	0.042	0.064	0.061	0.061
C16	0.369	0.375	0.356	0.362	0.371
C17	0.371	0.377	0.357	0.364	0.373
C18	0.035	0.034	0.059	0.056	0.055
C19	0.236	0.235	0.243	0.241	0.244
C20	0.053	0.052	0.046	0.048	0.046
C21	0.029	0.029	0.023	0.023	0.023
C22	0.265	0.264	0.268	0.268	0.269
C23	0.047	0.045	0.046	0.043	0.044
C24	0.363	0.369	0.343	0.350	0.360

C25	0.365	0.371	0.345	0.352	0.361
C26	0.041	0.038	0.048	0.045	0.046
C27	0.249	0.248	0.255	0.254	0.256
C28	0.280	0.280	0.279	0.280	0.280
C29	0.278	0.278	0.278	0.279	0.279
C30	0.251	0.251	0.254	0.254	0.256
C31	0.031	0.029	0.043	0.040	0.040
C32	0.370	0.377	0.350	0.357	0.367
C33	0.066	0.066	0.055	0.054	0.055
C34	0.061	0.061	0.058	0.058	0.058
C35	0.065	0.065	0.051	0.050	0.050
C36	0.065	0.065	0.057	0.057	0.057
C37	0.798	0.798	0.807	0.807	0.807
C38	0.800	0.800	0.827	0.827	0.828
C39	0.810	0.810	0.825	0.825	0.825
C40	0.803	0.803	0.806	0.806	0.806
C41	0.805	0.805	0.812	0.812	0.812
C42	0.807	0.807	0.821	0.822	0.821
C43	0.799	0.799	0.809	0.809	0.809
C44	0.806	0.806	0.825	0.825	0.825
F1	-0.268	-0.268	-0.271	-0.271	-0.271
F2	-0.291	-0.291	-0.293	-0.293	-0.293
F3	-0.276	-0.276	-0.277	-0.277	-0.277
F4	-0.254	-0.254	-0.254	-0.254	-0.254
F5	-0.259	-0.259	-0.259	-0.258	-0.258
F6	-0.272	-0.273	-0.273	-0.272	-0.272
F7	-0.273	-0.273	-0.274	-0.273	-0.273
F8	-0.261	-0.261	-0.261	-0.260	-0.260
F9	-0.261	-0.261	-0.261	-0.260	-0.260
F10	-0.273	-0.273	-0.274	-0.273	-0.273
F11	-0.272	-0.273	-0.273	-0.272	-0.272
F12	-0.259	-0.259	-0.259	-0.258	-0.258
F13	-0.256	-0.256	-0.255	-0.255	-0.255
F14	-0.276	-0.276	-0.277	-0.276	-0.276
F15	-0.289	-0.289	-0.294	-0.293	-0.294
F16	-0.268	-0.268	-0.261	-0.268	-0.268
F17	-0.258	-0.258	-0.258	-0.258	-0.258
F18	-0.246	-0.246	-0.247	-0.247	-0.247
F19	-0.241	-0.241	-0.247	-0.247	-0.247
F20	-0.242	-0.242	-0.243	-0.243	-0.243
F21	-0.235	-0.235	-0.251	-0.251	-0.250
F22	-0.262	-0.262	-0.260	-0.259	-0.239
F23	-0.260	-0.260	-0.261	-0.260	-0.261
F24	-0.239	-0.239	-0.239	-0.239	-0.239
F25	-0.240	-0.240	-0.246	-0.245	-0.246
F26	-0.257	-0.257	-0.251	-0.251	-0.251
F27	-0.244	-0.245	-0.248	-0.248	-0.248

F28	-0.233	-0.233	-0.238	-0.238	-0.238
F29	-0.258	-0.258	-0.256	-0.256	-0.256
F30	-0.236	-0.236	-0.239	-0.239	-0.239
F31	-0.242	-0.242	-0.244	-0.245	-0.244
F32	-0.239	-0.239	-0.258	-0.258	-0.258
F33	-0.341	-0.241	-0.245	-0.240	-0.245
F34	-0.258	-0.258	-0.240	-0.237	-0.240
F35	-0.262	-0.262	-0.263	-0.263	-0.262
F36	-0.236	-0.236	-0.238	-0.238	-0.237
F37	-0.244	-0.244	-0.248	-0.250	-0.247
F38	-0.256	-0.256	-0.267	-0.268	-0.268
F39	-0.246	-0.246	-0.250	-0.250	-0.250
F40	-0.245	-0.245	-0.243	-0.243	-0.243

The calculated 2-body bond lengths, 3-body bond angles, and atomic charges for F_{52}MPc are presented in Tables B.13-15 following the atom labeling scheme depicted in Figure B.5.

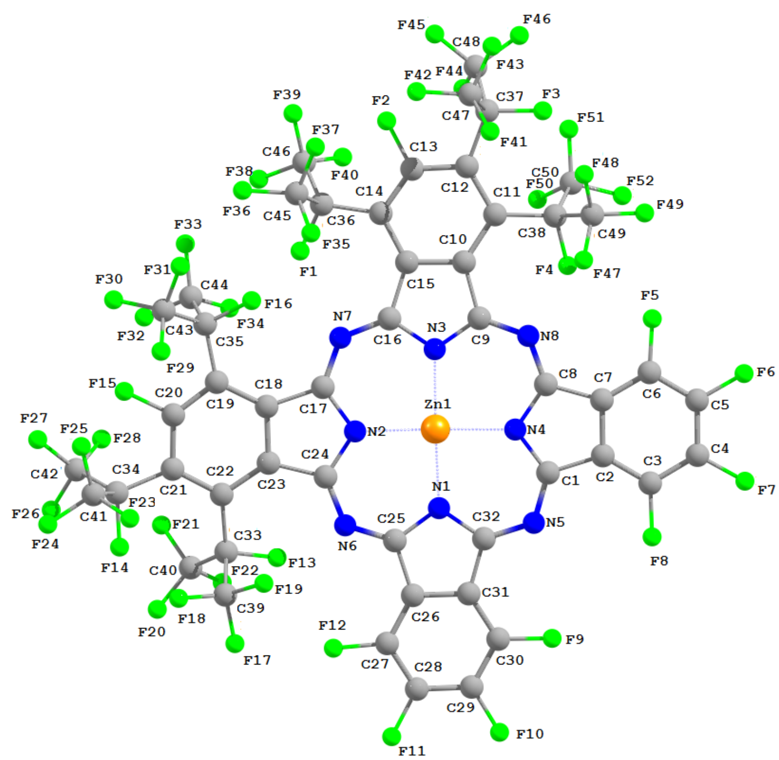

Figure B.5. Atom labeling scheme for F_{52}MPc bond lengths, 3-body angles, and atomic charges.

Table B.13. Calculated bond lengths of $F_{52}MPc$ with B3LYP functional and 6-31G basis set.

	$F_{52}ZnPc$	$F_{52}MgPc$	$F_{52}CoPc$	$F_{52}CuPc$	$F_{52}FePc$
M-N1	2.015	2.015	1.945	1.969	1.968
M-N2	2.038	2.038	1.981	1.999	2.003
M-N3	2.034	2.034	1.978	1.995	2.001
M-N4	2.022	2.022	1.952	1.975	1.974
N1-C25	1.389	1.389	1.396	1.393	1.394
N1-C32	1.380	1.380	1.388	1.384	1.387
N2-C17	1.388	1.388	1.397	1.393	1.395
N2-C24	1.375	1.375	1.384	1.380	1.382
N3-C9	1.375	1.375	1.383	1.379	1.381
N3-C16	1.387	1.387	1.396	1.392	1.395
N4-C1	1.377	1.377	1.386	1.382	1.385
N4-C8	1.388	1.388	1.396	1.394	1.394
N5-C1	1.328	1.328	1.321	1.324	1.324
N5-C32	1.328	1.328	1.321	1.324	1.323
N6-C24	1.333	1.333	1.326	1.330	1.328
N6-C25	1.315	1.315	1.309	1.311	1.311
N7-C16	1.335	1.335	1.328	1.332	1.331
N7-C17	1.334	1.334	1.327	1.331	1.330
N8-C8	1.313	1.313	1.306	1.309	1.308
N8-C9	1.331	1.331	1.324	1.328	1.326
C1-C2	1.457	1.457	1.452	1.456	1.453
C2-C3	1.390	1.390	1.393	1.392	1.394
C2-C7	1.419	1.419	1.414	1.416	1.416
C3-C4	1.395	1.395	1.394	1.395	1.394
C3-F8	1.371	1.371	1.371	1.370	1.371
C4-C5	1.397	1.397	1.396	1.396	1.397
C4-F7	1.371	1.371	1.371	1.371	1.371
C5-C6	1.397	1.397	1.397	1.398	1.397
C5-F6	1.371	1.371	1.372	1.372	1.371
C6-C7	1.391	1.391	1.394	1.393	1.393
C6-F5	1.369	1.369	1.368	1.368	1.369
C7-C8	1.472	1.472	1.468	1.472	1.470
C9-C10	1.484	1.484	1.481	1.485	1.482
C10-C11	1.441	1.441	1.447	1.445	1.446
C10-C15	1.446	1.446	1.440	1.443	1.442
C11-C12	1.420	1.420	1.421	1.421	1.421
C11-C38	1.551	1.551	1.551	1.551	1.551
C12-C12	1.397	1.397	1.397	1.397	1.397
C12-C37	1.543	1.543	1.547	1.545	1.546
C13-C14	1.382	1.382	1.382	1.383	1.382
C13-F2	1.384	1.384	1.384	1.384	1.385
C14-C15	1.417	1.417	1.421	1.420	1.421
C14-C36	1.522	1.522	1.522	1.522	1.522

C15-C16	1.503	1.503	1.501	1.504	1.502
C17-C18	1.504	1.504	1.502	1.505	1.503
C18-C19	1.416	1.416	1.421	1.419	1.420
C18-C23	1.448	1.448	1.441	1.445	1.444
C19-C20	1.381	1.381	1.381	1.382	1.381
C19-C35	1.523	1.523	1.523	1.523	1.523
C20-C21	1.394	1.394	1.393	1.393	1.394
C20-F15	1.385	1.385	1.386	1.386	1.386
C21-C22	1.418	1.418	1.419	1.419	1.419
C21-C34	1.537	1.537	1.541	1.539	1.540
C22-C23	1.445	1.445	1.451	1.448	1.450
C22-C33	1.558	1.558	1.558	1.558	1.558
C23-C24	1.489	1.489	1.486	1.489	1.487
C25-C26	1.471	1.471	1.467	1.471	1.469
C26-C27	1.389	1.389	1.392	1.391	1.391
C26-C31	1.418	1.418	1.413	1.415	1.415
C27-C28	1.397	1.397	1.396	1.397	1.397
C27-F12	1.367	1.367	1.367	1.367	1.367
C28-C29	1.397	1.397	1.397	1.396	1.397
C28-C11	1.371	1.371	1.372	1.372	1.371
C29-C30	1.395	1.395	1.394	1.395	1.394
C29-F10	1.371	1.371	1.371	1.372	1.372
C30-C31	1.390	1.390	1.393	1.392	1.393
C30-F9	1.371	1.371	1.371	1.371	1.371
C31-C32	1.456	1.456	1.451	1.455	1.452
C35-F16	1.408	1.408	1.407	1.407	1.407
C35-C43	1.581	1.581	1.583	1.582	1.582
C35-C44	1.554	1.554	1.555	1.555	1.555
C43-F29	1.376	1.376	1.377	1.377	1.377
C43-F30	1.378	1.378	1.378	1.377	1.378
C43-F31	1.386	1.386	1.385	1.385	1.385
C44-F32	1.382	1.382	1.382	1.382	1.382
C44-F33	1.383	1.383	1.383	1.383	1.383
C44-F34	1.374	1.374	1.374	1.374	1.374
C34-F25	1.414	1.414	1.414	1.414	1.414
C34-C42	1.582	1.582	1.583	1.582	1.583
C34-C41	1.567	1.567	1.568	1.567	1.568
C42-F26	1.380	1.380	1.381	1.381	1.381
C42-F27	1.375	1.375	1.375	1.375	1.375
C42-F28	1.382	1.382	1.381	1.381	1.381
C41-F23	1.384	1.384	1.384	1.384	1.384
C41-F24	1.375	1.375	1.374	1.374	1.374
C41-F25	1.379	1.379	1.379	1.379	1.379
C33-F13	1.421	1.421	1.421	1.420	1.421
C33-C40	1.601	1.601	1.602	1.601	1.601
C33-C39	1.564	1.564	1.564	1.564	1.564
C40-F20	1.388	1.388	1.388	1.387	1.388

C40-F21	1.377	1.377	1.376	1.376	1.377
C40-F22	1.377	1.377	1.377	1.377	1.377
C39-F17	1.382	1.382	1.381	1.381	1.381
C39-F18	1.377	1.377	1.377	1.376	1.377
C39-F19	1.378	1.378	1.378	1.377	1.378
C36-F1	1.409	1.409	1.408	1.408	1.408
C36-C45	1.556	1.556	1.556	1.556	1.556
C36-C46	1.578	1.578	1.580	1.578	1.579
C45-F37	1.384	1.384	1.384	1.384	1.384
C45-F36	1.373	1.373	1.373	1.373	1.373
C45-F35	1.382	1.382	1.382	1.382	1.382
C46-F40	1.384	1.384	1.384	1.385	1.384
C46-F39	1.377	1.377	1.377	1.377	1.377
C46-F38	1.378	1.378	1.378	1.378	1.378
C37-F3	1.413	1.413	1.412	1.413	1.413
C37-C48	1.578	1.578	1.579	1.578	1.578
C37-C47	1.566	1.566	1.566	1.566	1.567
C48-F45	1.380	1.380	1.380	1.380	1.380
C48-F46	1.375	1.375	1.375	1.375	1.375
C48-F44	1.383	1.383	1.382	1.383	1.383
C47-F41	1.383	1.383	1.384	1.384	1.384
C47-F42	1.375	1.375	1.375	1.376	1.375
C47-F43	1.378	1.378	1.379	1.379	1.379
C38-F4	1.433	1.433	1.433	1.433	1.433
C38-C50	1.586	1.586	1.588	1.587	1.587
C38-C49	1.571	1.571	1.571	1.571	1.571
C50-F51	1.373	1.373	1.373	1.373	1.373
C50-F52	1.376	1.376	1.376	1.376	1.377
C50-F50	1.390	1.390	1.390	1.390	1.390
C49-F47	1.381	1.381	1.381	1.381	1.381
C49-F48	1.375	1.375	1.375	1.375	1.376
C49-F49	1.378	1.378	1.377	1.377	1.377

Table B.14. Calculated 3-body bond angles of $F_{52}MPc$ with B3LYP functional and 6-31G basis set.

	$F_{52}ZnPc$	$F_{52}MgPc$	$F_{52}CoPc$	$F_{52}CuPc$	$F_{52}FePc$
N1-M-N2	90.75	90.75	90.66	90.74	90.84
N1-M-N3	174.69	174.69	176.28	176.54	176.73
N1-M-N4	87.15	87.15	87.84	87.51	87.64
M-N1-C25	123.80	123.80	125.35	124.72	124.68
M-N1-C32	127.07	127.07	127.75	127.53	127.48
N2-M-N3	91.09	91.09	90.79	90.94	90.64
N2-M-N4	177.01	177.01	178.48	178.22	178.43
M-N2-C17	124.16	124.16	125.59	125.05	125.19
M-N2-C24	124.71	124.71	125.81	125.40	125.21

N3-M-N4	90.83	90.83	90.69	90.79	90.85
M-N3-C9	124.37	124.37	125.54	125.09	124.94
M-N3-C16	124.56	124.56	125.89	125.35	125.53
M-N4-C1	127.21	127.21	127.88	127.70	127.61
M-N4-C8	123.70	123.70	125.28	124.60	124.60
C25-N1-C32	109.12	109.12	106.89	107.74	107.83
N1-C25-N6	126.48	126.48	126.30	126.65	126.57
N1-C25-C26	108.37	108.37	109.68	109.19	109.01
N1-C32-N5	127.58	127.58	127.42	127.66	127.57
N1-C32-C31	109.23	109.23	110.57	110.14	109.95
C17-N2-C24	111.11	111.11	108.59	109.53	109.57
N2-C17-N7	124.68	124.68	124.45	124.82	124.71
N2-C17-C18	106.96	106.96	108.42	107.93	107.81
N2-C24-N6	124.83	124.83	124.66	124.97	124.85
N2-C24-C23	109.48	109.48	111.04	110.52	110.35
C9-N3-C16	111.07	111.07	108.57	109.55	109.53
N3-C9-N8	125.01	125.01	124.83	125.08	124.99
N3-C9-C10	109.56	109.56	111.08	110.55	110.43
N3-C16-N7	124.44	124.44	124.25	124.52	124.44
N3-C16-C15	107.03	107.03	108.46	107.97	107.87
C1-N4-C8	109.08	109.08	106.84	107.69	107.77
N4-C1-N5	127.34	127.34	127.17	127.41	127.33
N4-C1-C2	109.30	109.30	110.67	110.21	110.07
N4-C8-N8	126.01	126.01	125.89	126.20	126.15
N4-C8-C7	108.57	108.57	109.89	109.37	109.21
C1-N5-C32	123.51	123.51	121.75	121.98	122.14
N5-C1-C2	123.36	123.36	122.15	122.37	122.56
N5-C32-C31	123.18	123.18	122.01	122.16	122.48
C24-N6-C25	128.96	128.96	126.78	127.12	127.44
N6-C24-C23	125.59	125.59	124.19	124.41	124.69
N6-C25-C26	125.06	125.06	123.93	124.07	124.26
C16-N7-C17	130.61	130.61	128.62	128.80	129.01
N7-C16-C15	128.47	128.47	127.23	127.33	127.62
N7-C17-C18	128.28	128.28	127.04	127.21	127.37
C8-N8-C9	129.25	129.25	127.02	127.36	127.72
N8-C8-C7	125.34	125.34	124.16	124.33	124.50
N8-C9-C10	125.37	125.37	124.05	124.27	124.53
C1-C2-C3	131.91	131.91	132.07	132.08	131.97
C1-C2-C7	106.80	106.80	106.55	106.60	106.69
C3-C2-C7	121.27	121.27	121.34	121.29	121.34
C2-C3-C4	118.76	118.76	118.74	118.82	118.77
C2-C3-F8	122.43	122.43	122.68	122.69	122.64
C2-C7-C6	119.29	119.29	119.23	119.20	119.19
C2-C7-C8	106.26	106.26	106.06	106.14	106.25
C4-C3-F8	118.81	118.81	118.58	118.49	118.58
C3-C4-C5	120.34	120.34	120.30	120.29	120.27
C3-C4-F7	120.21	120.21	120.28	120.31	120.32

C5-C4-F7	119.45	119.45	119.42	119.40	119.42
C4-C5-C6	121.05	121.05	121.04	121.00	121.10
C4-C5-F6	119.25	119.25	119.20	119.19	119.16
C6-C5-F6	119.71	119.71	119.76	119.80	119.74
C5-C6-C7	119.28	119.28	119.32	119.39	119.33
C5-C6-F5	117.53	117.53	117.16	117.11	117.18
C7-C6-F5	123.19	123.19	123.52	123.48	123.49
C6-C7-C8	134.36	134.36	134.56	134.58	134.47
C9-C10-C11	131.83	131.83	132.07	132.11	131.96
C9-C10-C15	105.17	105.17	104.89	104.94	105.08
C11-C10-C15	122.99	122.99	123.03	122.95	122.95
C10-C11-C12	116.69	116.69	116.79	116.84	116.78
C10-C11-C38	121.38	121.38	121.74	121.63	121.63
C10-C15-C14	117.99	117.99	117.90	117.89	117.97
C10-C15-C16	107.13	107.13	106.91	106.94	107.02
C12-C11-C38	121.53	121.53	121.06	121.13	121.16
C11-C12-C13	116.66	116.66	116.45	116.48	116.54
C11-C12-C37	129.63	129.63	129.92	129.81	129.79
C11-C38-F4	108.32	108.32	108.18	108.09	108.25
C11-C38-C50	113.70	113.70	113.81	113.87	113.89
C11-C38-C49	115.63	115.63	115.66	115.61	115.56
C13-C12-C37	113.56	113.56	113.49	113.55	113.52
C12-C13-C14	128.13	128.13	128.23	128.16	128.19
C12-C13-F2	115.30	115.30	115.14	115.16	115.17
C12-C37-F3	110.95	110.95	110.99	110.96	110.98
C12-C37-C48	115.78	115.78	116.02	115.93	115.99
C12-C37-C47	111.55	111.55	111.63	111.62	111.59
C14-C13-F2	116.53	116.53	116.58	116.64	116.60
C13-C14-C15	116.09	116.09	116.15	116.15	116.13
C13-C14-C36	116.78	116.78	116.30	116.39	116.45
C15-C14-C36	126.96	126.96	127.38	127.24	127.27
C14-C15-C16	134.88	134.88	135.19	135.14	135.01
C14-C36-F1	107.11	107.11	106.92	106.85	107.02
C14-C36-C45	109.49	109.49	109.60	109.62	109.45
C14-C36-C46	116.82	116.82	116.99	116.95	117.04
C17-C18-C19	134.57	134.57	134.91	134.89	134.72
C17-C18-C23	107.09	107.09	106.87	106.90	106.99
C19-C18-C23	118.33	118.33	118.21	118.20	118.28
C18-C19-C20	116.02	116.02	116.07	116.10	116.06
C18-C19-C35	127.71	127.71	128.12	127.99	128.01
C18-C23-C22	122.78	122.78	122.84	122.75	122.76
C18-C23-C24	104.86	104.86	104.58	104.63	104.79
C20-C19-C35	116.26	116.26	115.78	115.89	115.91
C19-C20-C21	128.19	128.19	128.34	128.28	128.30
C19-C20-F15	116.51	116.51	116.54	116.61	116.57
C19-C35-F16	107.29	107.29	107.13	107.05	107.15
C19-C35-C43	116.20	116.20	116.42	116.37	116.35

C19-C35-C44	110.24	110.24	110.31	110.33	110.33
C21-C20-F15	115.28	115.28	115.10	115.09	115.11
C20-C21-C22	117.50	117.50	117.24	117.28	117.32
C20-C21-C34	113.31	113.31	113.24	113.30	113.27
C22-C21-C34	129.17	129.17	129.50	129.40	129.39
C21-C22-C23	116.42	116.42	116.49	116.53	116.53
C21-C22-C33	122.77	122.77	122.28	122.35	122.38
C21-C34-F14	109.35	109.35	109.38	109.38	109.39
C21-C34-C42	115.21	115.21	115.48	115.37	115.44
C21-C34-C41	113.05	113.05	113.12	113.14	113.09
C23-C22-C33	120.70	120.70	121.13	121.01	120.96
C22-C23-C24	132.35	132.35	132.58	132.61	132.45
C22-C33-F13	107.15	107.15	107.09	106.99	107.15
C22-C33-C40	117.17	117.17	117.12	117.22	117.24
C22-C22-C39	114.41	114.41	114.51	114.41	114.39
C25-C26-C27	134.06	134.06	134.26	134.29	134.18
C25-C26-C31	106.49	106.49	106.29	106.38	106.48
C27-C26-C31	119.36	119.36	119.31	119.27	119.27
C26-C27-C28	119.39	119.39	119.43	119.49	119.41
C26-C27-F12	122.68	122.68	122.91	122.92	122.94
C26-C31-C30	121.20	121.20	121.30	121.22	121.29
C26-C31-C32	106.71	106.71	106.46	106.50	106.60
C28-C27-F12	117.93	117.93	117.67	117.59	117.65
C27-C28-C29	120.91	120.91	120.90	120.88	120.98
C27-C28-F11	119.81	119.81	119.83	119.86	119.82
C29-C28-F11	119.27	119.27	119.26	119.26	119.20
C28-C29-C30	120.36	120.36	120.33	120.32	120.29
C28-C29-F10	119.46	119.46	119.39	119.38	119.41
C30-C29-F10	120.18	120.18	120.27	120.30	120.30
C29-C30-C31	118.76	118.76	118.73	118.81	118.75
C29-C30-F9	118.81	118.81	118.59	118.49	118.59
C31-C30-F9	122.42	122.42	122.68	122.70	122.64
C30-C31-C32	132.07	132.07	132.23	132.19	132.10
F16-C35-C43	102.28	102.28	102.25	102.29	102.27
F16-C35-C44	108.10	108.10	108.21	108.18	108.15
C43-C35-C44	112.05	112.05	111.83	111.92	111.89
C35-C43-F29	113.95	113.95	114.04	114.04	114.05
C35-C43-F30	109.62	109.62	109.54	109.58	109.55
C35-C43-F31	110.01	110.01	110.06	110.02	110.04
C35-C44-F32	109.58	109.58	109.62	109.61	109.60
C35-C44-F33	111.33	111.33	111.47	111.42	111.46
C35-C44-F34	111.75	111.75	111.67	111.71	111.69
F29-C43-F30	106.68	106.68	106.62	106.61	106.64
F29-C43-F31	109.07	109.07	109.07	109.07	109.06
F30-C43-F31	107.25	107.25	107.25	107.25	107.24
F32-C44-F33	106.59	106.59	106.50	106.55	106.54
F32-C44-F34	109.41	109.41	109.46	109.42	109.42

F33-C44-F34	108.04	108.04	107.96	107.98	107.97
F14-C34-C42	104.72	104.72	104.57	104.57	104.61
F14-C43-C41	100.82	100.82	100.79	100.79	100.76
C42-C34-C41	112.28	112.28	112.04	112.13	112.09
C34-C42-F26	111.98	111.98	111.97	111.97	112.00
C34-C42-F27	110.04	110.04	110.01	110.06	110.04
C34-C42-F28	111.34	111.34	111.44	111.35	111.37
C34-C41-F23	108.40	108.40	108.32	108.28	108.35
C34-C41-F24	115.76	115.76	115.79	115.75	115.79
C34-C41-F25	108.85	108.85	108.84	108.93	108.87
F26-C42-F27	107.40	107.40	107.27	107.27	107.30
F26-C42-F28	108.15	108.15	108.22	108.25	108.19
F27-C42-F28	107.75	107.75	107.76	107.75	107.76
F23-C41-F24	106.99	106.99	107.07	107.08	107.06
F23-C41-F25	108.67	108.67	108.63	108.61	108.61
F24-C41-F25	107.98	107.98	108.01	108.00	107.97
F13-C33-C40	99.40	99.40	99.49	99.54	99.44
F13-C33-C39	103.74	103.74	103.81	103.80	103.79
C40-C33-C39	112.65	112.65	112.51	112.57	112.54
C33-C40-F20	111.33	111.33	111.44	111.36	111.42
C33-C40-F21	113.42	113.42	113.46	113.51	113.47
C33-C40-F22	110.29	110.29	110.24	110.27	110.27
C33-C39-F17	109.03	109.03	108.88	108.91	108.92
C33-C39-F18	115.23	115.23	115.38	115.33	115.34
C33-C39-F19	109.87	109.87	109.80	109.78	109.82
F20-C40-F21	109.40	109.40	109.42	109.44	109.38
F20-C40-F22	105.84	105.84	105.75	105.74	105.78
F21-C40-F22	106.17	106.17	106.13	106.11	106.13
F17-C39-F18	105.82	105.82	105.80	105.87	105.80
F17-C39-F19	109.38	109.38	109.59	109.55	109.51
F18-C39-F19	107.34	107.34	107.25	107.24	107.28
F1-C36-C45	108.62	108.62	108.79	108.73	108.71
F1-C36-C46	102.25	102.25	102.18	102.25	102.20
C45-C36-C46	111.95	111.95	111.75	111.82	111.81
C36-C45-F37	110.94	110.94	111.03	111.03	111.02
C36-C45-F36	112.06	112.06	112.02	112.03	112.02
C36-C45-F35	109.66	109.66	109.64	109.63	109.65
C36-C46-F40	109.99	109.99	110.11	110.03	110.06
C36-C46-F39	114.17	114.17	114.21	114.23	114.22
C36-C46-F38	109.48	109.48	109.42	109.46	109.44
F37-C45-F36	108.07	108.07	107.99	107.99	108.01
F37-C45-F35	106.47	106.47	106.37	106.43	106.41
F36-C45-F35	109.49	109.49	109.62	109.56	109.56
F40-C46-F39	109.05	109.05	108.97	108.97	109.00
F40-C46-F38	107.34	107.34	107.37	107.38	107.37
F39-C46-F38	106.55	106.55	106.49	106.50	106.49
F3-C37-C48	104.57	104.57	104.44	104.48	104.48

F3-C37-C47	100.32	100.32	100.29	100.29	100.27
C48-C37-C47	112.33	112.33	112.07	112.17	112.14
C37-C48-F45	112.37	112.37	112.41	112.42	112.43
C37-C48-F46	110.28	110.28	110.24	110.28	110.28
C37-C48-F44	110.51	110.51	110.61	110.51	110.54
C37-C47-F41	108.16	108.16	108.10	108.09	108.12
C37-C47-F42	115.36	115.36	115.39	115.34	115.38
C37-C47-F43	109.20	109.20	109.20	109.25	109.21
F45-C48-F46	107.12	107.12	107.01	107.02	107.03
F45-C48-F44	108.49	108.49	108.50	108.52	108.49
F46-C48-F44	107.92	107.92	107.90	107.92	107.91
F41-C47-F42	107.16	107.16	107.20	107.22	107.21
F41-C47-F43	108.57	108.57	108.55	108.54	108.53
F42-C47-F43	108.21	108.21	108.21	108.20	108.20
F4-C38-C50	94.10	94.10	94.14	94.16	94.12
F4-C38-C49	102.38	102.38	102.55	102.52	102.50
C50-C38-C49	118.85	118.85	118.66	118.74	118.69
C38-C50-F51	120.16	120.16	120.34	120.26	120.33
C38-C50-F52	109.50	109.50	109.41	109.47	109.45
C38-C50-F50	105.69	105.69	105.74	105.72	105.73
C38-C49-F47	108.22	108.22	108.07	108.11	108.10
C38-C49-F48	116.17	116.17	116.36	116.31	116.30
C38-C49-F49	110.69	110.69	110.62	110.60	110.65
F51-C50-F52	106.44	106.44	106.34	106.34	106.35
F51-C50-F50	106.12	106.12	106.08	106.12	106.08
F52-C50-F50	108.47	108.47	108.45	108.45	108.43
F47-C49-F48	104.72	104.72	104.64	104.71	104.68
F47-C49-F49	109.27	109.27	109.44	109.39	109.36
F48-C49-F49	107.50	107.50	107.43	107.45	107.46

Table B.15. Calculated Mullikan Atomic Charges of F_{52}MPc with B3LYP functional and 6-31G basis set.

	F_{52}ZnPc	F_{52}MgPc	F_{52}CoPc	F_{52}CuPc	F_{52}FePc
M	1.041	1.272	1.077	0.989	1.155
N1	-0.673	-0.738	-0.688	-0.672	-0.714
N2	-0.671	-0.732	-0.683	-0.668	-0.708
N3	-0.674	-0.735	-0.684	-0.670	-0.709
N4	-0.670	-0.733	-0.686	-0.669	-0.712
N5	-0.326	-0.327	-0.314	-0.319	-0.320
N6	-0.345	-0.373	-0.332	-0.336	-0.335
N7	-0.364	-0.364	-0.351	-0.355	-0.356
N8	-0.340	-0.340	-0.326	-0.331	-0.330

C1	0.358	0.365	0.344	0.353	0.358
C2	0.009	0.006	0.019	0.015	0.014
C3	0.260	0.259	0.264	0.263	0.266
C4	0.277	0.277	0.276	0.276	0.275
C5	0.281	0.281	0.280	0.280	0.281
C6	0.242	0.242	0.245	0.244	0.243
C7	0.075	0.073	0.083	0.078	0.082
C8	0.360	0.367	0.347	0.358	0.352
C9	0.370	0.376	0.349	0.362	0.353
C10	0.002	-0.001	0.013	0.008	0.014
C11	0.073	0.072	0.075	0.075	0.073
C12	0.027	0.027	0.028	0.026	0.027
C13	0.282	0.282	0.279	0.280	0.275
C14	0.021	0.019	0.023	0.023	0.025
C15	0.037	0.035	0.044	0.040	0.040
C16	0.410	0.416	0.394	0.405	0.405
C17	0.407	0.413	0.394	0.402	0.404
C18	0.025	0.023	0.032	0.030	0.028
C19	0.027	0.026	0.031	0.028	0.031
C20	0.275	0.275	0.272	0.274	0.271
C21	0.036	0.036	0.037	0.037	0.037
C22	0.092	0.090	0.093	0.092	0.091
C23	-0.007	-0.010	0.004	-0.002	0.005
C24	0.379	0.386	0.358	0.371	0.362
C25	0.366	0.373	0.353	0.363	0.358
C26	0.069	0.067	0.076	0.072	0.072
C27	0.240	0.239	0.242	0.241	0.240
C28	0.281	0.281	0.280	0.281	0.282
C29	0.277	0.277	0.276	0.276	0.275
C30	0.277	0.260	0.266	0.264	0.267
C31	0.013	0.100	0.022	0.019	0.019
C32	0.358	0.365	0.342	0.352	0.356
C33	0.056	0.056	0.055	0.055	0.055
C34	0.056	0.056	0.058	0.057	0.057
C35	0.081	0.081	0.082	0.081	0.081
C36	0.081	0.081	0.082	0.081	0.082
C37	0.060	0.060	0.062	0.061	0.061
C38	0.069	0.069	0.069	0.069	0.070
C39	0.819	0.819	0.820	0.820	0.819
C40	0.822	0.822	0.822	0.822	0.822
C41	0.811	0.811	0.811	0.811	0.811
C42	0.833	0.833	0.834	0.834	0.834
C43	0.814	0.813	0.814	0.814	0.814
C44	0.815	0.815	0.815	0.815	0.815
C45	0.816	0.816	0.816	0.816	0.817
C46	0.812	0.812	0.812	0.812	0.812
C47	0.810	0.810	0.810	0.811	0.810

C48	0.829	0.829	0.829	0.829	0.829
C49	0.813	0.813	0.813	0.813	0.813
C50	0.792	0.792	0.792	0.792	0.792
F1	-0.270	-0.270	-0.270	-0.270	-0.270
F2	-0.294	-0.294	-0.294	-0.293	-0.294
F3	-0.286	-0.287	-0.286	-0.286	-0.286
F4	-0.269	-0.269	-0.270	-0.270	-0.269
F5	-0.266	-0.266	-0.266	-0.266	-0.266
F6	-0.272	-0.272	-0.272	-0.272	-0.271
F7	-0.273	-0.273	-0.273	-0.273	-0.273
F8	-0.260	-0.261	-0.261	-0.260	-0.260
F9	-0.261	-0.261	-0.261	-0.260	-0.260
F10	-0.273	-0.273	-0.273	-0.273	-0.273
F11	-0.272	-0.272	-0.272	-0.272	-0.272
F12	-0.264	-0.264	-0.264	-0.264	-0.264
F13	-0.273	-0.273	-0.273	-0.273	-0.273
F14	-0.290	-0.290	-0.290	-0.290	-0.290
F15	-0.296	0.296	-0.296	-0.296	-0.297
F16	-0.271	-0.271	-0.271	-0.270	-0.271
F17	-0.249	-0.249	-0.248	-0.248	-0.249
F18	-0.244	-0.244	-0.244	-0.244	-0.244
F19	-0.252	-0.252	-0.253	-0.252	-0.253
F20	-0.245	-0.245	-0.245	-0.245	-0.245
F21	-0.270	-0.270	-0.270	-0.270	-0.270
F22	-0.245	-0.245	-0.245	-0.245	-0.245
F23	-0.256	-0.256	-0.256	-0.256	-0.256
F24	-0.245	-0.245	-0.245	-0.245	-0.245
F25	-0.237	-0.237	-0.237	-0.237	-0.237
F26	-0.241	-0.241	-0.242	-0.241	-0.241
F27	-0.248	-0.248	-0.249	-0.249	-0.249
F28	-0.258	-0.258	-0.258	-0.258	-0.258
F29	-0.265	-0.265	-0.265	-0.265	-0.265
F30	-0.244	-0.245	-0.245	-0.245	-0.245
F31	-0.242	-0.242	-0.242	-0.242	-0.242
F32	-0.248	-0.248	-0.248	-0.248	-0.247
F33	-0.244	-0.244	-0.244	-0.244	-0.244
F34	-0.259	-0.259	-0.259	-0.259	-0.259
F35	-0.260	-0.260	-0.260	-0.260	-0.260
F36	-0.244	-0.244	-0.244	-0.244	-0.244
F37	-0.248	-0.248	-0.248	-0.248	-0.248
F38	-0.242	-0.242	-0.243	-0.243	-0.243
F39	-0.245	-0.245	-0.245	-0.248	-0.245
F40	-0.263	-0.263	-0.263	-0.263	-0.263
F41	-0.256	-0.256	-0.256	-0.256	-0.256
F42	-0.237	-0.237	-0.237	-0.237	-0.237
F43	-0.246	-0.246	-0.245	-0.245	-0.246
F44	-0.259	-0.259	-0.259	-0.259	-0.259

F45	-0.248	-0.248	-0.248	-0.248	-0.248
F46	-0.241	-0.241	-0.241	-0.241	-0.241
F47	-0.247	-0.247	-0.247	-0.247	-0.247
F48	-0.242	-0.242	-0.241	-0.241	-0.241
F49	-0.247	-0.247	-0.247	-0.247	-0.247
F50	-0.262	-0.262	-0.262	-0.262	-0.262
F51	-0.241	-0.241	-0.241	-0.241	-0.241
F52	-0.243	-0.243	-0.243	-0.243	-0.243

The calculated 2-body bond lengths, 3-body bond angles, and atomic charges for F_{52a}MPc are presented in Tables B.16-18 following the atom labeling scheme depicted in Figure B.6.

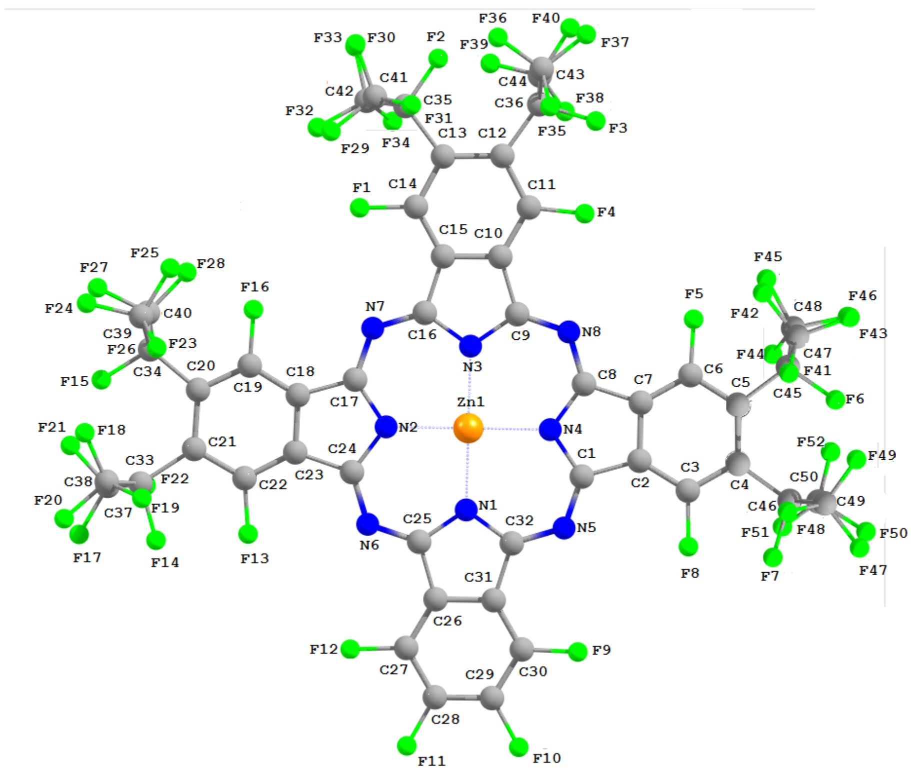

Figure B.6. Atom labeling scheme for F_{52s}MPc bond lengths, 3-body angles, and atomic charges.

Table B.16. Calculated bond lengths of $F_{52s}MPc$ with B3LYP functional and 6-31G basis set.

	$F_{52s}ZnPc$	$F_{52s}MgPc$	$F_{52s}CoPc$	$F_{52s}CuPc$	$F_{52s}FePc$
M-N1	1.997	2.010	1.942	1.963	1.950
M-N2	2.016	2.024	1.963	1.983	1.970
M-N3	2.009	2.022	1.958	1.977	1.966
M-N4	2.012	2.021	1.958	1.979	1.966
N1-C25	1.388	1.386	1.397	1.391	1.393
N1-C32	1.387	1.386	1.396	1.391	1.393
N2-C17	1.382	1.382	1.391	1.385	1.388
N2-C24	1.386	1.385	1.396	1.390	1.393
N3-C9	1.386	1.385	1.396	1.390	1.392
N3-C16	1.381	1.380	1.389	1.384	1.386
N4-C1	1.386	1.384	1.396	1.389	1.392
N4-C8	1.385	1.384	1.394	1.388	1.390
N5-C1	1.333	1.336	1.326	1.329	1.328
N5-C32	1.332	1.335	1.326	1.328	1.327
N6-C24	1.332	1.335	1.325	1.329	1.327
N6-C25	1.333	1.336	1.326	1.329	1.328
N7-C16	1.327	1.330	1.321	1.324	1.323
N7-C17	1.325	1.328	1.319	1.322	1.321
N8-C8	1.328	1.331	1.322	1.325	1.324
N8-C9	1.329	1.332	1.322	1.325	1.324
C1-C2	1.471	1.472	1.470	1.471	1.467
C2-C3	1.395	1.395	1.400	1.398	1.398
C2-C7	1.401	1.402	1.397	1.399	1.398
C3-C4	1.423	1.423	1.425	1.424	1.424
C3-F8	1.372	1.372	1.372	1.372	1.371
C4-C5	1.451	1.451	1.451	1.452	1.452
C4-C46	1.554	1.553	1.557	1.556	1.556
C5-C6	1.400	1.400	1.401	1.401	1.401
C5-C45	1.541	1.540	1.544	1.542	1.542
C6-C7	1.381	1.381	1.386	1.384	1.384
C6-F5	1.376	1.376	1.376	1.376	1.375
C7-C8	1.455	1.455	1.454	1.454	1.451
C9-C10	1.464	1.464	1.463	1.463	1.460
C10-C11	1.394	1.393	1.398	1.396	1.396
C10-C15	1.399	1.401	1.395	1.397	1.396
C11-C12	1.420	1.420	1.422	1.421	1.421
C11-F4	1.372	1.372	1.372	1.372	1.371
C12-C13	1.451	1.451	1.452	1.452	1.452
C12-C36	1.552	1.552	1.556	1.554	1.554
C13-C14	1.399	1.399	1.400	1.400	1.400
C13-C35	1.538	1.538	1.541	1.540	1.540
C14-C15	1.381	1.381	1.385	1.383	1.383
C14-F1	1.377	1.377	1.377	1.377	1.376

C15-C16	1.452	1.453	1.451	1.452	1.448
C17-C18	1.450	1.451	1.449	1.450	1.447
C18-C19	1.379	1.379	1.384	1.382	1.382
C18-C23	1.399	1.400	1.395	1.397	1.396
C19-C20	1.399	1.399	1.400	1.399	1.399
C19-F16	1.376	1.376	1.376	1.376	1.375
C20-C21	1.451	1.450	1.451	1.451	1.452
C20-C34	1.535	1.535	1.538	1.537	1.537
C21-C22	1.428	1.427	1.429	1.428	1.428
C21-C33	1.563	1.562	1.567	1.565	1.566
C22-C23	1.396	1.395	1.401	1.399	1.399
C22-F13	1.373	1.373	1.373	1.373	1.372
C23-C24	1.474	1.474	1.473	1.473	1.469
C25-C26	1.461	1.462	1.459	1.460	1.456
C26-C27	1.390	1.389	1.393	1.391	1.392
C26-C31	1.422	1.423	1.419	1.419	1.418
C27-C28	1.396	1.396	1.395	1.396	1.396
C27-F12	1.370	1.369	1.371	1.370	1.370
C28-C29	1.398	1.397	1.402	1.399	1.401
C28-F11	1.370	1.371	1.372	1.370	1.370
C29-C30	1.396	1.396	1.397	1.396	1.396
C29-F10	1.370	1.371	1.372	1.370	1.370
C30-C31	1.389	1.390	1.393	1.391	1.391
C30-F9	1.371	1.371	1.369	1.371	1.369
C31-C32	1.462	1.463	1.459	1.461	1.457
C33-F14	1.439	1.440	1.439	1.439	1.439
C33-C38	1.576	1.576	1.578	1.577	1.578
C33-C37	1.575	1.575	1.577	1.576	1.576
C38-F21	1.372	1.372	1.372	1.372	1.372
C38-F20	1.379	1.379	1.379	1.379	1.379
C38-F22	1.388	1.388	1.387	1.388	1.388
C37-F19	1.388	1.388	1.387	1.388	1.387
C37-F18	1.372	1.372	1.372	1.372	1.372
C37-F17	1.379	1.379	1.380	1.379	1.380
C34-F15	1.414	1.414	1.415	1.414	1.414
C34-C40	1.564	1.564	1.563	1.564	1.563
C34-C39	1.561	1.561	1.561	1.561	1.561
C40-F27	1.374	1.374	1.374	1.374	1.374
C40-F26	1.378	1.378	1.378	1.378	1.378
C40-F28	1.385	1.385	1.385	1.385	1.385
C39-F23	1.385	1.385	1.385	1.385	1.385
C39-F25	1.375	1.375	1.375	1.375	1.375
C39-F24	1.377	1.377	1.377	1.377	1.377
C35-F2	1.416	1.416	1.416	1.416	1.416
C35-C42	1.563	1.563	1.563	1.563	1.563
C35-C41	1.570	1.570	1.569	1.570	1.569
C42-F29	1.375	1.375	1.375	1.375	1.375

C42-F30	1.378	1.378	1.378	1.378	1.378
C42-F31	1.384	1.385	1.384	1.384	1.384
C41-F34	1.384	1.384	1.383	1.383	1.383
C41-F32	1.376	1.376	1.376	1.376	1.376
C41-F33	1.377	1.377	1.378	1.377	1.377
C36-F3	1.442	1.442	1.442	1.442	1.442
C36-C43	1.578	1.578	1.579	1.578	1.579
C36-C44	1.571	1.571	1.573	1.572	1.572
C43-F36	1.370	1.370	1.371	1.370	1.370
C43-F37	1.377	1.377	1.377	1.377	1.377
C43-F35	1.390	1.391	1.390	1.390	1.390
C44-F40	1.388	1.388	1.388	1.388	1.388
C44-F38	1.374	1.374	1.374	1.374	1.374
C44-F39	1.377	1.377	1.377	1.377	1.377
C45-F6	1.417	1.417	1.417	1.417	1.417
C45-C47	1.566	1.567	1.566	1.566	1.566
C45-C48	1.567	1.567	1.566	1.567	1.567
C47-F42	1.376	1.376	1.375	1.376	1.376
C47-F43	1.378	1.377	1.378	1.378	1.378
C47-F41	1.384	1.384	1.384	1.384	1.384
C48-F46	1.384	1.384	1.384	1.384	1.384
C48-F44	1.375	1.375	1.375	1.375	1.375
C48-F45	1.378	1.378	1.378	1.378	1.378
C46-F7	1.443	1.443	1.443	1.443	1.443
C46-C49	1.576	1.576	1.577	1.577	1.577
C46-C46	1.575	1.574	1.576	1.576	1.576
C49-F48	1.372	1.372	1.372	1.372	1.372
C49-F49	1.377	1.377	1.377	1.377	1.377
C49-F47	1.390	1.390	1.389	1.389	1.389
C46-F50	1.390	1.390	1.389	1.389	1.389
C46-F51	1.371	1.371	1.371	1.371	1.371
C46-F52	1.377	1.377	1.377	1.377	1.377

Table B.17. Calculated 3-body bond angles of F_{52a}MPc with B3LYP functional and 6-31G basis set.

	F_{52a}ZnPc	F_{52a}MgPc	F_{52a}CoPc	F_{52a}CuPc	F_{52a}FePc
N1-M-N2	89.45	89.58	89.64	89.60	89.66
N1-M-N3	174.17	176.99	179.79	178.38	178.67
N1-M-N4	90.07	90.17	90.23	90.21	90.22
M-N1-C25	125.34	125.10	126.23	125.89	126.06
M-N1-C32	124.95	124.76	125.90	125.48	125.74
N2-M-N3	90.26	90.37	90.33	90.37	90.33
N2-M-N4	174.47	177.25	179.23	178.65	179.02
M-N2-C17	124.18	124.03	125.23	124.77	125.07
M-N2-C24	126.14	125.97	127.13	126.66	126.88

N3-M-N4	89.66	89.74	89.81	89.79	89.76
M-N3-C9	125.90	125.70	126.81	126.40	126.61
M-N3-C16	124.70	124.49	125.69	125.22	125.48
M-N4-C1	125.53	125.35	126.55	126.08	126.29
M-N4-C8	124.58	124.45	125.61	125.16	125.47
C25-N1-C32	109.70	110.14	107.83	108.63	108.20
N1-C25-N6	127.54	127.55	127.37	127.59	127.61
N1-C25-C26	108.24	108.00	109.37	108.87	109.21
N1-C32-N5	127.41	127.35	127.20	127.47	127.42
N1-C32-C31	108.36	108.11	109.40	109.05	109.11
C17-N2-C24	109.65	110.01	107.60	108.58	108.05
N2-C17-N7	127.88	127.93	127.68	127.92	127.90
N2-C17-C18	108.13	107.90	109.32	108.82	109.06
N2-C24-N6	126.02	126.07	125.65	126.05	125.97
N2-C24-C23	107.84	107.61	109.07	108.53	108.81
C9-N3-C16	109.40	109.80	107.47	108.36	107.90
N3-C9-N8	126.41	126.40	126.21	126.46	126.48
N3-C9-C10	108.09	107.86	109.20	108.76	108.98
N3-C16-N7	127.55	127.51	127.35	127.61	127.56
N3-C16-C15	108.21	107.98	109.38	108.90	109.13
C1-N4-C8	109.84	110.20	107.82	108.77	108.24
N4-C1-N5	126.23	126.30	125.91	126.25	126.28
N4-C1-C2	107.86	107.64	109.04	108.54	108.83
N4-C8-N8	127.91	127.96	127.70	127.96	127.92
N4-C8-C7	107.86	107.62	109.02	108.54	108.77
C1-N5-C32	125.65	126.05	124.18	124.50	124.04
N5-C1-C2	125.90	126.05	125.04	125.19	124.89
N5-C32-C31	124.23	124.54	123.40	123.48	123.46
C24-N6-C25	125.36	125.71	123.97	124.21	123.81
N6-C24-C23	126.14	126.32	125.28	125.42	125.22
N6-C25-C26	124.20	124.44	123.24	123.52	123.19
C16-N7-C17	125.28	125.65	123.70	124.09	123.64
N7-C16-C15	124.24	124.51	123.27	123.49	123.31
N7-C17-C18	123.96	124.16	122.99	123.21	123.03
C8-N8-C9	125.36	125.72	123.86	124.20	123.75
N8-C8-C7	124.20	124.40	123.28	123.46	123.31
N8-C9-C10	125.50	125.74	124.57	124.78	124.54
C1-C2-C3	133.96	133.90	134.20	134.15	134.03
C1-C2-C7	106.55	106.61	106.36	106.41	106.40
C3-C2-C7	119.48	119.50	119.45	119.45	119.57
C2-C3-C4	122.70	122.69	122.80	122.80	122.69
C2-C3-F8	114.05	114.03	114.26	114.16	114.25
C2-C7-C6	119.21	119.17	119.18	119.19	119.18
C2-C7-C8	107.89	107.93	107.76	107.74	107.76
C4-C3-F8	123.24	123.28	122.95	123.04	123.06
C3-C4-C5	116.78	116.80	116.69	116.70	116.70
C3-C4-C46	117.32	117.27	117.53	117.47	117.46

C5-C4-C46	125.90	125.93	125.78	125.83	125.84
C4-C5-C6	118.55	118.56	118.54	118.53	118.61
C4-C5-C45	126.69	126.73	126.51	126.56	126.46
C4-C46-C7	109.27	109.33	109.20	109.22	109.22
C4-C46-C49	114.81	114.75	115.02	114.88	114.95
C4-C46-C46	114.70	114.65	114.82	114.84	114.81
C6-C5-C45	114.76	114.71	114.94	114.91	114.93
C5-C6-C7	123.26	123.27	123.34	123.33	123.25
C5-C6-F5	119.24	119.27	118.98	119.04	119.09
C5-C45-F6	108.89	108.90	108.88	108.89	108.82
C5-C45-C47	114.61	114.60	114.64	114.58	114.64
C5-C45-C48	114.47	114.42	114.67	114.61	114.58
C7-C6-F5	117.49	117.46	117.68	117.62	117.67
C6-C7-C8	132.90	132.89	133.06	133.07	133.06
C9-C10-C11	133.41	133.37	133.64	133.59	133.51
C9-C10-C15	106.67	106.72	106.49	106.51	106.53
C11-C10-C15	119.91	119.92	119.87	119.88	119.95
C10-C11-C12	122.47	122.46	122.54	122.53	122.45
C10-C11-F4	113.95	113.91	114.13	114.06	114.10
C10-C15-C14	119.04	119.01	119.06	119.04	119.09
C10-C15-C16	107.62	107.65	107.45	107.47	107.47
C12-C11-F4	123.58	123.62	123.34	123.41	123.45
C11-C12-C13	116.75	116.77	116.68	116.68	116.70
C11-C12-C36	117.10	117.06	117.26	117.22	117.21
C13-C12-C36	126.15	126.17	126.06	126.08	126.09
C12-C13-C14	118.78	118.78	118.77	118.75	118.82
C12-C13-C35	126.42	126.47	126.30	126.31	126.25
C12-C36-F3	109.10	109.14	109.06	109.06	109.04
C12-C36-C43	115.45	115.45	115.52	115.42	115.55
C12-C36-C44	114.08	113.98	114.26	114.27	114.18
C14-C13-C35	114.78	114.73	114.93	114.91	114.93
C13-C14-C15	123.05	123.06	123.08	123.10	122.99
C13-C14-F1	119.36	119.39	119.13	119.18	119.22
C13-C35-F2	108.73	108.76	108.71	108.73	108.68
C13-C35-C42	113.86	113.74	113.83	113.93	113.80
C13-C35-C41	114.97	115.01	115.20	115.01	115.16
C15-C14-F1	117.59	117.56	117.79	117.71	117.78
C14-C15-C16	133.34	133.34	133.48	133.49	133.44
C17-C1-C19	132.62	132.62	132.78	132.78	132.77
C17-C18-C23	107.96	107.99	107.84	107.83	107.83
C19-C18-C23	119.41	119.37	119.38	119.40	119.39
C18-C19-C20	123.06	123.08	123.13	123.13	123.05
C18-C19-F16	117.45	117.42	117.65	117.58	117.63
C18-C23-C22	119.42	119.44	119.41	119.38	119.50
C18-C23-C24	106.42	106.49	106.17	106.25	106.25
C20-C19-F16	119.49	119.51	119.22	119.29	119.32
C19-C20-C21	118.99	118.98	119.00	118.96	119.03

C19-C20-C34	114.85	114.82	115.01	114.99	115.02
C21-C20-C34	126.16	126.20	126.00	126.04	125.94
C20-C21-C22	116.32	116.34	116.23	116.23	116.25
C20-C21-C33	126.54	126.57	126.41	126.46	126.47
C20-C34-F15	107.98	108.00	107.96	107.97	107.91
C20-C34-C40	115.09	115.07	115.29	115.11	115.25
C20-C34-C39	114.37	114.35	114.39	114.48	114.37
C22-C21-C33	117.15	117.09	117.36	117.31	117.28
C21-C22-C23	122.80	122.79	122.86	122.88	122.78
C21-C22-F13	124.04	124.07	123.74	123.83	123.85
C21-C33-F14	107.03	107.09	106.96	106.97	106.98
C21-C33-C38	116.12	116.00	116.27	116.41	116.22
C21-C33-C37	116.05	116.06	116.21	115.97	116.23
C23-C22-F13	113.17	113.14	113.40	113.29	113.36
C22-C23-C24	134.17	134.08	134.42	134.37	134.25
C25-C26-C27	132.53	132.68	132.91	132.54	132.83
C25-C26-C31	106.96	106.97	106.74	106.89	106.69
C27-C26-C31	120.51	120.34	120.34	120.57	120.47
C26-C27-C28	118.73	118.94	118.96	118.72	118.77
C26-C27-F12	122.68	122.39	122.19	122.89	122.50
C26-C31-C30	120.35	120.24	120.36	120.36	120.44
C26-C31-C32	106.74	106.78	106.65	106.55	106.78
C28-C27-F12	118.58	118.66	118.85	118.39	118.72
C27-C28-C29	120.76	120.75	120.82	120.75	120.73
C27-C28-F11	120.21	120.17	119.76	120.26	120.09
C29-C28-F11	119.02	119.07	119.42	118.99	119.18
C28-C29-C30	120.91	120.78	120.51	120.89	120.82
C28-C29-F10	119.38	119.41	119.31	119.46	119.01
C30-C29-F10	119.71	119.81	120.19	119.65	120.16
C29-C30-C31	118.73	118.94	119.01	118.73	118.76
C29-C30-F9	118.98	119.01	119.18	119.01	118.55
C31-C30-F9	122.27	122.05	121.81	122.26	122.68
C30-C31-C32	132.91	132.99	132.99	133.09	132.78
F14-C33-C38	97.51	97.49	97.60	97.53	97.52
F14-C33-C37	97.22	97.18	97.24	97.21	97.20
C38-C33-C37	117.96	118.08	117.60	117.77	117.71
C33-C38-F21	118.89	118.87	118.94	118.91	118.94
C33-C38-F20	109.30	109.32	109.25	109.28	109.26
C33-C38-F22	106.40	106.36	106.33	106.37	106.35
C33-C37-F19	106.21	106.19	106.37	106.26	106.29
C33-C37-F18	119.08	119.09	119.20	119.11	119.18
C33-C37-F17	109.19	109.21	109.14	109.17	109.18
F21-C38-F20	106.13	106.18	106.13	106.10	106.15
F21-C38-F22	107.26	107.23	107.24	107.28	107.24
F20-C38-F22	108.53	108.54	108.63	108.56	108.57
F19-C37-F18	107.08	107.06	107.14	107.10	107.08
F19-C37-F17	108.69	108.68	108.63	108.68	108.64

F18-C37-F17	106.26	106.28	106.02	106.18	106.13
F15-C34-C40	101.43	101.43	101.33	101.35	101.40
F15-C34-C39	102.60	102.64	102.46	102.55	102.54
C40-C34-C39	113.49	113.49	113.45	113.46	113.44
C34-C40-F27	115.09	115.12	115.02	115.05	115.04
C34-C40-F26	109.45	109.44	109.51	109.48	109.47
C34-C40-F28	108.23	108.26	108.24	108.26	108.24
C34-C39-F23	108.53	108.52	108.55	108.50	108.55
C34-C39-F25	114.24	114.24	114.16	114.18	114.16
C34-C39-F24	110.04	110.03	110.07	110.07	110.06
F27-C40-F26	107.26	107.22	107.22	107.23	107.24
F27-C40-F28	108.17	108.17	108.27	108.21	108.22
F26-C40-F28	108.47	108.46	108.40	108.44	108.45
F23-C39-F25	108.11	108.09	108.16	108.14	108.12
F23-C39-F24	108.39	108.41	108.33	108.39	108.38
F25-C39-F24	107.38	107.40	107.42	107.41	107.41
F2-C35-C42	102.14	102.14	102.07	102.11	102.05
F2-C35-C41	102.72	102.79	102.58	102.64	102.75
C42-C35-C41	112.85	112.84	112.83	112.82	112.79
C35-C42-F29	114.55	114.58	114.44	114.48	114.52
C35-C42-F30	109.61	109.58	109.64	109.64	109.60
C35-C42-F31	108.74	108.73	108.78	108.71	108.75
C35-C41-F34	109.33	109.37	109.31	109.35	109.37
C35-C41-F32	114.22	114.18	114.22	114.20	114.14
C35-C41-F33	109.51	109.53	109.55	109.54	109.55
F29-C42-F30	107.52	107.55	107.54	107.54	107.55
F29-C42-F31	107.68	107.64	107.76	107.72	107.68
F30-C42-F31	108.59	108.61	108.54	108.59	108.60
F34-C41-F32	108.14	108.14	108.17	108.15	108.16
F34-C41-F33	108.44	108.42	108.40	108.43	108.42
F32-C41-F33	107.05	107.03	107.02	107.02	107.04
F3-C36-C43	96.01	96.01	96.03	96.01	96.00
F3-C36-C44	97.23	97.26	97.22	97.21	97.27
C43-C36-C44	120.43	120.50	120.18	120.29	120.23
C36-C43-F36	119.54	119.53	119.62	119.56	119.63
C36-C43-F37	109.91	109.92	109.89	109.90	109.88
C36-C43-F35	105.24	105.20	105.30	105.25	105.26
C36-C44-F40	106.23	106.27	106.18	106.22	106.24
C36-C44-F38	117.99	117.94	118.12	118.04	118.02
C36-C44-F39	110.35	110.38	110.31	110.34	110.33
F36-C43-F37	106.64	106.67	106.53	106.60	106.57
F36-C43-F35	106.60	106.60	106.62	106.61	106.61
F37-C43-F35	108.48	108.49	108.45	108.48	108.45
F40-C44-F38	105.54	105.51	105.58	105.56	105.51
F40-C44-F39	108.71	108.71	108.72	108.71	108.73
F38-C44-F39	107.63	107.65	107.54	107.59	107.62
F6-C45-C47	102.44	102.48	102.28	102.38	102.40

F6-C45-C48	102.04	102.05	101.94	101.98	102.00
C47-C45-C48	112.77	112.77	112.73	112.74	112.73
C45-C47-F42	114.43	114.44	114.35	114.37	114.36
C45-C47-F43	109.60	109.59	109.64	109.63	109.64
C45-C47-F41	109.04	109.02	109.08	109.04	109.06
C45-C48-F46	108.99	109.02	108.96	108.98	108.99
C45-C48-F44	114.64	114.66	114.55	114.59	114.59
C45-C48-F45	109.40	109.39	109.46	109.43	109.41
F42-C47-F43	107.20	107.21	107.19	107.21	107.20
F42-C47-F41	107.90	107.89	107.97	107.93	107.93
F43-C47-F41	108.52	108.53	108.44	108.50	108.50
F46-C48-F44	107.84	107.82	107.92	107.87	107.86
F46-C48-F45	108.57	108.56	108.52	108.56	108.56
F44-C48-F45	107.25	107.23	107.27	107.25	107.27
F7-C46-F49	96.30	96.30	96.32	96.30	96.30
F7-C46-F46	96.60	96.60	96.62	96.59	96.59
C49-C46-F46	120.56	120.65	120.23	120.38	120.32
C46-C49-F48	118.96	118.92	119.09	119.00	119.04
C46-C49-F49	110.13	110.14	110.09	110.12	110.11
C46-C49-F47	105.61	105.59	105.65	105.61	105.62
C46-C46-F50	105.62	105.64	105.62	105.62	105.64
C46-C46-F51	118.71	118.69	118.84	118.76	118.80
C46-C46-F52	110.28	110.31	110.24	110.26	110.25
F48-C49-F49	107.10	107.15	106.95	107.04	107.04
F48-C49-F47	106.04	106.02	106.08	106.06	106.04
F49-C49-F47	108.59	108.60	108.56	108.59	108.56
F50-C46-F51	105.98	105.96	106.03	106.01	105.98
F50-C46-F52	108.59	108.58	108.58	108.60	108.57
F51-C46-F52	107.22	107.24	107.11	107.18	107.17

Table B.18. Calculated Mullikan Atomic Charges of F_{52a}MPc with B3LYP functional and 6-31G basis set.

	F_{52a}ZnPc	F_{52a}MgPc	F_{52a}CoPc	F_{52a}CuPc	F_{52a}FePc
M	1.050	1.283	1.084	0.994	1.022
N1	-0.685	-0.719	-0.696	-0.681	-7.080
N2	-0.680	-0.743	-0.692	-0.677	-7.050
N3	-0.682	-0.744	-0.694	-0.679	-7.060
N4	-0.681	-0.745	-0.694	-0.678	-7.050
N5	-0.328	-0.381	-0.317	-0.320	-0.322
N6	-0.327	-0.381	-0.317	-0.320	-0.322
N7	-0.312	-0.316	-0.304	-0.307	-0.309
N8	-0.315	-0.318	-0.306	-0.309	-0.311
C1	0.368	0.379	0.353	0.363	0.367

C2	0.052	0.047	0.063	0.058	0.060
C3	0.268	0.267	0.270	0.269	0.272
C4	0.014	0.013	0.014	0.014	0.014
C5	0.062	0.062	0.059	0.060	0.060
C6	0.235	0.233	0.238	0.237	0.239
C7	0.032	0.030	0.040	0.036	0.039
C8	0.376	0.386	0.364	0.373	0.378
C9	0.358	0.368	0.344	0.352	0.358
C10	0.047	0.042	0.057	0.053	0.055
C11	0.271	0.270	0.273	0.272	0.274
C12	0.015	0.014	0.015	0.016	0.015
C13	0.061	0.062	0.050	0.060	0.050
C14	0.234	0.233	0.238	0.237	0.239
C15	0.041	0.040	0.050	0.045	0.040
C16	0.373	0.382	0.359	0.369	0.374
C17	0.374	0.383	0.362	0.371	0.376
C18	0.028	0.026	0.035	0.031	0.034
C19	0.237	0.236	0.241	0.240	0.242
C20	0.054	0.055	0.051	0.053	0.052
C21	0.031	0.031	0.031	0.032	0.032
C22	0.266	0.265	0.267	0.267	0.269
C23	0.055	0.049	0.067	0.061	0.063
C24	0.366	0.377	0.350	0.361	0.365
C25	0.371	0.381	0.357	0.367	0.371
C26	0.032	0.032	0.040	0.040	0.040
C27	0.253	0.250	0.254	0.255	0.257
C28	0.280	0.280	0.280	0.280	0.280
C29	0.280	0.281	0.282	0.280	0.280
C30	0.252	0.250	0.254	0.254	0.256
C31	0.039	0.036	0.044	0.045	0.041
C32	0.371	0.381	0.357	0.366	0.375
C33	0.068	0.068	0.071	0.069	0.070
C34	0.061	0.061	0.062	0.062	0.062
C35	0.065	0.065	0.066	0.066	0.066
C36	0.065	0.065	0.067	0.066	0.066
C37	0.796	0.796	0.796	0.796	0.796
C38	0.797	0.797	0.797	0.798	0.797
C39	0.805	0.805	0.805	0.805	0.805
C40	0.803	0.803	0.803	0.803	0.803
C41	0.805	0.804	0.804	0.805	0.805
C42	0.807	0.808	0.807	0.807	0.808
C43	0.800	0.800	0.800	0.800	0.800
C44	0.803	0.803	0.803	0.803	0.803
C45	0.806	0.806	0.806	0.806	0.806
C46	0.805	0.805	0.805	0.805	0.805
C47	0.800	0.800	0.800	0.800	0.800
C48	0.802	0.802	0.801	0.801	0.801

C49	0.796	0.796	0.796	0.796	0.796
C50	0.797	0.797	0.797	0.798	0.797
F1	-0.267	-0.267	-0.267	-0.267	-0.266
F2	-0.290	-0.290	-0.290	-0.290	-0.290
F3	-0.275	-0.275	-0.275	-0.275	-0.275
F4	-0.252	-0.252	-0.252	-0.252	-0.251
F5	-0.265	-0.265	-0.265	-0.265	-0.264
F6	-0.290	-0.290	-0.290	-0.290	-0.290
F7	-0.276	-0.276	-0.276	-0.276	-0.276
F8	-0.254	-0.254	-0.253	-0.253	-0.252
F9	-0.258	-0.259	-0.258	-0.258	-0.257
F10	-0.271	-0.271	-0.271	-0.271	-0.270
F11	-0.271	-0.271	-0.271	-0.271	-0.270
F12	-0.258	-0.258	-0.258	-0.258	-0.257
F13	-0.255	-0.255	-0.255	-0.254	-0.254
F14	-0.275	-0.275	-0.276	-0.276	-0.276
F15	-0.287	-0.287	-0.287	-0.287	-0.287
F16	-0.265	-0.265	-0.265	-0.265	-0.264
F17	-0.261	-0.261	-0.261	-0.261	-0.261
F18	-0.243	-0.243	-0.244	-0.243	-0.243
F19	-0.236	-0.236	-0.236	-0.236	-0.236
F20	-0.243	-0.243	-0.243	-0.243	-0.242
F21	-0.235	-0.235	-0.235	-0.234	-0.235
F22	-0.261	-0.261	-0.261	-0.261	-0.261
F23	-0.258	-0.258	-0.258	-0.257	-0.257
F24	-0.240	-0.240	-0.240	-0.240	-0.239
F25	-0.236	-0.236	-0.236	-0.236	-0.236
F26	-0.258	-0.258	-0.258	-0.258	-0.257
F27	-0.241	-0.241	-0.241	-0.241	-0.241
F28	-0.234	-0.235	-0.235	-0.235	-0.234
F29	-0.257	-0.257	-0.257	-0.257	-0.257
F30	-0.236	-0.236	-0.236	-0.236	-0.236
F31	-0.242	-0.242	-0.242	-0.241	-0.242
F32	-0.238	-0.239	-0.238	-0.238	-0.239
F33	-0.240	-0.240	-0.240	-0.240	-0.240
F34	-0.258	-0.259	-0.258	-0.258	-0.258
F35	-0.262	-0.262	-0.261	-0.261	-0.261
F36	-0.236	-0.236	-0.236	-0.236	-0.363
F37	-0.242	-0.242	-0.243	-0.242	-0.242
F38	-0.258	-0.258	-0.258	-0.258	-0.258
F39	-0.243	-0.243	-0.243	-0.243	-0.243
F40	-0.244	-0.244	-0.244	-0.244	-0.244
F41	-0.258	-0.260	-0.260	-0.258	-0.260
F42	-0.236	-0.239	-0.238	-0.236	-0.236
F43	-0.241	-0.243	-0.243	-0.240	-0.240
F44	-0.258	-0.260	-0.260	-0.258	-0.258
F45	-0.236	-0.239	-0.238	-0.236	-0.238

F46	-0.241	-0.243	-0.243	-0.241	-0.241
F47	-0.243	-0.241	-0.241	-0.241	-0.240
F48	-0.260	-0.259	-0.258	-0.260	-0.258
F49	-0.239	-0.236	-0.237	-0.239	-0.236
F50	-0.243	-0.236	-0.236	-0.238	-0.236
F51	-0.260	-0.258	-0.258	-0.260	-0.258
F52	-0.243	-0.241	-0.241	-0.243	-0.241

The calculated 2-body bond lengths, 3-body bond angles, and atomic charges for F_{64}MPc are presented in Tables B.16-18 following the atom labeling scheme depicted in Figure B.7.

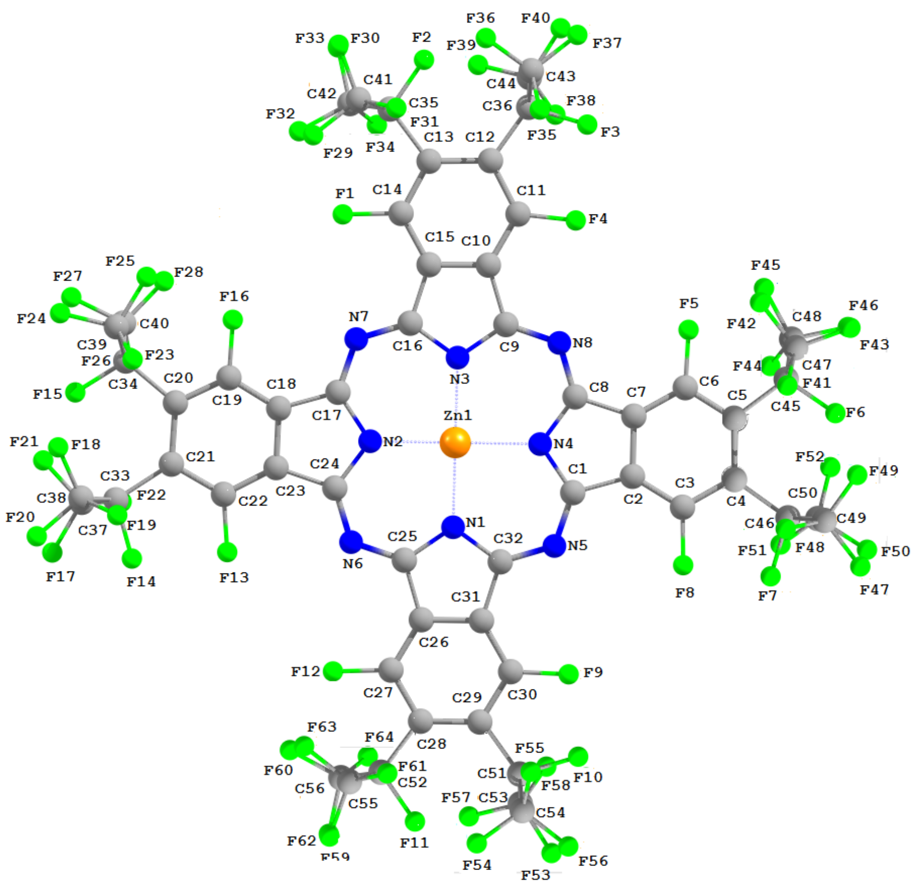

Figure B.7. Atom labeling scheme for F_{64}MPc bond lengths, 3-body angles, and atomic charges.

Table B.19. Calculated bond lengths of $F_{64}MPc$ with B3LYP functional and 6-31G basis set.

	$F_{64}ZnPc$	$F_{64}MgPc$	$F_{64}CoPc$	$F_{64}CuPc$	$F_{64}FePc$
M-N1	2.009	2.015	1.937	1.956	1.956
M-N2	2.017	2.028	1.945	1.963	1.963
M-N3	2.009	2.024	1.946	1.964	1.964
M-N4	2.012	2.022	1.940	1.958	1.958
N1-C25	1.386	1.385	1.393	1.387	1.387
N1-C32	1.389	1.388	1.395	1.389	1.389
N2-C17	1.379	1.379	1.388	1.382	1.382
N2-C24	1.389	1.388	1.396	1.390	1.390
N3-C9	1.387	1.385	1.394	1.388	1.388
N3-C16	1.381	1.380	1.388	1.383	1.383
N4-C1	1.389	1.388	1.396	1.390	1.390
N4-C8	1.382	1.382	1.390	1.384	1.384
N5-C1	1.331	1.335	1.322	1.324	1.324
N5-C32	1.333	1.337	1.324	1.326	1.326
N6-C24	1.330	1.333	1.322	1.324	1.324
N6-C25	1.334	1.337	1.324	1.326	1.326
N7-C16	1.325	1.328	1.318	1.321	1.321
N7-C17	1.327	1.330	1.320	1.322	1.322
N8-C8	1.330	1.334	1.322	1.324	1.324
N8-C9	1.327	1.330	1.320	1.322	1.322
C1-C2	1.472	1.475	1.462	1.461	1.461
C2-C3	1.395	1.395	1.396	1.393	1.393
C2-C7	1.401	1.402	1.395	1.396	1.396
C3-C4	1.424	1.425	1.422	1.421	1.421
C3-F8	1.371	1.371	1.371	1.371	1.371
C4-C5	1.450	1.450	1.451	1.451	1.451
C4-C46	1.554	1.554	1.554	1.553	1.553
C5-C6	1.401	1.401	1.400	1.400	1.400
C5-C45	1.541	1.541	1.542	1.540	1.540
C6-C7	1.381	1.381	1.383	1.381	1.381
C6-F5	1.375	1.376	1.376	1.376	1.376
C7-C8	1.455	1.456	1.449	1.449	1.449
C9-C10	1.466	1.468	1.458	1.458	1.458
C10-C11	1.393	1.393	1.394	1.392	1.392
C10-C15	1.398	1.400	1.394	1.395	1.395
C11-C12	1.421	1.422	1.420	1.420	1.420
C11-F4	1.371	1.371	1.371	1.371	1.371
C12-C13	1.450	1.450	1.450	1.450	1.450
C12-C36	1.553	1.553	1.553	1.552	1.552
C13-C14	1.400	1.400	1.400	1.400	1.400
C13-C35	1.539	1.539	1.538	1.537	1.537
C14-C15	1.380	1.380	1.382	1.380	1.380
C14-F1	1.376	1.376	1.377	1.377	1.377

C15-C16	1.453	1.455	1.448	1.448	1.448
C17-C18	1.451	1.452	1.446	1.445	1.445
C18-C19	1.379	1.379	1.381	1.379	1.379
C18-C23	1.398	1.400	1.393	1.394	1.394
C19-C20	1.399	1.399	1.399	1.399	1.399
C19-F16	1.375	1.375	1.376	1.375	1.375
C20-C21	1.450	1.449	1.451	1.451	1.451
C20-C34	1.535	1.535	1.536	1.535	1.535
C21-C22	1.429	1.429	1.426	1.425	1.425
C21-C33	1.564	1.564	1.563	1.562	1.562
C22-C23	1.396	1.397	1.396	1.394	1.394
C22-F13	1.372	1.373	1.372	1.372	1.372
C23-C24	1.474	1.477	1.464	1.463	1.463
C25-C26	1.459	1.461	1.453	1.453	1.453
C26-C27	1.383	1.383	1.385	1.382	1.382
C26-C31	1.402	1.403	1.396	1.398	1.398
C27-C28	1.402	1.402	1.402	1.401	1.401
C27-F12	1.376	1.376	1.376	1.376	1.376
C28-C29	1.448	1.448	1.448	1.448	1.448
C28-C52	1.537	1.538	1.537	1.536	1.536
C29-C3	1.422	1.422	1.421	1.420	1.420
C29-C51	1.556	1.556	1.556	1.555	1.555
C30-C31	1.394	1.394	1.395	1.393	1.393
C30-F9	1.371	1.371	1.371	1.371	1.371
C31-C32	1.467	1.469	1.459	1.458	1.458
C33-F14	1.438	1.438	1.440	1.440	1.440
C33-C38	1.577	1.577	1.577	1.576	1.576
C33-C37	1.575	1.575	1.575	1.574	1.574
C38-F21	1.371	1.371	1.371	1.371	1.371
C38-F20	1.379	1.378	1.378	1.378	1.378
C38-F22	1.388	1.388	1.388	1.389	1.389
C37-F19	1.387	1.387	1.388	1.388	1.388
C37-F18	1.372	1.372	1.372	1.372	1.372
C37-F17	1.379	1.379	1.379	1.379	1.379
C34-F15	1.414	1.414	1.414	1.414	1.414
C34-C40	1.563	1.563	1.563	1.563	1.563
C34-C39	1.560	1.560	1.560	1.560	1.560
C40-F27	1.374	1.374	1.374	1.374	1.374
C40-F26	1.377	1.377	1.378	1.377	1.377
C40-F28	1.385	1.385	1.385	1.385	1.385
C39-F23	1.385	1.385	1.385	1.385	1.385
C39-F25	1.375	1.375	1.376	1.376	1.376
C39-F24	1.377	1.377	1.377	1.377	1.377
C35-F2	1.415	1.415	1.416	1.415	1.415
C35-C41	1.563	1.563	1.562	1.561	1.561
C35-C42	1.569	1.568	1.570	1.570	1.570
C41-F29	1.375	1.375	1.375	1.376	1.376

C41-F30	1.377	1.377	1.378	1.378	1.378
C41-F31	1.384	1.384	1.385	1.385	1.385
C42-F34	1.383	1.383	1.384	1.384	1.384
C42-F32	1.376	1.376	1.377	1.377	1.377
C42-F33	1.377	1.377	1.376	1.376	1.376
C36-F3	1.442	1.442	1.441	1.441	1.441
C36-C36	1.577	1.577	1.580	1.579	1.579
C36-C44	1.571	1.572	1.572	1.572	1.572
C36-F36	1.370	1.370	1.370	1.370	1.370
C36-F37	1.377	1.377	1.377	1.377	1.377
C36-F35	1.390	1.390	1.391	1.391	1.391
C44-F40	1.388	1.389	1.387	1.387	1.387
C44-F38	1.373	1.373	1.376	1.376	1.376
C44-F39	1.376	1.376	1.376	1.376	1.376
C45-F6	1.416	1.416	1.416	1.416	1.416
C45-C47	1.566	1.566	1.567	1.566	1.566
C45-C48	1.566	1.567	1.567	1.567	1.567
C47-F42	1.375	1.375	1.376	1.376	1.376
C47-F43	1.377	1.377	1.377	1.377	1.377
C47-F41	1.384	1.384	1.384	1.384	1.384
C48-F46	1.384	1.384	1.384	1.384	1.384
C48-F44	1.375	1.375	1.375	1.375	1.375
C48-F45	1.377	1.377	1.378	1.377	1.377
C46-F7	1.442	1.442	1.443	1.443	1.443
C46-F49	1.575	1.575	1.576	1.576	1.576
C46-F50	1.575	1.575	1.576	1.575	1.575
C49-F48	1.371	1.371	1.372	1.372	1.372
C49-F49	1.376	1.376	1.376	1.376	1.376
C49-F47	1.389	1.389	1.389	1.390	1.390
C50-F50	1.389	1.389	1.389	1.390	1.390
C50-F51	1.371	1.371	1.372	1.372	1.372
C50-F52	1.376	1.376	1.376	1.376	1.376
C51-F10	1.443	1.443	1.444	1.444	1.444
C51-C54	1.571	1.571	1.570	1.569	1.569
C51-C53	1.578	1.579	1.579	1.579	1.579
C54-F56	1.373	1.373	1.373	1.373	1.373
C54-F58	1.376	1.376	1.377	1.376	1.376
C54-F57	1.389	1.390	1.390	1.390	1.390
C53-F55	1.389	1.389	1.389	1.389	1.389
C53-F54	1.371	1.372	1.372	1.372	1.372
C53-F53	1.377	1.377	1.377	1.377	1.377
C52-F11	1.417	1.417	1.417	1.417	1.417
C52-C56	1.565	1.565	1.564	1.564	1.564
C52-C55	1.563	1.563	1.564	1.564	1.564
C56-C63	1.373	1.373	1.374	1.374	1.374
C56-C62	1.378	1.378	1.379	1.379	1.379
C56-F64	1.383	1.383	1.384	1.384	1.384

C55-F61	1.384	1.384	1.385	1.385	1.385
C55-F60	1.377	1.377	1.377	1.378	1.378
C55-F59	1.375	1.376	1.376	1.375	1.375

Table B.20. Calculated 3-body bond angles of F_{64}MPc with B3LYP functional and 6-31G basis set.

	F_{64}ZnPc	F_{64}MgPc	F_{64}CoPc	F_{64}CuPc	F_{64}FePc
N1-M-N2	89.62	89.70	89.85	89.86	89.86
N1-M-N3	174.30	177.29	178.99	179.12	179.12
N1-M-N4	90.07	90.18	90.17	90.14	90.14
M-N1-C25	124.84	124.63	126.06	125.77	125.77
M-N1-C32	125.11	124.87	126.24	125.93	125.93
N2-M-N3	90.16	90.30	90.16	90.18	90.18
N2-M-N4	174.65	177.48	179.50	179.61	179.61
M-N2-C17	124.26	124.00	125.67	125.39	125.39
M-N2-C24	126.19	126.05	127.02	126.70	126.70
N3-M-N4	89.62	89.70	89.81	89.82	89.82
M-N3-C9	125.91	125.74	126.85	126.54	126.54
M-N3-C16	124.73	124.48	125.98	125.68	125.68
M-N4-C1	125.49	125.30	126.54	126.24	126.24
M-N4-C8	124.65	124.44	125.92	125.62	125.62
C25-N1-C32	110.03	110.49	107.70	108.29	108.29
N1-C25-N6	127.89	127.89	127.67	127.54	127.54
N1-C25-C26	107.62	107.35	109.04	108.79	108.79
N1-C32-N5	126.96	126.92	126.93	126.80	126.80
N1-C32-C31	107.68	107.40	109.10	108.85	108.85
C17-N2-C24	109.54	109.96	107.30	107.90	107.90
N2-C17-N7	127.90	127.98	127.84	127.69	127.69
N2-C17-C18	108.28	108.03	109.52	109.23	109.23
N2-C24-N6	125.69	125.68	126.12	126.04	126.04
N2-C24-C23	107.87	107.60	109.21	108.98	108.98
C9-N3-C16	109.36	109.77	107.16	107.76	107.76
N3-C9-N8	126.40	126.32	126.46	126.36	126.36
N3-C9-C10	108.11	107.86	109.44	109.20	109.20
N3-C16-N7	127.60	127.54	127.44	127.28	127.28
N3-C16-C15	108.27	108.03	109.58	109.30	109.30
C1-N4-C8	109.82	110.25	107.54	108.14	108.14
N4-C1-N5	126.15	126.17	126.47	126.38	126.38
N4-C1-C2	107.75	107.46	109.13	108.89	108.89
N4-C8-N8	127.93	128.01	127.88	127.72	127.72
N4-C8-C7	107.98	107.72	109.26	108.98	108.98
C1-N5-C32	126.10	126.54	123.62	124.45	124.45
N5-C1-C2	126.10	126.36	124.40	124.73	124.73
N5-C32-C31	125.36	125.68	123.96	124.32	124.32
C24-N6-C25	125.62	126.03	123.25	124.07	124.07

N6-C24-C23	126.44	126.71	124.67	124.98	124.98
N6-C25-C26	124.47	124.74	123.26	123.65	123.65
C16-N7-C17	125.21	125.67	122.88	123.74	123.74
N7-C16-C15	124.13	124.43	122.98	123.41	123.41
N7-C17-C18	123.80	123.98	122.62	123.07	123.07
C8-N8-C9	125.34	125.77	123.06	123.90	123.90
N8-C8-C7	124.08	124.26	122.84	123.25	123.25
N8-C9-C10	125.49	125.81	124.10	124.44	124.44
C1-C2-C3	134.00	134.04	133.73	133.68	133.68
C1-C2-C7	106.59	106.63	106.48	106.45	106.45
C3-C2-C7	119.42	119.33	119.80	119.87	119.87
C2-C3-C4	122.72	122.79	122.45	122.38	122.38
C2-C3-F8	114.01	113.97	114.27	114.23	114.23
C2-C7-C6	119.27	119.25	119.27	119.28	119.28
C2-C7-C8	107.86	107.93	107.59	107.54	107.54
C4-C3-F8	123.26	123.23	123.28	123.39	123.39
C3-C4-C5	116.80	116.79	116.80	116.81	116.81
C3-C4-C46	117.30	117.33	117.27	117.18	117.18
C5-C4-C46	125.90	125.88	125.93	126.00	126.00
C4-C5-C6	118.52	118.50	118.66	118.70	118.70
C4-C5-C45	126.69	126.69	126.42	126.44	126.44
C4-C46-F7	109.16	109.13	109.33	109.38	109.38
C4-C46-C49	114.90	114.98	114.83	114.70	114.70
C4-C46-C50	114.69	114.68	114.54	114.56	114.56
C6-C5-C45	114.79	114.80	114.92	114.87	114.87
C5-C6-C7	123.27	123.33	123.00	122.93	122.93
C5-C6-F5	119.22	119.18	119.24	119.38	119.38
C5-C45-F6	108.93	108.94	108.76	108.76	108.76
C5-C45-C47	114.56	114.60	114.60	114.70	114.70
C5-C45-C48	114.55	114.56	114.48	114.32	114.32
C7-C6-F5	117.51	117.49	117.75	117.69	117.69
C6-C7-C8	132.87	132.82	133.13	133.17	133.17
C9-C10-C11	133.46	133.50	133.33	133.31	133.31
C9-C10-C15	106.65	106.68	106.49	106.46	106.46
C11-C10-C15	119.89	119.81	120.16	120.22	120.22
C10-C11-C12	122.45	122.53	122.25	122.18	122.18
C10-C11-F4	113.96	113.90	114.19	114.14	114.14
C10-C15-C14	119.11	119.10	119.13	119.14	119.14
C10-C15-C16	107.61	107.65	107.32	107.27	107.27
C12-C11-F4	123.59	123.57	123.56	123.68	123.68
C11-C12-C13	116.76	116.74	116.74	116.76	116.76
C11-C12-C36	117.05	117.07	117.19	117.13	117.13
C13-C12-C36	126.19	126.20	126.06	126.10	126.10
C12-C13-C14	118.76	118.74	118.92	118.97	118.97
C12-C13-C35	126.47	126.46	126.17	126.19	126.19
C12-C36-F3	109.05	109.03	108.98	109.00	109.00
C12-C36-C36	115.38	115.36	115.85	116.15	116.15

C12-C36-C44	114.14	114.20	113.75	113.39	113.39
C14-C13-C35	114.77	114.79	114.89	114.83	114.83
C13-C14-C15	123.03	123.08	122.78	122.72	122.72
C13-C14-F1	119.39	119.35	119.24	119.34	119.34
C13-C35-F2	108.72	108.72	108.72	108.75	108.75
C13-C35-C41	113.85	113.79	113.62	113.52	113.52
C13-C35-C42	114.98	115.09	115.14	115.16	115.16
C15-C14-F1	117.58	117.57	117.96	117.90	117.90
C14-C15-C16	133.27	133.25	133.55	133.58	133.58
C17-C18-C19	132.58	132.49	132.94	132.99	132.99
C17-C18-C23	107.96	108.04	107.66	107.61	107.61
C19-C18-C23	119.46	119.46	119.40	119.40	119.40
C18-C19-C20	123.07	123.12	122.82	122.75	122.75
C18-C19-F16	117.46	117.44	117.67	117.60	117.60
C18-C23-C22	119.37	119.27	119.80	119.87	119.87
C18-C23-C24	106.35	106.37	106.31	106.28	106.28
C20-C19-F16	119.48	119.44	119.51	119.65	119.65
C19-C20-C21	118.99	118.97	119.11	119.15	119.15
C19-C20-C34	114.83	114.85	115.04	114.99	114.99
C21-C20-C34	126.18	126.17	125.86	125.86	125.86
C20-C21-C22	116.30	116.31	116.31	116.32	116.32
C20-C21-C33	126.50	126.44	126.62	126.71	126.71
C20-C34-F15	108.01	108.02	107.88	107.89	107.89
C20-C34-C40	115.15	115.11	115.09	115.04	115.04
C20-C34-C39	114.34	114.38	114.39	114.39	114.39
C22-C21-C33	117.20	117.25	117.07	116.97	116.97
C21-C22-C23	122.81	122.86	122.55	122.48	122.48
C21-C22-F13	124.03	124.00	124.10	124.22	124.22
C21-C33-F14	106.91	106.88	107.11	107.17	107.17
C21-C33-C38	116.04	116.17	115.94	115.91	115.91
C21-C33-C37	116.20	116.13	116.15	116.08	116.08
C23-C22-F13	113.16	113.13	113.35	113.29	113.29
C22-C23-C24	134.28	134.36	133.89	133.83	133.83
C25-C26-C27	133.59	133.57	133.83	133.84	133.84
C25-C26-C31	107.75	107.80	107.43	107.36	107.36
C27-C26-C31	118.65	118.61	118.73	118.76	118.76
C26-C27-C28	123.13	123.22	122.86	122.79	122.79
C26-C27-F12	117.67	117.63	118.00	117.94	117.94
C26-C31-C30	120.06	119.99	120.33	120.37	120.37
C26-C31-C32	106.92	106.94	106.72	106.68	106.68
C28-C27-F12	119.19	119.15	119.14	119.26	119.26
C27-C28-C29	119.00	118.97	119.10	119.12	119.12
C27-C28-C52	115.31	115.31	115.43	115.38	115.38
C29-C28-C52	125.69	125.72	125.46	125.49	125.49
C28-C29-C30	116.49	116.48	116.50	116.53	116.53
C28-C29-C51	126.41	126.38	126.45	126.52	126.52
C28-C52-F11	108.35	108.37	108.38	108.41	108.41

C28-C52-C56	115.03	115.15	114.88	114.78	114.78
C28-C52-C55	114.22	114.12	114.43	114.47	114.47
C30-C29-C51	117.10	117.14	117.05	116.95	116.95
C29-C30-C51	122.59	122.66	122.34	122.27	122.27
C29-C30-F9	123.40	123.36	123.37	123.48	123.48
C29-C51-F10	108.40	108.44	108.22	108.19	108.19
C29-C51-C54	114.14	114.10	114.36	114.44	114.44
C29-C51-C53	116.12	116.19	116.06	115.93	115.93
C31-C30-F9	114.01	113.97	114.29	114.23	114.23
C30-C31-C32	133.02	133.08	132.95	132.95	132.95
F14-C33-C38	97.64	97.66	97.41	97.37	97.37
F14-C33-C37	97.31	97.33	97.01	96.99	96.99
C38-C33-C37	117.83	117.75	118.19	118.30	118.30
C33-C38-F21	118.83	118.88	118.96	118.99	118.99
C33-C38-F20	109.20	109.21	109.35	109.41	109.41
C33-C38-F22	106.33	106.30	106.20	106.24	106.24
C33-C37-F19	106.31	106.37	106.12	106.03	106.03
C33-C37-F18	119.09	119.11	119.22	119.19	119.19
C33-C37-F17	109.18	109.17	109.21	109.25	109.25
F21-C38-F20	106.22	106.22	106.27	106.26	106.26
F21-C38-F22	107.31	107.26	107.14	107.07	107.07
F20-C38-F22	108.62	108.65	108.59	108.50	108.50
F19-C37-F18	107.11	107.13	106.99	106.92	106.92
F19-C37-F17	108.69	108.69	108.69	108.71	108.71
F18-C37-F17	106.13	106.05	106.27	106.41	106.41
F15-C34-C40	101.42	101.38	101.47	101.52	101.52
F15-C34-C39	102.53	102.49	102.73	102.78	102.78
C40-C34-C39	113.50	113.54	113.42	113.38	113.38
C34-C40-F27	115.10	115.11	115.02	115.07	115.07
C34-C40-F26	109.45	109.45	109.47	109.47	109.47
C34-C40-F28	108.20	108.19	108.25	108.22	108.22
C34-C39-F23	108.50	108.47	108.63	108.65	108.65
C34-C39-F25	114.24	114.25	114.08	114.14	114.14
C34-C39-F24	110.02	110.02	110.08	110.09	110.09
F27-C40-F26	107.24	107.23	107.30	107.35	107.35
F27-C40-F28	108.20	108.21	108.17	108.10	108.10
F26-C40-F28	108.48	108.48	108.47	108.47	108.47
F23-C39-F25	108.11	108.09	108.10	108.04	108.04
F23-C39-F24	108.41	108.40	108.39	108.36	108.36
F25-C39-F24	107.42	107.45	107.42	107.40	107.40
F2-C35-C41	102.25	102.27	101.83	101.83	101.83
F2-C35-C42	102.59	102.50	103.35	103.46	103.46
C41-C35-C42	112.87	112.87	112.66	112.61	112.61
C35-C41-F29	114.47	114.41	114.67	114.75	114.75
C35-C41-F30	109.62	109.64	109.50	109.52	109.52
C35-C41-F31	108.75	108.79	108.66	108.73	108.73
C35-C42-F34	109.21	109.17	109.64	109.62	109.62

C35-C42-F32	114.36	114.44	113.64	113.61	113.61
C35-C42-F33	109.46	109.44	109.70	109.68	109.68
F29-C41-F30	107.53	107.52	107.73	107.69	107.69
F29-C41-F31	107.74	107.76	107.48	107.39	107.39
F30-C41-F31	108.59	108.58	108.64	108.59	108.59
F34-C42-F32	108.11	108.09	108.21	108.20	108.20
F34-C42-F33	108.50	108.51	108.36	108.34	108.34
F32-C42-F33	107.04	107.03	107.14	107.24	107.24
F3-C36-C36	96.09	96.13	95.96	96.00	96.00
F3-C36-C44	97.20	97.13	97.61	97.63	97.63
C43-C36-C44	120.44	120.43	120.22	120.23	120.23
C36-C43-F36	119.46	119.42	119.82	119.78	119.78
C36-C43-F37	109.93	109.95	109.76	109.79	109.79
C36-C43-F35	105.26	105.27	105.10	105.04	105.04
C36-C44-F40	106.15	106.12	106.49	106.59	106.59
C36-C44-F38	118.04	118.13	117.66	117.65	117.65
C36-C44-F39	110.28	110.23	110.45	110.48	110.48
F36-C36-F37	106.67	106.70	106.50	106.57	106.57
F36-C36-F35	106.60	106.59	106.73	106.72	106.72
F37-C36-F35	108.50	108.50	108.49	108.51	108.51
F40-C44-F38	105.62	105.65	105.27	105.19	105.19
F40-C44-F39	108.73	108.72	108.81	108.76	108.76
F38-C44-F39	107.64	107.60	107.79	107.78	107.78
F6-C45-C47	102.36	102.34	102.61	102.69	102.69
F6-C45-C48	102.03	102.00	102.07	102.10	102.10
C47-C45-C48	112.76	112.74	112.71	112.67	112.67
C45-C47-F42	114.42	114.43	114.29	114.36	114.36
C45-C47-F43	109.60	109.60	109.66	109.67	109.67
C45-C47-F41	109.02	109.02	109.16	109.15	109.15
C45-C48-F46	108.93	108.93	109.00	109.00	109.00
C45-C48-F44	114.62	114.63	114.60	114.65	114.65
C45-C48-F45	109.41	109.40	109.38	109.37	109.37
F42-C47-F4	107.20	107.20	107.19	107.19	107.19
F42-C47-F41	107.92	107.93	107.88	107.83	107.83
F43-C47-F41	108.52	108.52	108.49	108.47	108.47
F46-C48-F44	107.87	107.88	107.76	107.67	107.67
F46-C48-F45	108.59	108.58	108.60	108.59	108.59
F44-C48-F45	107.28	107.27	107.35	107.39	107.39
F7-C46-C49	96.37	96.40	96.23	96.20	96.20
F7-C46-C50	96.66	96.64	96.62	96.64	96.64
C49-C46-C50	120.47	120.40	120.70	120.80	120.80
C46-C49-F48	118.97	118.98	118.97	118.92	118.92
C46-C49-F49	110.08	110.07	110.17	110.20	110.20
C46-C49-F47	105.63	105.61	105.57	105.55	105.55
C46-50-F50	105.60	105.62	105.59	105.61	105.61
C46-C50-F51	118.72	118.75	118.70	118.68	118.68
C46-C50-F52	110.22	110.20	110.32	110.37	110.37

F48-C49-F49	107.07	107.06	107.15	107.24	107.24
F48-C49-F47	106.07	106.09	105.92	105.85	105.85
F49-C49-F47	108.61	108.61	108.63	108.64	108.64
F50-C50-F51	106.03	106.05	105.89	105.84	105.84
F50-C50-F52	108.62	108.61	108.62	108.59	108.59
F51-C50-F52	107.23	107.19	107.29	107.32	107.32
F10-C51-C54	97.47	97.45	97.65	97.70	97.70
F10-C51-C53	95.50	95.51	95.38	95.36	95.36
C54-C51-C53	120.26	120.22	120.16	120.21	120.21
C51-C54-F56	118.49	118.49	118.45	118.40	118.40
C51-C54-F58	110.45	110.44	110.47	110.50	110.50
C51-C54-F57	105.68	105.66	105.75	105.77	105.77
C51-C53-F55	105.47	105.50	105.52	105.54	105.54
C51-C53-F54	120.00	119.99	120.02	119.99	119.99
C51-C53-F53	109.50	109.52	109.50	109.53	109.53
F56-C54-F58	107.18	107.20	107.14	107.18	107.18
F56-C54-F57	106.03	106.03	106.05	106.02	106.02
F58-C54-F57	108.62	108.62	108.57	108.56	108.56
F55-C53-F54	106.18	106.18	106.15	106.10	106.10
F55-C53-F53	108.67	108.67	108.68	108.66	108.66
F54-C53-F53	106.59	106.56	106.54	106.59	106.59
F11-C52-C56	100.88	100.89	100.67	100.70	100.70
F11-C52-C55	103.73	103.70	103.87	103.92	103.92
C56-C52-C55	112.94	112.92	112.90	112.86	112.86
C52-C56-F63	115.40	115.43	115.41	115.46	115.46
C52-C56-F62	108.93	108.93	108.92	108.94	108.94
C52-C56-F64	108.46	108.48	108.35	108.32	108.32
C52-C55-F61	109.24	109.24	109.34	109.34	109.34
C52-C55-F60	113.31	113.31	113.17	113.22	113.22
C52-C55-F59	110.28	110.26	110.32	110.34	110.34
F63-C56-F62	107.30	107.26	107.48	107.52	107.52
F63-C56-F64	107.92	107.90	107.85	107.78	107.78
F62-C56-F64	108.68	108.67	108.67	108.66	108.66
F61-C55-F60	107.97	107.97	108.04	107.99	107.99
F61-C55-F59	108.43	108.43	108.35	108.32	108.32
F60-C55-F59	107.49	107.50	107.48	107.47	107.47

Table B.21. Calculated Mullikan Atomic Charges of $F_{64}MPc$ with B3LYP functional and 6-31G basis set.

	$F_{64}ZnPc$	$F_{64}MgPc$	$F_{64}CoPc$	$F_{64}CuPc$	$F_{64}FePc$
M	1.053	1.284	0.976	1.000	1.192
N1	-0.681	-0.744	-0.701	-0.680	-0.738
N2	-0.687	-0.750	-0.678	-0.681	-0.707
N3	-0.679	-0.741	-0.700	-0.679	-0.787
N4	-0.682	-0.743	-0.675	-0.678	-0.704
N5	-0.315	-0.319	-0.301	-0.304	-0.308
N6	-0.321	-0.326	-0.303	-0.306	-0.311
N7	-0.321	-0.326	-0.305	-0.308	-0.313
N8	-0.312	-0.316	-0.300	-0.303	-0.306
C1	0.361	0.372	0.347	0.350	0.342
C2	0.049	0.045	0.057	0.054	0.061
C3	0.272	0.271	0.276	0.275	0.274
C4	0.016	0.016	0.016	0.016	0.015
C5	0.062	0.062	0.060	0.061	0.060
C6	0.235	0.234	0.241	0.240	0.239
C7	0.041	0.037	0.053	0.051	0.055
C8	0.376	0.386	0.363	0.366	0.357
C9	0.378	0.388	0.375	0.369	0.371
C10	0.025	0.020	0.039	0.039	0.036
C11	0.238	0.237	0.243	0.240	0.243
C12	0.055	0.054	0.053	0.054	0.052
C13	0.033	0.032	0.031	0.032	0.032
C14	0.267	0.265	0.273	0.272	0.273
C15	0.060	0.057	0.063	0.061	0.064
C16	0.364	0.375	0.358	0.352	0.356
C17	0.386	0.397	0.371	0.373	0.365
C18	0.043	0.038	0.055	0.054	0.058
C19	0.235	0.234	0.240	0.239	0.238
C20	0.058	0.058	0.055	0.056	0.055
C21	0.019	0.019	0.019	0.018	0.018
C22	0.275	0.273	0.279	0.279	0.277
C23	0.038	0.034	0.046	0.043	0.049
C24	0.372	0.383	0.355	0.357	0.350
C25	0.368	0.380	0.361	0.355	0.359
C26	0.055	0.051	0.060	0.059	0.060
C27	0.270	0.268	0.275	0.274	0.275
C28	0.015	0.015	0.013	0.014	0.014
C29	0.063	0.062	0.061	0.062	0.060
C30	0.236	0.235	0.241	0.238	0.241
C31	0.031	0.026	0.043	0.042	0.040
C32	0.381	0.391	0.377	0.371	0.373
C33	0.066	0.067	0.067	0.066	0.068
C34	0.062	0.063	0.061	0.061	0.062

C35	0.069	0.069	0.068	0.067	0.069
C36	0.061	0.061	0.062	0.061	0.062
C37	0.797	0.797	0.796	0.796	0.796
C38	0.805	0.805	0.806	0.806	0.805
C39	0.809	0.809	0.811	0.811	0.810
C40	0.803	0.803	0.803	0.803	0.803
C41	0.796	0.796	0.797	0.797	0.796
C42	0.798	0.798	0.799	0.799	0.798
C43	0.805	0.805	0.805	0.805	0.805
C44	0.804	0.803	0.804	0.804	0.804
C45	0.066	0.066	0.064	0.063	0.065
C46	0.805	0.805	0.805	0.805	0.805
C47	0.807	0.807	0.811	0.811	0.809
C48	0.066	0.066	0.065	0.065	0.066
C49	0.800	0.800	0.801	0.801	0.800
C50	0.803	0.803	0.805	0.805	0.804
C51	0.067	0.067	0.067	0.067	0.067
C52	0.067	0.067	0.068	0.067	0.068
C53	0.806	0.806	0.807	0.807	0.806
C54	0.805	0.805	0.805	0.805	0.805
C55	0.800	0.800	0.801	0.801	0.800
C56	0.802	0.802	0.803	0.803	0.802
F1	-0.251	-0.254	-0.252	-0.252	-0.253
F2	-0.275	-0.275	-0.274	-0.274	-0.275
F3	-0.286	-0.286	-0.286	-0.286	-0.236
F4	-0.264	-0.265	-0.263	-0.264	-0.264
F5	-0.265	-0.265	-0.265	-0.265	-0.265
F6	-0.289	-0.289	-0.290	-0.290	-0.289
F7	-0.274	-0.274	-0.274	-0.274	-0.274
F8	-0.251	-0.251	-0.250	-0.250	-0.251
F9	-0.264	-0.264	-0.263	-0.264	-0.264
F10	-0.289	-0.289	-0.289	-0.289	-0.289
F11	-0.274	-0.274	-0.274	-0.274	-0.274
F12	-0.251	-0.251	-0.249	-0.249	-0.250
F13	-0.250	-0.251	-0.249	-0.249	-0.250
F14	-0.274	-0.274	-0.274	-0.274	-0.274
F15	-0.289	-0.289	-0.289	-0.289	-0.289
F16	-0.265	-0.265	-0.264	-0.264	-0.265
F17	-0.242	-0.242	-0.242	-0.242	-0.242
F18	-0.238	-0.238	-0.239	-0.239	-0.238
F19	-0.260	-0.260	-0.259	-0.260	-0.260
F20	-0.242	-0.242	-0.242	-0.242	-0.242
F21	-0.239	-0.238	-0.238	-0.238	-0.238
F22	-0.260	-0.260	-0.260	-0.259	-0.260
F23	-0.259	-0.259	-0.259	-0.259	-0.259
F24	-0.238	-0.238	-0.237	-0.237	-0.238
F25	-0.238	-0.238	-0.239	-0.239	-0.239

F26	-0.242	-0.242	-0.242	-0.242	-0.242
F27	-0.234	-0.234	-0.234	-0.234	-0.234
F28	-0.256	-0.256	-0.256	-0.256	-0.256
F29	-0.261	-0.261	-0.260	-0.261	-0.261
F30	-0.242	-0.242	-0.242	-0.242	-0.243
F31	-0.236	-0.236	-0.236	-0.236	-0.236
F32	-0.261	-0.261	-0.261	-0.262	-0.252
F33	-0.242	-0.242	-0.241	-0.242	-0.242
F34	-0.235	-0.235	-0.235	-0.235	-0.235
F35	-0.257	-0.257	-0.257	-0.257	-0.257
F36	-0.239	-0.234	-0.239	-0.239	-0.239
F37	-0.236	-0.236	-0.236	-0.236	-0.236
F38	-0.257	-0.257	-0.257	-0.258	-0.257
F39	-0.240	-0.240	-0.240	-0.240	-0.240
F40	-0.234	-0.239	-0.235	-0.235	-0.235
F41	-0.257	-0.257	-0.256	-0.256	-0.257
F42	-0.236	-0.236	-0.236	-0.236	-0.236
F43	-0.240	-0.240	-0.241	-0.242	-0.241
F44	-0.238	-0.238	-0.238	-0.238	-0.239
F45	-0.258	-0.258	-0.250	-0.250	-0.259
F46	-0.239	-0.240	-0.240	-0.240	-0.239
F47	-0.261	-0.261	-0.262	-0.262	-0.261
F48	-0.236	-0.236	-0.235	-0.234	-0.235
F49	-0.241	-0.241	-0.242	-0.241	-0.242
F50	-0.258	-0.258	-0.258	-0.258	-0.257
F51	-0.242	-0.241	-0.246	-0.246	-0.244
F52	-0.243	-0.243	-0.243	-0.244	-0.243
F53	-0.258	-0.258	-0.258	-0.258	-0.258
F54	-0.237	-0.237	-0.237	-0.237	-0.237
F55	-0.240	-0.240	-0.240	0.240	-0.240
F56	-0.257	-0.258	-0.257	-0.257	-0.257
F57	-0.236	-0.236	-0.236	-0.236	-0.236
F58	-0.240	-0.240	-0.240	-0.240	-0.400
F59	-0.242	-0.242	-0.242	-0.242	-0.242
F60	-0.260	-0.260	-0.260	-0.260	-0.260
F61	-0.238	-0.238	-0.239	-0.239	-0.239
F62	-0.242	-0.242	-0.242	-0.242	-0.242
F63	-0.259	-0.260	-0.259	-0.259	-0.260
F64	-0.238	-0.238	-0.238	-0.239	-0.239

APPENDIX C

F_xMPc DOS, PDOS, and Electron Density Distribution Plots

The calculated DOS and PDOS of $F_{16}MPc$ are provided in Figure C.1. A summary of the energy and atom contributions of select MOs is also provided in Table C.1 with corresponding electron density plots illustrated in Figures C.2-6.

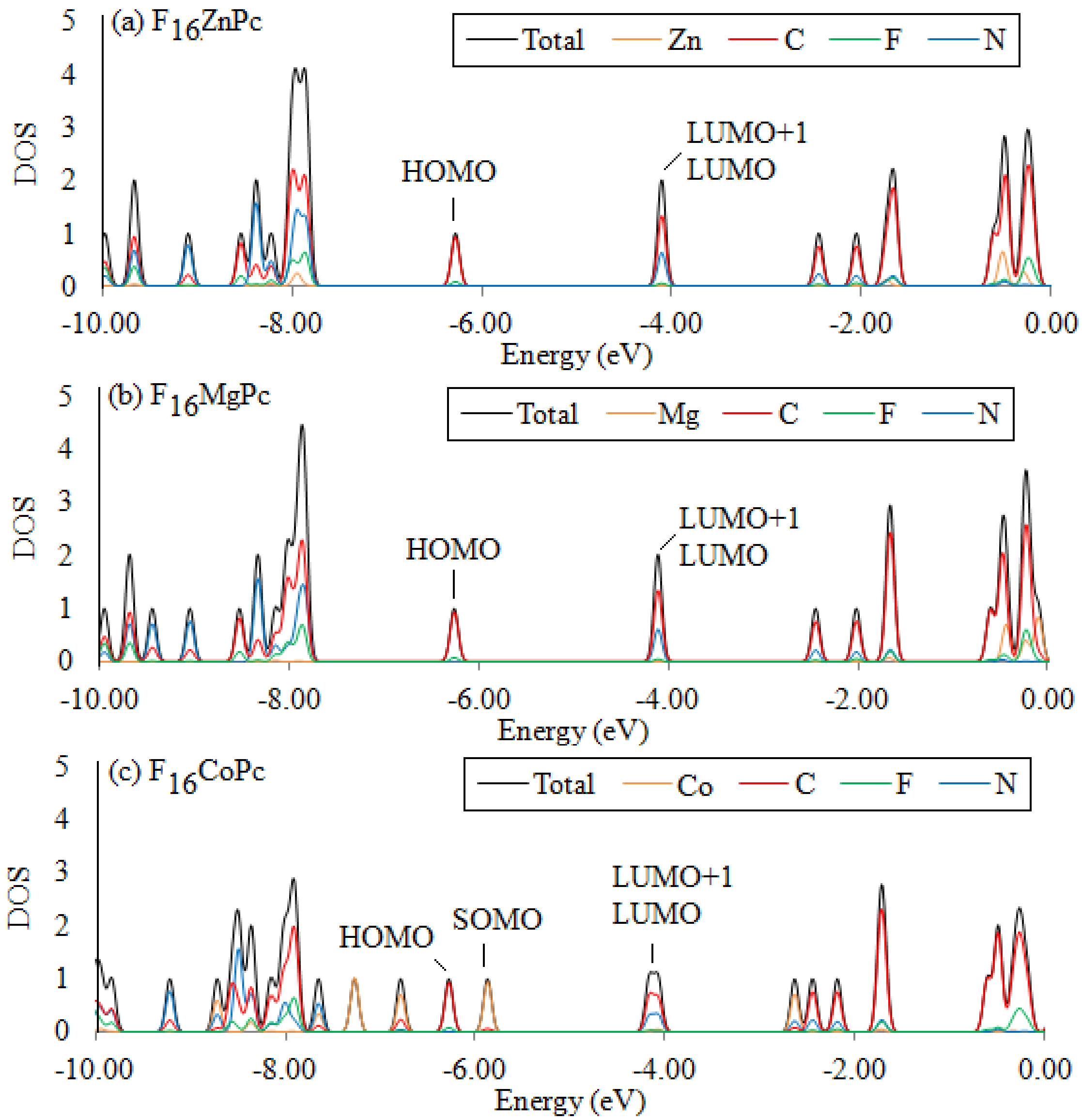

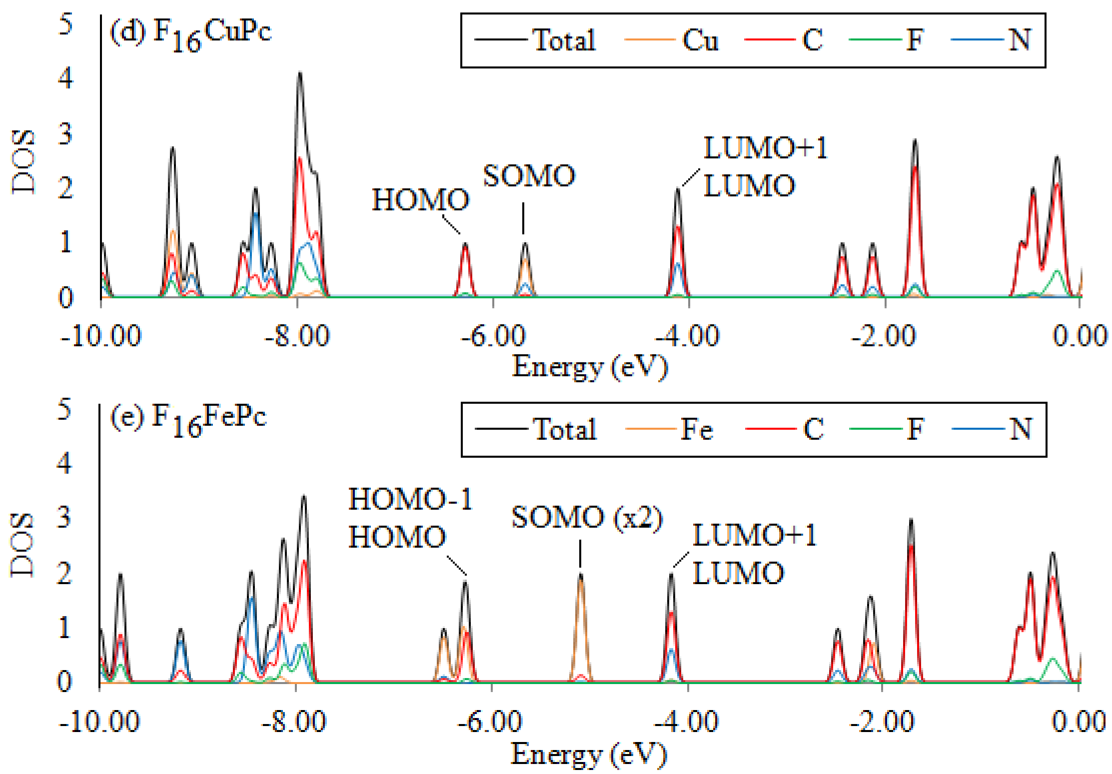

Figure C.1. DOS and PDOS of (a) F_{16}ZnPc, (b) F_{16}MgPc, (c) F_{16}CoPc, (d) F_{16}CuPc, and (e) F_{16}FePc.

Table C.1. Calculated energy and atom contributions of select MOs for F_{16}MPc.

			% Contribution to MO			
Pc	MO	Energy(eV)	Zn	N	C	F
F_{16}ZnPc	HOMO	-6.286	0.00	0.00	91.87	8.13
	LUMO	-4.114	0.31	31.23	65.93	2.53
	LUMO+1	-4.114	0.31	31.23	65.93	2.53
F_{16}MgPc	HOMO	-6.264	0.00	0.00	91.93	8.06
	LUMO	-4.114	0.00	30.99	66.47	2.54
	LUMO+1	-4.112	0.00	30.99	66.47	2.54
F_{16}CoPc	HOMO	-6.286	0.00	0.00	91.87	8.13
	SOMO	-5.878	93.71	6.65	5.43	0.21
	LUMO	-4.169	2.25	29.92	65.28	2.56
	LUMO+1	-4.076	4.55	31.45	61.64	2.37
F_{16}CuPc	HOMO	-6.294	0.00	0.00	91.85	8.13
	SOMO	-5.682	70.04	24.25	5.60	0.09
	LUMO	-4.123	1.00	31.11	65.38	2.51
	LUMO+1	-4.120	1.00	31.11	65.38	2.51
F_{16}FePc	HOMO-1	-6.291	100.00	0.00	0.00	0.00

	HOMO	-6.259	0.00	0.00	92.00	8.00
	SOMO	-5.097	93.17	0.41	6.19	0.22
	SOMO	-5.097	93.17	0.41	6.19	0.22
	LUMO	-4.172	2.80	30.55	64.14	2.50
	LUMO+1	-4.172	2.80	30.55	64.14	2.50

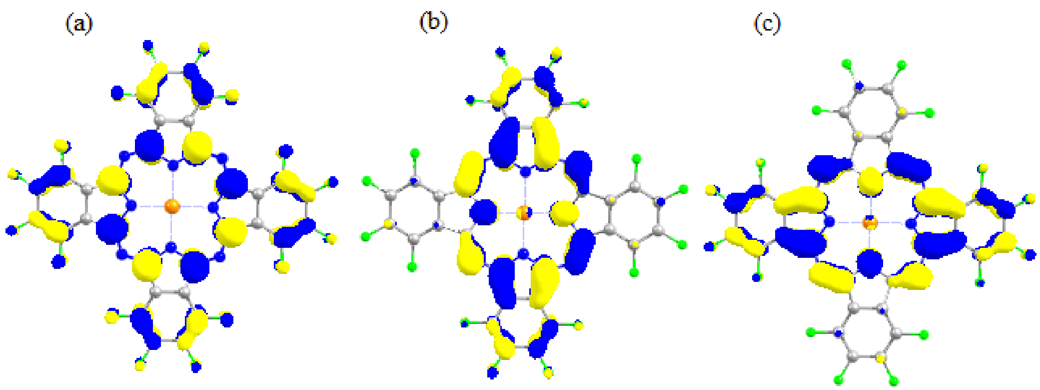

Figure C.2. Electron density distribution plots of $F_{16}ZnPc$ (a) HOMO, (b) LUMO, and (c) LUMO+1. Surfaces sampled at 0.03 e/au.

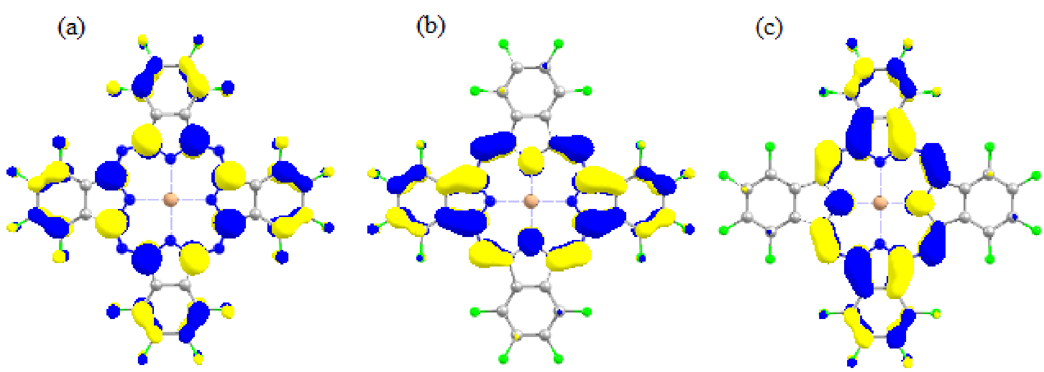

Figure C.3. Electron density distribution plots of $F_{16}MgPc$ (a) HOMO, (b) LUMO, and (c) LUMO+1. Surfaces sampled at 0.03 e/au.

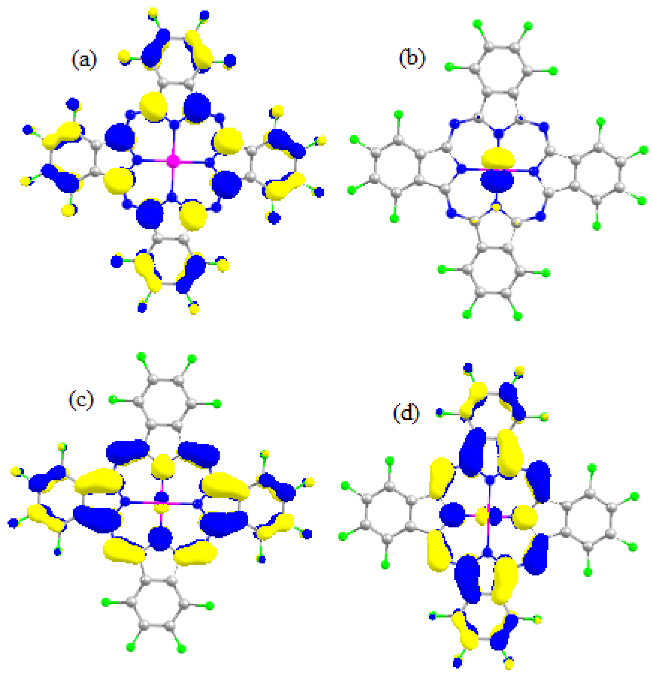

Figure C.4. Electron density distribution plots of $F_{16}CoPc$ (a) HOMO, (b) SOMO, (c) LUMO and (d) LUMO+1. Surfaces sampled at 0.03 e/au.

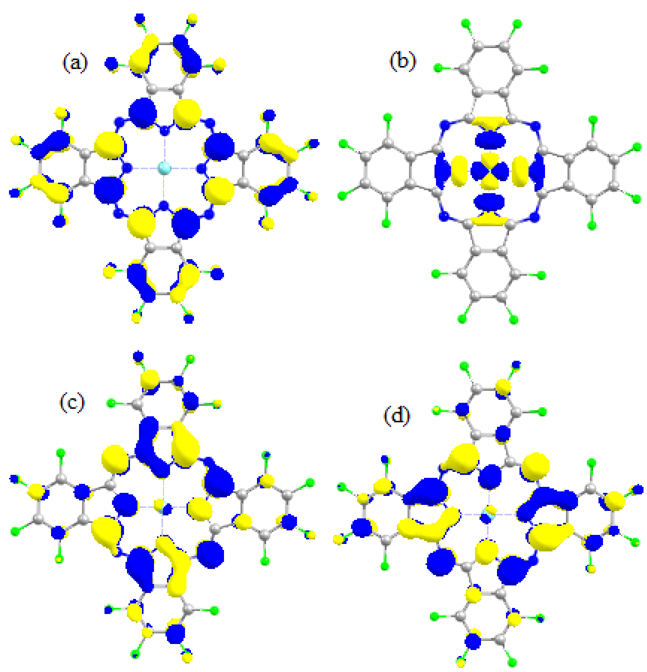

Figure C.5. Electron density distribution plots of $F_{16}CuPc$ (a) HOMO, (b) SOMO, (c) LUMO and (d) LUMO+1. Surfaces sampled at 0.03 e/au.

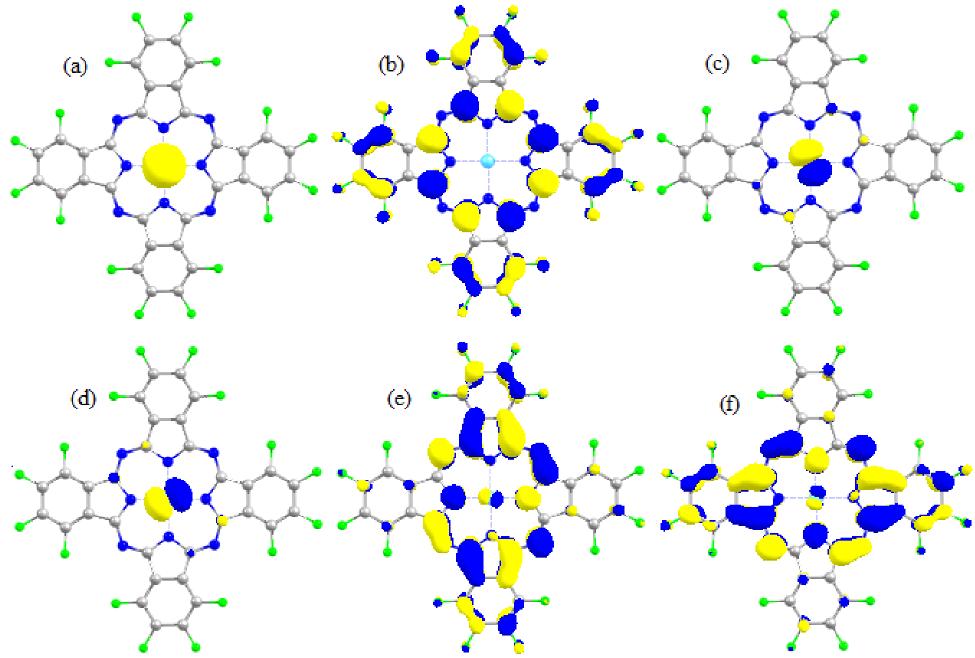

Figure C.6. Electron density distribution plots of $F_{16}FePc$ (a) HOMO-1, (b) HOMO, (c) SOMO (d) SOMO, (e) LUMO, and (f) LUMO+1. Surfaces sampled at 0.03 e/au.

The calculated DOS and PDOS of $F_{34}MPc$ are provided in Figure C.7. A summary of the energy and atom contributions of select MOs is also provided in Table C.2 with corresponding electron density plots illustrated in Figures C.8-12.

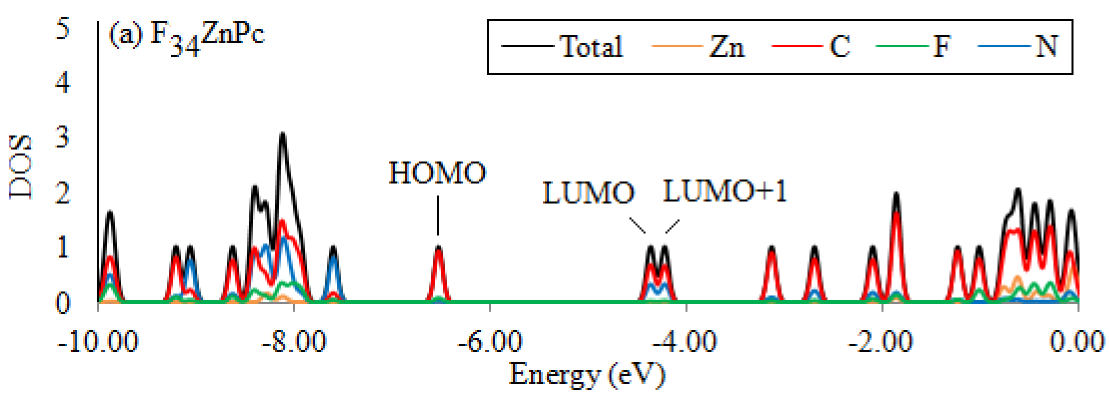

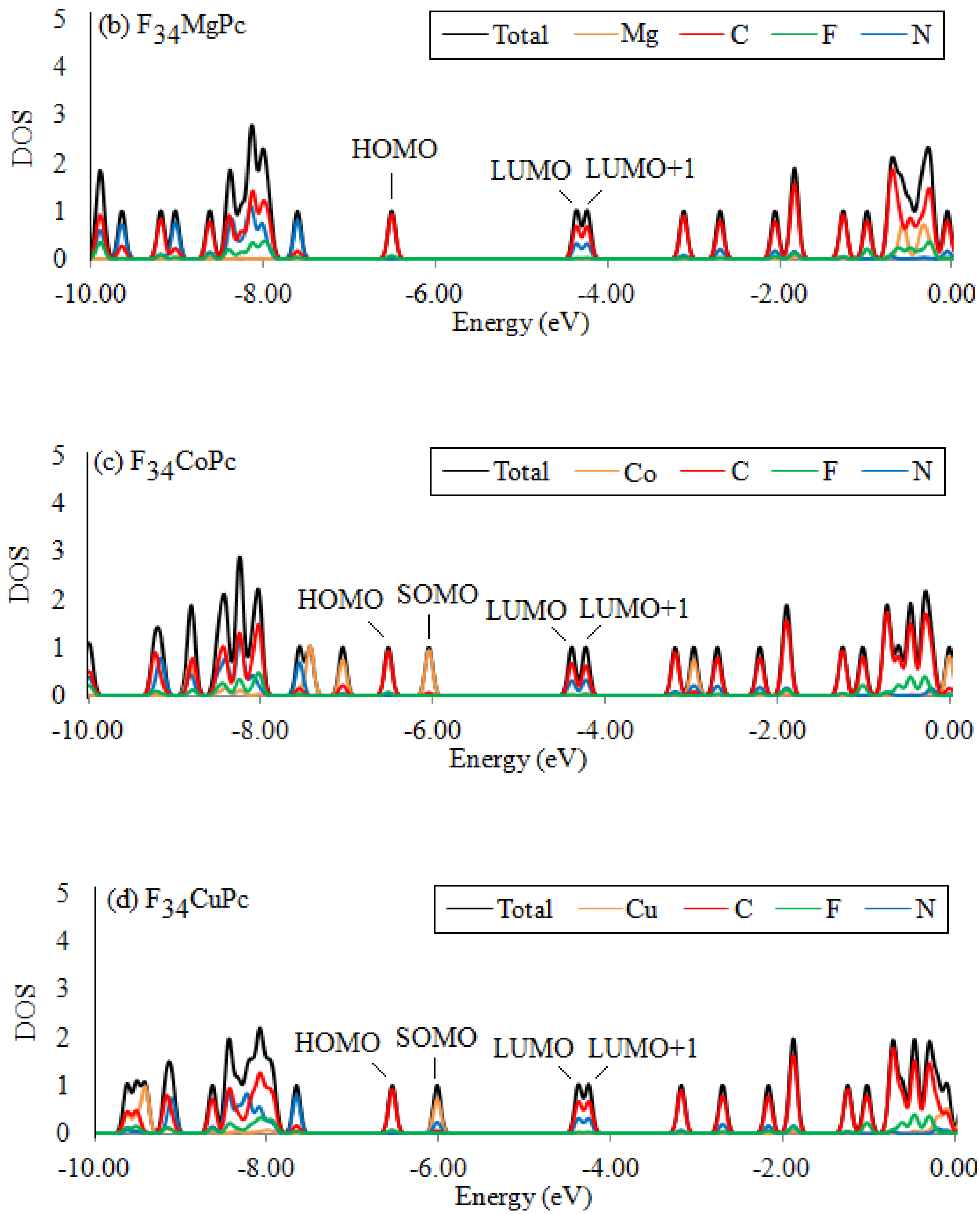
(b) F34MgPc
Total
Mg
C
F
N
HOMO
LUMO
LUMO+1
DOS
Energy (eV)
(c) F34CoPc
Total
Co
C
F
N
HOMO
SOMO
LUMO
LUMO+1
DOS
Energy (eV)
(d) F34CuPc
Total
Cu
C
F
N
HOMO
SOMO
LUMO
LUMO+1
DOS
Energy (eV)

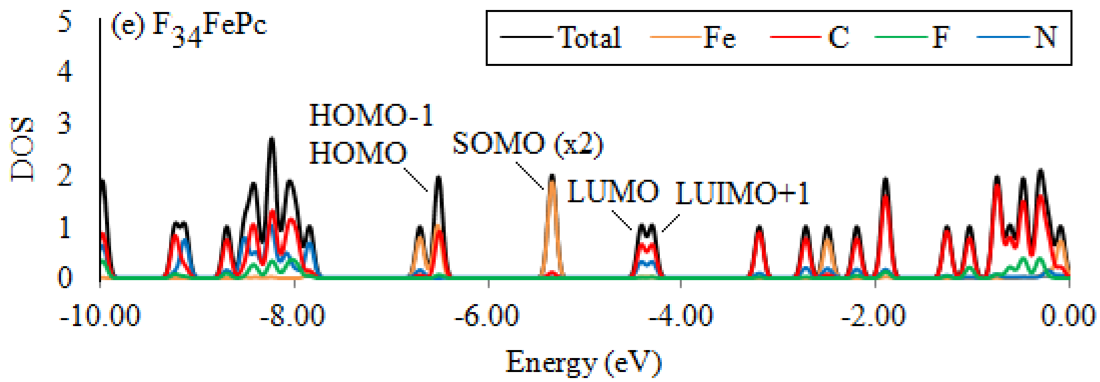

Figure C.7. DOS and PDOS of (a) F_{34}ZnPc, (b) F_{34}MgPc, (c) F_{34}CoPc, (d) F_{34}CuPc, and (e) F_{34}FePc.

Table C.2. Calculated energy and atom contributions of select MOs for F_{34}MPc.

			% Contribution to MO			
Pc	MO	Energy(eV)	Zn	N	C	F
F_{34}ZnPc	HOMO	-6.536	0.00	0.54	92.32	7.13
	LUMO	-4.373	0.32	31.11	66.62	1.94
	LUMO+1	-4.229	0.30	31.72	65.58	2.41
F_{34}MgPc	HOMO	-6.520	0.00	0.55	92.42	7.03
	LUMO	-4.370	0.00	31.11	66.93	1.94
	LUMO+1	-4.245	0.02	31.27	66.29	2.43
F_{34}CoPc	HOMO	-6.539	0.07	0.42	92.42	7.08
	SOMO	-6.065	93.57	0.62	5.62	0.20
	LUMO	-4.408	1.85	30.06	66.14	1.94
	LUMO+1	-4.245	4.39	31.61	61.72	2.28
F_{34}CuPc	HOMO	-6.544	0.02	0.52	92.31	7.15
	SOMO	-6.022	70.46	23.87	5.59	0.09
	LUMO	-4.378	1.02	31.28	65.79	1.92
	LUMO+1	-4.259	0.90	31.29	65.41	2.40
F_{34}FePc	HOMO-1	-6.531	100.00	0.00	0.00	0.00
	HOMO	-6.512	0.00	0.00	~92.00	~8.00
	SOMO	-5.350	93.60	0.41	5.81	0.17
	SOMO	-5.342	93.60	0.41	5.81	0.17
	LUMO	-4.422	2.81	30.83	64.47	1.89
	LUMO+1	-4.308	2.47	30.62	64.52	2.39

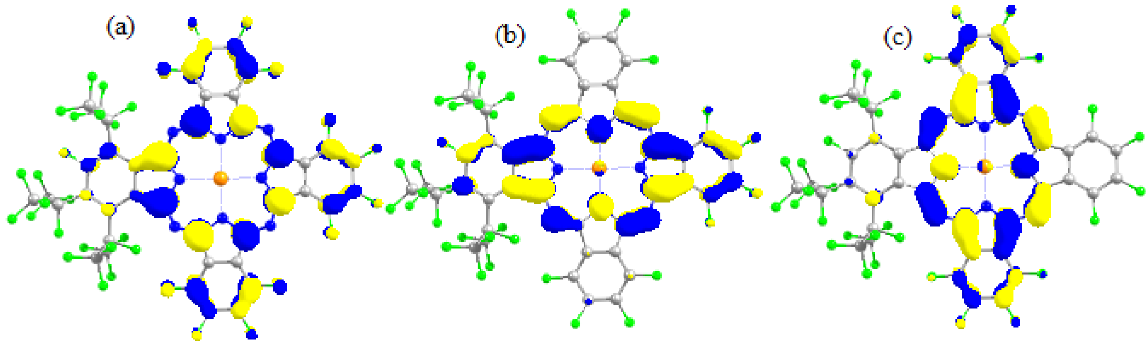

Figure C.8. Electron density distribution plots of $F_{34}ZnPc$ (a) HOMO, (b) LUMO, and (c) LUMO+1. Surfaces sampled at 0.03 e/au.

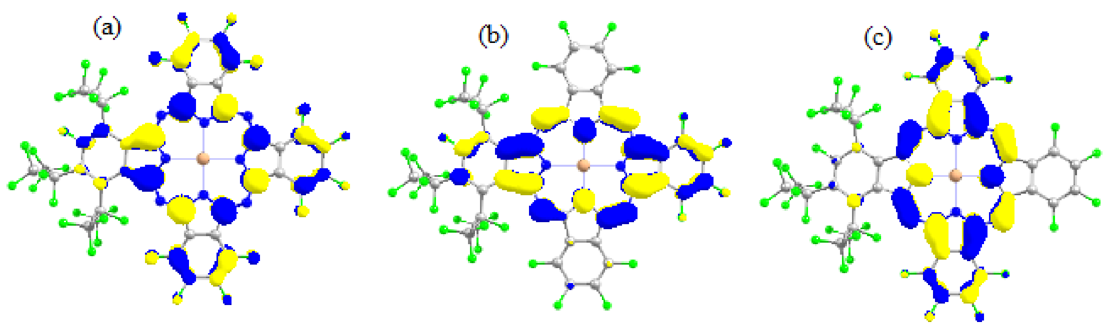

Figure C.9. Electron density distribution plots of $F_{34}MgPc$ (a) HOMO, (b) LUMO, and (c) LUMO+1. Surfaces sampled at 0.03 e/au.

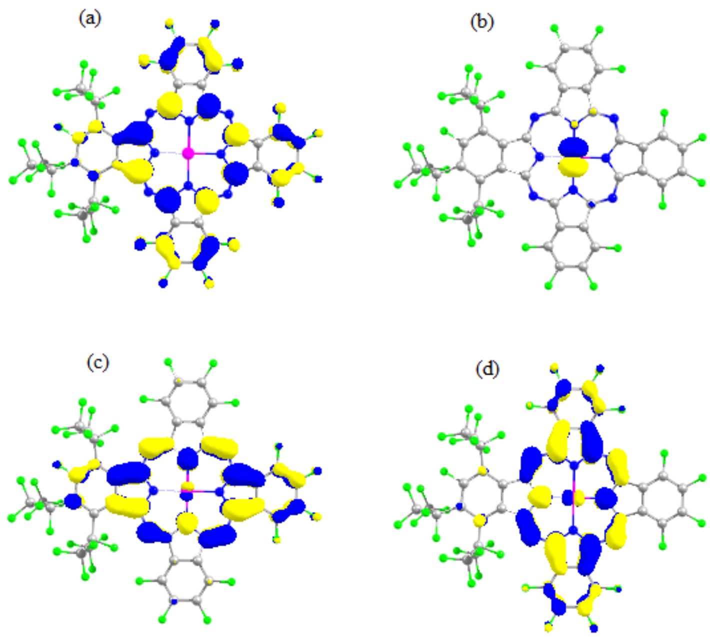

Figure C.10. Electron density distribution plots of $F_{34}CoPc$ (a) HOMO, (b) SOMO, (c) LUMO and (d) LUMO+1. Surfaces sampled at 0.03 e/au.

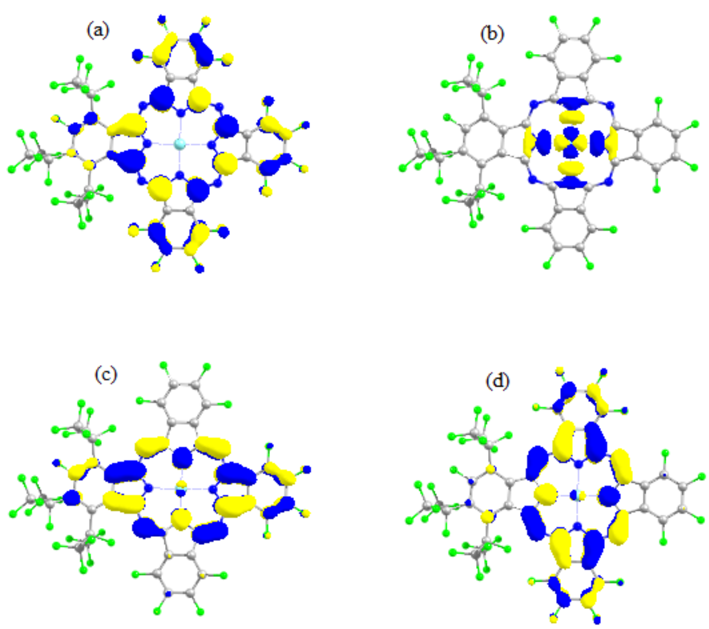

Figure C.11. Electron density distribution plots of $F_{34}CuPc$ (a) HOMO, (b) SOMO, (c) LUMO and (d) LUMO+1. Surfaces sampled at 0.03 e/au.

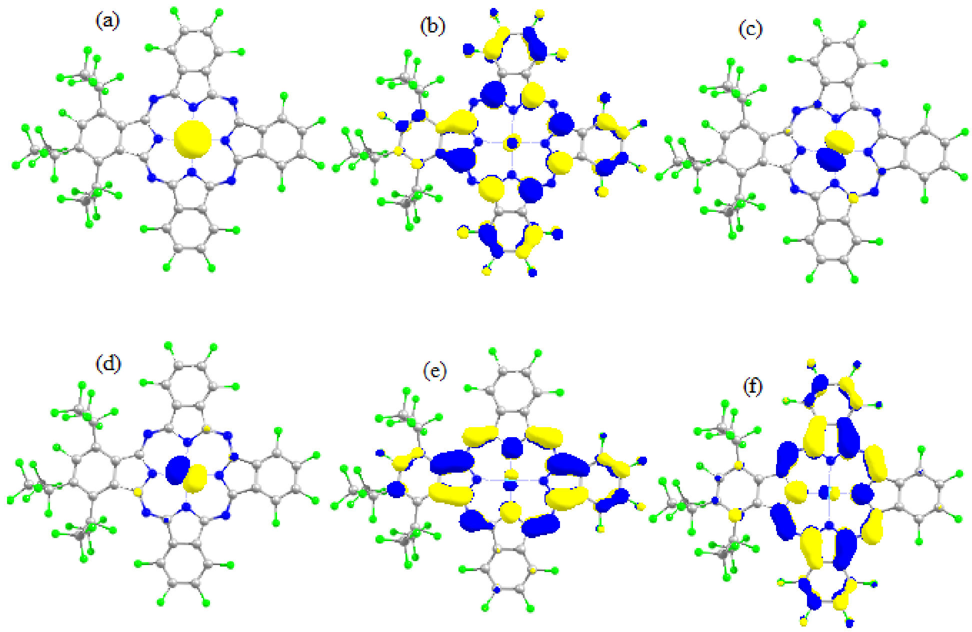

Figure C.12. Electron density distribution plots of $F_{34}FePc$ (a) HOMO-1, (b) HOMO, (c) SOMO (d) SOMO, (e) LUMO, and (f) LUMO+1. Surfaces sampled at 0.03 e/au.

The calculated DOS and PDOS of $F_{40}MPc$ are provided in Figure C.13. A summary of the energy and atom contributions of select MOs is also provided in Table C.3 with corresponding electron density plots illustrated in Figures C.14-18.

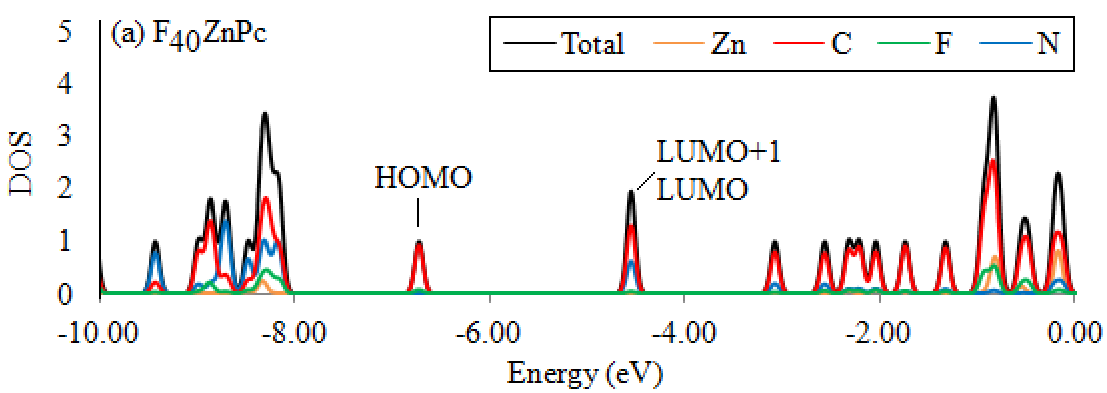

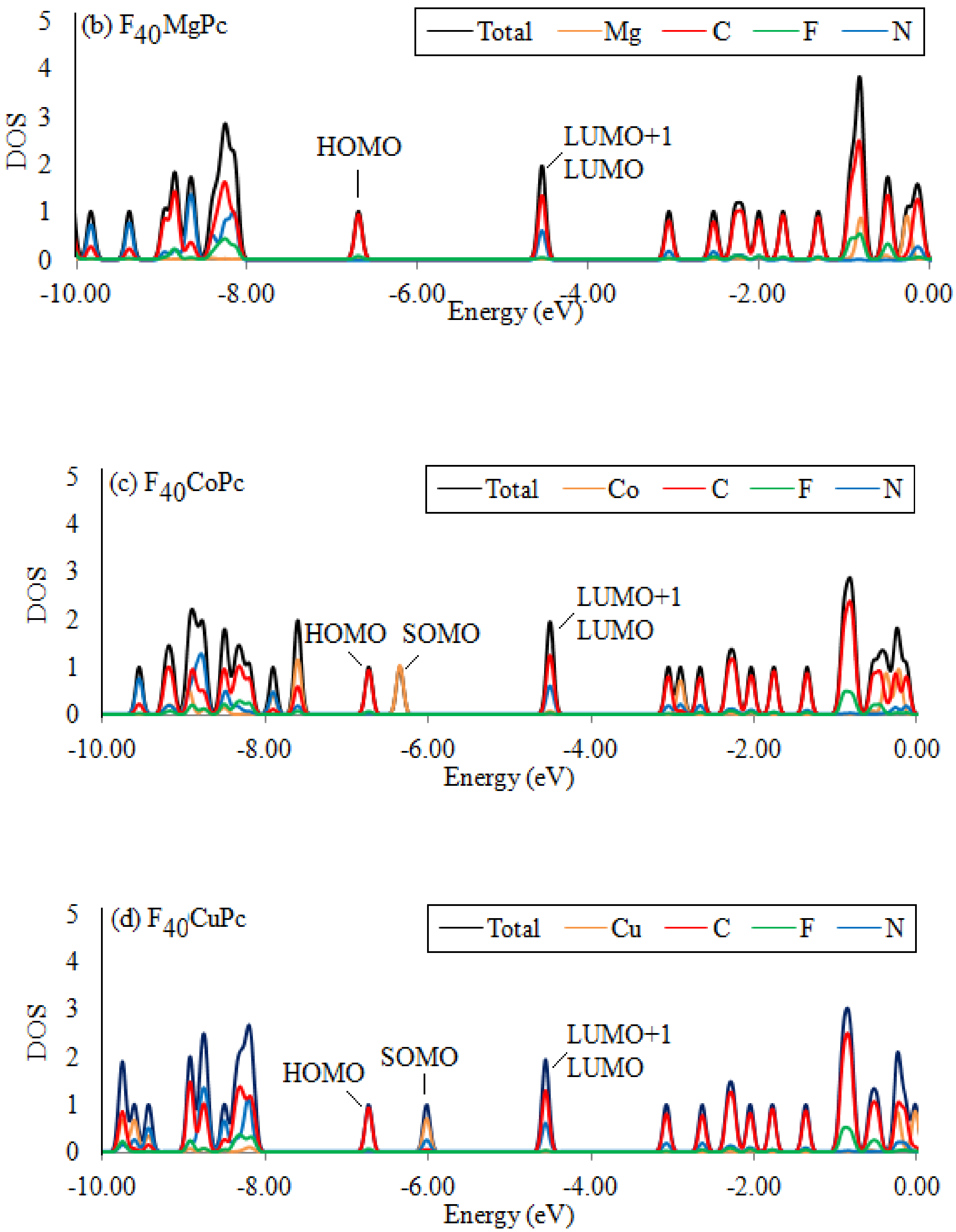
(b) F40MgPc
Total
Mg
C
F
N
DOS
HOMO
LUMO+1
LUMO
Energy (eV)
(c) F40CoPc
Total
Co
C
F
N
DOS
HOMO
SOMO
LUMO+1
LUMO
Energy (eV)
(d) F40CuPc
Total
Cu
C
F
N
DOS
HOMO
SOMO
LUMO+1
LUMO
Energy (eV)

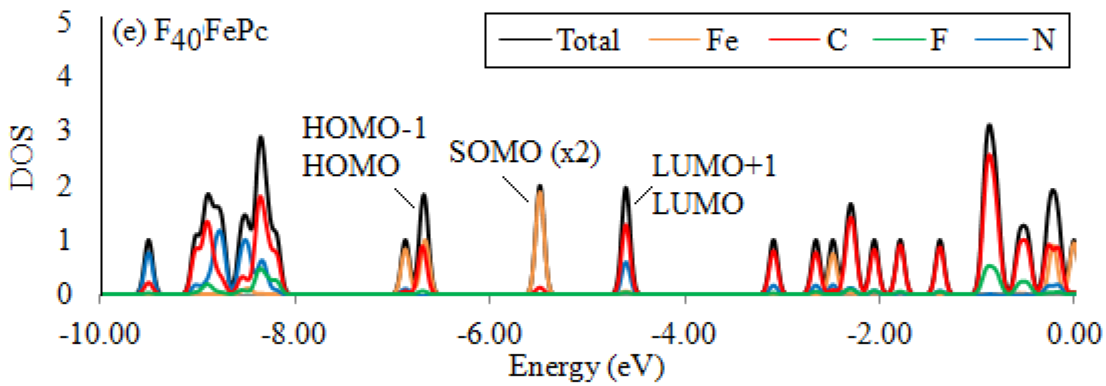

Figure C.13. DOS and PDOS of (a) F_{40}ZnPc, (b) F_{40}MgPc, (c) F_{40}CoPc, (d) F_{40}CuPc, and (e) F_{40}FePc.

Table C3. Calculated energy and atom contributions of select MOs for F_{40}MPc.

			% Contribution to MO			
Pc	MO	Energy(eV)	Zn	N	C	F
F_{40}ZnPc	HOMO	-6.740	0.00	0.35	92.94	6.71
	LUMO	-4.572	0.31	30.95	66.97	1.78
	LUMO+1	-4.553	0.31	30.95	66.97	1.78
F_{40}MgPc	HOMO	-6.713	0.00	0.35	93.05	6.60
	LUMO	-4.563	0.01	30.58	67.61	1.79
	LUMO+1	-4.547	0.01	30.58	67.61	1.79
F_{40}CoPc	HOMO	-6.740	0.17	0.39	92.63	6.80
	SOMO	-6.359	100.00	0.00	0.00	0.00
	LUMO	-4.525	3.69	30.81	63.81	1.70
	LUMO+1	-4.506	3.69	30.81	63.81	1.70
F_{40}CuPc	HOMO	-6.738	0.02	0.40	92.90	6.68
	SOMO	-6.025	69.93	24.34	5.65	0.07
	LUMO	-4.574	1.03	30.78	66.39	1.79
	LUMO+1	-4.555	1.03	30.78	66.39	1.79
F_{40}FePc	HOMO-1	-6.710	59.06	0.00	39.40	2.77
	HOMO	-6.675	93.13	0.41	6.29	0.18
	SOMO	-5.502	93.13	0.41	6.29	0.18
	SOMO	-5.499	93.13	0.41	6.29	0.18
	LUMO	-4.626	2.87	30.23	65.13	1.78
	LUMO+1	-4.610	2.87	30.23	65.13	1.78

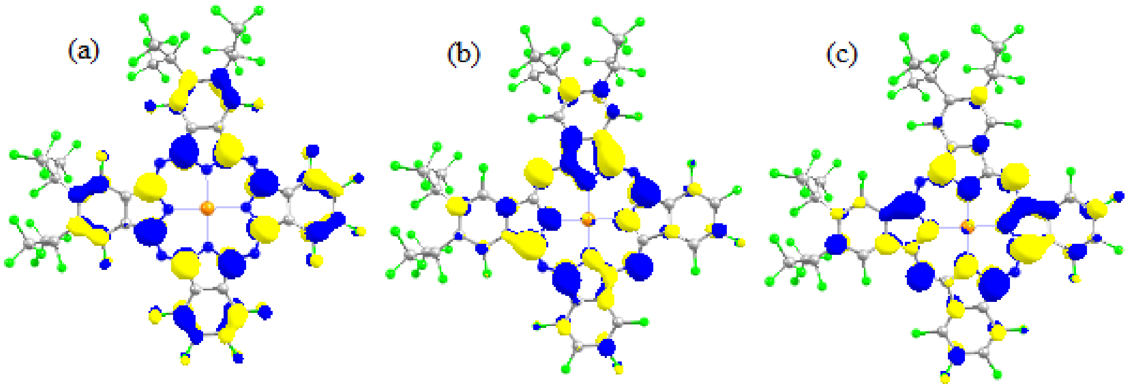

Figure C.14. Electron density distribution plots of $F_{40}ZnPc$ (a) HOMO, (b) LUMO, and (c) LUMO+1. Surfaces sampled at 0.03 e/au.

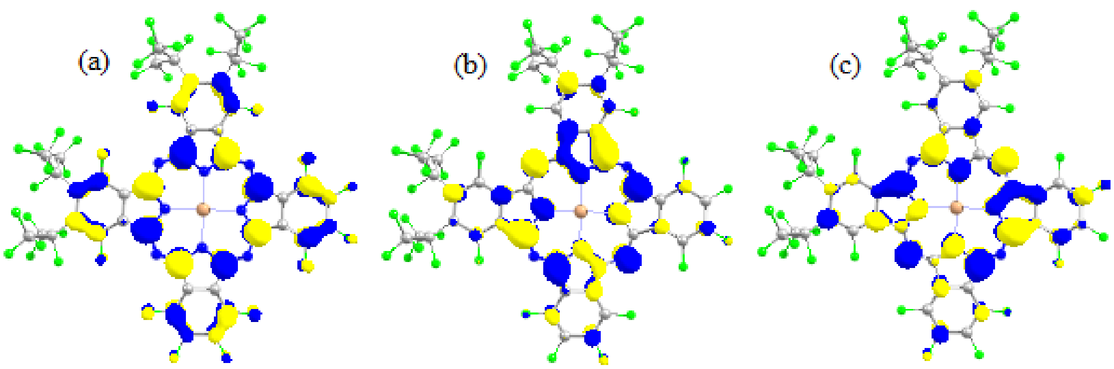

Figure C.15. Electron density distribution plots of $F_{40}MgPc$ (a) HOMO, (b) LUMO, and (c) LUMO+1. Surfaces sampled at 0.03 e/au.

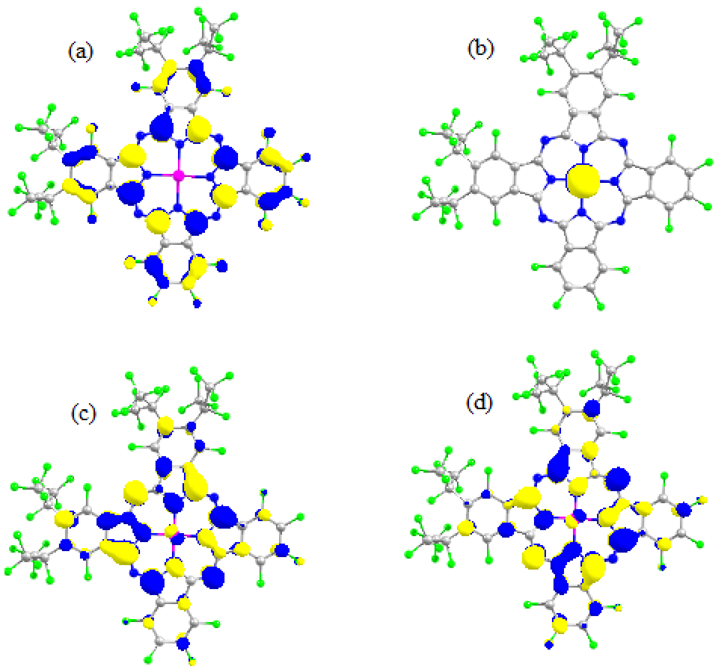

Figure C.16. Electron density distribution plots of $F_{40}CoPc$ (a) HOMO, (b) SOMO, (c) LUMO and (d) LUMO+1. Surfaces sampled at 0.03 e/au.

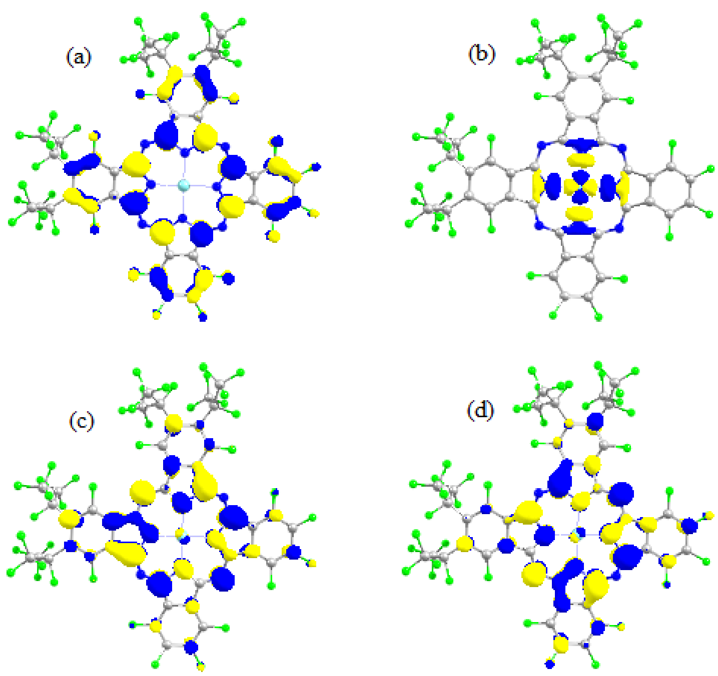

Figure C.17. Electron density distribution plots of $F_{40}CuPc$ (a) HOMO, (b) SOMO, (c) LUMO and (d) LUMO+1. Surfaces sampled at 0.03 e/au.

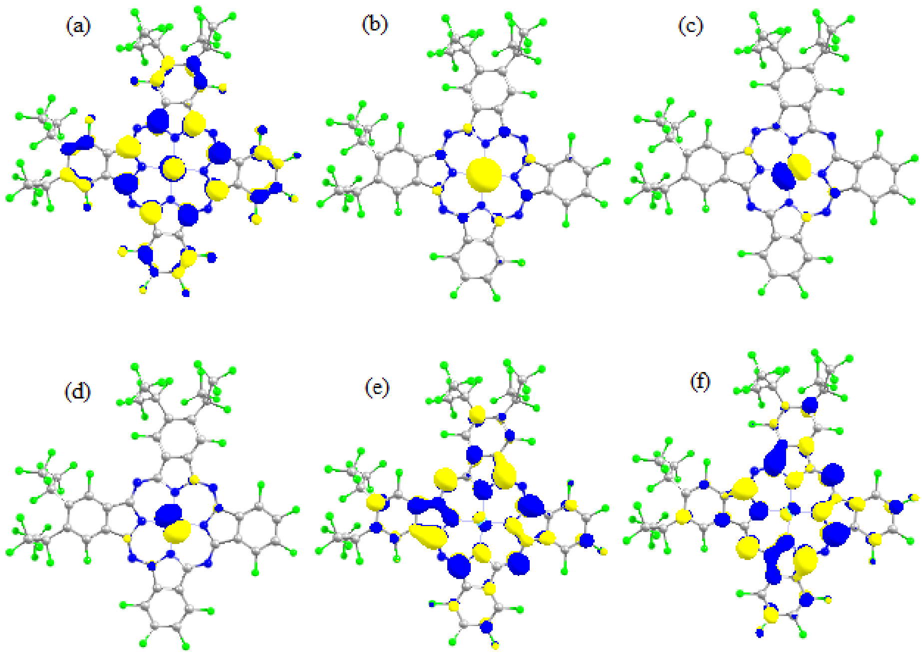

Figure C.18. Electron density distribution plots of $F_{40}FePc$ (a) HOMO-1, (b) HOMO, (c) SOMO (d) SOMO, (e) LUMO, and (f) LUMO+1. Surfaces sampled at 0.03 e/au.

The calculated DOS and PDOS of $F_{52}MPc$ are provided in Figure C.19. A summary of the energy and atom contributions of select MOs is also provided in Table C.4 with corresponding electron density plots illustrated in Figures C.20-24.

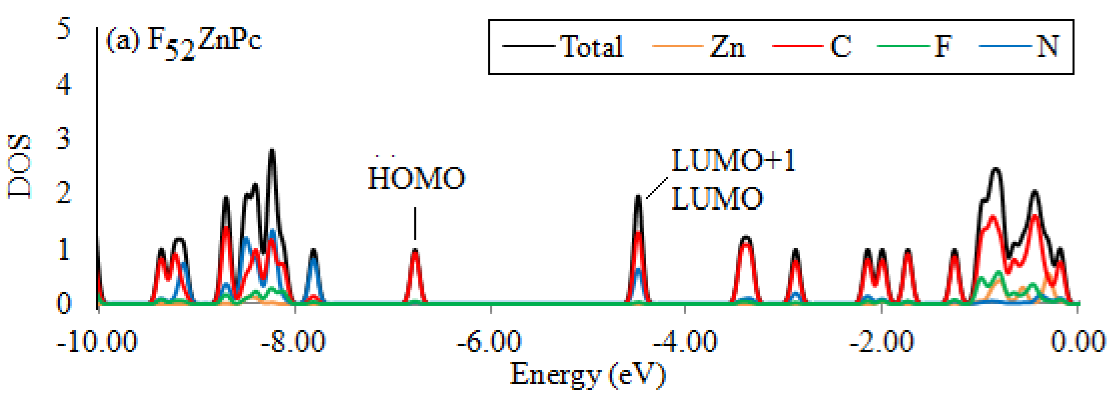

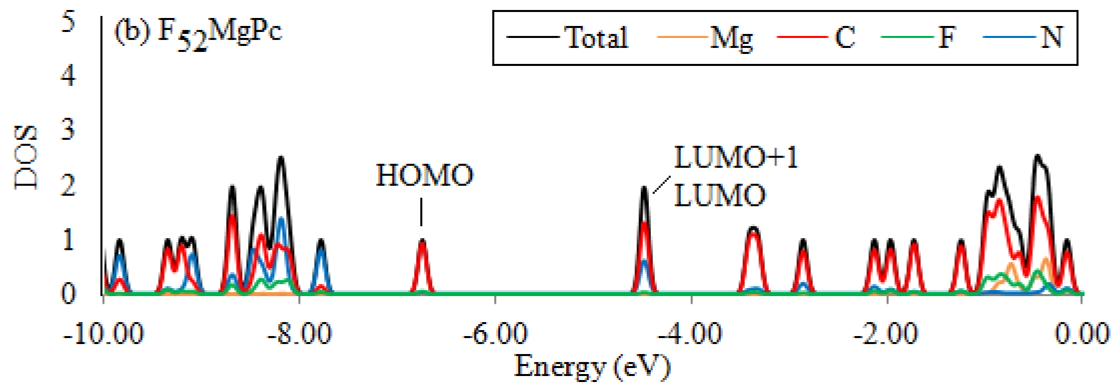
(b) F52MgPc
Total
Mg
C
F
N
DOS
HOMO
LUMO+1
LUMO
Energy (eV)
5
4
3
2
1
0
-10.00
-8.00
-6.00
-4.00
-2.00
0.00

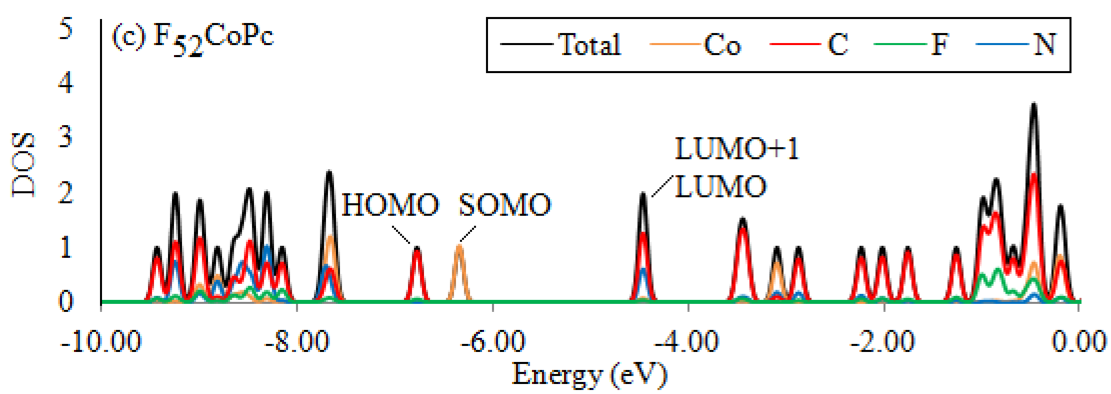
(c) F52CoPc
Total
Co
C
F
N
DOS
HOMO
SOMO
LUMO+1
LUMO
Energy (eV)
5
4
3
2
1
0
-10.00
-8.00
-6.00
-4.00
-2.00
0.00

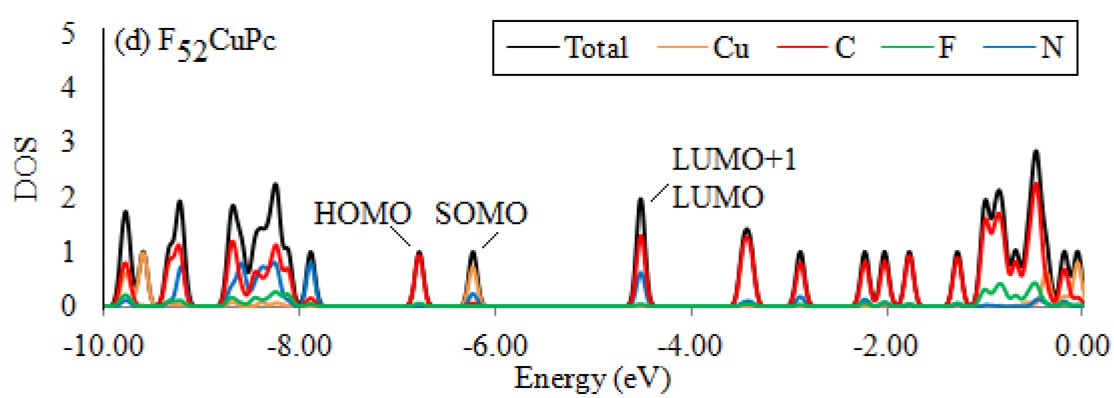
(d) F52CuPc
Total
Cu
C
F
N
DOS
HOMO
SOMO
LUMO+1
LUMO
Energy (eV)
5
4
3
2
1
0
-10.00
-8.00
-6.00
-4.00
-2.00
0.00

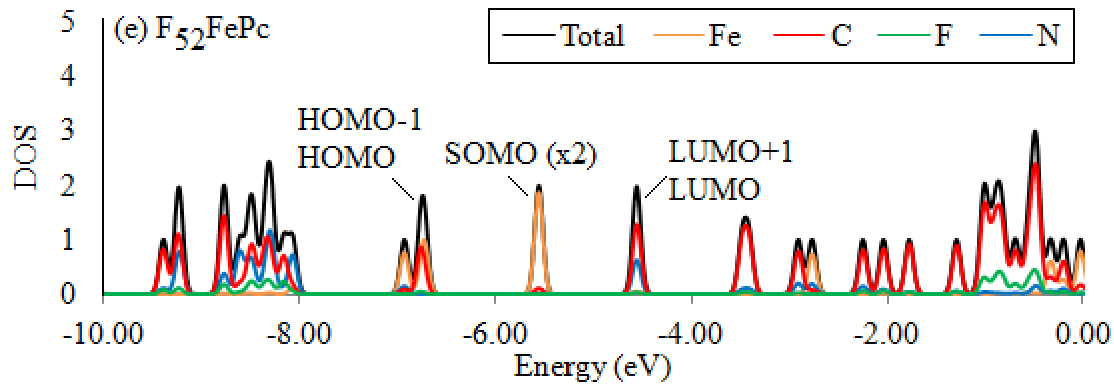

Figure C.19. DOS and PDOS of (a) F_{52}ZnPc, (b) F_{52}MgPc, (c) F_{52}CoPc, (d) F_{52}CuPc, and (e) F_{52}FePc.

Table C.4. Calculated energy and atom contributions of select MOs for F_{52}MPc

			% Contribution to MO			
Pc	MO	Energy(eV)	Zn	N	C	F
F_{52}ZnPc	HOMO	-6.787	0.02	1.47	92.93	5.56
	LUMO	-4.512	0.31	31.69	66.06	1.94
	LUMO+1	-4.442	0.31	31.69	66.06	1.94
F_{52}MgPc	HOMO	-6.759	0.02	1.47	93.05	5.47
	LUMO	-4.504	0.02	31.34	66.70	1.94
	LUMO+1	-4.487	0.02	31.34	66.70	1.94
F_{52}CoPc	HOMO	-6.787	0.64	1.40	92.19	5.77
	SOMO	-6.354	100.00	0.00	0.00	0.00
	LUMO	-4.476	3.48	31.47	63.20	1.85
	LUMO+1	-4.463	3.48	31.47	63.20	1.85
F_{52}CuPc	HOMO	-6.787	0.09	1.35	93.00	5.56
	SOMO	-6.237	70.54	23.74	5.66	0.07
	LUMO	-4.533	0.98	31.37	65.73	1.91
	LUMO+1	-4.517	0.98	31.37	65.73	1.91
F_{52}FePc	HOMO-1	-6.768	59.06	0.00	39.40	2.77
	HOMO	-6.729	93.13	0.41	6.29	0.18
	SOMO	-5.565	93.95	0.42	5.49	0.14
	SOMO	-5.557	93.95	0.42	5.49	0.14
	LUMO	-4.577	2.57	30.99	64.55	1.90
	LUMO+1	-4.563	2.57	30.99	64.55	1.90

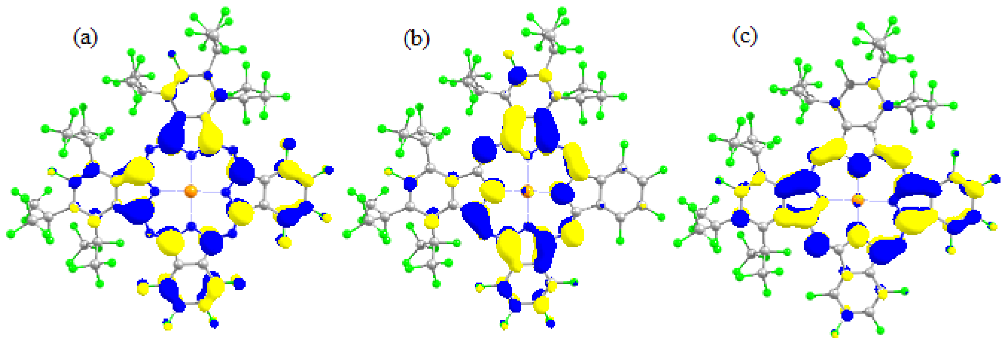

Figure C.20. Electron density distribution plots of $F_{52}ZnPc$ (a) HOMO, (b) LUMO, and (c) LUMO+1. Surfaces sampled at 0.03 e/au.

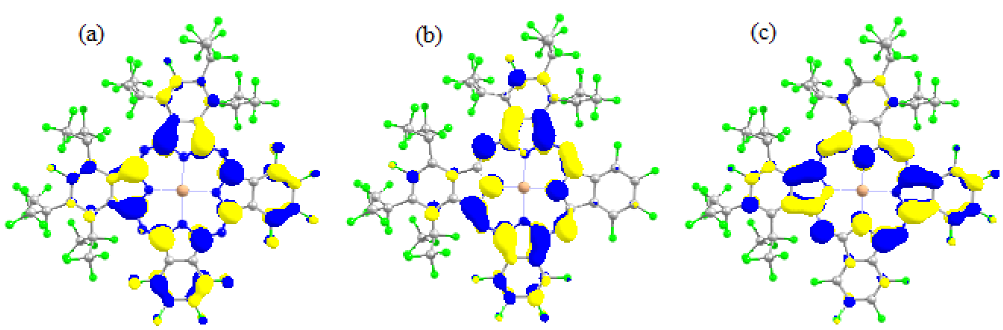

Figure C.21. Electron density distribution plots of $F_{52}MgPc$ (a) HOMO, (b) LUMO, and (c) LUMO+1. Surfaces sampled at 0.03 e/au.

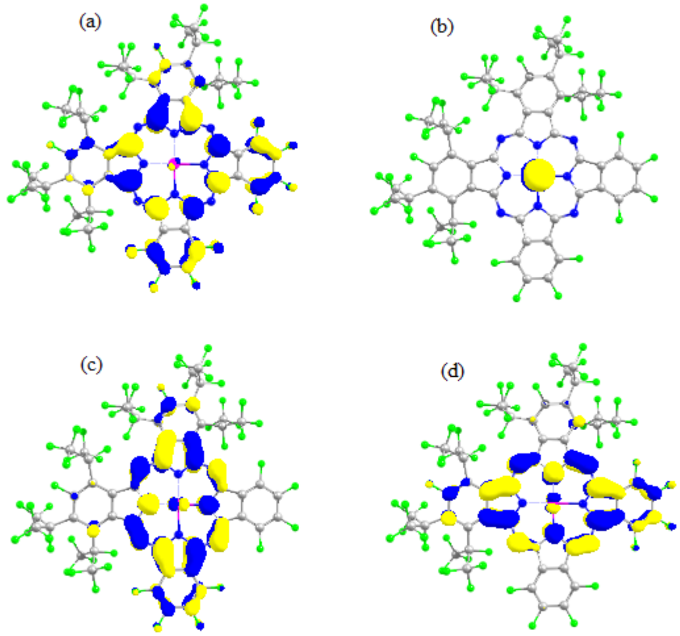

Figure C.22. Electron density distribution plots of $F_{52}CoPc$ (a) HOMO, (b) SOMO, (c) LUMO and (d) LUMO+1. Surfaces sampled at 0.03 e/au.

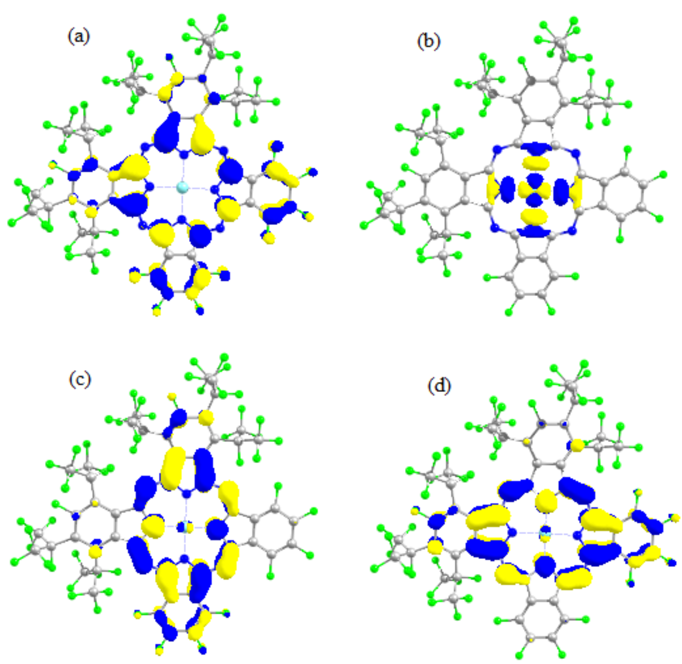

Figure C.23. Electron density distribution plots of $F_{52}CuPc$ (a) HOMO, (b) SOMO, (c) LUMO and (d) LUMO+1. Surfaces sampled at 0.03 e/au.

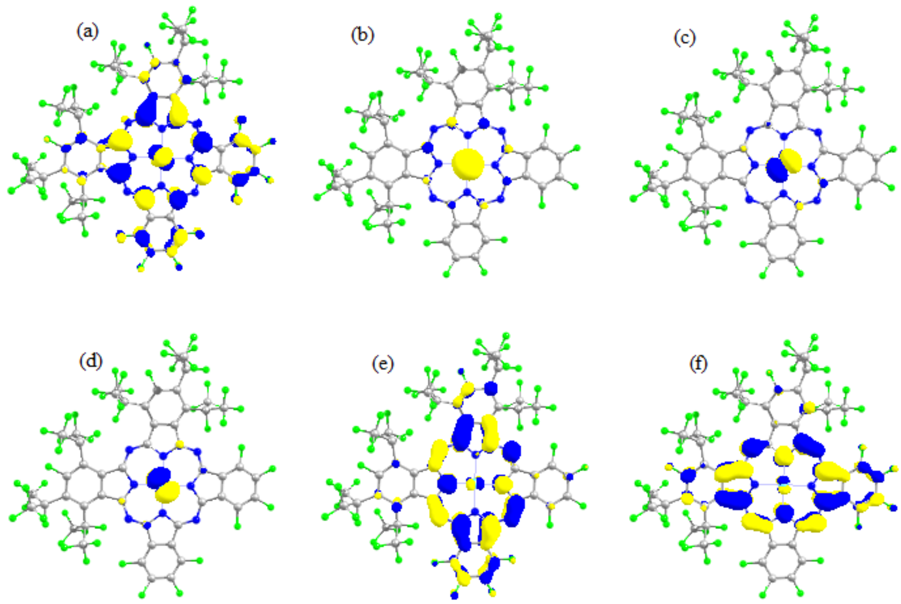

Figure C.24. Electron density distribution plots of $F_{52}FePc$ (a) HOMO-1, (b) HOMO, (c) SOMO (d) SOMO, (e) LUMO, and (f) LUMO+1. Surfaces sampled at 0.03 e/au.

The calculated DOS and PDOS of $F_{52a}MPc$ are provided in Figure C.25. A summary of the energy and atom contributions of select MOs is also provided in Table C.5 with corresponding electron density plots illustrated in Figures C.26-30.

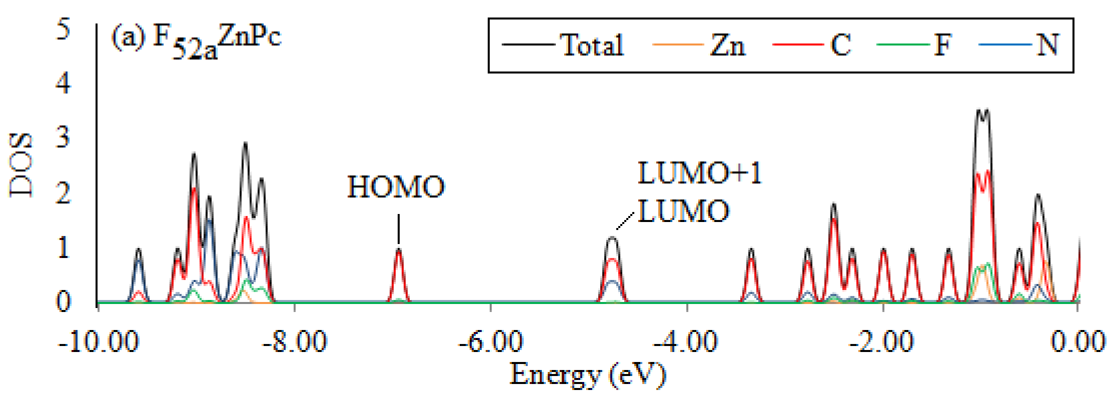

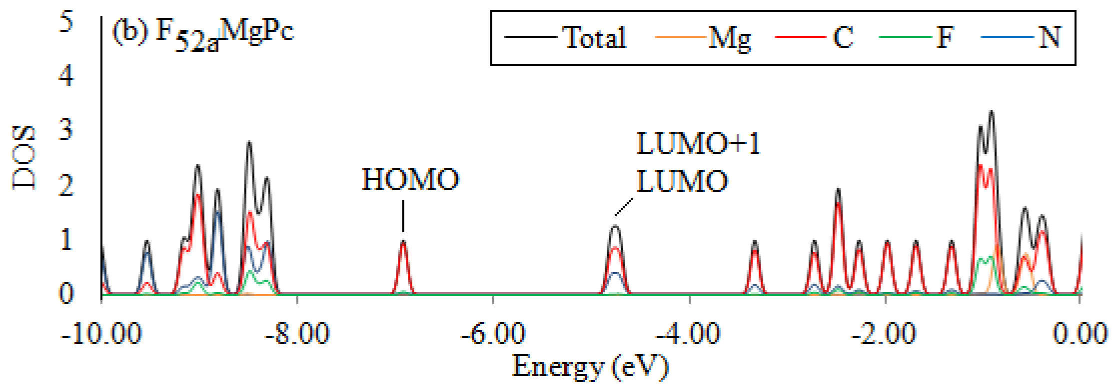
(b) F_{52a}MgPc
Total
Mg
C
F
N
DOS
HOMO
LUMO+1
LUMO
Energy (eV)

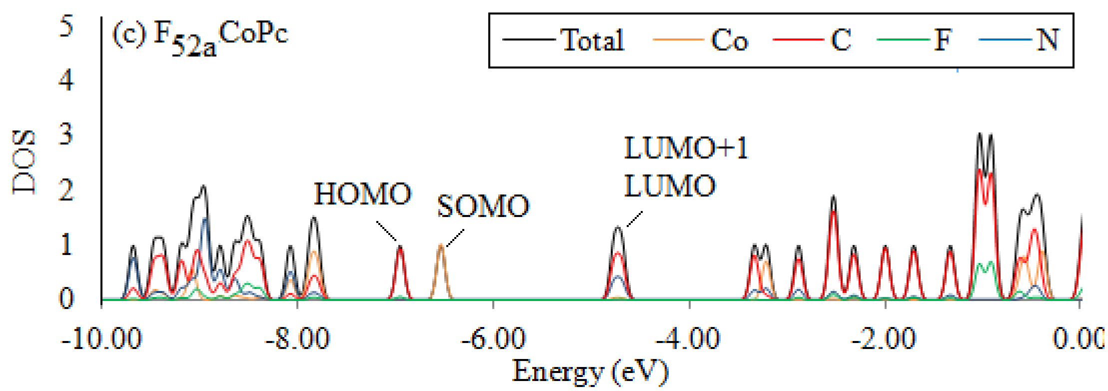
(c) F_{52a}CoPc
Total
Co
C
F
N
DOS
HOMO
SOMO
LUMO+1
LUMO
Energy (eV)

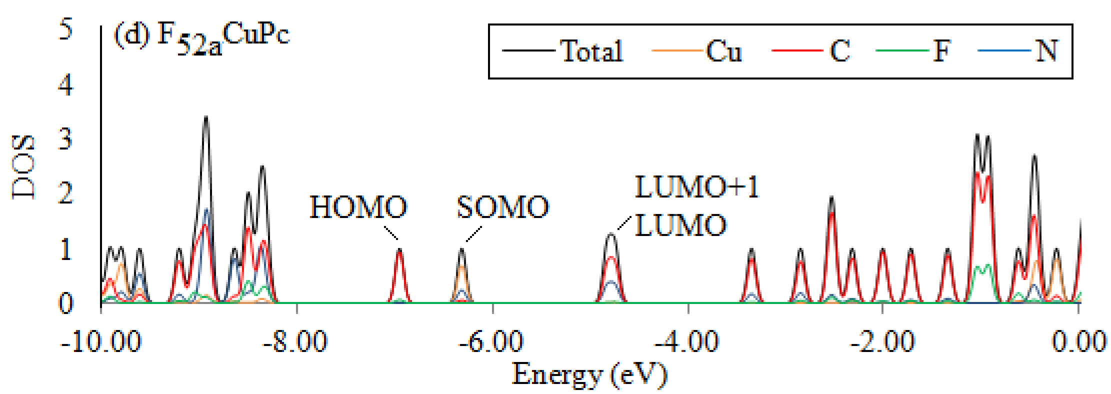
(d) F_{52a}CuPc
Total
Cu
C
F
N
DOS
HOMO
SOMO
LUMO+1
LUMO
Energy (eV)

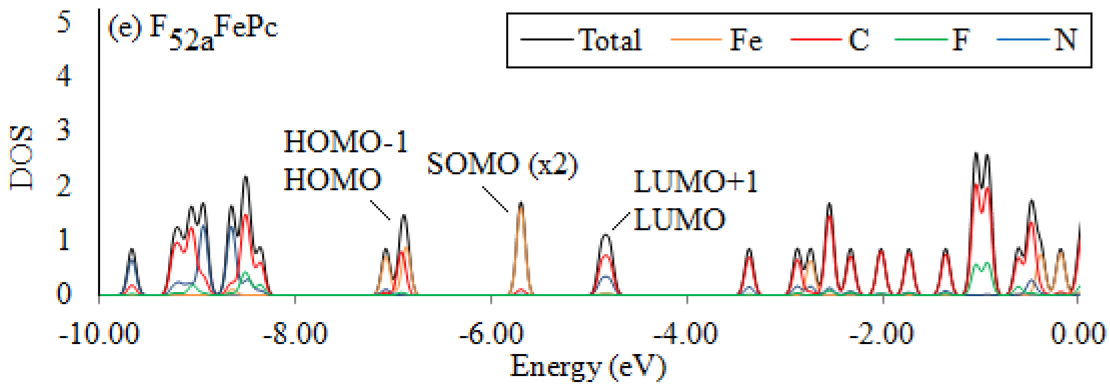

Figure C.25. DOS and PDOS of (a) F_{52a}ZnPc, (b) F_{52a}MgPc, (c) F_{52a}CoPc, (d) F_{52a}CuPc, and (e) F_{52a}FePc.

Table C.5. Calculated energy and atom contributions of select MOs for F_{52a}MPc

			% Contribution to MO			
Pc	MO	Energy(eV)	Zn	N	C	F
F_{52a}ZnPc	HOMO	-6.944	0.00	0.26	93.66	6.07
	LUMO	-4.811	0.31	31.10	67.45	1.15
	LUMO+1	-4.724	0.31	31.03	66.99	1.68
F_{52a}MgPc	HOMO	-6.923	0.00	0.26	93.73	6.00
	LUMO	-4.806	0.00	30.91	67.93	1.15
	LUMO+1	-4.724	0.00	30.78	67.54	1.67
F_{52a}CoPc	HOMO	-6.958	0.09	0.26	93.46	6.20
	SOMO	-6.542	100.00	0.00	0.00	0.00
	LUMO	-4.773	3.56	31.08	64.29	1.08
	LUMO+1	-4.697	3.55	30.98	63.95	1.51
F_{52a}CuPc	HOMO	-6.955	0.00	0.25	93.65	6.09
	SOMO	-6.319	70.30	24.03	5.63	0.04
	LUMO	-4.827	0.98	31.00	66.87	1.14
	LUMO+1	-4.745	0.99	30.90	66.46	1.66
F_{52a}FePc	HOMO-1	-6.920	59.06	0.00	39.40	2.77
	HOMO	-6.874	93.13	0.41	6.29	0.18
	SOMO	-5.740	93.26	0.39	6.19	0.15
	SOMO	-5.698	93.26	0.39	6.19	0.15
	LUMO	-4.874	2.80	30.45	65.49	1.25
	LUMO+1	-4.795	2.81	30.35	65.20	1.64

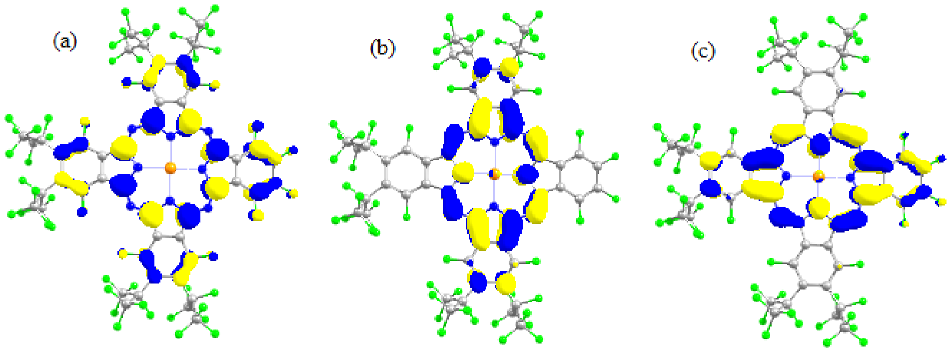

Figure A.26. Electron density distribution plots of $F_{52a}ZnPc$ (a) HOMO, (b) LUMO, and (c) LUMO+1. Surfaces sampled at 0.03 e/au.

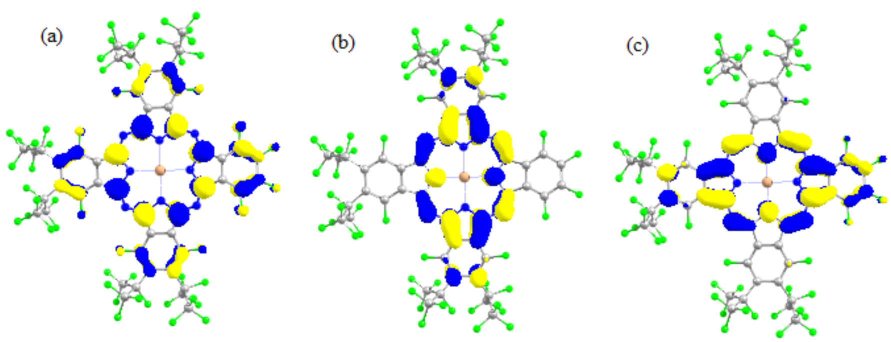

Figure A.27. Electron density distribution plots of $F_{52a}MgPc$ (a) HOMO, (b) LUMO, and (c) LUMO+1. Surfaces sampled at 0.03 e/au.

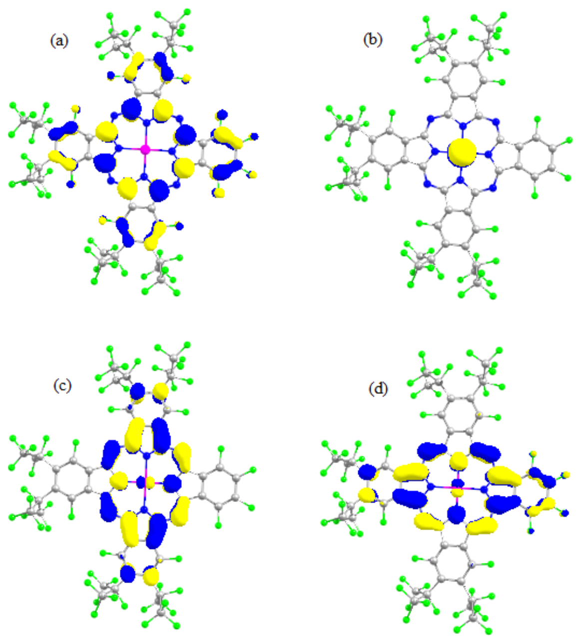

Figure A.28. Electron density distribution plots of $F_{52a}CoPc$ (a) HOMO, (b) SOMO, (c) LUMO and (d) LUMO+1. Surfaces sampled at 0.03 e/au.

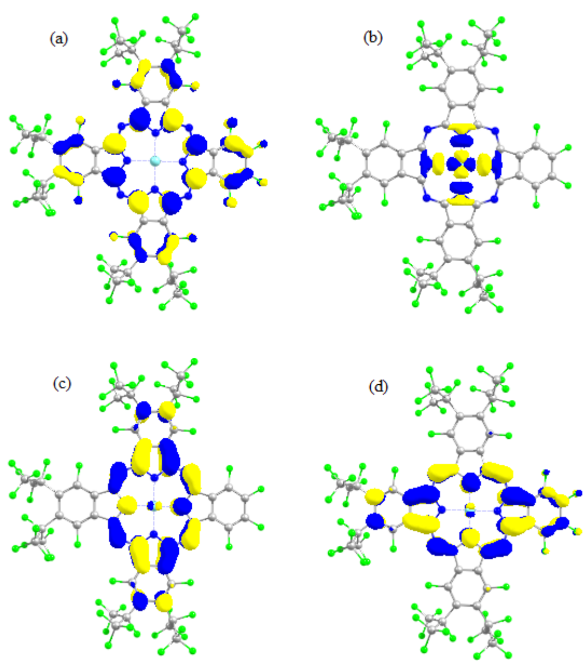

Figure A.29. Electron density distribution plots of $F_{52a}CuPc$ (a) HOMO, (b) SOMO, (c) LUMO and (d) LUMO+1. Surfaces sampled at 0.03 e/au.

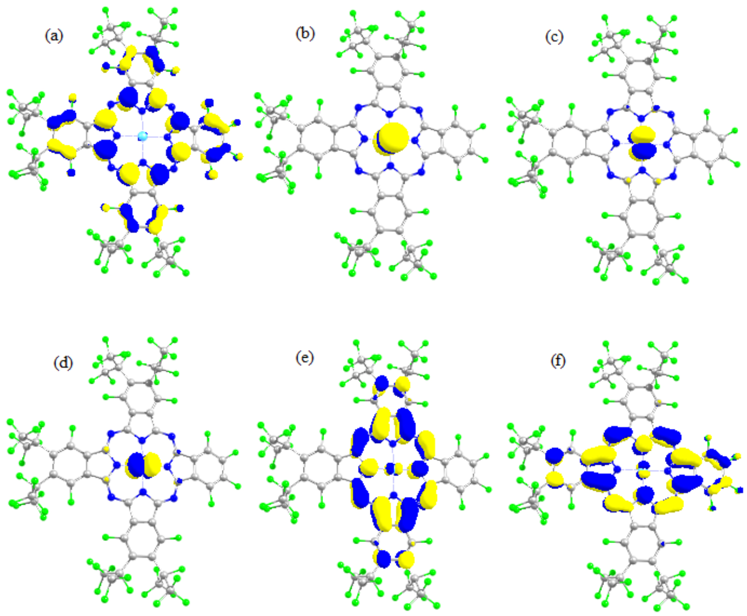

Figure A.30. Electron density distribution plots of F_{52a}FePc (a) HOMO-1, (b) HOMO, (c) SOMO (d) SOMO, (e) LUMO, and (f) LUMO+1. Surfaces sampled at 0.03 e/au.

The calculated DOS and PDOS of F_{64}MPc are provided in Figure C.31. A summary of the energy and atom contributions of select MOs is also provided in Table C.6 with corresponding electron density plots illustrated in Figures C.32-36

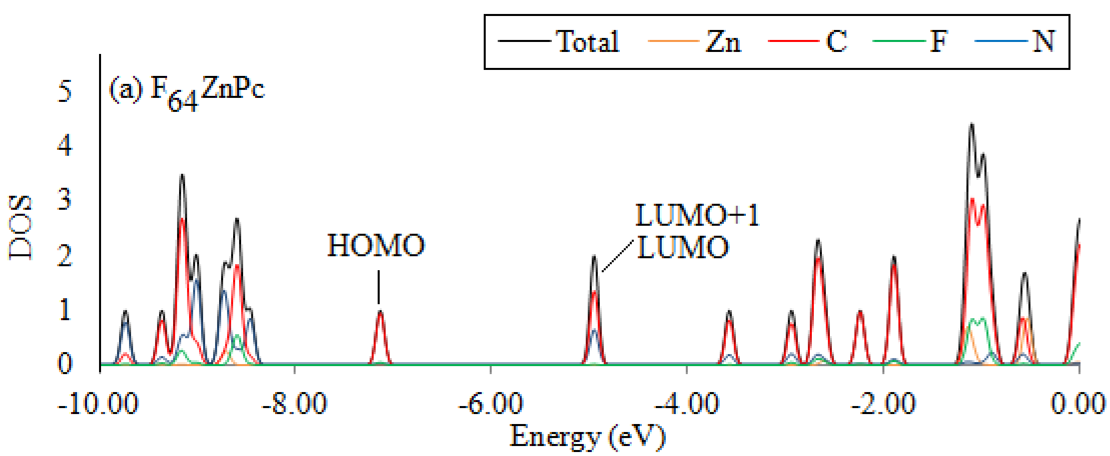

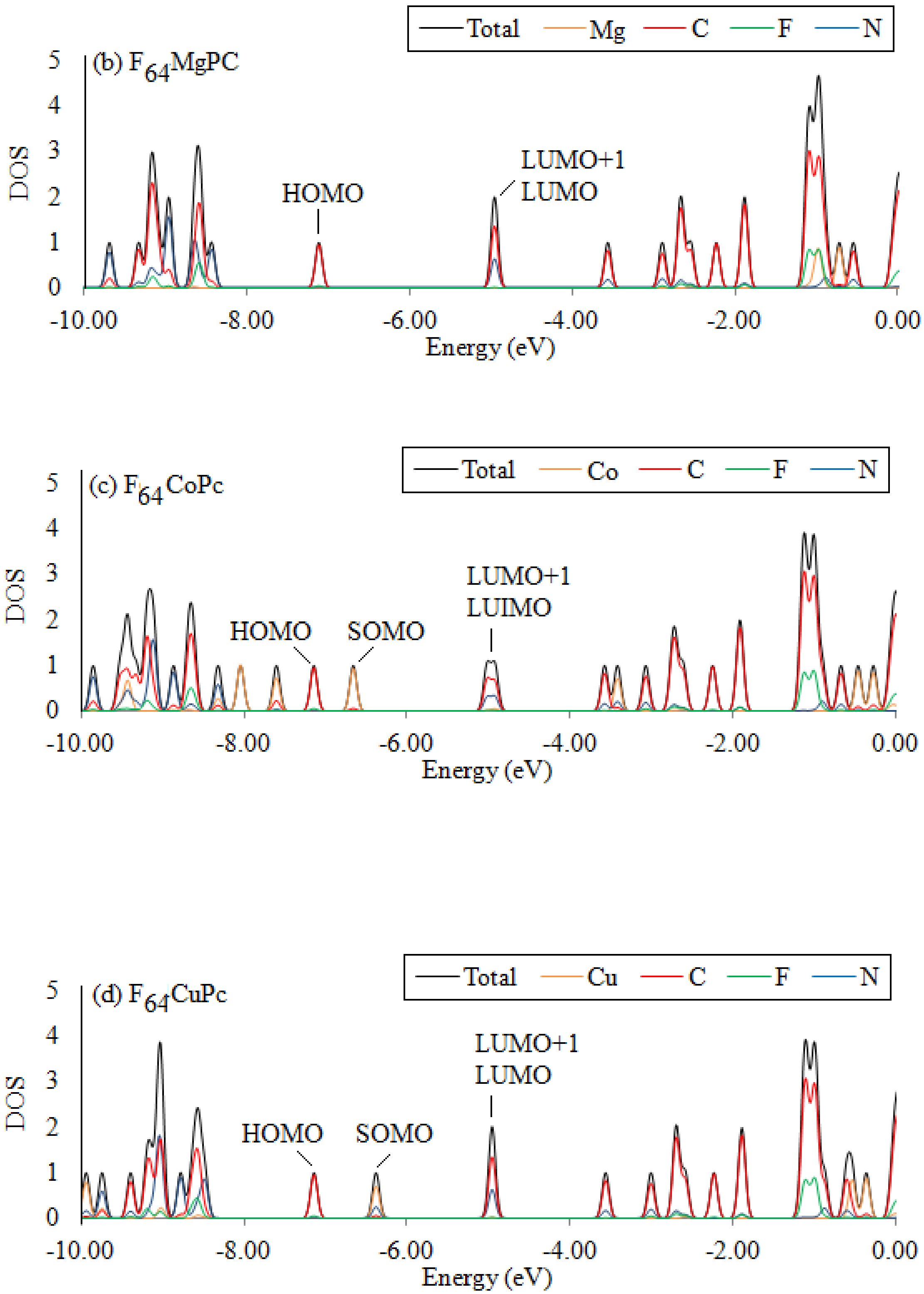
Total
Mg
C
F
N
(b) F64MgPC
DOS
HOMO
LUMO+1
LUMO
Energy (eV)
-10.00
-8.00
-6.00
-4.00
-2.00
0.00
Total
Co
C
F
N
(c) F64CoPc
DOS
HOMO
SOMO
LUMO+1
LUIMO
Energy (eV)
Total
Cu
C
F
N
(d) F64CuPc
DOS
HOMO
SOMO
LUMO+1
LUMO
Energy (eV)

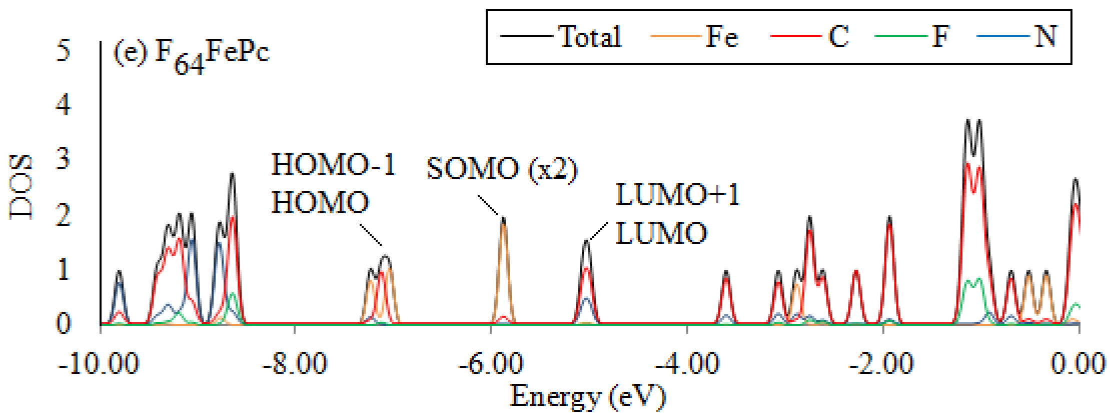

Figure C.31. DOS and PDOS of (a) F_{64}ZnPc, (b) F_{64}MgPc, (c) F_{64}CoPc, (d) F_{64}CuPc, and (e) F_{64}FePc.

Table C.6. Calculated energy and atom contributions of select MOs for F_{64}MPc.

			% Contribution to MO			
Pc	MO	Energy(eV)	Zn	N	C	F
F_{64}ZnPc	HOMO	-7.146	0.00	0.02	94.74	5.22
	LUMO	-4.961	0.31	31.25	67.44	0.99
	LUMO+1	-4.958	0.31	31.25	67.44	0.99
F_{64}MgPc	HOMO	-7.124	0.00	0.02	94.82	5.16
	LUMO	-4.963	0.00	31.06	67.94	1.00
	LUMO+1	-4.958	0.00	31.06	67.94	1.00
F_{64}CoPc	HOMO	-7.151	0.04	0.04	94.74	5.20
	SOMO	-6.667	93.84	0.56	5.50	0.12
	LUMO	-5.026	2.99	30.38	65.64	0.99
	LUMO+1	-4.931	2.99	30.38	65.64	0.99
F_{64}CuPc	HOMO	-7.154	0.00	0.03	94.76	5.22
	SOMO	-6.392	69.95	24.33	5.67	0.00
	LUMO	-4.972	1.06	31.11	66.83	1.00
	LUMO+1	-4.969	1.06	31.11	66.83	1.00
F_{64}FePc	HOMO-1	-7.123	31.38	0.00	65.72	3.47
	HOMO	-7.040	100.00	0.00	0.00	0.00
	SOMO	-5.883	93.05	0.39	6.44	0.13
	SOMO	-5.867	93.05	0.39	6.44	0.13
	LUMO	-5.059	2.86	30.56	65.60	0.98
	LUMO+1	-4.999	2.86	30.56	65.60	0.98

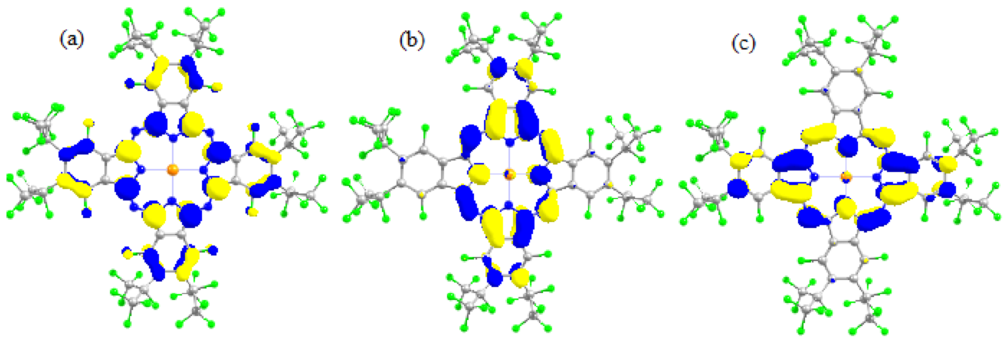

Figure C.32. Electron density distribution plots of $F_{64}ZnPc$ (a) HOMO, (b) LUMO, and (c) LUMO+1. Surfaces sampled at 0.03 e/au.

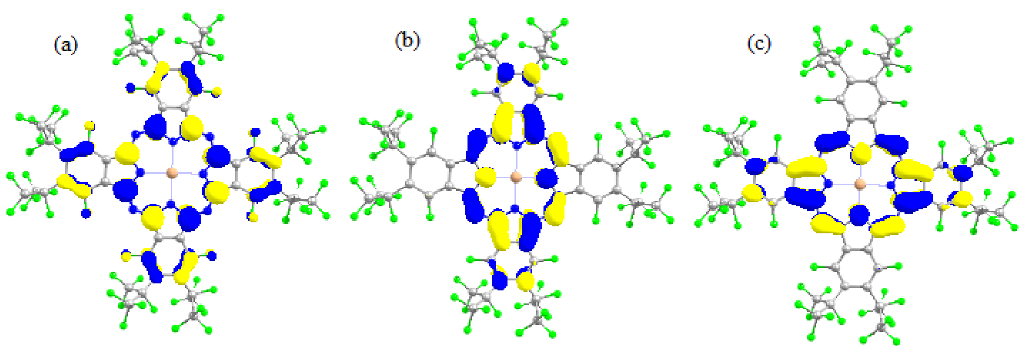

Figure C33. Electron density distribution plots of $F_{64}MgPc$ (a) HOMO, (b) LUMO, and (c) LUMO+1. Surfaces sampled at 0.03 e/au.

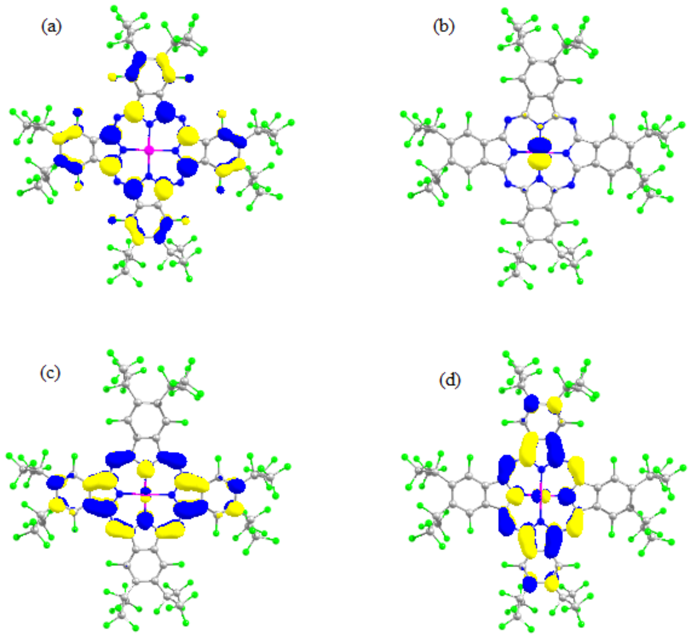

Figure C34. Electron density distribution plots of $F_{64}CoPc$ (a) HOMO, (b) SOMO, (c) LUMO and (d) LUMO+1. Surfaces sampled at 0.03 e/au.

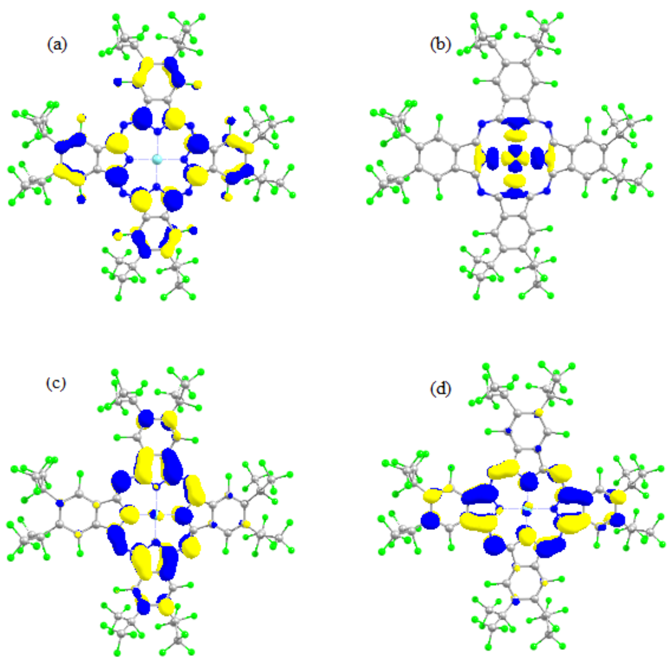

Figure C35. Electron density distribution plots of $F_{64}CuPc$ (a) HOMO, (b) SOMO, (c) LUMO and (d) LUMO+1. Surfaces sampled at 0.03 e/au.

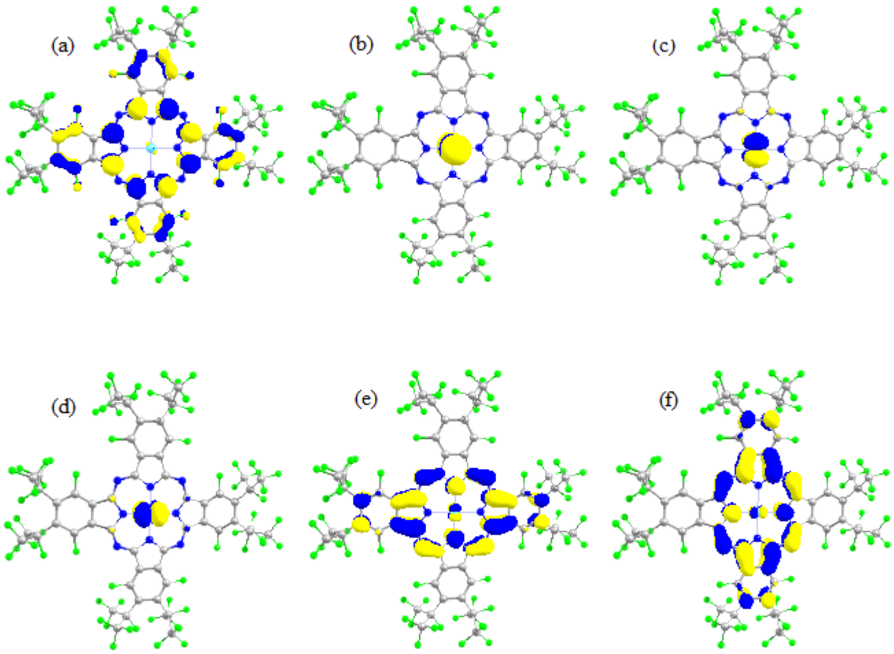

Figure C36. Electron density distribution plots of $F_{64}FePc$ (a) HOMO-1, (b) HOMO, (c) SOMO (d) SOMO, (e) LUMO, and (f) LUMO+1. Surfaces sampled at 0.03 e/au.

APPENDIX D

Supporting Information for All-Atom CHARMM Force Field Development

Given the symmetry of the phthalocyanine molecule, each atom was assigned an atom type according to the labeling schemes in Figure D.1.

$H_{16}ZnPc$

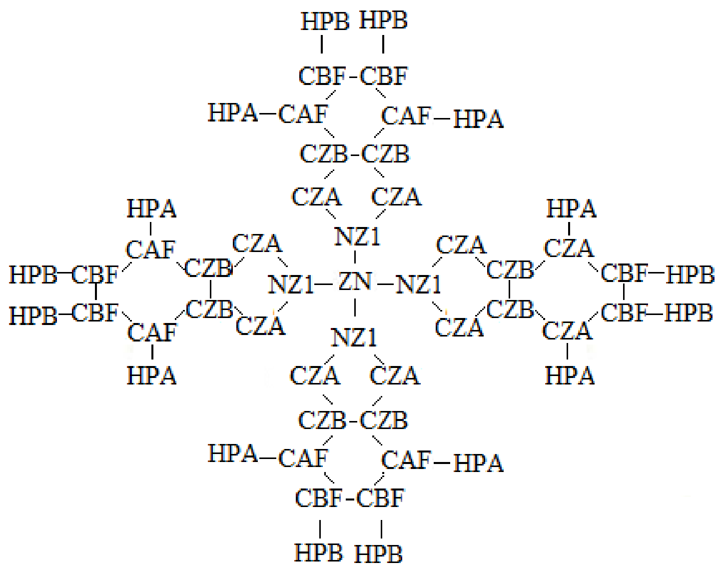

$F_{16}ZnPc$

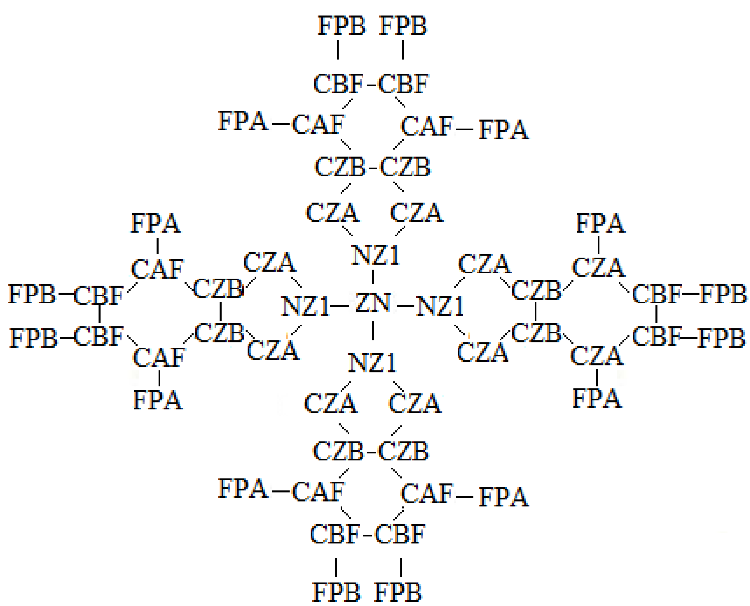

$F_{34}ZnPc$

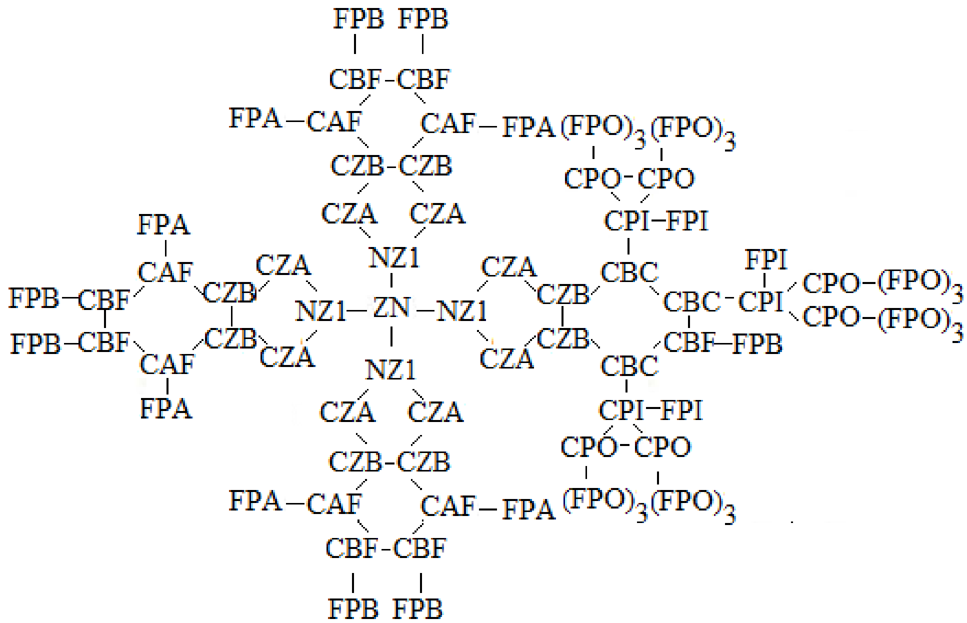

$F_{40}ZnPc$

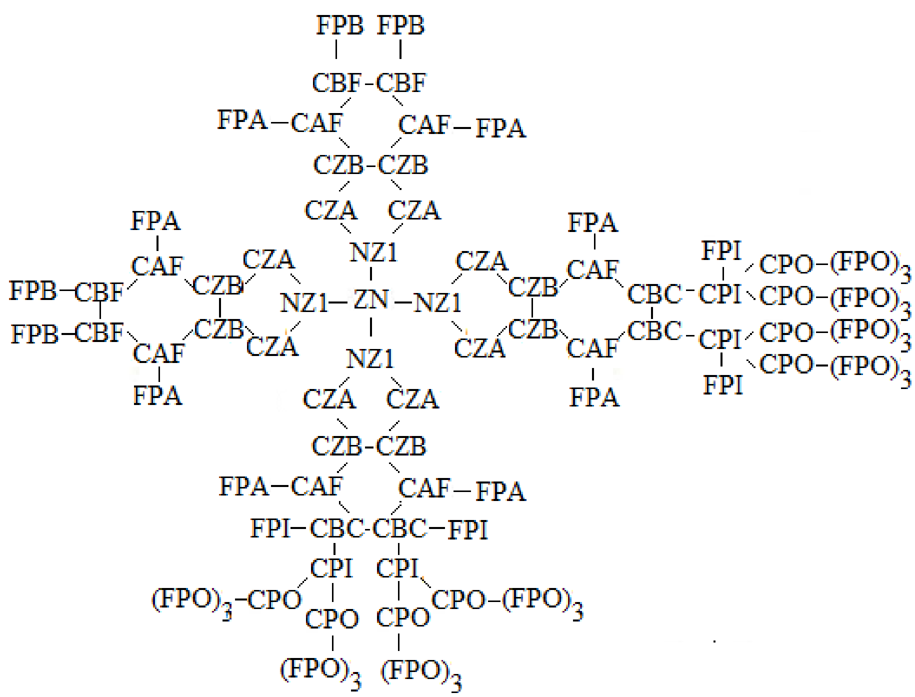

$F_{64}ZnPc$

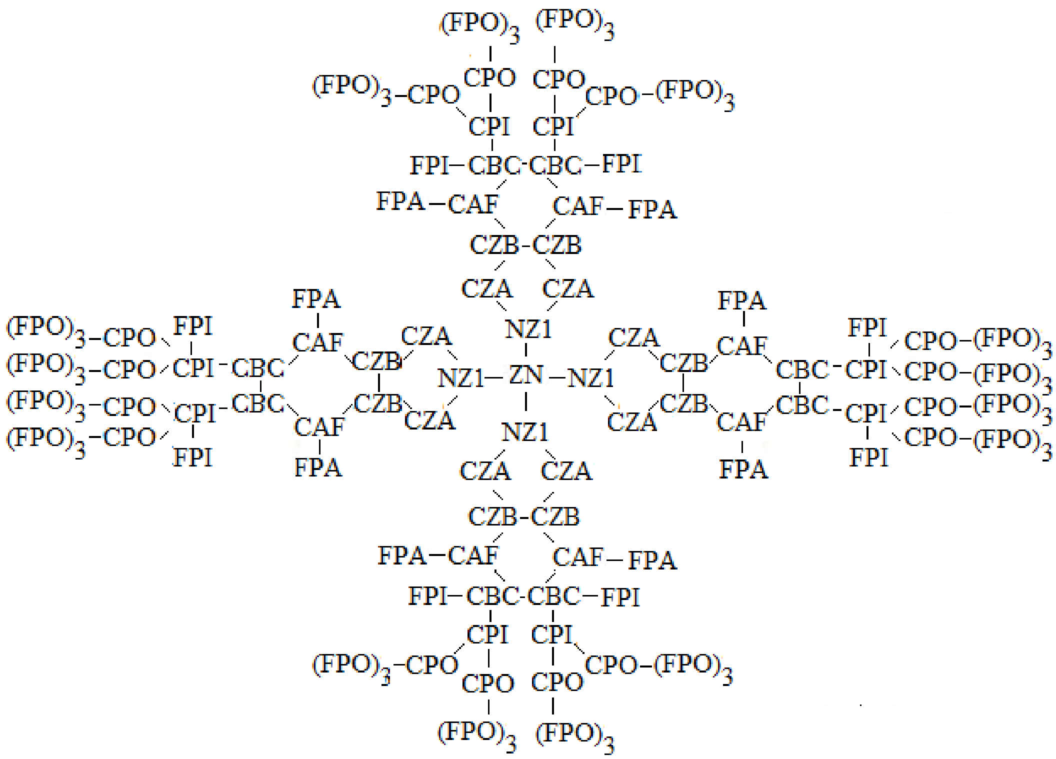

Figure D.1. Label schematics for force field atom types in $H_{16}ZnPc$, $F_{16}ZnPc$, $F_{34}ZnPc$, cis-$F_{40}ZnPc$, and $F_{64}ZnPc$.

Comparison of the molecular geometry obtained from the 6-31G and 6-31G* level of theory are presented in Table D.1. All 3-body angles are compared to available experimental XRD data. Given the computation cost of the increased basis set, only a fragment of the $F_{64}ZnPc$ molecule was optimized at the 6-31G* level. Indicated by the overall RMSD values, there is no significant improvement in the geometry when employing the expanded basis set.

Table D.1. Basis set 3-body angle comparison. Absolute percent deviation from XRD data.

Angle Type	XRD (°)	6-31G (%)	6-31G* (%)
$H_{16}ZnPc$			
NZ1-ZN-ZN1	90.000	0.110%	0.002%
NZ1-ZN-NZ1	179.980	2.635%	0.417%
ZN-NZ1-CZA	125.425	0.019%	0.358%
NZ1-CZA-NZ2	127.792	0.658%	0.267%
CZA-NZ1-CZA	109.114	0.023%	0.843%
CZA-NZ2-CZA	123.476	1.392%	1.350%
NZ1-CZA-CZB	108.887	0.178%	0.471%
NZ2-CZA-CZB	123.315	0.841%	0.694%
CZA-CZB-CZB	106.551	0.197%	0.052%
CZA-CZB-CAH	132.159	0.030%	0.196%
CZB-CZB-CAH	121.283	0.212%	0.256%
CZB-CAH-CBH	117.260	0.517%	0.555%
CAH-CBH-CBH	121.454	0.287%	0.280%
CZB-CAH-HPA	121.176	0.503%	0.462%
CBH-CAH-HPA	121.291	0.227%	0.150%
CAH-CBH-HPB	119.347	0.206%	0.234%
CBH-CBH-HPB	119.200	0.085%	0.047%
RMSD (°)	-	0.8252	0.5462
$F_{16}ZnPc$			
NZ1-ZN-ZN1	90.000	0.144%	0.666%
NZ1-ZN-NZ1	179.355	2.687%	6.186%
ZN-NZ1-CZA	125.362	0.117%	0.238%
NZ1-CZA-NZ2	129.107	1.531%	1.184%
CZA-NZ1-CZA	109.325	0.213%	0.306%
CZA-NZ2-CZA	120.972	3.585%	2.929%
NZ1-CZA-CZB	107.964	0.475%	0.680%
NZ2-CZA-CZB	122.871	1.235%	0.689%
CZA-CZB-CZB	107.388	0.598%	0.854%
CZA-CZB-CAF	132.070	0.643%	0.597%
CZB-CZB-CAF	120.468	0.112%	0.167%
CZB-CAF-CBF	119.297	0.346%	0.740%
CAF-CBF-CBF	120.112	0.559%	0.669%
CZB-CAF-FPA	122.069	0.163%	0.444%

CBF-CAF-FPA	118.557	0.245%	0.352%
CAF-CBF-FPB	121.751	1.306%	1.302%
CBF-CBF-FPB	117.903	0.978%	0.861%
RMSD (°)	-	1.3653	1.8024
F_{64}ZnPc fragment			
CZA-CZB-CZB	106.518	0.503%	1.717%
CZA-CZB-CAF	133.529	0.108%	1.536%
CZB-CZB-CAF	119.951	0.456%	0.232%
CZB-CAF-CBF	120.574	1.916%	1.685%
CAF-CBF-CBF	119.274	1.319%	0.533%
CZB-CAF-FPA	120.236	2.797%	2.568%
CBF-CAF-FPA	119.175	1.904%	2.154%
CBC-CBC-CPI	126.183	0.056%	0.065%
CAF-CBC-CPI	115.970	0.064%	0.106%
CBC-CPI-CPO	113.649	1.095%	0.613%
CBC-CPI-FPI	110.858	2.182%	1.606%
CPO-CPI-FPI	103.931	1.346%	1.265%
CPO-CPI-CPO	109.915	5.885%	5.733%
CPI-CPO-FPO	110.580	0.602%	0.218%
FPO-CPO-FPO	107.886	0.257%	0.150%
RMSD (°)	-	1.863	1.691

Table D.2 contains a listing comparing the atomic charges obtained using the 6-31G and 6-31G* basis set and the Mulliken and Merz-Kollman methods for atomic charge calculation.

Table D.2. Mulliken and MK Charge comparison.

Atom Type	**6-31G**		**6-31G***	
	Mulliken	**MK**	**Mulliken**	**MK**
H_{16}ZnPc				
ZN	1.040	0.7845	0.8910	0.8212
NZ1	-0.6835	-0.5978	-0.3383	-0.5845
NZ2	-0.3913	-0.7110	-0.2390	-0.6960
CZA	0.3468	0.6273	0.0623	0.58413

CZB	0.0291	-0.0921	0.0968	-0.0736
CAH	-0.1184	-0.0811	-0.1021	-0.1084
CBH	-0.1330	-0.1159	-0.1075	-0.1163
HPA	0.1559	0.1186	0.1174	0.1227
HPB	0.1302	0.1188	0.1110	0.1192
F_{16}ZnPc				
ZN	1.040	0.9975	1.252	0.8104
NZ1	-0.680	-0.8889	-0.9065	-0.6911
NZ2	-0.334	-0.7675	-0.632	-0.6722
CZA	0.359	0.9054	0.6473	0.7500
CZB	0.035	-0.3655	-0.155	-0.2986
CAF	0.248	0.3329	0.344	0.2636
CBF	0.276	0.1565	0.232	0.1079
FPA	-0.264	-0.1799	-0.224	-0.1240
FPB	-0.277	-0.1584	-0.234	-0.1073

Table D.3 shows the atomic charges used in the final force field model. Minor adjustments were made to achieve overall charge neutrality of the phthalocyanine molecule

Table D.3: Force Field Atomic Charges.

Atom	Charge				
Type	H_{16}ZnPc	F_{16}ZnPc	F_{34}ZnPc	F_{40}ZnPc	F_{64}ZnPc
ZN	0.788	0.996	0.996	0.996	0.996
NZ1	-0.596	-0.889	-0.889	-0.889	-0.889
NZ2	-0.709	-0.768	-0.768	-0.768	-0.768
CZA	0.632	0.904	0.904	0.904	0.904
CZB	-0.090	-0.366	-0.366	-0.366	-0.366
CAF*	-0.093	0.332	0.332	0.332	0.332
CBF*	-0.143	0.174	0.174	0.174	0.174
CPI	-	-	-0.117	-0.121	-0.121
CPO	-	-	0.736	0.719	0.719
CBC	-	-	-0.110	-0.110	-0.110
FPA*	0.124	-0.181	-0.181	-0.181	-0.181

FPB*	0.124	-0.159	-0.159	-0.159	-0.159
FPI	-	-	-0.148	-0.148	-0.148
FPO	-	-	-0.174	-0.174	-0.174

*Note: For H_{16} system, atom types CAF, CBF. FPA, and FPB are replaced with CAH, CBH, HPA, and HPB respectively

Tables D.4, D.5, and D.6 contain the non-bonded, bonded 2-body, and 3-body angle parameters for the force field respectively.

Table D.4: Force Field Non-bonded Parameters

Atom Type	ε	R_{min}
ZN	-0.2500	1.0900
NZ1	-0.1100	2.0000
NZ2	-0.2000	1.8500
CZA	-0.0900	1.8000
CZB	-0.0900	1.8000
CAF	-0.0700	1.9924
CBF	-0.0700	1.9924
CBC	-0.0700	1.9924
CPI	-0.0800	1.8880
CPO	-0.0200	2.3000
FPA	-0.1200	1.7000
FPB	-0.1200	1.7000
FPI	-0.1350	1.6300
FPO	-0.0970	1.6000
CAH	-0.0700	1.9924
CBH	-0.0700	1.9924
HPA	-0.0300	1.3582
HPB	-0.0300	1.3582

Table D.5: Bond Parameters

Bond Type	K_b	b_0
ZN-NZ1	300.00	1.9400
NZ1-CZA	270.00	1.3847
CZA-CZB	350.00	1.4592
CZA-NZ2	400.00	1.3310
CZB-CZB	360.00	1.4215
CZB-CAF	305.00	1.3908
CZB-CBC	305.00	1.3908
CAF-CBF	305.00	1.3941
CAF-CBC	305.00	1.3941
CBC-CBF	305.00	1.3941
CAF-FPA	349.00	1.3716
CBF-FPB	349.00	1.3728
CBF-CBF	305.00	1.3994
CBC-CBC	305.00	1.3994
CZB-CAH	305.00	1.3963
CAH-CBH	305.00	1.3976
CAH-HPA	340.00	1.0840
CBH-HPB	340.00	1.0850
CBH-CBH	305.00	1.4110
CBC-CPI	300.00	1.5410
CAF-CPI	300.00	1.5495
CPI-CPO	270.00	1.5698
CPI-FPI	420.00	1.4167
CPO-FPO	265.00	1.3799

Table D.6: Force Field Angle Parameters

Angle Type	K_θ	θ_0
NZ1-ZN-NZ1	14.39	180.0000
ZN-NZ1-CZA	96.15	125.2150
NZ1-CZA-CZB	122.00	108.4775
NZ1-CZA-NZ2	88.00	127.1300
NZ2-CZA-CZB	61.60	124.3888
CZA-CZB-CZB	90.00	106.7675
CZA-CZB-CAF	160.00	132.9150
CZA-CZB-CBC	160.00	132.9150
CZA-NZ2-CZA	94.20	125.3075
CZA-NZ1-CZA	139.30	109.5550
CZB-CAF-CBF	60.00	118.8875
CZB-CAF-CBC	60.00	118.8875
CZB-CZB-CAF	60.00	120.3525
CZB-CZB-CBC	60.00	120.3525
CZB-CBC-CBC	60.00	118.8875
CZB-CBC-CBF	60.00	118.8875
CZB-CAF-FPA	50.00	122.2700
CZB-CBC-CPI	150.00	125.7370
CAF-CBF-CBF	40.00	120.8100
CAF-CBC-CBC	40.00	120.8100
CAF-CBF-FPB	50.00	120.1613
CAF-CBF-CPI	150.00	127.0750
CAF-CBC-CPI	150.00	127.0750
CBC-CBC-CBF	40.00	120.8100
CBC-CBF-CBC	40.00	120.8100
CBC-CBC-CPI	150.00	114.4000
CBC-CPI-CPO	90.00	114.8540
CBC-CPI-FPI	60.00	108.6130
CBF-CBF-FPB	50.00	119.0563
CBF-CAF-FPA	50.00	118.8475
CBC-CBF-FPB	50.00	120.1613
CBF-CBC-CPI	150.00	114.4000
CPI-CPO-FPO	60.00	111.3288
CPO-CPI-CPO	90.00	116.4680
FPI-CPI-CPO	60.00	99.36720
FPO-CPO-FPO	60.00	107.5157

CAH-CBH-CBH	40.00	121.1000
CAH-CZB-CZB	60.00	121.0750
CZB-CAH-CBH	60.00	117.9000
CAH-CZB-CZA	160.00	132.2500
CBH-CAH-HPA	29.00	121.6525
CBH-CBH-HPB	29.00	119.3125
CAH-CBH-HPB	29.00	119.6125
CZB-CAH-HPA	29.00	120.5625

To maintain the planar geometry of all Pc's shown in the DFT calculations, dihedral parameters were imposed on the central ring structure. The remaining periphery perfluoro-isopropyl groups were parameterized following the FUERZA method.[250] The method was applied to acquire dihedral parameters for which no published relevant analogs are available. A hessian calculation was performed on quarter sections of the F_{34}ZnPc and the F_{40}ZnPc. The broken bonds in these fragments were terminated with hydrogen on the NZ2-type nitrogen links. Following DFT B3LYP/6-31G energy minimization and determination of the second derivative force matrices; the dihedral force constants were extracted. Dihedral multiplicities were selected that best mimic available crystal data. To maintain reasonable force constants the values acquired from the DFT calculations were scaled relative the existing values obtained along the central ring. The resulting dihedral angle parameters are shown in Table D.7.

Table D.7: Force Field Dihedral Parameters

Dihedral Type	K_φ	φ_0	n
NZ1-CZA-NZ2-CZ1	18.30	180.00	2
NZ1-CZA-CZB-CZB	14.00	180.00	2
NZ1-CZA-CZB-CAF	14.00	180.00	2
NZ1-CZA-CZB-CBC	14.00	180.00	2

NZ2-CZA-NZ1-CZA	14.00	180.00	2
NZ2-CZA-CZB-CZB	3.00	180.00	2
NZ2-CZA-CZB-CAF	3.00	180.00	2
NZ2-CZA-CZB-CBC	3.00	180.00	2
CZA-NZ2-CZA-CZB	14.00	180.00	2
CZA-CZB-CZB-CZA	3.10	180.00	2
CZA-CZB-CZB-CAF	3.10	180.00	2
CZA-CZB-CZB-CBC	3.10	180.00	2
CZA-CZB-CAF-CBF	3.10	180.00	2
CZA-CZB-CAF-CBC	3.10	180.00	2
CZA-CZB-CBC-CBC	3.10	180.00	2
CZA-CZB-CBC-CBF	3.10	180.00	2
CZA-CZB-CAF-FPA	4.20 (3.00)	180.00	2
CZB-CZA-NZ1-CZA	14.00	180.00	2
CZB-CZB-CAF-CBF	3.10	180.00	2
CZB-CZB-CAF-CBC	3.10	180.00	2
CZB-CZB-CBC-CBC	3.10	180.00	2
CZB-CZB-CBC-CBF	3.10	180.00	2
CZB-CZB-CAF-FPA	4.20 (3.00)	180.00	2
CZB-CAF-CBF-CBF	3.10	180.00	2
CZB-CAF-CBC-CBC	3.10	180.00	2
CZB-CBC-CBF-CBC	3.10	180.00	2
CZB-CAF-CBF-FPB	4.20 (3.50)	180.00	2
CZB-CBC-CBF-FPB	4.20	180.00	2
CAF-CBF-CBF-CAF	3.10	180.00	2
CAF-CBC-CBC-CAF	3.10	180.00	2
CAF-CBF-CBF-FPB	4.20 (3.50)	180.00	2
CBC-CBC-CBF-CBC	3.10	180.00	2
CBC-CBC-CBF-FPB	4.20	180.00	2
CBF-CBF-CAF-FPA	4.20 (3.50)	180.00	2
CBC-CBC-CAF-FPA	4.20	180.00	2
FPA-CAF-CBF-FPB	2.40 (2.50)	180.00	2
FPB-CBF-CBF-FPB	2.40 (2.50)	180.00	2
CPI-CBC-CZB-CZA	11.5	0.00	2
CPI-CBC-CZB-CZB	14.0	180.00	2
CPI-CBC-CBC-CBF	12.8	180.00	2
CPI-CBC-BCF-CBC	12.8	180.00	2
CPI-CBC-CBF-FPB	15.3	0.00	2
CPI-CBC-CBF-FPB	15.7	0.00	2

CPI-CBC-CBC-CPI	11.5	0.00	2
CPI-CBC-CAF-CZB	12.2	180.00	2
CPI-CBC-CAF-FPA	11.0	0.00	2
CPI-CBC-CBC-CAF	11.9	180.00	2
FPI-CPI-CBC-CZB	15.8	0.00	2
FPI-CPI-CBC-CBF	15.5	180.00	2
FPI-CPI-CBC-CAF	14.9	180.00	2
FPI-CPI-CBC-CBC	13.4	0.00	2
CPO-CPI-CBC-CZB	11.9	0.00	6
CPO-CPI-CBC-CBF	11.7	0.00	6
CPO-CPI-CBC-CAF	12.6	0.00	6
CPO-CPI-CBC-CBC	11.1	0.00	6
FPO-CPO-CPI-CBC	10.5	0.00	6
FPO-CPO-CPI-FPI	10.5	0.00	6
FPO-CPO-CPI-CPO	9.8	0.00	6

*****Note: For H_{16}ZnPc parameter for H instead of F in parenthesis

APPENDIX E

DOS, PDOS, and Lorentzian Distribution of F_xZnPc on CdTe, GaAs, InAs, Si, and SiC

As discussed in Chapter 4, the high VB of NiO is located near the LUMO of F_xZnPc. This could lead to increased charge recombination at the NiO surface. Several additional p-type semiconductors with slightly lower VB were investigated as potential alternatives to NiO. These semiconductors include; AlAs, Cdte, GaAS, InAs, Si, and SiC. Discussion on the potential of these semiconductor's application as photocathodes in FxZnPc based DSSCs is presented in Chapter 4. The optimized structures of these systems, DOS, PDOS, and Lorentzian distribution of the HOMO(ads) supporting the discussion are presented below. All of these figures are generated from semiempirical PM7 calculations.

The optimized structure, DOS, and PDOS for the F_xZnPc | AlAs systems are illustrated in Figures E.1-2. There is not orbital coupling in these systems so a Lorentzian distribution of the HOMO(ads) is not provided.

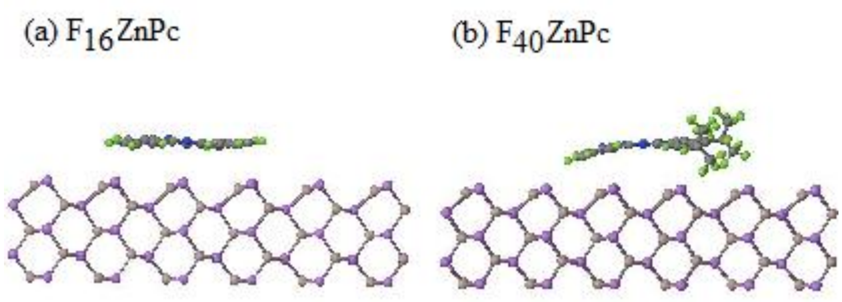

Figure E.1. PM7 Geometry Optimized Structure of F_xZnPc | AlAs Systems: (a) F_{16}ZnPc, (b) F_{40}ZnPc.

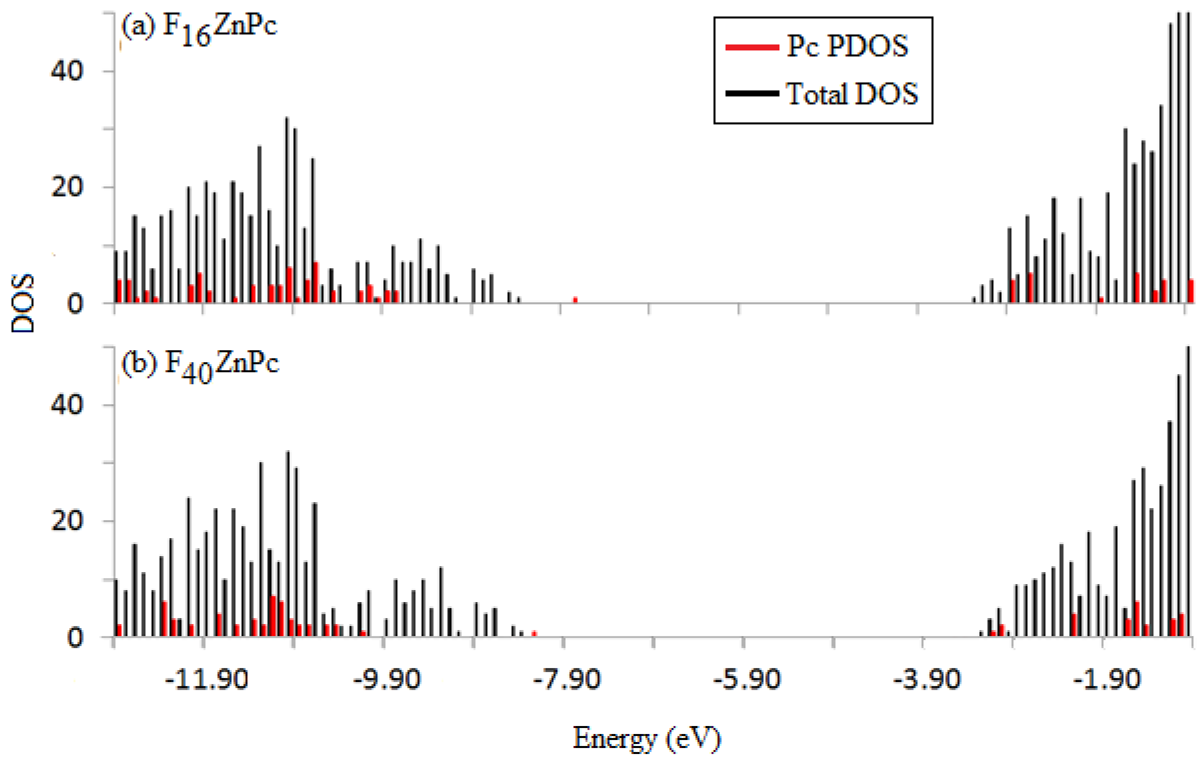

Figure E.2. PM7 Calculated DOS of AlAs (black lines) and F_xZnPc PDOS (red lines); a) $F_{16}ZnPc$ and b) $F_{40}ZnPc$

The optimized structure, DOS, and PDOS for the F_xZnPc | CdTe systems are illustrated in Figures E.3-4. Lorentzian distribution of the $F_{40}ZnPc$ Pc HOMO(ads) is illustrated in Figure E.5.

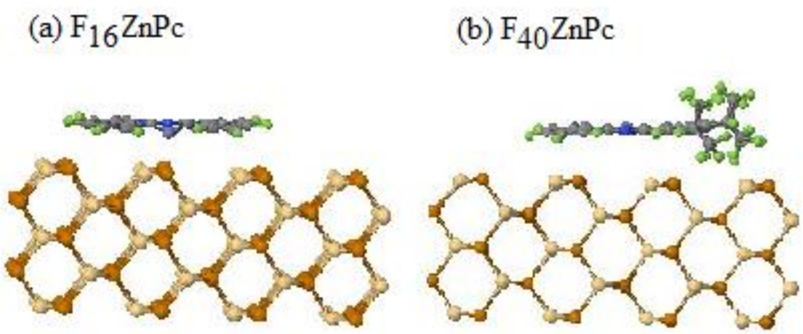

Figure E.3. PM7 Geometry Optimized Structure of F_xZnPc | CdTe Systems: (a) $F_{16}ZnPc$, (b) $F_{40}ZnPc$.

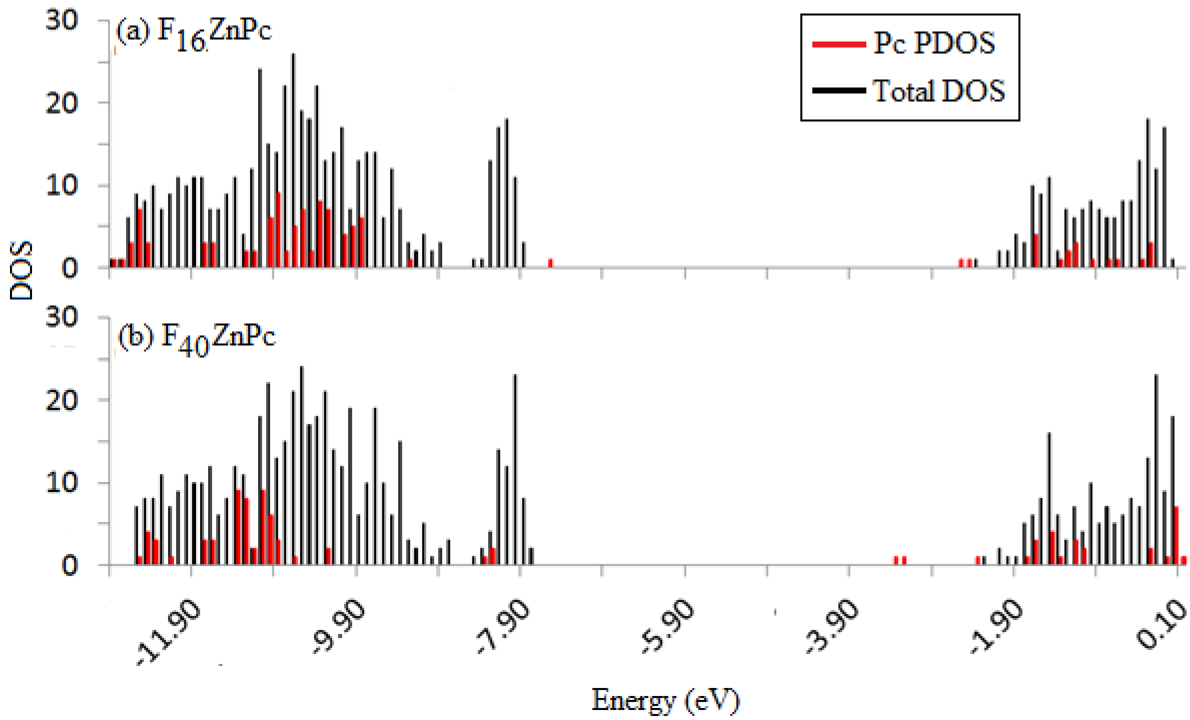

Figure E.4. PM7 Calculated DOS of CdTe (black lines) and F_xZnPc PDOS (red lines); a) $F_{16}ZnPc$ and b) $F_{40}ZnPc$

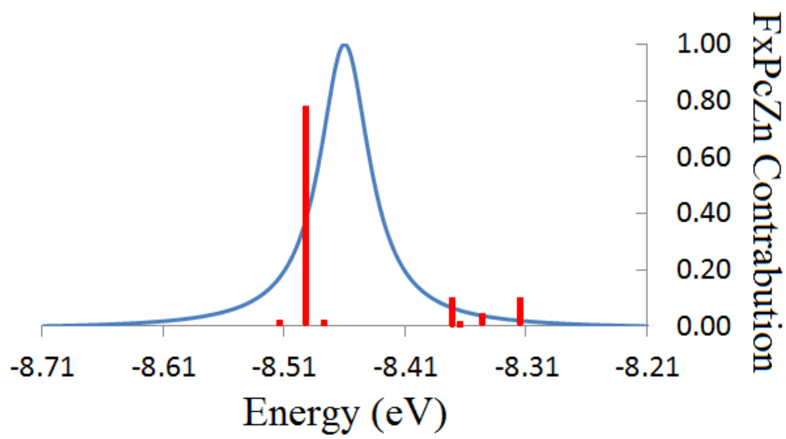

Figure E.5. Lorentzian distribution (blue curve) and HOMO(ads) levels (red lines) of $F_{40}ZnPc$ on the CdTe (110) surface. Distribution curve normalized to 1. Height of red lines indicates the portion of the MO which is located on the Pc.

The optimized structure, DOS, PDOS, and Lorentzian distribution of the HOMO(ads) for the F_xZnPc | GaAs systems are illustrated in Figures E.6-9.

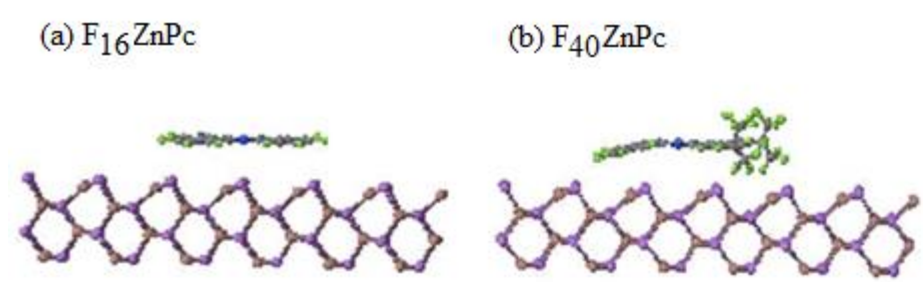

Figure E.6. PM7 Geometry Optimized Structure of F_xZnPc | GaAs Systems: (a) $F_{16}ZnPc$, (b) $F_{40}ZnPc$.

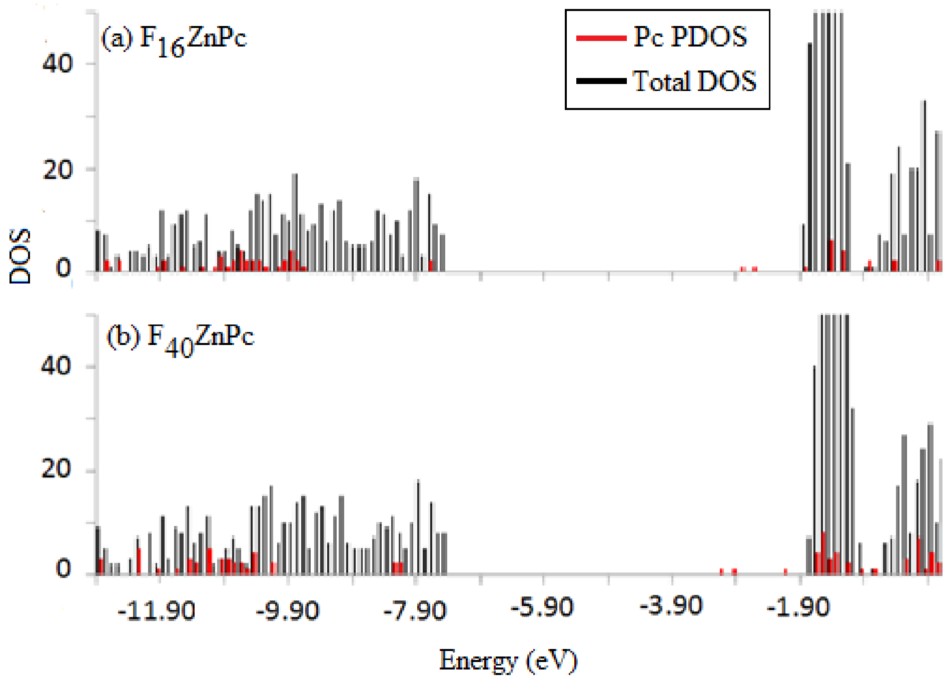

Figure E.7. PM7 Calculated DOS of GaAs (black lines) and F_xZnPc PDOS (red lines); a) $F_{16}ZnPc$ and b) $F_{40}ZnPc$

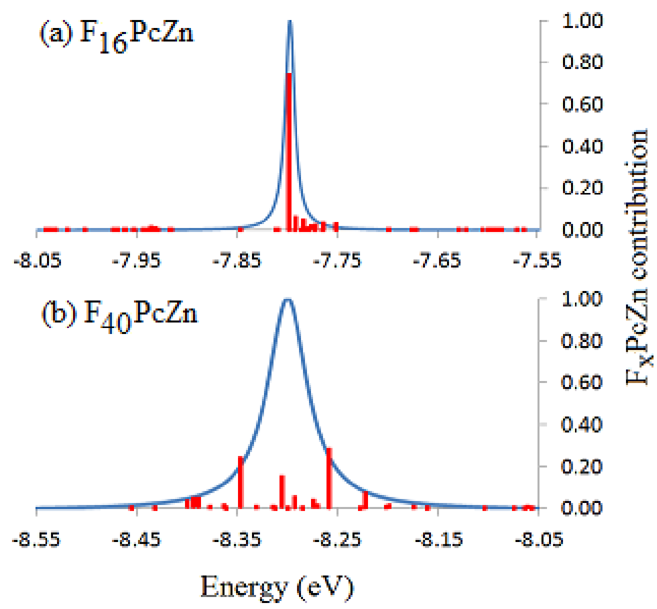

Figure E.8. Lorentzian distribution (blue curve) and HOMO(ads) levels (red lines) of (a) $F_{16}ZnPc$ and (b) $F_{40}ZnPc$ on the GaAs (110) surface. Distribution curve normalized to 1. Height of red lines indicates the portion of the MO which is located on the Pc.

The optimized structure, DOS, and PDOS for the F_xZnPc | InAs systems are illustrated in Figures E.9-10. Orbital Coupling was only observed in the $F_{40}ZnPc$ system; the and Lorentzian distribution of the $F_{40}ZnPc$ HOMO(ads) is illustrated in Figure E.11.

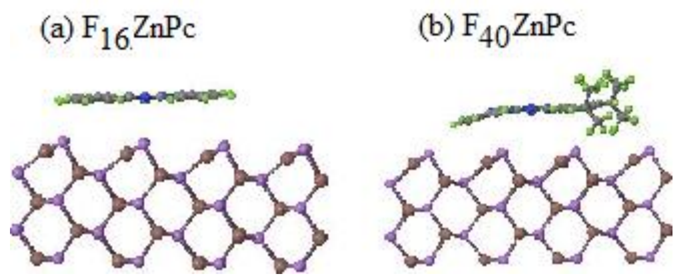

Figure E.9. PM7 Geometry Optimized Structure of F_xZnPc | InAs Systems: (a) $F_{16}ZnPc$, (b) $F_{40}ZnPc$.

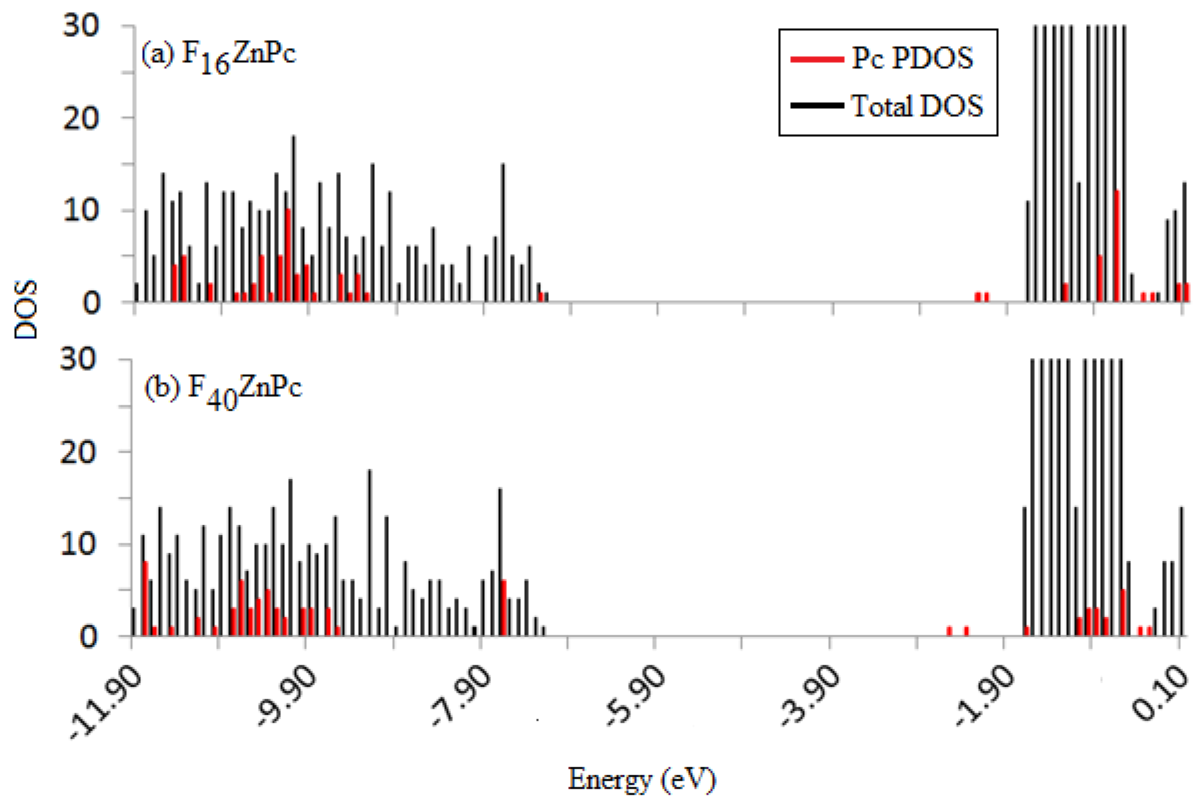

Figure E.10. PM7 Calculated DOS of InAs (black lines) and F_xZnPc PDOS (red lines); a) $F_{16}ZnPc$ and b) $F_{40}ZnPc$.

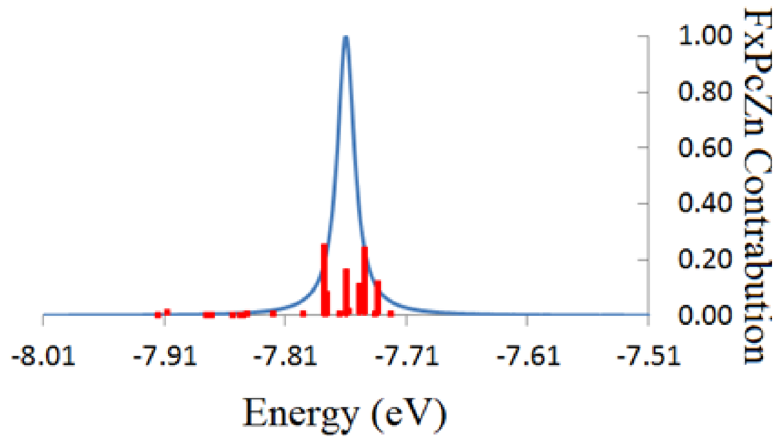

Figure E.11. Lorentzian distribution (blue curve) and HOMO(ads) levels (red lines) of $F_{40}ZnPc$ on the InAs (110) surface. Distribution curve normalized to 1. Height of red lines indicates the portion of the MO which is located on the Pc.

The optimized structure, DOS, PDOS, and Lorentzian distribution of the HOMO(ads) for the F_xZnPc | Si systems are illustrated in Figures E.12-14.

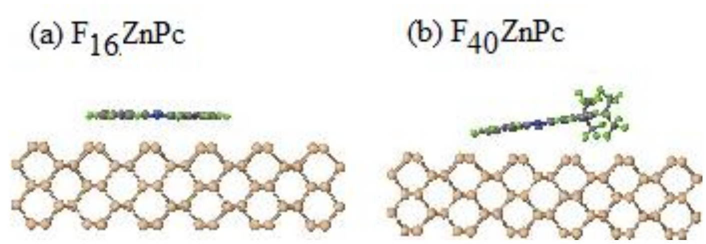

Figure E.12. PM7 Geometry Optimized Structure of F_xZnPc | Si Systems: (a) $F_{16}ZnPc$, (b) $F_{40}ZnPc$.

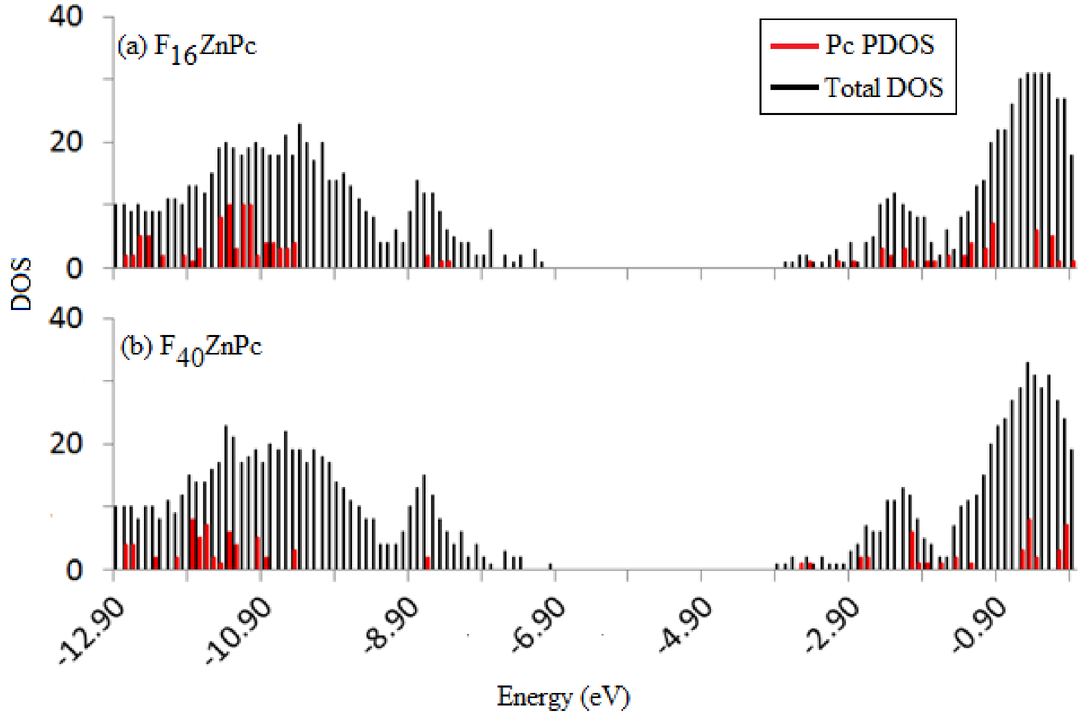

Figure E.13. PM7 Calculated DOS of Si (black lines) and F_xZnPc PDOS (red lines); a) F_{16}ZnPc and b) F_{40}ZnPc.

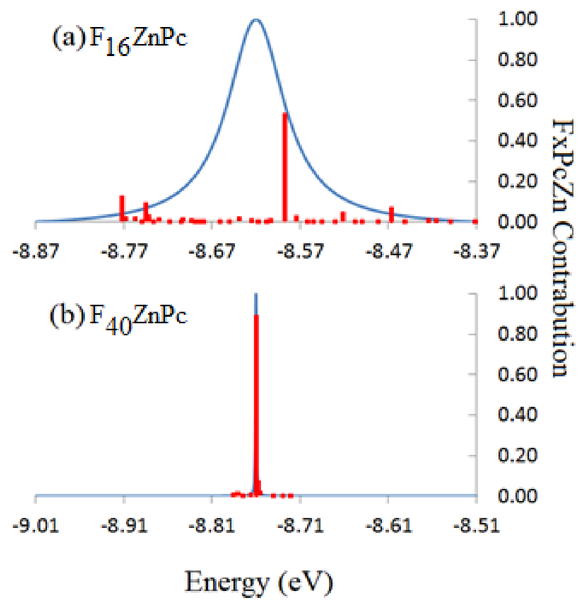

Figure E.14. Lorentzian distribution (blue curve) and HOMO(ads) levels (red lines) of (a) F_{16}ZnPc and (b) F_{40}ZnPc on the Si (110) surface. Distribution curve normalized to 1. Height of red lines indicates the portion of the MO which is located on the Pc.

The optimized structure, DOS, PDOS, and Lorentzian distribution of the HOMO(ads) for the F_xZnPc | SiC systems are illustrated in Figures E.15-17.

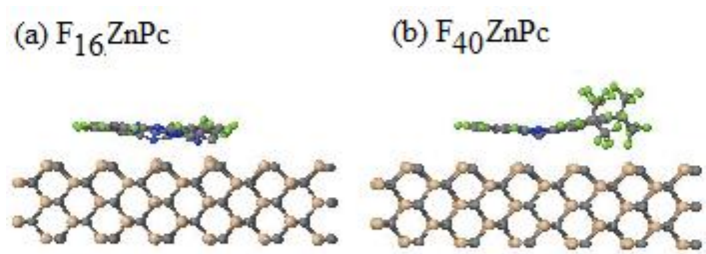

Figure E.15. PM7 Geometry Optimized Structure of F_xZnPc | SiC Systems: (a) $F_{16}ZnPc$, (b) $F_{40}ZnPc$.

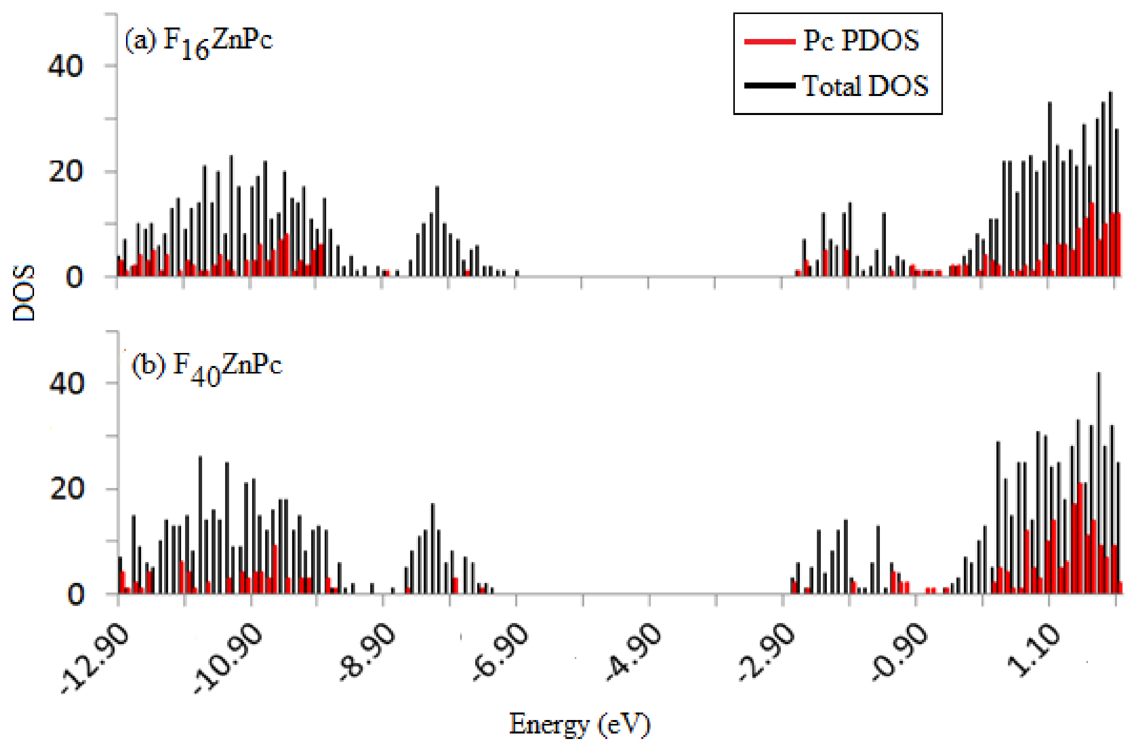

Figure E.16. PM7 Calculated DOS of SiC (black lines) and F_xZnPc PDOS (red lines); a) $F_{16}ZnPc$ and b) $F_{40}ZnPc$

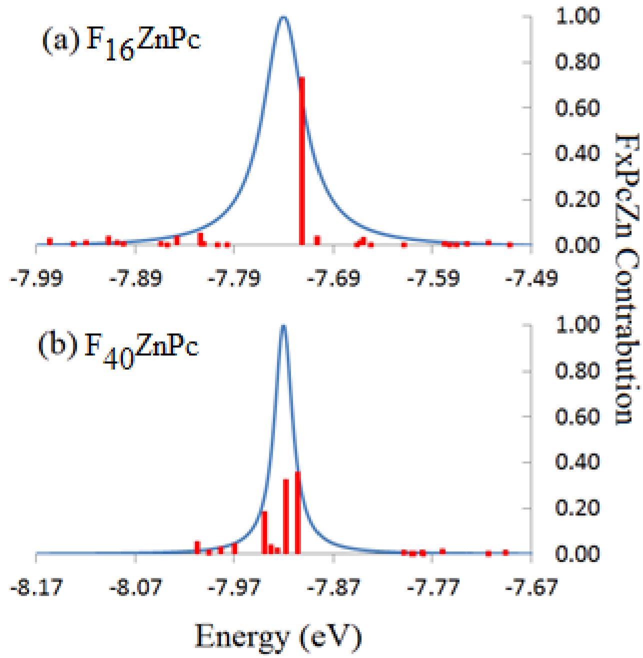

Figure E.17. Lorentzian distribution (blue curve) and HOMO(ads) levels (red lines) of (a) $F_{16}ZnPc$ and (b) $F_{40}ZnPc$ on the SiC (110) surface. Distribution curve normalized to 1. Height of red lines indicates the portion of the MO which is located on the Pc.

Appendix F

Calculated F_xZnPc Neutral, Cationic, and Anionic Geometry

The calculated Geometry of neutral F_xZnPc has already been reported in Appendix B. However, the geometry of the neutral F_xZnPc reporter here are calculated with the larger 6-31G+(d) basis set. The geometry of the F_xZnPc cation and anion are also reported. Due to the computational cost of the larger basis set, C_2 symmetry was imposed on all F_xZnPc, except $F_{34}ZnPc$. This appendix may then serve to compare the changes in geometry between neutral Pc and the charged states; as well as a comparison of geometry obtained using the different basis sets employed and symmetry constraints. The calculated bond lengths and 3-body angles of the neutral, cationic and anionic $F_{16}ZnPc$ are presented in Table F.1. Atoms labeling scheme is illustrated in Figure F.1, where the symmetry unique atoms are highlighted in red.

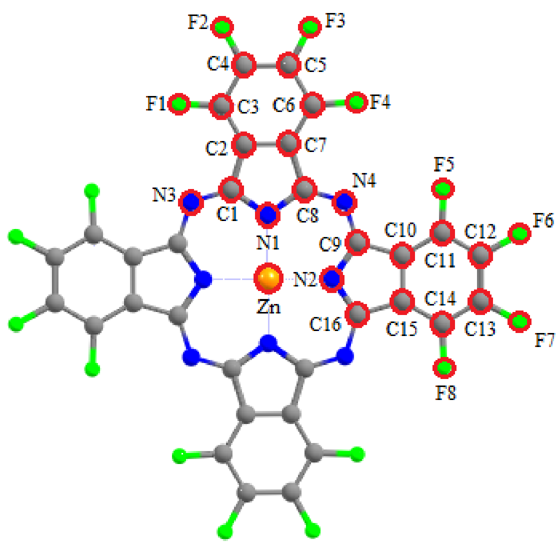

Figure F.1. Labeling scheme for $F_{16}ZnPc$ neutral, anionic, and cationic geometry. Symmetry unique atoms highlighted in red.

Table F.1. Calculated bond lengths and 3-body angles of $F_{16}ZnPc$ with the B3LYP functional and 6-31+G(d) basis set.

	Bonds				**Angles**		
	Pc	Pc^{-}	Pc^{+}		Pc	Pc^{-}	Pc^{+}
$ZN-N_1$	1.999	1.999	1.995	$ZN-N_1-C_1$	124.89	124.86	125.04
$ZN-N_2$	1.999	2.014	1.995	$ZN-N_1-C_8$	124.89	124.89	125.04
N_1-C_1	1.369	1.380	1.370	$ZN-N_2-C_9$	124.89	125.04	125.04
N_1-C_8	1.369	1.380	1.370	$ZN-N_2-C_{16}$	124.89	124.97	125.04
N_2-C_9	1.369	1.372	1.370	N_1-ZN-N_2	90.00	89.94	90.00
N_2-C_{16}	1.369	1.373	1.370	$N_1-C_1-N_3$	127.73	128.54	127.64
N_3-C_1	1.324	1.313	1.325	$N_1-C_8-N_4$	127.73	128.49	127.64
N_4-C_8	1.324	1.314	1.325	$N_1-C_1-C_2$	108.35	108.13	108.55
N_4-C_9	1.324	1.350	1.325	$N_1-C_8-C_7$	108.35	108.07	108.55
C_1-C_2	1.460	1.471	1.462	$N_2-C_9-N_4$	127.73	127.34	127.64
C_2-C_3	1.390	1.392	1.385	$N_2-C_9-C_{10}$	108.35	108.52	108.55
C_2-C_7	1.415	1.415	1.414	$N_2-C_{16}-C_{15}$	108.35	108.51	108.55
C_3-C_4	1.391	1.394	1.402	$C_1-C_2-C_3$	132.94	132.97	132.83
C_3-F_1	1.332	1.342	1.323	$C_1-C_2-C_7$	106.54	106.71	106.48
C_4-C_5	1.400	1.399	1.394	$C_2-C_3-C_4$	118.64	118.97	118.56
C_4-F_2	1.331	1.347	1.323	$C_2-C_7-C_6$	120.52	120.42	120.69
C_5-C_6	1.391	1.394	1.402	$C_2-C_3-F_1$	122.58	122.80	122.84
C_5-F_3	1.334	1.348	1.323	$C_3-C_4-C_5$	120.84	120.68	120.75
C_6-C_7	1.390	1.392	1.385	$C_3-C_4-F_2$	120.14	120.32	119.77
C_6-F_4	1.332	1.342	1.323	$C_4-C_5-F_3$	119.02	119.00	119.48
C_7-C_8	1.460	1.471	1.462	$C_5-C_4-F_2$	119.02	119.00	119.48
C_9-C_{10}	1.460	1.443	1.462	$C_6-C_5-C_4$	120.84	120.72	118.56
$C_{10}-C_{11}$	1.390	1.402	1.385	$C_6-C_5-F_3$	120.14	120.28	119.77
$C_{10}-C_{15}$	1.415	1.430	1.414	$C_7-C_6-C_5$	118.64	118.89	118.56
$C_{11}-C_{12}$	1.391	1.384	1.402	$C_7-C_2-C_3$	120.52	120.31	120.69
$C_{11}-F_5$	1.332	1.346	1.323	$C_7-C_6-F_4$	122.58	122.92	122.84
$C_{12}-C_{13}$	1.400	1.410	1.394	$C_8-C_7-C_6$	132.94	132.74	132.83
$C_{12}-F_6$	1.334	1.350	1.323	$C_8-C_7-C_2$	106.54	106.84	106.48
$C_{13}-C_{14}$	1.391	1.385	1.402	$C_8-N_4-C_9$	124.75	124.30	124.65
$C_{13}-F_7$	1.334	1.350	1.323	$C_9-C_{10}-C_{11}$	132.94	133.56	132.83
$C_{14}-C_{15}$	1.390	1.401	1.385	$C_9-C_{10}-C_{15}$	106.54	106.50	106.48
$C_{14}-F_8$	1.332	1.346	1.323	$C_{10}-C_{11}-C_{12}$	118.64	119.24	118.56
$C_{15}-C_{16}$	1.460	1.443	1.462	$C_{10}-C_{15}-C_{14}$	120.56	119.93	120.49
				$C_{10}-C_{11}-F_5$	122.58	122.07	122.84
				$C_{11}-C_{12}-C_{13}$	120.84	120.83	120.75
				$C_{11}-C_{12}-F_6$	120.14	120.52	119.77
				$C_{12}-C_{13}-F_7$	119.02	118.69	119.48
				$C_{13}-C_{12}-F_6$	119.02	118.65	119.48
				$C_{14}-C_{13}-C_{12}$	120.84	120.76	120.75
				$C_{14}-C_{13}-F_7$	120.14	120.55	119.77
				$C_{15}-C_{14}-C_{13}$	118.64	119.29	118.56
				$C_{15}-C_{10}-C_{11}$	120.52	119.94	120.69
				$C_{15}-C_{14}-F_8$	122.58	122.04	122.84
				$C_{16}-C_{15}-C_{14}$	132.94	133.59	132.83
				$C_{16}-C_{15}-C_{10}$	106.54	106.47	106.48

The calculated bond lengths and 3-body angles of the neutral, cationic and anionic $F_{34}ZnPc$ are presented in Table F.2. Atoms labeling scheme is illustrated in Figure F.2. No symmetry constrains were imposed on this Pc.

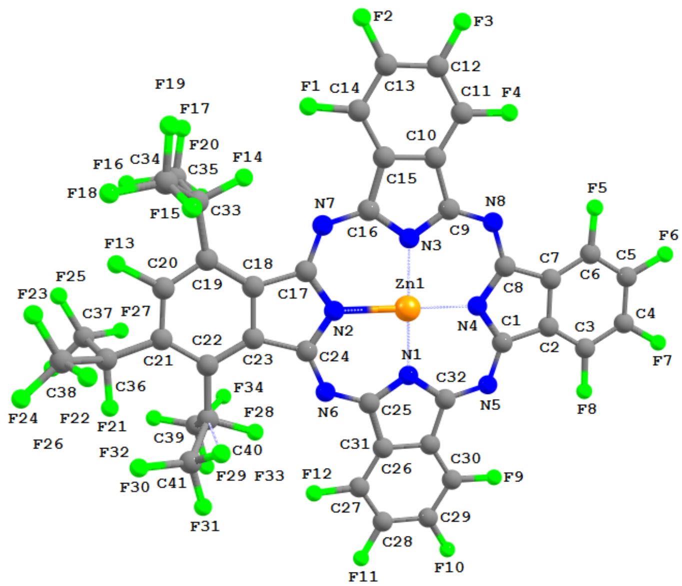

Figure F.2. Labeling scheme for $F_{34}ZnPc$ neutral, anionic, and cationic geometry.

Table F.2. Calculated bond lengths and 3-body angles of $F_{34}ZnPc$ with the B3LYP functional and 6-31+G(d) basis set.

Bonds				Angles			
	Pc	Pc^-	Pc^+		Pc	Pc^-	Pc^+
$ZN\text{-}N_1$	1.973	1.97	1.968	$N_1\text{-}ZN\text{-}N_2$	91.43	91.20	91.36
$ZN\text{-}N_2$	2.067	2.081	2.062	$N_1\text{-}ZN\text{-}N_3$	176.31	176.57	176.05
$ZN\text{-}N_3$	1.976	1.972	1.971	$N1\text{-}ZN\text{-}N_4$	88.29	88.45	88.38
$ZN\text{-}N_4$	2.047	2.056	2.041	$ZN\text{-}N_1\text{-}N_3$	88.15	88.29	88.03
$N_1\text{-}C_{25}$	1.377	1.379	1.375	$ZN\text{-}N_1\text{-}C_{25}$	122.78	122.79	123.03
$N_1\text{-}C_{32}$	1.367	1.379	1.373	$ZN\text{-}N_1\text{-}C_{32}$	127.07	126.81	127.13
$N_2\text{-}C_{17}$	1.359	1.366	1.358	$N_2\text{-}ZN\text{-}N_3$	91.25	91.33	91.14
$N_2\text{-}C_{24}$	1.364	1.361	1.368	$N_2\text{-}ZN\text{-}N_4$	177.44	178.00	176.79
$N_3\text{-}C_9$	1.368	1.377	1.375	$ZN\text{-}N_2\text{-}C_{17}$	123.77	123.68	123.96
$N_3\text{-}C_{16}$	1.379	1.385	1.377	$ZN\text{-}N_2\text{-}C_{24}$	124.84	125.02	125.00
$N_4\text{-}C_1$	1.370	1.371	1.372	$N_3\text{-}ZN\text{-}N_4$	88.92	88.95	88.95
$N_4\text{-}C_8$	1.370	1.368	1.371	$ZN\text{-}N_3\text{-}C_1$	88.15	88.29	88.03
$N_5\text{-}C_1$	1.324	1.345	1.327	$ZN\text{-}N_3\text{-}C_9$	126.13	125.95	126.21
$N_5\text{-}C_{32}$	1.330	1.313	1.329	$ZN\text{-}N_3\text{-}C_{16}$	123.71	123.59	123.94
$N_6\text{-}C_{24}$	1.326	1.348	1.322	$ZN\text{-}N_4\text{-}C_1$	125.34	125.23	125.47

N_6-C_{25}	1.312	1.301	1.318	ZN-N_4-C_8	125.09	125.08	125.29
N_7-C_{16}	1.317	1.303	1.323	C_{25}-N_1-C_{32}	110.14	110.39	109.82
N_7-C_{17}	1.330	1.352	1.326	N_1-C_{25}-N_6	127.89	128.98	127.80
N_8-C_8	1.324	1.346	1.326	N_1-C_{25}-C_{26}	108.09	107.81	108.39
N_8-C_9	1.331	1.315	1.329	N_1-C_{32}-C_5	127.94	128.73	127.84
C_1-C_2	1.465	1.445	1.464	N_1-C_{32}-C_{31}	108.77	108.27	108.82
C_2-C_3	1.391	1.400	1.388	C_{17}-N_2-C_{24}	111.39	111.29	111.03
C_2-C_7	1.415	1.427	1.416	N_2-C_{17}-N_7	125.07	124.60	125.19
C_3-C_5	1.396	1.386	1.406	N_2-C_{17}-C_{18}	108.62	108.79	108.83
C_3-F_8	1.336	1.344	1.328	N2-C24-N6	122.60	122.42	122.52
C_4-C_5	1.401	1.409	1.397	N_2-C_{24}-C_{23}	109.00	109.17	109.26
C_4-F_7	1.337	1.348	1.328	C_9-N_3-C_{16}	110.15	110.45	109.84
C_5-C_6	1.396	1.386	1.406	N_3-C_9-N_8	128.35	129.25	128.23
C_5-F_6	1.337	1.348	1.328	N_3-C_9-C_{10}	108.73	108.25	108.78
C_6-C_7	1.392	1.400	1.389	N_3-C_{16}-N_7	127.52	128.52	127.44
C_6-F_5	1.336	1.344	1.328	N_3-C_{16}-C_{15}	108.01	107.64	108.31
C_7-C_8	1.466	1.448	1.465	C_1-N_4-C_8	109.57	109.70	109.24
C_9-C_{10}	1.459	1.469	1.459	N_4-C_1-N_5	127.47	127.26	127.44
C_{10}-C_{11}	1.394	1.393	1.39	N_4-C_1-C_2	108.91	108.83	109.10
C_{10}-C_{15}	1.418	1.414	1.417	N_4-C_8-N_8	127.26	127.12	127.19
C_{11}-C_{12}	1.393	1.393	1.404	N_4-C_8-C_7	108.90	108.87	109.12
C_{11}-F_4	1.337	1.341	1.328	C_1-N_5-C_{32}	123.85	123.52	123.68
C_{12}-C_{13}	1.400	1.397	1.396	N_5-C_1-C_2	123.60	123.90	123.46
C_{12}-F_3	1.338	1.345	1.328	N_5-C_{32}-C_{31}	123.29	123.00	123.33
C_{13}-C_{14}	1.395	1.395	1.406	C_{24}-N_6-C_{25}	130.43	129.56	130.23
C_{13}-F_2	1.338	1.345	1.328	N_6-C_{24}-C_{23}	128.37	128.41	128.21
C_{14}-C_{15}	1.395	1.394	1.392	N_6-C_{25}-C_{26}	124.00	123.20	123.80
C_{14}-F_1	1.334	1.338	1.326	C_{16}-N_7-C_{17}	128.65	128.27	128.31
C_{15}-C_{16}	1.472	1.483	1.474	N_7-C_{16}-C_{15}	124.47	123.83	124.25
C_{17}-C_{18}	1.486	1.452	1.501	N_7-C_{17}-C_{18}	126.31	126.61	125.98
C_{18}-C_{19}	1.422	1.431	1.416	C_8-N_8-C_9	124.23	123.64	124.07
C_{18}-C_{23}	1.448	1.472	1.441	N_8-C_8-C_7	123.82	124.01	123.69
C_{19}-C_{20}	1.383	1.375	1.391	N_8-C_9-C_{10}	122.92	122.50	122.98
C_{19}-C_{33}	1.552	1.549	1.553	C_1-C_2-C_3	133.04	133.51	132.89
C_{20}-C_{21}	1.401	1.408	1.398	C_1-C_2-C_7	106.34	106.34	106.31
C_{20}-C_{13}	1.344	1.354	1.336	C_3-C_2-C_7	120.62	120.14	120.80
C_{21}-C_{22}	1.418	1.416	1.422	C_2-C_3-C_4	118.68	119.09	118.55
C_{21}-C_{36}	1.551	1.546	1.554	C_2-C_3-F_8	122.61	122.26	122.80
C_{22}-C_{23}	1.451	1.453	1.447	C_2-C_7-C_6	120.45	119.96	120.63
C_{22}-C_{39}	1.566	1.563	1.566	C_2-C_7-C_8	106.27	106.26	106.22
C_{23}-C_{24}	1.515	1.490	1.526	C_4-C_3-F_8	118.70	118.64	118.65
C_{25}-C_{26}	1.471	1.482	1.472	C_3-C_4-C_5	120.72	120.81	120.69
C_{26}-C_{27}	1.394	1.393	1.391	C_3-C_4-F_7	120.17	120.51	119.82
C_{26}-C_{31}	1.417	1.413	1.417	C_5-C_4-F_7	119.11	118.68	119.49
C_{27}-C_{28}	1.395	1.394	1.406	C_4-C_5-C_6	120.80	120.85	120.76
C_{27}-F_{12}	1.334	1.338	1.325	C_4-C_5-F_6	119.01	118.63	119.50
C_{28}-C_{29}	1.400	1.397	1.396	C_6-C_5-F_6	120.16	120.51	119.73
C_{28}-F_{11}	1.337	1.345	1.328	C_5-C_6-C_7	118.71	119.13	118.56
C_{29}-C_{30}	1.394	1.394	1.405	C_5-C_6-F_5	118.63	118.57	118.62
C_{29}-F_{10}	1.338	1.345	1.328	C_7-C_6-F_5	122.64	122.27	122.80
C_{30}-C_{31}	1.394	1.393	1.390	C_6-C_7-C_8	133.28	133.76	133.12
C_{30}-F_9	1.337	1.341	1.328	C_9-C_{10}-C_{11}	132.14	132.00	131.91
C_{31}-C_{32}	1.461	1.469	1.461	C_9-C_{10}-C_{15}	106.73	107.04	106.77
C_{33}-F_{14}	1.363	1.362	1.366	C_{11}-C_{10}-C_{15}	121.12	120.96	121.32

C_{33}-C_{34}	1.578	1.579	1.580
C_{33}-C_{35}	1.581	1.580	1.582
C_{34}-F_{16}	1.338	1.340	1.335
C_{34}-F_{17}	1.342	1.346	1.339
C_{34}-F_{15}	1.351	1.350	1.353
C_{35}-F_{20}	1.351	1.350	1.353
C_{35}-F_{18}	1.339	1.341	1.335
C_{35}-F_{19}	1.341	1.345	1.338
C_{36}-F_{21}	1.370	1.372	1.369
C_{36}-C_{38}	1.588	1.591	1.589
C_{36}-C_{37}	1.588	1.591	1.589
C_{38}-F_{25}	1.337	1.339	1.336
C_{38}-F_{26}	1.342	1.348	1.337
C_{38}-F_{27}	1.348	1.346	1.351
C_{37}-F_{22}	1.348	1.346	1.350
C_{37}-F_{23}	1.337	1.338	1.335
C_{37}-F_{24}	1.342	1.348	1.338
C_{39}-F_{28}	1.369	1.367	1.373
C_{39}-C_{40}	1.606	1.605	1.607
C_{39}-C_{41}	1.603	1.603	1.605
C_{40}-F_{32}	1.333	1.337	1.329
C_{40}-F_{33}	1.342	1.345	1.34
C_{40}-F_{34}	1.355	1.353	1.358
C_{41}-F_{29}	1.355	1.353	1.358
C_{41}-F_{31}	1.333	1.337	1.329
C_{41}-F_{30}	1.342	1.344	1.339

C_{10}-C_{11}-C_{12}	118.82	119.00	118.68
C_{10}-C_{11}-F_{4}	122.55	122.81	122.73
C_{10}-C_{15}-C_{14}	119.40	119.43	119.64
C_{10}-C_{15}-C_{16}	106.36	106.62	106.29
C_{12}-C_{11}-F_{4}	118.63	118.19	118.59
C_{11}-C_{12}-C_{13}	120.36	120.33	120.29
C_{11}-C_{12}- F_{3}	120.44	120.46	120.00
C_{13}-C_{12}-F_{3}	119.19	119.20	119.71
C_{12}-C_{13}-C_{14}	121.00	120.85	121.02
C_{12}-C_{13}-F_{2}	119.06	119.11	119.51
C_{14}-C_{13}-F_{2}	119.93	120.05	119.47
C_{13}-C_{14}-C_{15}	119.28	119.43	119.04
C_{13}-C_{14}-F_{1}	117.63	117.25	117.55
C_{15}-C_{14}-F_{1}	123.09	123.32	123.40
C_{14}-C_{15}-C_{16}	134.20	133.95	134.06
C_{17}-C_{18}-C_{19}	131.94	132.91	131.58
C_{17}-C_{18}-C_{23}	106.98	106.97	106.93
C_{19}-C_{18}-C_{23}	121.05	120.11	121.49
C_{18}-C_{19}-C_{20}	114.37	115.07	113.97
C_{18}-C_{19}-C_{33}	129.08	128.21	129.48
C_{18}-C_{23}-C_{22}	121.22	120.82	121.50
C_{18}-C_{23}-C_{24}	103.97	103.77	103.93
C_{20}-C_{19}-C_{33}	116.55	116.72	116.55
C_{19}-C_{20}-C_{21}	128.15	128.30	128.09
C_{19}-C_{20}-F_{13}	117.20	117.59	116.87
C_{19}-C_{33}-F_{14}	110.30	110.86	109.92
C_{19}-C_{33}-C_{34}	113.66	113.60	113.43
C_{19}-C_{33}-C_{35}	113.77	113.98	113.77
C_{21}-C_{20}-F_{13}	114.64	114.11	115.04
C_{20}-C_{21}-C_{22}	118.35	118.21	118.46
C_{20}-C_{21}-C_{36}	114.08	114.12	114.30
C_{22}-C_{21}-C_{36}	127.57	127.67	127.24
C_{21}-C_{22}-C_{23}	116.85	117.47	116.49
C_{21}-C_{22}-C_{39}	121.51	121.40	121.61
C_{21}-C_{36}-F_{21}	108.54	109.02	108.15
C_{21}-C_{36}-C_{38}	114.54	114.85	114.28
C_{21}-C_{36}-C_{37}	114.84	115.07	114.54
C_{23}-C_{22}-C_{39}	121.64	121.13	121.90
C_{22}-C_{23}-C_{24}	134.79	135.39	134.57
C_{22}-C_{39}-F_{28}	107.78	108.37	107.34
C_{22}-C_{39}-C_{40}	115.40	115.51	115.33
C_{22}-C_{39}-C_{41}	114.78	114.91	114.70
C_{22}-C_{39}-F_{29}	91.88	92.12	91.55
C_{25}-C_{26}-C_{27}	133.78	133.51	133.66
C_{25}-C_{26}-C_{31}	106.42	106.66	106.35
C_{27}-C_{26}-C_{31}	119.76	119.82	119.97
C_{26}-C_{27}-C_{28}	119.13	119.28	118.91
C_{26}-C_{27}-F_{12}	123.05	123.29	123.33
C_{26}-C_{31}-C_{30}	120.88	120.68	121.11
C_{26}-C_{31}-C_{32}	106.58	106.86	106.61
C_{28}-C_{27}-F_{12}	117.82	117.44	117.76
C_{27}-C_{28}-C_{29}	120.92	120.75	120.92
C_{27}-C_{28}-F_{11}	119.98	120.09	119.53
C_{29}-C_{28}-F_{11}	119.11	119.16	119.55

C_{28}-C_{29}-C_{30}	120.49	120.48	120.43
C_{28}-C_{29}-F_{10}	119.12	119.11	119.61
C_{30}-C_{29}-F_{10}	120.38	120.41	119.95
C_{29}-C_{30}-C_{31}	118.81	119.00	118.65
C_{29}-C_{30}-F_{9}	118.62	118.20	118.57
C_{31}-C_{30}-F_{9}	122.57	122.80	122.78
C_{30}-C_{31}-C_{32}	132.54	132.46	132.28
F_{14}-C_{33}-F_{34}	101.51	101.33	101.70
F_{14}-C_{33}-C_{35}	101.90	101.71	102.08
C_{34}-C_{33}-C_{35}	114.20	113.86	114.46
C_{33}-C_{34}-F_{16}	115.60	115.90	115.36
C_{33}-C_{34}-F_{17}	109.63	109.85	109.32
C_{33}-C_{34}-F_{15}	107.90	108.10	107.48
C_{33}-C_{35}-F_{20}	108.06	108.27	107.62
C_{33}-C_{35}-F_{18}	115.57	115.87	115.37
C_{33}-C_{35}-F_{19}	109.58	109.77	109.27
F_{16}-C_{34}-F_{17}	107.46	107.14	107.99
F_{16}-C_{34}-F_{15}	108.08	107.95	108.26
F_{17}-C_{34}-F_{15}	107.93	107.60	108.23
F_{20}-C_{35}-F_{18}	108.09	108.00	108.29
F_{20}-C_{35}-F_{19}	107.95	107.63	108.23
F_{18}-C_{35}-F_{19}	107.36	107.01	107.85
F_{21}-C_{36}-C_{38}	102.49	102.21	102.85
F_{21}-C_{36}-C_{37}	101.81	101.50	102.17
C_{38}-C_{36}-C_{37}	112.89	112.36	113.23
C_{36}-C_{36}-F_{25}	115.08	115.39	114.77
C_{36}-C_{38}-F_{26}	109.01	108.98	108.77
C_{36}-C38-F_{27}	109.13	109.38	108.69
C_{36}-C_{37}-F_{22}	108.84	109.15	108.47
C_{36}-C_{37}-F_{23}	115.56	115.90	115.22
C_{36}-C_{37}-F_{24}	108.70	108.67	108.48
F_{25}-C_{38}-F_{26}	107.23	106.90	107.81
F_{25}-C_{38}-F_{27}	107.98	108.10	108.09
F_{26}-C_{38}-F_{27}	108.20	107.83	108.56
F_{22}-C_{37}-F_{23}	107.98	108.10	108.09
F_{22}-C_{37}-F_{24}	108.27	107.87	108.63
F_{23}-C_{37}-F_{24}	107.28	106.88	107.79
F_{28}-C_{39}-C_{40}	96.00	95.82	96.10
F_{28}-C_{39}-C_{41}	96.56	96.40	96.64
F_{28}-C_{39}-F_{29}	80.37	80.58	80.23
C_{40}-C_{39}-C_{41}	120.96	120.57	121.28
C_{40}-C_{39}-F_{29}	152.03	151.59	152.51
C_{39}-C_{40}-F_{32}	121.22	121.37	121.05
C_{39}-C_{40}-F_{33}	108.63	108.88	108.32
C_{39}-C_{40}-F_{34}	104.95	105.22	104.57
C_{41}-C_{39}-F_{29}	33.82	33.66	34.02
C_{39}-C_{41}-F_{29}	105.02	105.27	104.61
C_{39}-C_{41}-F_{31}	120.75	120.94	120.64
C_{39}-C_{41}-F_{30}	109.00	109.20	108.63
C_{39}-F_{29}-C_{41}	41.16	41.07	41.37
F_{32}-C_{40}-F_{33}	106.85	106.41	107.30
F_{32}-C_{40}-F_{34}	106.44	106.11	106.64
F_{33}-C_{40}-F_{34}	108.18	108.30	108.43
F_{29}-C_{41}-F_{31}	106.50	106.14	106.63

	F_{29}-C_{41}-F_{30}	108.13	108.22	108.38
	F_{31}-C_{41}-F_{30}	106.88	106.52	107.42

The calculated bond lengths and 3-body angles of the neutral, cationic and anionic F_{40}ZnPc are presented in Table F.3. Atoms labeling scheme is illustrated in Figure F.3, with symmetry unique atoms highlighted in red.

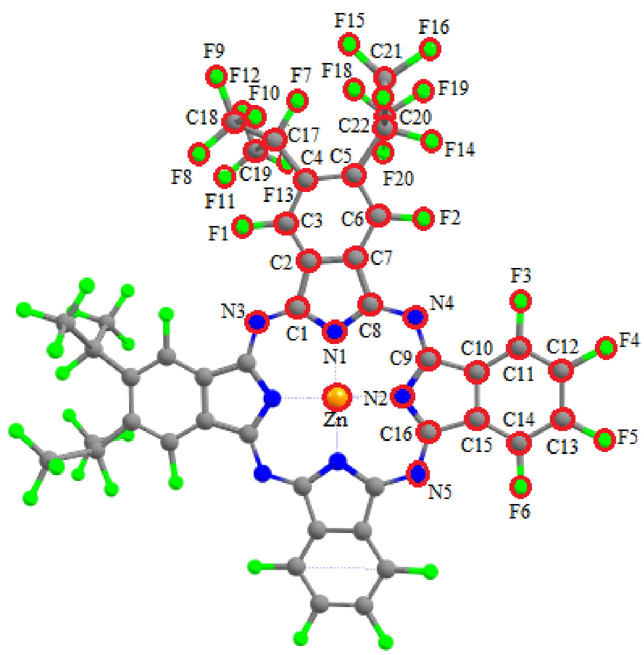

Figure F.3. Labeling scheme for F_{40}ZnPc neutral, anionic, and cationic geometry. Symmetry unique atoms highlighted in red.

Table F.3. Calculated bond lengths and 3-body angles of $F_{40}ZnPc$ with the B3LYP functional and 6-31+G(d) basis set.

Bonds				Angles			
	Pc	Pc^-	Pc^+		Pc	Pc^-	Pc^+
ZN-N_1	2.002	2.008	2.002	ZN-N_1-C_1	124.24	124.00	124.54
ZN-N_2	1.999	2.004	1.997	ZN-N_1-C_8	125.63	125.65	125.57
N_1-C_1	1.372	1.389	1.372	ZN-N_2-C_9	125.06	125.31	125.17
N_1-C_8	1.371	1.364	1.375	ZN-N_2-C_{16}	124.95	124.36	125.07
N_2-C_9	1.375	1.363	1.373	N_1-ZN-N_2	89.66	89.21	89.78
N_2-C_{16}	1.370	1.388	1.374	N_1-C_1-N_3	128.08	127.91	127.85
N_3-C_1	1.325	1.324	1.326	N_1-C_8-N_4	127.09	128.09	126.89
N_4-C_8	1.331	1.336	1.328	N_1-C_1-C_2	107.86	107.59	108.15
N_4-C_9	1.325	1.335	1.329	N_1-C_8-C_7	108.00	107.74	108.12
C_1-C_2	1.456	1.444	1.462	N_2-C_9-N_4	127.82	128.71	127.56
C_2-C_3	1.384	1.388	1.380	N_2-C_9-C_{10}	108.40	108.25	108.62
C_2-C_7	1.395	1.401	1.394	N_2-C_{16}-C_{15}	108.62	108.07	108.68
C_3-C_4	1.399	1.394	1.410	C_1-C_2-C_3	133.81	134.16	133.81
C_3-F_1	1.340	1.346	1.333	C_1-C_2-C_7	107.52	107.71	107.41
C_4-C_5	1.457	1.464	1.445	C_2-C_3-C_4	123.00	123.49	122.78
C_4-C_{17}	1.545	1.540	1.549	C_2-C_7-C_6	120.29	120.26	120.57
C_5-C_6	1.422	1.421	1.436	C_2-C_3-F_1	117.29	117.31	117.65
C_5-C_{20}	1.582	1.574	1.588	C_3-C_4-C_5	119.46	119.53	119.60
C_6-C_7	1.397	1.398	1.392	C_3-C_4-C_{17}	114.86	114.92	114.64
C_6-F_2	1.337	1.340	1.331	C_4-C_5-C_{20}	128.08	128.24	128.44
C_7-C_8	1.467	1.470	1.473	C_4-C_{17}-C_{18}	114.41	114.79	114.39
C_9-C_{10}	1.464	1.465	1.464	C_4-C_{17}-C_{19}	114.35	114.75	114.41
C_{10}-C_{11}	1.392	1.395	1.389	C_4-C_{17}-F_7	108.10	108.28	107.45
C_{10}-C_{15}	1.417	1.421	1.417	C_5-C_{20}-C_{21}	116.16	116.57	116.15
C_{11}-C_{12}	1.396	1.392	1.406	C_5-C_{20}-C_{22}	116.19	116.53	116.12
C_{11}-F_3	1.336	1.341	1.327	C_5-C_{20}-F_{14}	106.98	107.58	106.39
C_{12}-C_{13}	1.401	1.404	1.397	C_6-C_5-C_4	115.78	115.31	115.75
C_{12}-F_4	1.337	1.347	.328	C_6-C_5-C_{20}	116.15	116.46	116.44
C_{13}-C_{14}	1.396	1.391	1.405	C_7-C_6-C_5	122.80	123.29	122.52
C_{13}-F_5	1.337	1.346	1.328	C_7-C_2-C_3	118.67	118.12	118.78
C_{14}-C_{15}	1.392	1.396	1.390	C_7-C_6-F_2	113.06	113.16	113.24
C_{14}-F_6	1.336	1.343	1.328	C_8-C_7-C_6	133.24	133.15	133.00
C_{15}-C_{16}	1.464	1.454	1.463	C_8-C_7-C_2	106.47	106.59	106.43
C_{17}-C_{18}	1.582	1.582	1.584	C_8-N_4-C_9	124.74	123.03	125.03
C_{17}-C_{19}	1.582	1.581	1.584	C_9-C_{10}-C_{11}	132.95	132.97	132.87
C_{17}-F_7	1.368	1.372	1.366	C_9-C_{10}-C_{15}	106.54	106.68	106.49
C_{18}-F_8	1.337	1.337	1.337	C_{10}-C_{11}-C_{12}	118.68	119.04	118.64
C_{18}-F_9	1.342	1.348	1.337	C_{10}-C_{15}-C_{14}	120.53	120.12	120.62
C_{18}-F_{10}	1.350	1.350	1.350	C_{10}-C_{11}-F_3	122.57	122.55	122.75
C_{19}-F_{11}	1.337	1.337	1.337	C_{11}-C_{12}-C_{13}	120.80	120.60	120.75
C_{19}-F_{12}	1.343	1.348	1.337	C_{11}-C_{12}-F_4	120.15	120.46	119.72
C_{19}-F_{13}	1.350	1.350	1.350	C_{12}-C_{13}-F_5	119.09	118.81	119.57
C_{20}-C_{21}	1.594	1.595	1.595	C_{13}-C_{12}-F_4	119.05	118.94	119.53
C_{20}-C_{22}	1.594	1.596	1.596	C_{14}-C_{13}-C_{12}	120.79	120.88	120.70
C_{20}-F_{14}	1.385	1.387	1.383	C_{14}-C_{13}-F_5	120.12	120.31	119.73
C_{21}-F_{15}	1.351	1.350	1.353	C_{15}-C_{14}-C_{13}	118.68	119.02	118.67
C_{21}-F_{16}	1.336	1.338	1.332	C_{15}-C_{10}-C_{11}	120.52	120.35	120.64
C_{21}-F_{17}	1.344	1.348	1.339	C_{15}-C_{14}-F_6	122.56	122.46	122.77
C_{22}-F_{18}	1.351	1.350	1.352	C_{16}-C_{15}-C_{14}	133.00	133.23	132.94

C_{22}-F_{19}	1.335	1.338	1.332	C_{16}-C_{15}-C_{10}	106.47	106.66	106.44
C_{22}-F_{20}	1.344	1.348	1.339	C_{17}-C_{18}-F_8	114.72	115.08	114.34
				C_{17}-C_{18}-F_9	109.27	109.53	108.91
				C_{17}-C_{18}-F_{10}	108.59	108.81	108.33
				C_{17}-C_{19}-F_{11}	114.81	115.09	114.35
				C_{17}-C_{19}-F_{12}	109.35	109.51	108.90
				C_{17}-C_{19}-F_{13}	108.74	108.87	108.30
				C_{18}-C_{17}-C_{19}	112.98	112.55	113.12
				C_{20}-C_{21}-F_{15}	107.62	107.86	107.20
				C_{20}-C_{21}-F_{16}	117.45	117.62	116.91
				C_{20}-C_{21}-F_{17}	108.75	109.07	108.35
				C_{20}-C_{22}-F_{18}	107.56	108.00	107.17
				C_{20}-C_{22}-F_{19}	117.43	117.64	116.92
				C_{20}-C_{22}-F_{20}	108.71	109.07	108.33
				C_{22}-C_{20}-C_{21}	115.55	114.66	115.63
				F_8-C_{18}-F_9	107.69	107.32	108.12
				F_8-C_{18}-F_{10}	108.28	108.21	108.33
				F_9-C_{18}-F_{10}	108.11	107.64	108.69
				F_{11}-C_{19}-F_{12}	107.50	107.28	108.14
				F_{11}-C_{19}-F_{13}	108.21	108.21	108.33
				F_{12}-C_{19}-F_{13}	108.03	107.63	108.70
				F_{15}-C_{21}-F_{16}	108.05	107.92	108.40
				F_{15}-C_{21}-F_{17}	108.05	107.78	108.52
				F_{16}-C_{21}-F_{17}	106.59	106.23	107.23
				F_{18}-C_{22}-F_{19}	108.14	107.92	108.42
				F_{18}-C_{22}-F_{20}	108.05	107.77	108.54
				F_{19}-C_{22}-F_{20}	106.64	106.08	107.25

The calculated bond lengths and 3-body angles of the neutral, cationic and anionic F_{64}ZnPc are presented in Table F.4. Atoms labeling scheme is illustrated in Figure F.4, with symmetry unique atoms highlighted in red.

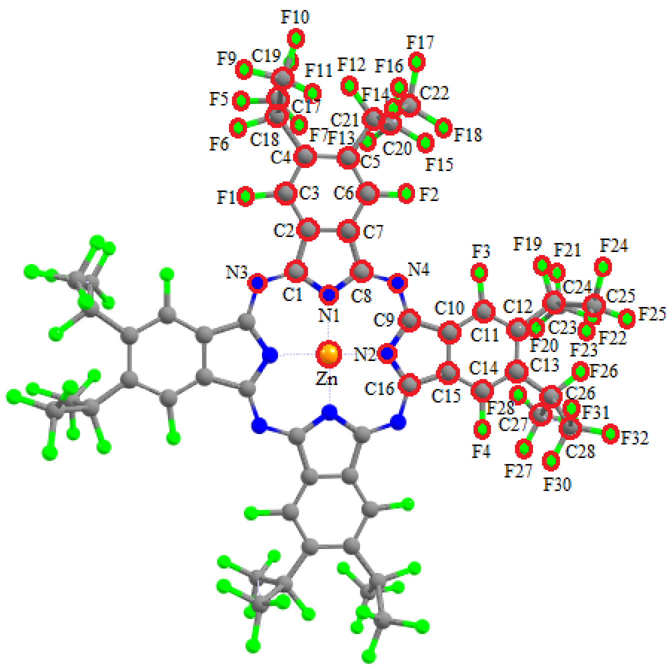

Figure F.4. Labeling scheme for $F_{64}ZnPc$ neutral, anionic, and cationic geometry. Symmetry unique atoms highlighted in red.

Table F.4. Calculated bond lengths and 3-body angles of $F_{64}ZnPc$ with the B3LYP functional and 6-31+G(d) basis set.

	Bonds				Angles		
	Pc	Pc$^-$	Pc$^+$		Pc	Pc$^-$	Pc$^+$
ZN-N_1	2.001	1.995	1.997	ZN-N_1-C_1	124.68	124.67	124.84
ZN-N_2	2.001	2.011	1.997	ZN-N_1-C_8	125.24	125.14	125.35
N_1-C_1	1.371	1.375	1.371	ZN-N_2-C_9	124.68	124.58	124.81
N_1-C_8	1.373	1.382	1.375	ZN-N_2-C_{16}	125.24	125.33	125.38
N_2-C_9	1.371	1.375	1.372	N_1-ZN-N_2	90.00	90.09	89.97
N_2-C_{16}	1.373	1.372	1.374	N_1-C_1-N_3	128.03	128.88	127.89
N_3-C_1	1.327	1.315	1.327	N_1-C_8-N_4	127.25	127.97	127.15
N_4-C_8	1.327	1.314	1.327	N_1-C_1-C_2	107.92	107.63	108.15
N_4-C_9	1.327	1.345	1.327	N_1-C_8-C_7	108.14	107.89	108.32
C_1-C_2	1.461	1.468	1.463	N_2-C_9-N_4	128.03	127.76	127.92
C_2-C_3	1.386	1.384	1.381	N_2-C_9-C_{10}	107.92	107.89	108.12
C_2-C_7	1.396	1.395	1.397	N_2-C_{16}-C_{15}	108.14	108.10	108.36
C_3-C_4	1.397	1.396	1.410	C_1-C_2-C_3	134.17	134.02	134.04
C_3-F_1	1.340	1.344	1.333	C_1-C_2-C_7	107.34	107.62	107.22
C_4-C_5	1.449	1.450	1.437	C_2-C_3-C_4	122.51	122.87	122.24
C_4-C_{17}	1.540	1.537	1.544	C_2-C_7-C_6	120.70	120.58	120.82
C_5-C_6	1.416	1.416	1.429	C_2-C_3-F_1	118.32	118.46	118.57
C_5-C_{20}	1.575	1.570	1.581	C_3-C_4-C_5	119.88	119.61	119.93
C_6-C_7	1.397	1.396	1.391	C_3-C_4-C_{17}	115.57	115.50	115.32
C_6-F_2	1.337	1.339	1.331	C_4-C_5-C_{20}	126.59	126.49	126.84

C_7-C_8	1.466	1.470	1.467	C_4-C_{17}-C_{18}	114.65	114.65	114.40
C_9-C_{10}	1.461	1.440	1.463	C_4-C_{17}-C_{19}	114.57	114.99	114.30
C_{10}-C_{11}	1.386	1.391	1.381	C_4-C_{17}-F_5	107.21	107.22	106.91
C_{10}-C_{15}	1.396	1.409	1.397	C_5-C_{20}-C_{21}	113.32	113.36	113.05
C_{11}-C_{12}	1.397	1.389	1.409	C_5-C_{20}-C_{22}	113.23	113.39	113.09
C_{11}-F_3	1.340	1.347	1.333	C_5-C_{20}-F_{12}	108.01	108.44	107.58
C_{12}-C_{13}	1.449	1.464	1.437	C_6-C_5-C_4	116.19	116.10	116.26
C_{12}-C_{23}	1.540	1.535	1.544	C_6-C_5-C_{20}	117.22	117.41	116.90
C_{13}-C_{14}	1.416	1.408	1.429	C_7-C_6-C_5	122.23	122.47	122.02
C_{13}-C_{26}	1.575	1.566	1.581	C_7-C_2-C_3	118.49	118.37	118.73
C_{14}-C_{15}	1.397	1.402	1.391	C_7-C_6-F_2	114.31	114.52	114.54
C_{14}-F_6	1.337	1.342	1.331	C_8-C_7-C_6	132.79	132.75	132.68
C_{15}-C_{16}	1.466	1.447	1.467	C_8-C_7-C_2	106.51	106.68	106.51
C_{17}-C_{18}	1.589	1.591	1.592	C_8-N_4-C_9	124.80	124.44	124.72
C_{17}-C_{19}	1.590	1.590	1.593	C_9-C_{10}-C_{11}	134.17	134.66	134.05
C_{17}-F_5	1.379	1.382	1.376	C_9-C_{10}-C_{15}	107.34	107.35	107.25
C_{18}-F_6	1.337	1.338	1.337	C_{10}-C_{11}-C_{12}	122.51	123.20	132.26
C_{18}-F_7	1.343	1.348	1.337	C_{10}-C_{15}-C_{14}	120.70	120.28	120.84
C_{18}-F_8	1.345	1.345	1.346	C_{10}-C_{11}-F_3	118.32	118.07	118.55
C_{19}-F_9	1.337	1.338	1.337	C_{11}-C_{12}-C_{13}	119.88	119.67	119.92
C_{19}-F_{10}	1.343	1.348	1.337	C_{11}-C_{12}-C_{23}	115.57	115.65	115.33
C_{19}-F_{11}	1.345	1.345	1.346	C_{12}-C_{13}-C_{26}	126.59	126.33	126.75
C_{20}-C_{21}	1.613	1.614	1.615	C_{13}-C_{12}-C_{23}	124.55	124.68	124.75
C_{20}-C_{22}	1.613	1.614	1.615	C_{14}-C_{13}-C_{12}	116.19	115.99	116.27
C_{20}-F_{12}	1.374	1.376	1.373	C_{14}-C_{13}-C_{26}	117.22	117.66	116.89
C_{21}-F_{13}	1.348	1.347	1.350	C_{12}-C_{23}-C_{24}	114.57	114.97	114.30
C_{21}-F_{14}	1.337	1.341	1.333	C_{12}-C_{23}-C_{25}	114.65	114.83	114.40
C_{21}-F_{15}	1.341	1.345	1.373	C_{12}-C_{23}-F_{19}	107.21	107.32	106.91
C_{22}-F_{16}	1.348	1.347	1.350	C_{13}-C_{26}-C_{27}	113.23	113.36	113.13
C_{22}-F_{17}	1.337	1.341	1.333	C_{13}-C_{26}-C_{28}	113.31	113.71	113.04
C_{22}-F_{18}	1.341	1.344	1.338	C_{13}-C_{26}-F_{26}	108.01	108.53	107.56
C_{23}-C_{24}	1.590	1.590	1.593	C_{15}-C_{14}-C_{13}	122.23	122.86	122.00
C_{23}-C_{25}	1.589	1.590	1.593	C_{15}-C_{10}-C_{11}	118.49	117.99	118.70
C_{23}-F_{19}	1.379	1.383	1.376	C_{15}-C_{14}-F_4	114.31	114.01	114.56
C_{24}-F_{20}	1.345	1.345	1.346	C_{16}-C_{15}-C_{14}	132.79	133.16	132.68
C_{24}-F_{21}	1.337	1.339	1.337	C_{16}-C_{15}-C_{10}	106.51	106.56	106.48
C_{24}-F_{22}	1.343	1.349	1.337	C_{17}-C_{18}-F_6	114.11	114.29	113.78
C_{25}-F_{23}	1.345	1.345	1.346	C_{17}-C_{18}-F_7	108.82	108.78	108.61
C_{25}-F_{24}	1.337	1.339	1.337	C_{17}-C_{18}-F_8	110.05	110.29	109.75
C_{25}-F_{25}	1.343	1.349	1.337	C_{17}-C_{19}-F_9	114.12	114.33	113.77
C_{26}-C_{27}	1.613	1.615	1.615	C_{17}-C_{19}-F_{10}	108.81	108.84	108.61
C_{26}-C_{28}	1.613	1.615	1.615	C_{17}-C_{19}-F_{11}	110.06	110.23	109.80
C_{26}-F_{26}	1.374	1.377	1.373	C_{18}-C_{17}-C_{19}	111.38	111.27	111.76
C_{27}-F_{27}	1.341	1.346	1.338	C_{20}-C_{21}-F_{13}	109.65	110.02	109.24
C_{27}-F_{28}	1.348	1.347	1.350	C_{20}-C_{21}-F_{14}	115.47	115.47	115.14
C_{27}-F_{29}	1.337	1.342	1.333	C_{20}-C_{21}-F_{15}	109.30	109.42	109.10
C_{28}-F_{30}	1.348	1.346	1.350	C_{20}-C_{22}-F_{16}	109.67	109.98	109.25
C_{28}-F_{31}	1.337	1.347	1.333	C_{20}-C_{22}-F_{17}	115.47	115.51	115.15
C_{28}-F_{32}	1.341	1.342	1.338	C_{20}-C_{22}-F_{18}	109.30	109.42	109.12
				C_{22}-C_{20}-C_{21}	116.55	116.47	117.02
				C_{23}-C_{24}-F_{20}	110.06	110.32	109.76
				C_{23}-C_{24}-F_{21}	114.12	114.31	113.77
				C_{23}-C_{24}-F_{22}	108.81	109.02	108.60
				C_{23}-C_{25}-F_{23}	110.05	110.32	109.78

C_{23}-C_{25}-F_{24}	114.11	114.31	113.78
C_{23}-C_{25}-F_{25}	108.82	109.02	108.63
C_{24}-C_{23}-C_{25}	111.38	111.25	111.78
C_{26}-C_{27}-F_{27}	109.30	109.45	109.10
C_{26}-C_{27}-F_{28}	109.67	110.13	109.21
C_{26}-C_{27}-F_{29}	115.47	115.59	115.16
C_{26}-C_{28}-F_{30}	109.30	109.48	109.10
C_{26}-C_{28}-F_{31}	109.65	110.07	109.27
C_{26}-C_{28}-F_{32}	115.47	115.65	115.14
C_{27}-C_{26}-C_{28}	116.55	116.19	117.01
F_{6}-C_{18}-F_{7}	107.81	107.45	108.11
F_{6}-C_{18}-F_{8}	107.68	107.77	107.86
F_{7}-C_{18}-F_{8}	108.21	108.06	108.61
F_{9}-C_{19}-F_{10}	107.81	107.42	108.09
F_{9}-C_{19}-F_{11}	107.67	107.76	107.85
F_{10}-C_{19}-F_{11}	108.21	108.06	108.59
F_{13}-C_{21}-F_{14}	108.04	107.95	108.38
F_{13}-C_{21}-F_{15}	107.07	107.08	107.33
F_{14}-C_{21}-F_{15}	106.97	106.54	107.37
F_{16}-C_{22}-F_{17}	108.03	107.93	108.38
F_{16}-C_{22}-F_{18}	107.06	107.09	107.32
F_{17}-C_{22}-F_{18}	106.97	106.55	107.34
F_{20}-C_{24}-F_{21}	107.67	107.72	107.88
F_{20}-C_{24}-F_{22}	108.21	107.96	108.60
F_{21}-C_{24}-F_{22}	107.81	107.31	108.11
F_{23}-C_{25}-F_{24}	107.68	107.71	107.86
F_{23}-C_{25}-F_{25}	108.21	107.93	108.60
F_{24}-C_{25}-F_{25}	107.81	107.34	108.07
F_{27}-C_{27}-F_{28}	107.06	107.02	107.31
F_{27}-C_{27}-F_{29}	106.97	106.42	107.40
F_{28}-C_{27}-F_{29}	108.03	107.85	108.37
F_{30}-C_{28}-F_{31}	107.07	107.02	107.30
F_{30}-C_{28}-F_{32}	106.97	106.38	107.38
F_{31}-C_{28}-F_{32}	108.04	107.85	108.37

Appendix G

Fundamentals of MD Simulations

G.1 Introduction

With applications in physics, chemistry, biochemistry, and materials science; molecular dynamics (MD) simulation offers the methodology for detailed microscopic modeling on the molecular scale. The central inquiry that MD simulations provide insight to is the relation between the bulk properties of matter (solid, liquid, or gaseous state) and the fundamental interactions among the constituent atoms or molecules. Simulations provide a bridge between microscopic length and time scales and the macroscopic world of the experimental laboratory. MD may also be employed to carry out simulations that are difficult in the laboratory such as working at high temperature or pressure. Given the continuous growth in computing power, the ability to answer questions of increasing complexity about microscopic behavior is possible through MD simulations.

Following the successes of Monte Carlo simulations, the molecular dynamics methodology was firth introduced by Alder and Wainwright to study the interaction of hard spheres in the late 1950's.[251-252] These initial studies using MD provided insight regarding the behavior of simple liquids. Rahman provided the next major advance in 1964 with the first simulation using a realistic potential for liquid argon.[253] The first simulation of a realistic system was done on liquid water in 1974 by Rahman and Stillinger[254]. This simulation of water is advancement over the previous Argon simulations due to the addition of Coulomb and hydrogen bond interactions present in water in addition to the van der Waal's interactions. The first protein simulations appeared in 1977 with the simulation of bovine pancreatic trypsin inhibitor (BPTI).[255]

G.2 Classical Mechanics

Molecular dynamics simulations consist of the numerical solution of the classical equations of motion. Integration of the equations of motion yields a trajectory that describes the positions, velocities, and accelerations of the particle as they vary with time. From this trajectory, the average values of properties may be determined. The MD method is deterministic, that is, once the positions and velocities of each particle are known, the state of the system may be predicted at any time in the future or the past. A simple application of Newton's second law of motion is presented below. Newton's equation of motion is given by:

$$F_i = m_i a_i \tag{G.1}$$

where F_i is the force exerted on particle i, m_i is the mass of particle i and a_i is the acceleration of particle i. The force may also be expressed as the gradient of the potential energy, V.

$$F_i = -\nabla_i V \tag{G.2}$$

Combining these two equations yields,

$$-\frac{dV}{dr_i} = m_i \frac{d^2 r_i}{dt^2} \tag{G.3}$$

Newton's equation of motion can then relate the derivative of the potential energy to the changes in position as a function of time. To calculate a trajectory, one only needs the initial positions of the atoms, an initial distribution of velocities and the acceleration, which is determined by the gradient of the potential energy function as follows:

$$F = ma = m\frac{dv}{dt} = m\frac{d^2x}{dt^2} \tag{G.4}$$

Taking the simple case where the acceleration is constant,

$$a = \frac{dv}{dt} \tag{G.5}$$

we obtain an expression for the velocity after integration

$$v = at + v_0 \tag{G.6}$$

and since

$$v = \frac{dx}{dt} \tag{G.7}$$

we can integrate once again to obtain

$$x = vt + x_0 \tag{G.8}$$

Combining this equation with the expression for velocity, we obtain the following relation which gives the value of x at time t as a function of the acceleration, a, the initial position, x_0, and the initial velocity, v_0.

$$x = at^2 + v_0 t + x_0 \tag{G.9}$$

Finally, the acceleration is given as the derivative of the potential energy with respect to the position, r,

$$a = -\frac{1}{m}\frac{dE}{dr} \tag{G.10}$$

G.3. Molecular Interactions

G.3.1 Non-bonded Interactions

In this section we will focus on the potential energy functions employed in the CHARMm forcefield.[256-257] While several other forcefields potentials exist, such as AMBER[258] and GROMACS,[259] the CHARMm potential was used for all MD investigations in this work. The most commonly used potential for non-bonded interactions of uncharged particles is that of the Lennard-Jones potential,[260]

$$V^{LJ}(r) = 4\varepsilon\left[\left(\frac{\sigma}{r}\right)^{12} - \left(\frac{\sigma}{r}\right)^{6}\right] \tag{G.11}$$

where σ is the diameter and ε the depth of the well. The potential describes a mild attraction as two particles approach each other from a distance, but a strong repulsive term when they get too close. The Lennard-Jones potential was employed for the early MD simulations on liquid argon previously mentioned.[253] Graphical representation of the potential may be seen in Figure G.1.

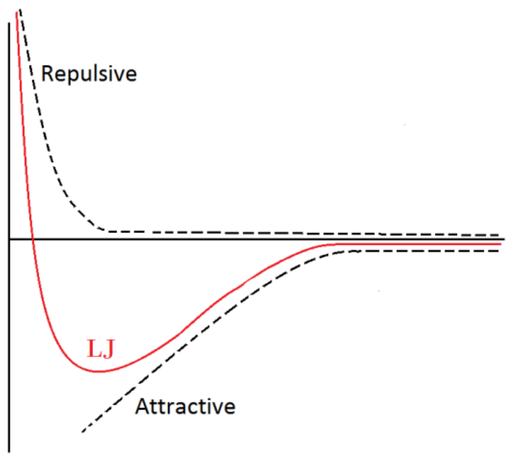

Figure G.1. Grapherical representation of the L-J potential.

To handle the electrostatic charges present in the system, a Coulomb potential is added,

$$V^{Coulomb}(r) = \frac{Q_1 Q_2}{4\pi\varepsilon_0 r} \tag{G.12}$$

where Q_1 *and* Q_2 are the charges of particle 1 and 2, and ε_0 is the permittivity of free space.

3.3.2 Bonding Potentials

In addition to the non-bonding interactions, we must also consider the bonding interactions for molecules. The CHARMm potential functions that describes these terms is shown below,

$$V^{\text{intermolecular}} = \sum_{Bonds} k_b (r - r_0)^2 \tag{G.13}$$

$$+ \sum_{\text{Angles}} \mathrm{k}_\theta (\theta - \theta_0)^2 \tag{G.14}$$

$$+ \sum_{Dihedrals} k_\varphi [1 + \cos(n\varphi - \delta)] \tag{G.15}$$

$$+ \sum_{\text{Impropers}} \mathrm{k}_\omega (\omega - \omega_0)^2 \tag{G.16}$$

$$+ \sum_{U-B} k_u (u - u_0)^2 \tag{G.17}$$

The first term in this potential accounts for the 2-body bond lengths where k_b is the bond force constant and r-r_0 is the band length deviation from equilibrium. The second term describes the band angles where k_θ is the angle force constant and θ-θ_0 is the angle from equilibrium between three bonded atoms. The third term is for the dihedral (tortion angles) where k_φ is the dihedral force constant, n represents the multiplicity of the angle, φ is the dihedral angle defined in terms of three connected bonds, and δ is the phase shift. The improper (out of plane) angles are described by the fourth term where k_ω is the improper force constant and ω-ω_0 is the improper angle deviation. The fifth term in the potential is the Urey-Bradley component. This accounts for the cross-term interaction for angle bending using 1-3 harmonic nonbonded interactions. For this term, k_u is the force constant and u-u_0 is the distance between atoms 1 and 3. The geometry of these terms is displayed for a simple molecule in Figure 2.

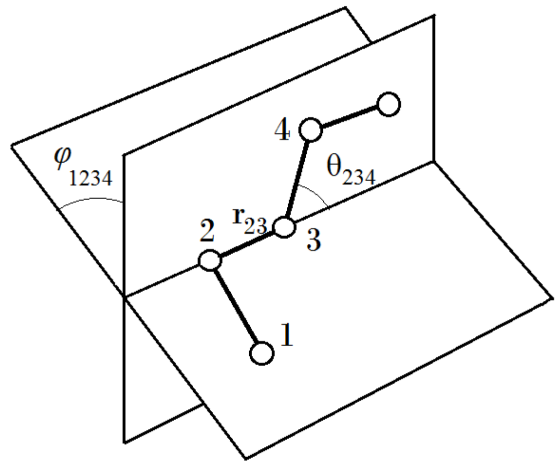

Figure G.2: Geometry of bond distance, r_{123}, bond angle, θ_{234}, and dihedral angle, φ_{1234}.

G.4. Integration Algorithms

The potential energy of a system is a function of the atomic positions (3N) of all the atoms in the systems. Due to the potential large scale of MD simulations and the inherit complexity of this function, there is no analytical solutions to the equations of motion. Therefore, these equations must be solved numerically. Several numerical algorithms have been developed to aid in the integration of the equations of motion. This section will give a brief introduction to the verlet,[261-262] leap-frog,[263] velocity verlet,[264] and Beeman's[265-266] algorithms. Several important factors must be considered when choosing which algorithm, including the following: The algorithm should conserve both energy and momentum, it should be computationally efficient, and it should allow a long time step for integration. All of the above integration algorithms mentioned assume the positions, velocities, and accelerations can be approximated by a Taylor series expansion as follows,

$$r(t+\delta t) = r(t) + v(t)\delta t + \frac{1}{2}a(t)\delta t^2 + \ldots \quad \text{(G.18)}$$

$$v(t=\delta t) = v(t) + a(t)\delta t + \frac{1}{2}b(t)\delta t^2 + \ldots \quad \text{(G.19)}$$

$$a(t=\delta t) = a(t) + b(t)\delta t + \ldots \quad \text{(G.20)}$$

Where *r* is the position, *v* is the first derivate with respect to time (velocity), and *a* is the second derivative with respect to time (acceleration), etc.

G.4.1 Verlet Algorithm

The Verlet algorithm[261-262] calculates new positions at time $t+\delta t$ from the positions and accelerations at time *t* and the positions from time $t-\delta t$. From this formulation, one can see that this algorithm uses no explicit velocities. The Verlet algorithm requires little data storage compared to the other algorithms but the precision of this method is relatively modest. The derivation is shown below;

$$r(t+\delta t) = r(t) + v(t)\delta t + \frac{1}{2}a(t)\delta t^2 \quad \text{(G.21)}$$

$$r(t-\delta t) = r(t) - v(t)\delta t + \frac{1}{2}a(t)\delta t^2 \quad \text{(G.22)}$$

Summation of these two equations provides;

$$r(t+\delta t) = 2r(t) - r(t-\delta t) + a(t)\delta t^2 \quad \text{(G.23)}$$

G.4.2 Leap-frog Algorithm

The leap-frog[263] algorithm is a modification to the original Verlet[261-262] algorithm. The positions, r, at time $t+\delta t$ are calculated from first calculating the velocities, v, at time $t+\frac{1}{2}\delta t$. This is where the name leap-frog comes from; the velocities leap over the positions, then the positions leap over the velocities as the simulation proceeds.

$$r(t+\delta t) = r(t) + v\left(t + \frac{1}{2}\delta t\right)\delta t \tag{G.24}$$

$$v(t+\frac{1}{2}\delta t) = v\left(t - \frac{1}{2}\delta t\right) + a(t)\delta t \tag{G.25}$$

The distinct advantage of this algorithm over the original Verlet algorithm is that the velocities are explicitly calculated. But it must again be emphasized that the velocities are not calculated at the same time as the positions. To approximate the velocities at time t, the following relation may be used;

$$v(t) = \frac{1}{2}\left[v\left(t - \frac{1}{2}\delta t\right) + v\left(t + \frac{1}{2}\delta t\right)\right] \tag{G.26}$$

G.4.3 Velocity Verlet Algorithm

The velocity verlet[264] algorithm is the best of the algorithms belonging to the verlet family. Its major advantage over the others is that it yields the positions, velocities, and accelerations at time t without any compromise on precision. However, it should be noted that this algorithm assumes that the acceleration at time $t+\delta t$ only depends on the position at time

$t+\delta t$ and does not depend on the velocity at time $t+\delta t$. It is the velocity verlet algorithm that is employed in the simulation package NAMD:[79]

$$r(t+\delta t) = r(t) + v(t)\delta t + \frac{1}{2}a(t)\delta t^2 \tag{G.27}$$

$$v(t+\delta t) = v(t) + \frac{1}{2}\left[a(t) + a(t+\delta t)\right]\delta t \tag{G.28}$$

G.4.4 Beeman's Algorithm

Beeman's[265-266] algorithm is a modification to the Verlet[261-262] integration method. It produces identical positions as verlet, but employs a different formula for calculation of the velocities. This method can be found in two forms; the more popular direct form published by Schofield[266] in 1973, and the implicit (predictor-corrector) multi-step form published by Beeman[265] in 1976. The popular direct form is shown below. This algorithm is considerably more complex making calculation more computationally expensive, but produces a more accurate expression for the velocity and better energy conservation.

$$r(t+\delta t) = r(t) + v(t)\delta t + \frac{2}{3}a(t)\delta t^2 - \frac{1}{6}a(t-\delta t)\delta t^2 \tag{G.29}$$

$$v(t+\delta t) = v(t) + v(t)\delta t + \frac{1}{3}a(t)\delta t + \frac{5}{6}a(t)\delta t - \frac{1}{6}a(t-\delta t)\delta t \tag{G.30}$$

G.5 Statistical Mechanics

Statistical mechanics is essential for the conversion of information gathered at the microscopic level in MD simulations to macroscopic observables. Statistical mechanics can be classified into two distinct parts; dealing with systems in equilibrium and dealing with systems not in equilibrium. The former is referred to as statistical thermodynamics and provides a mathematical relation between the various macroscopic experimental observables to the distribution and motion of the atoms and molecules of the MD simulation. The field of statistical mechanics is far too vast to be covered here in any detail; instead a simplified explanation of the various thermodynamic ensembles along with methods to calculate experimental observables in terms of ensemble averages will be presented in this section.

G.5.1 Ensemble Types

An ensemble is a very large collection of all possible microscopic states, but represents the same thermodynamic state. Simply stated, it is a probability distribution for the state of the system. The various properties of a given ensemble depend on the constraints imposed on the system. The possible ensembles and the corresponding constraints and partition functions are summarized in Table G.1.

Table G.1: Various ensembles with corresponding constraints and partition functions.

Ensemble	Constraint	Partition Function ($kT\ln(q)$)
Microcanonical	N, V, E	ST
Canonical	N, V, T	-A
Grand Canonical	V, T, μ	PV
Isothermal-Isobaric	N, T, P	-G

G.5.2 Ensemble Averages

In statistical mechanics, macroscopic observables are defined as ensemble averages. Ensemble averages incorporate a large number of replicas of the system considered at the same time and is given by;

$$\langle A \rangle_{ensemble} = \iint dp^N dr^N A\left(p^N, r^N\right)\rho\left(p^N, r^N\right) \quad \text{(G.31)}$$

where $A(p^N,r^N)$ is the observable of interest expressed as a function of the momenta, *p*, and the positions, *r*, and integrated over all possible values of *p* and *r*. The $\rho(p^N,r^N)$ term is the probability density of the ensemble and is expressed as;

$$\rho\left(p^N, r^N\right) = \frac{1}{Q}\exp\left[\frac{-H\left(p^N, r^N\right)}{k_b T}\right] \quad \text{(G.32)}$$

where H is the Hamiltonian, T is the temperature, k_b is Boltzmann's constant, and Q is the partition function:

$$Q = \iint dp^N dr^N \exp\left[\frac{-H\left(p^N, r^N\right)}{k_b T}\right] \tag{G.33}$$

As seen above, the partition function integral requires calculation of all possible states of the system. Since points in the ensemble are calculated sequentially in time during an MD simulation, this would require the MD simulation to pass through all possible states corresponding to the thermodynamic constraints to arrive at an ensemble average. Evaluation of this integral during a MD simulation would be extremely computational expensive if not impossible. Fortunately, statistical mechanics allows reasonable assumptions to be made to simplify the process. It is assumed that the random process we are attempting to measure is stationary in time. That is to say the probability distribution functions do not depend on a shift of the origin of time. This leads to the assumption known as the ergodic hypothesis in statistical mechanics. Making a large number of observations at M instants of time on a single system, as in MD simulations, have the same statistical properties as observing a large number of M systems at the same instant of time, as in an experimental observable. This allows the experimental observable (ensemble average) to be determined as a time average over the MD simulation.

$$\begin{aligned} \langle A \rangle_{time} &= \lim_{\tau \to \infty} \frac{1}{\tau} \int_{t=0}^{\tau} A\left(p^N(t), r^N(t)\right) dt \\ &\approx \frac{1}{M} \sum_{t=1}^{M} A\left(p^N, r^N\right) \end{aligned} \tag{G.34}$$

where t is the simulation time, M is the number of simulation time steps, and $A(p^N, r^N)$ is the instantaneous value of A (our observable). Some simple examples of MD time averages are the average potential and kinetic energy:

$$V = \langle V \rangle = \frac{1}{M}\sum_{i=1}^{M} V_i \tag{G.35}$$

$$K = \langle K \rangle = \frac{1}{M}\sum_{j=1}^{M}\left\{\sum_{i=1}^{N}\frac{m_i}{2}v_i v_j\right\}_j \tag{G.36}$$

where M is the number of configurations in the MD trajectory, V_i is the potential energy of each configuration, N is the number of atoms in the system, m_i and v_i is the mass and velocity of the particle i, respectively.

G.6. Temperature and Pressure Control

As seen in the ensemble discussion of the last section, simulation under the canonical, grand canonical and isobaric-isothermal ensembles requires methods to control the temperature and pressure of the system. Temperature is a thermodynamic quantity and function of the velocities. The temperature of a given system can be related to the average kinetic energy of the system through the equipartition of energy principle in statistical mechanics. This states that every degree of freedom will contribute ½ k_bT to the average energy[267].

$$\langle K \rangle = \left\langle \sum_{i}^{N}\frac{1}{2}mv_i^2 \right\rangle = \frac{N_f k_b T}{2} \tag{G.37}$$

where N_f is the number of degrees of freedom, k_b is Boltzmann's constant, and T is the temperature. In addition to the average kinetic energy, the instantaneous kinetic temperature can be defined as:

$$T_{ins} = \frac{2K}{N_f k_b} \qquad \text{(G.38)}$$

where the thermodynamic temperature of the system is equal to the average of the instantaneous kinetic temperature of all the particles in the system. Given the relation between kinetic energy of the temperature of the system, a common method for controlling the system temperature is to scale the velocities of the particles (atoms). Such adjustments simply add or subtract energy to or from the system to maintain constant temperature. However, this method is very inaccurate and not a realistic description of how energy is dissipated in real systems. To overcome such simplistic methods several algorithms has been developed, including Nosé -Hoover, Langevin, and Berendsen methods. These three most popular methods will be discussed below.

G.6.1. Nosé-Hoover Thermostat

The Nosé-Hoover thermostat began as a version proposed by Nosé[268-269] in which thermal reservoir was introduced to maintain constant temperature. Nosé's original method consisted of an addition degree of freedom that corresponded to the thermal reservoir and acted as a time scaling factor. Additionally, a parameter describing the mass of the thermal reservoir was introduced. Later, Hoover[270] simplified the Nosé method by eliminating the time scaling factor and introducing a new friction coefficient. This simplified Nosé method proposed by Hoover is what is known as the Nosé-Hoover thermostat. The temperature control mechanism for this thermostat is shown below;

$$\dot{\zeta} = \frac{1}{Q}\left(\sum_{i=1}^{N}\frac{p_i^2}{m_i} - N_f k_b T\right) \tag{G.39}$$

where ζ is the thermodynamic friction coefficient and Q is the parameter for the mass of the thermal reservoir. It should be noted that the value of Q is at the discretion of the user, but performance of the thermostat depends on the use of appropriate values. When this parameter was introduced, Nosé recommended values for Q be proportional to $N_f k_b T$. If Q values are too small the temperature of the system will fluctuate rapidly, while too large of a value of Q will lead to inefficient sampling of the system.

G.6.2 Generalized Langevin Equation Approach (GLEQ)

This temperature control approach was first introduced by Adelman and Doll[271] in 1976. In this approach the system is thought to be not in vacuum, but embedded in a constant temperature “solvent”. In this type of scheme the atoms or molecules making up the system are thought to be solutes. From the solvent effects on the solute, two new terms are introduced to the equations of motion. The frictional force (friction constant, β), which accounts for the frictional drag that occurs as solute passes through solvent, and the random force (R(t)), which accounts for the random collisions between solute and solvent. To maintain constant temperature in the system, the random force is balanced with the frictional force. The equation of motion for the new “solute” particle is as follows:

$$ma(t) = F(t) - \beta v(t) + R(t) \quad \text{(G.40)}$$

Therefore, through gradually modifying the velocity of the particle, the instantaneous kinetic temperature of the particle is close to the desired system temperature.

G.6.3 Berendsen Method

The Berendsen[272] method for temperature control was introduced in 1984 and is much like the earlier Andersen[273] method which was introduced in 1980. In both of these methods the system is coupled to an imagery external thermal bath which is held at a fixed temperature. The difference between the two methods is in the rate of the exchange of thermal energy between the bath and the system. The Anderson method is known for rapid exchange that leads to drastic changes in the system dynamics, while the Berendsen method involves a much more gradual exchange. Under the Berendsen method, the velocity of the particle is slowly scaled by multiplying it by a scaling factor, λ:

$$\lambda = \left[1 + \frac{\Delta t}{\tau_T}\left(\frac{T}{T_{ins}} - 1\right)\right]^{1/2} \quad \text{(G.41)}$$

where Δt is the time step and τ_T is the time constant of the coupling between the bath and the system.

G.7. Periodic Boundary Conditions

Unless a simulation is designed to investigate surface effects, periodic boundary conditions must be employed. Even in systems with a large number of atoms present in the simulation box, a large percent of these atoms will be on the outer faces of the box. Without periodic conditions, this will lead to large effects on any calculated properties during the simulation. By using periodic boundary conditions, the simulation box is replicated in all directions to give a periodic array. If a particle is to leave the box during simulation, it is substituted with an image particle that comes in from the opposite side. When calculating particle interactions within the cutoff range, both real and image neighbors are included. Therefore the number of particles inside the simulation box is conserved throughout the MD simulation. The concept of a periodic array is illustrated in Figure G.3.

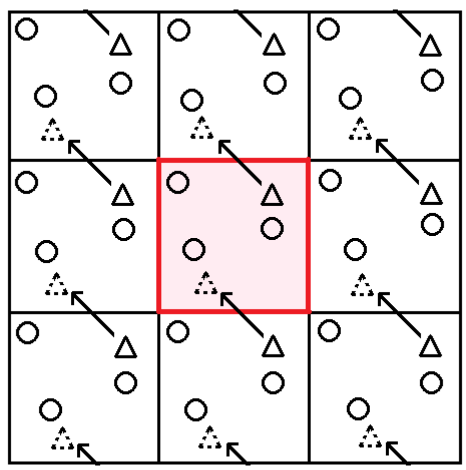

Figure G.3: Periodic boundary conditions. The simulation box is shaded in red with surrounding periodic array. The particle (solid triangle) moves out of the simulation box along the path specified by the arrow and is replaced by an image particle (dashed triangle).

G.8. Neighbor Lists

During any MD simulation, the calculation of the non-bonded interactions previously discussed involves a large number of pairwise calculations. In principle, for each atom *i*, we must loop over all other atoms, *j*, in the system to calculate the minimum separations, r_{ij}. With increased system size, comes increased number of pairwise calculations. The number of distinct pairs in any given system is $\frac{1}{2}N(N-1)$, where N is the number of atoms in the system. To save in computational time some methods have been developed to limit the number of pair interaction that needs to be considered. First, a potential cutoff, r_{cutoff}, is defined by the user in that if $r_{ij} > r_{cutoff}$ then $v(r_{ij})=0$ and the force calculation is skipped.

Verlet[261] introduced another technique for improving the speed of the pair calculations. This technique is known as creating neighbor lists, in which outside the potential cutoff radius another sphere of radius, r_{list}, is introduced. At the start of an MD simulation, a neighbor list is constructed for all atoms that consist of any atoms that are found within the r_{list} cutoff. Over the next few MD steps, only atoms within this neighbor list are run through the force calculation process. Because atoms may experience large positional displacements during the simulation, these neighbor lists need to be updates as the simulation progresses. This updating of the list must be done before any atoms not contained in the list move into range of the non-bonding potential cutoff. Like the potential cutoff, the neighbor list cutoff is defined by the user. Choosing the appropriate list cutoff is a compromise. Smaller list cutoffs include less neighbors, therefore less pair calculations, but require frequent updating. Larger list cutoffs need to be reconstructed much less frequently, but include larger number of atoms and therefore become more computationally demanding. A simple illustration of the potential and neighbor list cutoffs are displayed in Figure G.4.

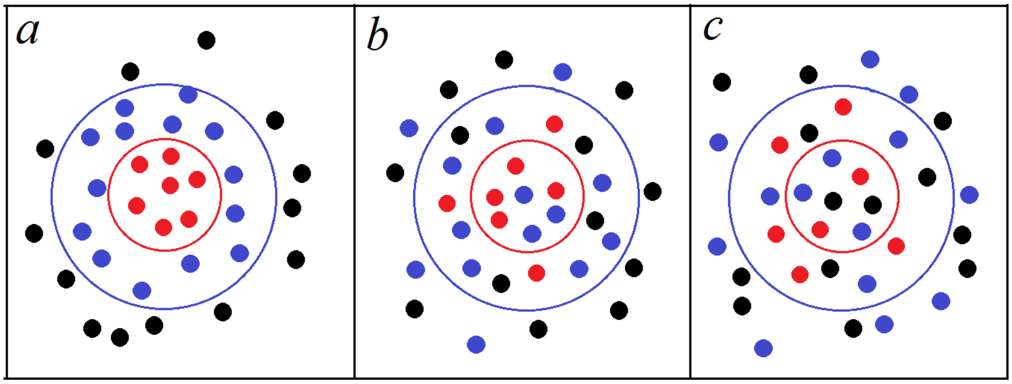

Figure G.4: The atomic potential cutoff (red line) and Verlet neighbor list cutoff (blue line). Three types of atoms depicted: atoms inside both cutoffs (red), atoms inside the neighbor list cutoff only (blue), and atoms outside both cutoffs (black). (a) Construction of the lists, (b) lists at some time later, and (c) lists that has not been updated soon enough; atoms not in the neighbor list have moved into the potential cutoff range.

Appendix H

Fundamentals of Density functional Theory

H.1. Introduction

Density functional theory (DFT) was first introduced in two groundbreaking papers published in the 1960's. First the Hohenberg-Kohn paper[274] in 1964, followed by the Kohn-Sham[275] paper one year later. Walter Kohn would later be awarded the Nobel Prize in chemistry in 1998 for his part in the development of DFT. The application of DFT encompasses many broad areas of research and continues to grow at a rapid pace every year. DFT is an extraordinarily effective approach to finding solutions to the fundamental equation that describes the quantum behavior of atoms or molecules; the Schrödinger equation. The primary motivation of DFT is to describe a many-body interacting system by its particle density; not its many-body wavefunction. Therefore, the systems 3N degrees of freedom are reduced to only three spatial coordinates. Practical application of DFT requires several approximations to be introduced. In this appendix, a condensed version of the basics behind DFT theory will be explored. It is important to note that atomic units will be used throughout this section.

H.2. Born-Oppenheimer Approximation

The Hamiltonian (*H*) operator for a many-body system consisting of *M* nuclei and *N* electrons is:

$$\hat{H} = -\frac{1}{2}\sum_{i=1}^{N}\nabla_i^2 - \frac{1}{2}\sum_{A=1}^{M}\frac{1}{M_A}\nabla_A^2 - \sum_{i=1}^{N}\sum_{A=1}^{M}\frac{Z_A}{r_{iA}} + \sum_{i=1}^{N}\sum_{i>j}^{N}\frac{1}{\mathrm{r}_{\mathrm{ij}}} + \sum_{A=1}^{M}\sum_{B>A}^{M}\frac{Z_A Z_B}{R_{AB}} \quad (\mathrm{H.1})$$

where *A* and *B* run over the *M* nuclei and *i, j* denote the *N* electrons in the systems. The kinetic energy of the electrons and nuclei are described by the first and second terms, respectively. The other three terms represent the attractive electrostatic interaction between the nuclei and the electrons and the repulsive potential due to the electron-electron and nucleus-nucleus interactions. The time-independent form of the Schrödinger equation for the many-body systems is:

$$\hat{H}\Psi(\{R_A\},\{r_i\}) = E\Psi(\{R_A\},\{r_i\}) \tag{H.2}$$

Solving the Schrödinger equation allows everything about the system to be known. However, in practice, it is impossible to solve. A fundamental observation in quantum mechanics is that atomic nuclei are much heavier than electrons. Therefore, electrons respond much more rapidly to changes in their surroundings than nuclei will on the timescale of nuclear motion. This means we may consider the electrons of a system as moving in a field of fixed nuclei, i.e. the nuclear kinetic energy is zero and their potential energy is a constant. This is known as the Born-Oppenheimer approximation.[276] Now, the total wavefunction may be written as:

$$\psi(\{R_A\},\{r_i\}) = \Theta(\{R_A\})\phi(\{r_i\}) \tag{H.3}$$

Where $\Theta(\{R_A\})$ describes the nuclei and $\phi(\{r_i\})$ the electrons of the system. Thus, the Hamiltonian (H.1) may be divided into nuclear and electronic parts; where the electronic Hamiltonian (H_{elec}) is written as:

$$\hat{H}_{elec} = -\frac{1}{2}\sum_{i=1}^{N}\nabla_i^2 - \sum_{i=1}^{N}\sum_{A=1}^{M}\frac{Z_A}{r_{iA}} + \sum_{i=1}^{N}\sum_{i>j}^{N}\frac{1}{\mathrm{r_{ij}}} \tag{H.4}$$

where the solution to the Schrödinger equation with H_{elec} is the electronic wave function, Ψ_{elec}, and the electronic energy, E_{elec}. The total energy of the system is simply the sum of the electronic energy and the constant nucleus energy, E_{nuc}:

$$\hat{H}_{elec}\,\psi_{elec} = E_{elec}\psi_{elec} \tag{H.5}$$

$$E_{total} = E_{elec} + E_{nuc} \tag{H.6}$$

$$E_{nuc} = \sum_{A=1}^{M}\sum_{B>A}^{M}\frac{Z_A Z_B}{R_{AB}} \tag{H.7}$$

H.3 Variational Principle

The variational method[277] is an approximation to find the ground-state energy of a system of several interacting particles without needing to explicitly solve the Schrödinger equation. First, when a system is in the state φ, the expectation value of the energy is given by:

$$E\varphi = \frac{\left\langle \varphi \,|\, \hat{H} \,|\, \varphi \right\rangle}{\left\langle \varphi \,|\, \varphi \right\rangle}$$

$$\left\langle \varphi \,|\, \hat{H} \,|\, \varphi \right\rangle = \int \varphi^{*}\,\hat{H}\,\varphi d\tau \tag{H.8}$$

The variational principle states if φ is any normalized well-behaved function that satisfies the boundary conditions of the problem, it is true that,

$$\int \varphi^* \hat{H} \varphi \, d\tau \geq E_0 \qquad \text{(H.9)}$$

where E_0 is the value of the lowest energy eigenvalue of the Hamiltonian operator, H.[278] The function φ is known as the trial wave function and the integral in Equation H.9 is the variational integral. This approximation method tries many trial wave functions and looks for one that gives the lowest value of the variational integral. The lower the value of the variational integral, the better approximation to E_0 is achieved. In practical applications of the variational method, several parameters are put into the trial wave function, and then these parameters are varied to minimize the variational integral. The ability to make a good choice of a trial function is essential in the success of this method.

H.4. Hohenberg-Kohn Theorems

To better understand the theorems that laid the foundation for DFT, we must first discuss the electron density. It is worth noting that although great emphasis has been placed on the wave function, it remains something that cannot be directly observed. The quantity that can (in principle) be observed is the probability that the N electrons are at a particular position. Therefore, the quantity of fundamental importance becomes the electron density; the density of electrons at a particular position in space. This may be written as the integral over all the spin coordinates of all electrons over all but one spatial variables (x ≡ r, s),

$$\rho(r) = N \int \ldots \int \left| \Psi(x_1, x_2, \ldots, x_N) \right|^2 ds_1 dx_2 \ldots dx_N \qquad \text{(H.10)}$$

The entire field of DFT is rooted in two fundamental mathematical theorems proved by Hohenberg and Kohn.[27,274] The first H-K theorem shows that the electron density uniquely determines the Hamiltonian operator, and thus all the properties of the system. That is, the external potential $V_{ext}(r)$ is a unique functional of the electron density $\rho(r)$. The importance of this theorem is that know solving the Schrödinger equation may be thought of as finding a function of three spatial variables (the electron density) rather than a function of the many body wave function (3*N* variables). The second H-K theorem states: $F_{HK}[\rho]$, the functional that delivers the ground state energy of the system, delivers the lowest energy if, and only if, the input density is the true ground state density. This is essentially the variational principle at work. If the HK functional were known, the electron density could be varied until the energy of the functional is minimized. In turn, this would lead to the ground-state electron density and energy.

The universal H-K functional, $F_{HK}[\rho]$, proposed contains the functional for the kinetic energy, $T[\rho]$, and the electron-electron interaction, $E_{ee}[\rho]$.

$$F_{HK}[\rho] = T[\rho] + E_{ee} \tag{H.11}$$

Unfortunately, the explicit form of both of these functional is completely unknown. The classical part, $J[\rho]$, of the electron-electron interaction, which is known, may be separated from the non-classical, E_{ncl}, part in Equation H.22:

$$\begin{aligned} E_{ee}[\rho] &= J[\rho] + E_{ncl}[\rho] \\ &= \frac{1}{2}\iint \frac{\rho(r_1)\rho(r_2)}{r_{12}} dr_1\, dr_2 + E_{ncl} \end{aligned} \tag{H.12}$$

H.5. Kohn-Sham Equations

In the year following the H-K paper, The Kohn-Sham paper was published;[275] which made practical application of DFT a possibility. The Kohn-Sham method suggested replacing the original many-body system with a non-interacting reference system, *S*, with the same electron density as the real, interacting system. For the reference system, the Kohn-Sham Hamiltonian is written as:

$$\hat{H}_{KS} = -\frac{1}{2}\nabla^2 + V_{KS}(r) \tag{H.13}$$

where the non-interacting electron are moving in the Kohn-Sham single particle potential, (V_{KS}). The ground state is then obtained by solving these one electron Schrödinger equations; with a single electron in each of the N orbitals (φ_i) and lowest eigenvalue (ε_i):

$$\hat{H}_{KS}\varphi_i(r) = \varepsilon_i\varphi_i(r) \tag{H.14}$$

The electron density (p_s) and kinetic energy (T_s) of the reference system (*S*) is then:

$$T_S = -\frac{1}{2}\sum_i^N \langle \varphi_i \mid \nabla^2 \mid \varphi_i \rangle \tag{H.15}$$

$$\rho_S(r) = \sum_i^N \sum_S |\varphi_i(r,s)|^2 = \rho(r) \tag{H.16}$$

Kohn and Sham accounted for the difference in kinetic energy between the reference system and the true kinetic energy by introducing the separation of the universal functional as follows:

$$F[\rho] = T_S[\rho] + J[\rho] + E_{XC}[\rho] \quad \text{(H.17)}$$

$$E_{XC}[\rho] \equiv (T[\rho] - T_S[\rho]) + (E_{ee}[\rho] - J[\rho]) \quad \text{(H.18)}$$

where *J[p]* is the classical electrostatic energy of the electrons:

$$J[p] = \frac{1}{2}\iint \frac{n(r_i)n(r_j)}{|r_i - r_j|} dr_i dr_j \quad \text{(H.19)}$$

The exchange and correlation energy, E_{xc}, contains the difference between the real and reference KE, as well as the non-classical electron-electron interactions. Next, in order to determine the orbitals in the reference system, a potential, V_S, must be defined that generates a Slater determinant with the same density as our real system. The expression for the energy of the interacting system in terms of the separation in Equation H. 17 would be:

$$E[\rho] = T_S[\rho] + J[\rho] + E_{XC}[\rho] + E_{Ne}[\rho]$$

$$= -\frac{1}{2}\sum_i^N \langle \varphi_i | \nabla^2 | \varphi_i \rangle + \frac{1}{2}\sum_i^N \sum_j^N \iint |\varphi_i(r_1)|^2 \frac{1}{r_{12}} |\varphi_j(r_2)|^2 dr_1 dr_2 + E_{XC}[\rho] \quad \text{(H.20)}$$

$$-\sum_i^N \int \sum_A^M \frac{Z_A}{r_{1A}} |\varphi_1(r_1)|^2 dr_1$$

The only term in Equation H.20 in which there is no explicit form is $E_{XC.}$ Through use of the variational principle to minimize this energy expression, the final component of the Kohn-Sham equations appears.

$$\left(-\frac{1}{2}\nabla^2 + \left[\int \frac{\rho(r_2)}{r_{12}} + V_{XC}(r_1) - \sum_{A}^{M} \frac{Z_A}{r_{1A}}\right]\right)\varphi_i = \left(-\frac{1}{2}\nabla^2 + V_S(r_1)\right)\varphi_i = \varepsilon_i \varphi_i \qquad \text{(H.21)}$$

$$V_S(r_1) = \int \frac{\rho(r_2)}{r_{12}} + V_{XC}(r_1) - \sum_{A}^{M} \frac{Z_A}{r_{1A}} \qquad \text{(H.22)}$$

By finding the various contributions in Equations H.21 and H.22, we achieve an understanding of the potential, V_S, which is needed to insert into the one-particle equations. This then determines the spin orbitals and later the ground state energy. The potential is dependent on the electron density, and therefore, the Kohn-Sham equations, which give the single-electron wave functions as solutions, depend only on the spatial variables. The exchange-correlation potential, V_{xc}, in Equation 22 is the functional derivative of the exchange-correlation energy, E_{XC}, with respect to the electron density.

$$V_{XC} = \frac{\delta E_{XC}}{\delta \rho} \qquad \text{(H.23)}$$

As can been seen in all of the previous discussion, solving the Kohn-Sham equations is circular process. The potential is needed to solve the Kohn-Sham equations, and the electron density is needed to define the potential. But to find the electron density, the single-electron wave functions must be known, and these wave functions are the solution to the Kohn-Sham equations. Therefore, these equations must be solved in an iterative manner. The process for solving the Kohn-Sham equations is depicted in Figure H.1.

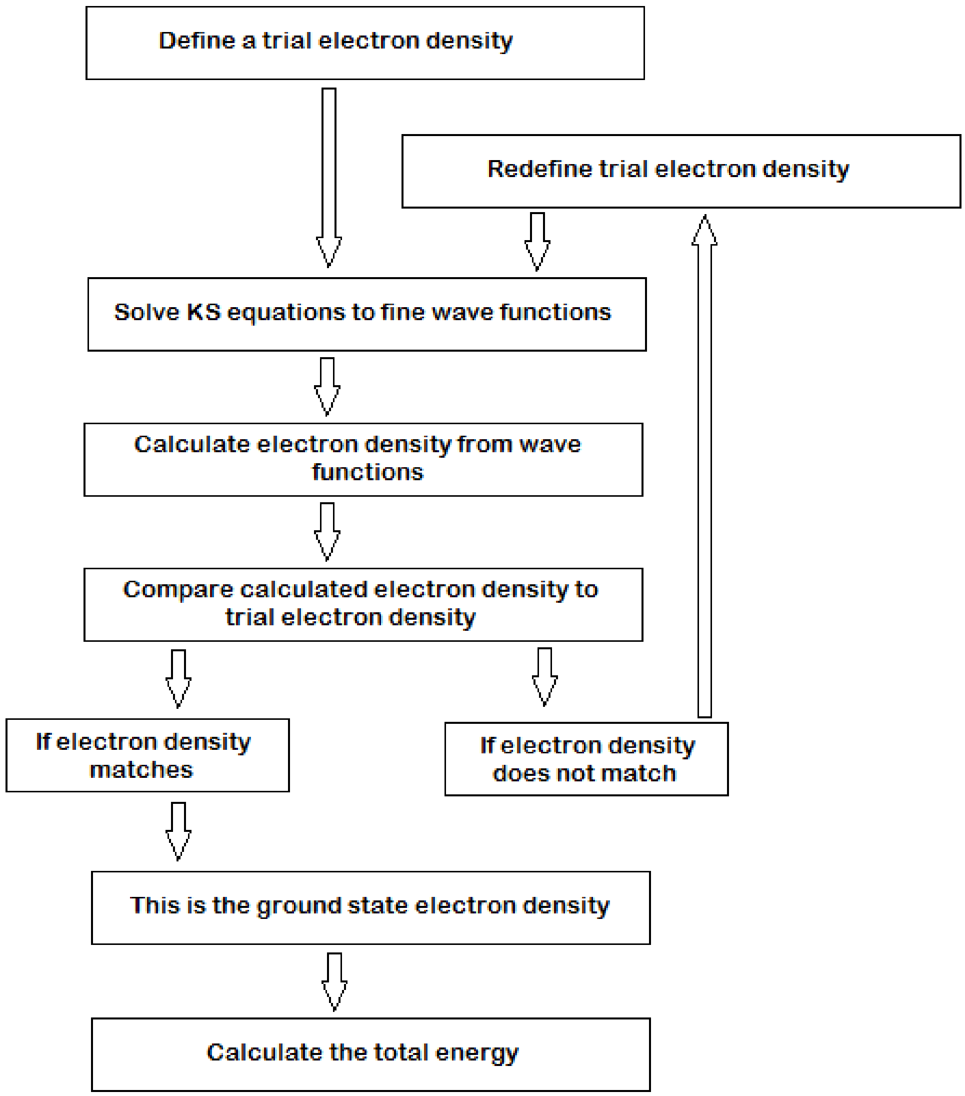

Figure H.1: Iterative method for solving the Kohn-Sham equations.

H.6. Local Density Approximation (LDA)

To solve the Kohn-Sham equations discussed in the previous section, an exchange-correlation functional must be specified. However, the exact form of the exchange-correlation functional is simply not known. Fortunately, simple but successful approximations to it have been proposed. These approximations allow for accurate predictions of various properties while greatly reducing the computational cost. The first of these approximations to be considered is the local density approximation (LDA).[275] In LDA, the exchange and correlation is solved in terms of a uniform electron gas. For this condition, the electron density is assumed constant at all points in space. That is the electron moves on a positive background charge distribution so that the total ensemble has a net charge of zero (neutral). This situation may seem to be of limited value since it is the deviation in electron density that defines chemical bonds, but the uniform electron gas model provides a practical way to employ the Kohn-Sham equations. This may be written in the following way,

$$E_{XC}^{LDA}[\rho] = \int \rho(r)\varepsilon_{XC}(\rho(r))\,dr \tag{H.24}$$

where $\varepsilon_{XC}(\rho(r))$ is the exchange-correlation energy per particle of a uniform electron gas. This exchange-correlation may be separated into an exchange and a correlation part:

$$\varepsilon_{XC}(\rho(r)) = \varepsilon_X(\rho(r)) + \varepsilon_C(\rho(r)) \tag{H.25}$$

For spin polarized systems,[279]

$$E_{XC}^{LDA}[\rho_{\uparrow,}\rho_{\downarrow}] = \int \rho(r)\varepsilon_{XC}(\rho_{\uparrow}(r), \rho_{\downarrow}(r))\,dr \tag{H.26}$$

The exchange energy of an electron in a uniform electron gas of a particular density was originally derived by Dirac.[280]

$$\varepsilon_X = -\frac{3}{4}\left(\frac{3\rho(r)}{\pi}\right)^{1/3} \tag{H.27}$$

No explicit expression is known for the correlation energy, except at high and low densities. Most local density approximations interpolate correlation energies at intermediate density from the known high and low limits. Some local density approximations include; Vosko-Wilk-Nusair,[281] Perdew-Zunger,[282] Cole-Perdew,[283] and Perdew-Wang.[284]

The major drawback to LDA is ignoring the inhomogeneities in the electron density; but this simple method works reasonability well. LDA tends to underestimate ground state energies and ionization energies, while overestimating binding energies. It is also known to be poor at predicting band gaps of some semiconductors. These shortcomings have lead to additional XC functionals; including the Generalized Gradient Approximation (GGA), which adds gradient corrections to the electron density; and LDA+U, which adds a correction term to account for stronger correlation of the *d* electron in transition elements. Both of these methods will be addressed in the following sections.

H.7. Generalized Gradient Approximation (GGA)

The best known class of functional after the LDA uses information about the local gradient of the electron density in addition to the local electron density. This method is known as the generalized gradient approximation (GGA).

$$E_{XC}^{GGA}\left[\rho_{\alpha},\rho_{\beta}\right]=\int f\left(\rho_{\alpha},\rho_{\beta},\nabla\rho_{\alpha},\nabla\rho_{\beta}\right)dr \qquad \text{(H.28)}$$

Contrary to conventional thought, GGA functionals are not always more accurate than LDA functionals even though they include more physical information. There is also a large number of different GGA functionals, which vary in the way the gradient information is included. Some of the most widely used GGAs were proposed by: Becke;[285] Perdew;[284] and Perdew, Burke, and Enzerhof.[286] GGA still tens to underperform in systems with localized and strongly correlated electrons, such as transition metal oxides.

H.8 LDA+U Method

Systems containing transition metals are strongly correlated due to the localized partially filled *d* orbitals. The orbital-independent potentials in LDA and GGA do not property describe these systems. The LDA+U[287] method is the most widely used approach to correctly model the strong *d* (or *f*) electron-electron correlation. Within the LDA+U methodology, the electron of the system are separated into two regimes; delocalized *s* and *p* electrons, and localized *d* and *f* electrons. The delocalized *s* and *p* electrons are well described by LDA and/or GGA. For the localized *d* and *f* electrons, an additional orbital-dependant Columbic term is introduced to treat the *d-d* and *f-f* electron interactions:

$$\frac{1}{2}U\sum_{i\neq j} n_i n_j \tag{H.29}$$

where n_i are *d* or *f* orbital occupancies. The total energy in LDA+U is given by:[287]

$$E_{LDA+U} = E_{LDA} + \frac{1}{2}U\sum_{i\neq j} n_i n_j - \frac{1}{2}UN(N-1) \tag{H.30}$$

The first term in Eq. H.30 is the standard LDA energy discussed previously, the second term is the electron-electron interaction, and the third term is a double counting term which removes an averaged LDA energy contribution of the *d* and/or *f* electrons from the LDA energy. The derivative of Eq. H.30 with respect to the orbital occupations (n_i) provides the orbital energies:

$$\varepsilon_i = \frac{\partial E}{\partial n_i} = \varepsilon_{LDA} + U\left(\frac{1}{2} - n_i\right) \tag{H.31}$$

For occupied orbitals ($n_i = 1$), the LDA+U orbital energies are shifted by –U/2 compared to the LDA orbital energies. For unoccupied orbitals ($n_i = 0$), the LDA+U orbital energies are shifted by +U/2. Therefore, the band gap is increased by *U* with the LDA+U method.

H.9. Basis Sets

For most KS applications in chemistry, a linear combination of atomic orbitals (LCAO) expansion is employed. A set of *N* predefined basis functions, $\{\eta_\mu\}$, are introduced and linearly expanded as:

$$\varphi_i = \sum_{\mu=1}^{N} c_{\mu i} \eta_u \tag{H.32}$$

This finite set of functions is called the basis set for the calculation. Naturally, increasing the size of the basis set will increase the accuracy of the calculation, but will also increase the computational cost of the calculation. There are two basic types of basis sets available, Slater-type-orbitals (STO),[288] and Gaussian-type-orbitals (GTO).[289] Slater-type-orbitals are exponential functions that mimic the exact eigenfunctions of the Hydrogen atom. A typical STO is shown below:

$$\eta^{STO} = Nr^{n-1} \exp[-\beta r] \mathrm{Y}_{lm}(\Theta, \phi) \tag{H.38}$$

This function contains the principle quantum number, n, the orbital exponent, β, and the spherical harmonics, Y_{lm}. STO basis functions are the simplest functions in quantum chemistry and are seldom used in calculations any more. The GTO functions are much more common and have the following form.

$$\eta^{GTO} = Nx^l y^m z^n \exp[-\alpha r] \tag{H.39}$$

where N is a normalization factor which ensures that $<\eta_\mu|\eta_\mu> = 1$, and α is the orbital exponent. $L= l +m +n$ is used to classify the function as s-function (L=0), p-function (L=1), etc.

There are numerous basis sets based of GTOs. The main difference in these basis sets is the number of functions employed. The smallest basis set allowed (minimal basis) is composed of the minimum number of functions required to represent all of the electrons on each atom. For example, the minimal basis set for a Hydrogen atom would only require a function approximating the *1s* atomic orbital. However, additional functions may be added to the basis set. The most common functions added to minimal basis sets are polarization and diffuse functions. Addition of polarization functions allow for increased flexibility within the molecular orbitals. A single polarization function added to the Hydrogen atom minimal basis would add a p-function; allowing for more asymmetry to molecular orbitals involving the Hydrogen atomic orbital. Diffuse functions are very shallow GTOs which better describe the tail portion of the atomic orbital at increased distance from the atomic nuclei. These additional functions are commonly added to charged molecular systems.

Since the valence electrons are key to most molecular properties; multiple basis functions are used to represent these electrons. This type of basis set was introduced by Pople and is simply known as a split-valence basis set. The commonly used notation for these basis sets is *a-bcG*. Where the number of core GTOs is represented by *a*, and *bc* indicate the valence electrons are described by two functions. The first by a linear combination of *b* GTOs, and the second by a linear combination of *c* GTOs. Within this basis set notation, additional polarization functions are represented with an asterisk or (d), and diffuse functions by a plus sign. For example, the most common basis set employed throughout this work is the 6-31G basis, but occasionally polarization and diffuse functions were added (6-31+G(d)).

However, these localized basis functions are not applicable in calculations where periodic boundary conditions are desired. For periodic calculations, plane wave basis sets are employed, which are independent of the atomic positions. The plane waves are expanded in the following form:

$$\varphi(r) = \frac{1}{\sqrt{\Omega}} \exp(iG \cdot r) \tag{H.40}$$

Where Ω is the volume of the periodic cell, G are the wave-vectors that the periodicity of the cell and r is the spacing of the sampling grid. Plane wave basis sets are used in conjunction with pseudopotentials, which restrict the plane waves to describing only the valence electrons; leaving the core electrons frozen.

H.10. Time-Dependant Density Functional Theory

Time-dependant density functional theory (TDDFT) is an extension traditional DFT for the treatment of time-dependant events, such as electronic excitations and molecular excited states. The foundation of TDDFT is in the Runge-Gross theorem,[279] which is the time dependant form of the Hohenberg-Kohn theorem. [274] The Runge-Gross theorem proves that in a many-body system evolving from an initial state, the time-dependant external potential is directly related to the one-body electron density. Therefore, by knowing the time-dependant density of a system, we find the external potential responsible for producing this density; which then describes the Hamiltonian and allows the time-dependant Schrödinger equation to be solved.

As expected, the introduction of time results is several fundamental quantum mechanical differences. The first involves the procedure for locating the ground state of the system. In static DFT, the ground state is determined through minimization of the total energy functional. In time dependent systems the total energy is not a conserved quantity, therefore employing the variational principle based on the total energy is not valid. Determination of the ground state of a time dependent system relies on the quantum mechanical action, A, an equivalent quantity to the total energy.

$$A\psi = \int_{t_0}^{t_1} \left\langle \psi(t) | \, i\frac{d}{dt} - \hat{H}(t) | \, \psi(t) \right\rangle dt \tag{H.41}$$

The time dependent Schrodinger equation may be obtained by equating the functional derivative in terms of ψ*(t) to zero. The solution to the time dependent problem can be found by calculation the function, Ψ(t), which makes the functional, Aψ, stationary. Therefore, the iterative process to minimize the total energy functional in static DFT is replaced by a "stationary principle" in TDDFT.

An additional important difference between DFT and TDDFT is that the time dependent problem is an "initial value" problem introduced earlier. Namely, the density depends on the initial state of the system and the Runge-Gross theorem can only hold for a fixed initial state. This is a direct consequence of the time dependent Schrödinger equation being a first order differential equation with respect to time. The static DFT problem is a "boundary value" problem; with the Schrödinger equation is a second order differential equation with respect to the special coordinates.

References

1. Dent, C. E.; Linstead, R. P., Phthalocyanines. Iv. Copper Phthalocyanines. *J. Chem. Soc.* **1934**, 1027-31.

2. Dent, C. E.; Linstead, R. P.; Lowe, A. R., Phthalocyanines. Vi. The Structure of the Phthalocyanines. *J. Chem. Soc.* **1934**, 1033-9.

3. Linstead, R. P.; Lowe, A. R., Phthalocyanines. V. The Molecular Weight of Magnesium Phthalocyanine. *J. Chem. Soc.* **1934**, 1031-3.

4. Linstead, R. P.; Lowe, A. R., Phthalocyanines. Iii. Preliminary Experiments on the Preparation of Phthalocyanines from Phthalonitrile. *J. Chem. Soc.* **1934**, 1022-7.

5. Rio, Y.; Rodriguez-Morgade, M. S.; Torres, T., Modulating the Electronic Properties of Porphyrinoids: A Voyage from the Violet to the Infrared Regions of the Electromagnetic Spectrum. *Org. Biomol. Chem.* **2008,** *6* (11), 1877-1894.

6. Kadish, K. M.; Smith, K. M.; Guilard, R.; Editors, *The Porphyrin Handbook: Volume 19 / Applications of Phthalocyanines*. Academic Press: 2003; p 194 pp.

7. Chen, Y., et al., Soluble Axially Substituted Phthalocyanines: Synthesis and Nonlinear Optical Response. *J. Mater. Sci.* **2006,** *41* (8), 2169-2185.

8. Claessens, C. G., et al., Phthalocyanines and Phthalocyanine Analogues: The Quest for Applicable Optical Properties. *Monatsh. Chem.* **2001,** *132* (1), 3-11.

9. Elemans, J. A. A. W.; van Hameren, R.; Nolte, R. J. M.; Rowan, A. E., Molecular Materials by Self-Assembly of Porphyrins, Phthalocyanines, and Perylenes. *Adv. Mater. (Weinheim, Ger.)* **2006,** *18* (10), 1251-1266.

10. He, N., et al., Phthalocyanine-Based Optical Limiting Functional Materials. *Zhongguo Jiguang* **2009,** *36* (8), 1909-1917.

11. Lukyanets, E. A.; Nemykin, V. N., The Key Role of Peripheral Substituents in the Chemistry of Phthalocyanines and Their Analogs. *J. Porphyrins Phthalocyanines* **2010,** *14* (1), 1-40.

12. McKeown, N. B., *Phthalocyanine Materials: Structure, Synthesis and Function*. Cambridge Univ Press: 1998; p 200 pp.

13. McKeown, N. B.; Budd, P. M., Polymers of Intrinsic Microporosity (Pims): Organic Materials for Membrane Separations, Heterogeneous Catalysis and Hydrogen Storage. *Chem. Soc. Rev.* **2006,** *35* (8), 675-683.

14. Minnes, R., et al., Enhanced Acidity, Photophysical Properties and Liposome Binding of Perfluoroalkylated Phthalocyanines Lacking C-H Bonds. *Photochem. Photobiol.* **2006,** *82* (Mar./Apr.), 593-599.

15. Patel, P., et al. In *Nucleic Acid Bioconjugates in Anticancer Applications*, American Chemical Society: 2014; pp MEDI-482.

16. Walter, M. G.; Rudine, A. B.; Wamser, C. C., Porphyrins and Phthalocyanines in Solar Photovoltaic Cells. *J. Porphyrins Phthalocyanines* **2010,** *14* (9), 759-792.

17. Yin, H.-s.; Liu, L.; Wu, G.-q., Review of Application of Phthalocyanines as Functional Materials in Battery. *Dianchi Gongye* **2006,** *11* (6), 425-428.

18. Jiang, J.; Editor, *Functional Phthalocyanine Molecular Materials. [In: Struct. Bonding (Berlin, Ger.), 2010; 135]*. Springer GmbH: 2010; p 325 pp.

19. Sayer, P.; Gouterman, M.; Connell, C. R., Metalloid Porphyrins and Phthalocyanines. *Acc. Chem. Res.* **1982,** *15* (3), 73-9.

20. Fukuda, T.; Homma, S.; Kobayashi, N., Deformed Phthalocyanines: Synthesis and Characterization of Zinc Phthalocyanines Bearing Phenyl Substituents at the 1-, 4-, 8-, 11-, 15-, 18-, 22-, and/or 25-Positions. *Chem. - Eur. J.* **2005,** *11* (18), 5205-5216.

21. Moons, H., et al., Synthesis, X-Ray Structure, Magnetic Resonance, and Dft Analysis of a Soluble Copper(Ii) Phthalocyanine Lacking C-H Bonds. *Inorg. Chem.* **2010,** *49* (19), 8779-8789.

22. de Oteyza, D. G., et al., Copper-Phthalocyanine Based Metal-Organic Interfaces: The Effect of Fluorination, the Substrate, and Its Symmetry. *J. Chem. Phys.* **2010,** *133* (21), 214703/1-214703/6.

23. Bao, Z.; Lovinger, A. J.; Brown, J., New Air-Stable N-Channel Organic Thin Film Transistors. *J. Am. Chem. Soc.* **1998,** *120* (1), 207-208.

24. Loas, A. Persional Communication.

25. Yang, C. H.; Lin, S. F.; Chen, H. L.; Chang, C. T., Electrosynthesis of the Metal Phthalocyanine Complexes. *Inorg. Chem.* **1980,** *19* (11), 3541-3.

26. Gaspard, S.; Maillard, P., Structure of Tetra-Tert-Butylphthalocyanines: Mechanism of the System. *Tetrahedron* **1987,** *43* (6), 1083-90.

27. Holdenberg, P.; Kohn, W., Inhomogeneous Electron Gas. *Phys. Rev. B* **1964,** *136*, 864-871.

28. Kohn, W.; Sham, L. J. *Self-Consistent Equations Including Exchange and Correlation Effects*; Univ. of California: 1965; p 21 pp.

29. Gordon, M. S.; Schmidt, M. W. In *Advances in Electronic Structure Theory: Gamess a Decade Later,* Elsevier B.V.: 2005; pp 1167-1189.

30. Schmidt, M. W., et al., General Atomic and Molecular Electronic Structure System. *Journal of Computational Chemistry* **1993,** *14* (11), 1347-63.

31. Becke, A. D., Density-Functional Thermochemistry. Iii. The Role of Exact Exchange. *J. Chem. Phys.* **1993,** *98* (7), 5648-52.

32. Lee, C.; Yang, W.; Parr, R. G., Development of the Colle-Salvetti Correlation-Energy Formula into a Functional of the Electron Density. *Phys. Rev. B: Condens. Matter* **1988,** *37* (2), 785-9.

33. Stephens, P. J.; Devlin, F. J.; Chabalowski, C. F.; Frisch, M. J., Ab Initio Calculation of Vibrational Absorption and Circular Dichroism Spectra Using Density Functional Force Fields. *J. Phys. Chem.* **1994,** *98* (45), 11623-7.

34. Hehre, W. J.; Ditchfield, R.; Pople, J. A., Selfconsistent Molecular Orbital Methods. Xii. Further Extensions of Gaussianâ€”Type Basis Sets for Use in Molecular Orbital Studies of Organic Molecules. *The Journal of Chemical Physics* **1972,** *56* (5), 2257-2261.

35. Mitin, A. V.; Baker, J.; Pulay, P., An Improved 6-31g* Basis Set for First-Row Transition Metals. *J. Chem. Phys.* **2003,** *118* (17), 7775-7782.

36. Dwyer, P. J., et al., All-Atom Charmm Force Field and Bulk Properties of Perfluorozinc Phthalocyanines. *Journal of Physical Chemistry A* **2014,** *118*, 11583-90.

37. Frisch, M. J.; Pople, J. A.; Binkley, J. S., Self Consistent Molecular Orbital Methods 25. Supplementary Functions for Gaussian Basis Sets. *The Journal of Chemical Physics* **1984,** *80* (7), 3265-3269.

38. Rassolov, V. A.; Pople, J. A.; Ratner, M. A.; Windus, T. L., 6-31g* Basis Set for Atoms K through Zn. *J. Chem. Phys.* **1998,** *109* (4), 1223-1229.

39. Runge, E.; Gross, E. K. U., Density-Functional Theory for Time-Dependent Systems. *Phys. Rev. Lett.* **1984,** *52* (12), 997-1000.

40. Tomasi, J.; Mennucci, B.; Cammi, R., Quantum Mechanical Continuum Solvation Models. *Chem. Rev. (Washington, DC, U. S.)* **2005,** *105* (8), 2999-3093.

41. Andrienko, G. A. e. a. Chemcraft. http://www.chemcraftprog.com.

42. Liao, M.-S.; Scheiner, S., Electronic Structure and Bonding in Metal Phthalocyanines, Metal = Fe, Co, Ni, Cu, Zn, Mg. *J. Chem. Phys.* **2001,** *114* (22), 9780-9791.

43. Kahl, J. L.; Faulkner, L. R.; Dwarakanath, K.; Tachikawa, H., Reversible Oxidation and Rereduction of Magnesium Phthalocyanine Electrodes. Electrochemical Behavior and in Situ Raman Spectroscopy. *J. Am. Chem. Soc.* **1986,** *108* (18), 5434-40.

44. Besler, B. H.; Merz, K. M., Jr.; Kollman, P. A., Atomic Charges Derived from Semiempirical Methods. *Journal of Computational Chemistry* **1990,** *11* (4), 431-9.

45. Mulliken, R. S., Electronic Population Analysis on Lcao-Mo Molecular-Wave Functions. Iv. Bonding and Antibonding in Lcao and Valence-Bond Theories. *J. Chem. Phys.* **1955,** *23*, 2343-6.

46. Mulliken, R. S., Electronic Population Analysis on Lcao-Mo Molecular-Wave Functions. Iii. Effects of Hybridization on Overlap and Gross Ao Populations. *J. Chem. Phys.* **1955,** *23*, 2338-42.

47. Mulliken, R. S., Electronic Population Analysis on Lcao-Mo [Linear Combination of Atomic Orbital-Molecular Orbital] Molecular Wave Functions. Ii. Overlap Populations, Bond Orders, and Covalent Bond Energies. *J. Chem. Phys.* **1955,** *23*, 1841-6.

48. Mulliken, R. S., Electronic Population Analysis on Lcao-Mo [Linear Combination of Atomic Orbital-Molecular Orbital] Molecular Wave Functions. I. *J. Chem. Phys.* **1955,** *23*, 1833-40.

49. Roothaan, C. C. J., Self-Consistent Field Theory for Open Shells of Electronic Systems. *Reviews of Modern Physics* **1960,** *32* (2), 179-185.

50. O'Boyle, N. M.; Tenderholt, A. L.; Langner, K. M., Software News and Updates Cclib: A Library for Package-Independent Computational Chemistry Algorithms. *Journal of Computational Chemistry* **2008,** *29* (5), 839-845.

51. Barea, E. M., et al., Energetic Factors Governing Injection, Regeneration and Recombination in Dye Solar Cells with Phthalocyanine Sensitizers. *Energy Environ. Sci.* **2010,** *3* (12), 1985-1994.

52. Clifford, J. N.; Martinez-Ferrero, E.; Viterisi, A.; Palomares, E., Sensitizer Molecular Structure-Device Efficiency Relationship in Dye Sensitized Solar Cells. *Chem. Soc. Rev.* **2011,** *40* (3), 1635-1646.

53. Kimura, M., et al., Molecular Design Rule of Phthalocyanine Dyes for Highly Efficient near-Ir Performance in Dye-Sensitized Solar Cells. *Chemistry* **2013,** *19* (23), 7496-502.

54. Sorokin, A. B., Phthalocyanine Metal Complexes in Catalysis. *Chem. Rev. (Washington, DC, U. S.)* **2013,** *113* (10), 8152-8191.

55. Royer, J. E.; Zhang, C.; Kummel, A. C.; Trogler, W. C., Air-Stable Spin-Coated Naphthalocyanine Transistors for Enhanced Chemical Vapor Detection. *Langmuir* **2012,** *28* (14), 6192-6200.

56. Nenon, S., et al., Shelf-Life Time Test of P- and N-Channel Organic Thin Film Transistors Using Copper Phthalocyanines. *Thin Solid Films* **2010,** *518* (19), 5593-5598.

57. Patel, P., et al., Chemically Robust Fluoroalkyl Phthalocyanine-Oligonucleotide Bioconjugates and Their Grp78 Oncogene Photocleavage Activity. *Chem. Commun. (Cambridge, U. K.)* **2014,** *50* (48), 6309-6311.

58. Chen, I.-J.; Yin, D.; MacKerell, J., A.D., Combined Ab Initio/Empirical Approach for Optimization of Lennard-Jones Parameters for Polar-Neutral Compounds. *Journal of Computational Chemistry* **2002,** *23* (2), 199-213.

59. Einstein, T. L.; Fisher, M. E.; Weeks, J. D., The Effect of Gravity on the Deposition of Thin Films: The Physical Vapor Transport of Copper Phthalocyanine. DoD-AFOSR, Ed. Gov. Rep. Announce.: Washington DC, 1994; Vol. 95, pp 21-03,752.

60. Forrest, S. R.; Zhang, Y., Ultrahigh-Vacuum Quasiepitaxial Growth of Model Van Der Waals Thin Films. I. Theory. *Phys. Rev. B: Condens. Matter Mater. Phys.* **1994,** *49* (16), 11297-308.

61. Heuts, J. P. A.; Schipper, E. T. W. M.; Piet, P.; German, A. L., Molecular Mechanics Calculations on Cobalt Phthalocyanine Dimers. *J. Mol. Struct. THEOCHEM* **1995,** *333*, 39-47.

62. Keil, C., et al., Growth and Characterization of Thin Films Prepared from Perfluoro-Isopropyl-Substituted Perfluorophthalocyanines. *Thin Solid Films* **2009,** *517* (15), 4379-4384.

63. Liu, D.-J.; Selinger, R. L. B.; Weeks, J. D., Representing Molecular Shape and Interactions: A Reduced Intermolecular Potential for Copper Phthalocyanine. *J. Chem. Phys.* **1996,** *105* (11), 4751-60.

64. Liu, Y.-H., et al., Stacking Behavior of 2-D Assemblies of Octa-Alkoxyl-Substituted Phthalocyanine Studied by Scanning Tunneling Microscopy. *Surf. Sci.* **2004,** *559*, 40-46.

65. Nakamura, M.; Tokumoto, H., Molecular Arrangement of Copper Phthalocyanine on Si (00 1)-(2 X 1)-H: A High-Resolution Frictional Force Microscopy and Molecular Mechanics Study. *Surf. Sci.* **1998,** *398*, 143-53.

66. Fendrich, M.; Wagner, T.; Stohr, M.; Moller, R., Hindered Rotation of a Copper Phthalocyanine Molecule on C60: Experiments and Molecular Mechanics Calculations. *Phys. Rev. B: Condens. Matter Mater. Phys.* **2006,** *73* (11), 115433/1-115433/7.

67. Kroger, I., et al., Modeling Intermolecular Interactions of Physisorbed Organic Molecules Using Pair Potential Calculations. *J Chem Phys* **2011,** *135* (23), 234703.

68. Kunzel, D.; Markert, T.; Gross, A.; Benoit, D. M., Bis(Terpyridine)-Based Surface Template Structures on Graphite: A Force Field and Dft Study. *Phys Chem Chem Phys* **2009,** *11* (39), 8867-78.

69. Olivier, Y., et al., Theoretical Characterization of the Structural and Hole Transport Dynamics in Liquid-Crystalline Phthalocyanine Stacks. *Journal of Physical Chemistry B* **2009,** *113* (43), 14102-14111.

70. Von Lilienfeld, O. A.; Andrienko, D., Coarse-Grained Interaction Potentials for Polyaromatic Hydrocarbons. *J. Chem. Phys.* **2006,** *124* (5), 054307/1-054307/6.

71. Yin, S.; Wang, C.; Xu, B.; Bai, C., Studies of Cupc Adsorption on Graphite Surface and Alkane Adlayer. *Journal of Physical Chemistry B* **2002,** *106* (35), 9044-9047.

72. Sun, H., Compass: An Ab Initio Force-Field Optimized for Condensed-Phase Applications - Overview with Details on Alkane and Benzene Compounds. *Journal of Physical Chemistry B* **1998,** *102* (38), 7338-7364.

73. Shao, C., et al., Simulation of Crystalline and Amorphous Copper Phthalocyanine: Force Field Development and Analysis of Thermal Transport Mechanisms. *Journal of Physical Chemistry C* **2014,** *118* (19), 9861-9870.

74. Brooks, B. R., et al., Charmm: A Program for Macromolecular Energy, Minimization, and Dynamics Calculations. *J. Comp. Chem.* **1983,** *4* (2), 187-217.

75. Liao, M.-S., et al., Structure and Properties of Perfluoroalkylated Phthalocyanines: A Theoretical Study. *Journal of Theoretical & Computational Chemistry* **2008,** *7* (4), 541-563.

76. Scheidt, W. R.; Dow, W., Molecular Stereochemistry of Phthalocyanatozinc(Ii). *J. Am. Chem. Soc.* **1977,** *99* (4), 1101-4.

77. Yoon, S. M., et al., Single Crystal Structure of Copper Hexadecafluorophthalocyanine (F16cupc) Ribbon. *Chem. Commun. (Cambridge, U. K.)* **2010,** *46* (2), 231-233.

78. Autenrieth, F.; Tajkhorshid, E.; Baudry, J.; Luthey-Schulten, Z., Classical Force Field Parameters for the Heme Prosthetic Group of Cytochrome C. *Journal of Computational Chemistry* **2004,** *25* (13), 1613-1622.

79. Phillips, J. C., et al., Scalable Molecular Dynamics with Namd. *Journal of Computational Chemistry* **2005,** *26* (16), 1781-1802.

80. Izaguirre, J. A.; Catarello, D. P.; Wozniak, J. M.; Skeel, R. D., Langevin Stabilization of Molecular Dynamics. *J. Chem. Phys.* **2001,** *114* (5), 2090-2098.

81. Lin, F.; Wang, R., Systematic Derivation of Amber Force Field Parameters Applicable to Zinc-Containing Systems. *Journal of Chemical Theory and Computation* **2010,** *6* (6), 1852-1870.

82. Peters, M. B., et al., Structural Survey of Zinc-Containing Proteins and Development of the Zinc Amber Force Field (Zaff). *Journal of Chemical Theory and Computation* **2010,** *6* (9), 2935-2947.

83. Zhang, Y.; Loas, A.; Patel, H.; Gorun, S., Fluorinated Phthalocyanines for Electronic Materials and Green Catalyst. *Abstracts of Papers, 242nd ACS National Meeting & Exposition, Denver, CO, United States, August 28-September 1, 2011* **2011**, INOR-431.

84. O'Regan, B.; Gratzel, M., A Low-Cost, High-Efficiency Solar Cell Based on Dye-Sensitized Colloidal TiO_2 Films. *Nature* **1991,** *353* (6346), 737-740.

85. Grätzel, M., Dye-Sensitized Solar Cells. *J. Photochem. PhotoBiol. C* **2003,** *4*, 145-153.

86. Hagfeldt, A., et al., Dye-Sensitized Solar Cells. *Chem. Rev.* **2010,** *110*, 6595-6663.

87. Toivola, M., et al., Nanostructured Dye Solar Cells on Flexible Substrates - Review. *Int. J. Energy Res.* **2009,** *33* (13), 1145-1160.

88. Lewcenko, N. A., et al., A New Family of Substituted Triethoxysilyl Iodides as Organic Iodide Sources for Dye-Sensitized Solar Cells. *Journal of Materials Chemistry* **2010,** *20* (18), 3694-3702.

89. Mathew, S., et al., Dye-Sensitized Solar Cells with 13% Efficiency Achieved through the Molecular Engineering of Porphyrin Sensitizers. *Nature Chemistry* **2014,** *6*, 242-247.

90. Batmunkh, M.; Biggs, M. J.; Shapter, J. G., Carbon Nanotubes for Dye-Sensitized Solar Cells. *Small* **2015**, Ahead of Print.

91. Bella, F.; Gerbaldi, C.; Barolo, C.; Gratzel, M., Aqueous Dye-Sensitized Solar Cells. *Chem. Soc. Rev.* **2015**, Ahead of Print.

92. Calogero, G., et al., Vegetable-Based Dye-Sensitized Solar Cells. *Chem. Soc. Rev.* **2015**, Ahead of Print.

93. Lee, C.-P., et al., Recent Progress in Organic Sensitizers for Dye-Sensitized Solar Cells. *RSC Adv.* **2015,** *5* (30), 23810-23825.

94. Ragoussi, M.-E.; Torres, T., New Generation Solar Cells: Concepts, Trends and Perspectives. *Chem. Commun. (Cambridge, U. K.)* **2015,** *51* (19), 3957-3972.

95. Rong, Y., et al., All-Solid-State Mesoscopic Solar Cells: From Dye-Sensitized to Perovskite. *Huaxue Xuebao* **2015,** *73* (3), 237-251.

96. Shen, H., et al., Application Progress of the Nanotechnology in Solar Cells. *Weinadianzi Jishu* **2014,** *51* (2), 78-82, 119.

97. Su'ait, M. S.; Rahman, M. Y. A.; Ahmad, A., Review on Polymer Electrolyte in Dye-Sensitized Solar Cells (Dsscs). *Sol. Energy* **2015,** *115*, 452-470.

98. Tian, H.; Sun, L. In *Organic Photovoltaics and Dye-Sensitized Solar Cells*, Elsevier B.V.: 2013; pp 567-605.

99. Urbani, M.; Gratzel, M.; Nazeeruddin, M. K.; Torres, T., Meso-Substituted Porphyrins for Dye-Sensitized Solar Cells. *Chem. Rev. (Washington, DC, U. S.)* **2014,** *114* (24), 12330-12396.

100. Weickert, J.; Schmidt-Mende, L. In *Solid-State Dye-Sensitized Solar Cells*, Wiley-VCH Verlag GmbH & Co. KGaA: 2014; pp 465-493.

101. Wu, J., et al., Electrolytes in Dye-Sensitized Solar Cells. *Chem. Rev. (Washington, DC, U. S.)* **2015,** *115* (5), 2136-2173.

102. Yu, Y., et al. In *Conducting Organic Polymers in Hybrid, Organic and Dye Sensitized Solar Cells*, Nova Science Publishers, Inc.: 2013; pp 315-343.

103. Zhang, L.; Cole, J. M., Anchoring Groups for Dye-Sensitized Solar Cells. *ACS Appl. Mater. Interfaces* **2015,** *7* (6), 3427-3455.

104. Manthou, V. S.; Pefkianakis, E. K.; Falaras, P.; Vougioukalakis, G. C., Co-Adsorbents: A Key Component in Efficient and Robust Dye-Sensitized Solar Cells. *ChemSusChem* **2015,** *8* (4), 588-599.

105. Gong, J.; Liang, J.; Sumathy, K., Review on Dye-Sensitized Solar Cells (Dsscs): Fundamental Concepts and Novel Materials. *Renewable Sustainable Energy Rev.* **2012,** *16* (8), 5848-5860.

106. Nazeeruddin, M. K., et al., Conversion of Light to Electricity by Cis-X2bis(2,2'-Bipyridyl-4,4'-Dicarboxylate)Ruthenium(Ii) Charge-Transfer Sensitizers (X = Cl-, Br-, I-, Cn-, and Scn-) on Nanocrystalline Titanium Dioxide Electrodes. *J. Am. Chem. Soc.* **1993,** *115* (14), 6382-90.

107. Chiba, Y., et al., Dye-Sensitized Solar Cells with Conversion Efficiency of 11.1%. *Jpn. J. Appl. Phys., Part 2* **2006,** *45* (24-28), L638-L640.

108. Mishra, A.; Fischer, M. K. R.; Bauerle, P., Metal-Free Organic Dyes for Dye-Sensitized Solar Cells: From Structure: Property Relationships to Design Rules. *Angewandte Chemie, International Edition* **2009,** *48* (14), 2474-2499.

109. Hwang, S., et al., A Highly Efficient Organic Sensitizer for Dye-Sensitized Solar Cells. *Chem. Commun. (Cambridge, U. K.)* **2007,** (46), 4887-4889.

110. Yella, A., et al., Porphyrin-Sensitized Solar Cells with Cobalt (Ii/Iii)-Based Redox Electrolyte Exceed 12% Efficiency. *Science (Washington, DC, U. S.)* **2011,** *334* (6056), 629-634.

111. Claessens, C. G.; Hahn, U.; Torres, T., Phthalocyanines: From Outstanding Electronic Properties to Emerging Applications. *Chem. Rec.* **2008,** *8* (2), 75-97.

112. de la Torre, G.; Claessens, C. G.; Torres, T., Phthalocyanines: Old Dyes, New Materials. Putting Color in Nanotechnology. *Chem. Commun. (Cambridge, U. K.)* **2007,** (20), 2000-2015.

113. Mack, J.; Kobayashi, N., Low Symmetry Phthalocyanines and Their Analogues. *Chem. Rev. (Washington, DC, U. S.)* **2011,** *111* (2), 281-321.

114. Eu, S., et al., Synthesis of Sterically Hindered Phthalocyanines and Their Applications to Dye-Sensitized Solar Cells. *Dalton Transactions* **2008,** (40), 5476-5483.

115. Giribabu, L., et al., Unsymmetrical Alkoxy Zinc Phthalocyanine for Sensitization of Nanocrystalline TiO_2 Films. *Sol. Energy Mater. Sol. Cells* **2007,** *91* (17), 1611-1617.

116. Giribabu, L.; Sudhakar, K.; Velkannan, V., Phthalocyanines: Potential Alternative Sensitizers to Ru(Ii) Polypyridyl Complexes for Dye-Sensitized Solar Cells. *Curr. Sci.* **2012,** *102* (7), 991-1000.

117. He, J., et al., Modified Phthalocyanines for Efficient near-Ir Sensitization of Nanostructured TiO_2 Electrode. *J. Am. Chem. Soc.* **2002,** *124* (17), 4922-4932.

118. He, J., et al., Phthalocyanine-Sensitized Nanostructured TiO_2 Electrodes Prepared by a Novel Anchoring Method. *Langmuir* **2001,** *17* (9), 2743-2747.

119. Martinez-Diaz, M. V.; de la Torre, G.; Torres, T., Lighting Porphyrins and Phthalocyanines for Molecular Photovoltaics. *Chem. Commun. (Cambridge, U. K.)* **2010,** *46* (38), 7090-7108.

120. Martinez-Diaz, M. V.; Ince, M.; Torres, T., Phthalocyanines: Colorful Macroheterocyclic Sensitizers for Dye-Sensitized Solar Cells. *Monatsh. Chem.* **2011,** *142* (7), 699-707.

121. Martinez-Diaz, M. V.; Torres, T. In *On the Significance of Phthalocyanines in Solar Cells*, World Scientific Publishing Co. Pte. Ltd.: 2010; pp 141-181.

122. Nazeeruddin, M. K., et al., Efficient near-Ir Sensitization of Nanocrystalline TiO_2 Films by Zinc and Aluminum Phthalocyanines. *J. Porphyrins Phthalocyanines* **1999,** *3* (3), 230-237.

123. Ragoussi, M.-E.; Ince, M.; Torres, T., Recent Advances in Phthalocyanine-Based Sensitizers for Dye-Sensitized Solar Cells. *European Journal of Organic Chemistry* **2013,** *2013* (29), 6475-6489.

124. Reddy, P. Y., et al., Efficient Sensitization of Nanocrystalline TiO_2 Films by a near-Ir-Absorbing Unsymmetrical Zinc Phthalocyanine. *Angew Chem Int Ed Engl* **2007,** *46* (3), 373-6.

125. Silvestri, F., et al., Carboxy-1,4-Phenylenevinylene- and Carboxy-2, 6-Naphthylene-Vinylene Unsymmetrical Substituted Zinc Phthalocyanines for Dye-Sensitized Solar Cells. *J. Porphyrins Phthalocyanines* **2009,** *13* (3), 369-375.

126. Ince, M., et al., Molecular Engineering of Phthalocyanine Sensitizers for Dye-Sensitized Solar Cells. *Journal of Physical Chemistry C* **2014,** *118* (30), 17166-17170.

127. Mori, S., et al., Enhancement of Incident Photon-to-Current Conversion Efficiency for Phthalocyanine-Sensitized Solar Cells by 3d Molecular Structuralization. *J. Am. Chem. Soc.* **2010,** *132* (12), 4054-4055.

128. Aranyos, V.; Hjelm, J.; Hagfeldt, A.; Grennberg, H., Free-Base Tetraarylphthalocyanines for Dye-Sensitized Nanostructured Solar Cell Applications. *J. Porphyrins Phthalocyanines* **2001,** *5* (8), 609-616.

129. Koehorst, R. B. M., et al., Spectral Sensitization of TiO_2Substrates by Monolayers of Porphyrin Heterodimers. *Journal of Physical Chemistry B* **2000,** *104* (10), 2371-2377.

130. Breckenridge, R. G.; Hosler, W. R., Electrical Properties of Titanium Dioxide Semiconductors. *Phys. Rev.* **1953,** *91*, 793-802.

131. Law, M., et al., Nanowire Dye-Sensitized Solar Cells. *Nat. Mater.* **2005,** *4* (6), 455-459.

132. Keis, K., et al., A 5% Efficient Photoelectrochemical Solar Cell Based on Nanostructured Zno Electrodes. *Sol. Energy Mater. Sol. Cells* **2002,** *73* (1), 51-58.

133. Jose, R.; Thavasi, V.; Ramakrishna, S., Metal Oxides for Dye-Sensitized Solar Cells. *J. Am. Ceram. Soc.* **2009,** *92* (2), 289-301.

134. Saito, M.; Fujihara, S., Large Photocurrent Generation in Dye-Sensitized Zno Solar Cells. *Energy Environ. Sci.* **2008,** *1* (2), 280-283.

135. Qian, J., et al., TiO_2-Coated Multilayered Sno2 Hollow Microspheres for Dye-Sensitized Solar Cells. *Adv. Mater. (Weinheim, Ger.)* **2009,** *21* (36), 3663-3667.

136. Green, A. N. M., et al., Charge Transport Versus Recombination in Dye-Sensitized Solar Cells Employing Nanocrystalline TiO_2 and SnO_2 Films. *Journal of Physical Chemistry B* **2005,** *109* (25), 12525-12533.

137. Fukai, Y.; Kondo, Y.; Mori, S.; Suzuki, E., Highly Efficient Dye-Sensitized Sno2 Solar Cells Having Sufficient Electron Diffusion Length. *Electrochem. Commun.* **2007,** *9* (7), 1439-1443.

138. Senevirathna, M. K. I., et al., Stability of the Sno2/Mgo Dye-Sensitized Photoelectrochemical Solar Cell. *Sol. Energy Mater. Sol. Cells* **2007,** *91* (6), 544-547.

139. Boschloo, G.; Hagfeldt, A., Characteristics of the Iodide/Triiodide Redox Mediator in Dye-Sensitized Solar Cells. *Acc. Chem. Res.* **2009,** *42* (11), 1819-1826.

140. Zanni, M. T.; Greenblatt, B. J.; Davis, A. V.; Neumark, D. M., Photodissociation of Gas Phase I3- Using Femtosecond Photoelectron Spectroscopy. *J. Chem. Phys.* **1999,** *111* (7), 2991-3003.

141. Daeneke, T., et al., Aqueous Dye-Sensitized Solar Cell Electrolytes Based on the Ferricyanide-Ferrocyanide Redox Couple. *Adv. Mater. (Weinheim, Ger.)* **2012,** *24* (9), 1222-1225.

142. Zakeeruddin, S. M.; Graetzel, M., Solvent-Free Ionic Liquid Electrolytes for Mesoscopic Dye-Sensitized Solar Cells. *Advanced Functional Materials* **2009,** *19* (14), 2187-2202.

143. Goncalves, L. M.; Bermudez, V. d. Z.; Ribeiro, H. A.; Mendes, A. M., Dye-Sensitized Solar Cells: A Safe Bet for the Future. *Energy Environ. Sci.* **2008,** *1* (6), 655-667.

144. Gorlov, M.; Pettersson, H.; Hagfeldt, A.; Kloo, L., Electrolytes for Dye-Sensitized Solar Cells Based on Interhalogen Ionic Salts and Liquids. *Inorg. Chem.* **2007,** *46* (9), 3566-3575.

145. Bai, Y., et al., High-Performance Dye-Sensitized Solar Cells Based on Solvent-Free Electrolytes Produced from Eutectic Melts. *Nat. Mater.* **2008,** *7* (8), 626-630.

146. Tennakone, K., et al., A Dye-Sensitized Nano-Porous Solid-State Photovoltaic Cell. *Semicond. Sci. Technol.* **1995,** *10* (12), 1689-93.

147. O'Regan, B.; Schwartz, D. T., Efficient Photo-Hole Injection from Adsorbed Cyanine Dyes into Electrodeposited Copper(I) Thiocyanate Thin Films. *Chemistry of Materials* **1995,** *7* (7), 1349-54.

148. Heng, L., et al., P-N-Junction-Based Flexible Dye-Sensitized Solar Cells. *Advanced Functional Materials* **2010,** *20* (2), 266-271.

149. Bach, U., et al., Solid-State Dye-Sensitized Mesoporous TiO_2 Solar Cells with High Photon-to-Electron Conversion Efficiencies. *Nature (London)* **1998,** *395* (6702), 583-585.

150. Shockley, W.; Queisser, H. J., Detailed Balance Limit of Efficiency of P-N Junction Solar Cells. *Journal of Applied Physics* **1961,** *32* (3), 510-519.

151. Green, M. A., *Third Generation Photovoltaics: Advanced Solar Energy Conversion*. Springer Berlin Heidelberg: 2003.

152. He, J.; Lindstroem, H.; Hagfeldt, A.; Lindquist, S.-E., Dye-Sensitized Nanostructured P-Type Nickel Oxide Film as a Photocathode for a Solar Cell. *Journal of Physical Chemistry B* **1999,** *103* (42), 8940-8943.

153. He, J.; Lindstrom, H.; Hagfeldt, A.; Lindquist, S.-E., Dye-Sensitized Nanostructured Tandem Cell-First Demonstrated Cell with a Dye-Sensitized Photocathode. *Sol. Energy Mater. Sol. Cells* **2000,** *62*, 265-73.

154. Morandeira, A.; Boschloo, G.; Hagfeldt, A.; Hammarstroem, L., Photoinduced Ultrafast Dynamics of Coumarin 343 Sensitized P-Type-Nanostructured Nio Films. *Journal of Physical Chemistry B* **2005,** *109* (41), 19403-19410.

155. Enea, O.; Moser, J.; Graetzel, M., Achievement of Incident Photon to Electric Current Conversion Yields Exceeding 80% in the Spectral Sensitization of Titanium Dioxide by Coumarin. *J. Electroanal. Chem. Interfacial Electrochem.* **1989,** *259* (1-2), 59-65.

156. Ghosh, H. N.; Asbury, J. B.; Lian, T., Direct Observation of Ultrafast Electron Injection from Coumarin 343 to TiO_2 Nanoparticles by Femtosecond Infrared Spectroscopy. *Journal of Physical Chemistry B* **1998,** *102* (34), 6482-6486.

157. Hara, K., et al., Molecular Design of Coumarin Dyes for Efficient Dye-Sensitized Solar Cells. *Journal of Physical Chemistry B* **2003,** *107* (2), 597-606.

158. Huber, R.; Moser, J. E.; Graetzel, M.; Wachtveitl, J., Real-Time Observation of Photoinduced Adiabatic Electron Transfer in Strongly Coupled Dye/Semiconductor Colloidal Systems with a 6 Fs Time Constant. *Journal of Physical Chemistry B* **2002,** *106* (25), 6494-6499.

159. Mikolajczyk, M. M., et al., Long-Range Corrected Dft Calculations of Charge-Transfer Integrals in Model Metal-Free Phthalocyanine Complexes [Erratum to Document Cited in Ca156:098742]. *J. Mol. Model.* **2011,** *17* (11), 3025.

160. Murakoshi, K.; Yanagida, S.; Capel, M.; Castner, E. W., Jr., Interfacial Electron Transfer Dynamics of Photosensitized Zinc Oxide Nanoclusters. *ACS Symp. Ser.* **1997,** *679* (Nanostructured Materials), 221-238.

161. Nattestad, A., et al., Highly Efficient Photocathodes for Dye-Sensitized Tandem Solar Cells. *Nat. Mater.* **2010,** *9* (1), 31-35.

162. Gibson, E. A., et al., A P-Type Nio-Based Dye-Sensitized Solar Cell with an Open-Circuit Voltage of 0.35 V. *Angewandte Chemie, International Edition* **2009,** *48* (24), 4402-4405.

163. Wang, Z.-S.; Yamaguchi, T.; Sugihara, H.; Arakawa, H., Significant Efficiency Improvement of the Black Dye-Sensitized Solar Cell through Protonation of TiO_2 Films. *Langmuir* **2005,** *21* (10), 4272-4276.

164. Zhang, J., et al., Density Functional Theory Characterization and Design of High-Performance Diarylamine-Fluorene Dyes with Different Π Spacers for Dye-Sensitized Solar Cells. *Journal of Materials Chemistry* **2012,** *22* (2), 568-576.

165. Bahers, T. L., et al., A Td-Dft Investigation of Ground and Excited State Properties in Indoline Dyes Used for Dye-Sensitized Solar Cells. *Phys. Chem. Chem. Phys.* **2009,** *11* (47), 11276-84.

166. Fujimori, A.; Minami, F., Valence-Band Photoemission and Optical Absorption in Nickel Compounds. *Phys. Rev. B: Condens. Matter* **1984,** *30* (2), 957-71.

167. Moreira, I. d. P. R.; Illas, F.; Martin, R. L., Effect of Fock Exchange on the Electronic Structure and Magnetic Coupling in Nio. *Phys. Rev. B: Condens. Matter Mater. Phys.* **2002,** *65* (15), 155102/1-155102/14.

168. Odobel, F.; Le Pleux, L.; Pellegrin, Y.; Blart, E., New Photovoltaic Devices Based on the Sensitization of P-Type Semiconductors: Challenges and Opportunities. *Acc. Chem. Res.* **2010,** *43* (8), 1063-71.

169. Odobel, F., et al., Recent Advances and Future Directions to Optimize the Performances of P-Type Dye-Sensitized Solar Cells. *Coordination Chemistry Reviews* **2012,** *256* (21-22), 2414-2423.

170. Morandeira, A.; Boschloo, G.; Hagfeldt, A.; Hammarstrom, L., Coumarin 343-Nio Films as Nanostructured Photocathodes in Dye-Sensitized Solar Cells: Ultrafast Electron Transfer, Effect of the I3-/I- Redox Couple and Mechanism of Photocurrent Generation. *Journal of Physical Chemistry C* **2008,** *112* (25), 9530-9537.

171. Mori, S., et al., Charge-Transfer Processes in Dye-Sensitized Nio Solar Cells. *Journal of Physical Chemistry C* **2008,** *112* (41), 16134-16139.

172. Muscat, J. P., Theory of the Interaction between Chemisorbed Atoms on Metal Surfaces. *Progress in Surface Science* **1987,** *25* (1-4), 211-27.

173. Muscat, J. P.; Newns, D. M., Chemisorption on Metals. *Progress in Surface Science* **1978,** *9* (1), 1-43.

174. Lundqvist, M. J., et al., Spacer and Anchor Effects on the Electronic Coupling in Ruthenium-Bis-Terpyridine Dye-Sensitized TiO_2 Nanocrystals Studied by Dft. *Journal of Physical Chemistry B* **2006,** *110* (41), 20513-20525.

175. Lundqvist, M. J.; Nilsing, M.; Persson, P.; Lunell, S., Dft Study of Bare and Dye-Sensitized TiO_2 Clusters and Nanocrystals. *Int. J. Quant. Chem.* **2006,** *106*, 3214-3234.

176. Persson, P.; Bergstrom, R.; Ojamae, L.; Lunell, S., Quantum-Chemical Studies of Metal Oxides for Photoelectrochemical Applications. *Adv. Quantum Chem.* **2002,** *41*, 203-263.

177. Persson, P.; Lundqvist, M. J., Calculated Structural and Electronic Interactions of the Ruthenium Dye N3 with a Titanium Dioxide Nanocrystal. *Journal of Physical Chemistry B* **2005,** *109* (24), 11918-11924.

178. Persson, P., et al., Quantum Chemical Calculations of the Influence of Anchor-Cum-Spacer Groups on Femtosecond Electron Transfer Times in Dye-Sensitized Semiconductor Nanocrystals. *Journal of Chemical Theory and Computation* **2006,** *2* (2), 441-451.

179. Persson, P.; Lunell, S.; Ojamae, L., Electronic Interactions between Aromatic Adsorbates and Metal Oxide Substrates Calculated from First Principles. *Chemical Physics Letters* **2002,** *364* (5,6), 469-474.

180. Nilsing, M.; Persson, P.; Lunell, S.; Ojamaee, L., Dye-Sensitization of the TiO_2 Rutile (110) Surface by Perylene Dyes: Quantum-Chemical Periodic B3lyp Computations. *Journal of Physical Chemistry C* **2007,** *111* (32), 12116-12123.

181. Nilsing, M.; Persson, P.; Ojamaee, L., Anchor Group Influence on Molecule-Metal Oxide Interfaces: Periodic Hybrid Dft Study of Pyridine Bound to TiO_2 Via Carboxylic and Phosphonic Acid. *Chemical Physics Letters* **2005,** *415* (4-6), 375-380.

182. Cohen-Tannoudji, C.; Diu, B.; Laloe, F., *Quantum Mechanics*. Wiley & Sons: Paris, 1977; Vol. 2.

183. Beltran, A., et al., Static Simulation of Bulk and Selected Surfaces of Anatase TiO_2. *Surf. Sci.* **2001,** *490* (1-2), 116-124.

184. Labat, F.; Baranek, P.; Adamo, C., Structural and Electronic Properties of Selected Rutile and Anatase TiO_2 Surfaces: An Ab Initio Investigation. *Journal of Chemical Theory and Computation* **2008,** *4* (2), 341-352.

185. Lazzeri, M.; Vittadini, A.; Selloni, A., Structure and Energetics of Stoichiometric TiO_2 Anatase Surfaces. *Phys. Rev. B: Condens. Matter Mater. Phys.* **2001,** *63* (15), 155409/1-155409/9.

186. Muscat, J.; Harrison, N. M.; Thornton, G., Effects of Exchange, Correlation, and Numerical Approximations on the Computed Properties of the Rutile TiO_2 (100) Surface. *Phys. Rev. B: Condens. Matter Mater. Phys.* **1999,** *59* (3), 2320-2326.

187. Perron, H., et al., Optimization of Accurate Rutile TiO_2 (110), (100), (101) and (001) Surface Models from Periodic Dft Calculations. *Theoretical Chemistry Accounts* **2007,** *117* (4), 565-574.

188. Scaranto, J., et al., A Quantum-Mechanical Study of the Vinyl Fluoride Adsorbed on the Rutile TiO_2(110) Surface. *Surf. Sci.* **2006,** *600* (2), 305-317.

189. Swamy, V.; Muscat, J.; Gale, J. D.; Harrison, N. M., Simulation of Low Index Rutile Surfaces with a Transferable Variable-Charge Ti-O Interatomic Potential and Comparison with Ab Initio Results. *Surf. Sci.* **2002,** *504* (1-3), 115-124.

190. Muscat, J.; Harrison, N. M., The Physical and Electronic Structure of the Rutile (001) Surface. *Surf. Sci.* **2000,** *446* (1-2), 119-127.

191. Sze, S. M.; Ng, K. K., *Physics of Semiconductor Devices*. 3 ed.; Wiley: 2006.

192. Stewart, J. J. P. Mopac2012. HTTP://OpenMOPAC.net.

193. Stewart, J. J. P., Optimization of Parameters for Semiempirical Methods Vi: More Modifications to the Nddo Approximations and Re-Optimization of Parameters. *J. Mol. Model.* **2013,** *19* (1), 1-32.

194. Dewar, M. J. S.; Thiel, W., A Semiempirical Model for the Two-Center Repulsion Integrals in the Nddo Approximation. *Theor. Chim. Acta* **1977,** *46* (2), 89-104.

195. Byrd, R. H.; Lu, P.; Nocedal, J., A Limited Memory Algorithm for Bound Constrained Optimization. *Scientif. Statistic. Comput.* **1995,** *16*, 1190–1208.

196. Kresse, G.; Hafner, J., Ab Initio Molecular-Dynamics Simulation of the Liquid-Metal-Amorphous-Semiconductor Transition in Germanium. *Phys. Rev. B: Condens. Matter* **1994,** *49* (20), 14251-69.

197. Kresse, G.; Furthmueller, J., Efficient Iterative Schemes for Ab Initio Total-Energy Calculations Using a Plane-Wave Basis Set. *Phys. Rev. B: Condens. Matter* **1996,** *54* (16), 11169-11186.

198. Kresse, G.; Furthmuller, J., Efficiency of Ab-Initio Total Energy Calculations for Metals and Semiconductors Using a Plane-Wave Basis Set. *Comput. Mater. Sci.* **1996,** *6* (1), 15-50.

199. Kresse, G.; Hafner, J., Ab Initio Molecular Dynamics of Liquid Metals. *Phys. Rev. B: Condens. Matter* **1993,** *47* (1), 558-61.

200. Blochl, P. E.; Jepsen, O.; Andersen, O. K., Improved Tetrahedron Method for Brillouin-Zone Integrations. *Phys. Rev. B: Condens. Matter* **1994,** *49* (23), 16223-33.

201. Kresse, G.; Joubert, D., From Ultrasoft Pseudopotentials to the Projector Augmented-Wave Method. *Phys. Rev. B: Condens. Matter Mater. Phys.* **1999,** *59* (3), 1758-1775.

202. Monkhorst, H. J.; Pack, J. D., *Phys. Rev. B* **1976,** *13*, 5188.

203. Dudarev, S. L., et al., Electron-Energy-Loss Spectra and the Structural Stability of Nickel Oxide: An Lsda+U Study. *Phys. Rev. B: Condens. Matter Mater. Phys.* **1998,** *57* (3), 1505-1509.

204. Visikovskiy, A., et al., The Atomic and Electronic Structures of Nio(001)/Au(001) Interfaces. *J. Chem. Phys.* **2013,** *139* (14), 144705/1-144705/7.

205. Venkataraman, D.; Yurt, S.; Venkatraman, B. H.; Gavvalapalli, N., Role of Molecular Architecture in Organic Photovoltaic Cells. *J. Phys. Chem. Lett.* **2010,** *1* (6), 947-958.

206. Jiang, Y., et al., Theoretical Design of Polythienylenevinylene Derivatives for Improvements of Light-Emitting and Photovoltaic Performances. *Journal of Materials Chemistry* **2012,** *22* (10), 4491-4501.

207. Shirota, Y.; Kageyama, H., Charge Carrier Transporting Molecular Materials and Their Applications in Devices. *Chem. Rev. (Washington, DC, U. S.)* **2007,** *107* (4), 953-1010.

208. Zaumseil, J.; Sirringhaus, H., Electron and Ambipolar Transport in Organic Field-Effect Transistors. *Chem. Rev. (Washington, DC, U. S.)* **2007,** *107* (4), 1296-1323.

209. Bredas, J.-L.; Beljonne, D.; Coropceanu, V.; Cornil, J., Charge-Transfer and Energy-Transfer Processes in Ï€-Conjugated Oligomers and Polymers: A Molecular Picture. *Chem. Rev. (Washington, DC, U. S.)* **2004,** *104* (11), 4971-5003.

210. Hummer, K.; Ambrosch-Draxl, C., Electronic Properties of Oligoacenes from First Principles. *Phys. Rev. B: Condens. Matter Mater. Phys.* **2005,** *72* (20), 205205/1-205205/10.

211. Zhou, Y., et al., Single Microwire Transistors of Oligoarenes by Direct Solution Process. *J. Am. Chem. Soc.* **2007,** *129* (41), 12386-12387.

212. de Boer, R. W. I.; Klapwijk, T. M.; Morpurgo, A. F., Field-Effect Transistors on Tetracene Single Crystals. *Applied Physics Letters* **2003,** *83* (21), 4345-4347.

213. Podzorov, V.; Pudalov, V. M.; Gershenson, M. E., Field-Effect Transistors on Rubrene Single Crystals with Parylene Gate Insulator. *Applied Physics Letters* **2003,** *82* (11), 1739-1741.

214. Zeis, R.; Siegrist, T.; Kloc, C., Single-Crystal Field-Effect Transistors Based on Copper Phthalocyanine. *Applied Physics Letters* **2005,** *86* (2), 022103/1-022103/3.

215. Irfan, A., et al., A Study on the Electronic and Charge Transfer Properties in Tin Phthalocyanine (Snpc) Derivatives by Density Functional Theory. *Comput. Theor. Chem.* **2011,** *977* (1-3), 9-12.

216. Song, D., et al., Tin (Iv) Phthalocyanine Oxide: An Air-Stable Semiconductor with High Electron Mobility. *Applied Physics Letters* **2008,** *92* (14), 143303/1-143303/3.

217. Rajesh, K. R., et al., High Mobility Polymer Gated Organic Field Effect Transistor Using Zinc Phthalocyanine. *Bull. Mater. Sci.* **2014,** *37* (1), 95-99.

218. Ye, R., et al., On the Correlation between Morphology and Electronic Properties of Fluorinated Copper Phthalocyanine (F16cupc) Thin Films. *Molecular Crystals and Liquid Crystals* **2006,** *444*, 203-210.

219. Sethuraman, K., et al., Fluorinated Copper-Phthalocyanine-Based N-Type Organic Field-Effect Transistors with a Polycarbonate Gate Insulator. *J. Korean Phys. Soc.* **2012,** *61* (1), 113-118.

220. Yadav, S.; Ghosh, S., Ambipolar Copper Phthalocyanine Heterojunction Field Effect Transistors Based Organic Inverter. *AIP Conf. Proc.* **2013,** *1512* (Solid State Physics), 466-467.

221. Yadav, S.; Sharma, A.; Ghosh, S., Organic Transistor and Inverter Based on Assembly of Organic Nanowires Achieved by Optimizing Surface Morphology. *Applied Physics Letters* **2013,** *102* (9), 093303/1-093303/5.

222. Coropceanu, V., et al., Charge Transport in Organic Semiconductors. *Chem Rev* **2007,** *107* (4), 926-52.

223. Hutchison, G. R.; Ratner, M. A.; Marks, T. J., Intermolecular Charge Transfer between Heterocyclic Oligomers. Effects of Heteroatom and Molecular Packing on Hopping Transport in Organic Semiconductors. *J. Am. Chem. Soc.* **2005,** *127* (48), 16866-16881.

224. Deng, W.-Q.; Goddard, W. A., III, Predictions of Hole Mobilities in Oligoacene Organic Semiconductors from Quantum Mechanical Calculations. *Journal of Physical Chemistry B* **2004,** *108* (25), 8614-8621.

225. Bredas, J. L.; Calbert, J. P.; Da Silva Filho, D. A.; Cornil, J., Organic Semiconductors: A Theoretical Characterization of the Basic Parameters Governing Charge Transport. *Proc. Natl. Acad. Sci. U. S. A.* **2002,** *99* (9), 5804-5809.

226. Marcus, R. A., Electron Transfer Reactions in Chemistry. Theory and Experiment. *Rev. Mod. Phys.* **1993,** *65* (3, Pt. 1), 599-610.

227. Marcus, R. A.; Eyring, H., Chemical and Electrochemical Electron-Transfer Theory. *Annu. Rev. Phys. Chem.* **1964,** *15*, 155-96.

228. Senevirathna, W.; Daddario, C. M.; Sauve, G., Density Functional Theory Study Predicts Low Reorganization Energies for Azadipyrromethene-Based Metal Complexes. *J. Phys. Chem. Lett.* **2014,** *5* (5), 935-941.

229. Lin, T., et al., Theoretical Study on Charge Injection and Transport Properties of Six Emitters with Push-Pull Structure. *Chem. Phys.* **2014,** *440*, 47-52.

230. Troisi, A.; Orlandi, G., The Hole Transfer in DNA: Calculation of Electron Coupling between Close Bases. *Chemical Physics Letters* **2001,** *344* (5,6), 509-518.

231. Yin, S., et al., Balanced Carrier Transports of Electrons and Holes in Silole-Based Compounds-a Theoretical Study. *Journal of Physical Chemistry A* **2006,** *110* (22), 7138-7143.

232. Huang, J.; Kertesz, M., Intermolecular Transfer Integrals for Organic Molecular Materials: Can Basis Set Convergence Be Achieved? *Chemical Physics Letters* **2004,** *390* (1-3), 110-115.

233. Yang, X.; Li, Q.; Shuai, Z., Theoretical Modelling of Carrier Transports in Molecular Semiconductors: Molecular Design of Triphenylamine Dimer Systems. *Nanotechnology* **2007,** *18* (42), 424029/1-424029/6.

234. Wang, C., et al., Theoretical Comparative Studies of Charge Mobilities for Molecular Materials: Pet Versus Bnpery. *Organic Electronics* **2008,** *9* (5), 635-640.

235. Valeev, E. F., et al., Effect of Electronic Polarization on Charge-Transport Parameters in Molecular Organic Semiconductors. *J. Am. Chem. Soc.* **2006,** *128* (30), 9882-9886.

236. Zhong, A.; Bian, Y.; Zhang, Y., Semiconductor Performance of Phthalocyaninato Lead Complex and Its Nonperipheral Substituted Derivatives for Organic Field Effect Transistors: Density Functional Theory Calculations. *J. Phys. Chem. C* **2010,** *114* (7), 3248-55.

237. Sanyal, S.; Manna, A. K.; Pati, S. K., Effect of Imide Functionalization on the Electronic, Optical, and Charge Transport Properties of Coronene: A Theoretical Study. *J. Phys. Chem. C* **2013,** *117*, 825-36.

238. Navarro, A., et al., A Dft Approach to the Charge Transport Related Properties in Columnar Stacked Π-Conjugated N-Heterocycle Cores Including Electron Donor and Acceptor Units. *Phys. Chem. Chem. Phys.* **2015,** *17* (1), 605-618.

239. Mikolajczyk, M. M., et al., Long-Range Corrected Dft Calculations of Charge-Transfer Integrals in Model Metal-Free Phthalocyanine Complexes. *J. Mol. Model.* **2011,** *17* (9), 2143-49.

240. Baba, M.; Ohishi, Y.; Mori, K.; Suzuki, K., On the Correlation between Morphology and Electronic Properties of Fluorinated Copper Phthalocyanine (F16cupc) Thin Films. *Mol. Cryst. Liq. Cryst.* **2006,** *444* (1), 203-10.

241. Yadav, S.; Ghosh, S., Ambipolar Copper Phthalocyanine Heterojunction Field Effect Transistors Based Organic Inverter. *AIP Conf. Proc., Sol. State. Ionics* **2013,** *1512*, 466-67.

242. Chai, J.-D.; Head-Gordon, M., Long-Range Corrected Hybrid Density Functionals with Damped Atom-Atom Dispersion Corrections. *Phys. Chem. Chem. Phys.* **2008,** *10*, 6615-20.

243. Gross, E. K. U.; Dobson, J. F.; Petersilka, M., Density Functional Theory of Time-Dependent Phenomena. *Top. Curr. Chem.* **1996,** *181* (Density Functional Theory II), 81-172.

244. Onida, G.; Reining, L.; Rubio, A., Electronic Excitations: Density-Functional Versus Many-Body Green's-Function Approaches. *Rev. Mod. Phys.* **2002,** *74* (2), 601-659.

245. Maitra, N. T.; Wasserman, A.; Burke, K., *Electron Correlations and Materials Properties 2*. Gonis, A

Kioussis, N.

Ciftan, M. ed.; Kluwer Academic/Plenum Press: New York, 2003.

246. Furche, F.; Burke, K., Time-Dependent Density Functional Theory in Quantum Chemistry. *Annu. Rep. Comput. Chem.* **2005,** *1*, 19-30.

247. Furche, F.; Rappoport, D., Density Functional Methods for Excited States: Equilibrium Structure and Electronic Spectra. *Theor. Comput. Chem.* **2005,** *16* (Computational Photochemistry), 93-128.

248. Adamo, C.; Barone, V., Toward Reliable Density Functional Methods without Adjustable Parameters: The Pbe0 Model. *J. Chem. Phys.* **1999,** *110* (13), 6158-6170.

249. Yanai, T.; Tew, D. P.; Handy, N. C., A New Hybrid Exchange-Correlation Functional Using the Coulomb-Attenuating Method (Cam-B3lyp). *Chemical Physics Letters* **2004,** *393* (1-3), 51-57.

250. Seminario, J. M., Calculation of Intramolecular Force Fields from Second-Derivative Tensors. *Int. J. Quantum Chem.* **1996,** *60* (7, Proceedings of the International Symposium on Atomic, Molecular, and Condensed Matter Theory and Computational Methods, 1996), 59-65.

251. Alder, B. J.; Wainwright, T. E., Phase Transition for a Hard-Sphere System. *J. Chem. Phys.* 1957, p 1208.

252. Alder, B. J.; Wainwright, T. E., Studies in Molecular Dynamics. I. General Method. *J. Chem. Phys.* **1959,** *31*, 459-66.

253. Rahman, A., Correlations in the Motion of Atoms in Liquid Argon. *Phys. Rev.* **1964,** *136* (2A), 405-11.

254. Stillinger, F. H.; Rahman, A. In *Molecular Dynamics Calculation of Neutron Inelastic Scattering from Water*, Reidel: 1974; pp 479-94.

255. McCammon, J. A.; Gelin, B. R.; Karplus, M., Dynamics of Folded Proteins. *Nature* **1977,** *267* (5612), 585-90.

256. MacKerell, A. D., Jr., et al., All-Atom Empirical Potential for Molecular Modeling and Dynamics Studies of Proteins. *Journal of Physical Chemistry B* **1998,** *102* (18), 3586-3616.

257. MacKerell, A. D., Jr.; Wiorkiewicz-Kuczera, J.; Karplus, M. In *An All-Atom Empirical Energy Function for the Simulation of Nucleic Acids*, American Chemical Society: 1995; pp COMP-068.

258. Weiner, P. K.; Kollman, P. A., Amber: Assisted Model Building with Energy Refinement. A General Program for Modeling Molecules and Their Interactions. *Journal of Computational Chemistry* **1981,** *2* (3), 287-303.

259. Van Der Spoel, D., et al., Gromacs: Fast, Flexible, and Free. *Journal of Computational Chemistry* **2005,** *26* (16), 1701-1718.

260. Jones, J. E., *On the Determination of Molecular Fields. Ii. From the Equation of State of a Gas*. 1924; Vol. 106, p 463-477.

261. Verlet, L., Computer Experiments on Classical Liquids. I. Thermodynamical Properties of Lennard-Jones Molecules. *Phys. Rev.* **1967,** *159*, 98-103.

262. Verlet, L., Computer Experiments on Classical Liquids. Ii. Equilibrium Correlation Functions. *Phys. Rev.* **1968,** *165*, 201-214.

263. Hockney, R. W. E., J. W., *Computer Simulations Using Particles*. Bristol, 1988.

264. Swope, W. C. A., H. C.; Berens, P. H.; Wilson, K. R., A Computer Simulation Method for the Calculation of Equilibrium Constants for the Formation of Physical Clusters of Molecules: Application to Small Water Clusters. *J. Chem. Phys.* **1982,** *76*, 637-649.

265. Beeman, D., Some Multistep Methods for Use in Molecular Dynamics Calculations. *Journal of Computational Physics* **1976,** *20* (2), 130-139.

266. Schofield, P., Computer Simulation Studies of the Liquid State. *Comput. Phys. Commun.* **1973,** *5* (1), 17-23.

267. McQuarrie, D. A., *Statistical Mechanics*. University Science Books: Mill Vally, California, 2000.

268. Nose, S., A Unified Formulation of the Constant-Temperature Molecular-Dynamics Methods. *J. Chem. Phys.* **1984,** *81* (1), 511-19.

269. Nose, S., A Molecular Dynamics Method for Simulations in the Canonical Ensemble. *Mol. Phys.* **1984,** *52* (2), 255-68.

270. Hoover, W. G., Canonical Dynamics – Equilibrium Phase-Space Distributions. *Phys. Rev. A* **1985,** *31*, 1695-1697.

271. Adelman, S. A.; Doll, J. D., Generalized Langevin Equation Approach for Atom/Solid-Surface Scattering: General Formulation for Classical Scattering Off Harmonic Solids. *J. Chem. Phys.* **1976,** *64* (6), 2375-88.

272. Berendsen, H. J. C., et al., Molecular Dynamics with Coupling to an External Bath. *J. Chem. Phys.* **1984,** *81* (8), 3684-90.

273. Andersen, H. C., Molecular Dynamics Simulations at Constant Pressure and/or Temperature. *J. Chem. Phys.* **1980,** *72* (4), 2384-93.

274. Hohenberg, P.; Kohn, W., Inhomogeneous Electron Gas. *Physical Review* **1964,** *136* (3B), B864-B871.

275. Kohn, W.; Sham, L. J., Self-Consistent Equations Including Exchange and Correlation Effects. *Physical Review* **1965,** *140* (4A), A1133-A1138.

276. Born, M.; Oppenheimer, R., Quantum Theory of the Molecules. *Ann. Phys. (Berlin, Ger.)* **1927,** *84*, 457-84.

277. Scholtz, F. G.; Geyer, H. B.; Hahne, F. J. W., Quasi-Hermitian Operators in Quantum Mechanics and the Variational Principle. *Annals of Physics* **1992,** *213* (1), 74-101.

278. Levine, I. N., *Quantum Chemistry*. Prentice Hall: 2008.

279. Runge, E., Gross, K. U., , Density-Functional Theory for Time-Dependent Systems. *phys. rev. lett* **1984,** *52* (997), 997-1000.

280. Dirac, P. A. M., Note on Exchange Phenomena in the Thomas Atom. *Mathematical Proceedings of the Cambridge Philosophical Society* **1930,** *26* (03), 376-385.

281. Vosko, S. H.; Wilk, L.; Nusair, M., Accurate Spin-Dependent Electron Liquid Correlation Energies for Local Spin Density Calculations: A Critical Analysis. *Can. J. Phys.* **1980,** *58* (8), 1200-11.

282. Perdew, J. P.; Zunger, A., Self-Interaction Correction to Density-Functional Approximations for Many-Electron Systems. *Phys. Rev. B: Condens. Matter* **1981,** *23* (10), 5048-79.

283. Cole, L. A.; Perdew, J. P., Calculated Electron Affinities of the Elements. *Phys. Rev. A* **1982,** *25* (3), 1265-71.

284. Perdew, J. P., et al., Atoms, Molecules, Solids, and Surfaces: Applications of the Generalized Gradient Approximation for Exchange and Correlation. *Phys. Rev. B: Condens. Matter* **1992,** *46* (11), 6671-87.

285. Becke, A. D., Density-Functional Exchange-Energy Approximation with Correct Asymptotic Behavior. *Phys. Rev. A: Gen. Phys.* **1988,** *38* (6), 3098-100.

286. Perdew, J. P.; Burke, K.; Ernzerhof, M., Generalized Gradient Approximation Made Simple. *Phys. Rev. Lett.* **1996,** *77* (18), 3865-3868.

287. Anisimov, V. I.; Aryasetiawan, F.; Lichtenstein, A. I., First-Principles Calculations of the Electronic Structure and Spectra of Strongly Correlated Systems: The Lda + U Method. *J. Phys.: Condens. Matter* **1997,** *9* (4), 767-808.

288. Slater, J. C., Atomic Shielding Constants. *Physical Review* **1930,** *36* (1), 57-64.

289. Boys, S. F., *Electronic Wave Functions. I. A General Method of Calculation for the Stationary States of Any Molecular System*. 1950; Vol. 200, p 542-554.